South Dakota
Department of Transportation
Office of Research

U.S. Department
of Transportation
Federal Highway
Administration

SD2002-01-A
TPF-5(042)-A

The Deleterious Chemical Effects of Concentrated Deicing Solutions on Portland Cement Concrete

Study SD2002-01
Technical Appendices

Prepared by
Michigan Tech Transportation Institute
1400 Townsend Drive
Houghton, MI

April 2008

DISCLAIMER

The contents of this report reflect the views of the authors who are responsible for the facts and accuracy of the data presented herein. The contents do not necessarily reflect the official views or policies of the South Dakota Department of Transportation, the State Transportation Commission, or the Federal Highway Administration. This report does not constitute a standard, specification, or regulation.

ACKNOWLEDGEMENTS

This work was performed under the supervision of the SD2002-01 Technical Panel:

Dan Johnston	Office of Research	Dennis Johnson	Office of Research
Craig Smith	SDDOT	Roger Surdahl	FHWA
Paul Virmani	FHWA	Brett Hestdalen	FHWA
Bob Dawson	Iowa DOT	Ron Wright	Idaho DOT
Chris Romo	Wyoming DOT	Mike Lynch	Montana DOT
Richard Williammee	Texas DOT	Kelley Morse	Illinois DOT
Rob Reis	Caltrans	Roberto de Dios	Colorado DOT

The work was performed in cooperation with the United States Department of Transportation Federal Highway Administration.

TECHNICAL REPORT STANDARD TITLE PAGE

1. Report No.	2. Government Accession No.	3. Recipient's Catalog No.
SD2002-01-A		

4. Title and Subtitle	5. Report Date
The Deleterious Chemical Effects of Concentrated Deicing Solutions on Portland Cement Concrete	April 30, 2008
	6. Performing Organization Code

7. Author(s)	8. Performing Organization
Lawrence Sutter (Michigan Tech), Karl Peterson (Michigan Tech), Gustavo Julio-Betancourt (Univ. of Toronto), Doug Hooton (Univ. of Toronto), Tom Van Dam (Applied Pavement Technology), Kurt Smith (Applied Pavement Technology)	Report No.

9. Performing Organization Name and Address	10. Work Unit No.
Michigan Tech Transportation Institute 1400 Townsend Dr. Houghton, MI 49931	11. Contract or Grant No. 310802

12. Sponsoring Agency Name and Address	13. Type of Report and Period Covered
South Dakota Department of Transportation Office of Research 700 East Broadway Avenue Pierre, SD 57501-2586	Technical Appendices September 2002 to April 2008
	14. Sponsoring Agency Code HRZ201(01), TPF-5(042)

15. Supplementary Notes

Additional published documents: Final Report (SD2002-01-F), Literature Review (SD2002-01-L), Implementation Guide (SD2002-01-G) and Technical Appendices (SD2002-01-A)

16. Abstract

This research project investigated the effects of concentrated brines of magnesium chloride, calcium chloride, sodium chloride, and calcium magnesium acetate on portland cement concrete. Although known to be effective at deicing and anti-icing, the deleterious effects these chemicals may have on concrete have not been well documented. As a result of this research, it was determined that there is significant evidence that magnesium chloride and calcium chloride chemically interact with hardened portland cement paste in concrete resulting in expansive cracking, increased permeability, and a significant loss in compressive strength. Although the same effects were not seen with sodium chloride brines, it was shown that sodium chloride brines have the highest rate of ingress into hardened concrete. This latter fact is significant with respect to corrosion of embedded steel. The mechanism for attack of hardened cement paste varies with deicer chemical but in general, a chemical reaction between chlorides and cement hydration products results in the dissolution of the hardened cement paste and formation of oxychloride phases, which are expansive. The chemical attack of the hardened cement paste is significantly reduced if supplementary cementitious materials are included in the concrete mixture. Both coal fly ash and ground granulated blast furnace slag were found to be effective at mitigating the chemical attack caused by the deicers tested. In the tests performed, ground granulated blast furnace slag performed better as a mitigation strategy as compared to coal fly ash. Additionally, siloxane and silane sealants were effective at slowing the ingress of deicing chemicals into the concrete and thereby reducing the observed distress. In general, the siloxane sealant appeared to be more effective than the silane, but both were effective and should be considered as a maintenance strategy.

17. Keywords	18. Distribution Statement
deicing chemicals, anti-icing chemicals, concrete distress, petrography, oxychloride	No restrictions. This document is available to the public from the sponsoring agency.

19. Security Classification (of this report)	20. Security Classification (of this page)	21. No. of Pages	22. Price
Unclassified	Unclassified	370	

Table of Contents

Table of Acronyms

Acronym	Definition
AASHTO	American Association of State Highway and Transportation Officials
ACI	American Concrete Institute
ACR	Alkali Carbonate Reaction
ASR	Alkali Silica Reaction
ASTM	American Society for Testing and Materials
AVA	Air Void Analyzer
BSE	Back-Scattered Electron
C_2S	Dicalcium Silicate
C_3A	Tricalcium Aluminate
C_3S	Tricalcium Silicate
C_4AF	Tetracalcium Aluminoferrite
$Ca(OH)_2$	Calcium Hydroxide
Ca^{2+}	Calcium Ion
$CaCl_2$	Calcium Chloride
$CaCO_3$	Calcite
$(CaMg)CO_3$	Dolomite
CANMET	Canada Center for Mineral and Energy Technology
CCD	Charge Coupled Device
CH	Calcium Hydroxide
Cl	Chlorine
Cl^-	Chloride Ion
CMA	Calcium Magnesium Acetate
C-N(K)-S-H	Calcium-Alkali-Silicate-Hydrate
CO_2	Carbon Dioxide
COV	Coefficient of Variation
CSH	Calcium Silicate Hydrate
DC	Direct Current
DOT	Department of Transportation
EDS	Energy Dispersive Spectrometry
EMPA	Electron Micro-Probe Analysis

Table of Acronyms

Acronym	Definition
ESEM	Environmental Scanning Electron Microscope
F-T	Freeze-Thaw
GGBFS	Ground Granulated Blast Furnace Slag
dpi	Dots per Inch
dpm	Dots per Millimeter
HPC	High Performance Concretes
ICP	Inductively Coupled Plasma Spectroscopy
ICP-OES	Inductively Coupled Plasma Optical Emission Spectroscopy
K	Potassium
LVSEM	Low-Vacuum Scanning Electron Microscope
MBAP	Magnesium Chloride Based Agricultural Product
MDOT	Michigan Department of Transportation
Mg	Magnesium
$Mg(OH)_2$	Brucite
Mg^{2+}	Magnesium Ion
$MgCl_2$	Magnesium Chloride
MIP	Mercury Intrusion Porosimetry
MSH	Magnesium-Silicate-Hydrate
N(K)-S-H	Alkali-Silicate-Hydrate
NaCl	Sodium Chloride
ODOT	Ohio Department of Transportation
OH^-	Hydroxide Ion
psi	Pounds per Square Inch
psia	Pounds per Square Inch Absolute
RCPT	Rapid Chloride Permeability Test
RGB	Red-Green-Blue
SCM	Supplementary Cementitious Materials
SDDOT	South Dakota Department of Transportation
SEM	Scanning Electron Microscopy

Table of Acronyms

Acronym	Definition
SHA	State Highway Agency
SHRP	Strategic Highway Research Program
UV	Ultra-Violet
vpm	Vibrations per Minute
w/c	Water-to-Cement Ratio
w/cm	Water-to-Cementitious Ratio
XRD	X-ray Diffraction
XRF	X-ray Fluorescence

Problem Statement

Keeping roads safe and passable are key concerns for any State Highway Agency (SHA), especially during the winter season when ice and snow accumulation on roads and bridges can create hazardous driving conditions. To accomplish this, SHAs are constantly seeking out, evaluating, and adapting new winter maintenance strategies that are cost effective and environmentally friendly. One such area where new strategies are being employed is the broad area of deicing and anti-icing. Deicing is defined as any effort to remove ice from road and bridge surfaces after ice deposition has occurred. This is in contrast to anti-icing, which is defined as a surface treatment applied prior to ice formation that eliminates ice accumulation or facilitates ice removal by lessening the bond between the ice and the riding surface. In general, deicing and anti-icing are accomplished through the use of various chemicals including aqueous solutions of chlorides (e.g. magnesium chloride, sodium chloride, and calcium chloride) or other chemicals such as calcium magnesium acetate and urea. Although the efficacy of these chemicals for deicing and anti-icing has been clearly demonstrated, possible detrimental effects to concrete in transportation structures have not been fully examined and documented. In this sense, the true cost effectiveness has not been determined as chemical attack on concrete is a possibility and in turn, the resulting deterioration of the structures from chemical attack may lead to costly rehabilitation or replacement. Based upon published research, the most problematic chemicals appear to be the chlorides of magnesium, calcium, and sodium and other chemicals containing calcium and magnesium (e.g. calcium magnesium acetate). Use of these chemicals has increased given their relatively low cost, ease of use, and effectiveness for deicing and anti-icing, in certain applications. Use of alternative chemicals such as propylene glycol and ethylene glycol have seen limited use given concerns about their environmental impact, whereas potassium acetate, sodium acetate, potassium formate, and sodium formate are used almost exclusively on airports (with some use in automated bridge deicing systems) due to high cost. In the end, chloride-based deicers appear to be the best choice for highway applications if they can be used in such a way as to minimize possible chemical attack to concrete.

The degradation of concrete used in pavements and bridges that may occur as a result of attack by chemical deicers/anti-icers is the result of an increased concentration of dissociated calcium and magnesium ions in the concrete pore water. In theory, these free ions are available to combine with materials in the concrete to form expansive or weak reaction products such as brucite or magnesium silicate hydrates, respectively. Of course, the dissociation of chlorides into ionic species also increases the concentration of chloride in the pore water solution, which has been well documented as a primary cause of scaling and corrosion of reinforcing steel. These possible and known effects must be fully understood if these chemicals are to be used as a mainstay of any deicing or anti-icing strategy. The goal of this proposed research is to examine the effects of deicing and anti-icing chemicals on portland cement concrete and to recommend changes to concrete mixture designs, construction practices, and winter maintenance procedures that will make these solutions non-detrimental to concrete durability.

Summary of Project Tasks

Task 1: Literature Review
Task 2: Conduct Survey
Task 3: Site Selection
Task 4: Meeting with Technical Panel
Task 5: Characterization of Field Specimens
Task 6: Laboratory Experiment
Task 7: Assessing and Minimizing the Impact of Deicing/Anti-Icing Chemicals
Task 8: Effects of Various Deicing/Anti-Icing Chemicals
Task 9: Life Cycle Cost Analyses
Task 10: Development of Guidelines
Task 11: Submit Interim Report
Task 12: Meeting With Technical Panel at Michigan Tech
Task 13: Prepare and Submit Final Report
Task 14: Executive Presentation to Research Panel
Task 15: Executive Presentation to SDDOT Executive Review Board

Report Organization and Distribution

The final report for this project is extensive. To facilitate distribution, the report has been broken down into a number of separate volumes and these are listed below.

- **Executive Summary** – Provides a concise overview of the entire project.
- **Final Report** – The final technical report organized into nine sections.

  Section 1 - A brief introduction
  Section 2 - An abridged background for the project based on the Task 1 literature review
  Section 3 - Presents the experimental approach for the entire project
  Section 4 An abridged summary of the Task 5 results
  Section 5 - An abridged summary of Task 6 laboratory results for Phase I and Phase II of
  Section 6 - Presents a discussion of the results of Tasks 5, 6, 7, 8 and 9
  Section 7 - Presents suggested mitigation strategies based upon the results of this study
  Section 8 - Conclusions based upon the results of this study
  Section 9 - Recommendations based upon the results of this study
  Section 10 - Bibliography used as the basis for Section 2

- **Appendix to Final Report** – The appendix contains details on specific analytical methods used in the study. Also, the appendix contains an unabridged summary of results for the characterization of field specimens and for all laboratory experiments.
- **Full Literature Review** – Provides the unabridged version of the literature review.
- **Guidelines** – A practical guideline document to assist DOT personnel in implementing this research.

Appendix 1

Experimental Methods

Table of Contents

List of Figures

List of Tables

Appendix 1 – Experimental Methods

Description of the *w/c* Determination Methodology

The method of *w/c* determination used in the characterization of the field specimens, relies upon the relationship between measurements of cement paste fluorescence and the *w/c* values of known concrete standards (Mayfield 1990, Elsen 1995, Jakobsen 1997). To determine the *w/c* of a concrete specimen, fluorescence measurements are made from the cement paste, and related back to fluorescence measurements from the concrete standards. The intensity of the fluorescence measured depends upon the amount of the UV light-sensitive dyed epoxy absorbed by the cement paste. Cement pastes of higher *w/c* absorb more of the dyed epoxy because they possess a larger volume of capillary porosity than do cement pastes of lower *w/c*. To measure the fluorescence of the cement paste, a concrete thin section is illuminated from above with blue light. The blue light causes the dyed epoxy to fluoresce yellow-green. A blocking filter is used remove the blue light reflected from the surface, allowing only the yellow-green fluorescence to reach the camera (Walker 1979). The camera generates a video signal, which is converted to an RGB digital image on a computer monitor. In the image, each pixel is assigned an intensity between 0 and 255, where 0 represents pure white (high intensity) and 255 represents pure black (low intensity). The G band of the image contains the most information about the fluorescence and is used to make the cement paste fluorescence measurement.

To ensure that the illumination of the blue light and the performance of the camera are constant, a method of calibration was needed. Prior to collecting any measurements, a thin section composed of quartz sand in a matrix of dyed epoxy is used to calibrate the system. A digital image of the calibration slide is collected. In the image, the quartz sand appears dark, and the dyed epoxy matrix appears bright. If a histogram is plotted of the image, two distinct peaks are present, one for the quartz sand, and the other for the dyed epoxy matrix. It is important that the positions of the peaks on the x-axis do not shift in order to ensure consistent measurements. Figure A1.1 shows a summary of histograms collected from the calibration thin section. If the peak positions are out of alignment, then adjustments need to be made either in the illumination, shutter speed of the camera, or gain and offset of the digital capture card. It has been reported that the fluorescence of the dyed epoxy decreases under constant illumination, but recovers to its initial fluorescence if allowed to sit in darkness for a period of two hours (Jakobsen 1995). Furthermore, the drop-off in fluorescence is most dramatic within the first two minutes, so it is important not to pause too long over any given area before collecting a fluorescence measurement.

Another set of parameters that can affect the fluorescence measurements is consistency in thickness of the thin sections, uniformity of impregnation by the dyed epoxy, and the consistency in dosage of dye. It is imperative that the thin sections used are of high quality (Elsen 1995, Jakobsen 1997).

Since concrete is a combination of cement paste, aggregate, and air voids, it is necessary to distinguish between the cement paste fluorescence and the fluorescence from aggregates and air voids. Generally, the aggregates are less porous than the cement paste, and therefore fluoresce at lower intensity levels, although this may not always be the case, especially when

porous aggregates are used. At the other extreme, air voids fluoresce at a higher intensity level than the cement paste. At intermediate intensity values, most of the fluorescence can be attributed to the cement paste. Rigorous schemes have been proposed to ensure that the pixels used to make the fluorescence measurements do not include air voids or aggregate (Elsen 1995, Gerold 2000). However, the wide variety of field concrete examined here precluded the possibility of a unified automated approach to air void and aggregate removal. Some of the factors that complicated an automated approach included the presence of secondary precipitation of minerals in entrained air voids, and the presence of porous fine aggregates. Therefore, in all cases, air voids and aggregates were removed manually to isolate the fluorescence contributed by the cement paste.

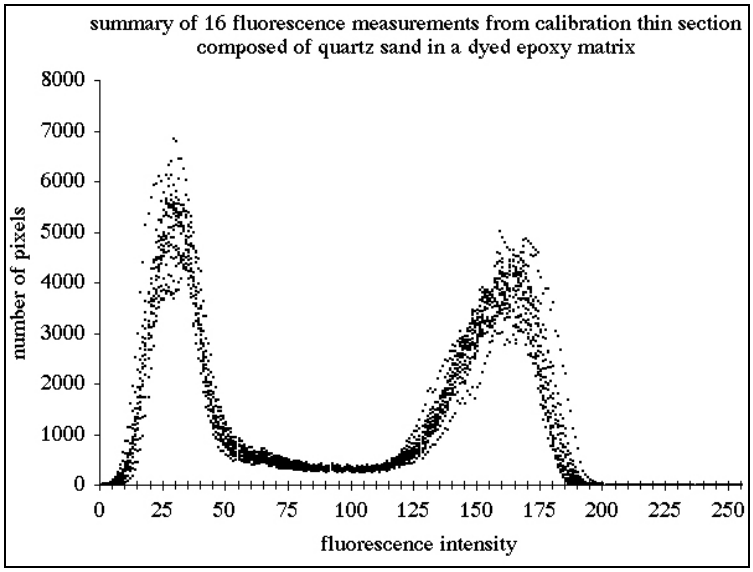

Figure A1.1. Histogram of fluorescence measurements from calibration thin section composed of quartz sand in a dyed epoxy matrix. The peak on the left represents the dyed epoxy matrix, and the peak on the right represents the quartz sand.

A set of three mortar cylinders were cast with *w/c* ratios of 0.40, 0.50, and 0.60, and moist cured for 28 days. The cylinders were cut into billets, and the billets impregnated with epoxy resin spiked with a fluorescent dye (DayGlo Tigris Yellow D-043 added at a dosage of 0.5 wt% to Epoxy Technologies EPO-TEK 301 resin). The impregnated billets were prepared in thin section, and images collected in epifluorescent mode with an Olympus BX-60 petrographic microscope equipped with an Optronics DEI-750 CCD video camera. The G-band was extracted from each 640 x 480 pixel, 2.612 x 1.959 mm, 24 bit, RGB image, and the fine aggregate and air voids manually masked to isolate fluorescence due to the uptake of the dyed resin into the capillary pores of the hardened cement paste. Figures A1.2 through A1.7 show images collected from each of the standards both before and after the masking operation. Figure A1.8 compares histograms of cement paste fluorescence from the standards. The average intensity from each masked image was used as measurement of cement paste fluorescence, as summarized in Table A1.1, and used to develop the calibration curve shown in Figure A1.9. This calibration curve was applied to measurements collected from field concrete samples to yield equivalent *w/c* values as compared to the 28 day moist cured mortar standards.

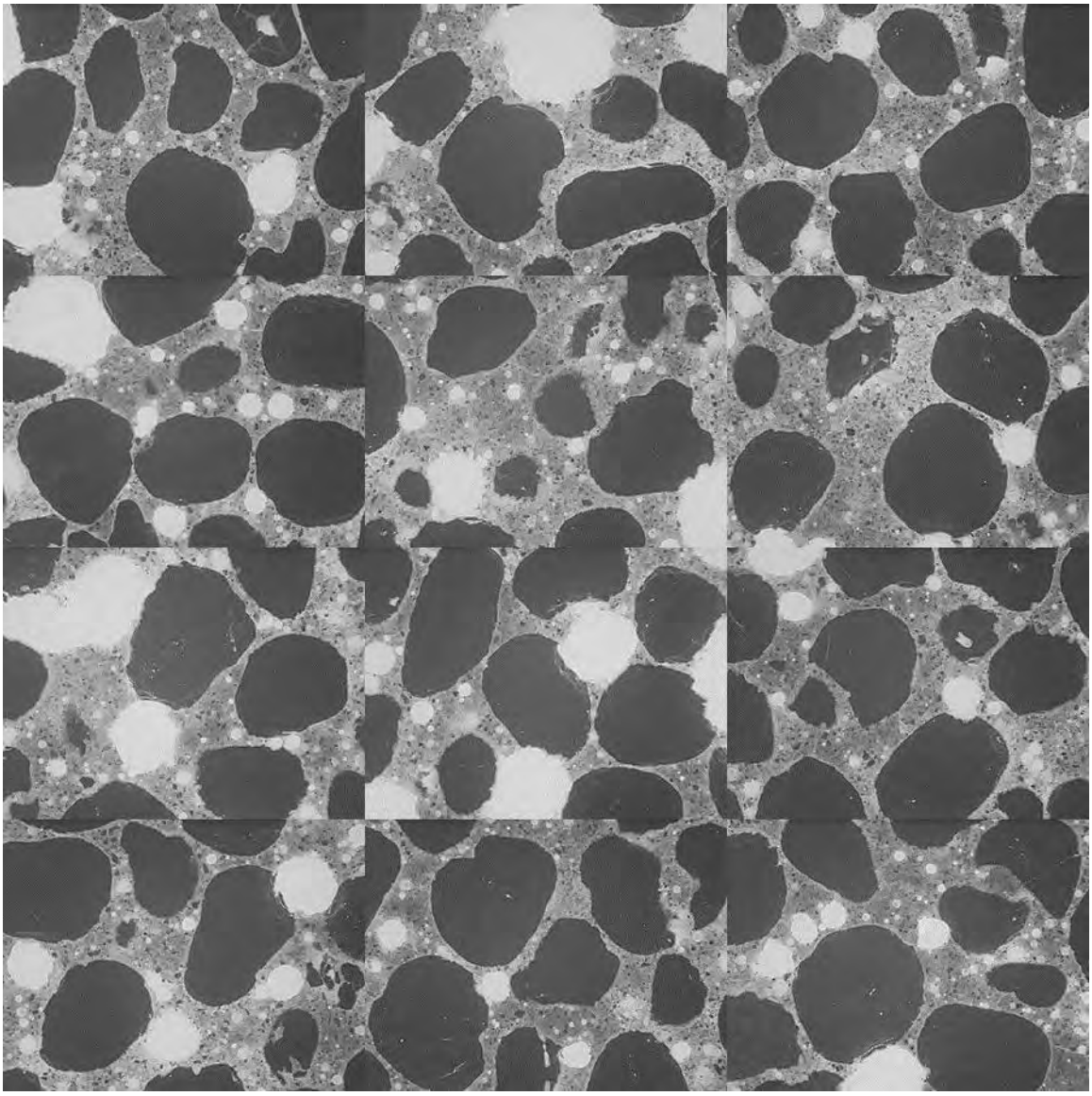

Figure A1.2. Mosaic of 12 frames collected from 0.40 *w/c* 28 day moist cured mortar standards (each individual frame measures 2.612 x 1.959 mm).

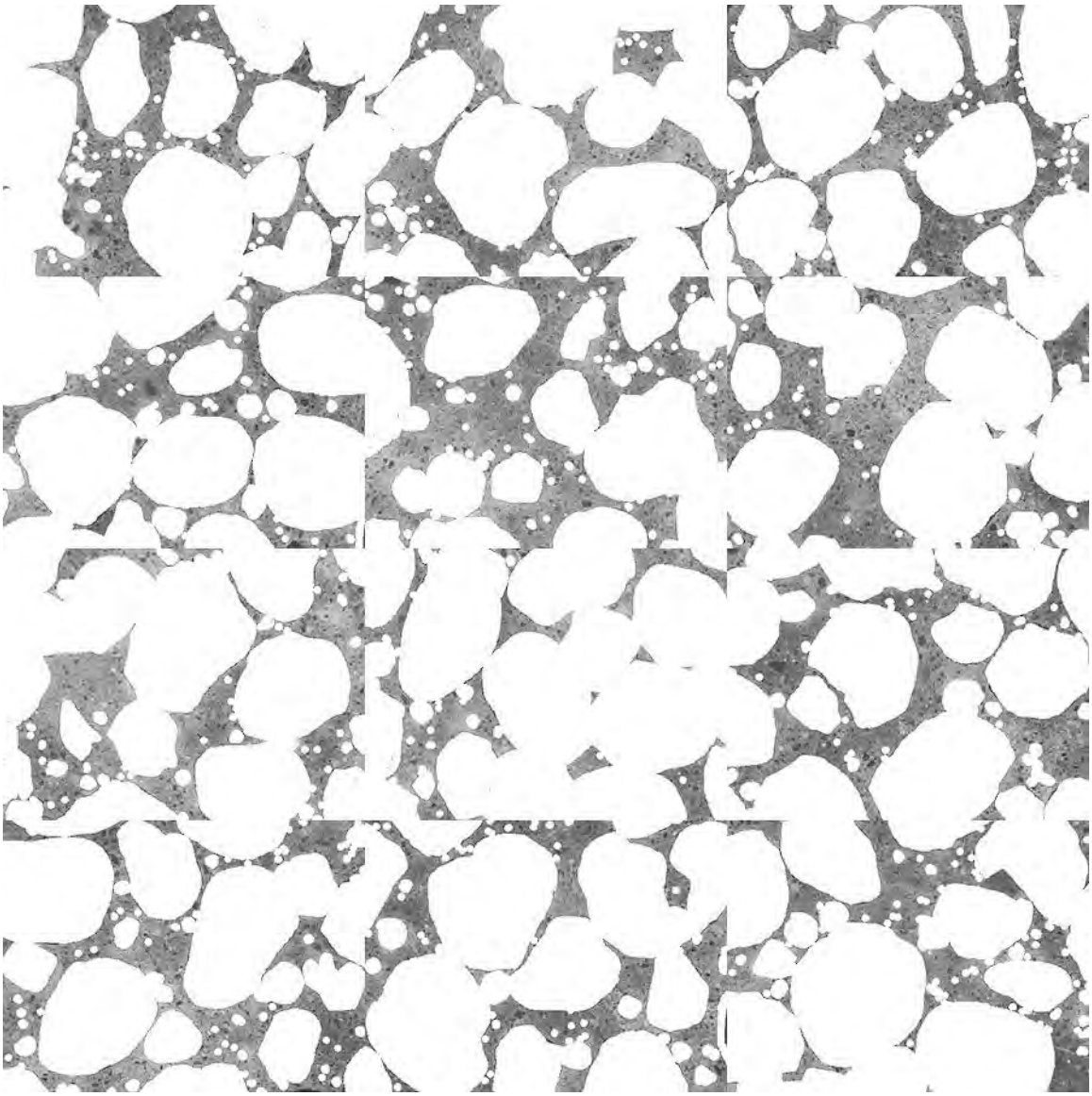

Figure A1.3. Mosaic of 12 frames collected from 0.40 *w/c* 28 day moist cured mortar standards after masking out air voids and fine aggregate to isolate cement paste (each individual frame measures 2.612 x 1.959 mm).

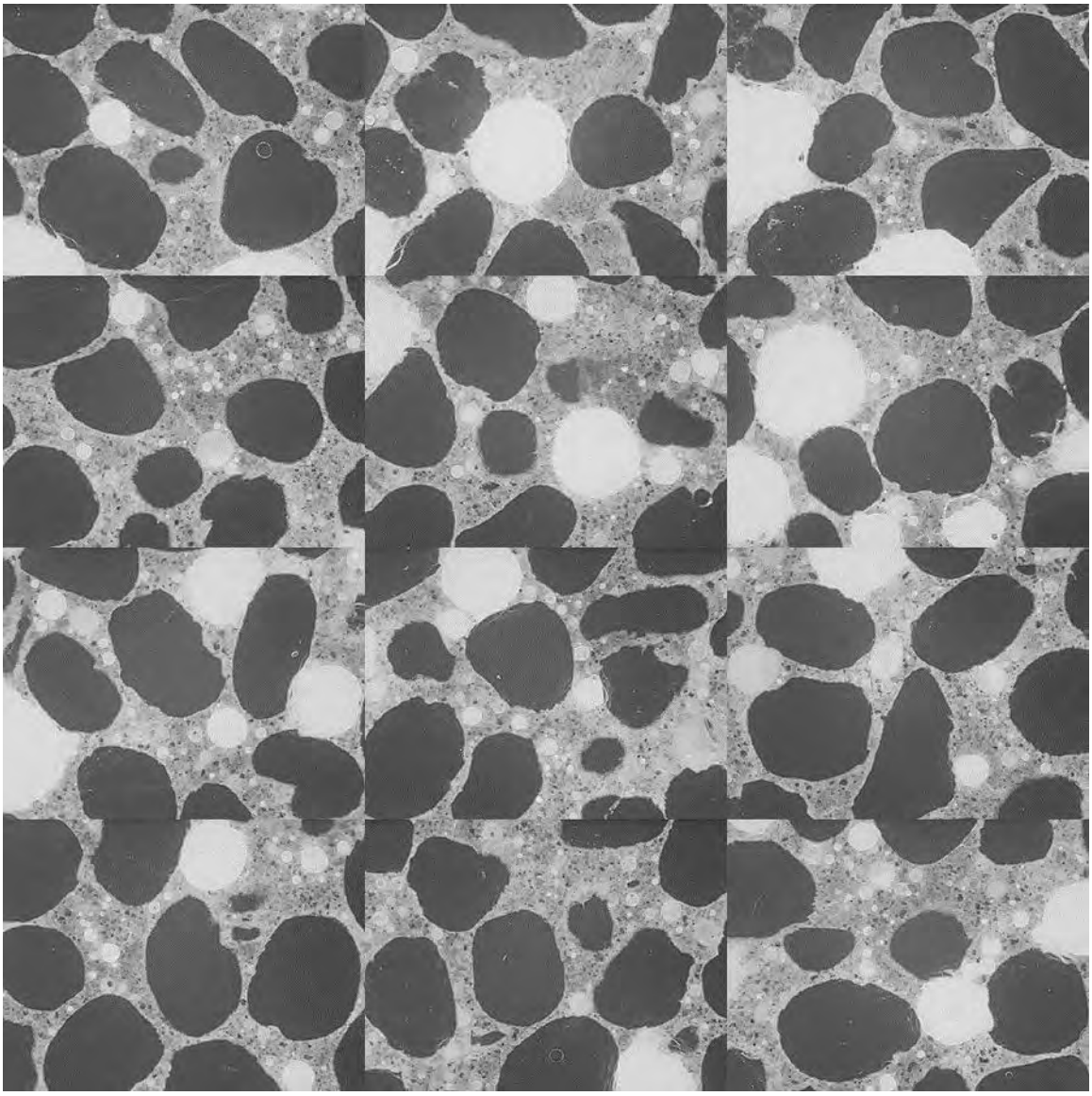

Figure A1.4. Mosaic of 12 frames collected from 0.50 *w/c* 28 day moist cured mortar standards (each individual frame measures 2.612 x 1.959 mm).

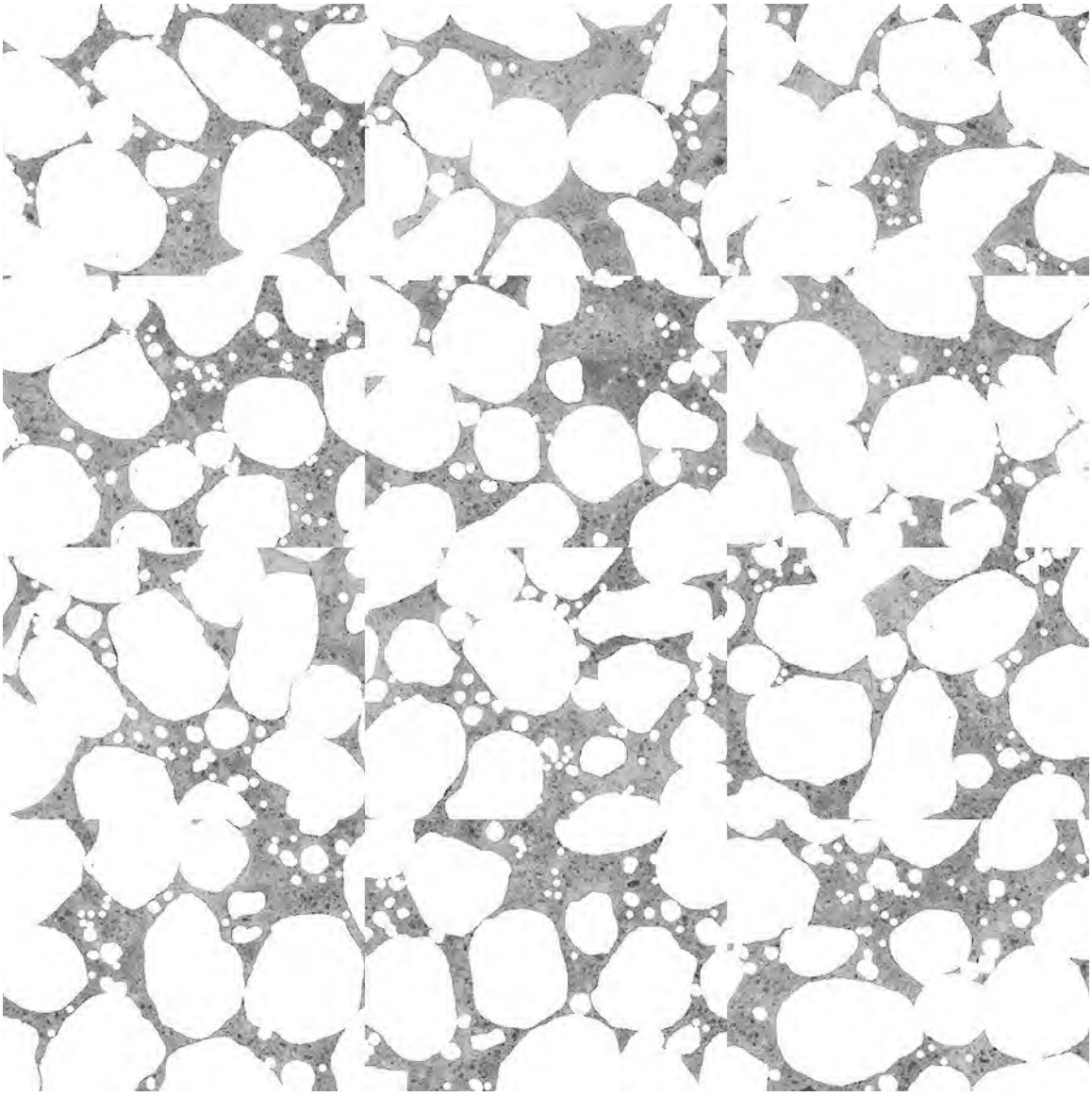

Figure A1.5. Mosaic of 12 frames collected from 0.50 *w/c* 28 day moist cured mortar standards after masking out air voids and fine aggregate to isolate cement paste (each individual frame measures 2.612 x 1.959 mm).

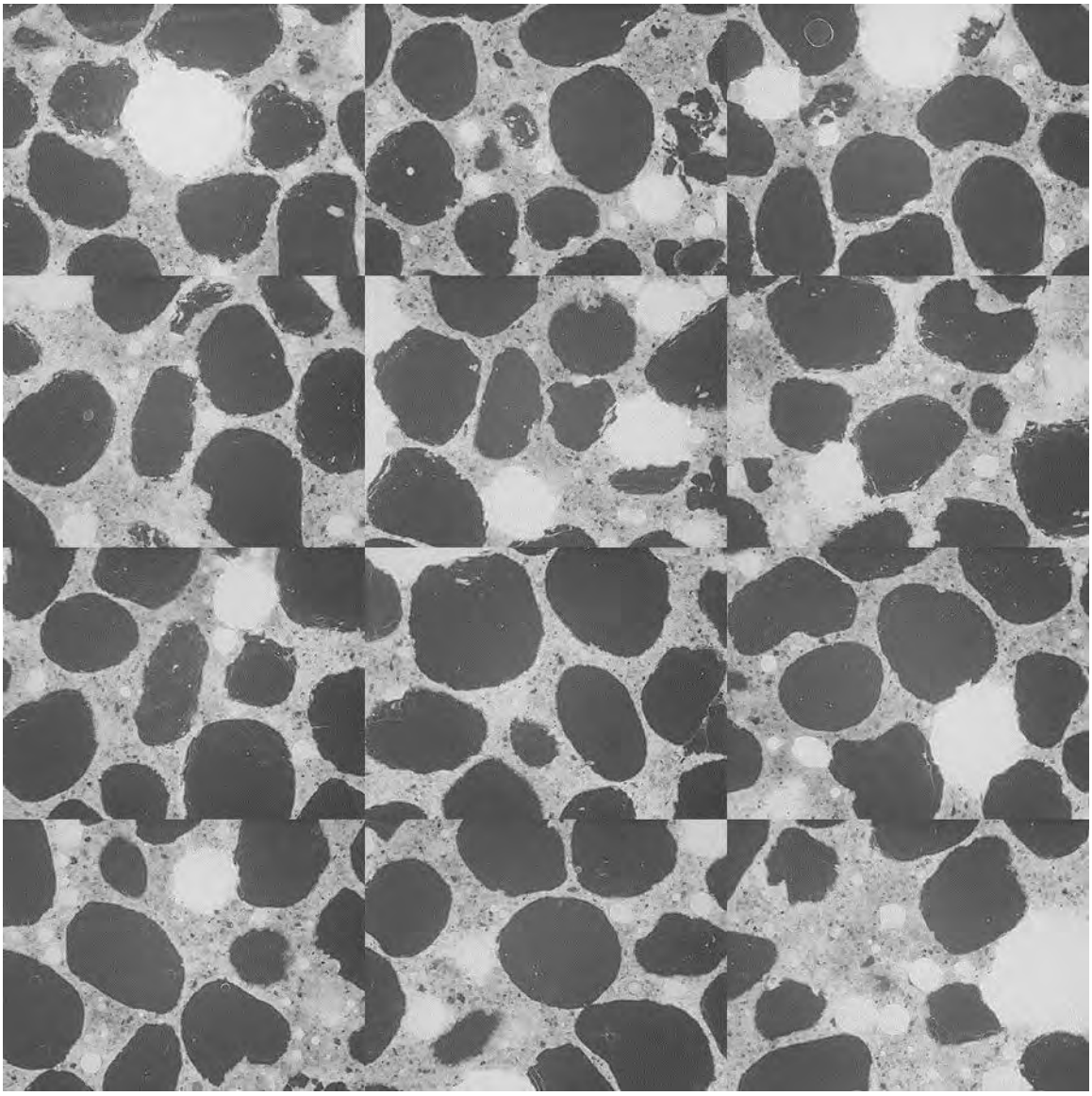

Figure A1.6. Mosaic of 12 frames collected from 0.60 *w/c* 28 day moist cured mortar standards (each individual frame measures 2.612 x 1.959 mm).

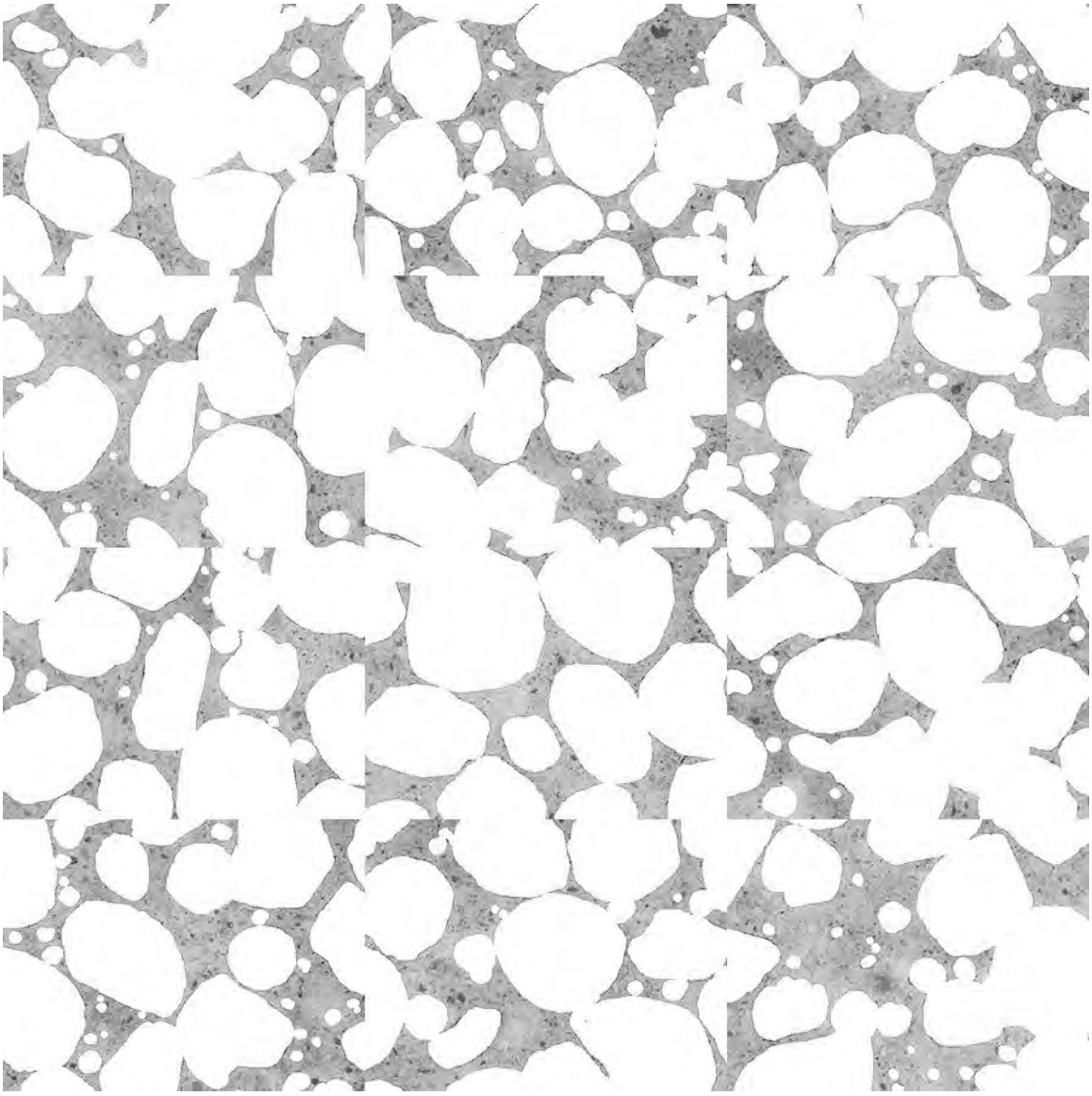

Figure A1.7. Mosaic of 12 frames collected from 0.60 *w/c* 28 day moist cured mortar standards after masking out air voids and fine aggregate to isolate cement paste (each individual frame measures 2.612 x 1.959 mm).

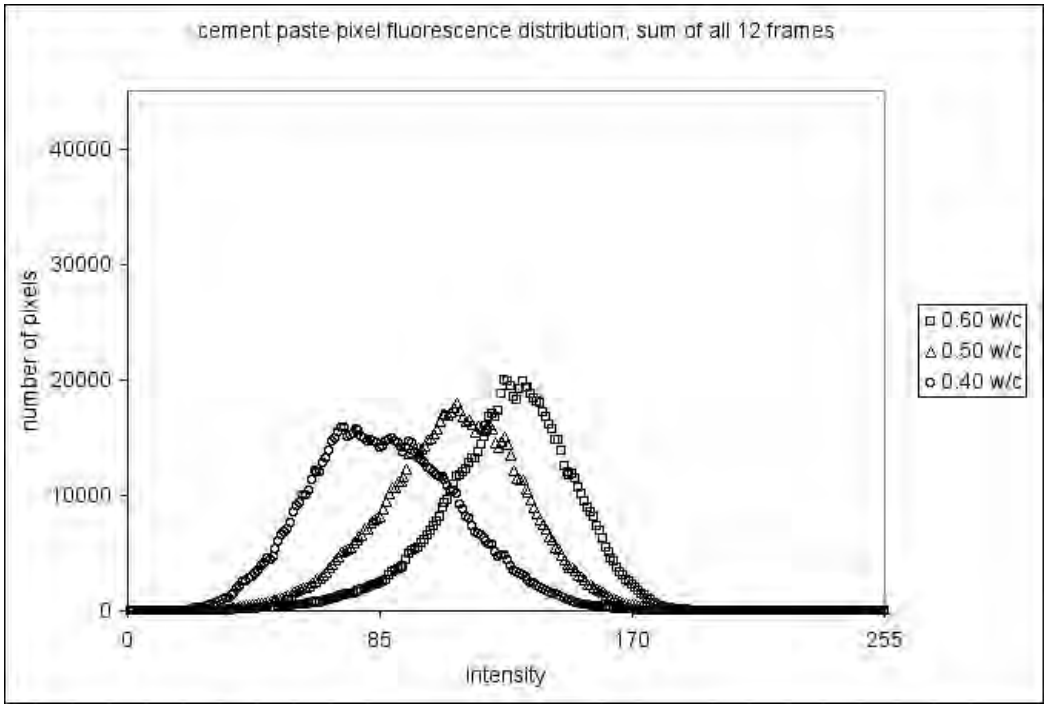

Figure A1.8. Histogram plotting cement paste pixel intensities using all 12 frames collected from each of the 28 day moist cured mortar standards.

Table A1.1. Average cement paste pixel intensities per frame collected from *w/c* standards.

w/c	Cement Paste Pixel Fluorescence Measurements (average intensity per frame)			
0.6	130 123 119	118 132 121	122 127 124	132 134 134
0.5	106 103 106	118 114 106	110 114 103	106 113 108
0.4	80 93 78	94 86 86	79 99 77	87 93 77

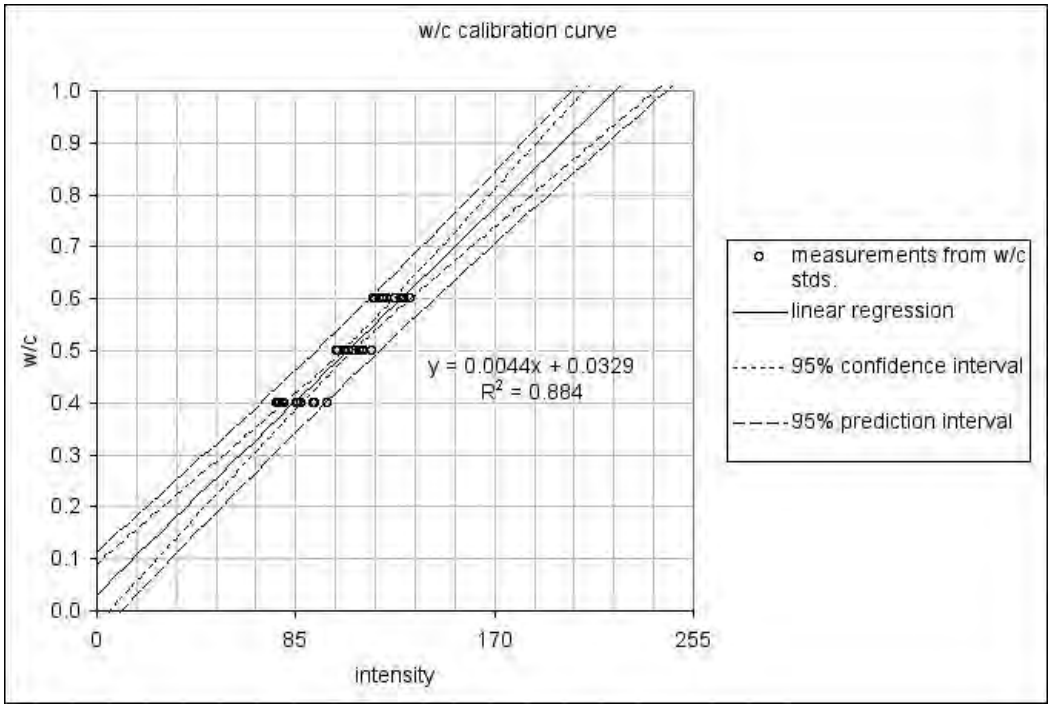

Figure A1.9. Calibration curve plotting average cement paste pixel fluorescence intensity per frame versus *w/c*.

X-ray Microscope Methodology

The x-ray microscope is a relatively new instrument that provides innovative ways of analyzing materials. It uses a precisely shaped glass tube to "focus" x-rays to a user selectable spot source of 10 to 300 microns. The specimen is stepped under the focused x-ray flux in a regular grid pattern or a specific point on the specimen is analyzed by moving the point of interest to the focal point of the guide tube. The incident x-rays fluoresce characteristic x-rays from the specimen in a manner analogous to a SEM producing x-rays with a focused electron beam. These characteristic x-rays are used to perform a quantitative analysis of the analysis point or to produce an x-ray map of a scanned area.

The instrument used was a Horiba/Oxford XGT-2000W x-ray analytical microscope. In this study, the x-ray microscope was one method used to determine the chloride profiles from field and laboratory prepared specimens. The profiles were determined by developing a calibration curve for x-ray intensity versus chlorine concentration.

A series of 0.45 and 0.55 *w/c* ratio mortar cylinders were cast and moist cured for 28 days. The cylinders were spiked with known concentrations of $CaCl_2$. The x-ray microscope was used to collect characteristic Cl Kα radiation (2.51 - 2.76 keV) from regions of cement paste by placing diamond ground cross-sections cut from the cylinders beneath the 300 micrometer diameter x-ray beam. Figures A1.10 and A1.11 plot the calibration curves from the 0.45 and 0.55 *w/c* mortar samples. The slopes and intercepts of the regression lines are very similar. Given the limited range of *w/c* for the laboratory portion of this study, this calibration was sufficient. However, the effect of paste density was studied further by preparing standards with a *w/c* of 0.35. This investigation showed that cement paste density can make a difference in the calibration. Figure A1.12 plots the calibration curve from the 0.35 *w/c* samples. The slope of the regression line from the 0.35 *w/c* samples is noticeably lower than the slopes from the 0.45 and 0.55 *w/c* samples. Therefore, before performing analyses of field concrete, it was necessary to estimate the *w/c* for the specimens before performing the chloride profiling. Figure A1.13 plots calibration curves for various *w/c* values as interpolated from the calibration curves from the 0.45, 0.55, and 0.35 *w/c* standards. Determined values for wt% chloride in paste were corrected to wt% chloride in concrete based on paste content by weight according to mix design. When mix design information was unavailable, paste content by weight was estimated from volume % paste measurements from point counting.

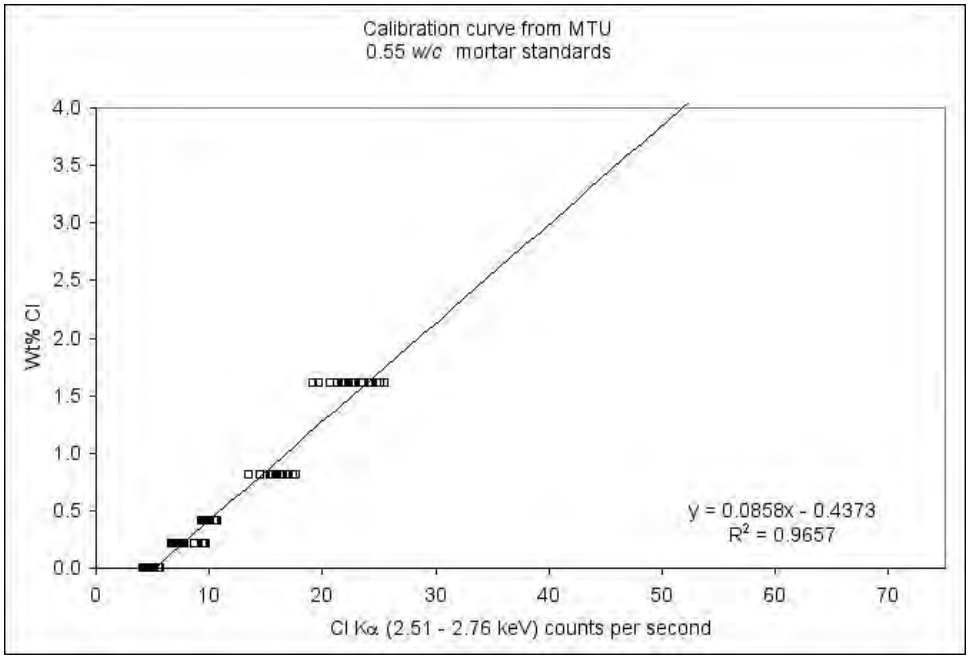

Figure A1.10 Calibration curve plotting Cl Kα counts per second versus wt% Cl from cement paste of 0.55 *w/c* mortar standards.

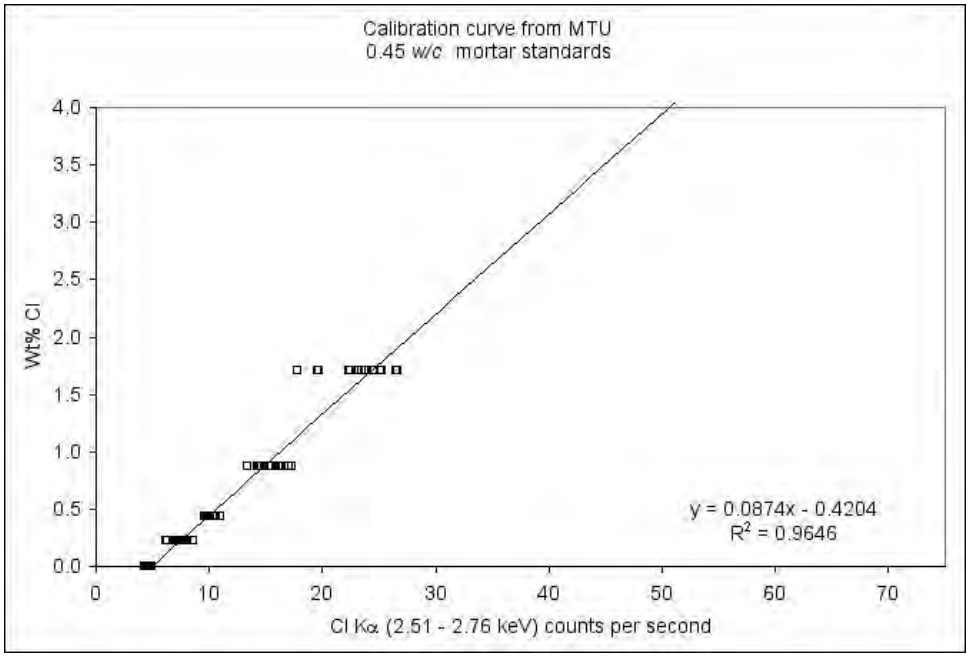

Figure A1.11. Calibration curve plotting Cl Kα counts per second versus wt% Cl from cement paste of 0.45 *w/c* mortar standards.

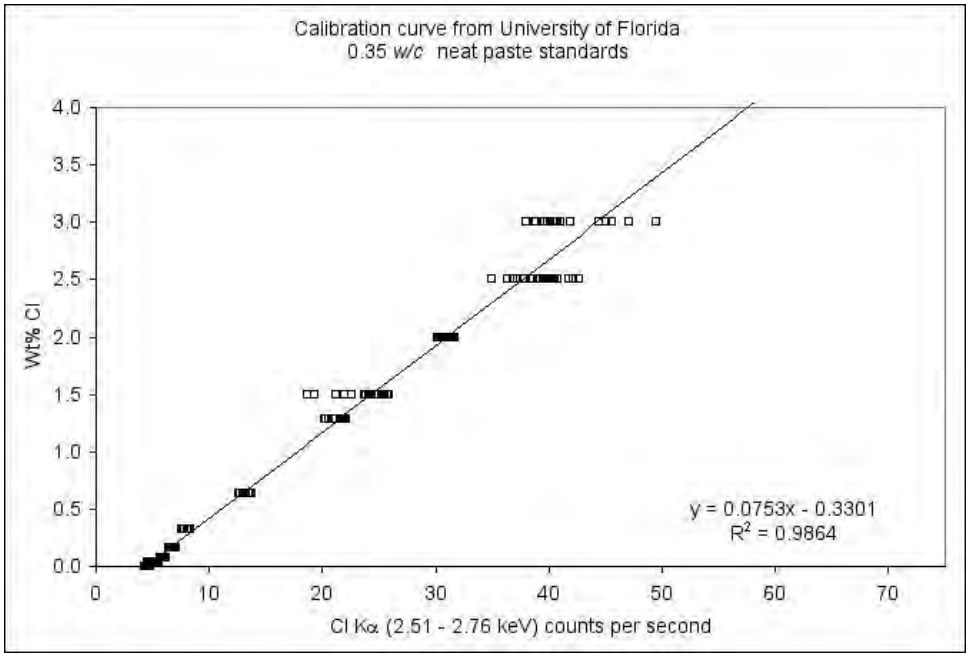

Figure A1.12. Calibration curve plotting Cl Kα counts per second versus wt% Cl from cement paste of 0.35 *w/c* neat cement standards.

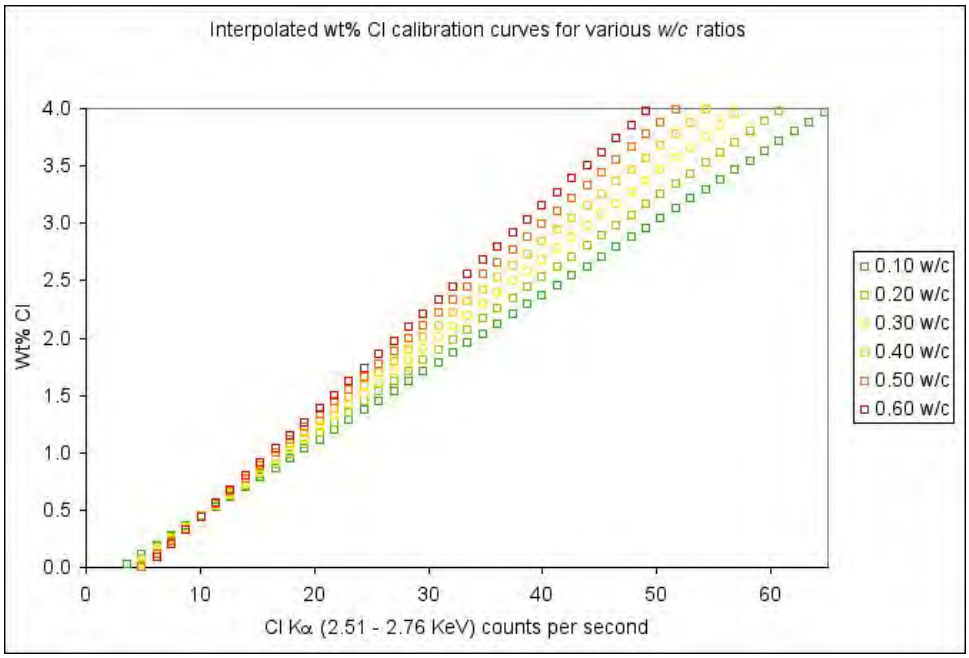

Figure A1.13. Interpolated calibration curves plotting Cl Kα counts per second versus wt% Cl for cement pastes at various *w/c* levels.

Methodology for the Analysis of Field Specimens

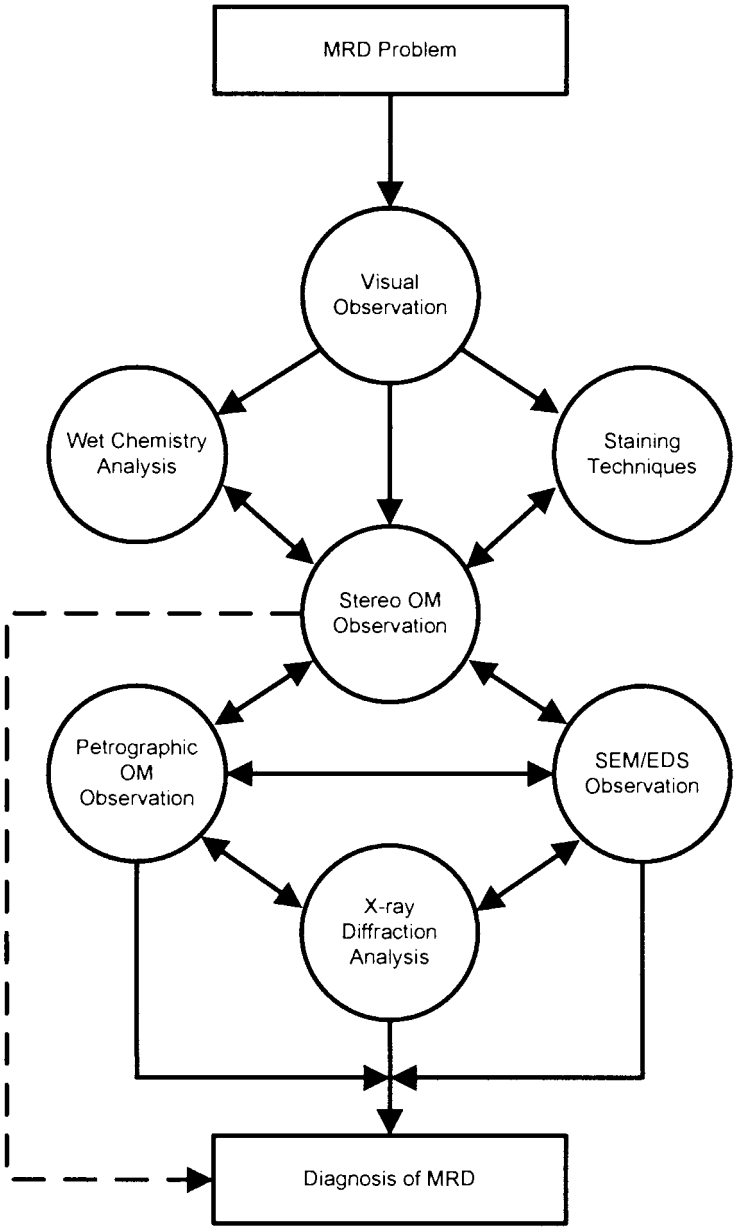

Figure A1.14. General approach to analyzing concrete exhibiting materials related distress. The general approach is to move down the diagram, first applying visual inspection, staining, and stereo optical microscopy. Other techniques are applied in an iterative manner as needed.

The cores received from each site were cataloged and photographed. They were then examined by various laboratory methods, as described in Section 3 of the Final Report, under the supervision of an ASTM C 856 qualified petrographer. The general application of analytical techniques follows the flow sheet presented in Figure A1.14. Systematically, the

concrete is inspected with various techniques including visual inspection, staining, stereo optical microscopy, petrographic optical microscopy, scanning electron microscopy, and x-x-ray diffraction. In this study, the x-ray microscope was used to perform many of the tasks normally performed with the SEM, specifically chloride concentration profiles.

For field specimens, selected cores were cut into slabs for stereo optical microscopy and determination of hardened air content in accordance with ASTM C 457. Cores were first embedded in fluorescent dyed epoxy resin, and then cut into slabs. The slabs were further cut into billets and prepared in thin section for examination with the petrographic microscope and the scanning electron microscope. Some cores were not embedded with epoxy, but also cut into slabs. From each of the non-embedded cores, one of the slabs was polished for examination with a flatbed scanner and the stereo microscope, and the other slab was cut into billets and prepared for chloride profiling with the x-ray microscope. A similar approach was applied to samples resulting from laboratory experiments. It should be noted that a flatbed scanner is often used to accomplish the observations performed by a stereo microscope. This approach is only applicable to flat specimens, such as slabs removed from cores. The flatbed scanner provides a convenient approach to capturing images of entire slabs, and it can be used to determine the air content of hardened concrete.

Appendix 2

Summary of Results for the Characterization of Field Specimens

Table of Contents

List of Figures

List of Figures

List of Figures

List of Figures

List of Figures

List of Figures

List of Tables

Characterization of Field Specimens

Approach

To approach Task 5, Characterization of Field Specimens, the research team began by meeting with the technical advisory panel and discussing possible sites that 1) represent the range of deicers being currently studied and 2) either exhibit some level of distress or represent new pavements that have been exposed only to one specific deicer. The intent of the study was to identify distress mechanisms that are visible in field concrete and study field concrete that has been exposed to a specific deicer, to assess how that one specific deicer is interacting with the concrete. The sites identified are listed below in Table A2.1.

Table A2.1. Pavement sites identified in cooperation with the technical advisory panel for examination as part of Task 5.

Colorado, State Highway 83, South of Denver near Milepost 57
Iowa, eastbound US Highway 34, western end of the Burlington Bridge.
Idaho, westbound Interstate Highway 184 west of Boise, near milepost 3
Montana, westbound Interstate Highway 90 bridge deck near milepost 117
South Dakota, Sioux Falls, eastbound 26th Street left turn lane

In general, the sites initially identified lacked unambiguous evidence of distress associated with deicers. To continue the field study, the research team obtained cores from a number of bridge decks in Montana that were exhibiting distress. Although these bridge decks are maintained using various non-NaCl deicers, they are all bridge decks that have been in service for numerous years and as a result, have been exposed to NaCl deicers for a significant portion of their service lives. Ultimately, because of this maintenance history, any distress identified would be difficult to associate with a specific deicing chemical. However, the team felt it was important to examine these bridge decks to determine if any visible mechanisms of chemical attack could be identified. The specific bridge decks sampled are listed below in Table A2.2.

Table A2.2. Bridge decks identified as additional field sites for examination as part of Task 5.

Montana, eastbound Interstate Highway 90 bridge deck, near milepost 61.8, Tarkio interchange
Montana, westbound Interstate Highway 90 bridge deck, near milepost 37.2, Sloway interchange

Presented in the remainder of this chapter are the results obtained from petrographic analyses of the samples representing the sites identified in Tables A2.1 and A2.2.

Petrographic Analysis of Identified Sites

Colorado, State Highway 83, South of Denver near Milepost 57

This pavement, constructed in 1996, exhibited visible signs of distress. Figure A2.1 shows the type of cracking observed in the field. The pavement has been exposed primarily to NaCl deicer. Figure A2.2 shows the location of the cores taken, and Figures A2.3 and A2.4 show photographs of the individual cores. Two of the cores were cut into slabs and polished: core CO-1 (near a joint), and core CO-5 (mid-panel). Figures A2.5 through A2.8 show the slabs as polished, after staining with phenolphthalein, and after treatment to enhance air voids and cracks. The phenolphthalein stain showed normal carbonation depths. The black and white treatment did not reveal any macro-cracking in either of the cores. Table A2.3 summarizes the air void parameters. Both sets of slabs showed adequate entrained air, with spacing factors of 0.182 mm and 0.175 mm for cores CO-1 and CO-5, respectively. Figure A2.9 shows an example stereomicroscope image of the air void structure. Some alkali silica reactivity (ASR) was observed with minor gel production and cracking, as illustrated in Figure A2.10. A *w/c* ratio estimation was performed on a thin section prepared from the top of core CO-6. Figures A2.11 and A2.12 show the images used to make the measurements. The results of the *w/c* estimation are summarized in Table A2.4, with an average *w/c* value of 0.47 as compared to the 28-day moist cured mortar sample standards. Figures A2.13 through A2.16 show chloride profiles from cores CO-6 and CO-8. Figure A2.17 shows fly ash particles present in the concrete. The exact cause of the observed distress is indeterminable but the most dominant symptoms seem to be associated with ASR.

Figure A2.1. Photograph of cracks in pavement.

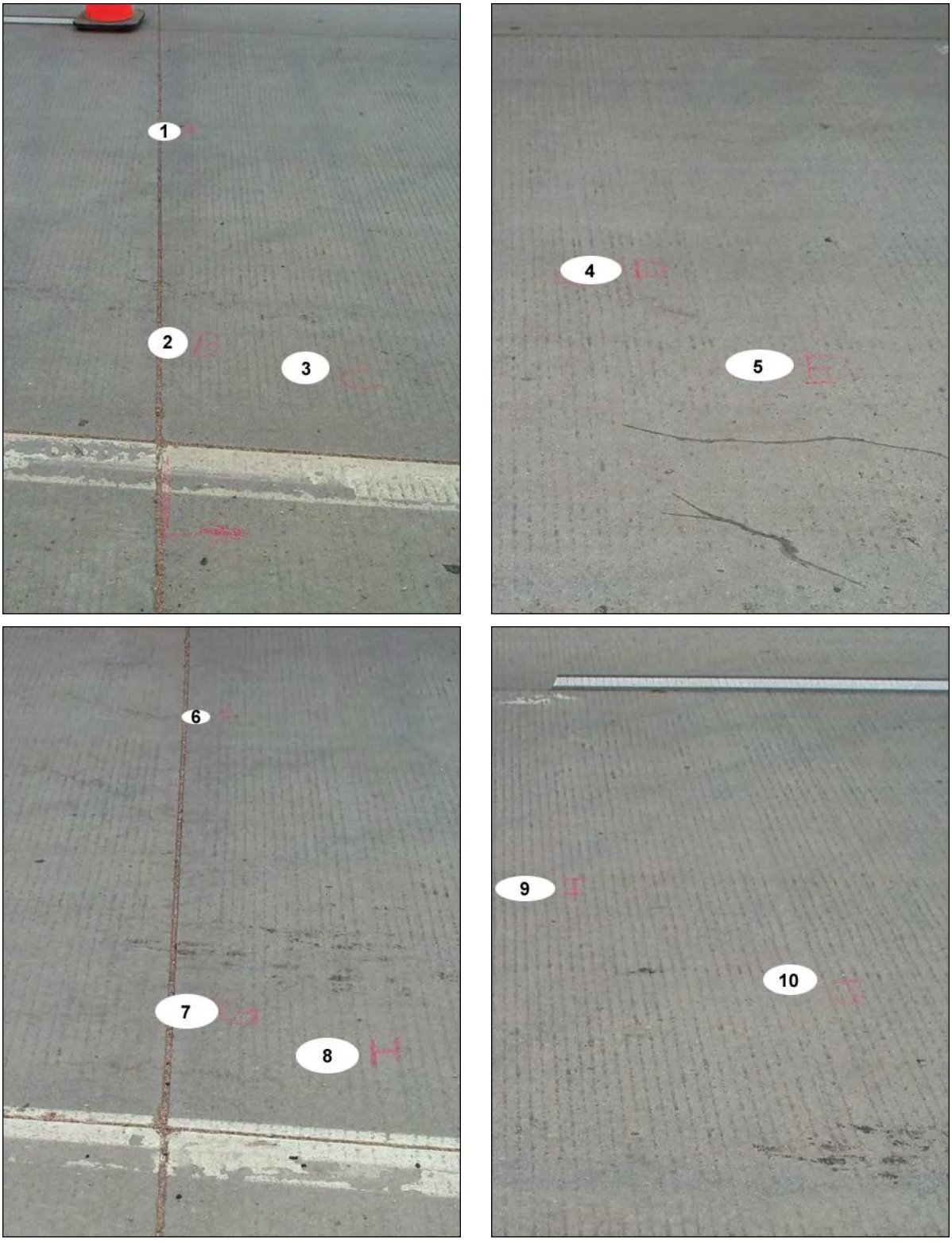

Figure A2.2. Photographs to show core locations.

Figure A2.3. Cores taken at joint.

Figure A2.4. Cores taken away from joint.

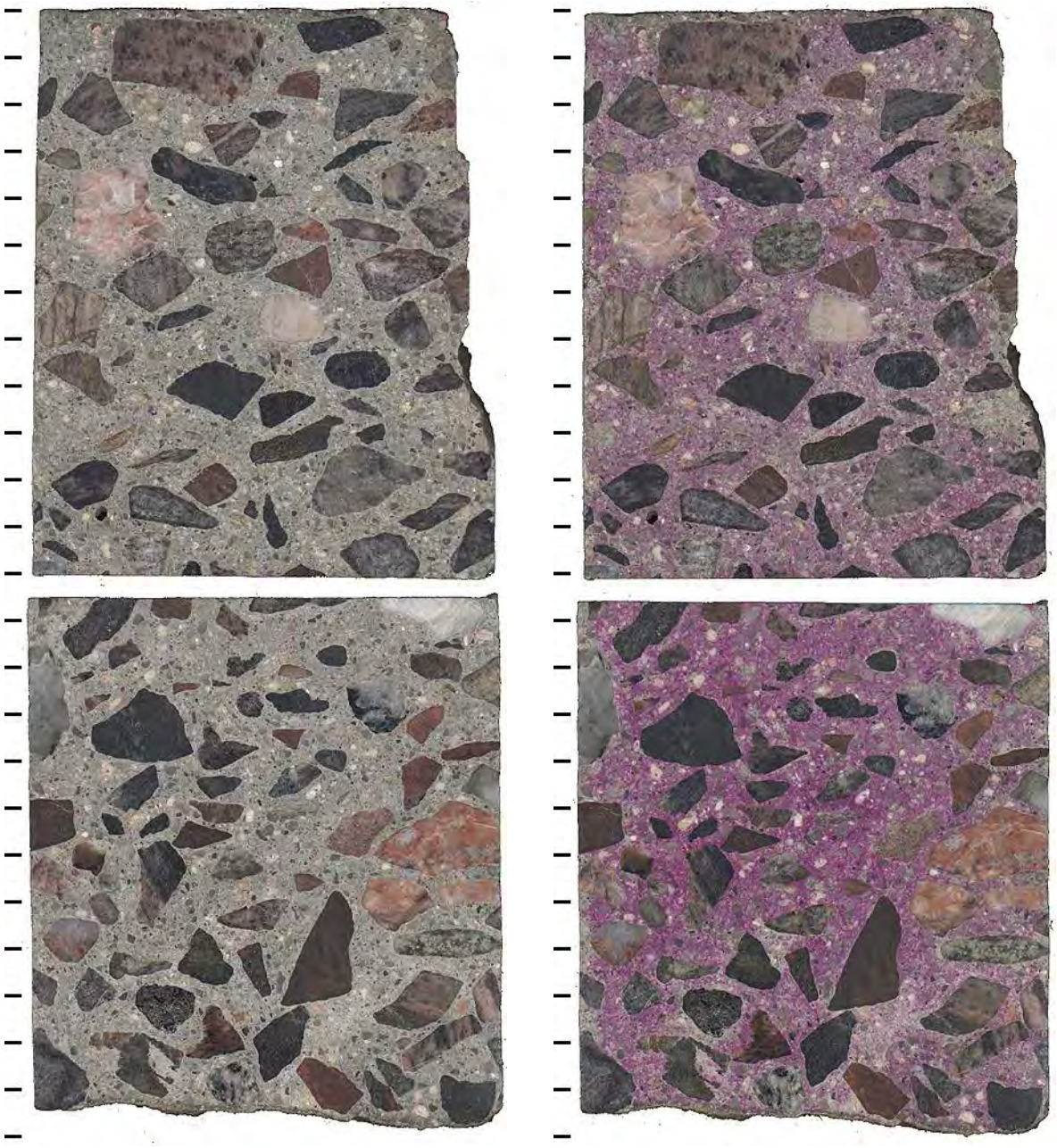

Figure A2.5. Polished slabs to show complete cross-section through core CO-1 both before (left) and after application of phenolphthalein stain (right) tic marks every cm.

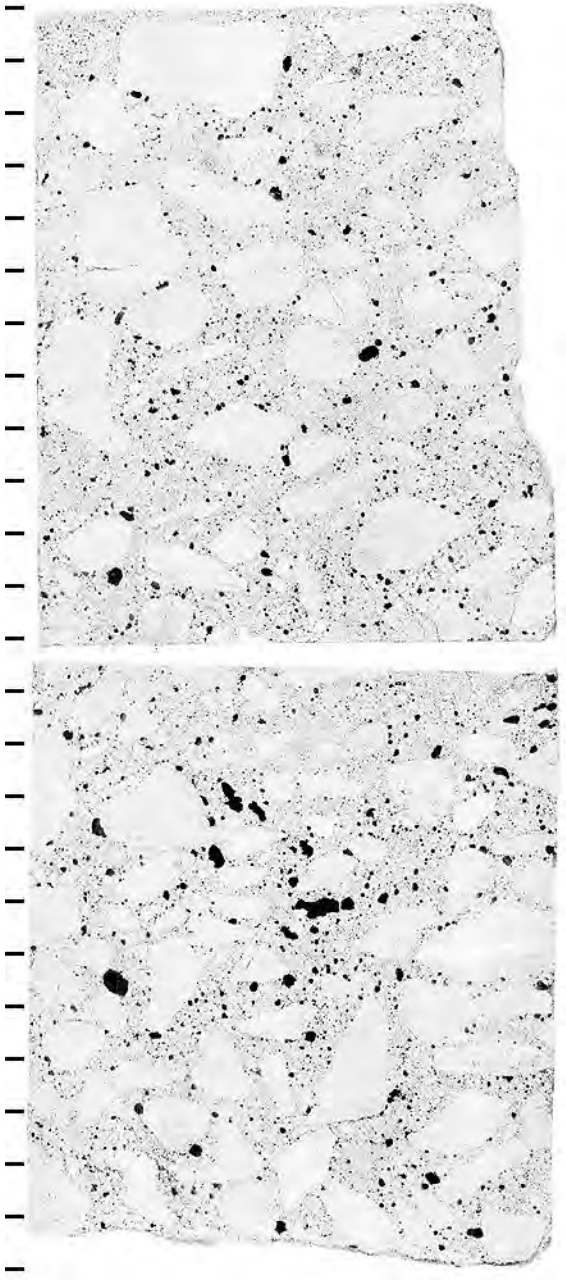

Figure A2.6. Polished slabs to show complete cross-section through core CO-1 after treatment to enhance appearance of air voids and cracks, tic marks every cm.

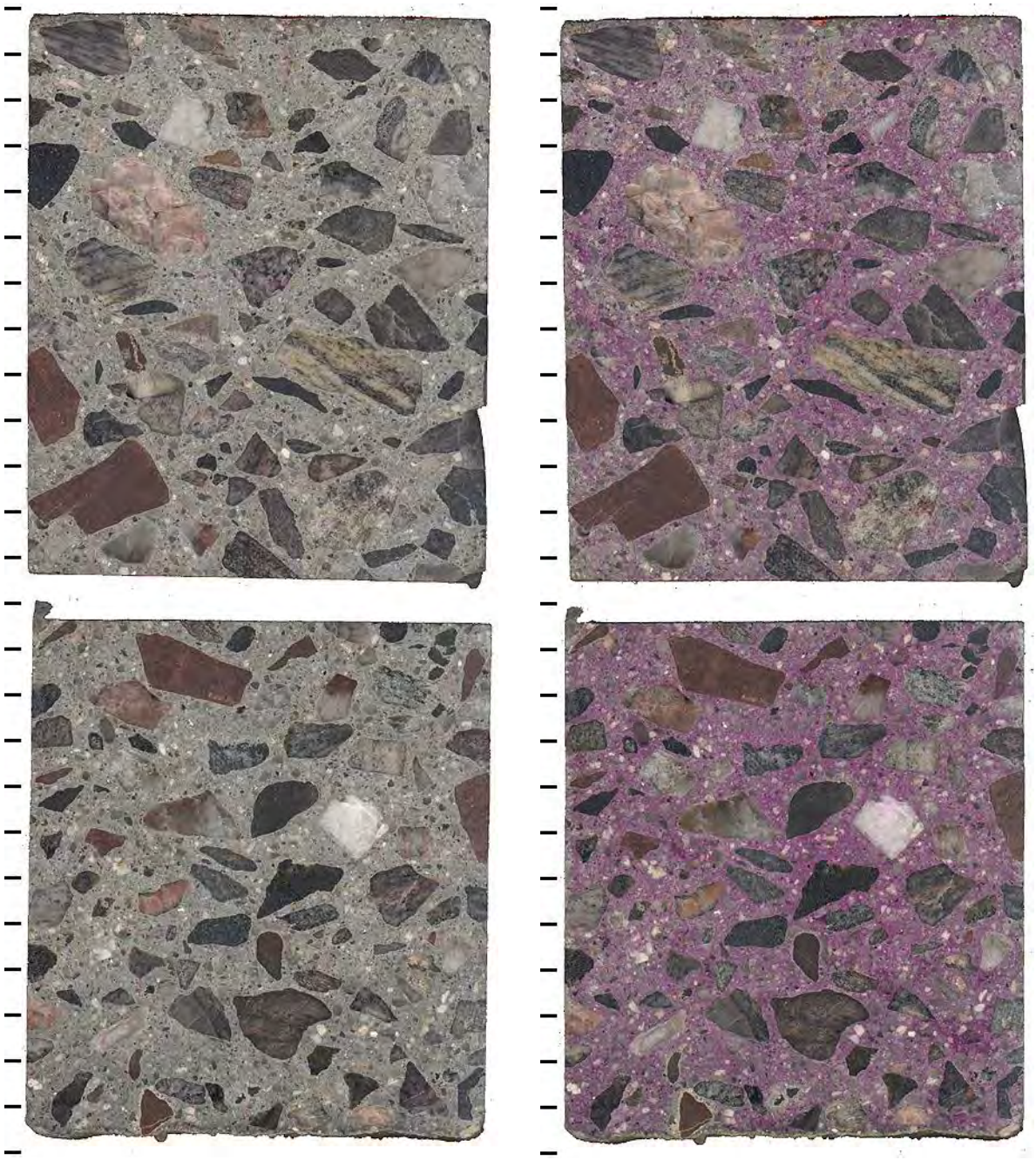

Figure A2.7. Polished slabs to show complete cross-section through core CO-5 both before (left) and after application of phenolphthalein stain (right) tic marks every cm.

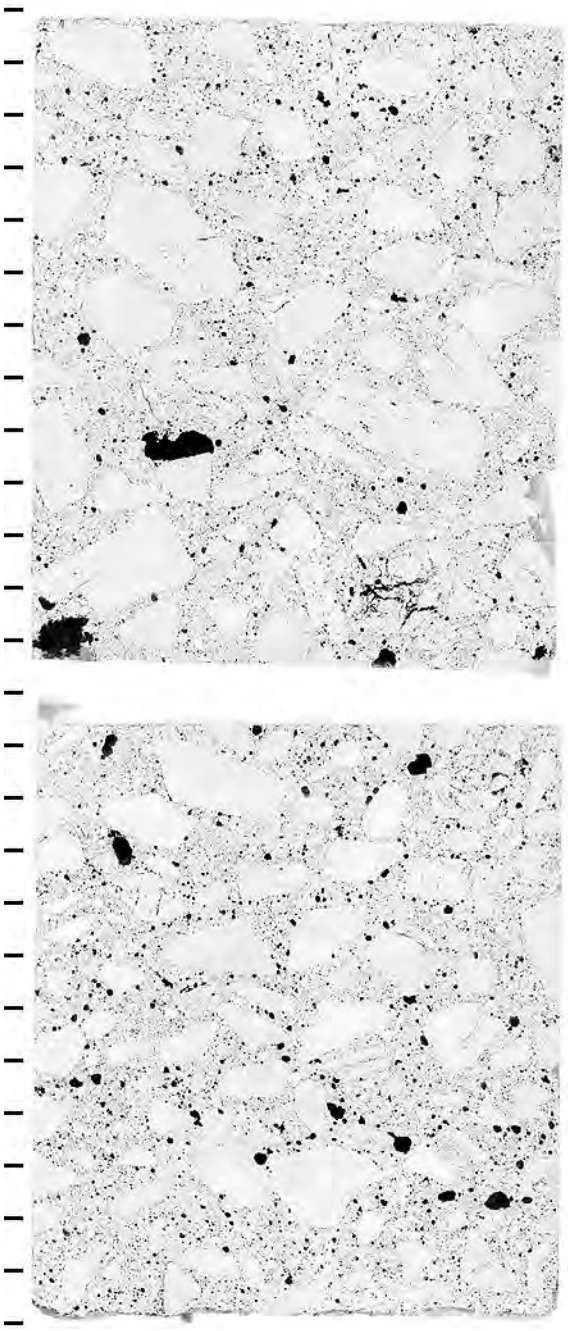

Figure A2.8. Polished slabs to show complete cross-section through core CO-5 after treatment to enhance appearance of air voids and cracks, tic marks every cm.

Table A2.3. Air void parameters.

Sample ID	CO-01	CO-05
Location	At joint	Away from Joint
Raw data		
Total traverse length (mm)	3625.5	3625.5
Area analyzed (cm^2)	71.0	71.0
Air stops	79	83
Paste stops	300	282
Aggregate stops	1009	1023
Secondary deposit stops	0	0
Total stops	1388	1388
Number of air intercepts	1072	1051
Number of filled void intercepts	3	0
Results		
Air vol%	5.7	6.0
Paste vol%	21.6	20.3
Aggregate vol%	72.7	73.7
Secondary deposit vol%	0.0	0.0
Existing average chord length (mm)	0.192	0.206
Existing paste/air ratio	3.8	3.4
Existing air void specific surface (mm^{-1})	20.8	19.4
Existing air void frequency (voids/m)	296	290
Existing spacing factor (mm)	0.183	0.175
Original average chord length (mm)	0.192	0.206
Original paste/air ratio	3.8	3.4
Original air void specific surface (mm^{-1})	20.8	19.4
Original air void frequency (voids/m)	297	290
Original spacing factor (mm)	0.182	0.175

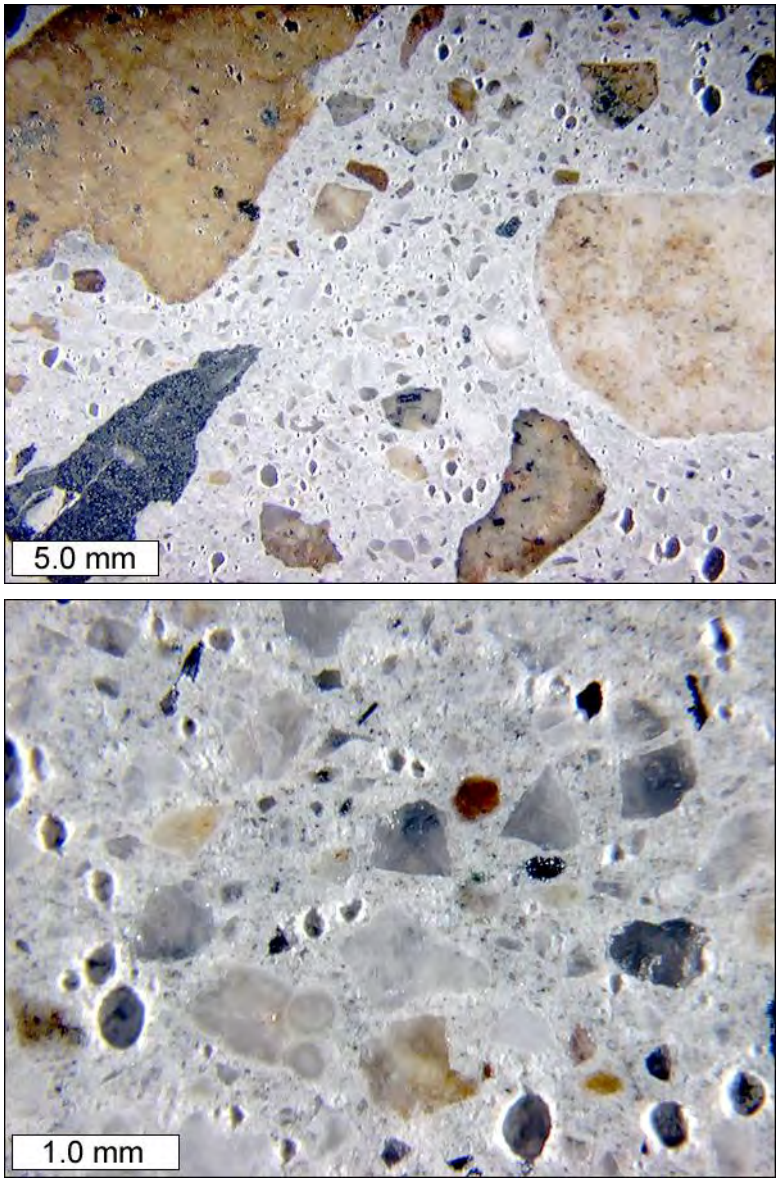

Figure A2.9. Stereo microscope images to show air void structure on polished slab from core CO-1.

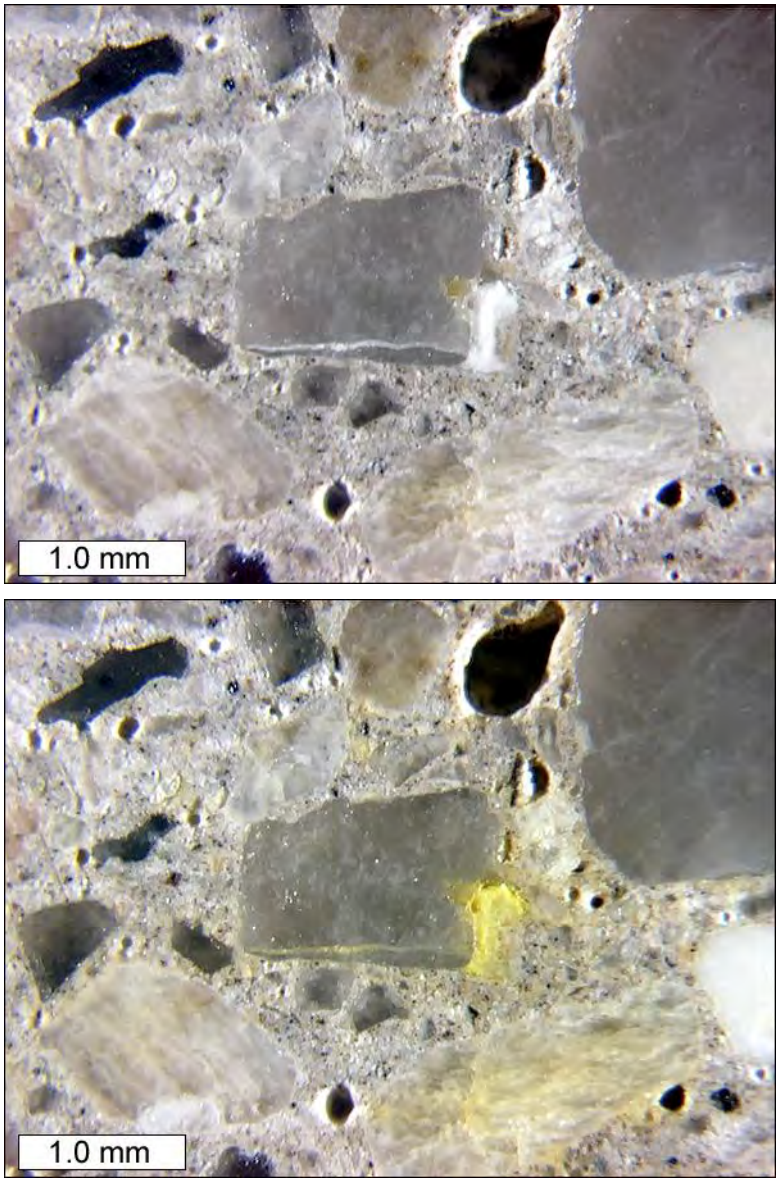

Figure A2.10. Stereo microscope images to show reactive aggregate particle both before (top) and after (bottom) treatment with sodium cobaltinitrite stain (sample CO-5).

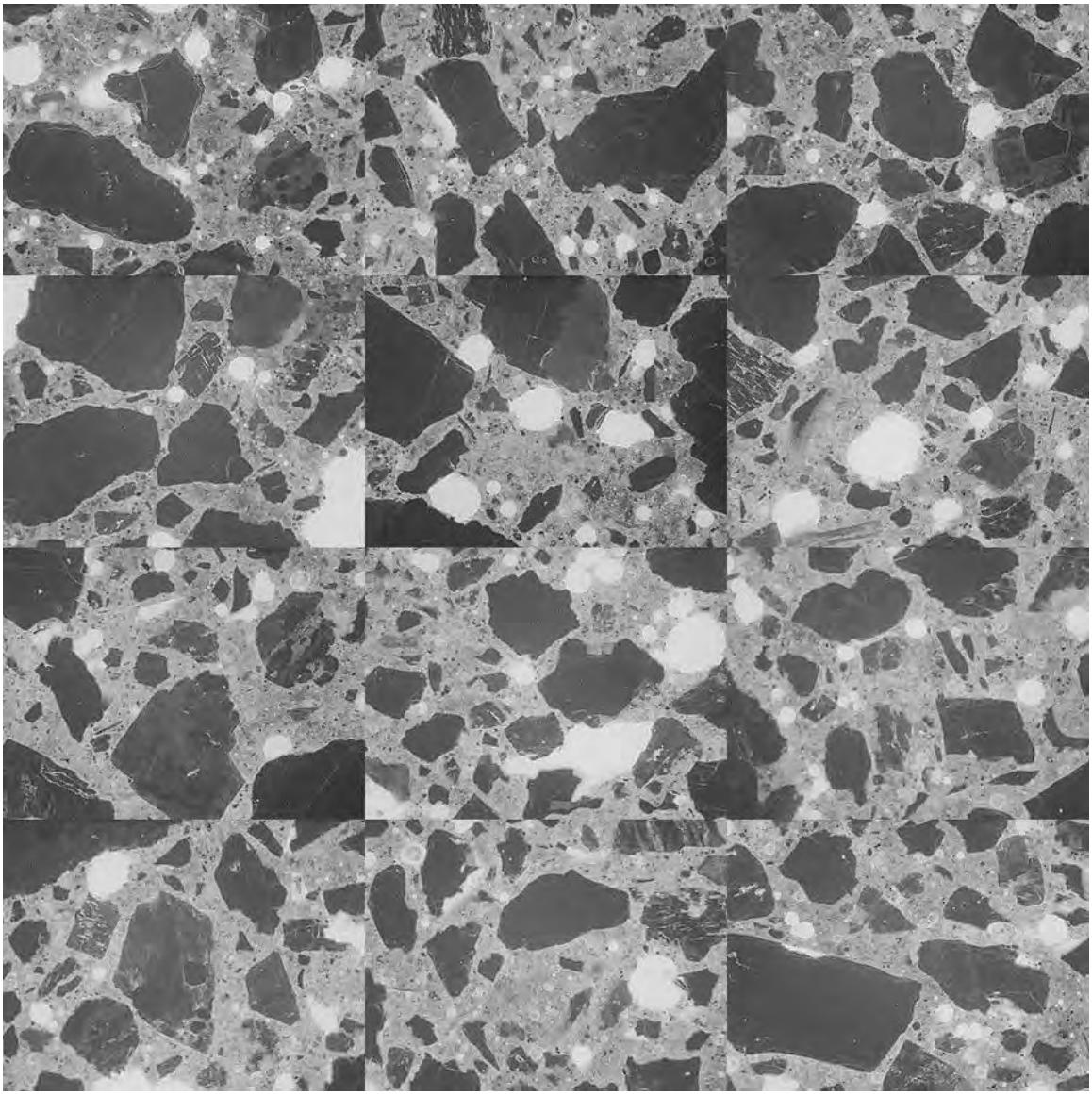

Figure A2.11. Mosaic of 12 frames collected from thin section prepared from billet cut from top portion of core CO-6 (each individual frame measures 2.612 x 1.959 mm).

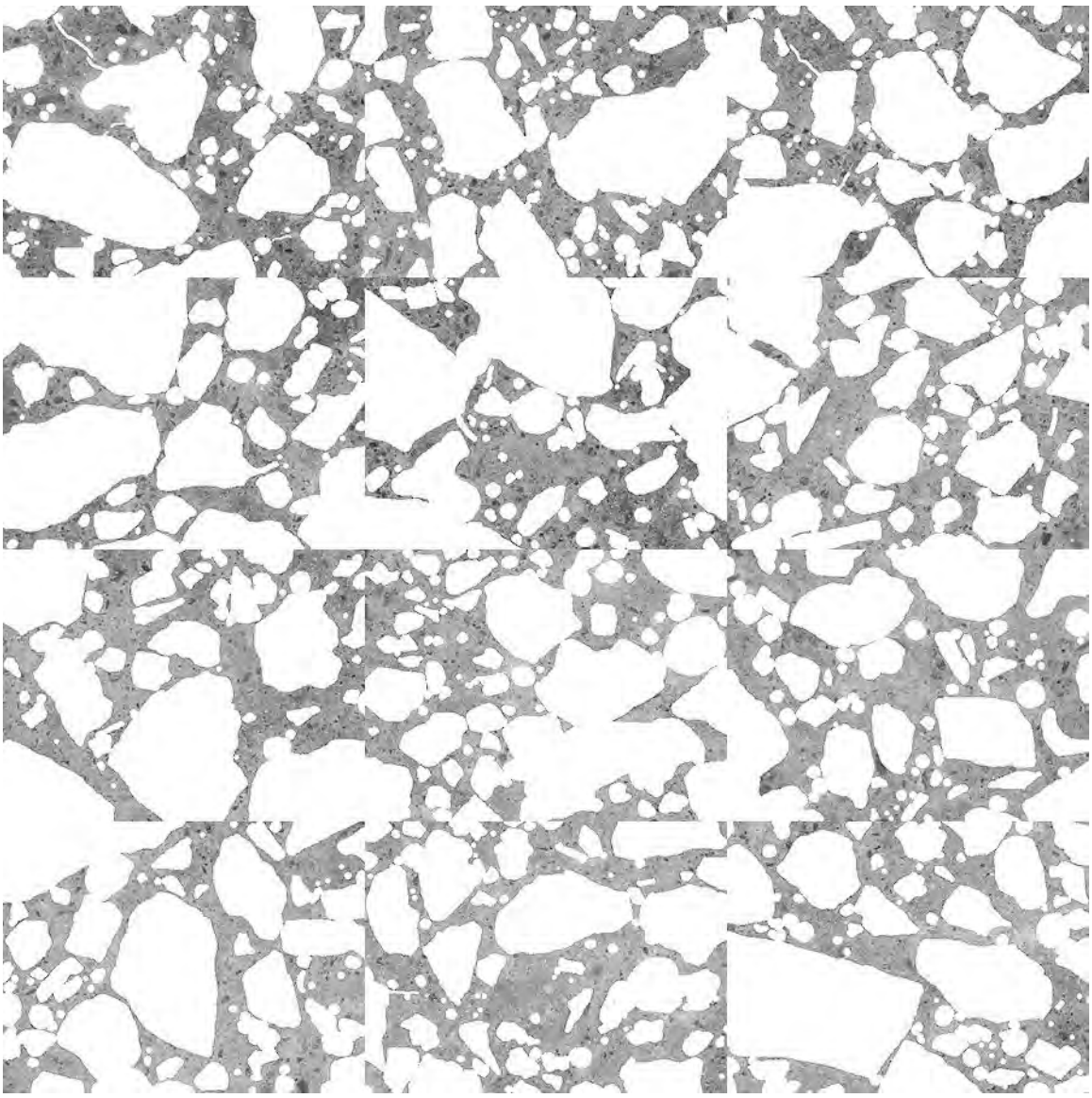

Figure A2.12. Mosaic of 12 frames collected from thin section prepared from billet cut from top portion of core CO-6 after masking out air voids and fine aggregate to isolate cement paste (each individual frame measures 2.612 x 1.959 mm).

Table A2.4. Average cement paste pixel intensities per frame, and equivalent *w/c* values (as compared to 28-day moist cured mortar samples).

Cement Paste Pixel Fluorescence Measurements (average intensity per frame)			
88	96	90	93
87	108	102	115
110	116	115	113
Equivalent *w/c* (y = 0.0044x + 0.0329)			
0.42	0.45	0.43	0.44
0.41	0.50	0.48	0.53
0.51	0.54	0.54	0.53

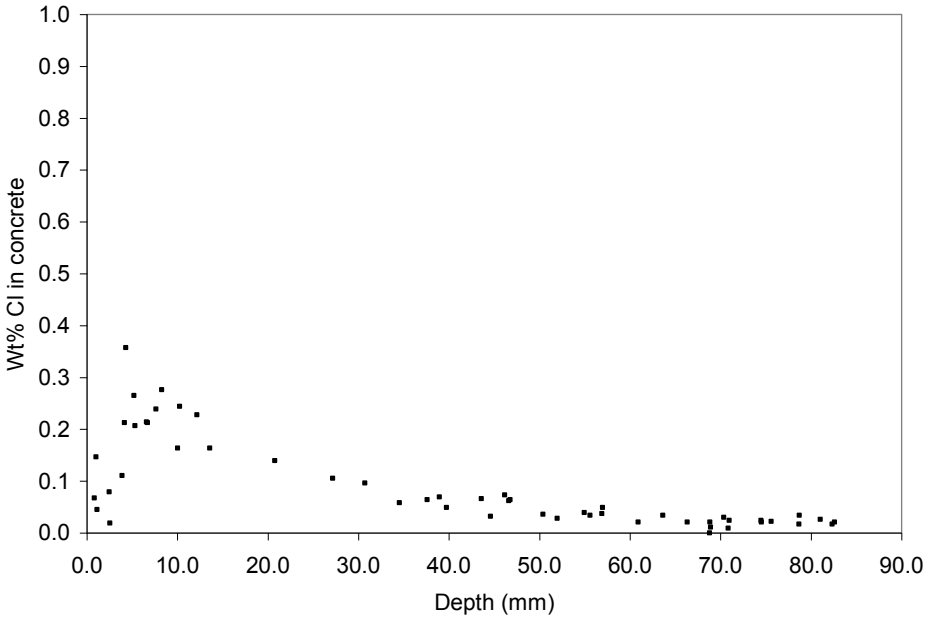

Figure A2.13. Chloride profile from billet prepared from core CO-6, immediately adjacent to joint.

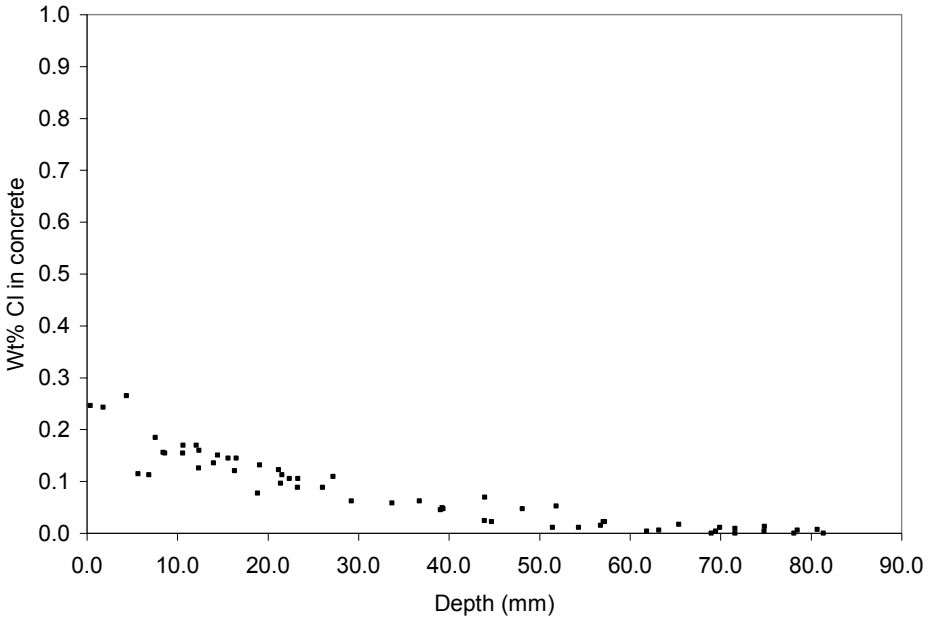

Figure A2.14. Chloride profile from billet prepared from core CO-6, approximately 25 mm from joint.

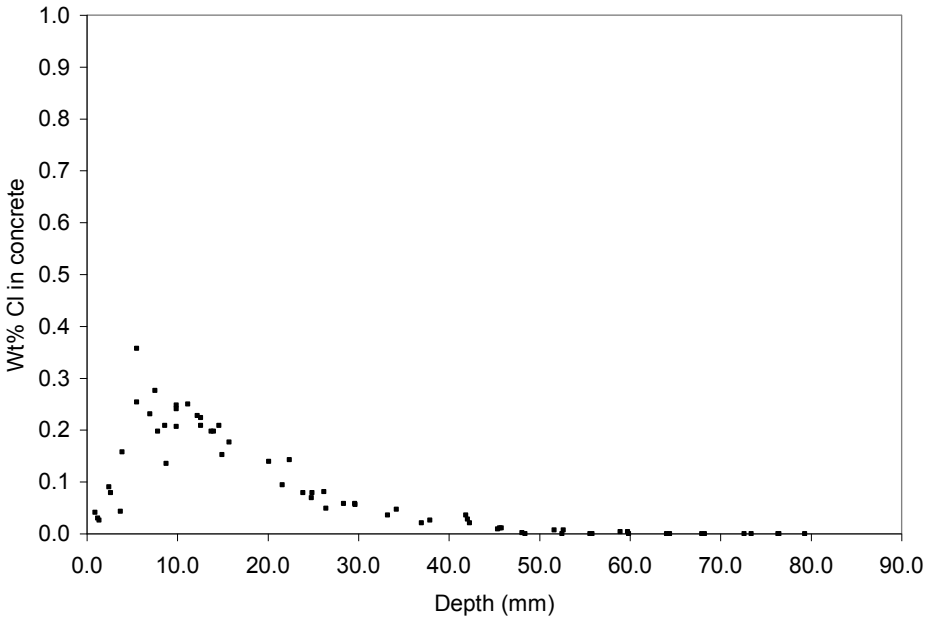

Figure A2.15. Chloride profile from billet prepared from core CO-8, mid-panel.

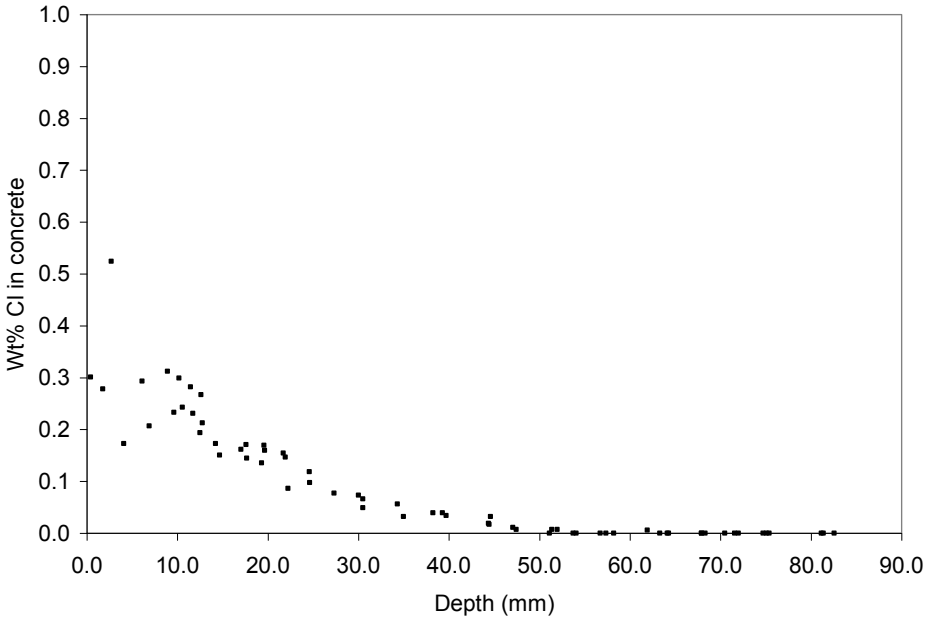

Figure A2.16. Duplicate chloride profile from additional billet prepared from core CO-8.

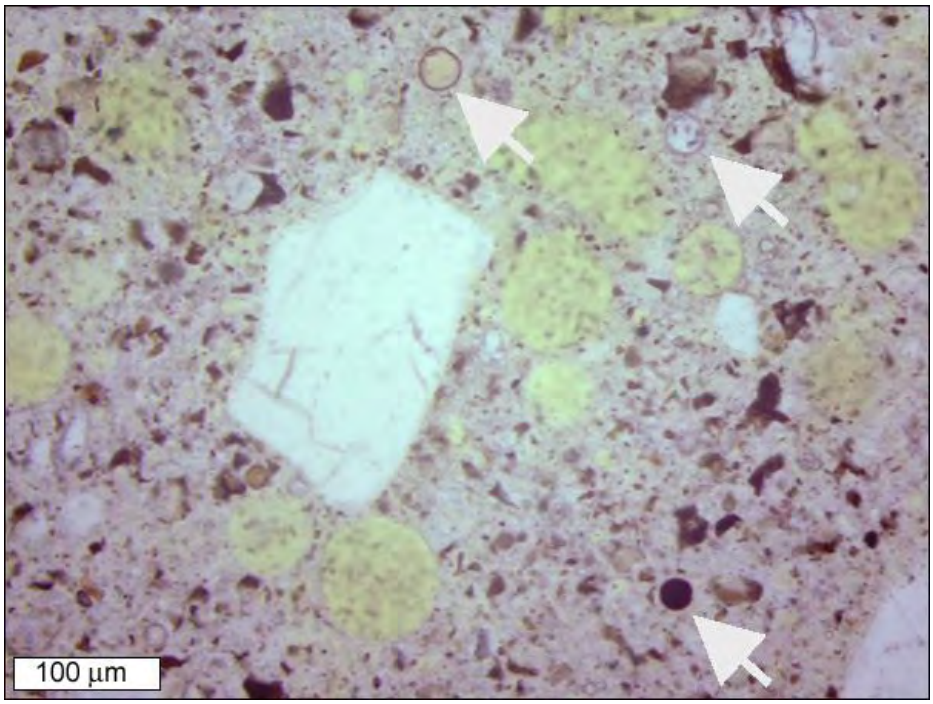

Figure A2.17. Transmitted light image, with arrows indicating some of the fly ash particles.

Iowa, eastbound US Highway 34, western end of the Burlington Bridge.

This bridge deck, overlaid in 1993, is reported to have been exposed exclusively to calcium magnesium acetate deicer. Figure A2.18 shows the locations of the cores, and Figure A2.19 shows an example of surface cracking observed in the field. Figures A2.20 and A2.21 show photographs of the partial depth cores, which primarily sampled the approximately 2" thick concrete overlay. Two of the cores were cut into slabs and polished: core IA-6 (over a surface crack), and core IA-5 (no surface crack). Figures A2.22 and A2.23 show the slabs as polished, after staining with phenolphthalein, and after treatment to enhance air voids and cracks. The phenolphthalein stain showed normal carbonation depths. The black and white treatment did not reveal any macro-cracking in either of the cores, other than the obvious surface crack of core IA-6, which extended both through the overlay and into the original concrete below. Table A2.5 summarizes the air void parameters. The overlay from both slabs exhibited borderline entrained air parameters, with spacing factors of 0.276 mm and 0.217 mm for cores IA-5 and IA-6 respectively. Figure A2.24 shows an example stereomicroscope image of the air void structure. Some alkali silica reactivity was observed with minor gel production but no cracking, as illustrated in Figure A2.25. A *w/c* ratio estimation was performed on a thin section prepared from the top concrete overlay portion of core IA-3, and from the original concrete below in core IA-11. Figures A2.26 through A2.29 show the images used to make the measurements. The results of the *w/c* estimations are summarized in Tables A2.6 and A2.7, with an average *w/c* value of 0.30 for the overlay, and an average *w/c* value of 0.42 for the original concrete, (as compared to 28-day moist cured mortar sample standards). Figures A2.30 through A2.33 show chloride profiles collected from core IA-3 (over a surface crack) and core IA-11 (no surface crack). All of the profiles show an increase in chloride concentration near the pavement surface. Although CMA may have been used exclusively on the bridge deck, it is possible that contamination from the preceding roadway contributed to the observed chloride gradient. A careful comparison of the profiles from cores IA-3 and IA-11 shows an increased chloride penetration in core IA-3, which was taken directly over a surface crack in the pavement. Figure A2.34 shows secondary calcium hydroxide deposits in air voids, which were commonly observed in the concrete overlay. The petrographic analysis of these cores did not reveal any specific degradation related to chemical attack from deicers. The only significant observation was the marginal air-void system, which may have contributed to the observed distress.

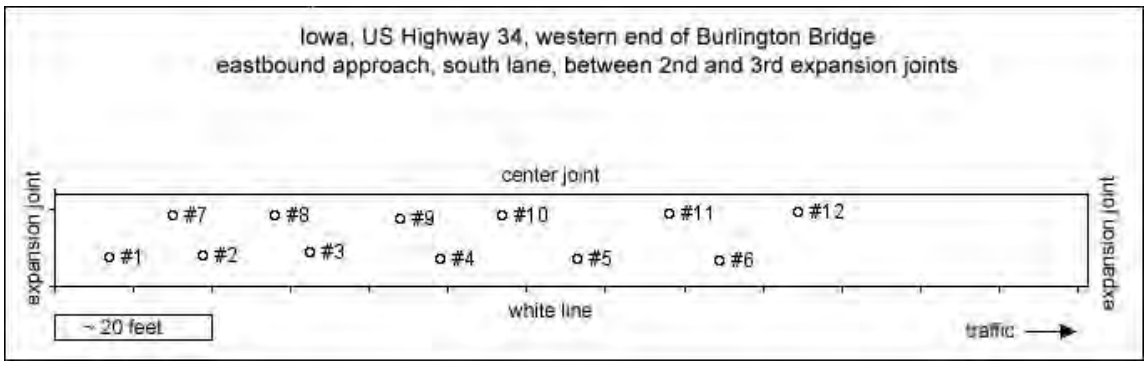

Figure A2.18. Diagram of core locations based on submitted field information.

Figure A2.19. Photograph of crack in bridge deck.

Figure A2.20. Partial depth cores through bridge deck from right hand side of lane.

Figure A2.21. Partial depth cores through bridge deck from left hand side of lane.

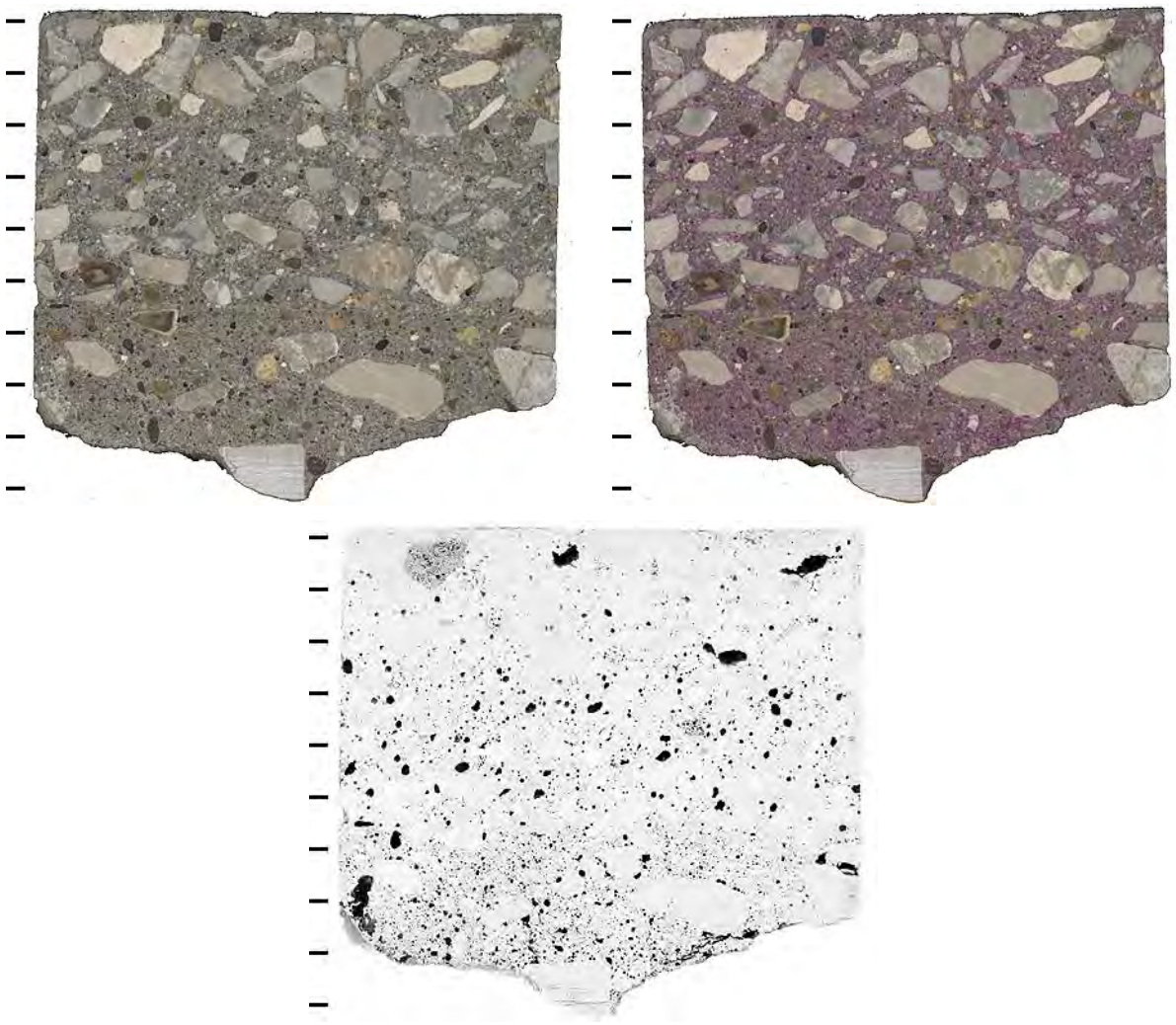

Figure A2.22. Polished slabs to show complete cross-section through core IA-4, before (upper left) and after application of phenolphthalein stain (upper right) and after treatment to enhance appearance of air voids and cracks (bottom) tic marks every cm.

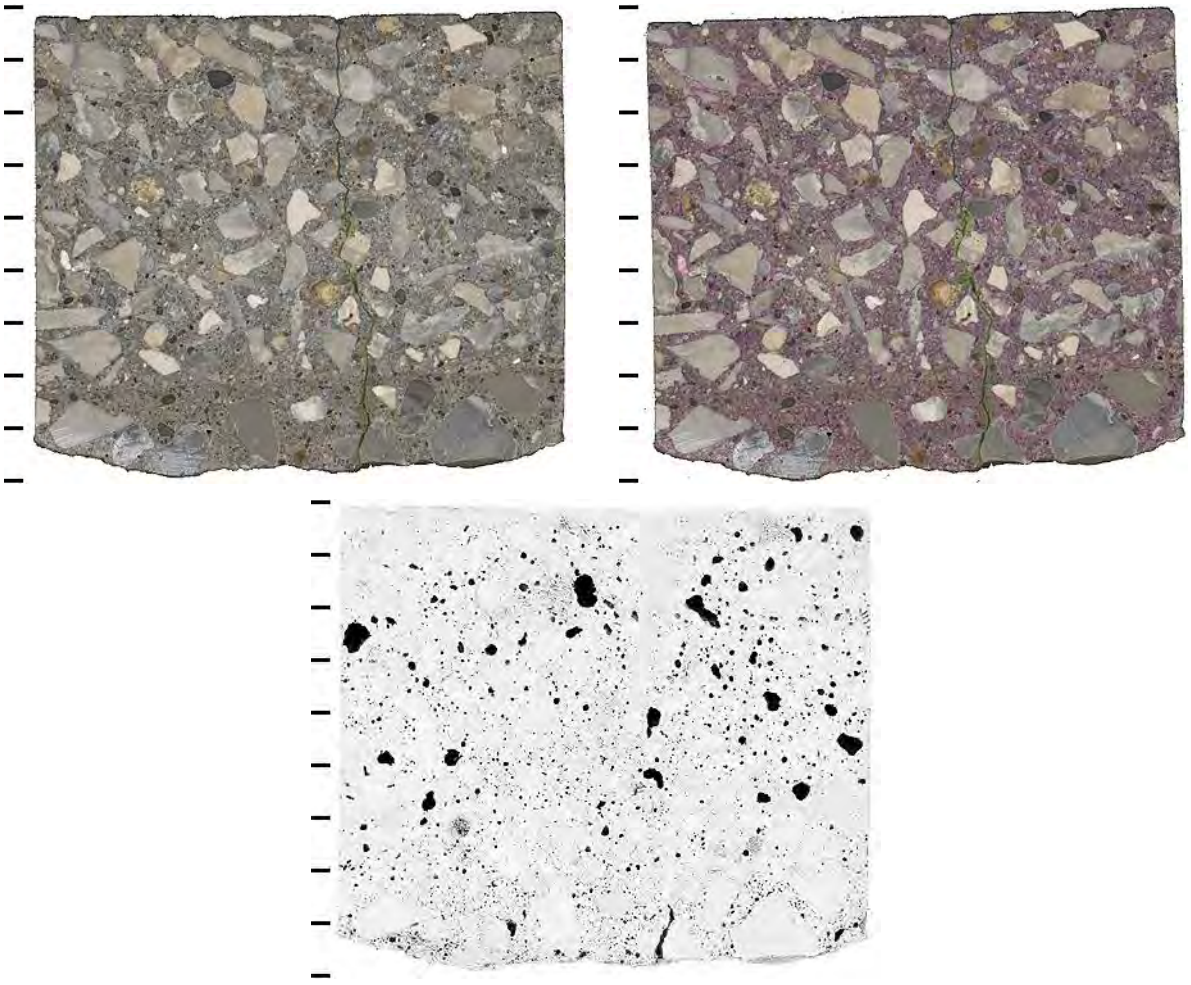

Figure A2.23. Polished slabs to show complete cross-section through core IA-7, before (upper left) and after application of phenolphthalein stain (upper right) and after treatment to enhance appearance of air voids and cracks (bottom) tic marks every cm. The slab was stabilized with epoxy prior to polishing due to the large crack running the down the middle of the core. Since the crack was filled with epoxy, it does not appear in the black and white enhanced image.

Table A2.5. Air void parameters of concrete overlay.

Sample ID	IA-07	IA-04
Location	At crack	Away from crack
Raw data		
Total traverse length (mm)	3411.3	4197.5
Area analyzed (cm^2)	66.8	82.2
Air stops	86	123
Paste stops	400	400
Aggregate stops	817	1083
Secondary deposit stops	3	1
Total stops	1306	1607
Number of air intercepts	835	1198
Number of filled void intercepts	6	5
Results		
Air vol%	6.6	7.7
Paste vol%	30.6	24.9
Aggregate vol%	62.8	67.5
Secondary deposit vol%	0.2	0.1
Existing average chord length (mm)	0.302	0.268
Existing paste/air ratio	4.7	3.3
Existing air void specific surface (mm^{-1})	14.9	14.9
Existing air void frequency (voids/m)	245	285
Existing spacing factor (mm)	0.269	0.219
Original average chord length (mm)	0.305	0.269
Original paste/air ratio	4.5	3.2
Original air void specific surface (mm^{-1})	14.5	14.9
Original air void frequency (voids/m)	247	287
Original spacing factor (mm)	0.276	0.217

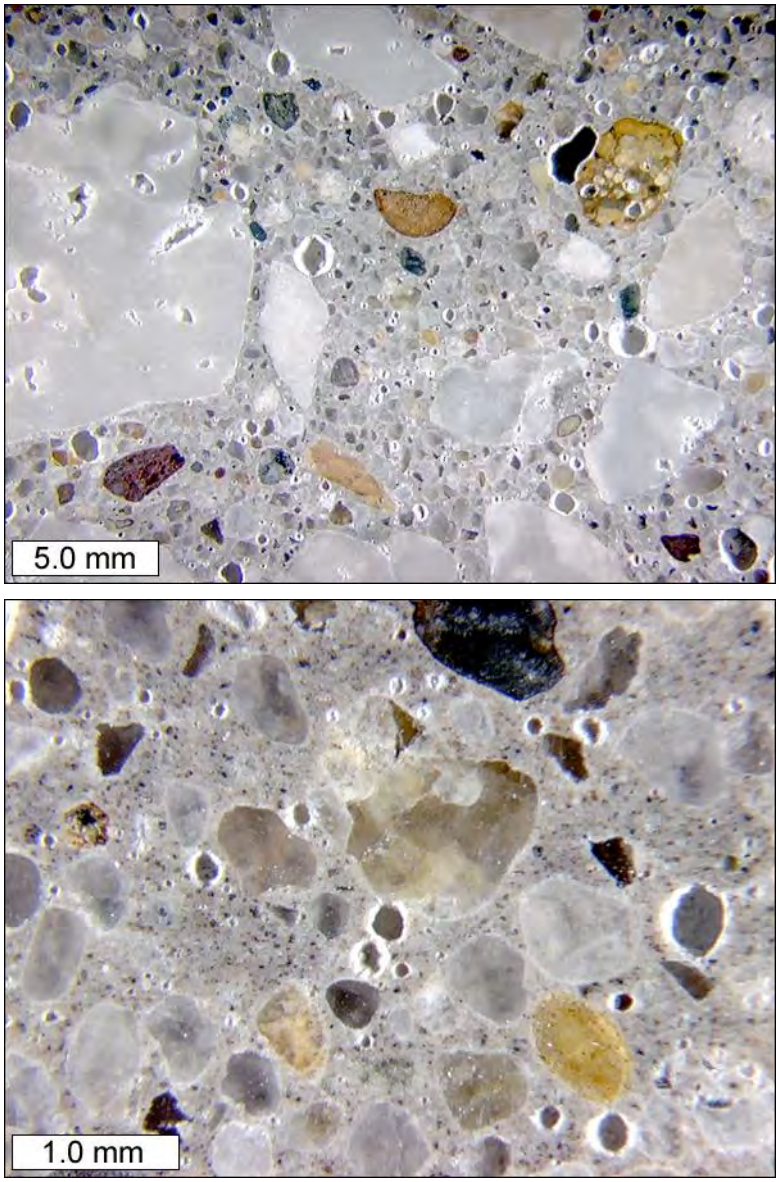

Figure A2.24. Stereo microscope images to show air void structure of concrete overlay on polished slab from core IA-4.

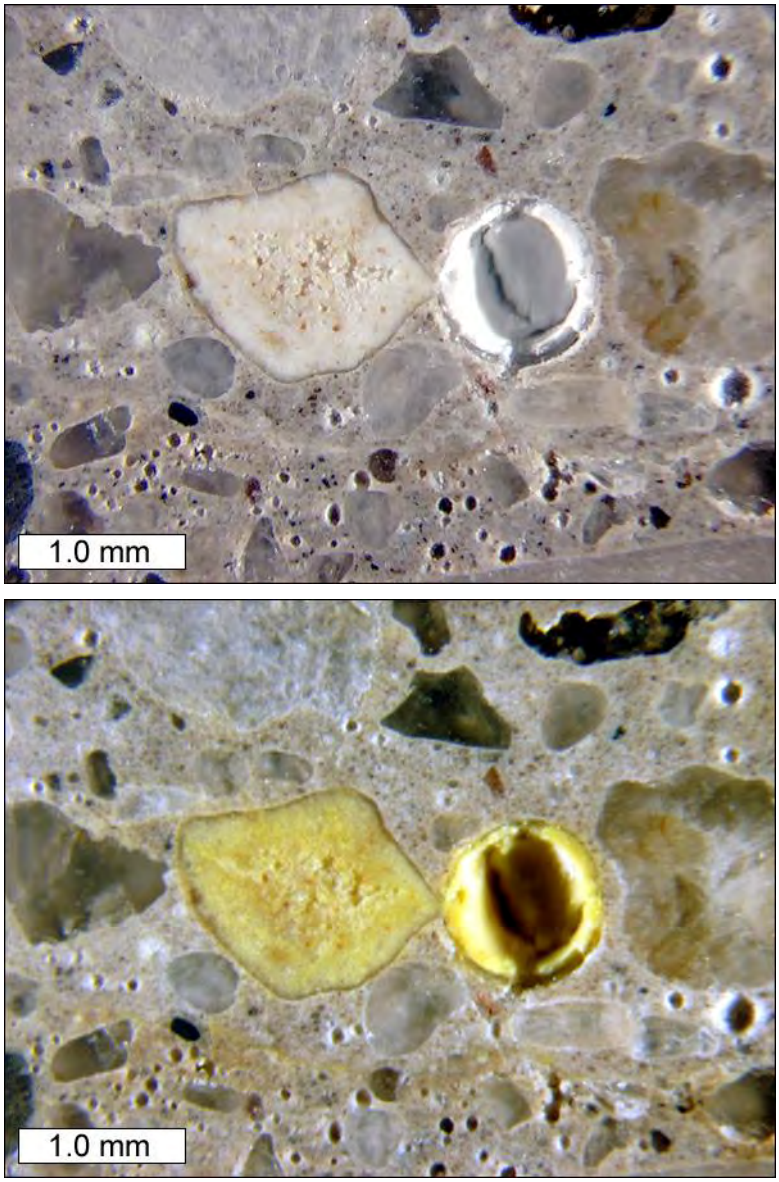

Figure A2.25. Stereo microscope images to show reactive aggregate particle both before (top) and after (bottom) treatment with sodium cobaltinitrite stain (sample IA-7). Image also illustrates the contrast in texture between the concrete overlay (top $^{3}/_{4}$ of image) and the original concrete below (bottom $^{1}/_{4}$ of image).

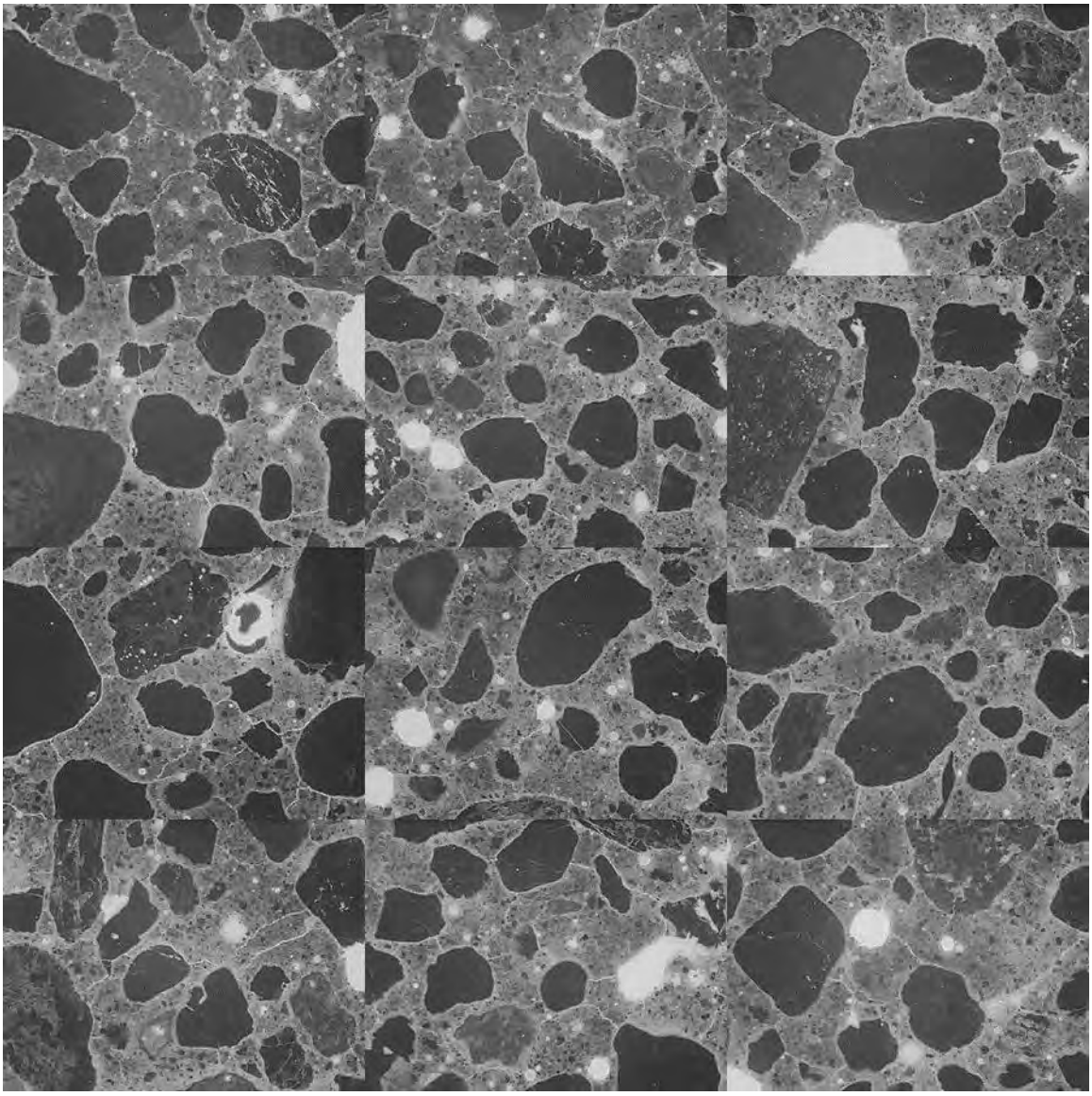

Figure A2.26. Mosaic of 12 frames collected from thin section prepared from billet cut from top portion of concrete overlay, core IA-3 (each individual frame measures 2.612 x 1.959 mm).

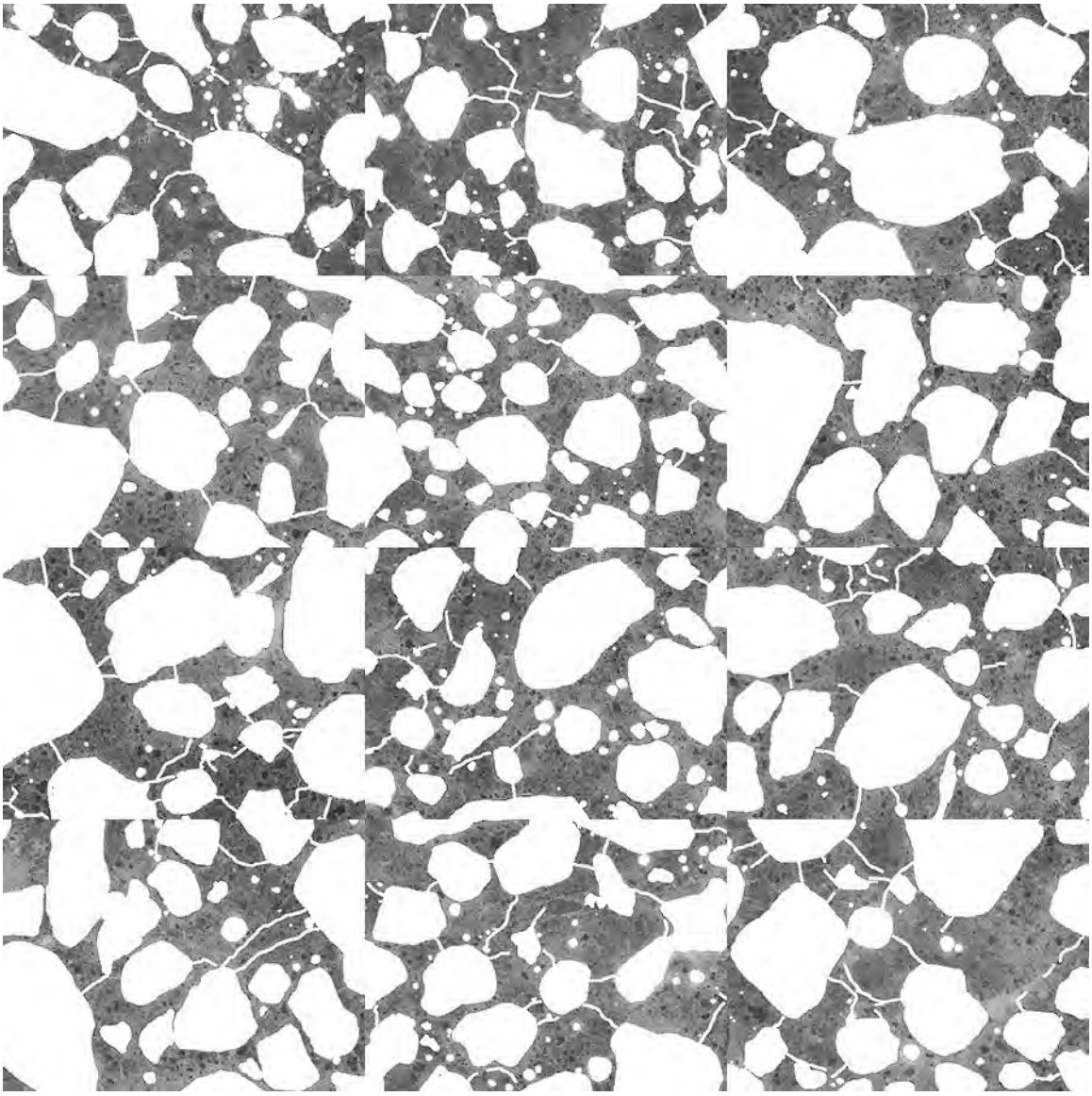

Figure A2.27. Mosaic of 12 frames collected from thin section prepared from billet cut from top portion of concrete overlay, core IA-3, after masking out air voids, fine aggregate, and micro-cracks to isolate cement paste (each individual frame measures 2.612 x 1.959 mm).

Table A2.6. Average cement paste pixel intensities per frame, and equivalent *w/c* values (as compared to 28-day moist cured mortar samples) from concrete overlay, core IA-3.

Cement Paste Pixel Fluorescence Measurements (average intensity per frame)			
54	54	55	69
68	64	55	61
64	67	68	68
equivalent *w/c* (y = 0.0044x + 0.0329)			
0.27	0.27	0.27	0.34
0.33	0.31	0.27	0.30
0.31	0.32	0.33	0.33

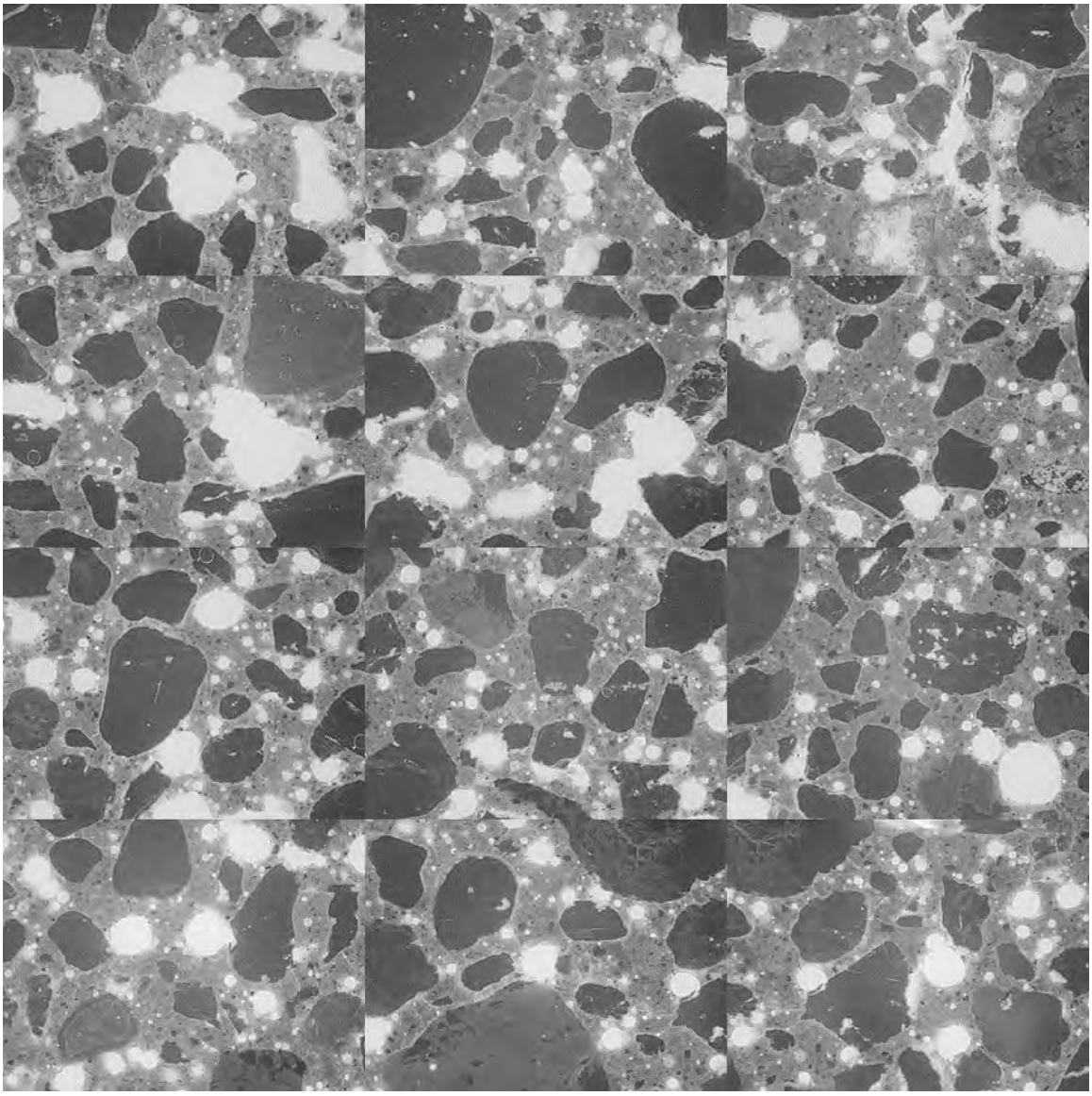

Figure A2.28. Mosaic of 12 frames collected from area of thin section representing the original concrete below the concrete overlay, core IA-11 (each individual frame measures 2.612 x 1.959 mm).

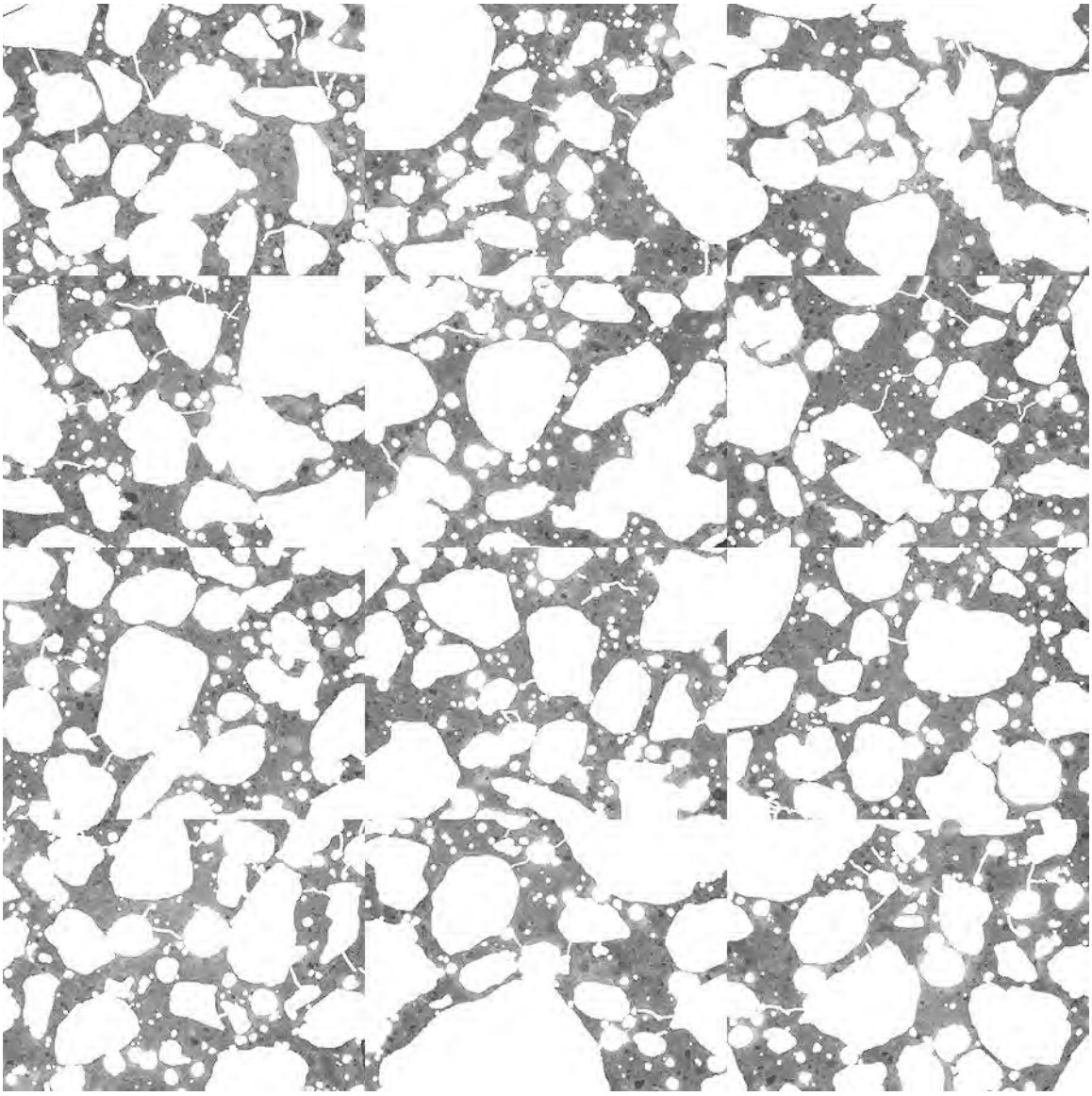

Figure A2.29. Mosaic of 12 frames collected area of thin section representing the original concrete below the concrete overlay, core IA-11, after masking out air voids, fine aggregate, and micro-cracks to isolate cement paste (each individual frame measures 2.612 x 1.959 mm).

Table A2.7. Average cement paste pixel intensities per frame, and equivalent *w/c* values (as compared to 28-day moist cured mortar samples) from original concrete below the overlay, core IA-11.

Cement Paste Pixel Fluorescence Measurements (average intensity per frame)			
90	91	87	85
90	81	88	92
85	96	88	90
equivalent *w/c* (y = 0.0044x + 0.0329)			
0.42	0.43	0.41	0.40
0.42	0.39	0.42	0.43
0.40	0.45	0.41	0.43

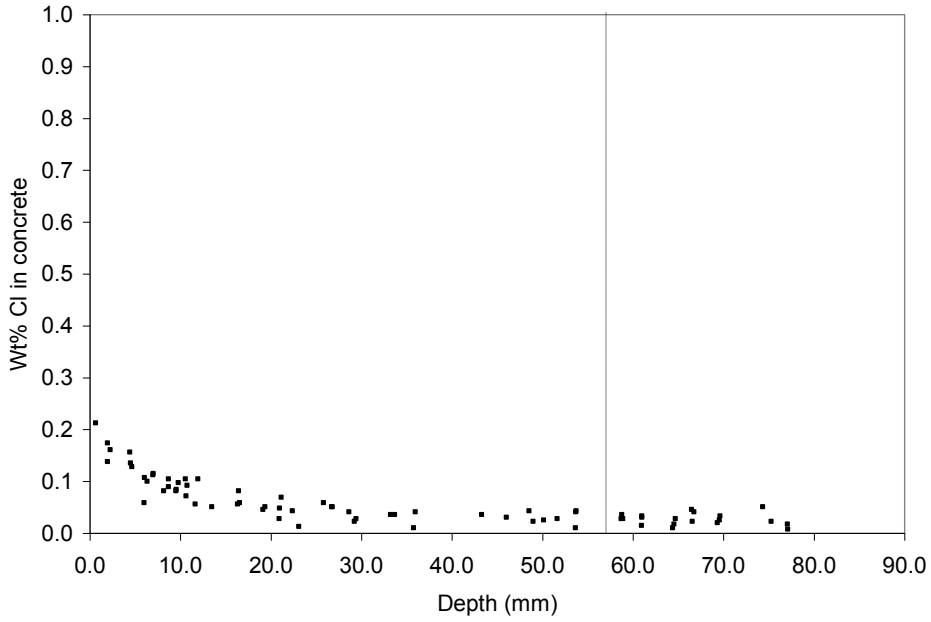

Figure A2.30. Chloride profile from billet prepared from core IA-3, about 25 mm away from visible surface crack, dashed line marks the transition point between the concrete overlay and the original concrete below the overlay.

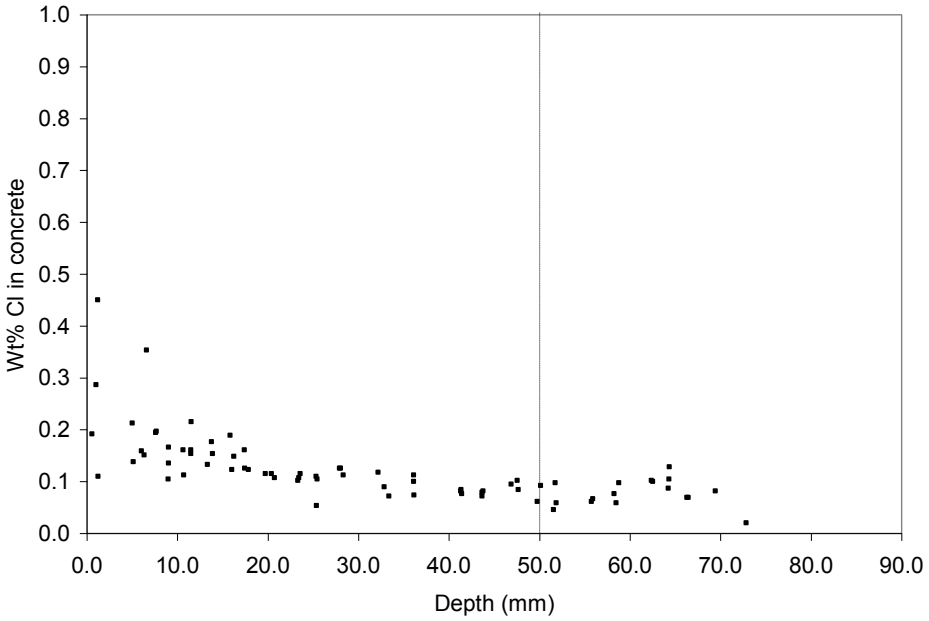

Figure A2.31. Chloride profile from billet prepared from core IA-3, directly adjacent to visible surface crack, dashed line marks the transition point between the concrete overlay and the original concrete below the overlay.

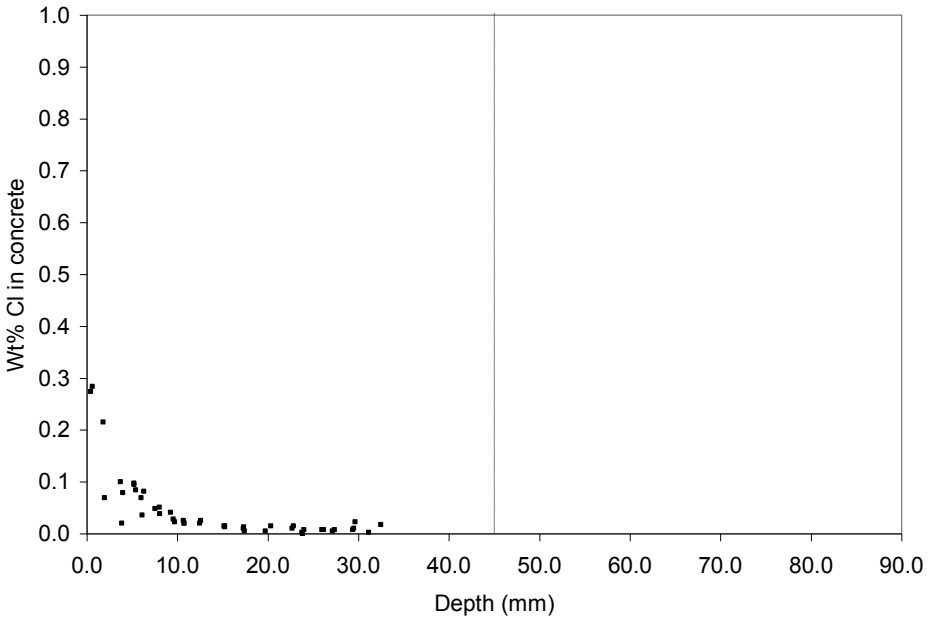

Figure A2.32. Chloride profile from billet prepared from core IA-11, dashed line marks the transition point between the concrete overlay and the original concrete below the overlay.

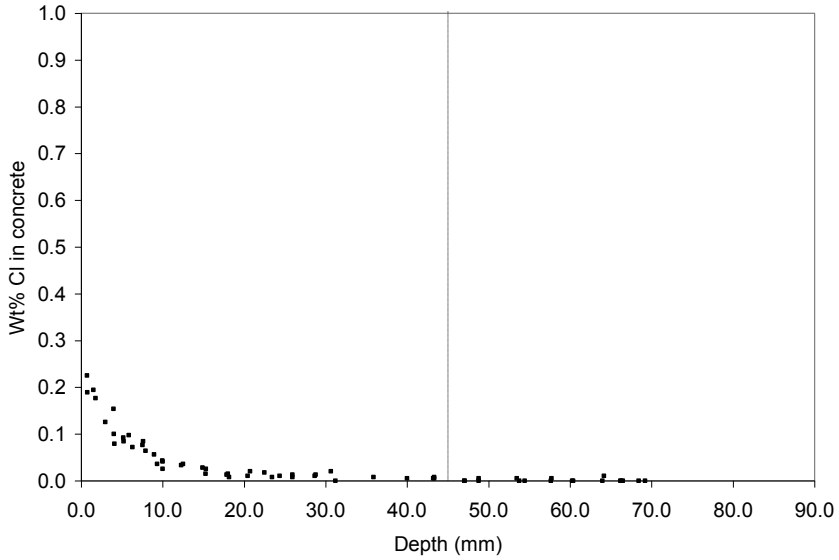

Figure A2.33. Duplicate chloride profile from additional billet prepared from core IA-11, dashed line marks the transition point between the concrete overlay and the original concrete below the overlay.

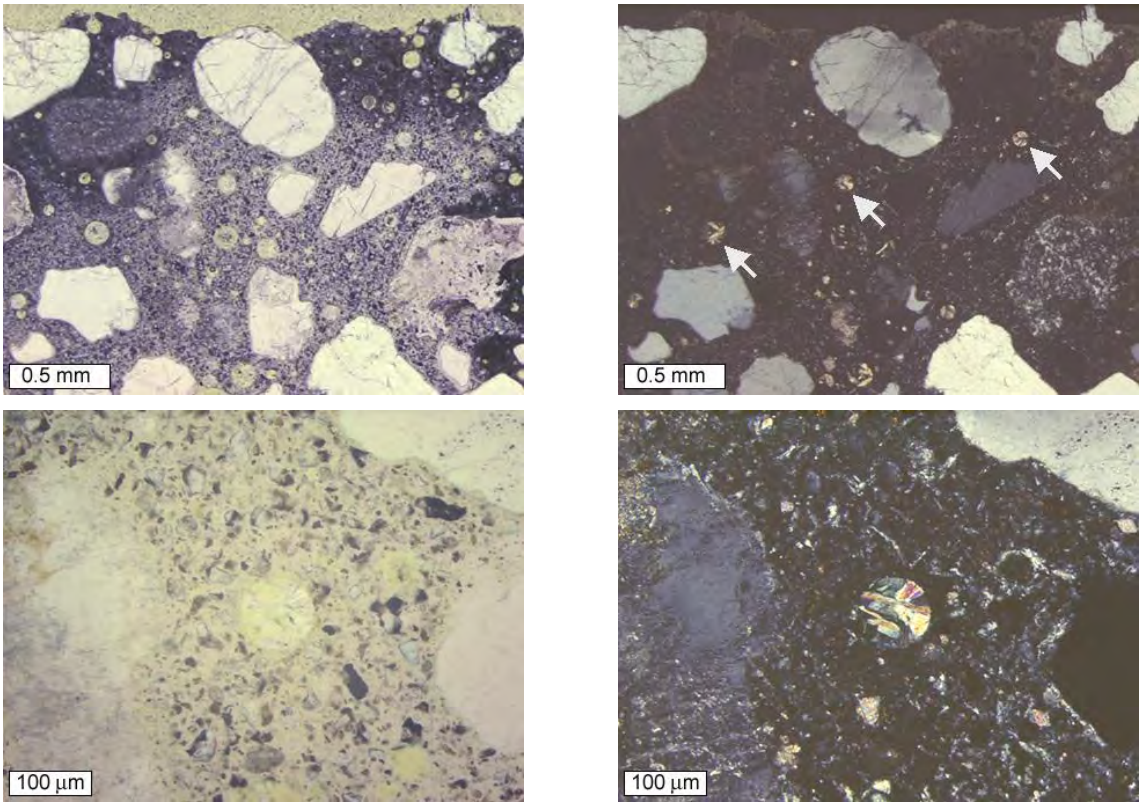

Figure A2.34. Transmitted light (left) and crossed-polars (right) images showing calcium hydroxide deposits in air voids just below the pavement wear surface. White arrows in crossed polars image indicate some of the filled voids.

Idaho, westbound Interstate Highway 184 west of Boise, near milepost 3.

This pavement was constructed in 1992 and is reported to have been exposed to $MgCl_2$ for anti-icing, and NaCl for deicing. Figure A2.35 shows the locations of the cores, which came from both the far left and far right lanes. Figures A2.36 through A2.39 show photographs of the cores. Cores were slabbed and polished from both lanes, both at the joint, and away from the joint. Figures A2.40 through A2.47 show the slabs as polished, after staining with phenolphthalein, and after treatment to enhance air voids and cracks. The phenolphthalein stain showed normal carbonation depths. The black and white treatment did not reveal any macro-cracking in any of the cores, except for one crack at depth in core IDR-7, as shown in Figure A2.45. Table A2.8 summarizes the air void parameters, which varied considerably, from a low spacing factor value of 0.118 mm for core IDR-3, to a high spacing factor value of 0.267 mm for core IDL-6. Figure A2.48 shows an example stereomicroscope image of the more borderline air void structure from core IDR-7, (spacing factor 0.238 mm). A *w/c* ratio estimation was performed on a thin section prepared from the top of core IDL-1. Figures A2.49 and A2.50 show the images used to make the measurements. The results of the *w/c* estimation are summarized in Table A2.9, with an average *w/c* value of 0.46 as compared to the 28-day moist cured mortar sample standards. Figures A2.51 through A2.54 show chloride profiles from cores IDL-1 (at joint) and IDL-5 (mid-panel). The profiles from core IDL-1 show increased chloride penetration as compared to the profiles from core IDL-5.

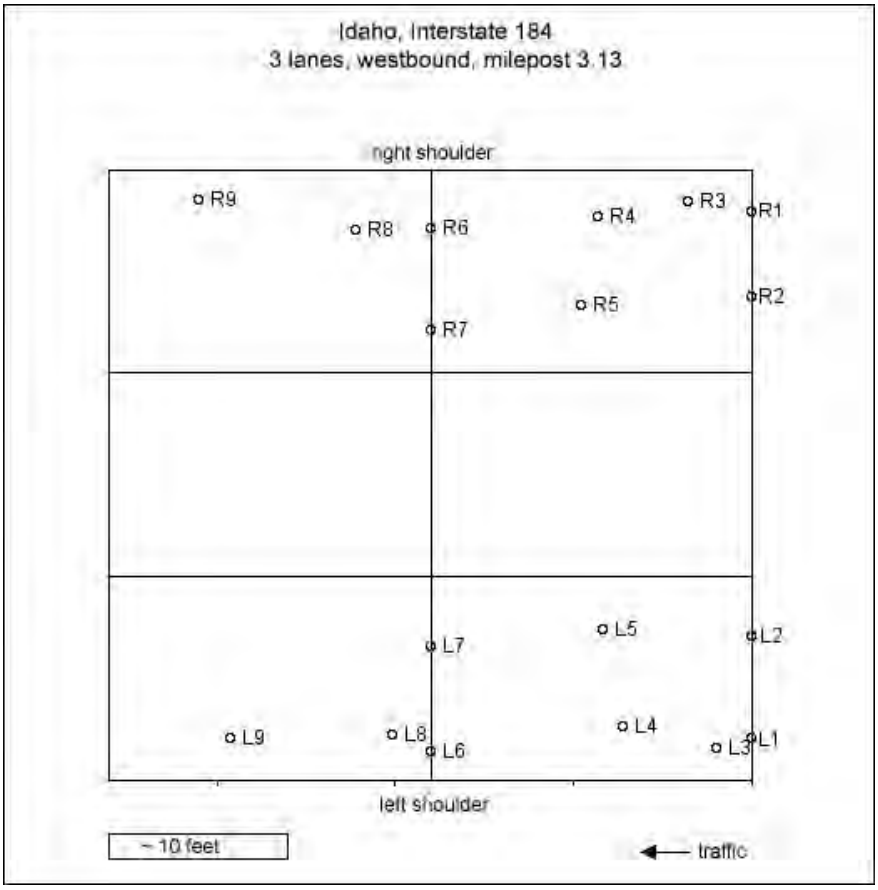

Figure A2.35. Diagram of core locations based on submitted field information.

Figure A2.36. Cores from left lane taken near pavement joints.

Figure A2.37. Cores from left lane taken away from pavement joints.

Figure A2.38. Cores from right lane taken near pavement joints.

Figure A2.39. Cores from right lane taken away from pavement joints.

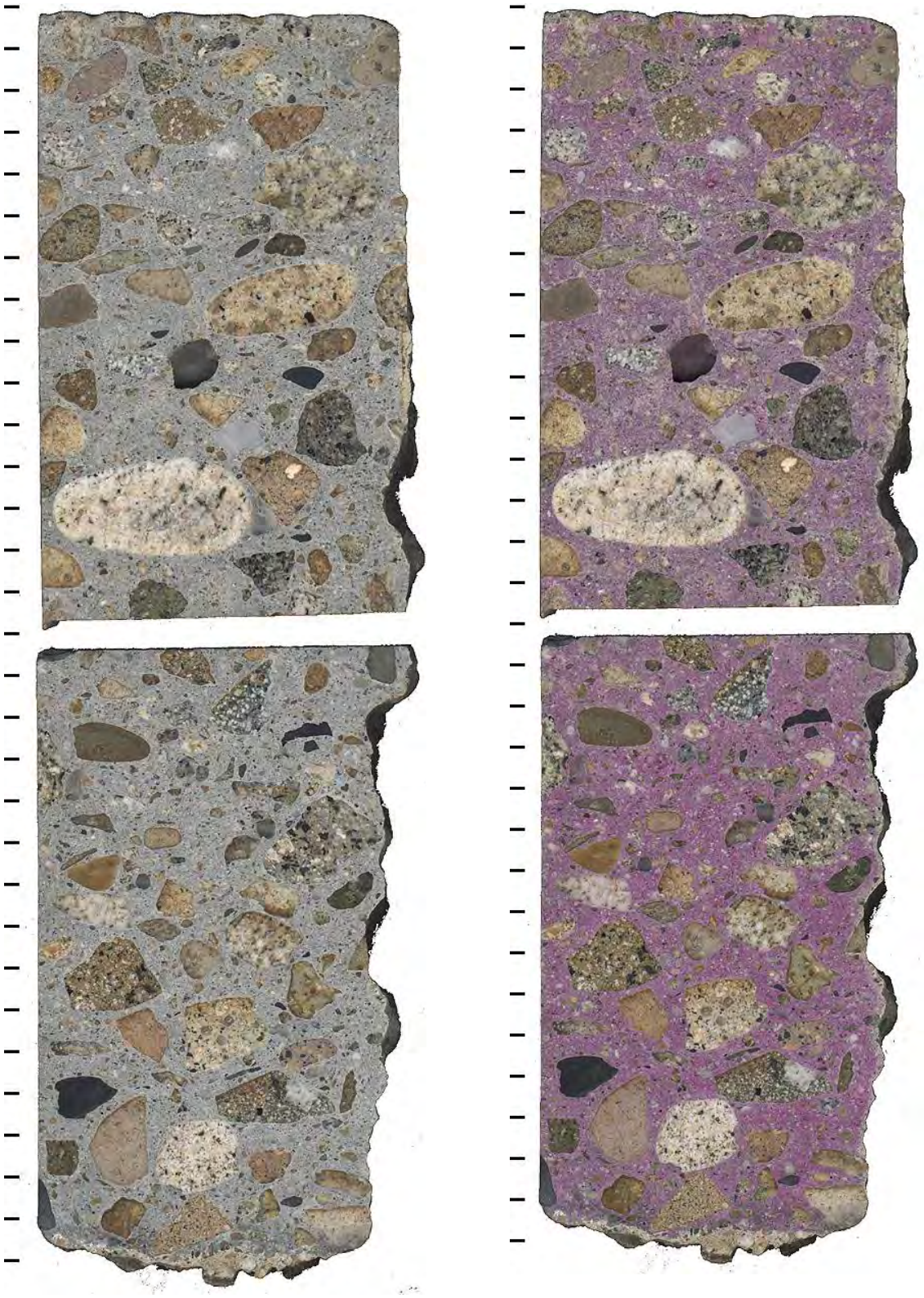

Figure A2.40. Polished slabs to show complete cross-section through core IDL-6 both before (left) and after application of phenolphthalein stain (right) tic marks every cm.

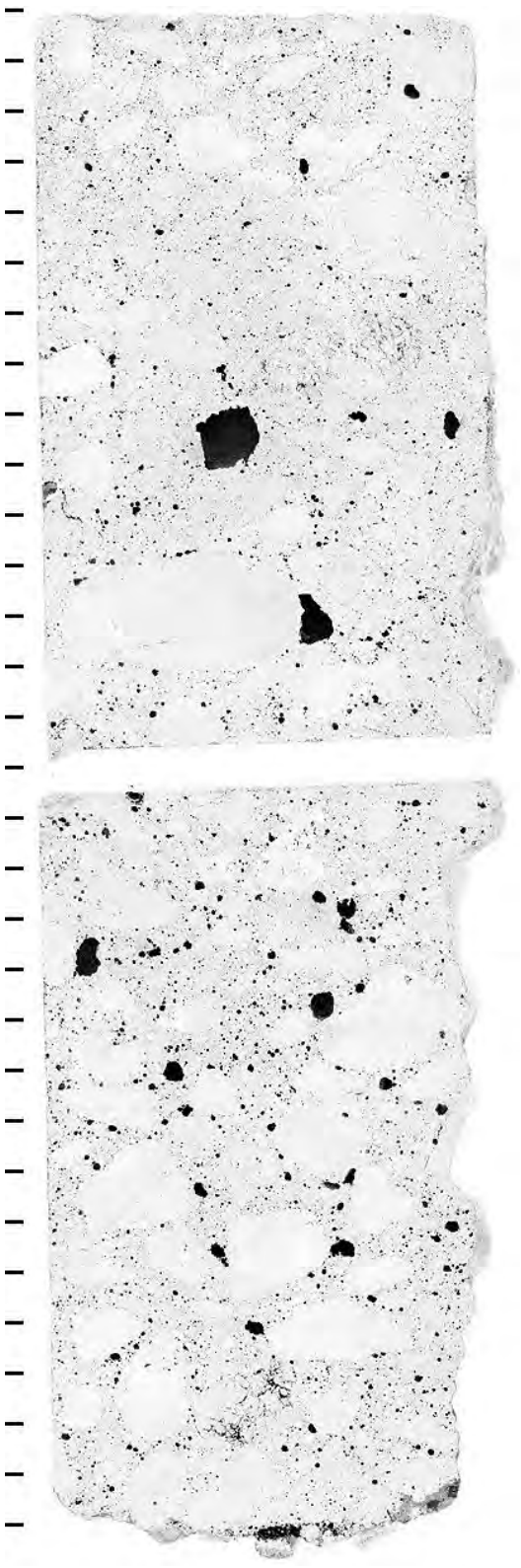

Figure A2.41. Polished slabs to show complete cross-section through core IDL-6 after treatment to enhance appearance of air voids and cracks, tic marks every cm.

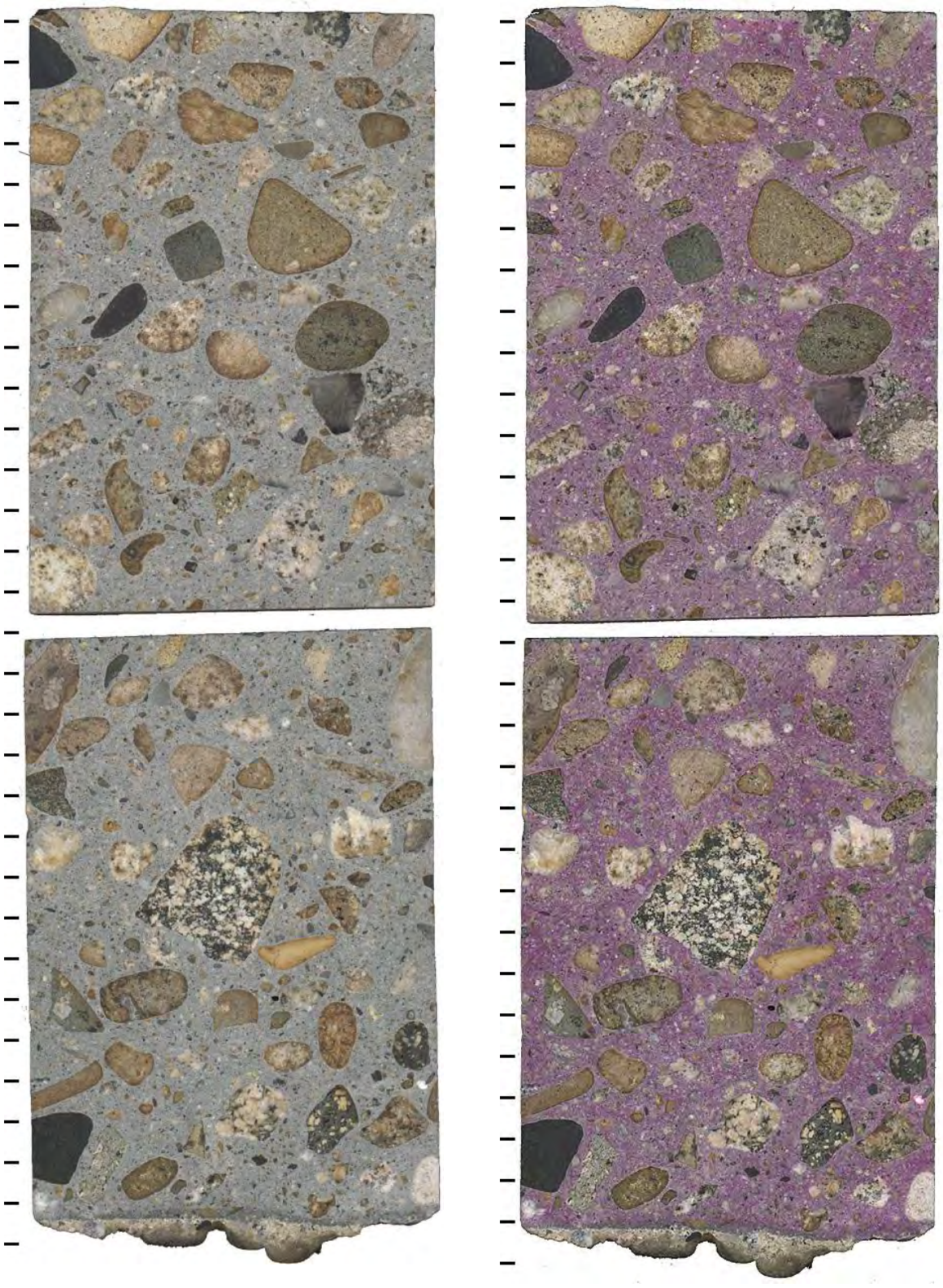

Figure A2.42. Polished slabs to show complete cross-section through core IDL-4 both before (left) and after application of phenolphthalein stain (right) tic marks every cm.

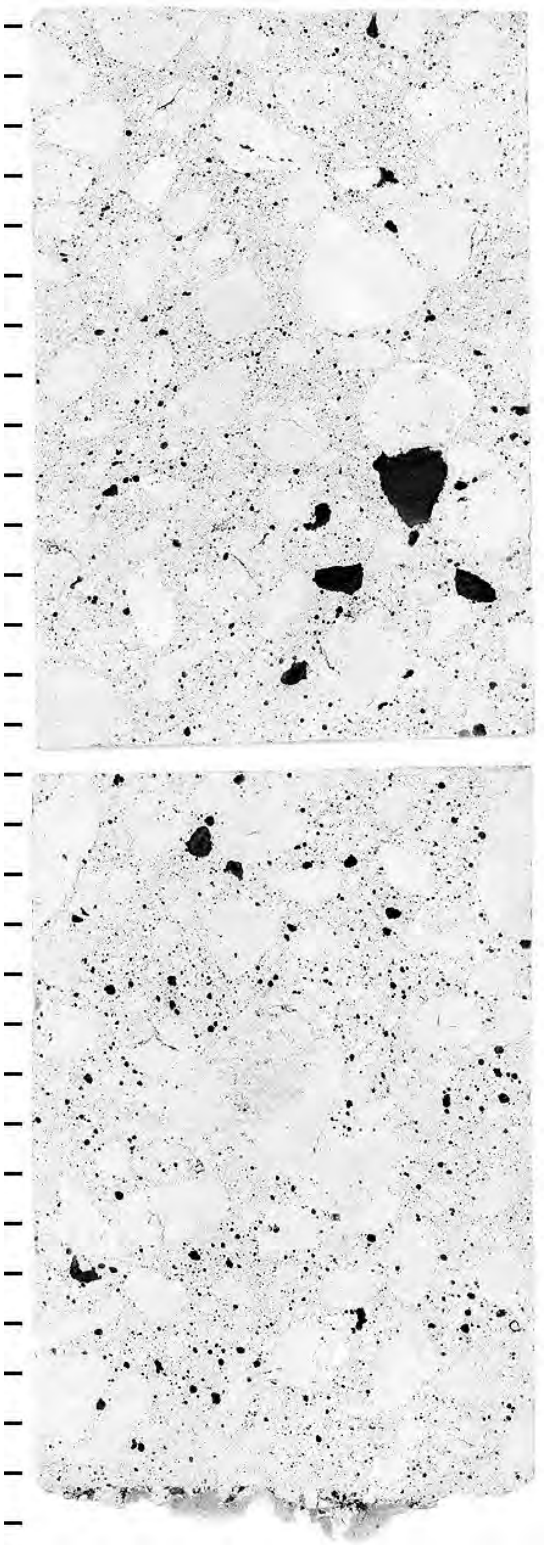

Figure A2.43. Polished slabs to show complete cross-section through core IDL-4 after treatment to enhance appearance of air voids and cracks, tic marks every cm.

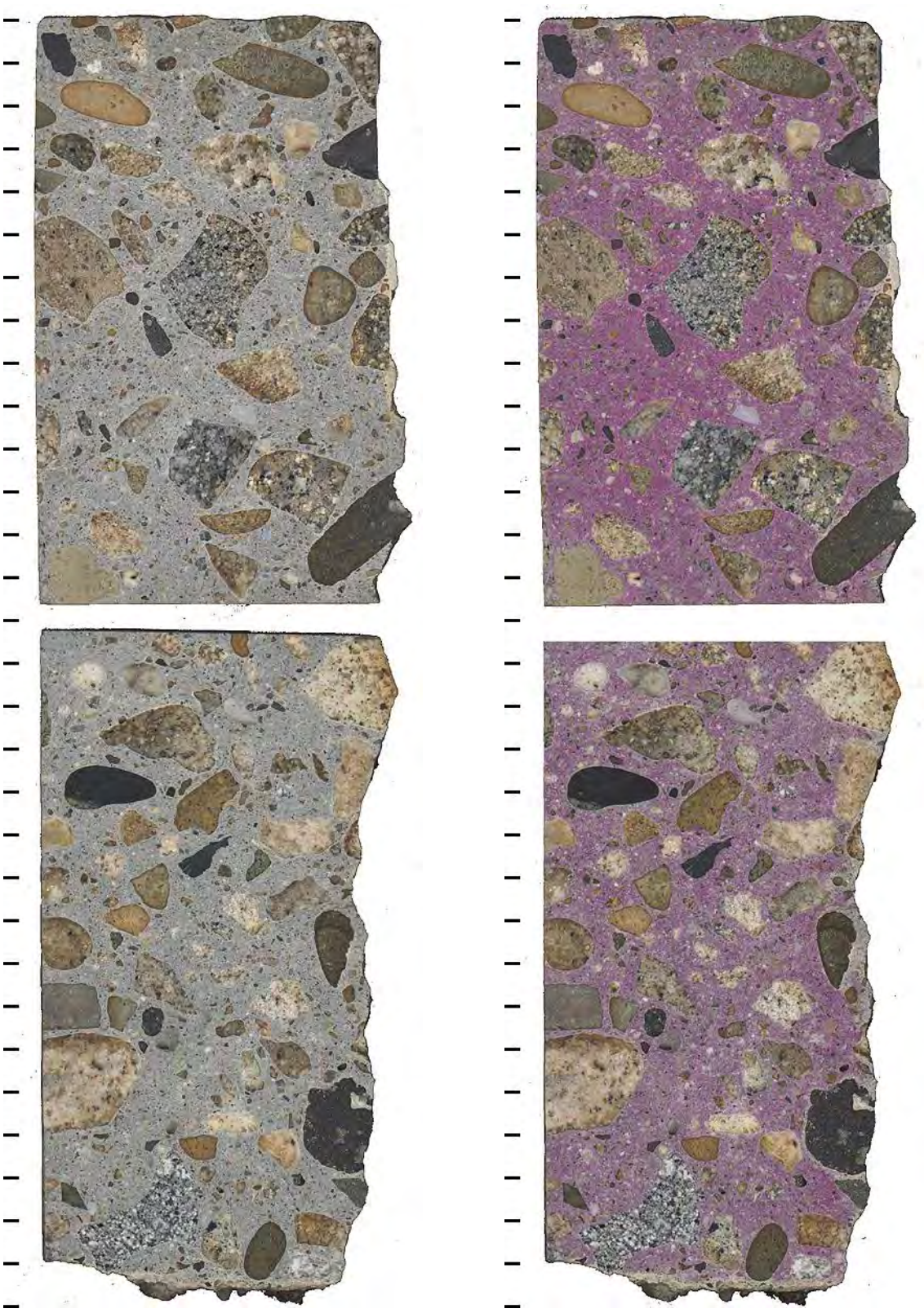

Figure A2.44. Polished slabs to show complete cross-section through core IDR-7 both before (left) and after application of phenolphthalein stain (right) tic marks every cm.

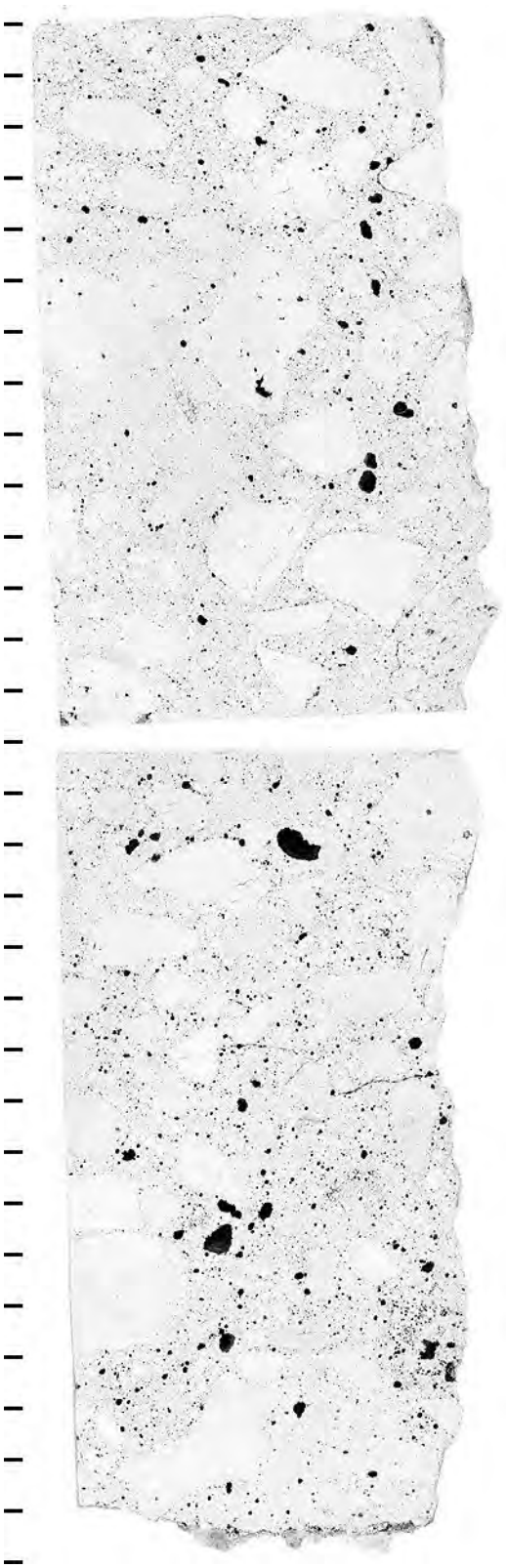

Figure A2.45. Polished slabs to show complete cross-section through core IDR-7 after treatment to enhance appearance of air voids and cracks, tic marks every cm.

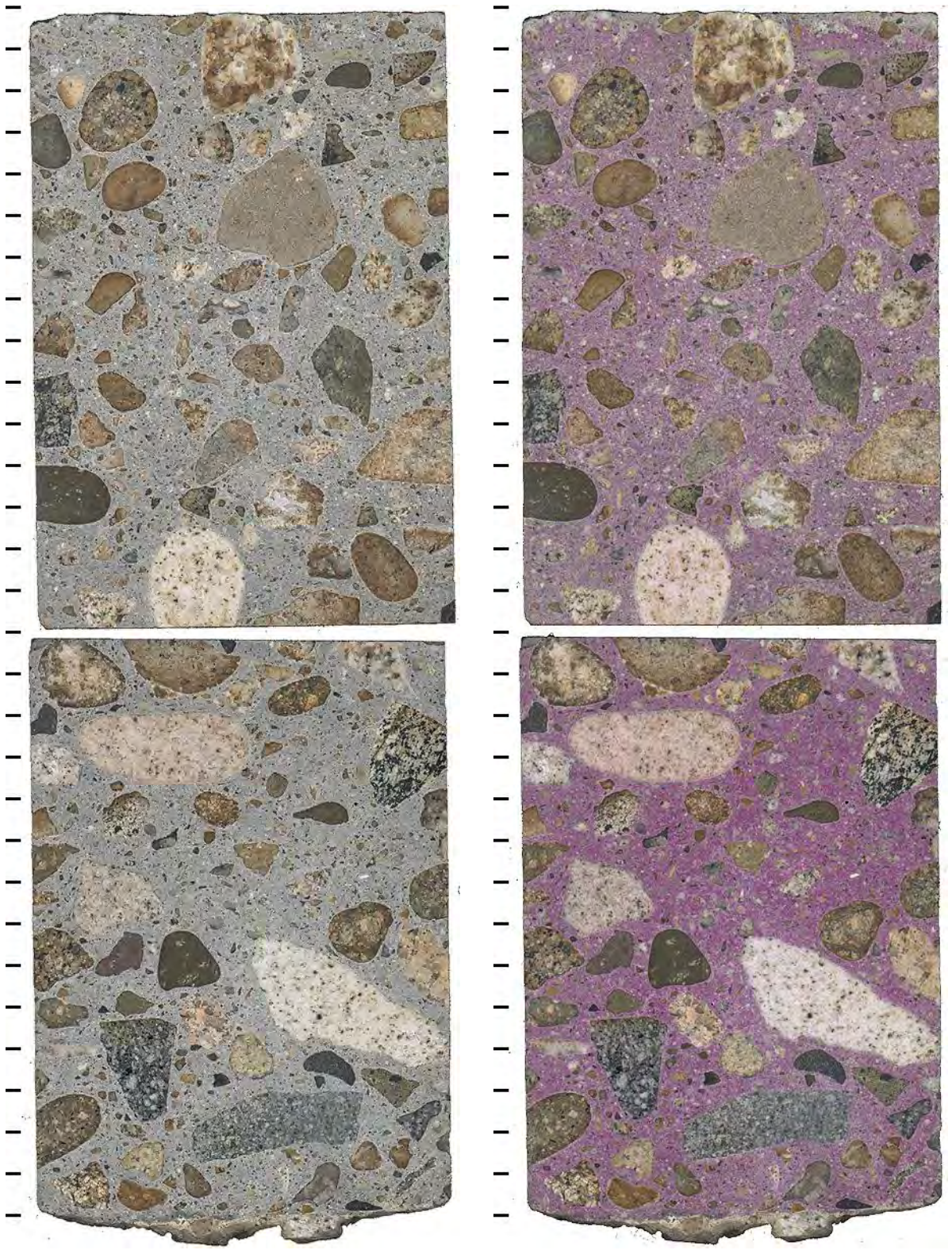

Figure A2.46. Polished slabs to show complete cross-section through core IDR-3 both before (left) and after application of phenolphthalein stain (right) tic marks every cm.

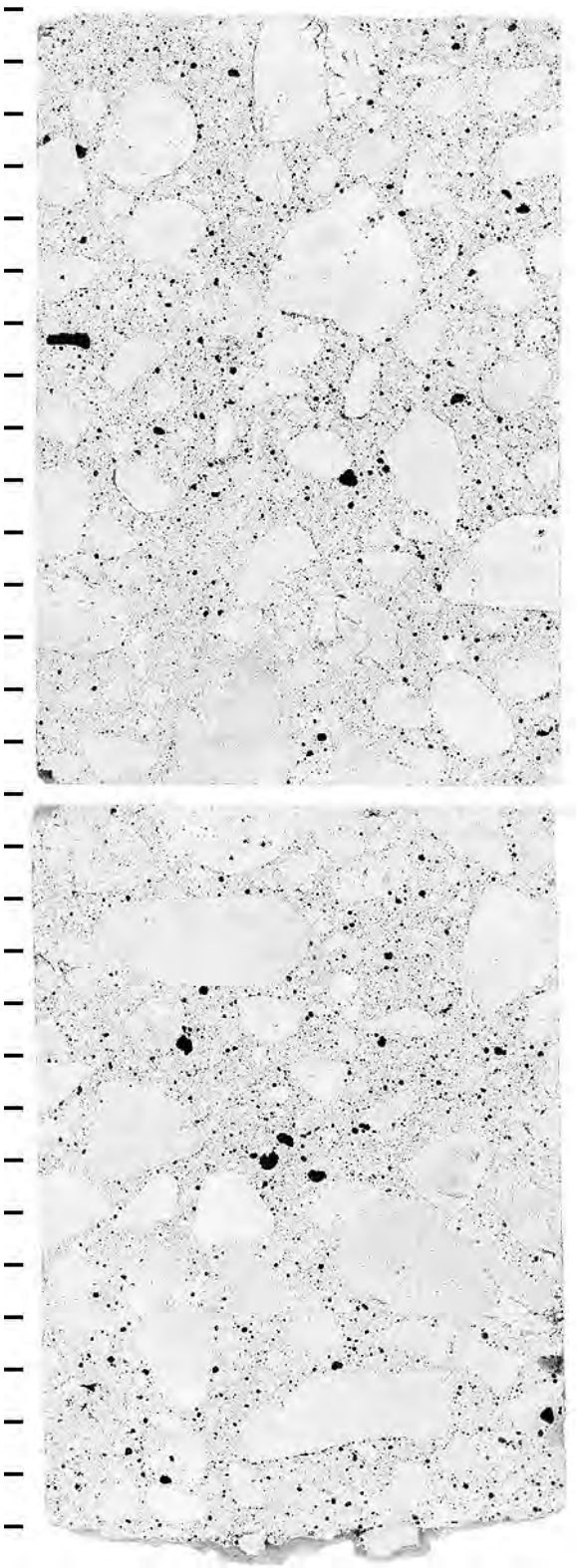

Figure A2.47. Polished slabs to show complete cross-section through core IDR-3 after treatment to enhance appearance of air voids and cracks, tic marks every cm.

Table A2.8. Air void parameters.

Sample ID	ID-L06	ID-L04	ID-R07	ID-R03
Location	Left-most lane, At joint	Left-most lane, Away from joint	Right-most lane, At joint	Right-most lane, Away from joint
Raw Data				
Total traverse length (mm)	3931.1	3931.1	3931.1	3931.1
Area analyzed (cm^2)	77.0	77.0	77.0	77.0
Air stops	102	143	100	152
Paste stops	365	358	433	353
Aggregate stops	1038	1004	972	1000
Secondary deposit stops	0	0	0	0
Total stops	1505	1505	1505	1505
Number of air intercepts	875	1630	1178	1949
Number of filled void intercepts	18	0	10	1
Results				
Air vol%	6.8	9.5	6.6	10.1
Paste vol%	24.3	23.8	28.8	23.5
Aggregate vol%	69.0	66.7	64.6	66.4
Secondary deposit vol%	0.0	0.0	0.0	0.0
Existing average chord length (mm)	0.304	0.229	0.222	0.204
Existing paste/air ratio	3.6	2.5	4.3	2.3
Existing air void specific surface (mm^{-1})	13.1	17.5	18.0	19.6
Existing air void frequency (voids/m)	223	415	300	496
Existing spacing factor (mm)	0.272	0.143	0.240	0.118
Original average chord length (mm)	0.298	0.229	0.220	0.204
Original paste/air ratio	3.6	2.5	4.3	2.3
Original air void specific surface (mm^{-1})	13.4	17.5	18.2	19.6
Original air void frequency (voids/m)	227	415	302	496
Original spacing factor (mm)	0.267	0.143	0.238	0.118

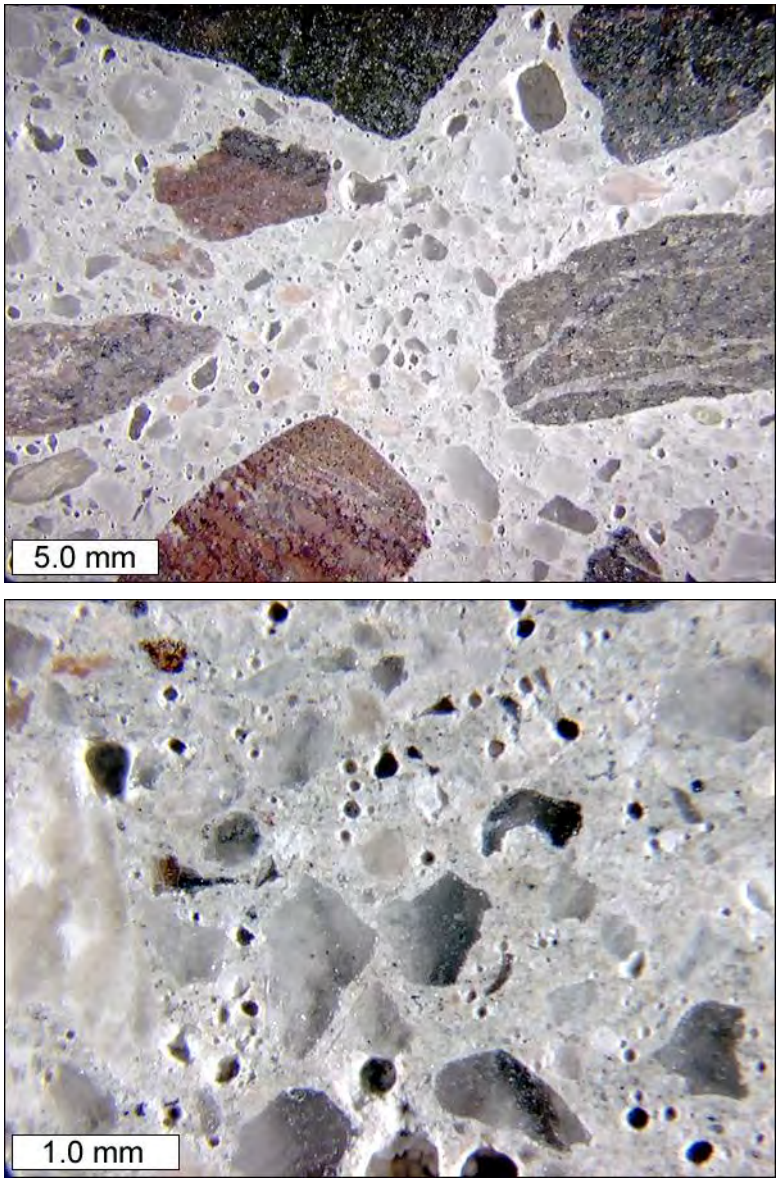

Figure A2.48. Stereo microscope images to show air void structure on polished slab from core IDR-7.

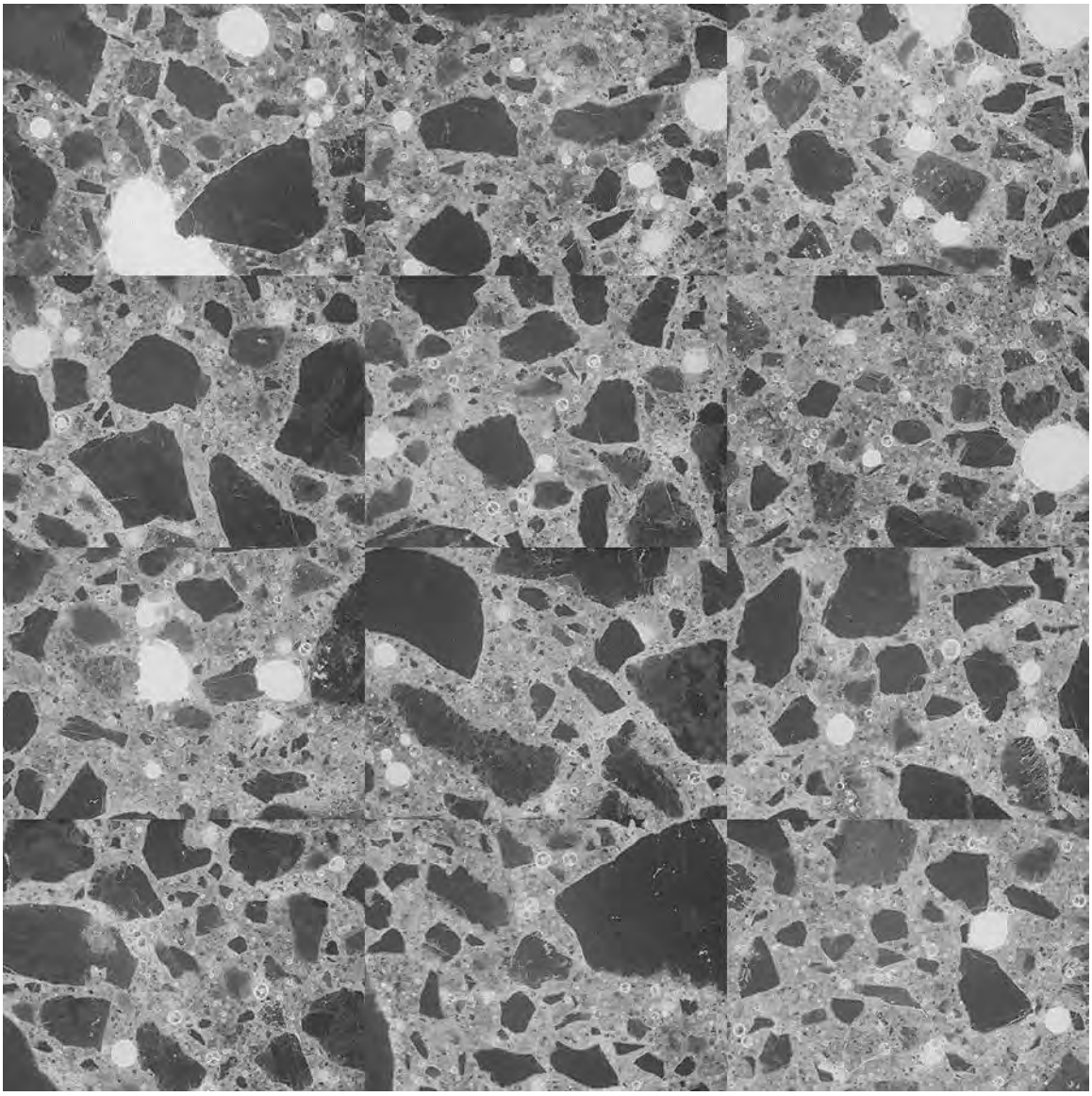

Figure A2.49. Mosaic of 12 frames collected from thin section prepared from billet cut from top portion of core IDL-1 (each individual frame measures 2.612 x 1.959 mm).

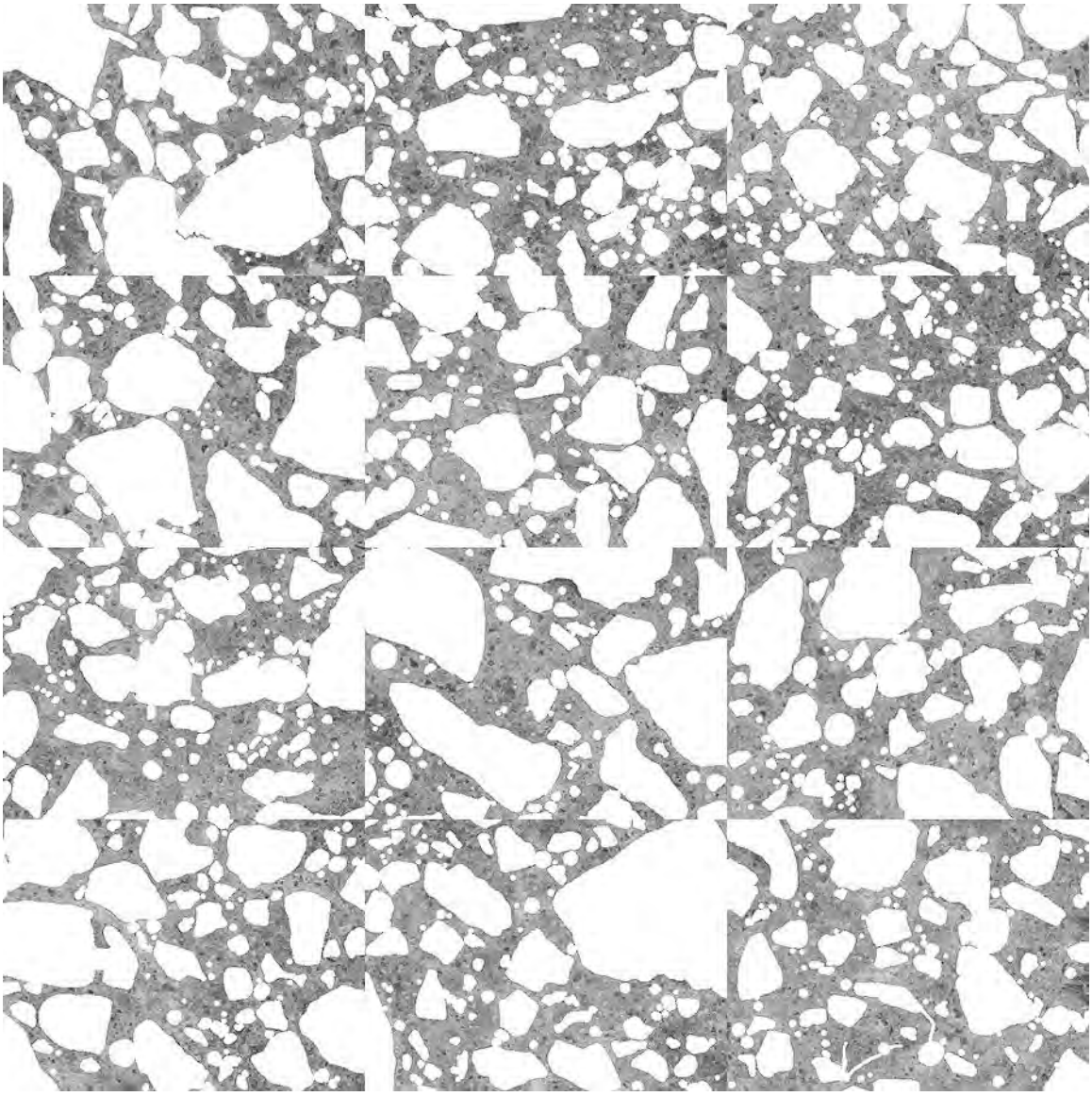

Figure A2.50. Mosaic of 12 frames collected from thin section prepared from billet cut from top portion of core IDL-1 after masking out air voids and fine aggregate to isolate cement paste (each individual frame measures 2.612 x 1.959 mm).

Table A2.9. Average cement paste pixel intensities per frame, and equivalent *w/c* values (as compared to 28-day moist cured mortar samples).

Cement Paste Pixel Fluorescence Measurements (average intensity per frame)			
90	88	105	105
101	86	99	98
105	98	99	104
equivalent *w/c* (y = 0.0044x + 0.0329)			
0.43	0.42	0.49	0.49
0.47	0.41	0.47	0.46
0.49	0.46	0.47	0.49

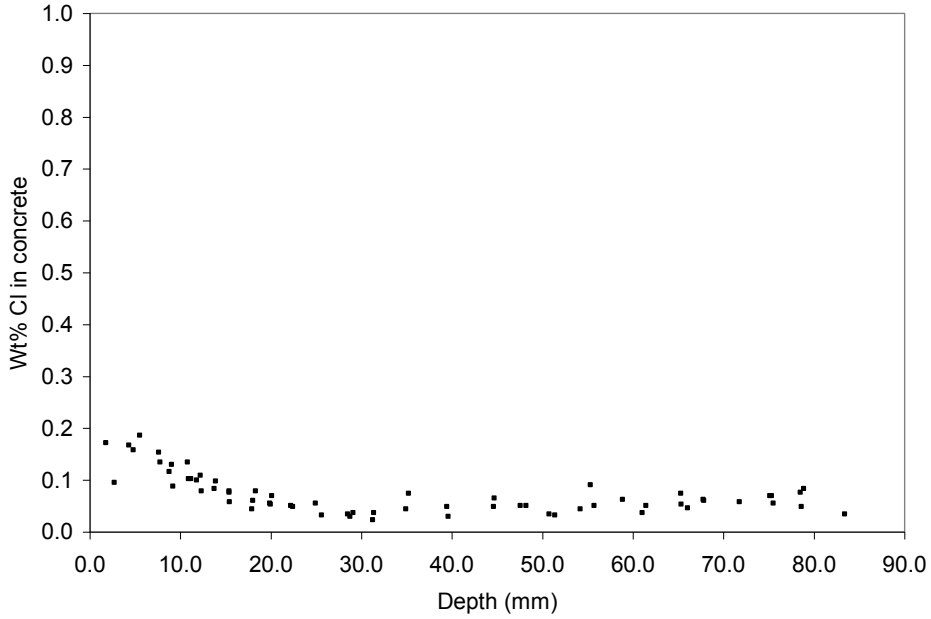

Figure A2.51. Chloride profile from billet prepared from core IDL-1, immediately adjacent to joint.

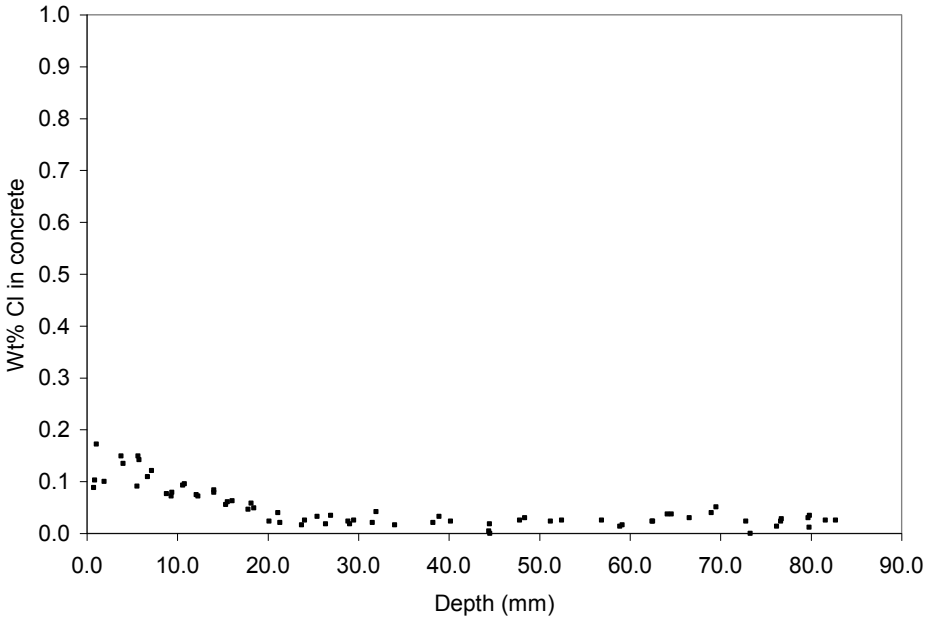

Figure A2.52. Chloride profile from billet prepared from core IDL-1, 25 mm away from joint.

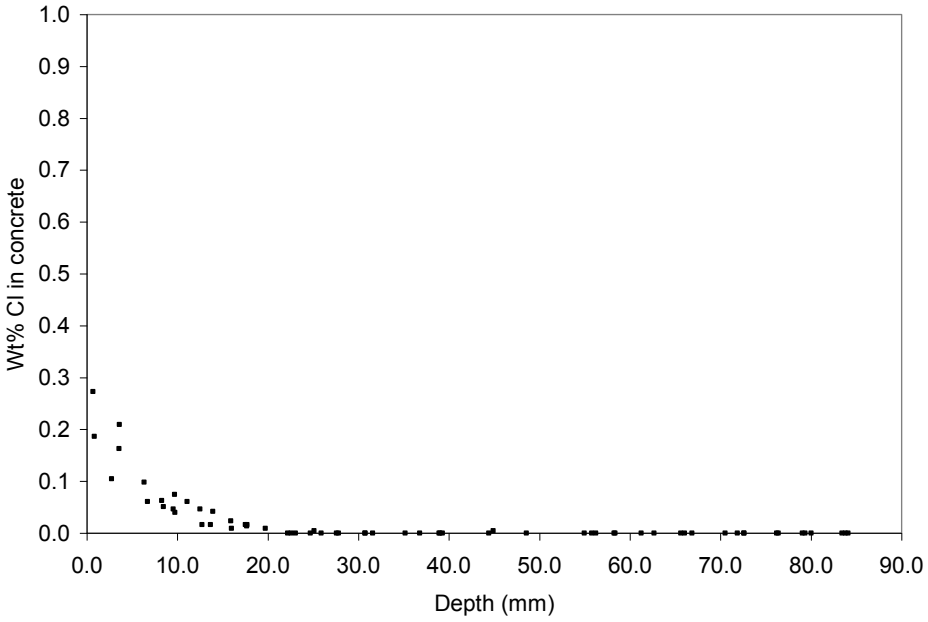

Figure A2.53. Chloride from billet prepared from core IDL-5, mid-panel.

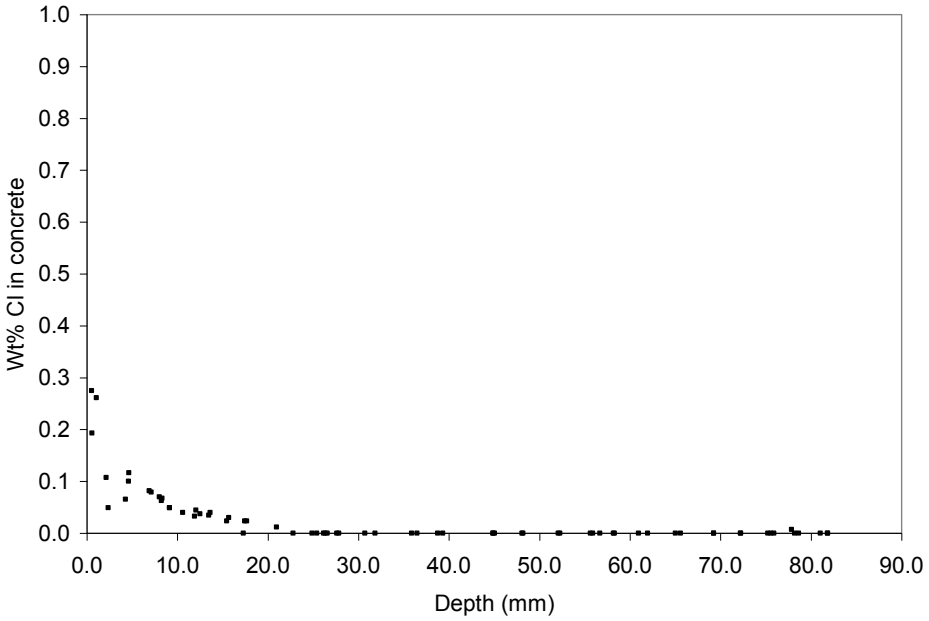

Figure A2.54. Duplicate chloride from additional billet prepared from core IDL-5, mid-panel.

Montana, westbound Interstate Highway 90 bridge deck near milepost 117

Partial depth cores 5 to 6 inches in depth were received from this bridge deck. The top 2 inches of the cores consisted of a latex modified concrete overlay. The deck is reported to have been exposed to $MgCl_2$ for anti-icing, and NaCl for deicing. Figure A2.55 shows the locations of the cores, and Figure A2.56 shows an incomplete series of photographs of the cores as received. Figure A2.57 shows the variation in surface wear observed on some of the cores. Two of the cores were cut into slabs and polished: core MT-2 and core MT-8. Figures A2.58 through A2.60 show the slabs as polished, after staining with phenolphthalein, and after treatment to enhance air voids and cracks. The phenolphthalein stain showed normal carbonation depths. The black and white treatment did not reveal any macro-cracking in either of the cores. Table A2.10 summarizes the air void parameters. The overlay from both slabs exhibited inadequate entrained air parameters, with spacing factors of 0.432 mm and 0.687 mm for cores MT-2 and MT-8 respectively. However, considering the extreme density of the cement paste, air entrainment is not likely a requirement for the latex-modified overlay. Figure A2.61 shows an example stereomicroscope image of the air void structure. A *w/c* ratio estimation was performed on a thin section prepared from the top concrete overlay portion and from the original concrete portion of core MT-3. Figures A2.62 through A2.65 show the images used to make the measurements. The results of the *w/c* estimations are summarized in Tables A2.11 and A2.12, with an average *w/c* value of 0.13 for the overlay, and an average *w/c* value of 0.42 for the original concrete. The unusual *w/c* value of 0.13 should not be interpreted as an accurate measure of the actual *w/c*, but rather as a comparison to the 28-day moist cured straight portland cement mortar standards. Figures A2.66 through A2.69 show chloride profiles collected from core MT-1 and core MT-3. The transition from overlay to original concrete is apparent in the profiles, and it appears that there is some diffusion of chlorine from the original concrete up into the base of the overlay.

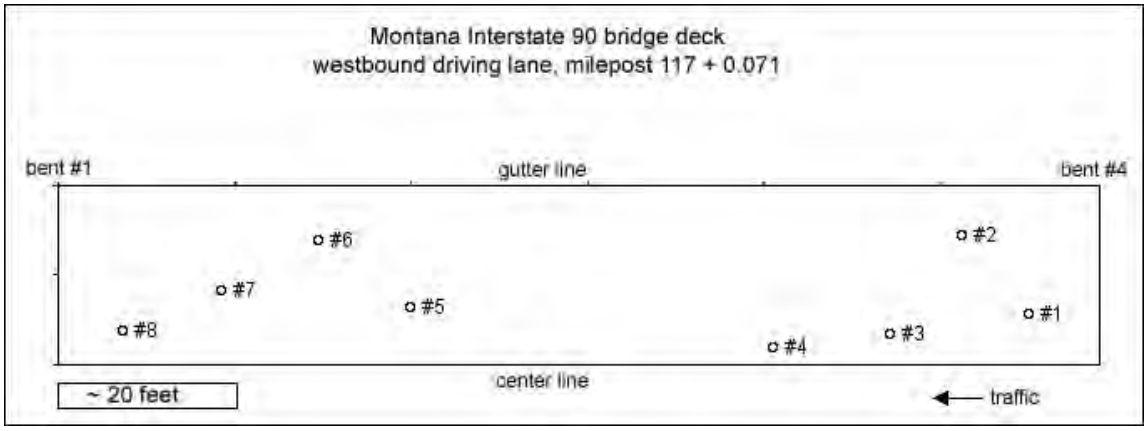

Figure A2.55. Diagram to show core locations based on submitted field information.

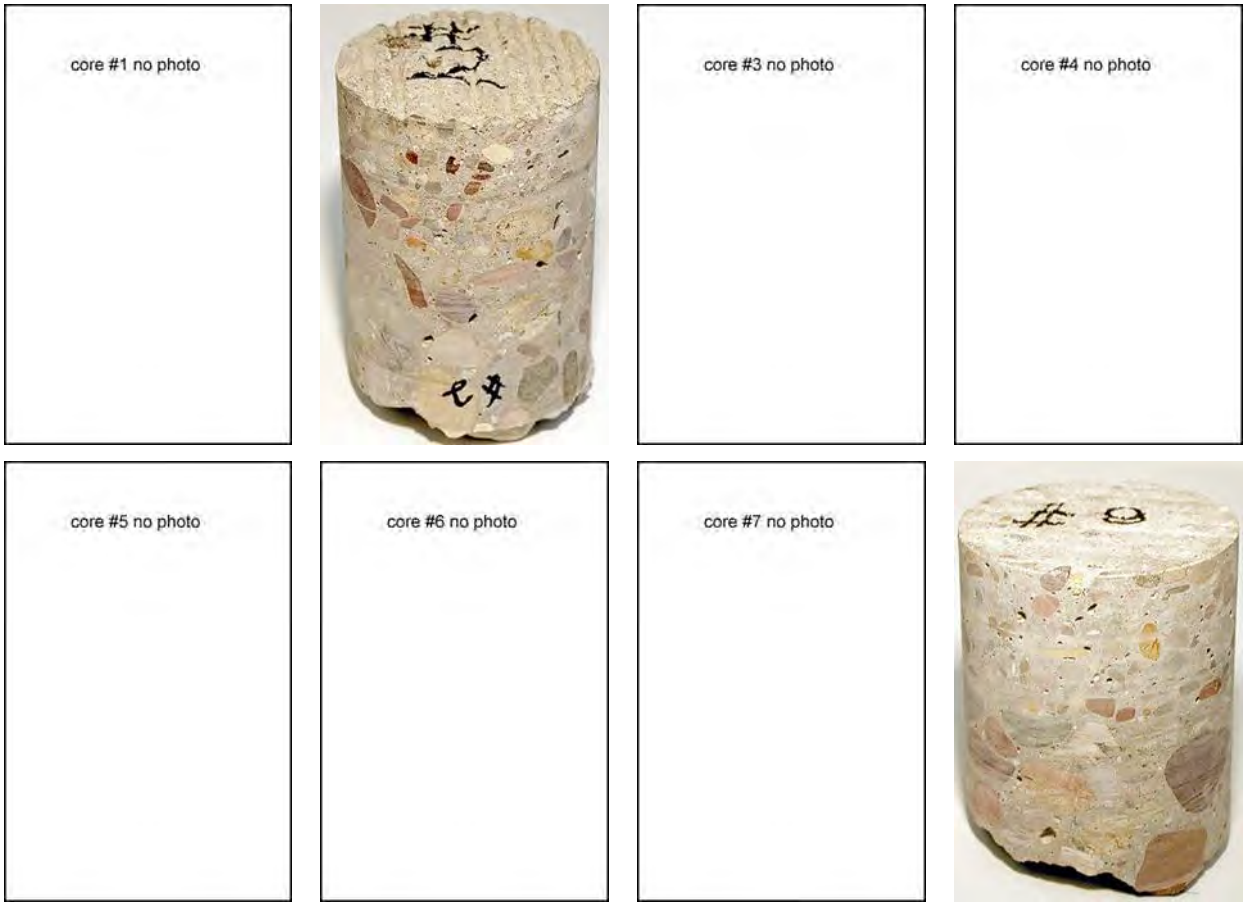

Figure A2.56. Photographs of cores.

Figure A2.57. Photograph to show variation in surface wear from core to core.

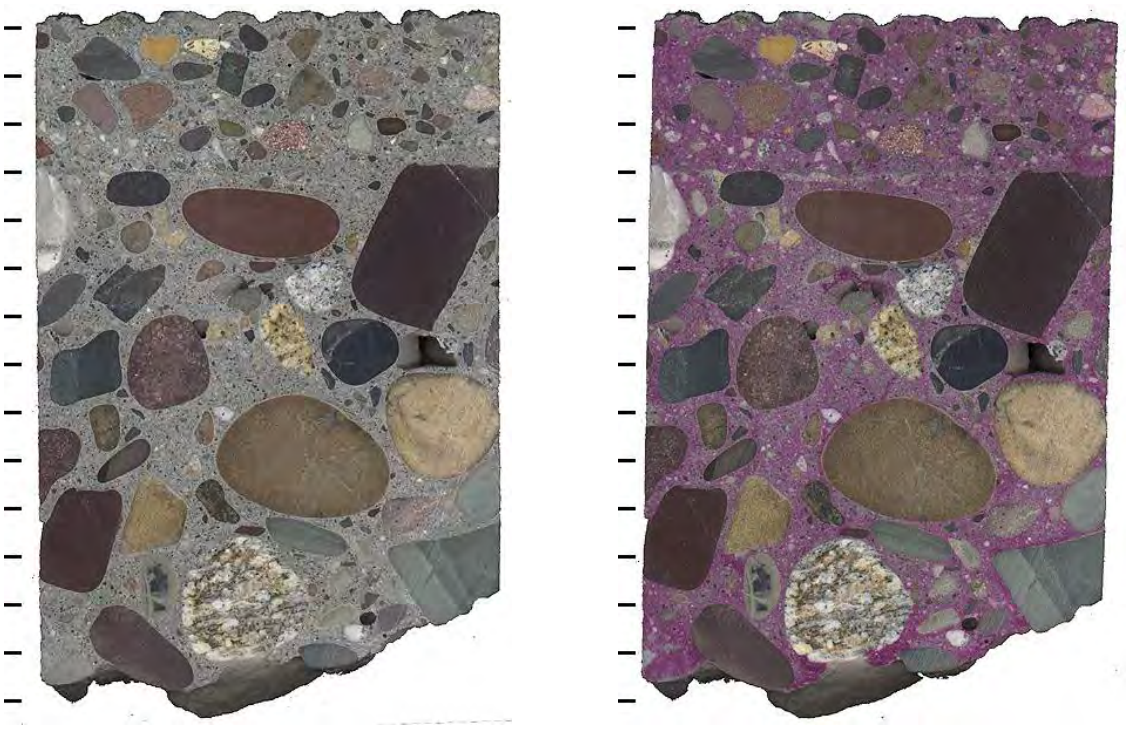

Figure A2.58. Polished slabs to show complete cross-section through core MT-2 both before (left) and after application of phenolphthalein stain (right) tic marks every cm.

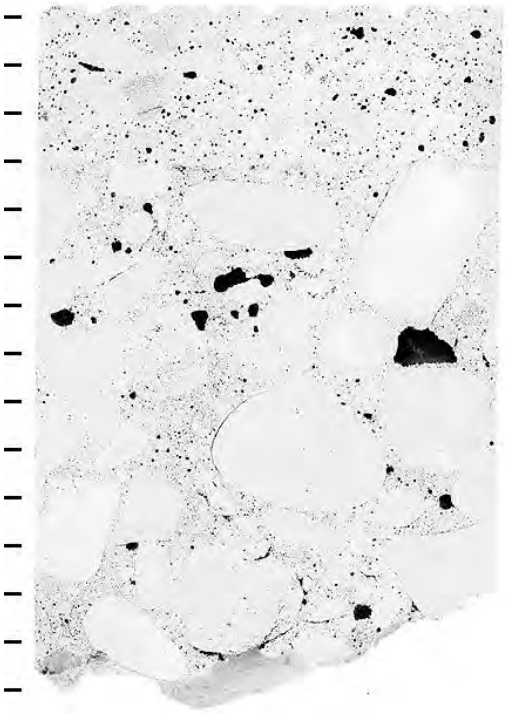

Figure A2.59. Polished slabs to show complete cross-section through core MT-2 after treatment to enhance appearance of air voids and cracks, tic marks every cm.

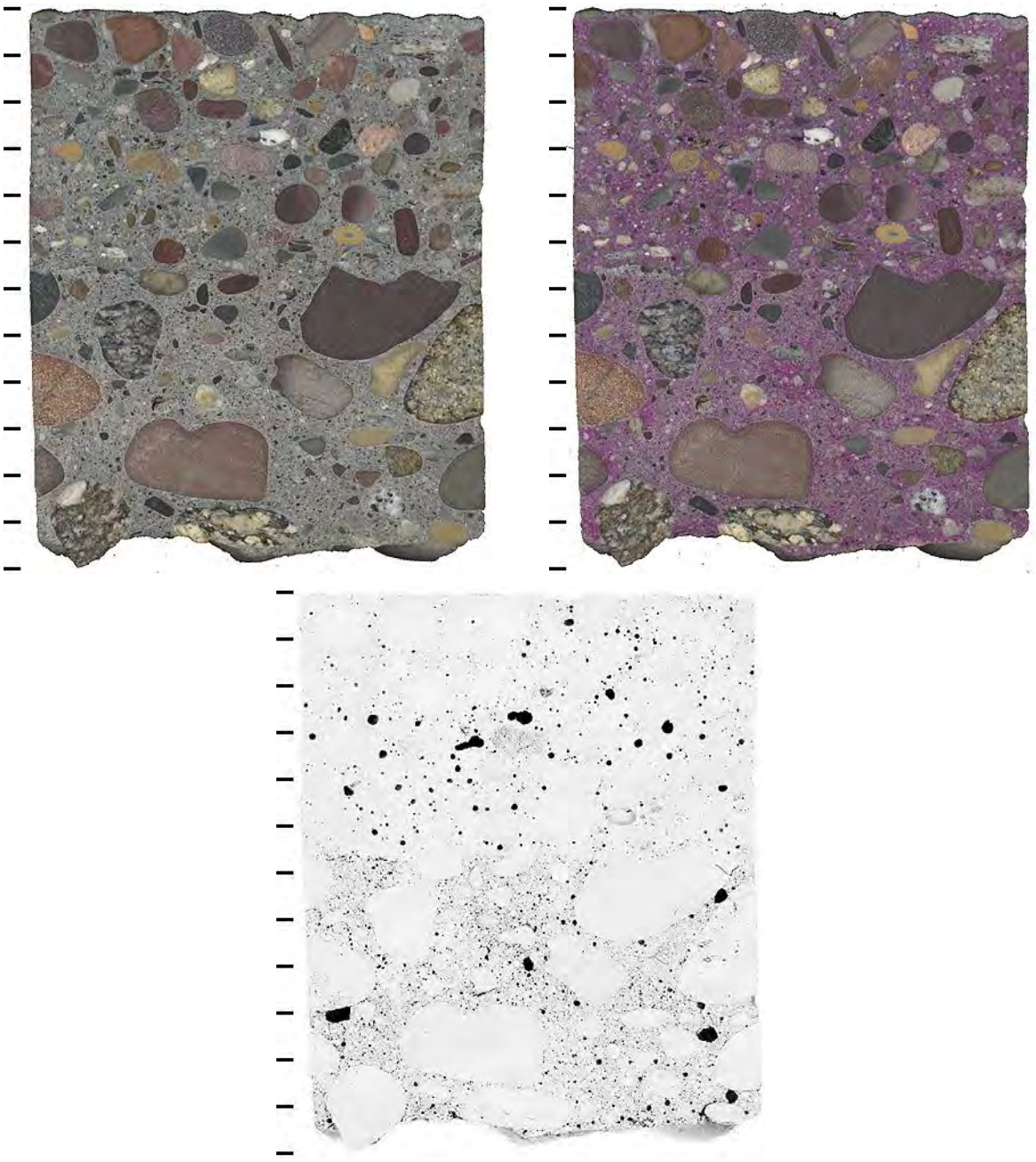

Figure A2.60. Polished slabs to show complete cross-section through core MT-8, before (upper left) and after application of phenolphthalein stain (upper right) and after treatment to enhance appearance of air voids and cracks (bottom) tic marks every cm.

Table A2.10. Air void parameters from concrete overlay.

Sample ID	MT-02	MT-08
Location	Tining Intact	Tining Worn
Raw Data		
Total traverse length (mm)	3400.8	3408.7
Area analyzed (cm^2)	66.6	66.8
Air stops	47	43
Paste stops	419	424
Aggregate stops	833	836
Secondary deposit stops	3	2
Total stops	1302	1305
Number of air intercepts	419	234
Number of filled void intercepts	24	30
Results		
Air vol%	3.6	3.3
Paste vol%	32.2	32.5
Aggregate vol%	64.2	64.2
Secondary deposit vol%	0.2	0.2
Existing average chord length (mm)	0.293	0.480
Existing paste/air ratio	9.0	9.9
Existing air void specific surface (mm^{-1})	13.7	8.3
Existing air void frequency (voids/m)	123	69
Existing spacing factor (mm)	0.443	0.758
Original average chord length (mm)	0.295	0.445
Original paste/air ratio	8.4	9.4
Original air void specific surface (mm^{-1})	13.6	9.0
Original air void frequency (voids/m)	130	77
Original spacing factor (mm)	0.432	0.687

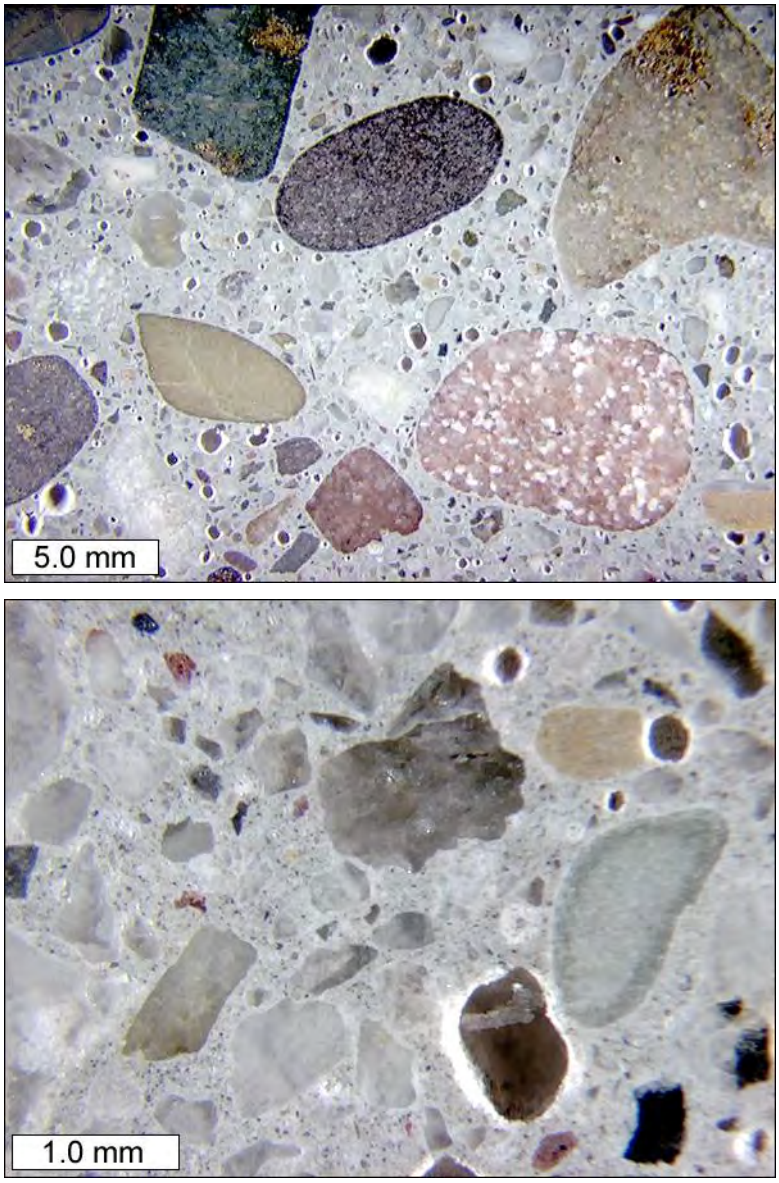

Figure A2.61. Stereo microscope images to show air void structure of concrete overlay on polished slab from core MT-2.

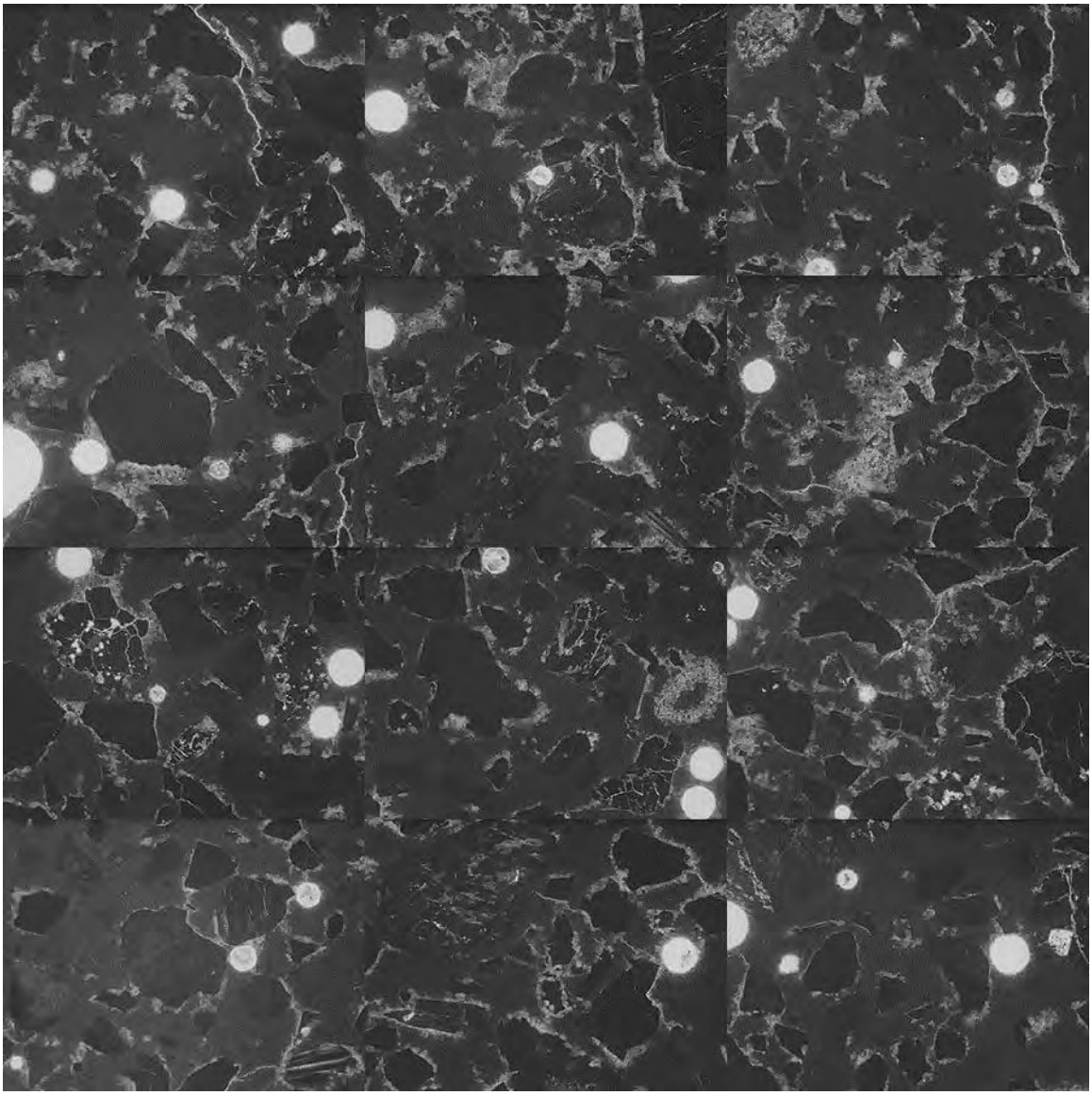

Figure A2.62. Mosaic of 12 frames collected from thin section prepared from billet cut from top portion of concrete overlay, core MT-3 (each individual frame measures 2.612 x 1.959 mm).

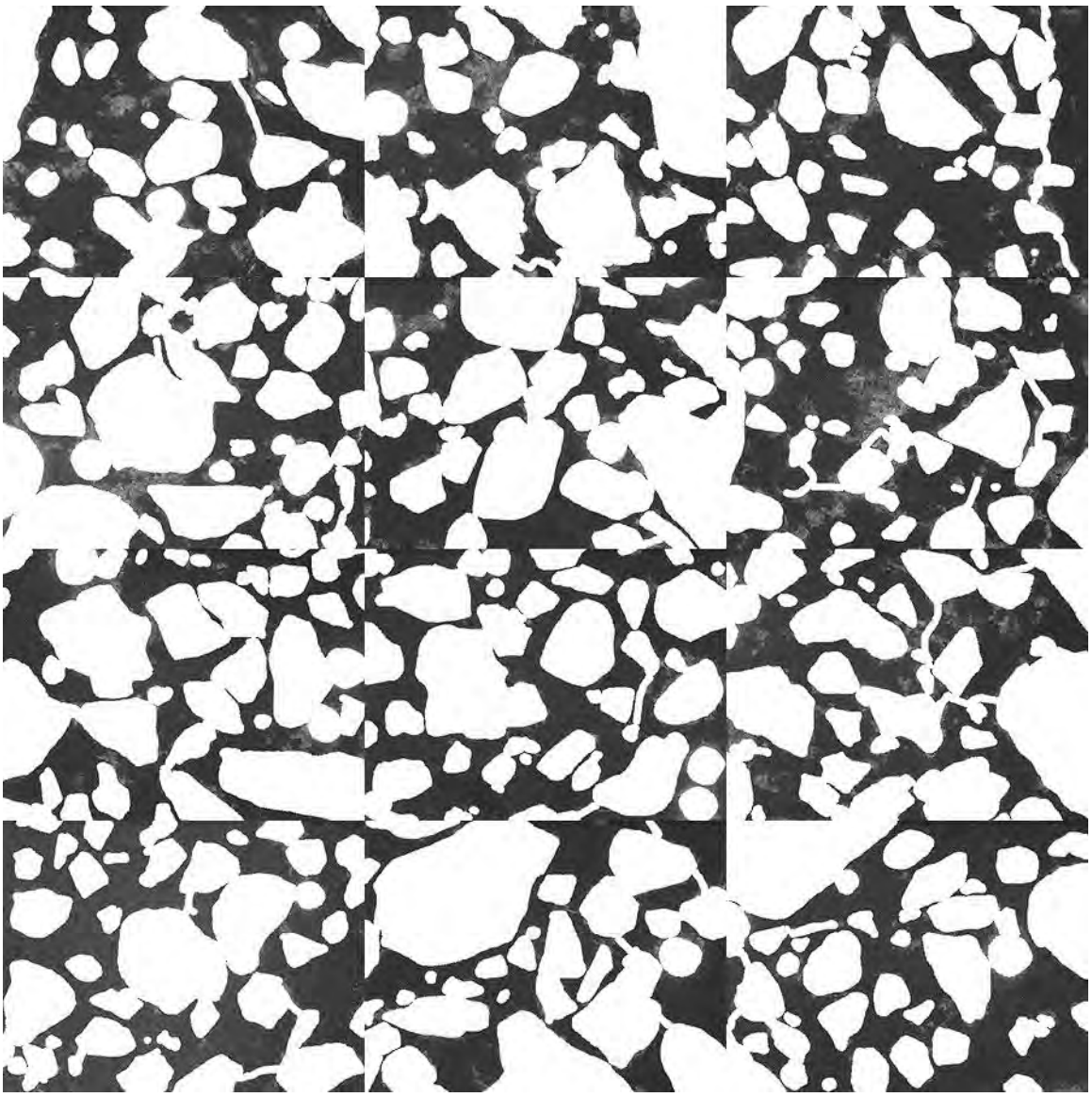

Figure A2.63. Mosaic of 12 frames collected from thin section prepared from billet cut from top portion of concrete overlay, core MT-3, after masking out air voids, fine aggregate, and micro-cracks to isolate cement paste (each individual frame measures 2.612 x 1.959 mm).

Table A2.11. Average cement paste pixel intensities per frame, and equivalent *w/c* values (as compared to 28-day moist cured mortar samples) from concrete overlay, core MT-3.

Cement Paste Pixel Fluorescence Measurements (average intensity per frame)			
23	23	20	25
20	23	20	19
21	24	18	19
equivalent *w/c* ($y = 0.0044x + 0.0329$)			
0.13	0.14	0.12	0.14
0.12	0.13	0.12	0.12
0.13	0.14	0.11	0.12

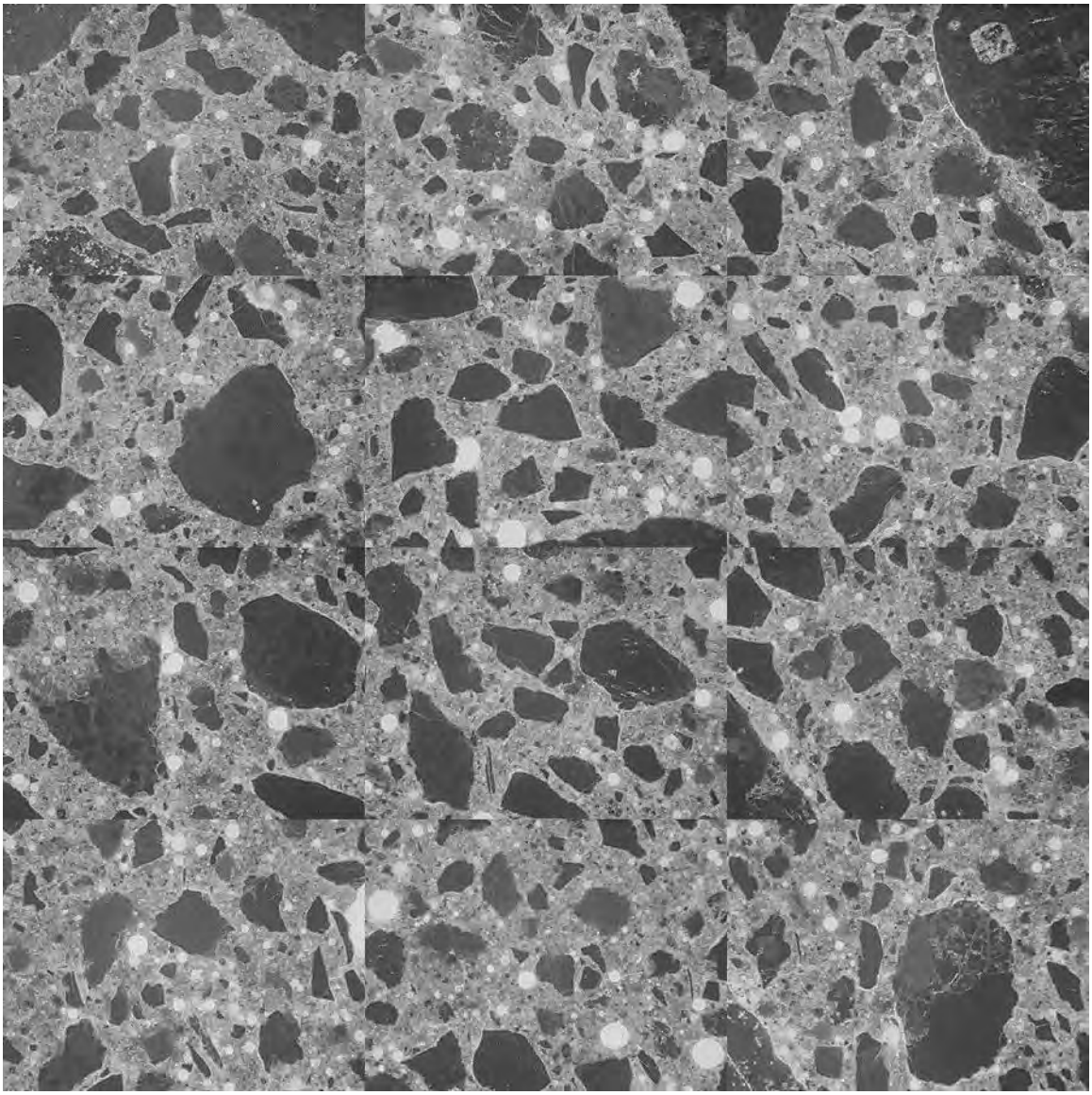

Figure A2.64. Mosaic of 12 frames collected from area of thin section representing the original concrete below the concrete overlay, core MT-3 (each individual frame measures 2.612 x 1.959 mm).

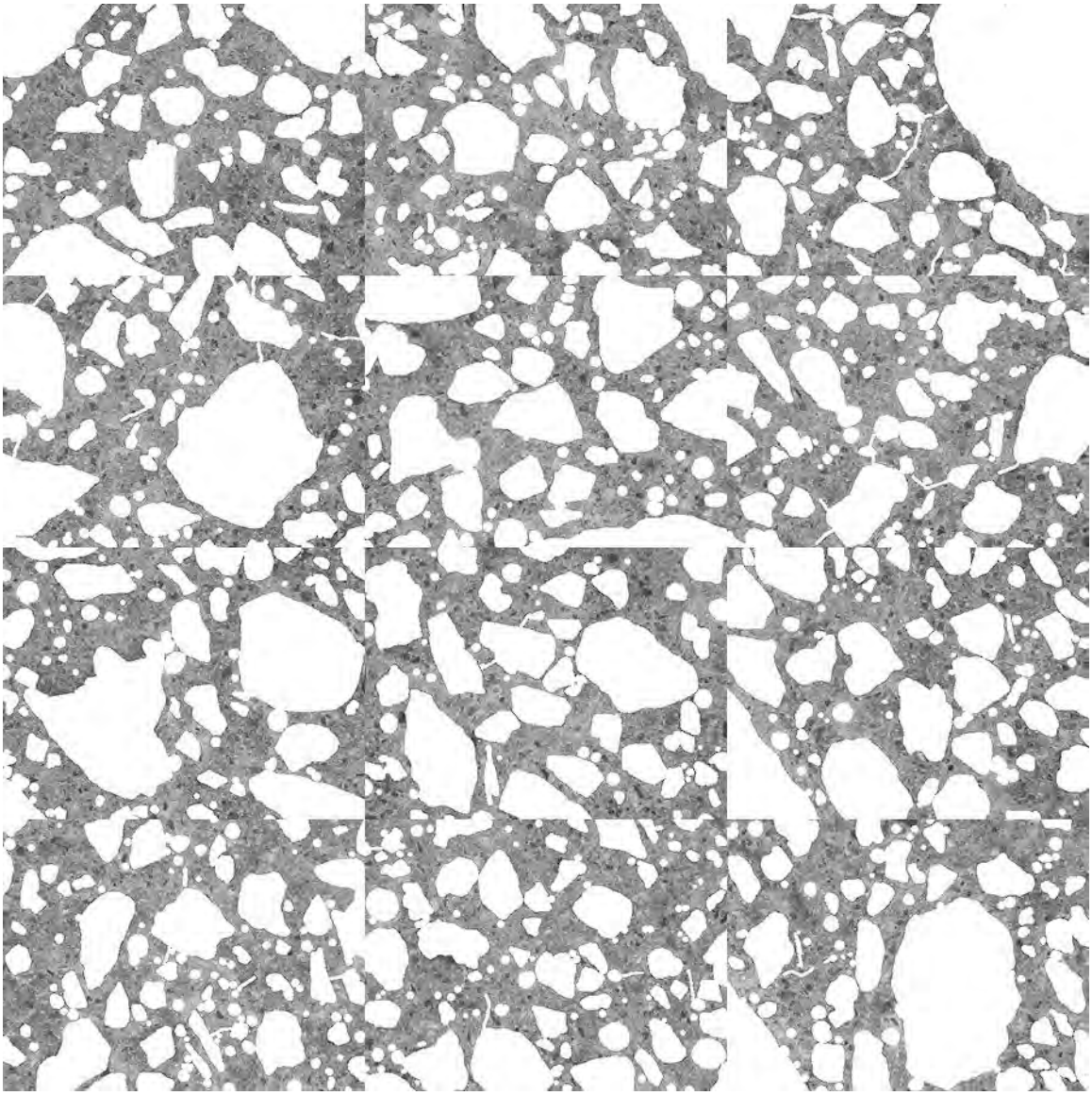

Figure A2.65. Mosaic of 12 frames collected area of thin section representing the original concrete below the concrete overlay, core MT-3, after masking out air voids, fine aggregate, and micro-cracks to isolate cement paste (each individual frame measures 2.612 x 1.959 mm).

Table A2.12. Average cement paste pixel intensities per frame, and equivalent *w/c* values (as compared to 28-day moist cured mortar samples) from original concrete below the overlay, core MT-3.

Cement Paste Pixel Fluorescence Measurements (average intensity per frame)			
83	93	85	87
92	91	84	86
85	92	89	91
equivalent *w/c* (y = 0.0044x + 0.0329)			
0.40	0.44	0.41	0.41
0.43	0.43	0.40	0.41
0.40	0.44	0.42	0.43

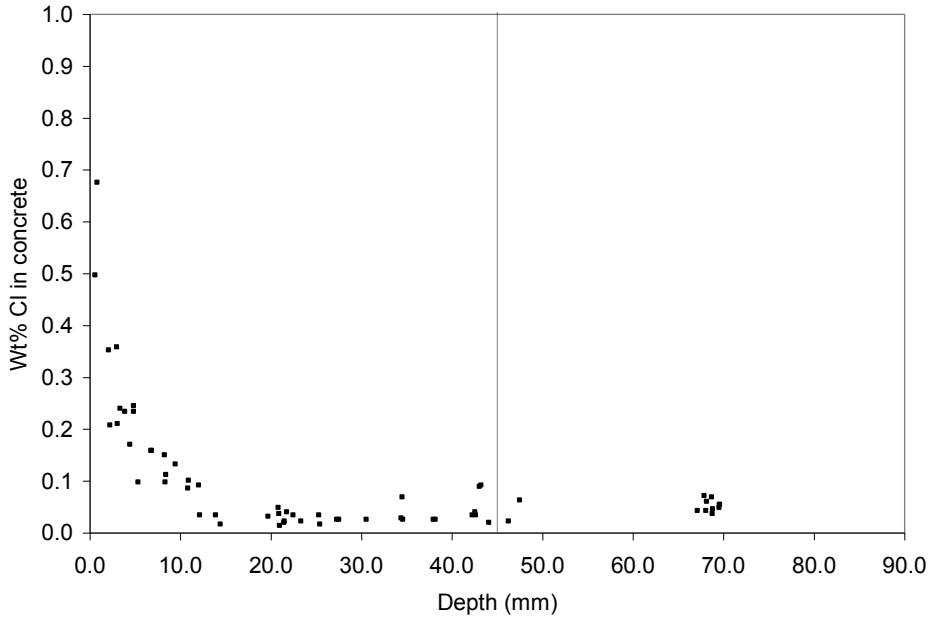

Figure A2.66. Chloride profile from billet prepared from core MT-1, dashed line marks the transition between the overlay and the original concrete below.

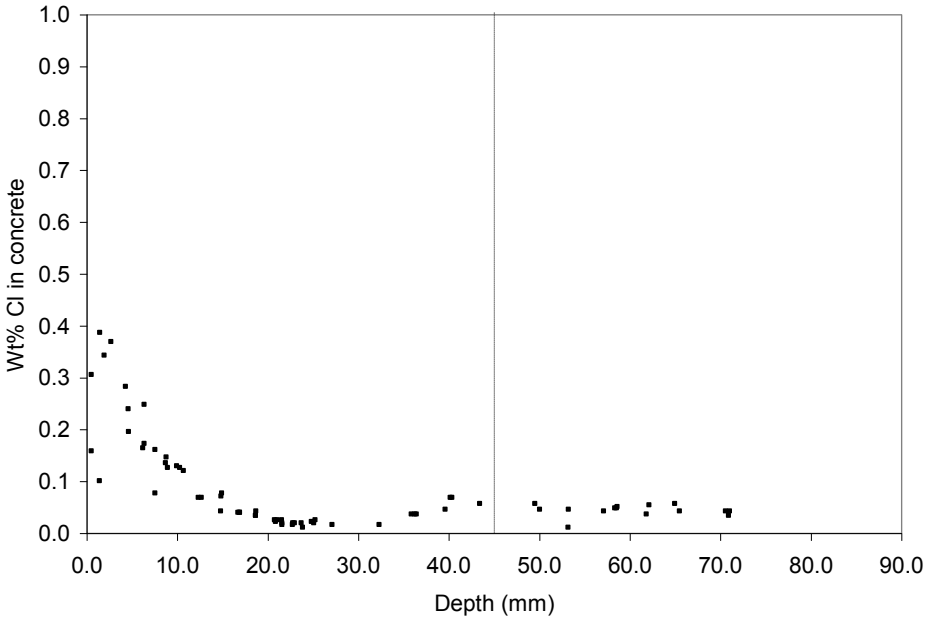

Figure A2.67. Duplicate chloride profile from additional billet prepared from core MT-1, dashed line marks the transition between the overlay and the original concrete below.

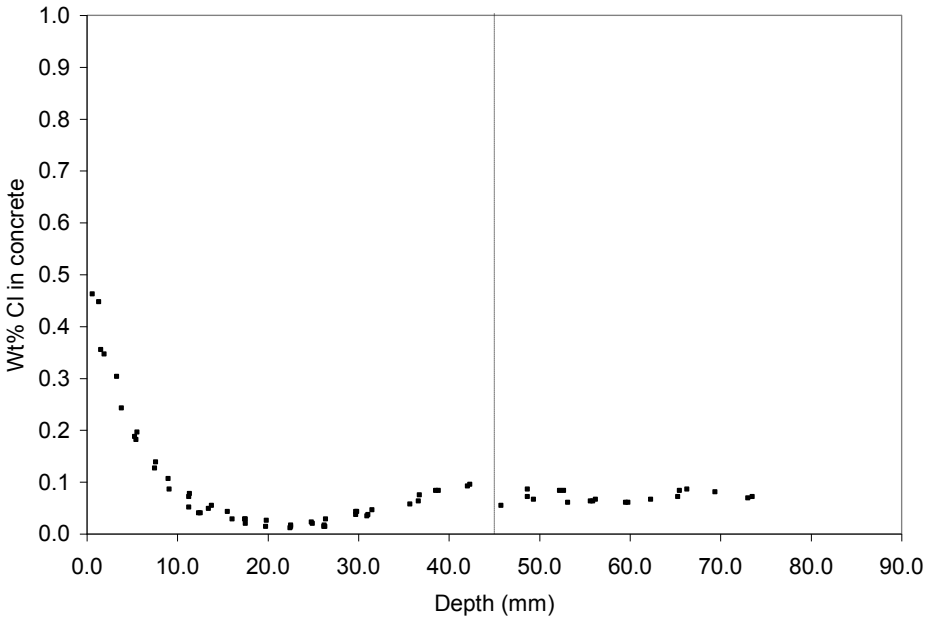

Figure A2.68. Chloride profile through billet prepared from core MT-3, dashed line marks the transition between the overlay and the original concrete below.

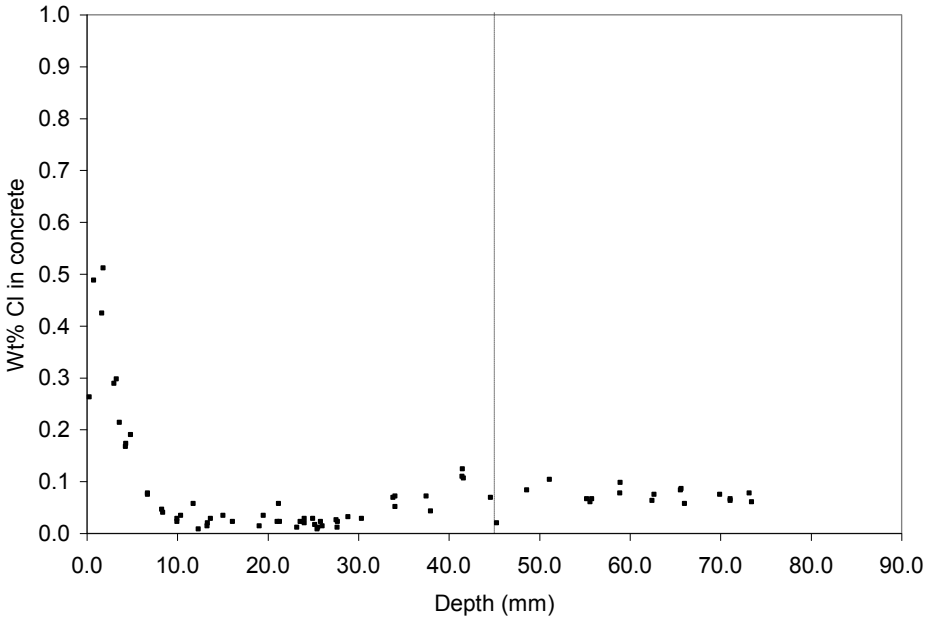

Figure A2.69. Duplicate chloride profile through additional billet prepared from core MT-3, dashed line marks the transition between the overlay and the original concrete below.

South Dakota, Sioux Falls, eastbound 26th Street left-turn lane onto northbound, Interstate Highway 29

This pavement was placed on November 1, 1996, and exposed to $MgCl_2$ brine shortly thereafter on November 15, 1996. A letter came with the cores that described the pavement surface to be in good condition, but stated that the cores taken near the joint looked like they had been eaten away. Figure A2.70 shows the locations of the cores, and Figure A2.71 shows an overview of the turn lane. Figure A2.72 shows the core holes from near the joint. What had been interpreted in the letter as deterioration was just the normal appearance of a concrete joint as exposed in cross section. Figures A2.73 and A2.74 show photographs of the individual cores. Two of the cores were cut into slabs and polished: core SD-1 (at a joint), and core SD-4 (mid-panel). Figures A2.75 through A2.78 show the slabs as polished, after staining with phenolphthalein, and after treatment to enhance air voids and cracks. The phenolphthalein stain showed normal carbonation depths. The black and white treatment did not reveal any macro-cracking in either of the cores. Table A2.13 summarizes the air void parameters. Both sets of slabs showed adequate entrained air, with spacing factors of 0.158 mm and 0.176 mm for cores SD-1 and SD-4 respectively. Figure A2.79 shows an example stereomicroscope image of the air void structure. Initially, water to cement ratio estimations were performed both on a thin section prepared from a core taken at the joint, (SD-1) and on a thin section prepared from a core taken at mid-panel, (SD-4). The *w/c* estimates were consistently higher for the core taken at the joint versus the core taken at mid-panel. To double-check the results, an additional thin section was prepared from the same pair of cores. To further investigate the trend, thin sections were also prepared from another pair of cores representing the joint, (SD-7) and the mid-panel, (SD-5). The same trend of higher *w/c* estimates near the joint was observed. Figures A2.80 and A2.81 show the images used to make the measurements from the first thin section prepared from the top of core SD-1 (at a joint). The results of the *w/c* estimation are summarized in Table A2.14, with an average *w/c* value of 0.47 as compared to the 28-day moist cured mortar sample standards. Figure A2.82 shows images collected from the second thin section prepared from core SD-1. These images were not masked and used for *w/c* measurement, but provided as a visual check on the first thin section. Figures A2.83 and A2.84 show the images used to make the measurements from the thin section prepared from the top of core SD-7 (also at a joint). The results of the *w/c* estimation are summarized in Table A2.15, with an average *w/c* value of 0.45. Figures A2.85 and A2.86 show the images used to make the measurements from the thin section prepared from the top of core SD-4 (from mid-panel). The results of the *w/c* estimation are summarized in Table A2.16, with an average *w/c* value of 0.38. Figure A2.87 shows images collected from the second thin section prepared from core SD-4. These images were not masked and used for *w/c* measurement, but provided as a visual check on the first thin section. Figures A2.88 and A2.89 show the images used to make the measurements from the thin section prepared from the top of core SD-5 (also from mid-panel). The results of the *w/c* estimation are summarized in Table A2.17, with an average *w/c* value of 0.35. Figure A2.90 compares cement paste fluorescence histograms from the four cores. The samples prepared from the joint fluoresced consistently brighter than the samples prepared from mid-panel. Figures A2.91 through A2.94 show chloride profiles from cores SD-3 and SD-7.

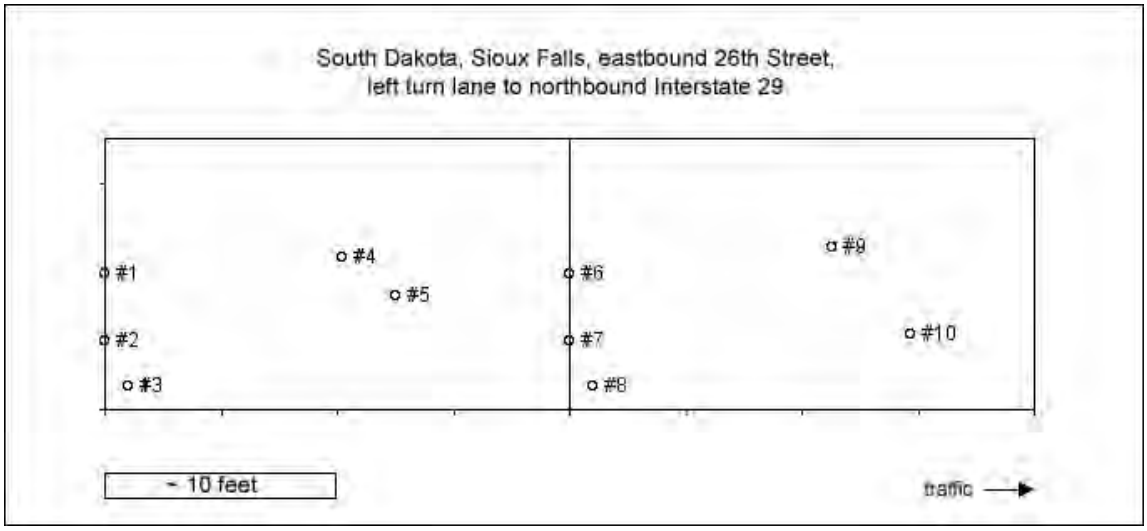

Figure A2.70. Diagram to show core locations based on submitted field information.

Figure A2.71. Photograph of core site.

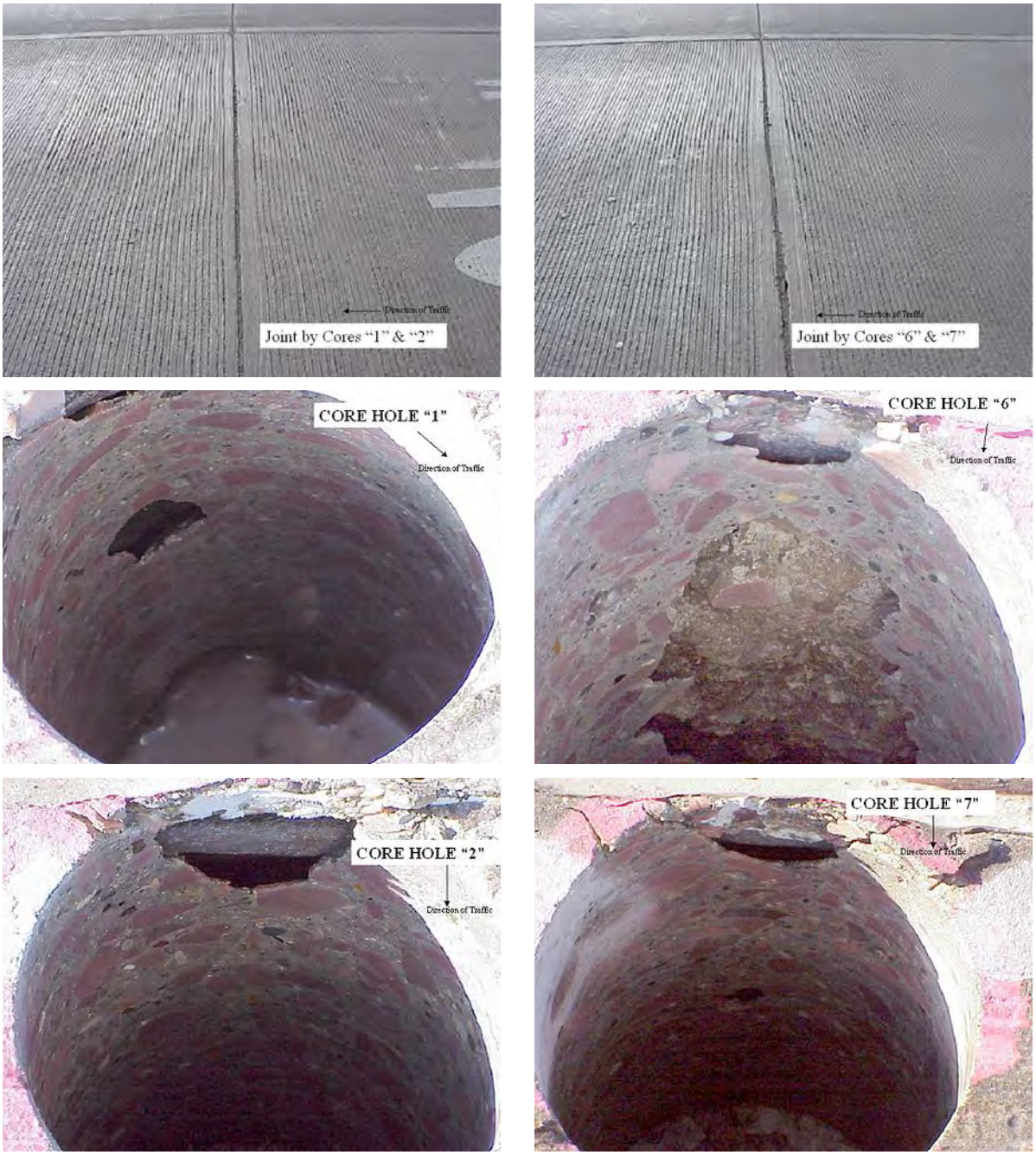

Figure A2.72. Photographs of the joints sampled, and of the holes after the coring operation.

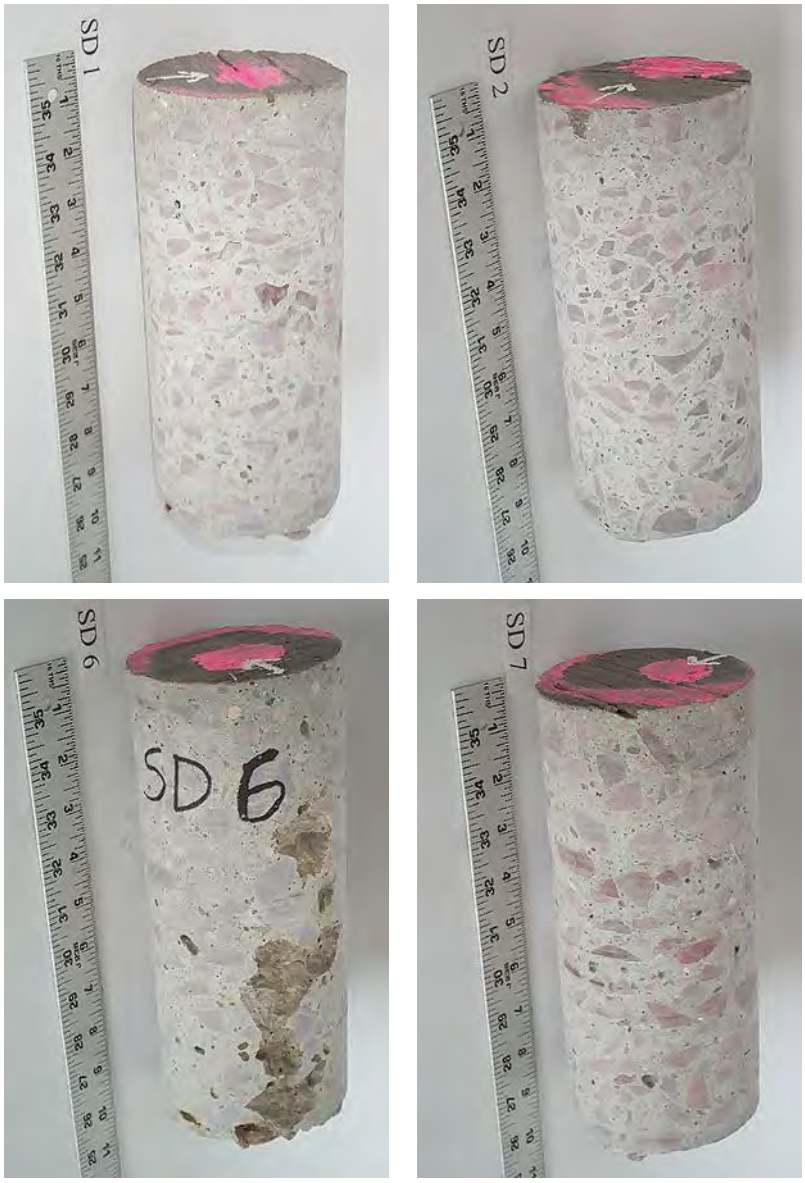

Figure A2.73. Cores taken at joint.

Figure A2.74. Cores taken away from joint.

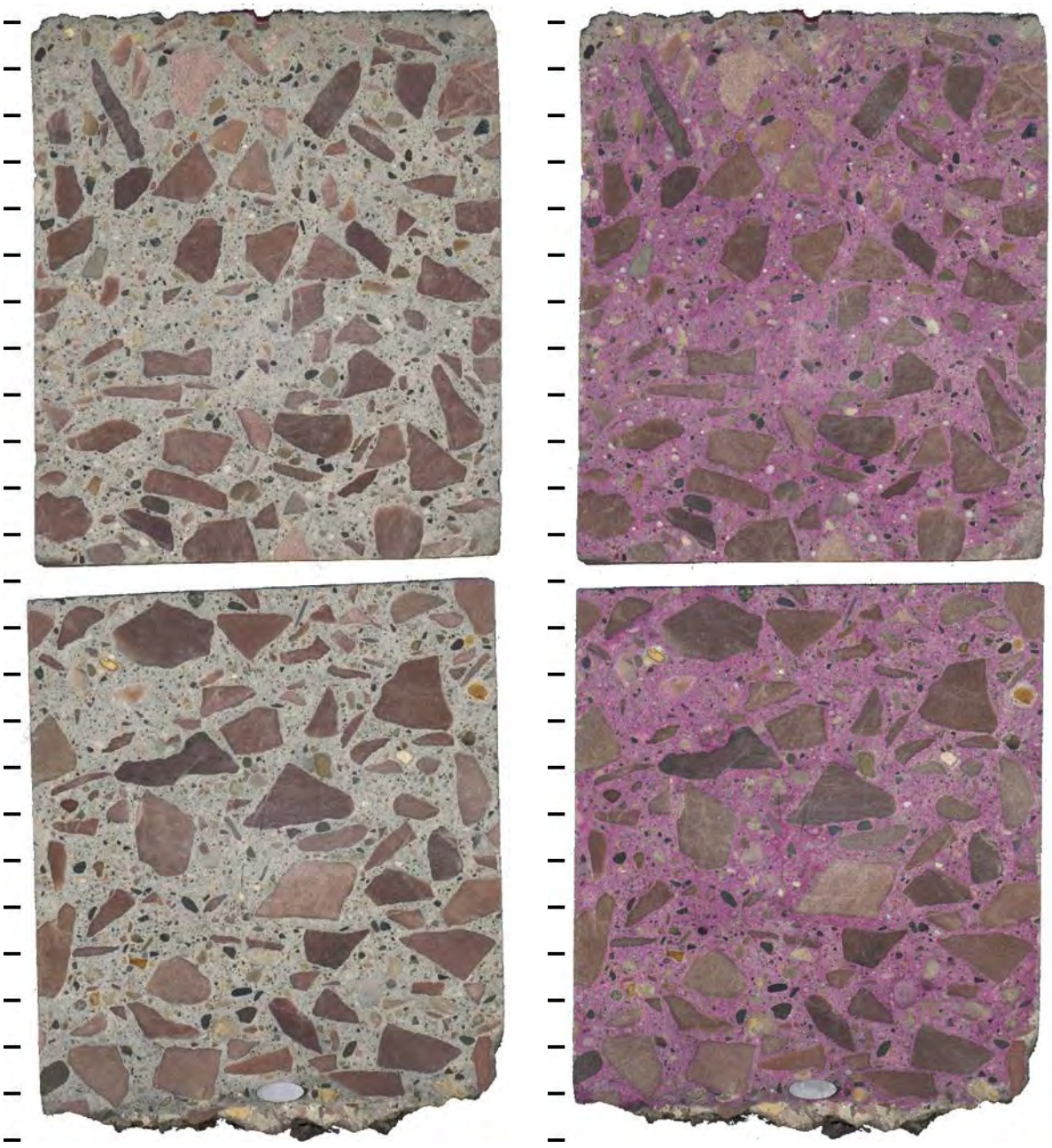

Figure A2.75. Polished slabs to show complete cross-section through core SD-1 both before (left) and after application of phenolphthalein stain (right) tic marks every cm.

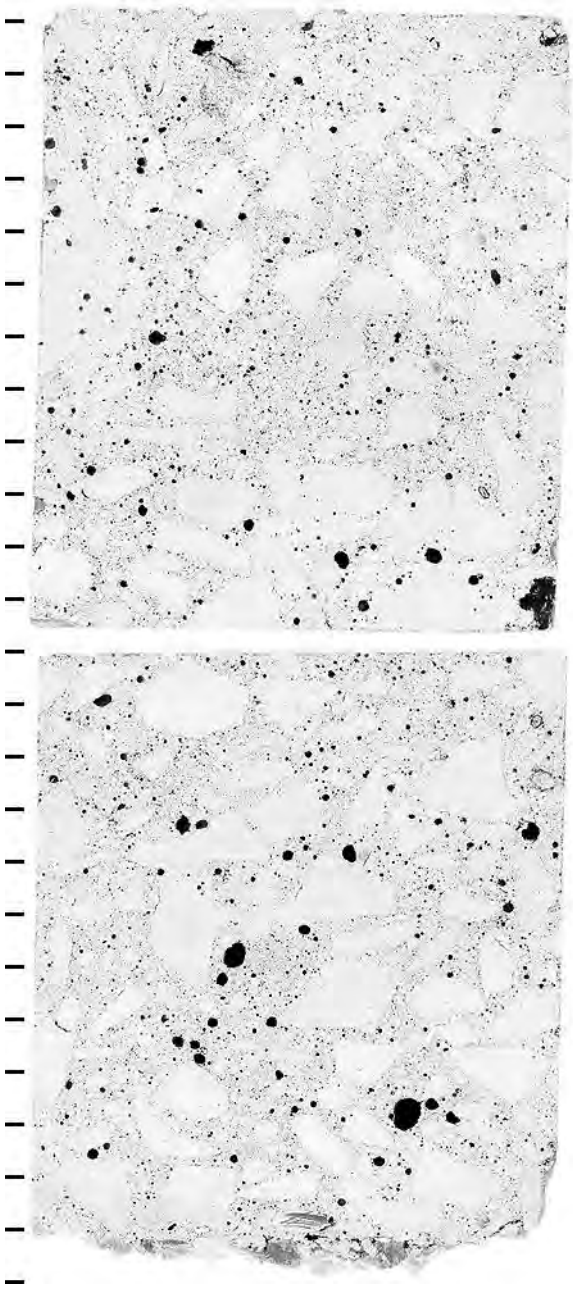

Figure A2.76. Polished slabs to show complete cross-section through core SD-1 after treatment to enhance appearance of air voids and cracks, tic marks every cm.

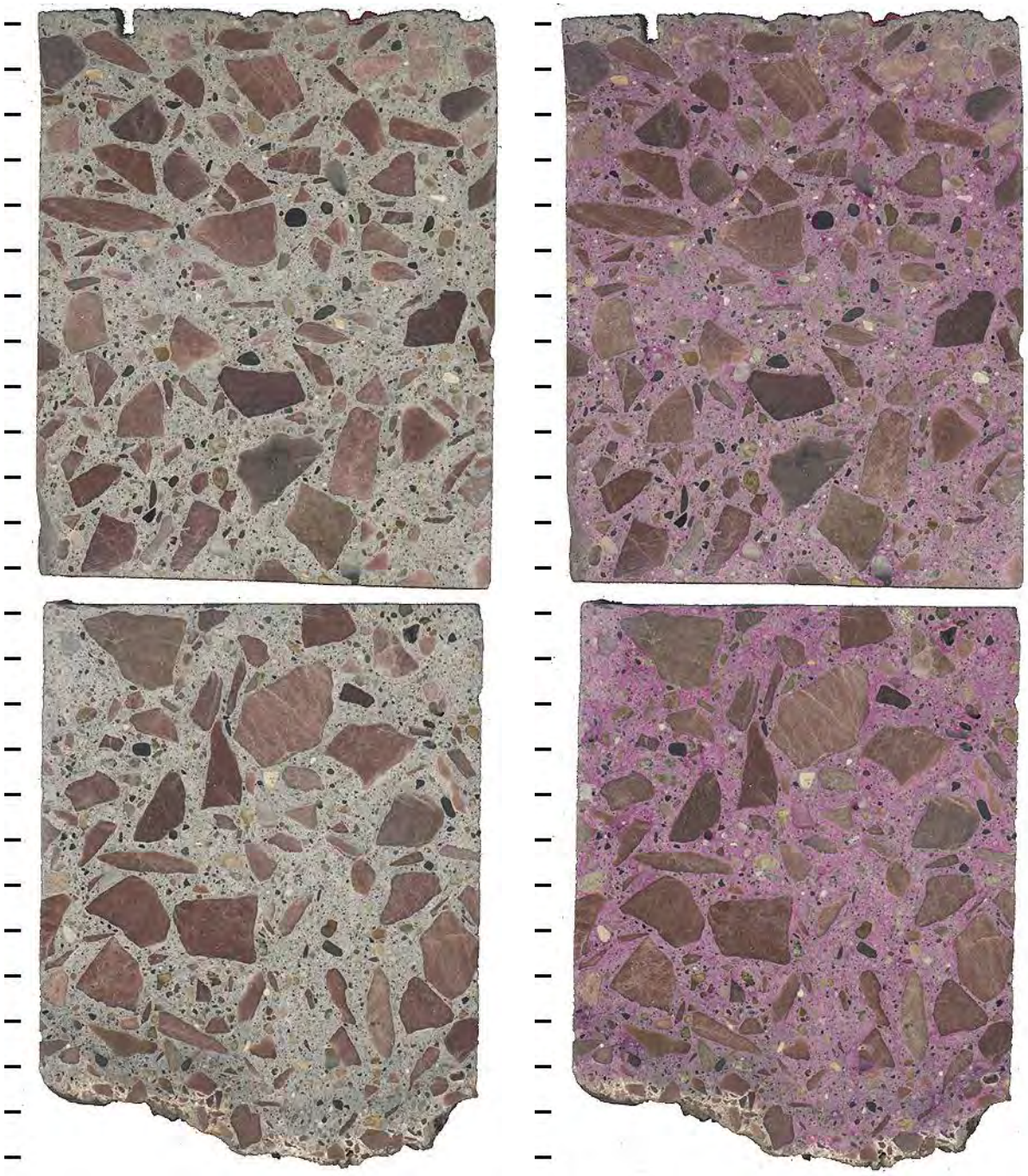

Figure A2.77. Polished slabs to show complete cross-section through core SD-4 both before (left) and after application of phenolphthalein stain (right) tic marks every cm.

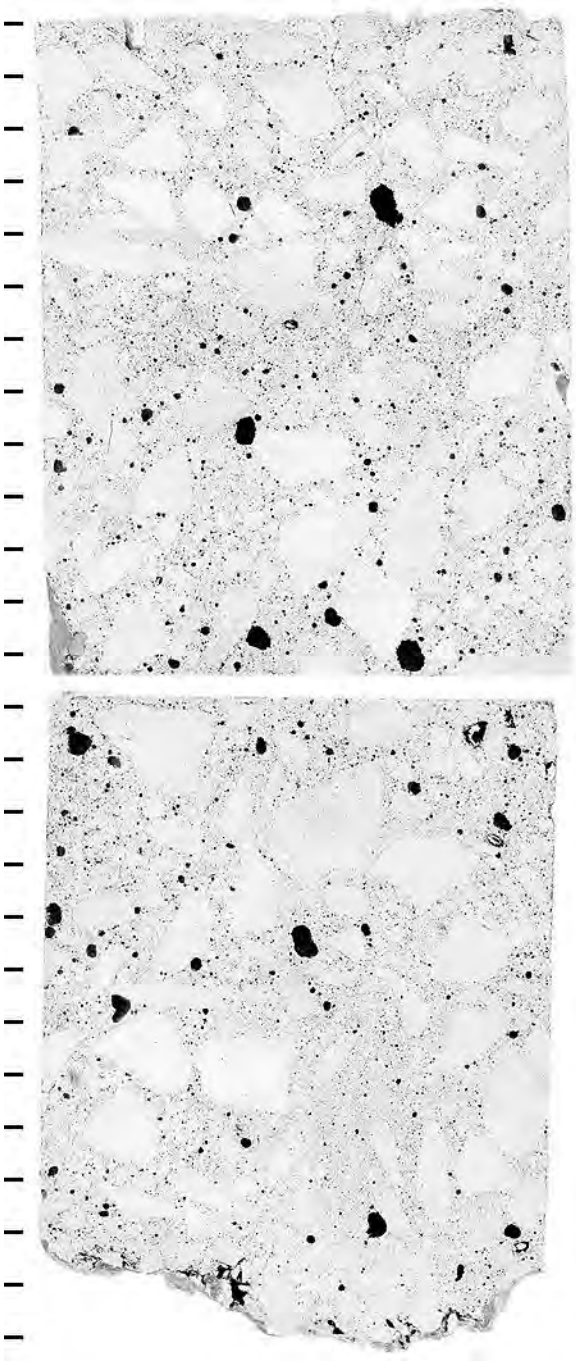

Figure A2.78. Polished slabs to show complete cross-section through core SD-4 after treatment to enhance appearance of air voids and cracks, tic marks every cm.

Table A2.13. Air void parameters

Sample ID	SD-01	SD-04
Location	At joint	Away from Joint
Raw data		
Total traverse length (mm)	3625.5	3625.5
Area analyzed (cm^2)	71.0	71.0
Air stops	85	91
Paste stops	396	382
Aggregate stops	907	915
Secondary deposit stops	0	0
Total stops	1388	1388
Number of air intercepts	1577	1420
Number of filled void intercepts	2	0
Results		
Air vol%	6.1	6.6
Paste vol%	28.5	27.5
Aggregate vol%	65.3	65.9
Secondary deposit vol%	0.0	0.0
Existing average chord length (mm)	0.141	0.167
Existing paste/air ratio	4.7	4.2
Existing air void specific surface (mm^{-1})	28.4	23.9
Existing air void frequency (voids/m)	435	392
Existing spacing factor (mm)	0.158	0.176
Original average chord length (mm)	0.141	0.167
Original paste/air ratio	4.7	4.2
Original air void specific surface (mm^{-1})	28.4	23.9
Original air void frequency (voids/m)	436	392
Original spacing factor (mm)	0.158	0.176

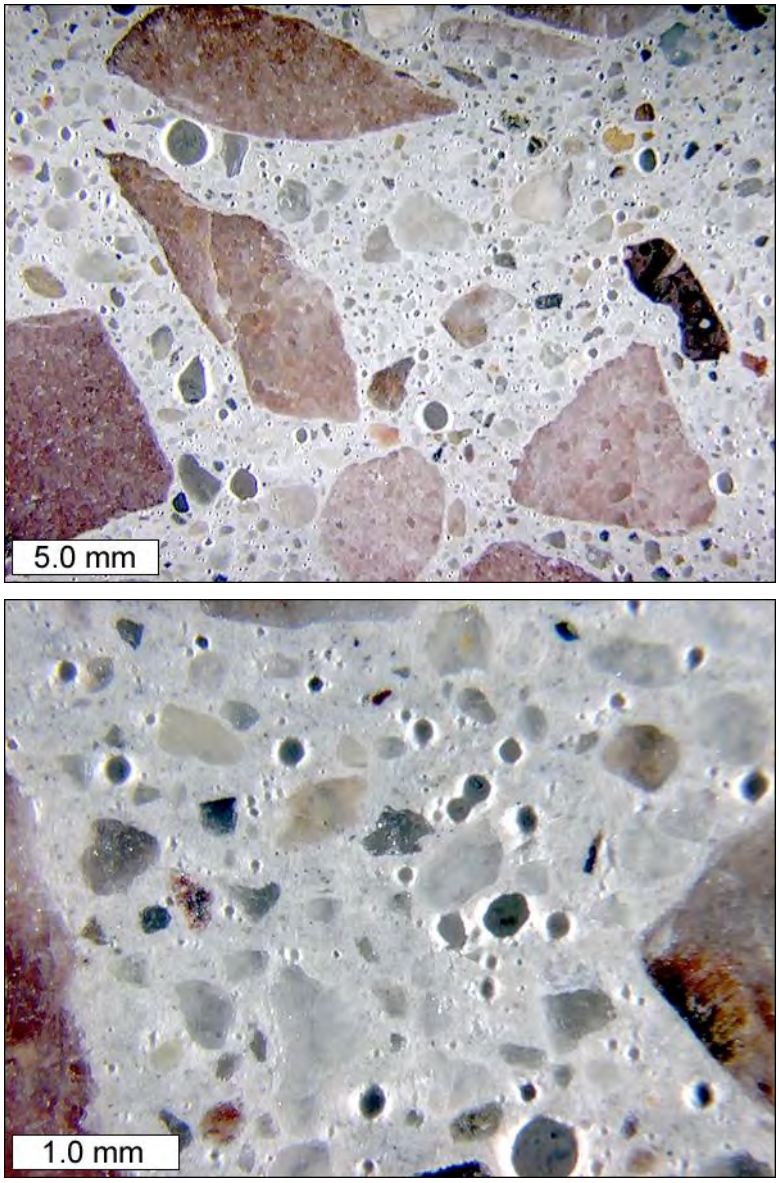

Figure A2.79. Stereo microscope images to show air void structure on polished slab from core SD-4.

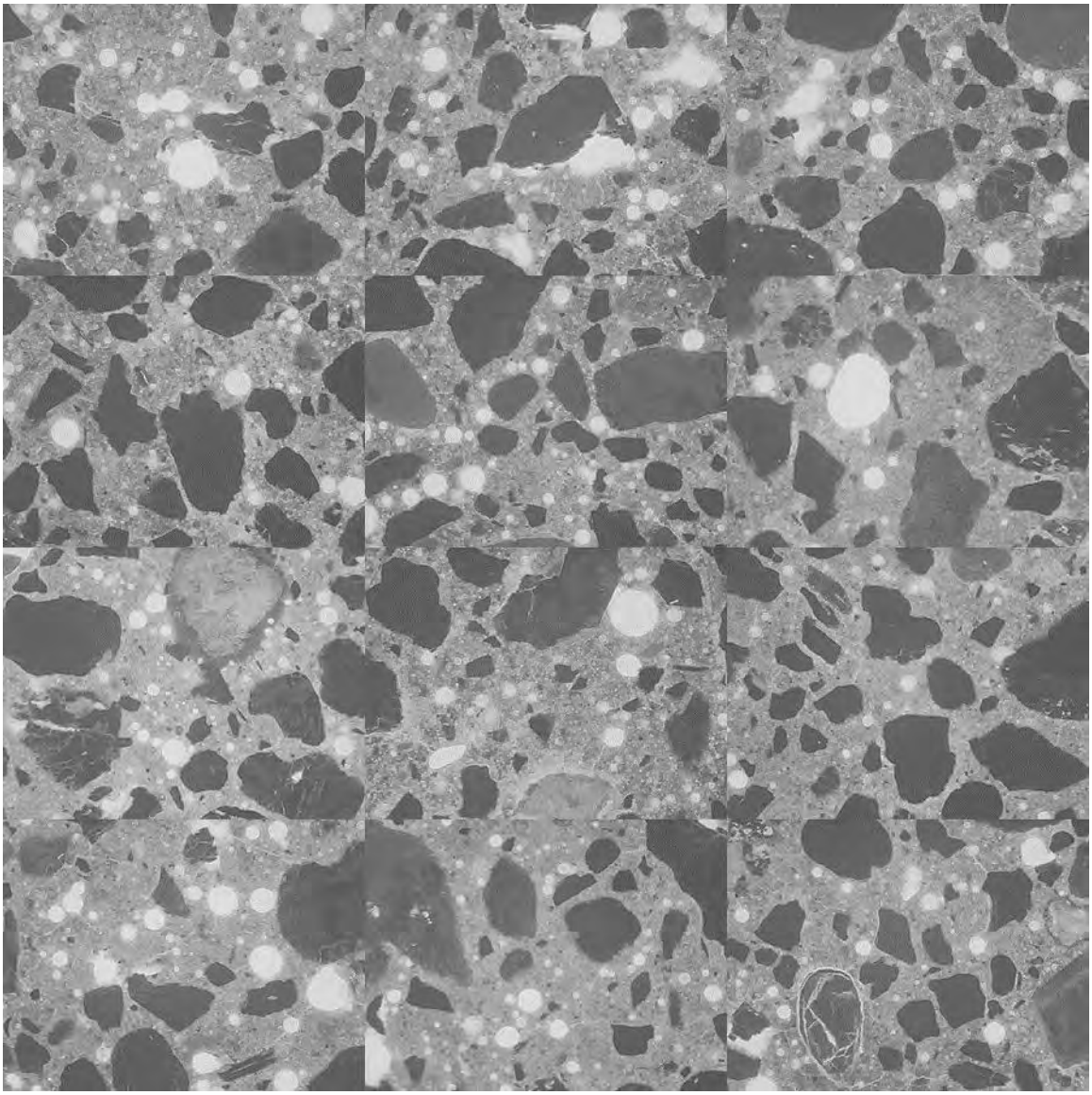

Figure A2.80. Mosaic of 12 frames collected from thin section prepared from billet cut from top portion of core SD-1 (each individual frame measures 2.612 x 1.959 mm).

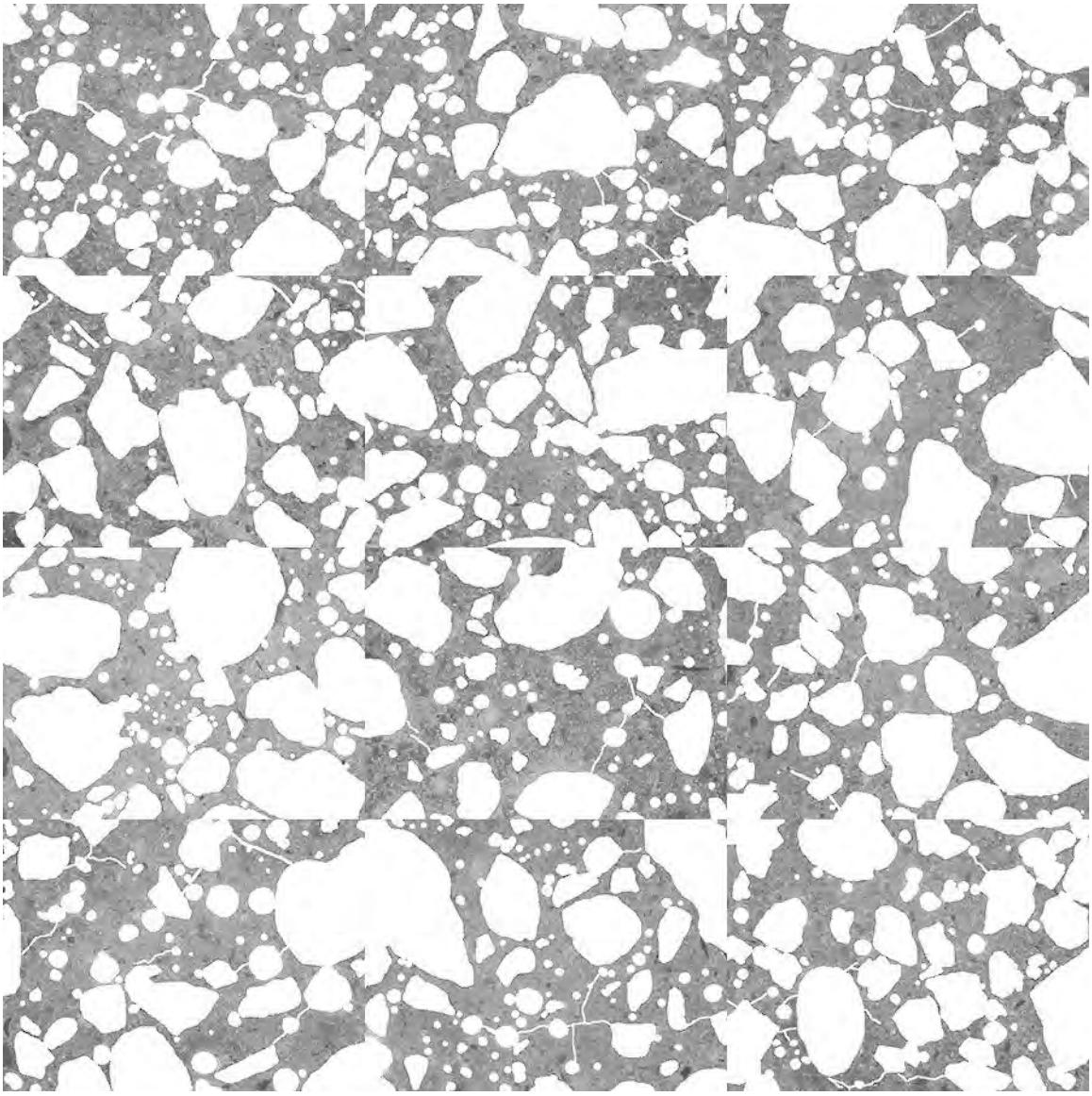

Figure A2.81. Mosaic of 12 frames collected from thin section prepared from billet cut from top portion of core SD-1 after masking out air voids, fine aggregate, and micro-cracks to isolate cement paste (each individual frame measures 2.612 x 1.959 mm).

Table A2.14. Average cement paste pixel intensities per frame, and equivalent *w/c* values (as compared to 28-day moist cured mortar samples) for core SD-1.

Cement Paste Pixel Fluorescence Measurements (average intensity per frame)			
101	101	95	95
93	98	120	97
101	102	101	97
equivalent *w/c* ($y = 0.0044x + 0.0329$)			
0.47	0.47	0.45	0.45
0.44	0.46	0.56	0.46
0.47	0.48	0.47	0.46

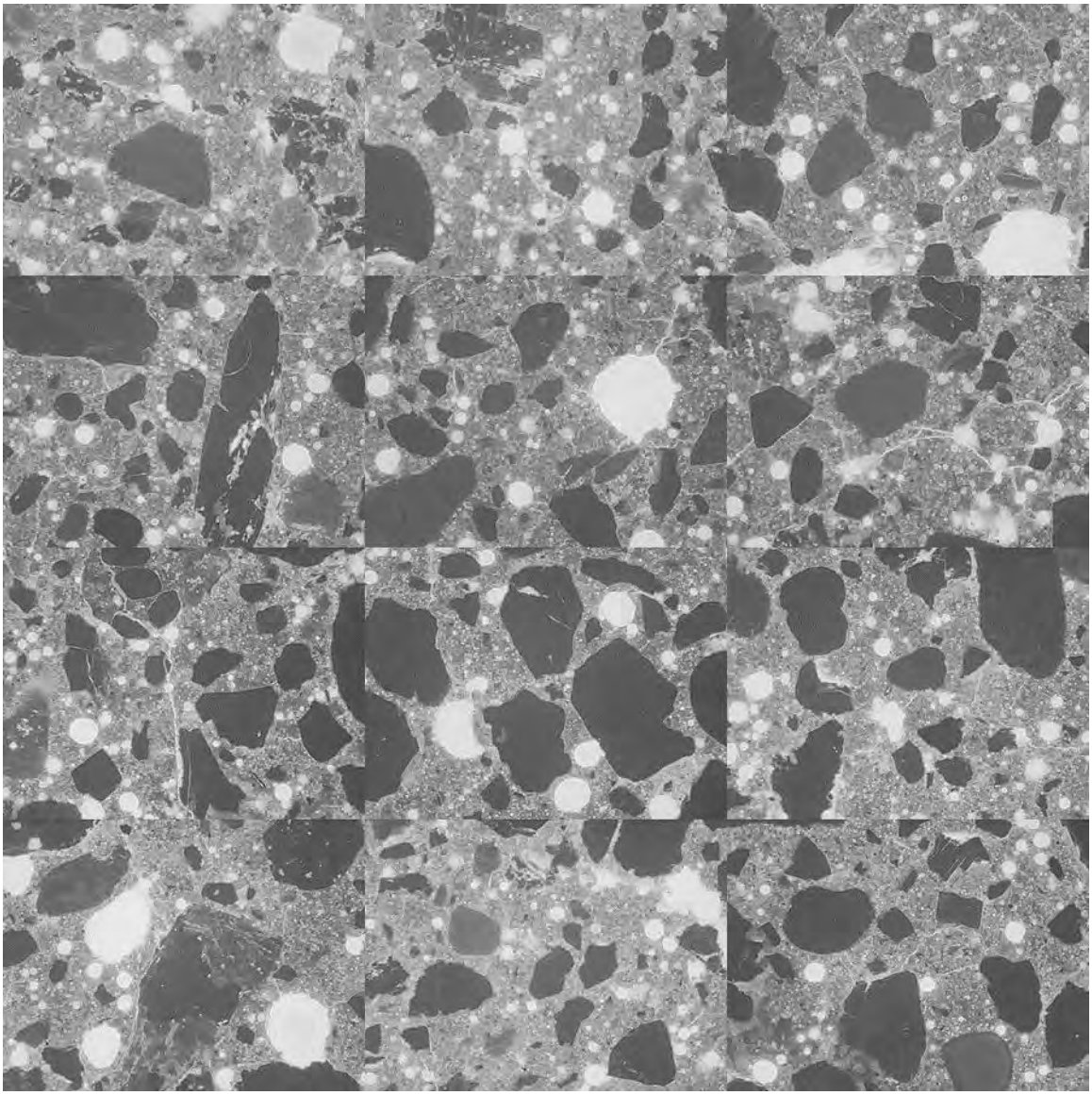

Figure A2.82. Mosaic of 12 frames collected from thin section prepared from a second billet cut from top portion of core SD-1 (each individual frame measures 2.612 x 1.959 mm). These frames were not masked and used for *w/c* determination, but recorded as visual check against the first section prepared from core SD-1.

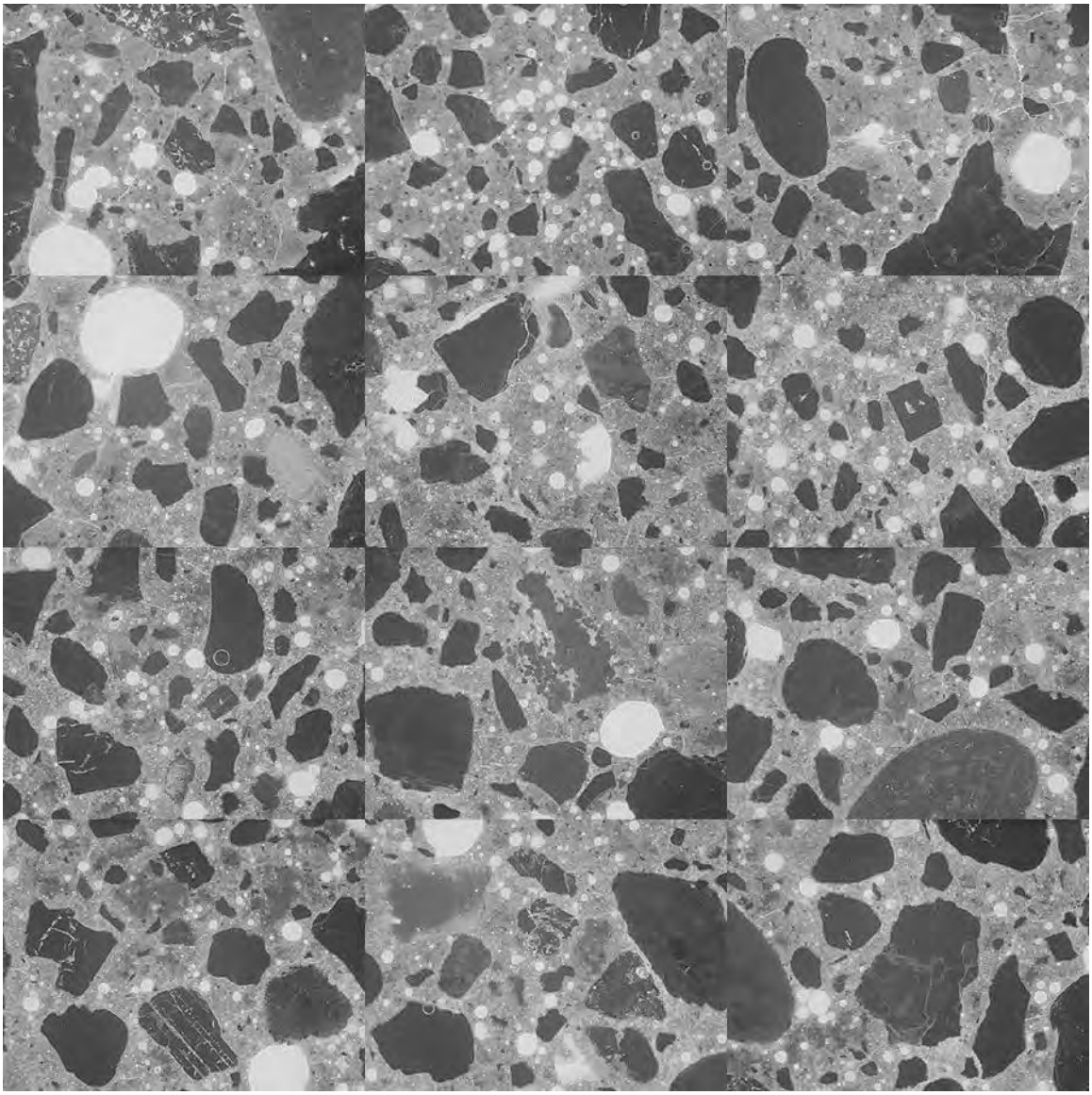

Figure A2.83. Mosaic of 12 frames collected from thin section prepared from billet cut from top portion of core SD-7 (each individual frame measures 2.612 x 1.959 mm).

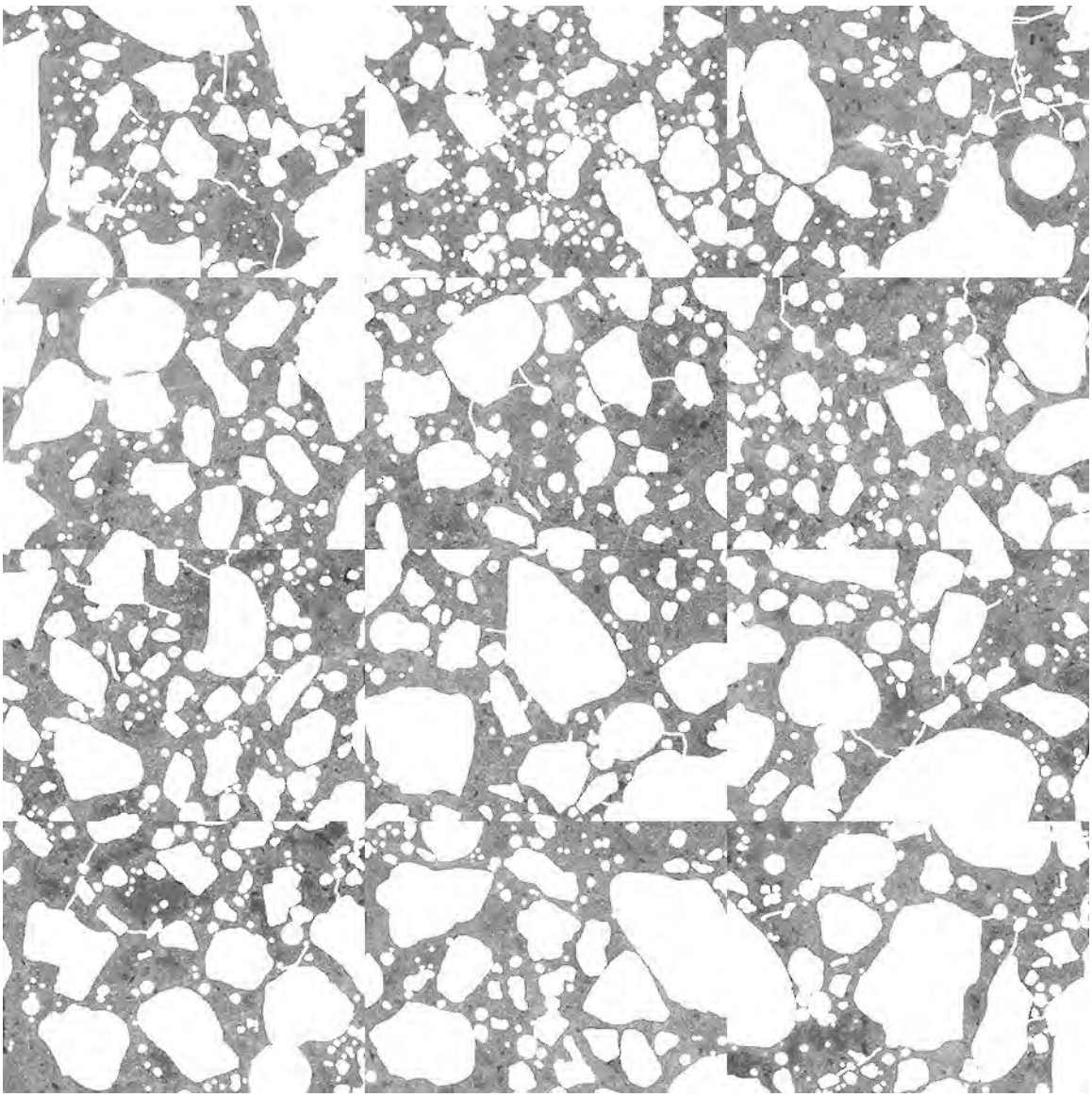

Figure A2.84. Mosaic of 12 frames collected from thin section prepared from billet cut from top portion of core SD-7 after masking out air voids, fine aggregate, and micro-cracks to isolate cement paste (each individual frame measures 2.612 x 1.959 mm).

Table A2.15. Average cement paste pixel intensities per frame, and equivalent *w/c* values (as compared to 28-day moist cured mortar samples) for core SD-7.

Cement Paste Pixel Fluorescence Measurements (average intensity per frame)			
97	97	96	103
92	102	91	95
95	89	103	95
equivalent *w/c* (y = 0.0044x + 0.0329)			
0.46	0.45	0.45	0.48
0.44	0.48	0.43	0.45
0.45	0.42	0.48	0.45

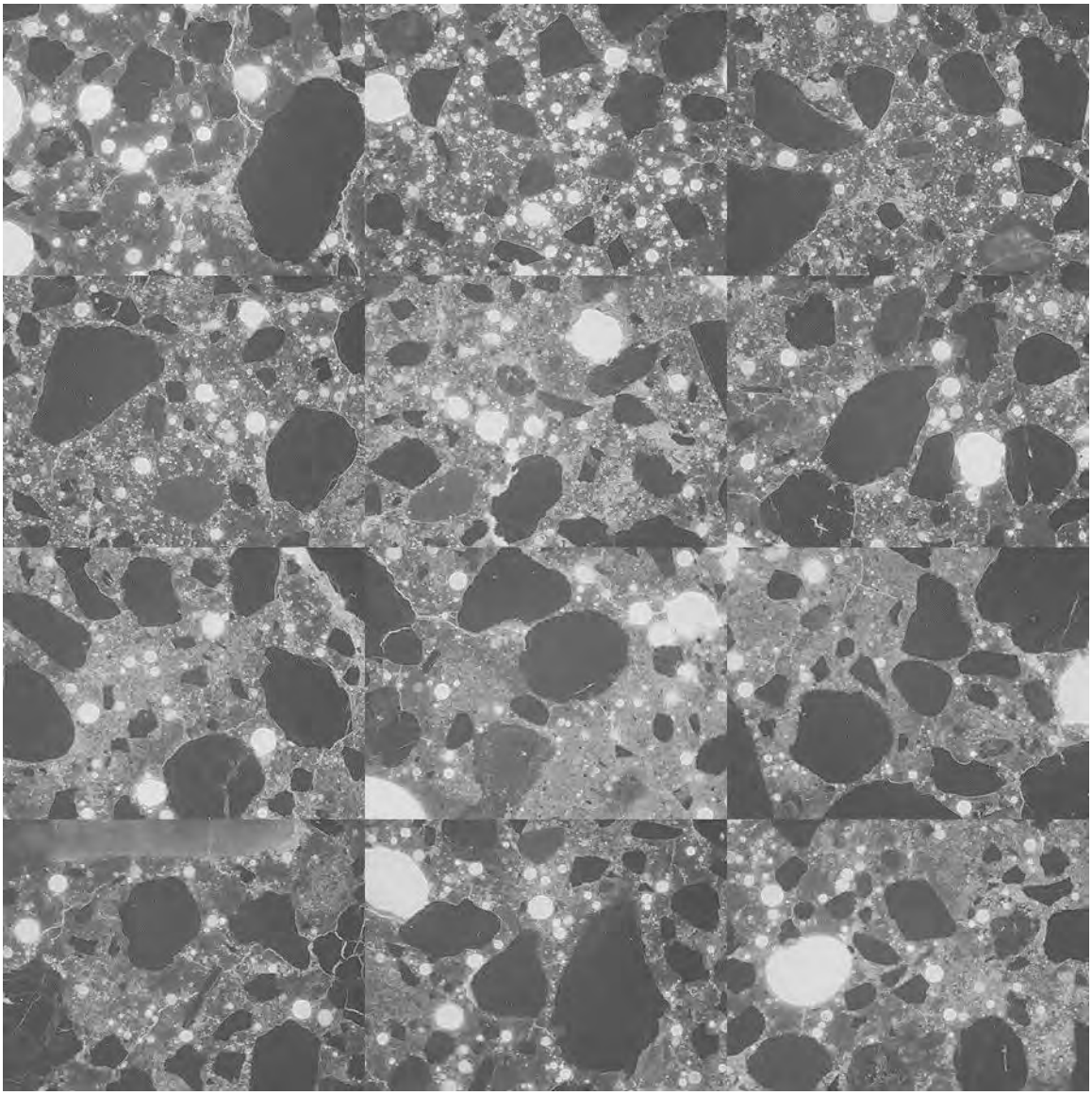

Figure A2.85. Mosaic of 12 frames collected from thin section prepared from billet cut from top portion of core SD-4 (each individual frame measures 2.612 x 1.959 mm).

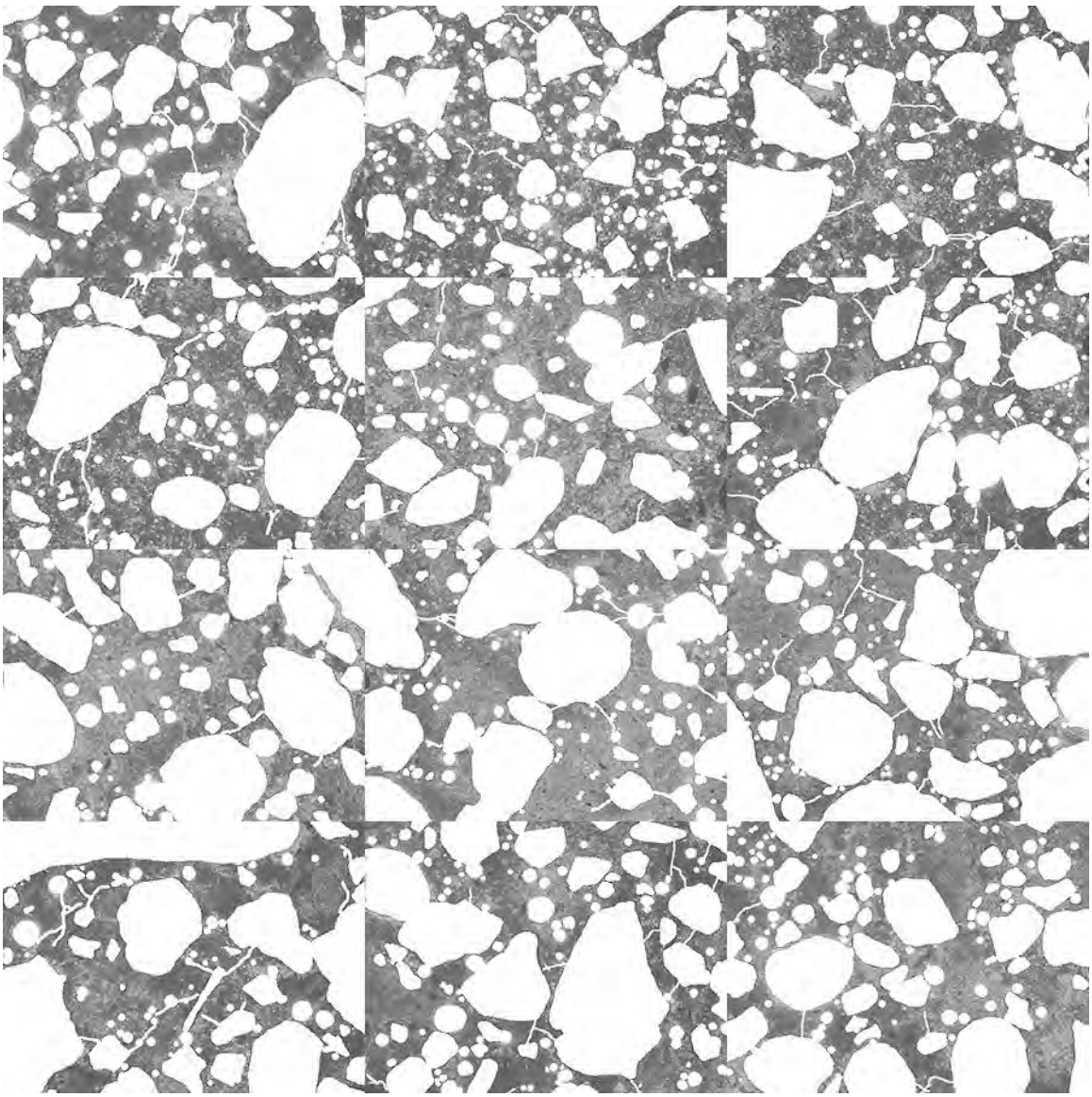

Figure A2.86. Mosaic of 12 frames collected from thin section prepared from billet cut from top portion of core SD-4 after masking out air voids, fine aggregate, and micro-cracks to isolate cement paste (each individual frame measures 2.612 x 1.959 mm).

Table A2.16. Average cement paste pixel intensities per frame, and equivalent *w/c* values (as compared to 28-day moist cured mortar samples) from core SD-4.

Cement Paste Pixel Fluorescence Measurements (average intensity per frame)			
78	78	71	76
93	90	94	85
85	68	70	70
equivalent *w/c* (y = 0.0044x + 0.0329)			
0.37	0.37	0.34	0.37
0.44	0.35	0.43	0.44
0.40	0.33	0.34	0.34

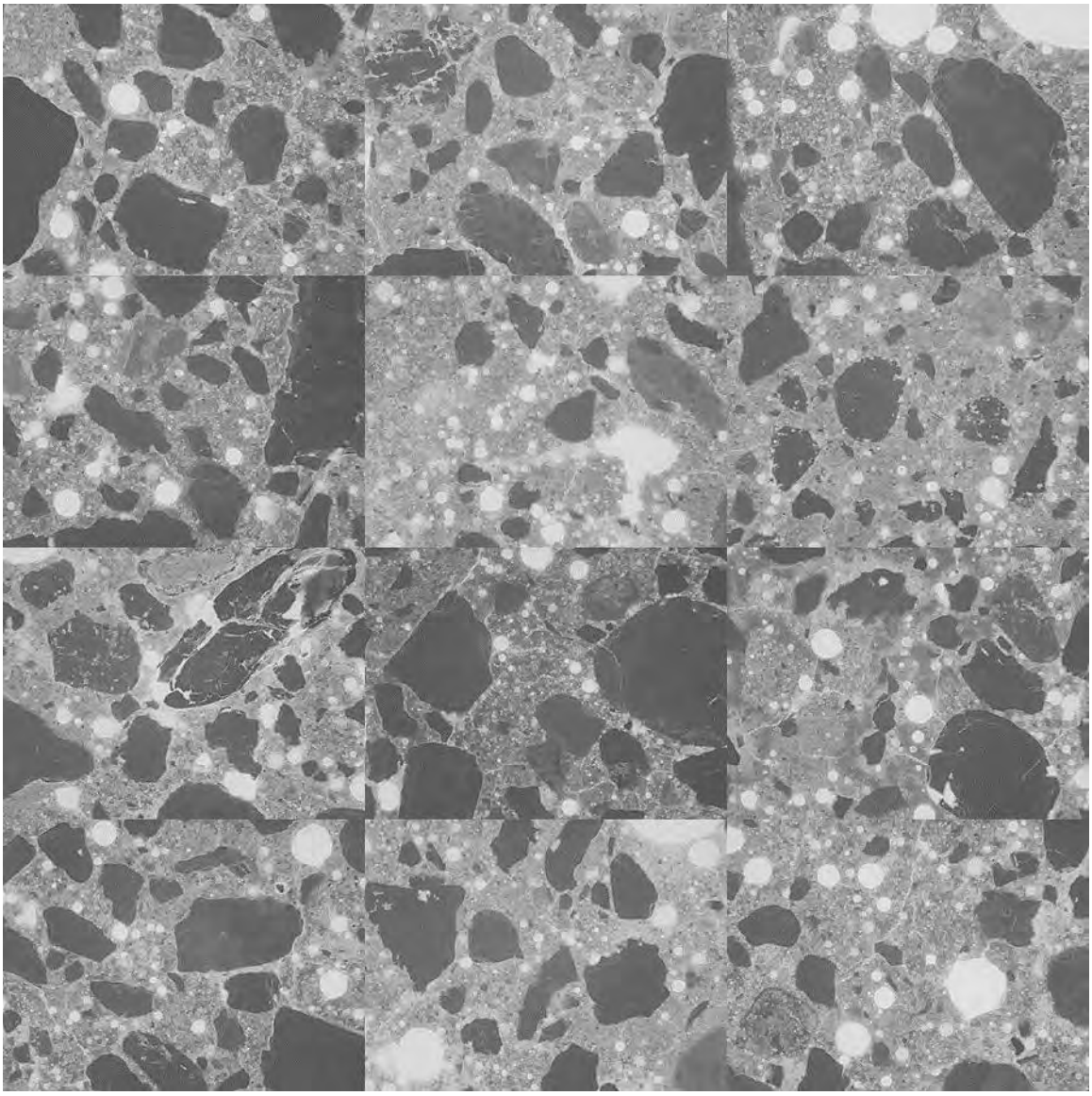

Figure A2.87. Mosaic of 12 frames collected from thin section prepared from a second billet cut from top portion of core SD-4 (each individual frame measures 2.612 x 1.959 mm). These frames were not masked and used for *w/c* determination, but recorded as visual check against the first section prepared from core SD-4.

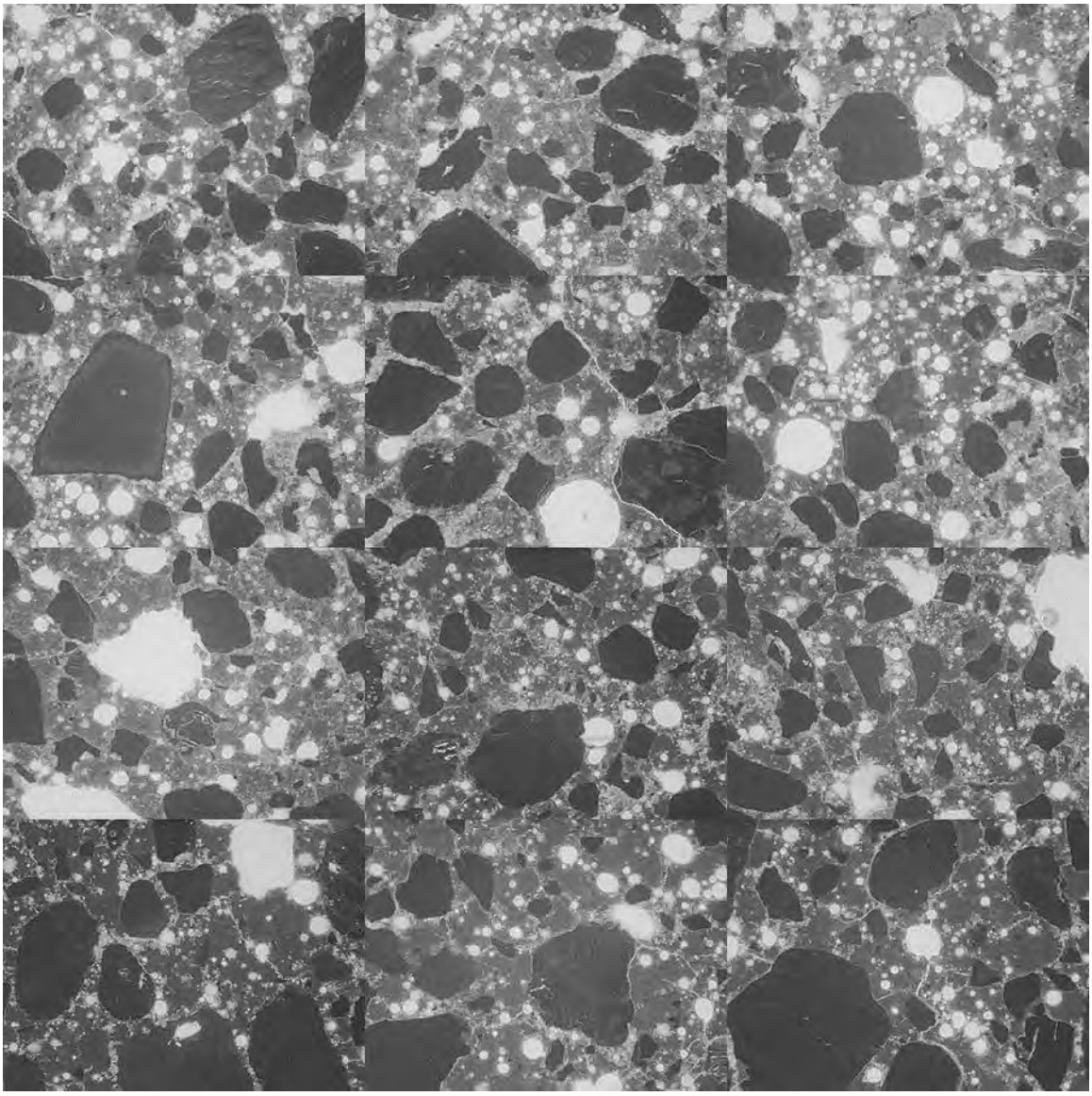

Figure A2.88. Mosaic of 12 frames collected from thin section prepared from billet cut from top portion of core SD-5 (each individual frame measures 2.612 x 1.959 mm).

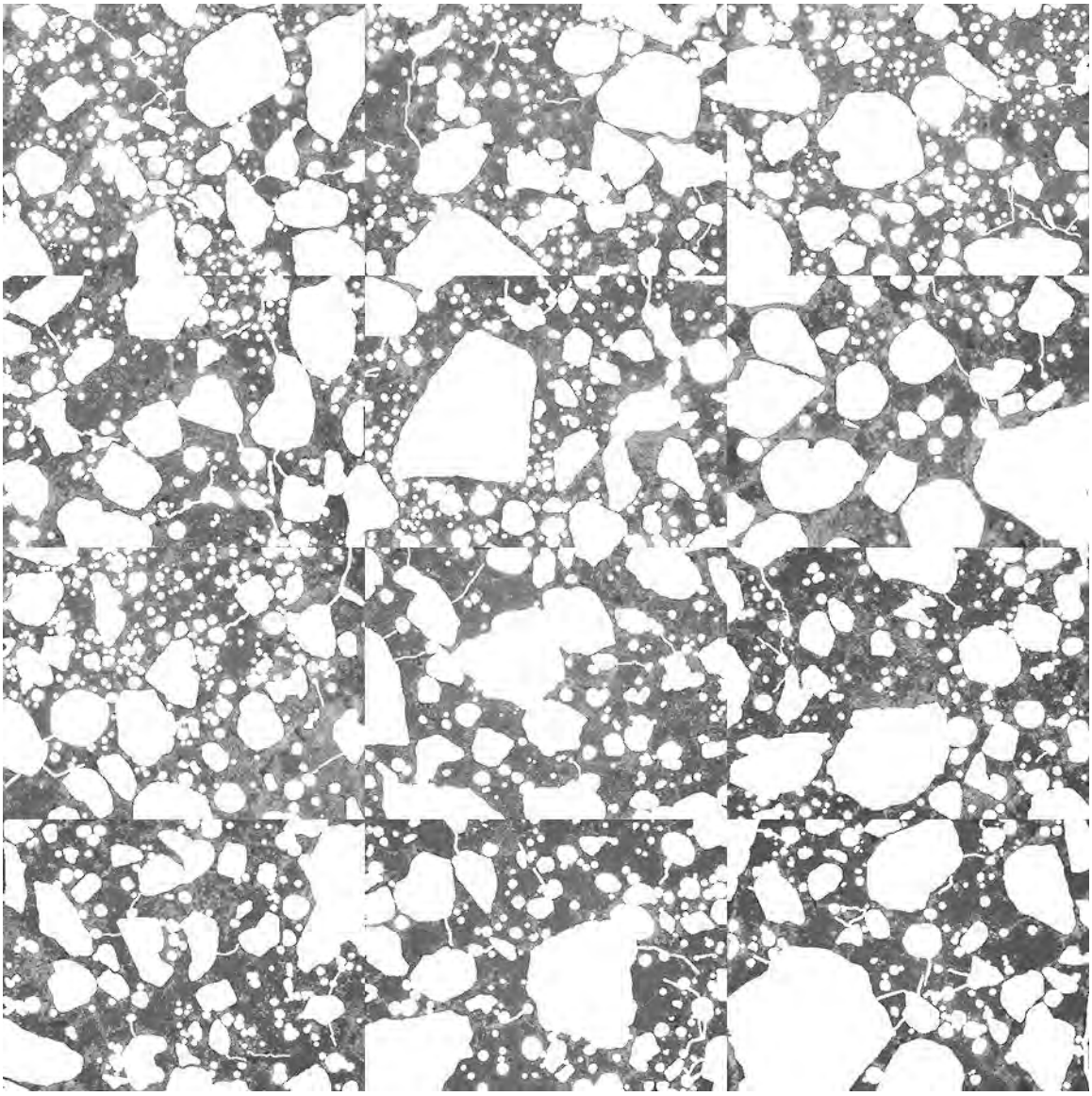

Figure A2.89. Mosaic of 12 frames collected from thin section prepared from billet cut from top portion of core SD-5 after masking out air voids, fine aggregate, and micro-cracks to isolate cement paste (each individual frame measures 2.612 x 1.959 mm).

Table A2.17. Average cement paste pixel intensities per frame, and equivalent *w/c* values (as compared to 28-day moist cured mortar samples) core SD-5.

Cement Paste Pixel Fluorescence Measurements (average intensity per frame)			
86	84	86	74
82	74	83	75
58	64	62	52
equivalent *w/c* ($y = 0.0044x + 0.0329$)			
0.41	0.40	0.41	0.36
0.39	0.36	0.39	0.36
0.29	0.31	0.30	0.26

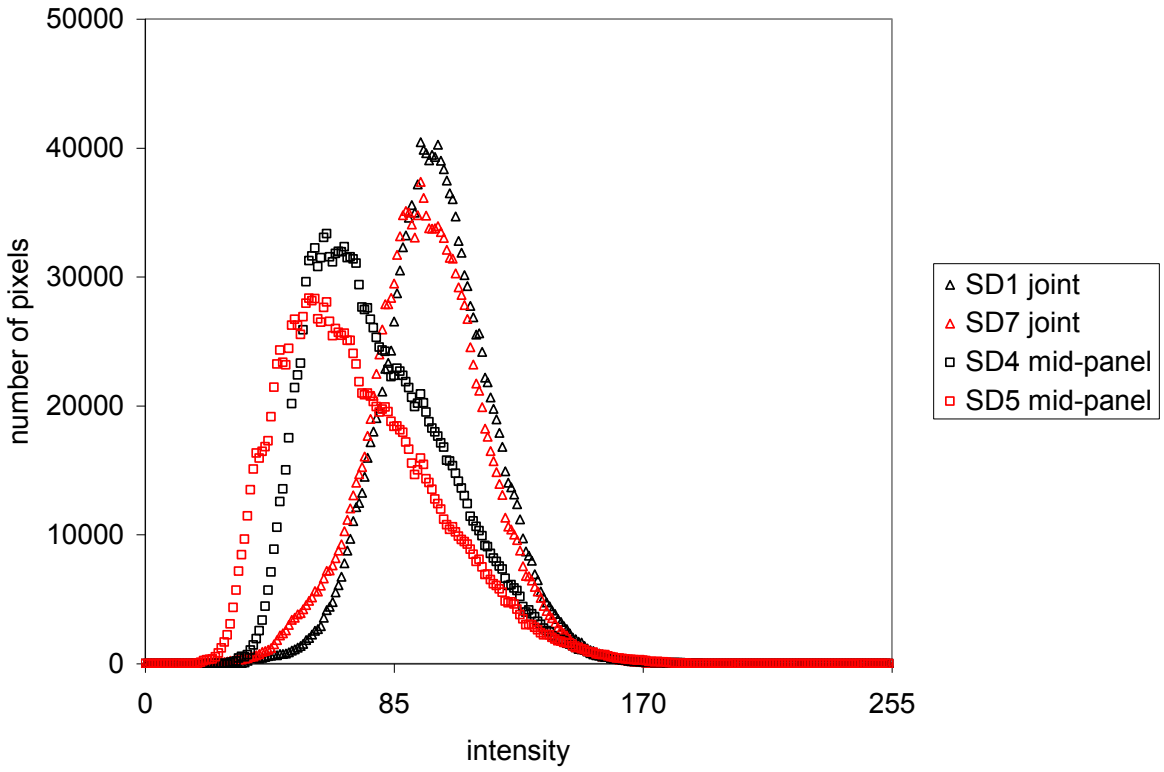

Figure A2.90. Histogram comparing cement paste pixel intensities using all 12 frames as collected from thin sections prepared from cores taken at the joint versus cores taken mid-panel.

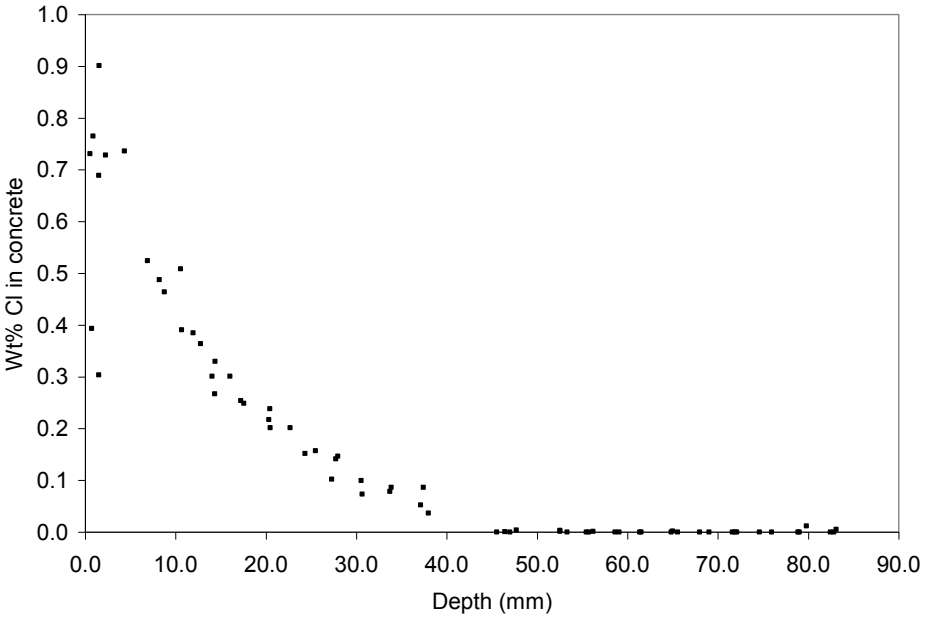

Figure A2.91. Chloride profile from billet prepared from core SD-3, panel corner.

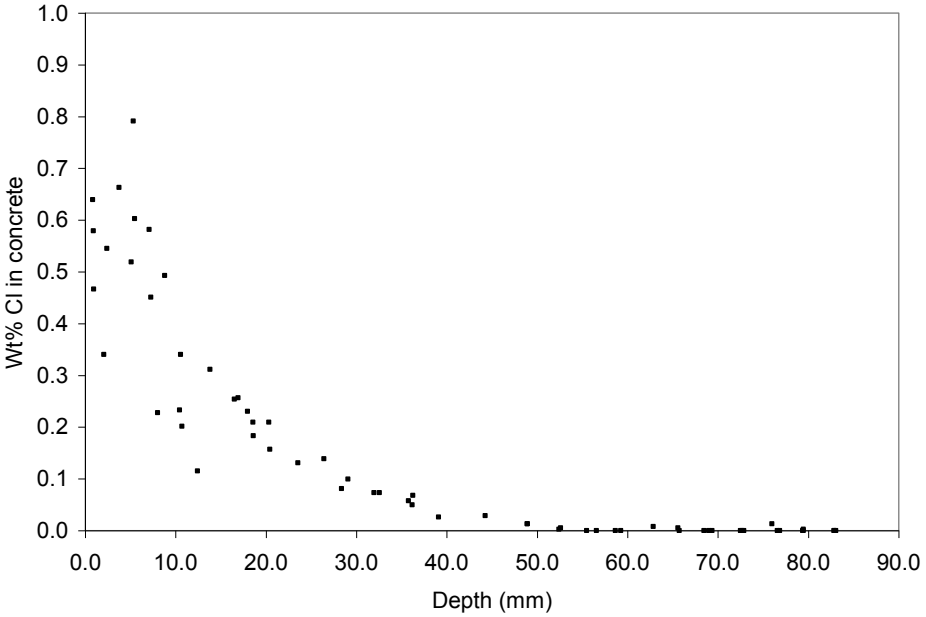

Figure A2.92. Duplicate chloride profile from additional billet prepared from core SD-3, panel corner.

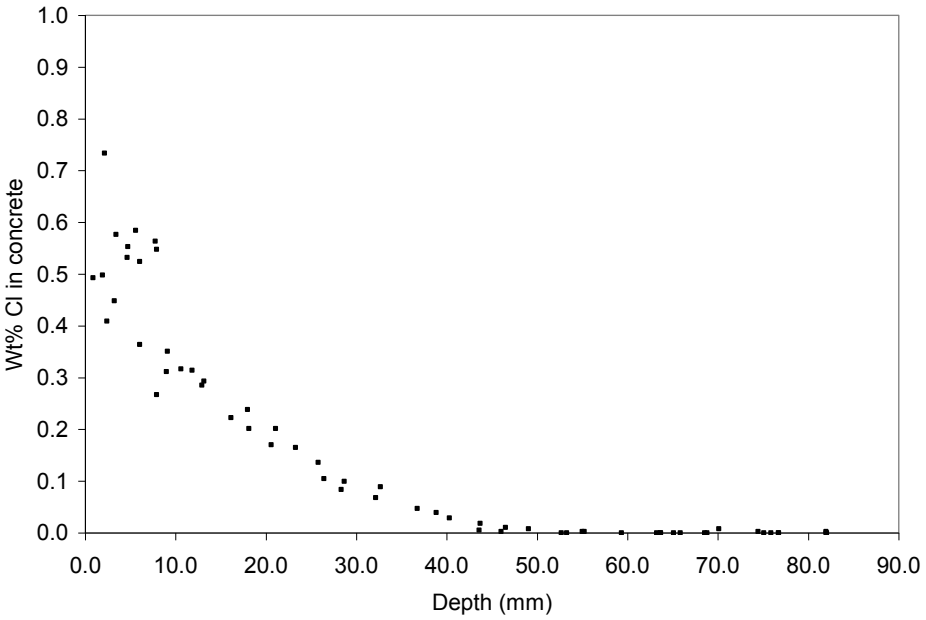

Figure A2.93. Chloride profile from billet prepared from core SD-7, mid-panel.

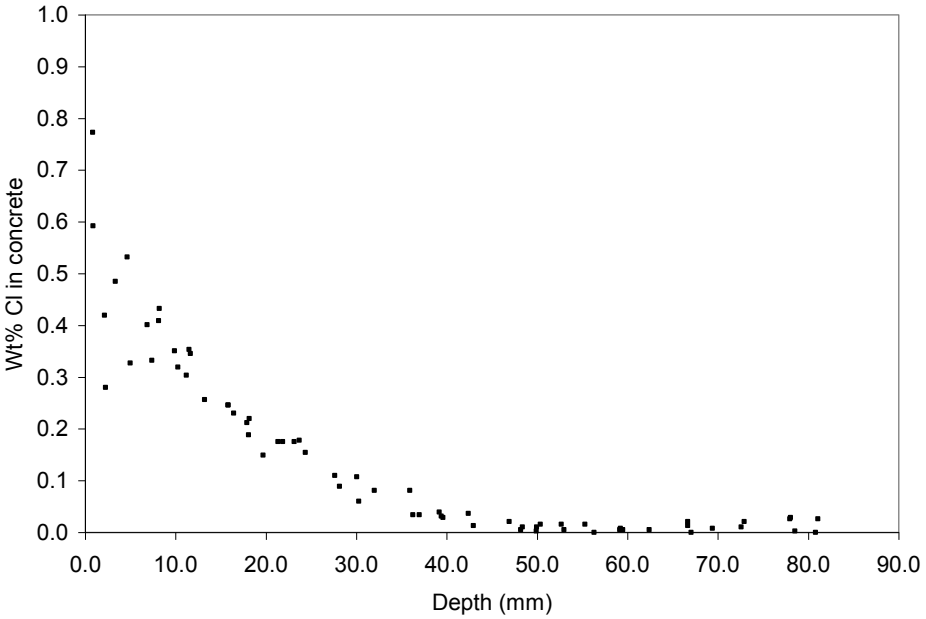

Figure A2.94. Duplicate chloride profile from additional billet prepared from core SD-7, mid-panel.

Montana, eastbound Interstate Highway 90 bridge deck, near milepost 61.8, Tarkio interchange

The Tarkio interchange was constructed in 1958, and lies at the border of two maintenance areas: 1113, and 1114. Maintenance personnel indicated they used both $MgCl_2$ brine, and a combination of NaCl and sand on this bridge deck. Maintenance personnel described spalling at many of the bridge decks in the area that had been coated with a thick (~ 1/4") layer of epoxy and aggregate. In order to patch the spalls, they had to first scrape away the epoxy layer, which debonded and came off in sheets. It was never stated that this was the case at the Tarkio interchange, which appeared to be uncoated. Figure A2.95 shows the locations of the cores, and Figure A2.96 shows the condition of the bridge deck, covered with cold patch material. Figure A2.97 shows the underside of the bridge deck with pronounced efflorescence, especially in areas directly below regions covered with cold patch material. Figure A2.98 shows photographs of the cores. Core T-1 exhibited a crack plane at a depth of about 45 mm. The entire core was vacuum impregnated with epoxy and used only for thin section preparation. Core T-2 was intact, and cut into slabs and polished. Figures A2.99 and A2.100 show the slab as polished, after staining with phenolphthalein, and after treatment to enhance air voids and cracks. The phenolphthalein stain showed normal carbonation at the surface, but pronounced carbonation of over a centimeter thick at the base of the deck. The black and white treatment did not reveal any macro-cracking. Table A2.18 summarizes the air void parameters. The slab showed inadequate entrained air, with a spacing factor of 0.296 mm. Figure A2.101 shows an example stereomicroscope image of the air void structure. A *w/c* ratio estimation was performed on a thin section prepared from the top of core T-2. Figures A2.102 and A2.103 show the images used to make the measurements. The results of the *w/c* estimation are summarized in Table A2.19, with an average *w/c* value of 0.33 as compared to the 28-day moist cured mortar sample standards. Figures A2.104 through A2.106 show chloride profiles from cores T-2. Figures A2.107 and A2.108 show locations on the thin sections prepared from core T-1 that were used for elemental mapping. Regions were mapped to represent the pavement surface and the crack at depth. Figures A2.109 and A2.110 show the elemental maps from the two regions. Chloride profiles were not recorded from core T-1 because it had been epoxy impregnated; the epoxy contains chlorine. The most interesting feature of the elemental maps is the Mg map from Figure A2.110 that shows magnesium enrichment at the surface of the bridge deck.

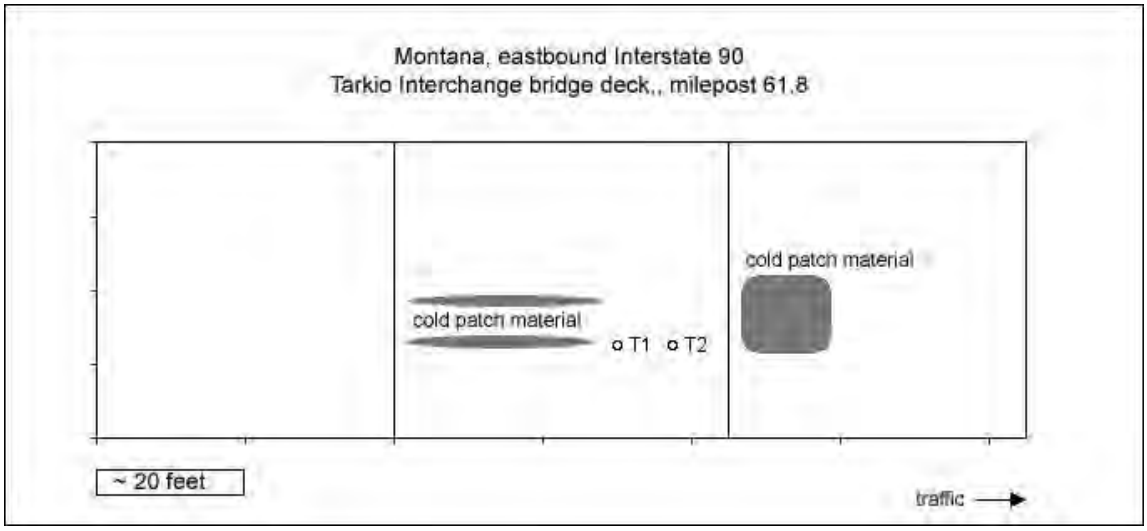

Figure A2.95. Diagram to show location of cores according to field notes.

Figure A2.96. Photograph of core site.

Figure A2.97. Photograph from beneath bridge deck after coring operation. Hole from core T-2 is visible. Dampness permeating through cracks visible beneath the area of core T-1. White efflorescence common in areas directly below regions covered with cold patch material.

Figure A2.98. Cores retrieved from site, core T-1 (top), core T-2 (bottom).

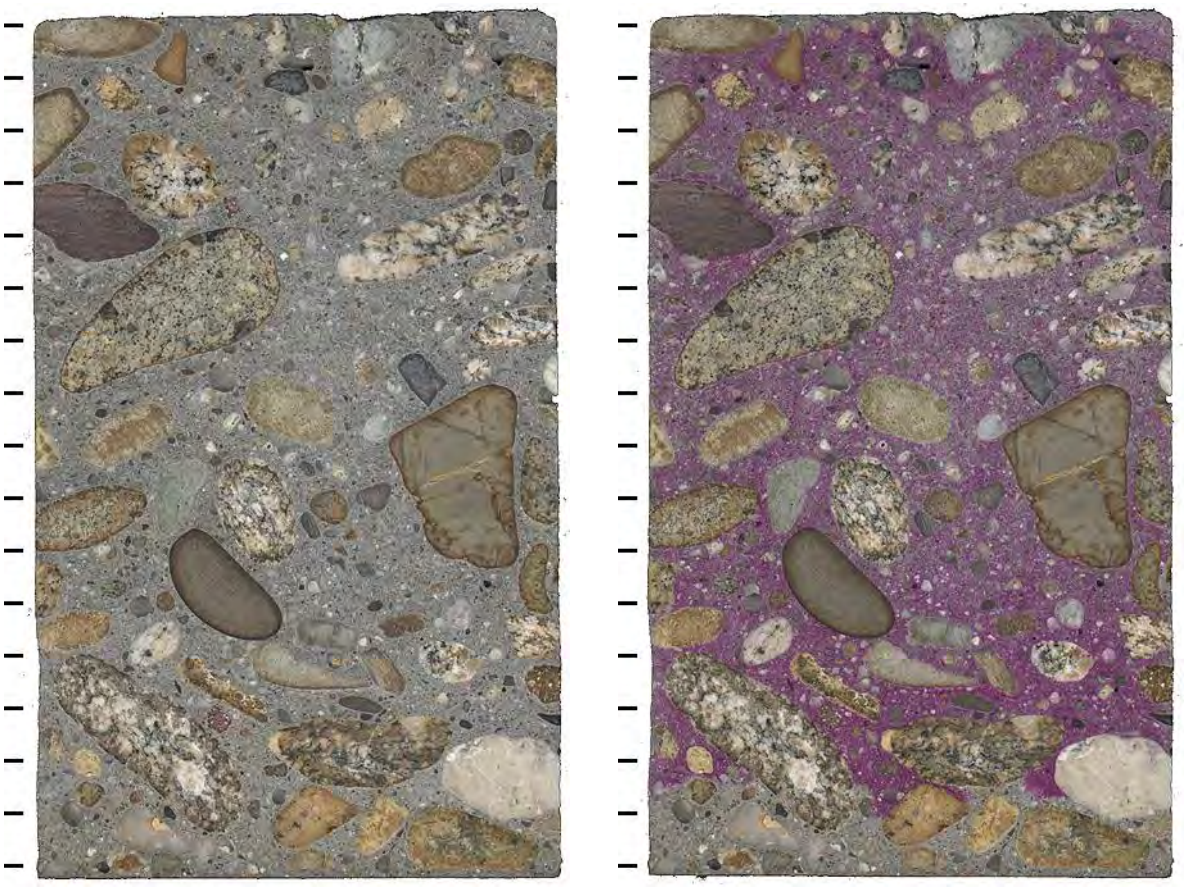

Figure A2.99. Polished slabs to show complete cross-section through core T-2 both before (left) and after application of phenolphthalein stain (right) tic marks every cm.

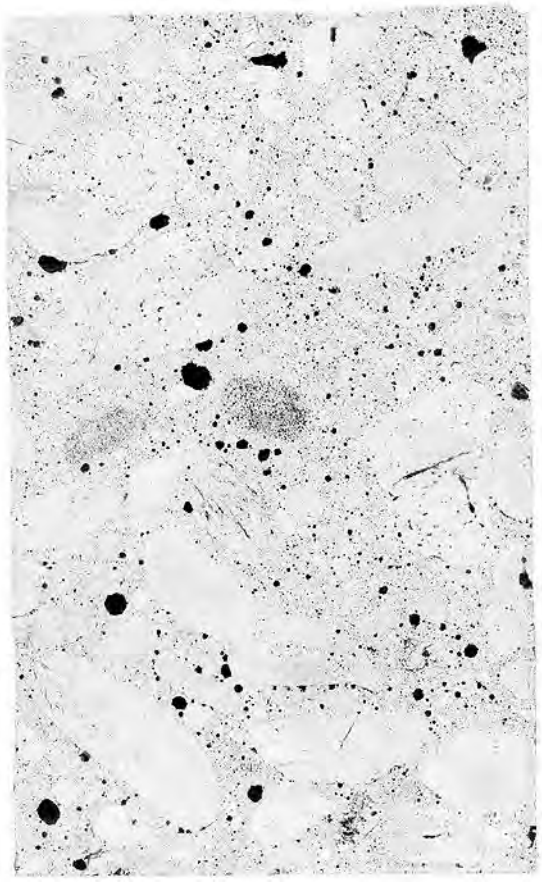

Figure A2.100. Polished slabs to show complete cross-section through core T-2 after treatment to enhance appearance of air voids and cracks, tic marks every cm.

Table A2.18. Air void parameters.

Sample ID	T-2
Location	Area in Good Condition
Raw data	
Total traverse length (mm)	3772.1
Area analyzed (cm^2)	73.9
Air stops	70
Paste stops	413
Aggregate stops	961
Secondary deposit stops	0
Total stops	1444
Number of air intercepts	617
Number of filled void intercepts	0
Results	
Air vol%	4.9
Paste vol%	28.6
Aggregate vol%	66.6
Secondary deposit vol%	0.0
Existing average chord length (mm)	0.370
Existing paste/air ratio	5.9
Existing air void specific surface (mm^{-1})	13.5
Existing air void frequency (voids/m)	164
Existing spacing factor (mm)	0.296
Original average chord length (mm)	0.370
Original paste/air ratio	5.9
Original air void specific surface (mm^{-1})	13.5
Original air void frequency (voids/m)	164
Original spacing factor (mm)	0.296

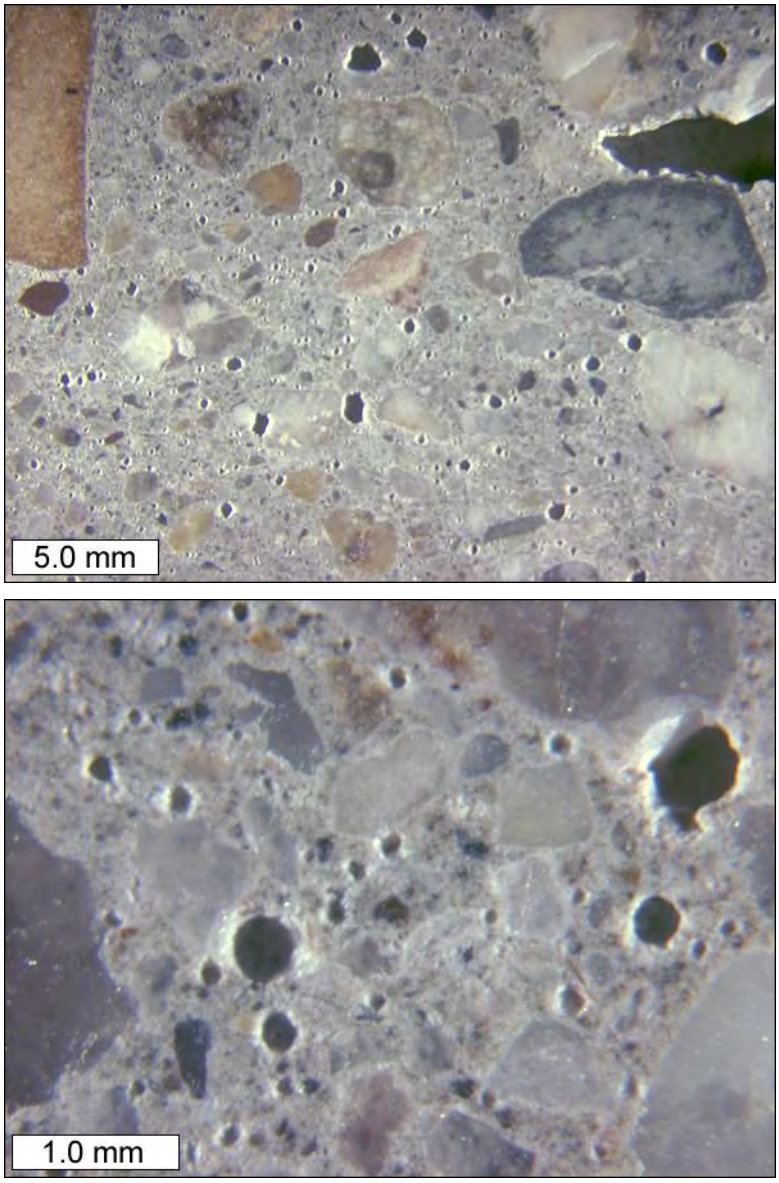

Figure A2.101. Stereo microscope images to show air void structure on polished slab from core T-2.

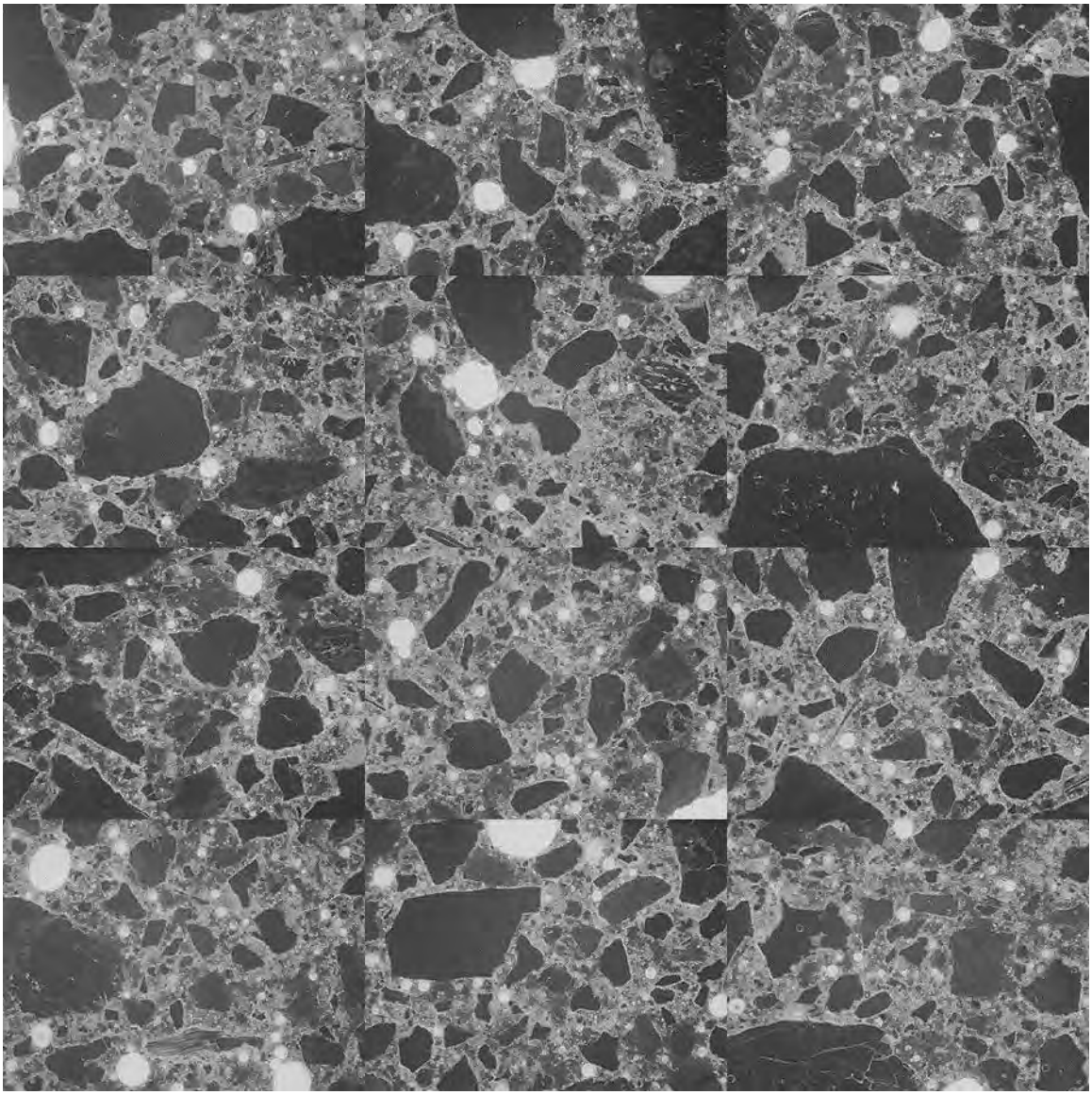

Figure A2.102. Mosaic of 12 frames collected from thin section prepared from billet cut from top portion of core T-2 (each individual frame measures 2.612 x 1.959 mm).

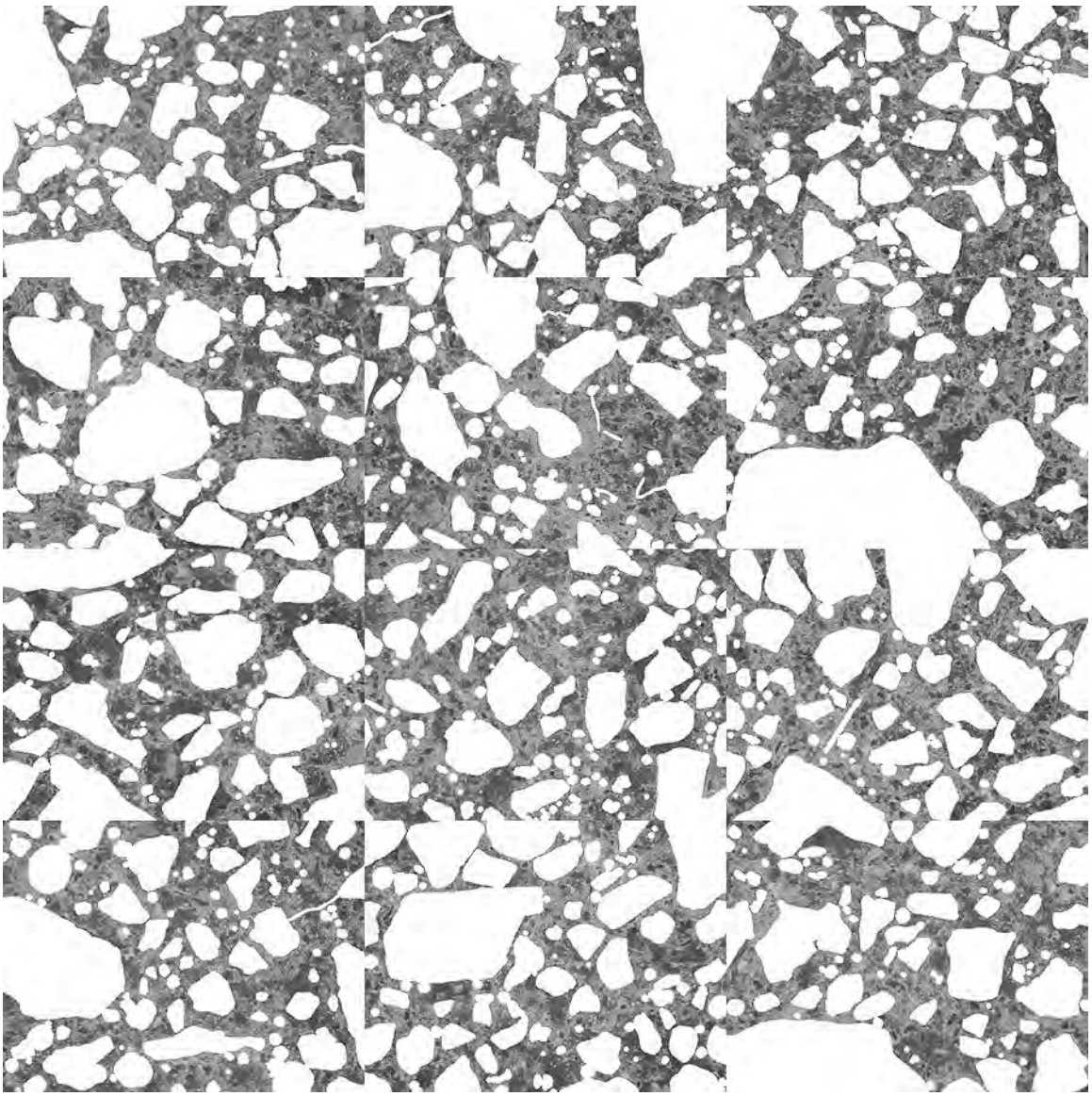

Figure A2.103. Mosaic of 12 frames collected from thin section prepared from billet cut from top portion of core T-2 after masking out air voids, fine aggregate, and micro-cracks to isolate cement paste (each individual frame measures 2.612 x 1.959 mm).

Table A2.19. Average cement paste pixel intensities per frame, and equivalent *w/c* values (as compared to 28-day moist cured mortar samples).

Cement Paste Pixel Fluorescence Measurements (average intensity per frame)			
71	67	63	68
72	67	62	72
75	68	69	72
equivalent *w/c* (y = 0.0044x + 0.0329)			
0.34	0.33	0.31	0.33
0.35	0.32	0.31	0.35
0.36	0.33	0.33	0.35

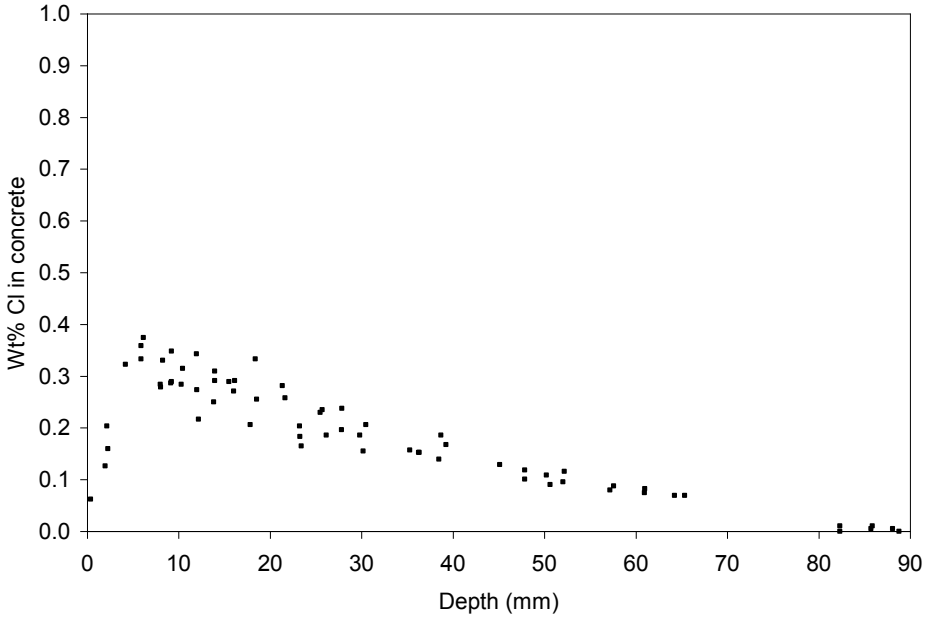

Figure A2.104. Chloride profile from billet prepared from core T-2.

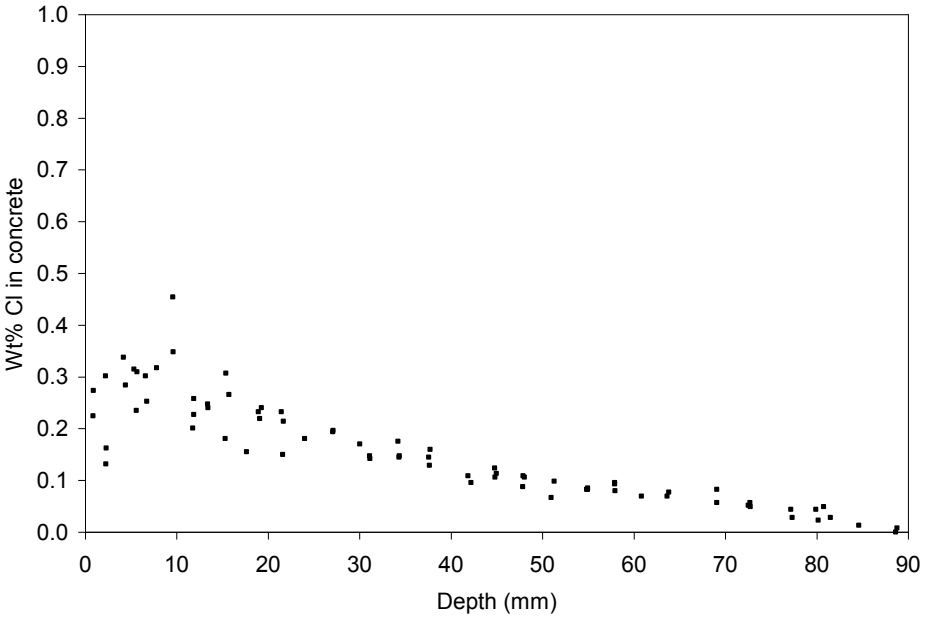

Figure A2.105. Duplicate chloride profile from additional billet prepared from core T-2.

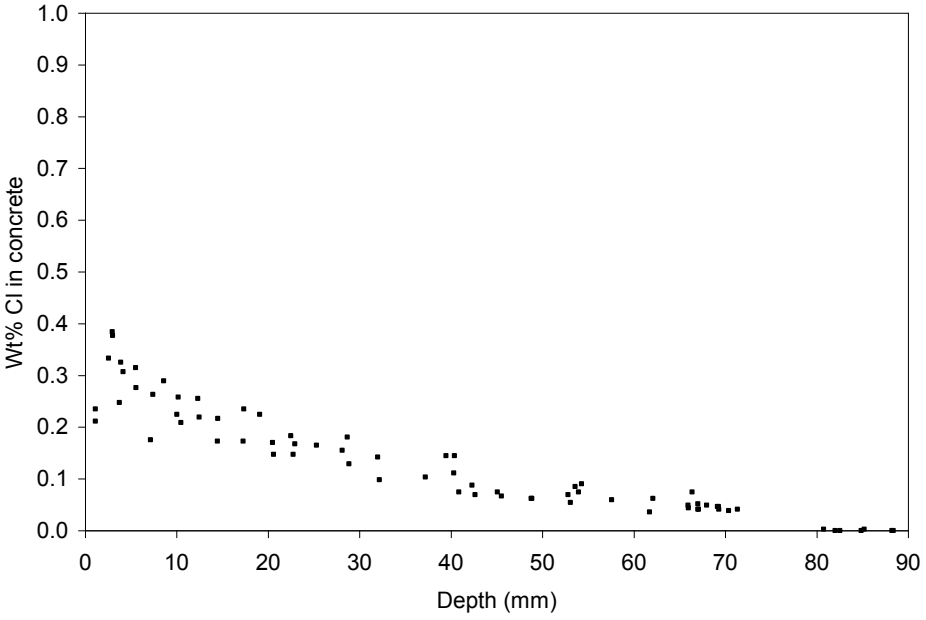

Figure A2.106. Duplicate chloride profile from additional billet prepared from core T-2.

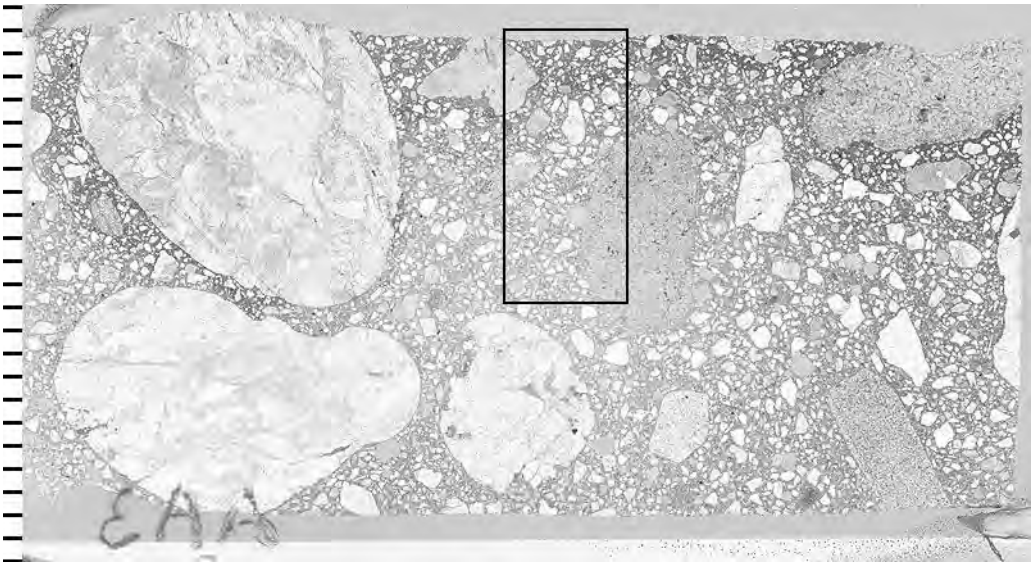

Figure A2.107. Transmitted light scanned image of thin section to show location of elemental maps shown in Figure A2.109. The top of the thin section represents the wear surface of the pavement, (tic marks every mm).

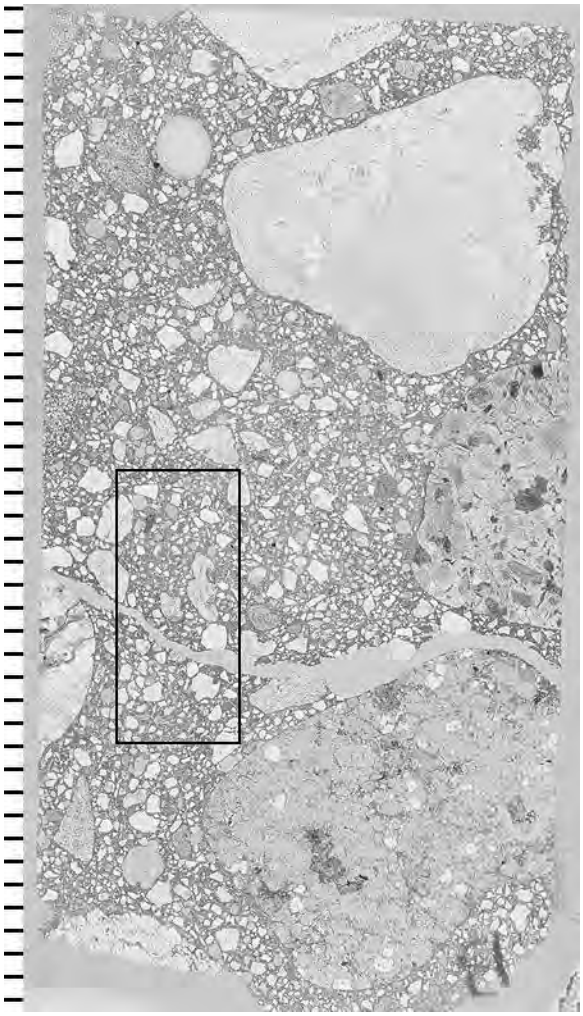

Figure A2.108. Transmitted light scanned image of thin section to show location of elemental maps shown in Figure A2.110. The large crack, sub-parallel to the pavement surface, is at a depth of about 40 mm, (tic marks every mm).

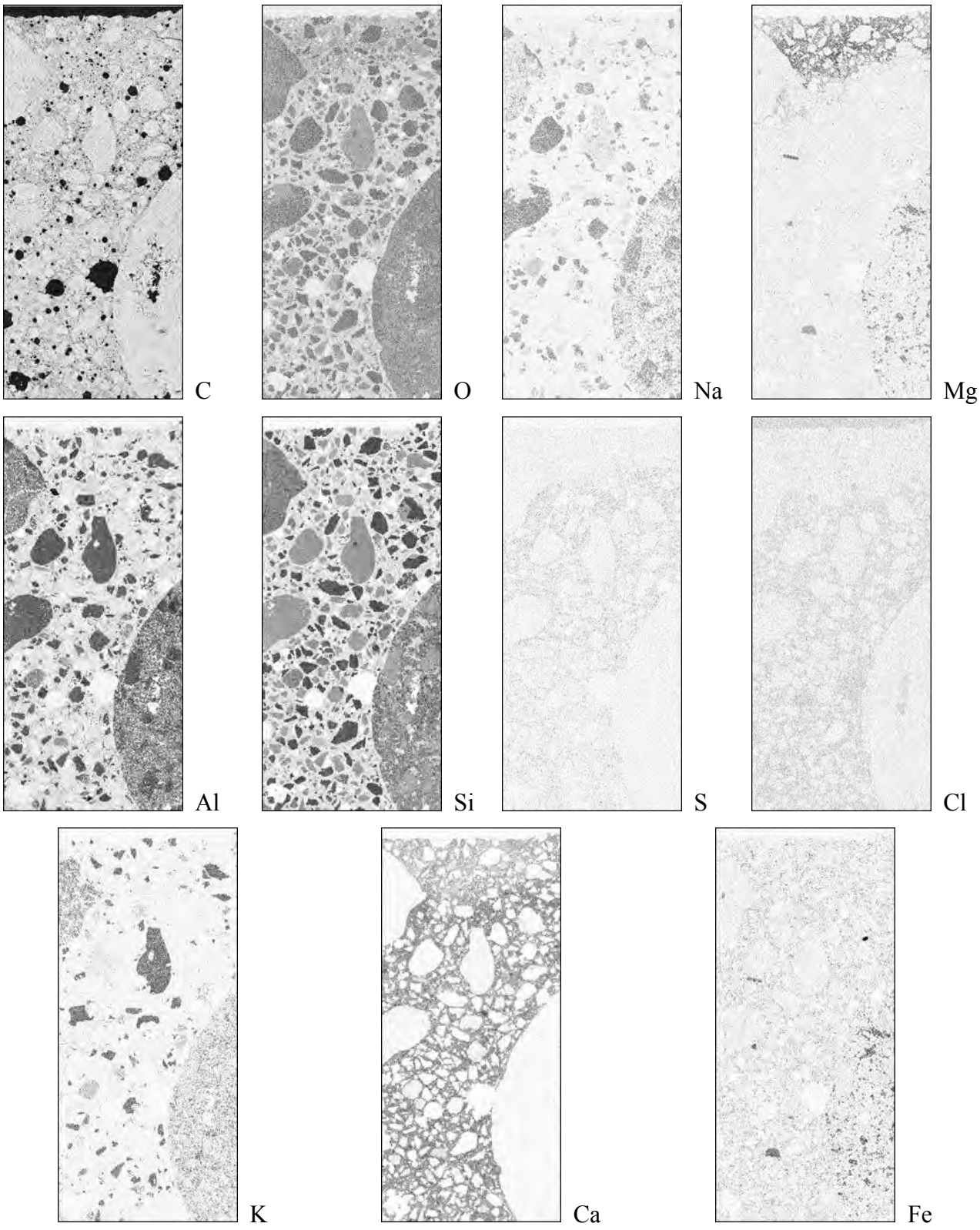

Figure A2.109. Elemental maps from pavement surface, darker regions indicate higher concentrations.

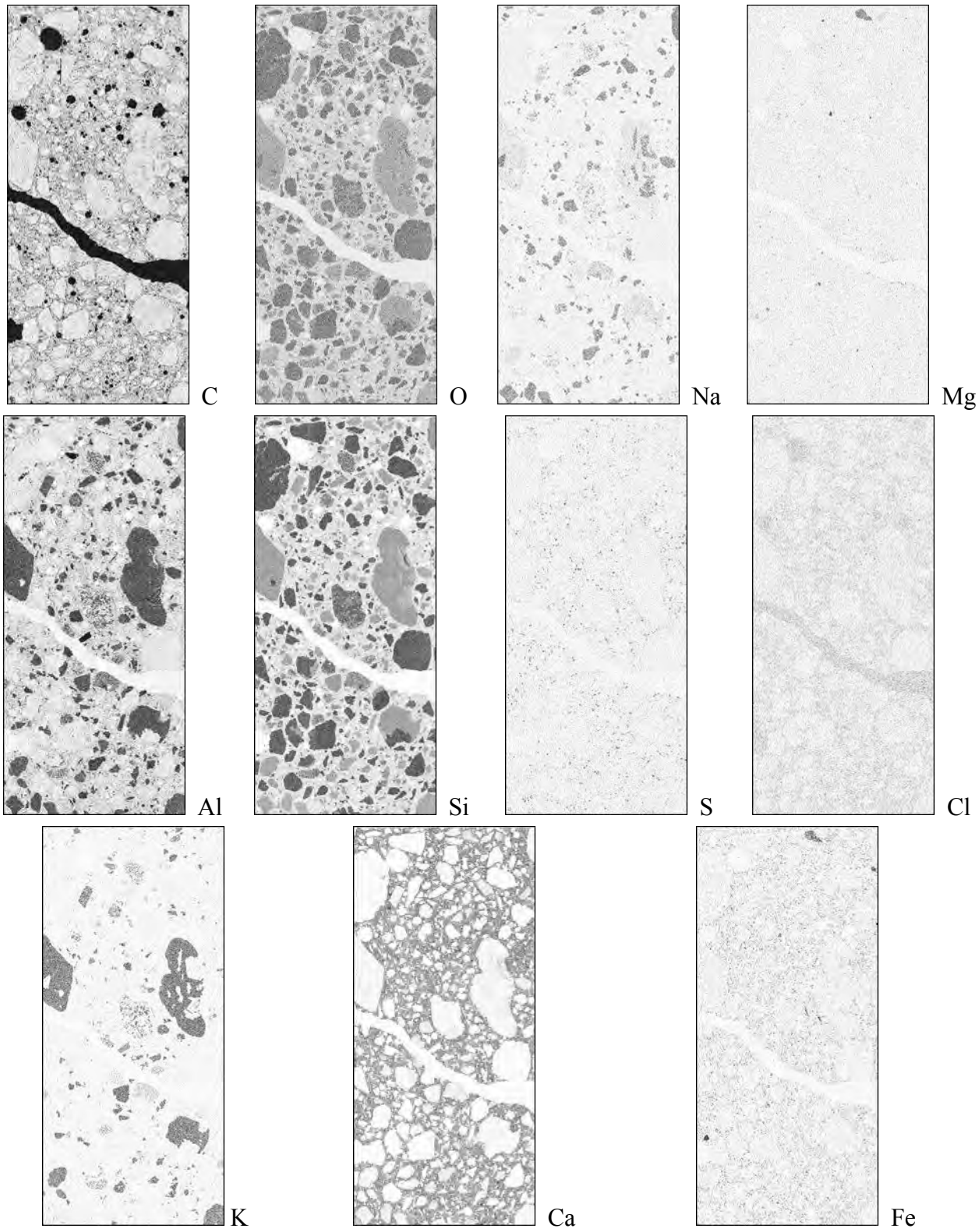

Figure A2.110. Elemental maps from crack at depth, darker regions indicate higher concentrations.

Montana, westbound Interstate Highway 90 bridge deck, near milepost 37.2, Sloway interchange

This bridge deck was constructed in 1977, part of maintenance area 1114, and exposed to $MgCl_2$ brine and a combination of NaCl and sand. Figure A2.111 shows the locations of the cores, and Figure A2.112 shows the condition of the bridge deck, with some spalling. Figure A2.113 shows the underside of the bridge deck. Figure A2.114 shows photographs of the cores. Core S-1 exhibited a crack plane at a depth of about 30 mm coinciding with reinforcement steel. Upon extraction from the bridge deck, the top 30 mm portion of the core was easily separated from the remainder of the core, and the reinforcement steel did not exhibit corrosion. The corrosion products visible in the photograph of the core in Figure A2.114 occurred subsequent to the coring operation, as the core was stored in a damp state wrapped in plastic for a period of one week. After unwrapping and photographing core S-1, the core was dried overnight in a 50 degree C oven, vacuum impregnated with epoxy, and used for thin section preparation. Core S-2 was intact, and cut into slabs and polished. Figures A2.115 and A2.116 show the slab as polished, after staining with phenolphthalein, and after treatment to enhance air voids and cracks. The phenolphthalein stain showed normal carbonation depths. The black and white treatment did not reveal any macro-cracking, with the exception of a small crack perpendicular to the pavement surface. Table A2.20 summarizes the air void parameters. The slab showed adequate entrained air, with a spacing factor of 0.173 mm. Figure A2.117 shows an example stereomicroscope image of the air void structure. A *w/c* ratio estimation was performed on a thin section prepared from the top of core S-2. Figures A2.118 and A2.119 show the images used to make the measurements. The results of the *w/c* estimation are summarized in Table A2.21, with an average *w/c* value of 0.33 as compared to the 28-day moist cured mortar sample standards. Figures A2.120 and A2.121 show chloride profiles from cores S-2. Figure A2.122 shows the locations on the thin sections prepared from core S-1 that were used for elemental mapping. Regions were mapped to represent the pavement surface and the crack at depth. Figures A2.123 and A2.124 show the elemental maps from the two regions. Chloride profiles were not recorded from core S-1 because it had been epoxy impregnated; the epoxy contains chlorine. The most interesting feature in the elemental maps is the chlorine map from Figure A2.124 that shows chlorine enrichment along the top surface of the crack at depth.

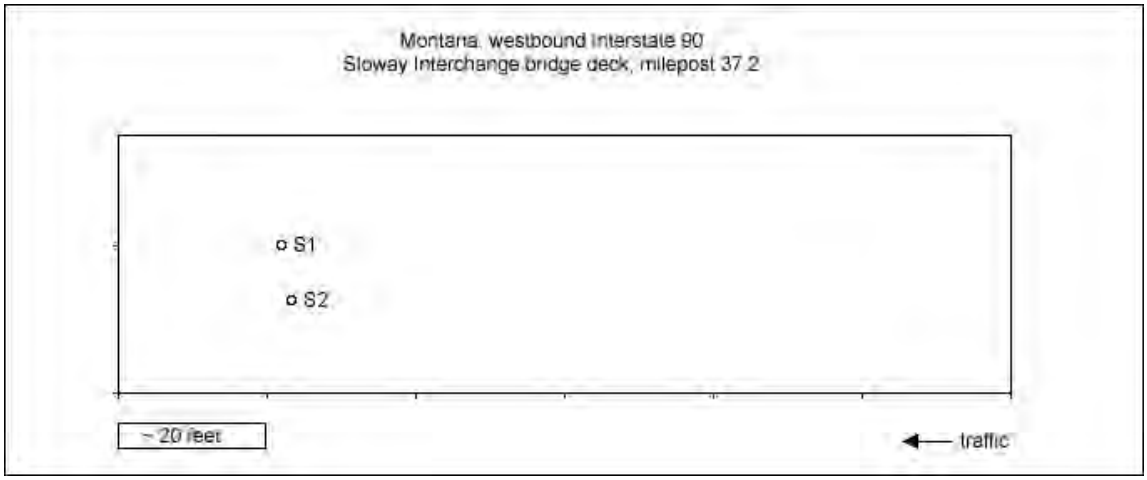

Figure A2.111. Diagram to show location of cores based on field information.

Figure A2.112. Photograph of core site.

Figure A2.113. Photograph from beneath bridge deck after coring operation, hole from core S-1 is clearly visible, light coming through hole from core S-2 is partly obscured by the pre-stressed beam.

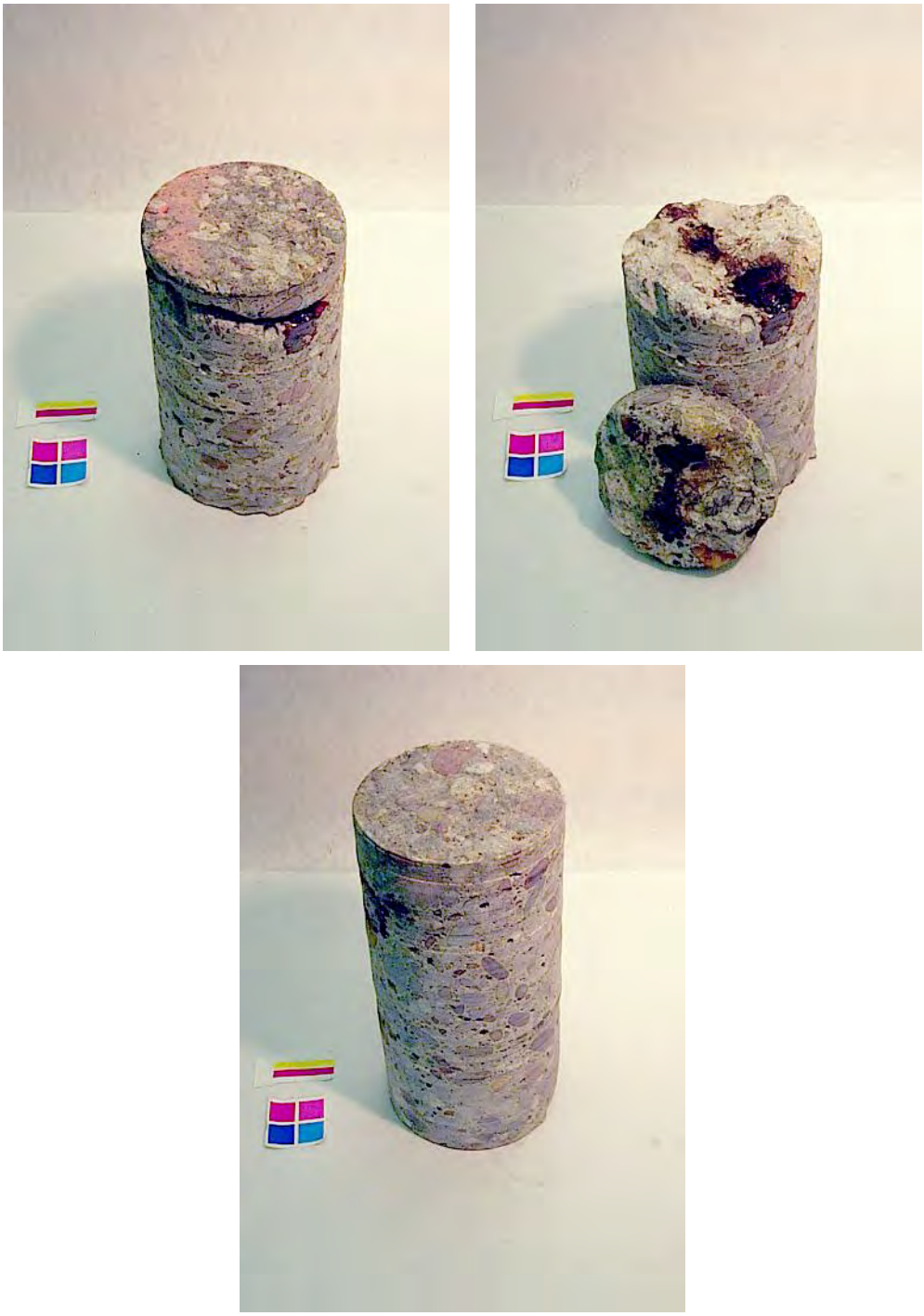

Figure A2.114. Cores retrieved from site, core S-1 (top), core S-2 (bottom).

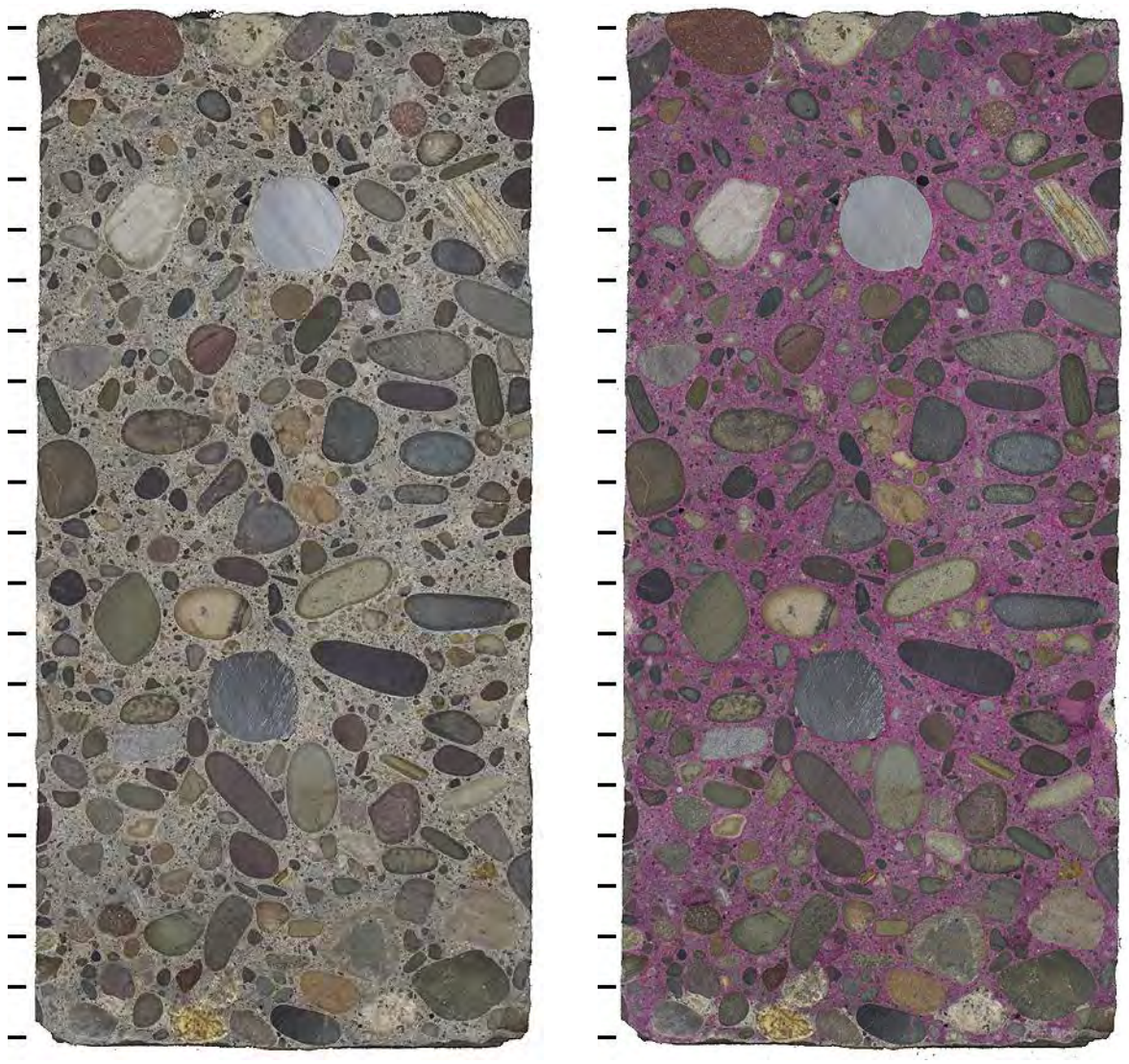

Figure A2.115. Polished slabs to show complete cross-section through core S-2 both before (left) and after application of phenolphthalein stain (right) tic marks every cm.

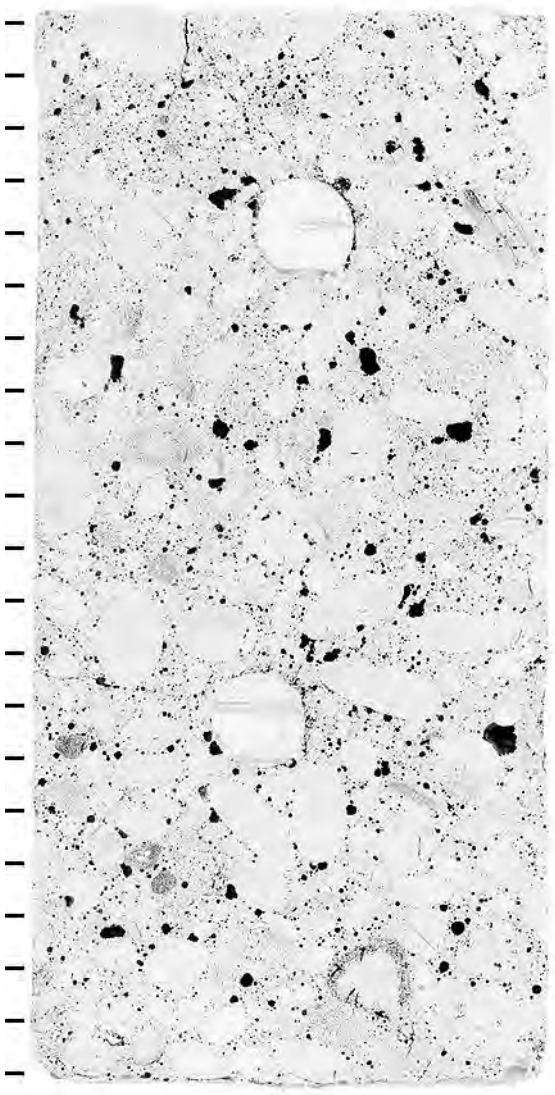

Figure A2.116. Polished slabs to show complete cross-section through core S-2 after treatment to enhance appearance of air voids and cracks, tic marks every cm.

Table A2.20. Air void parameters.

Sample ID	S-2
Location	Area in Good Condition
Raw data	
Total traverse length (mm)	4242.3
Area analyzed (cm^2)	83.1
Air stops	65
Paste stops	464
Aggregate stops	1092
Secondary deposit stops	3
Total stops	1624
Number of air intercepts	958
Number of filled void intercepts	66
Results	
Air vol%	4.0
Paste vol%	28.6
Aggregate vol%	67.2
Secondary deposit vol%	0.2
Existing average chord length (mm)	0.242
Existing paste/air ratio	7.2
Existing air void specific surface (mm^{-1})	22.6
Existing air void frequency (voids/m)	226
Existing spacing factor (mm)	0.177
Original average chord length (mm)	0.231
Original paste/air ratio	6.8
Original air void specific surface (mm^{-1})	23.1
Original air void frequency (voids/m)	241
Original spacing factor (mm)	0.173

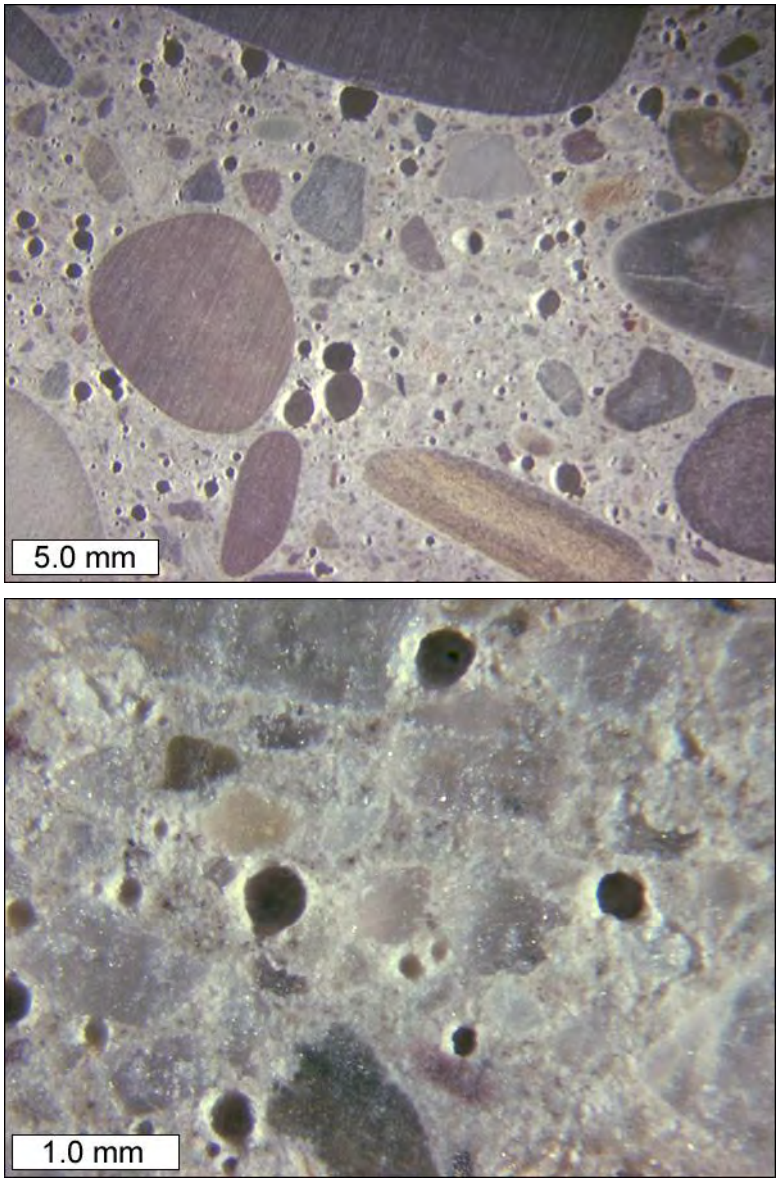

Figure A2.117. Stereo microscope images to show air void structure on polished slab from core S-2.

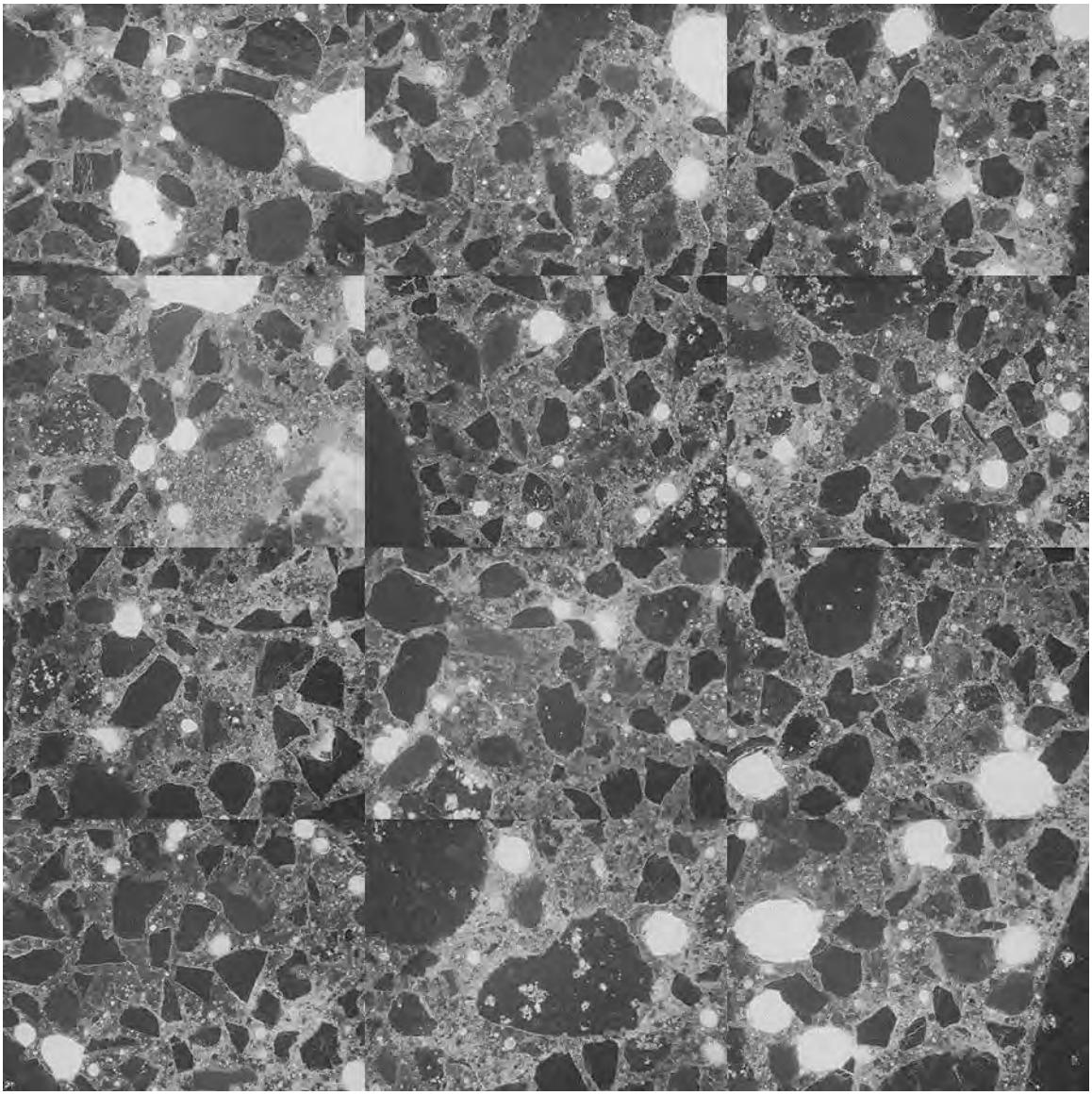

Figure A2.118. Mosaic of 12 frames collected from thin section prepared from billet cut from top portion of core S-2 (each individual frame measures 2.612 x 1.959 mm).

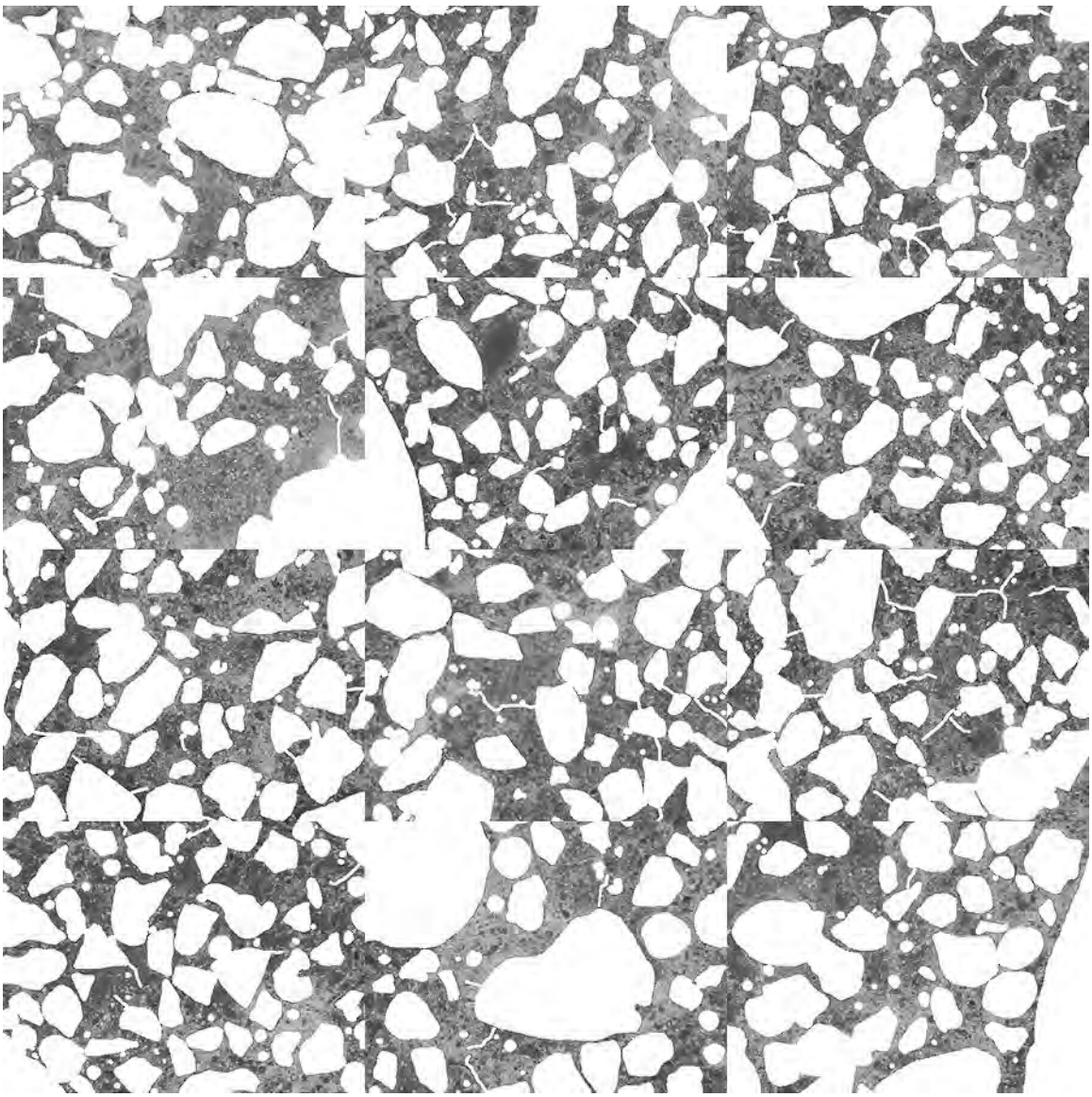

Figure A2.119. Mosaic of 12 frames collected from thin section prepared from billet cut from top portion of core S-2 after masking out air voids, fine aggregate, and micro-cracks to isolate cement paste (each individual frame measures 2.612 x 1.959 mm).

Table A2.21. Average cement paste pixel intensities per frame, and equivalent *w/c* values (as compared to 28-day moist cured mortar samples).

Cement Paste Pixel Fluorescence Measurements (average intensity per frame)			
78	73	64	78
57	66	60	68
59	58	75	73
equivalent *w/c* (y = 0.0044x + 0.0329)			
0.37	0.35	0.31	0.37
0.28	0.32	0.30	0.33
0.29	0.28	0.36	0.35

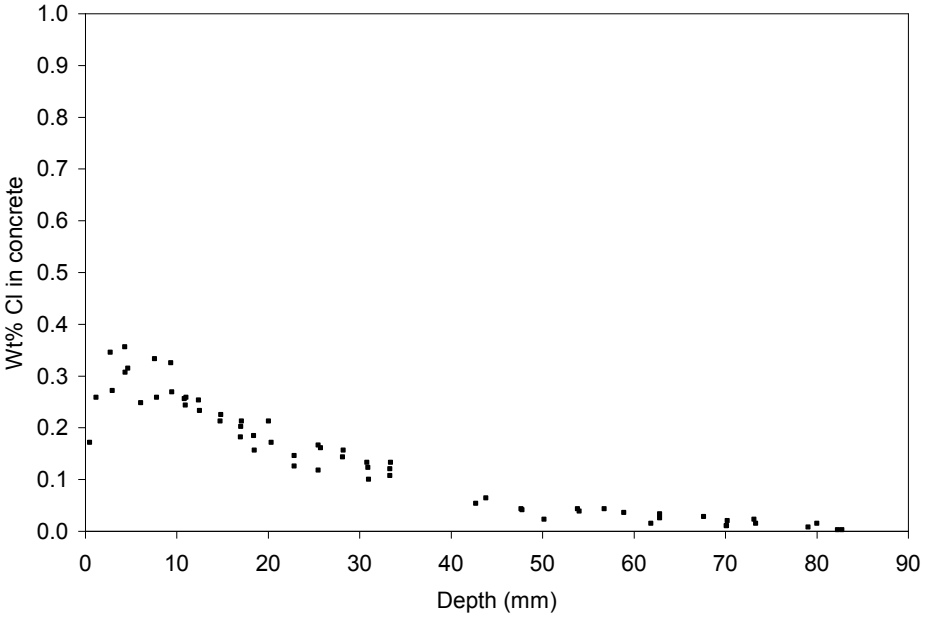

Figure A2.120. Chloride profile from billet prepared from core S-2.

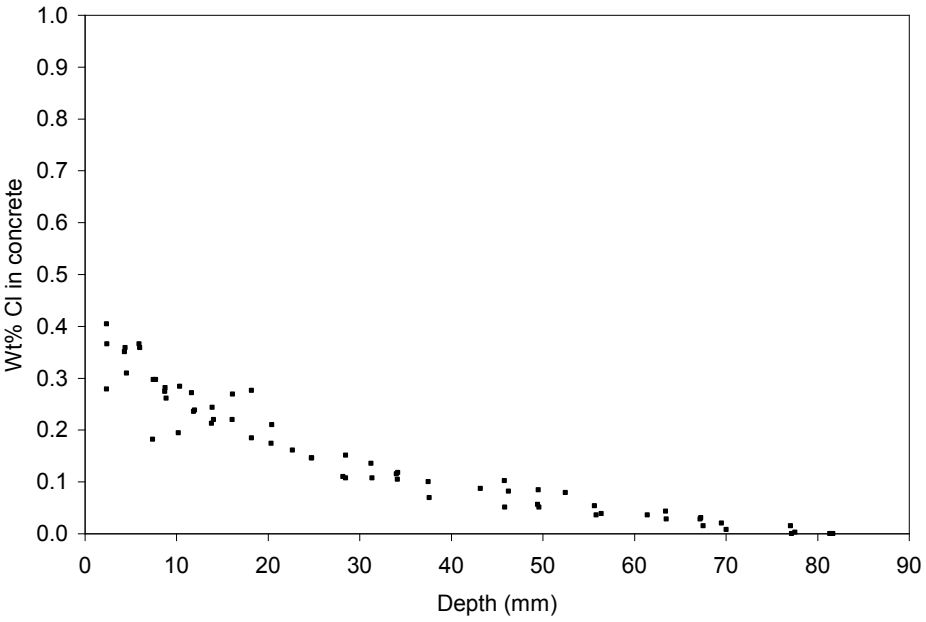

Figure A2.121. Duplicate chloride profile from additional billet prepared from core S-2.

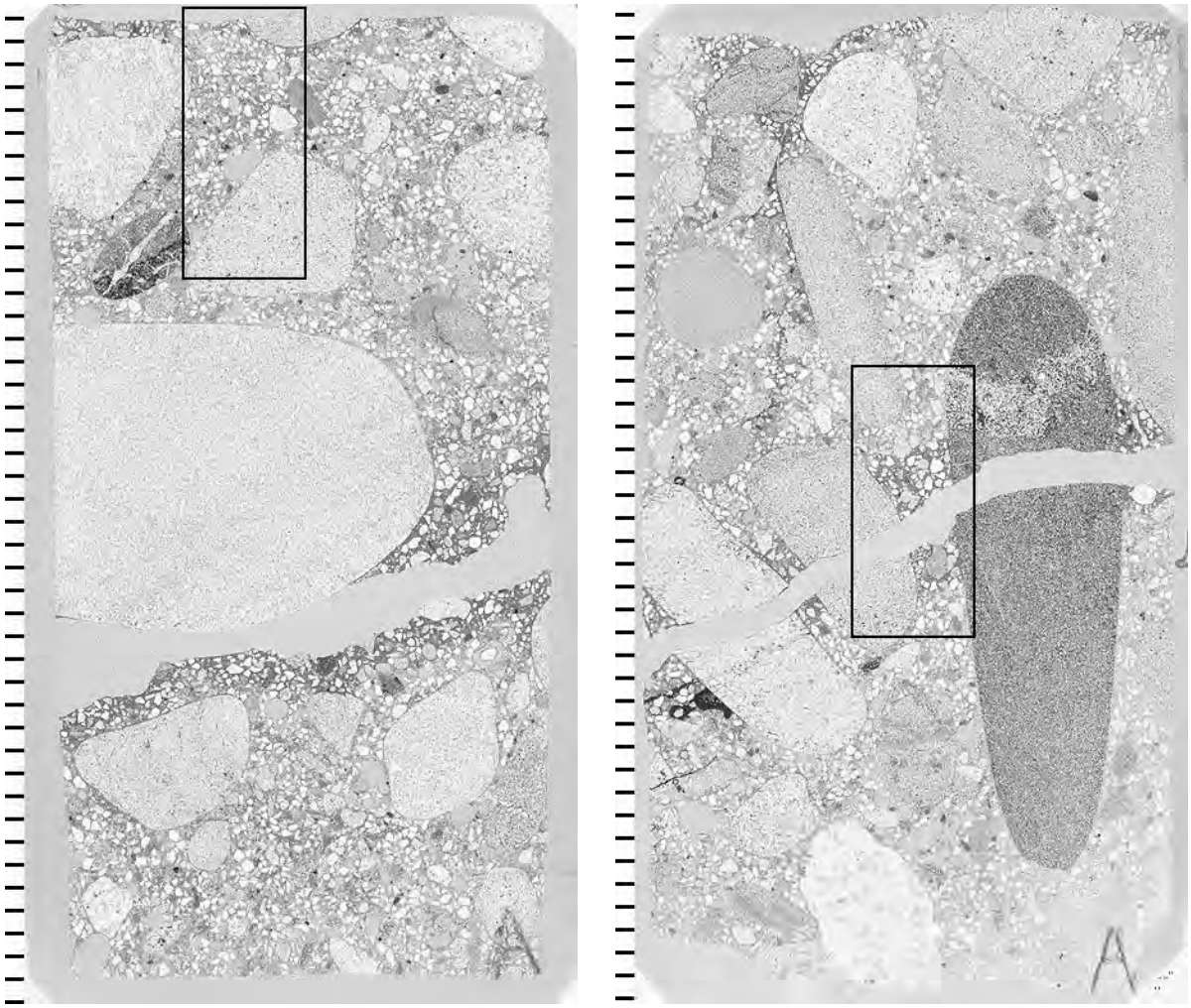

Figure A2.122. Transmitted light scanned images of thin sections to show locations of elemental maps. The top of each thin section represents the wear surface of the pavement, the large cracks, sub-parallel to the surface, are at a depth of about 25 mm, (tic marks every mm).

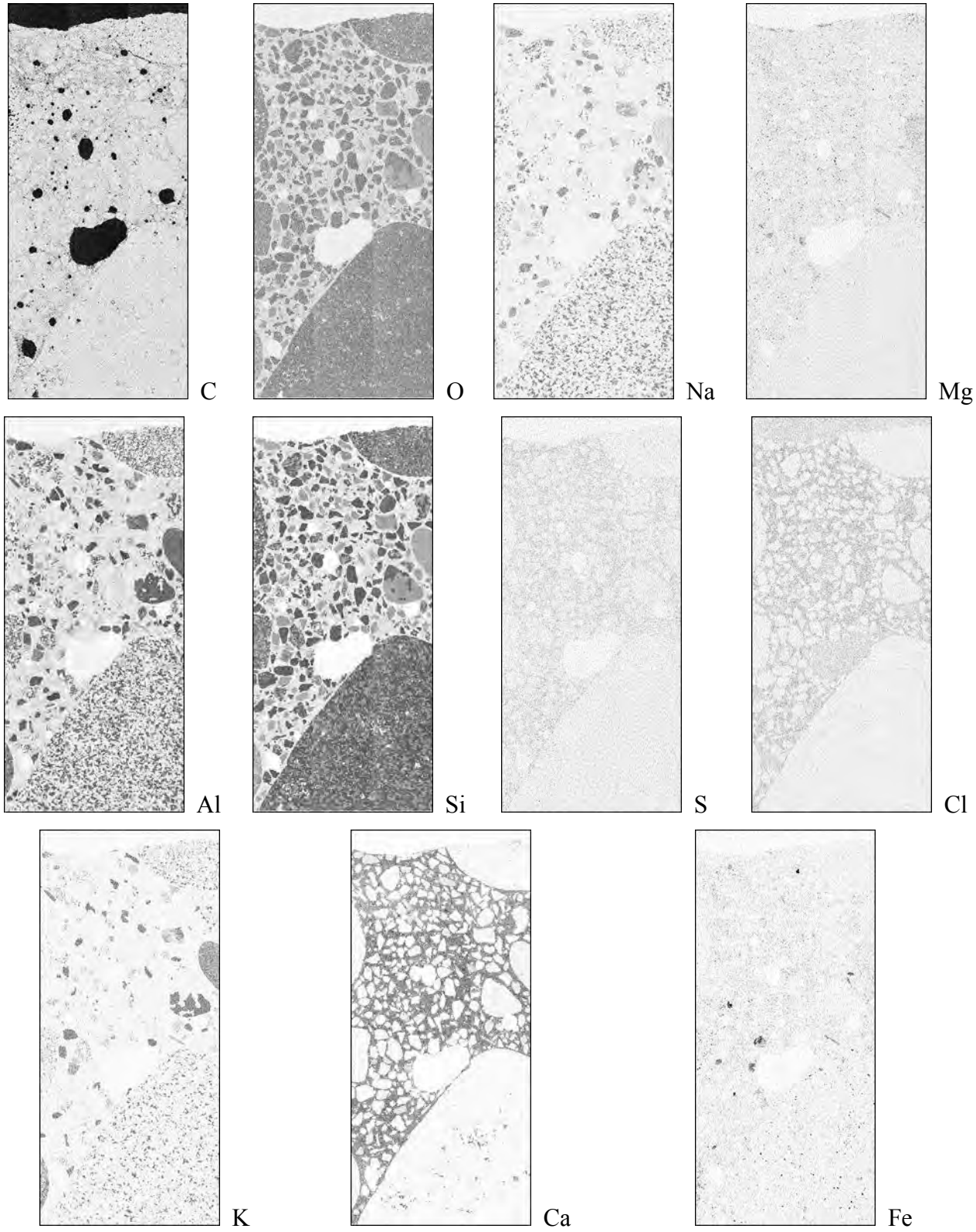

Figure A2.123. Elemental maps from pavement surface, darker regions indicate higher concentrations.

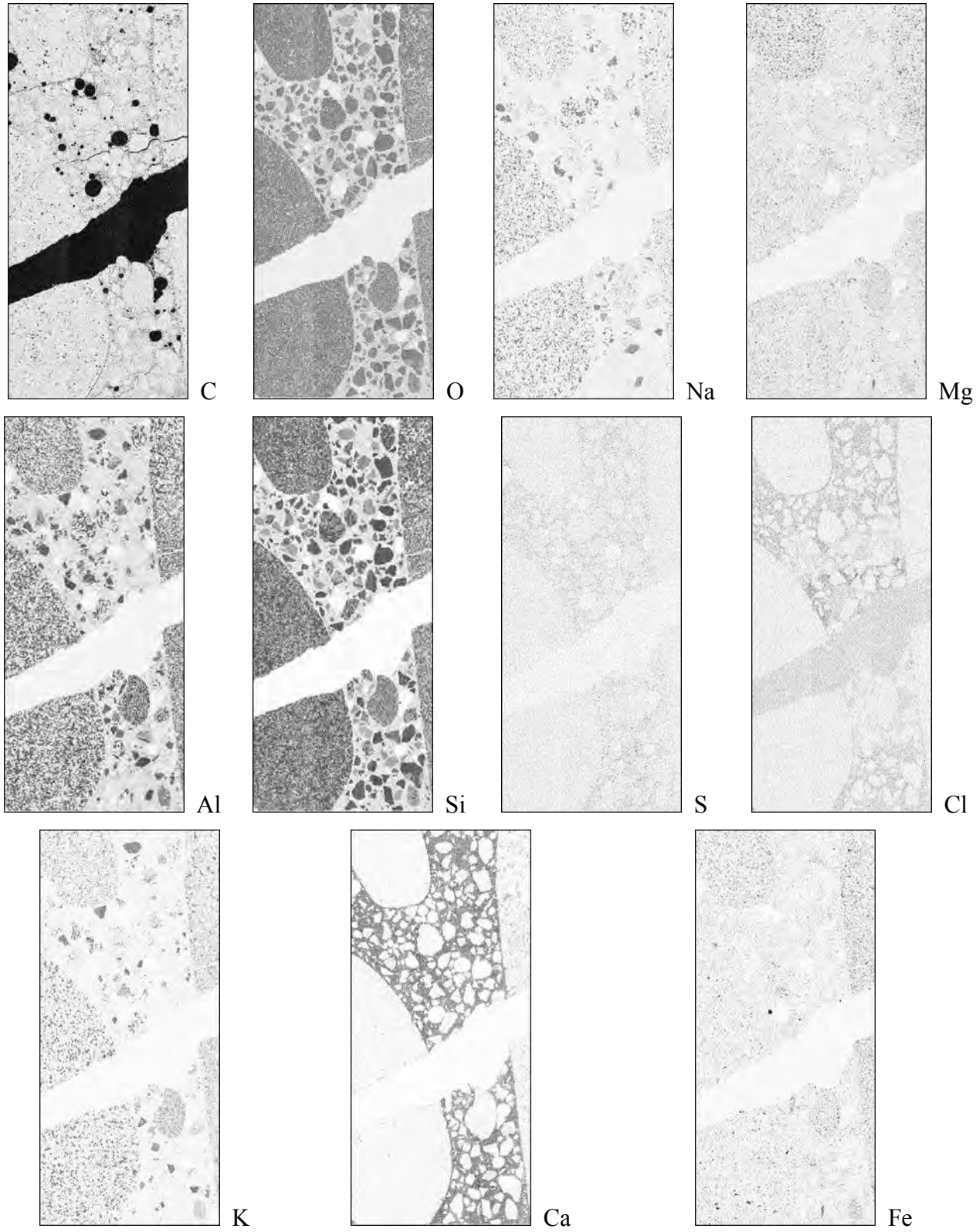

Figure A2.124. Elemental maps from crack at depth, darker regions indicate higher concentrations.

Appendix 3

Summary of Results from All Laboratory Experiments

Table of Contents

Table of Contents

List of Figures

List of Figures

List of Figures

List of Figures

List of Figures

List of Figures

List of Figures

List of Figures

List of Figures

List of Figures

List of Figures

List of Figures

List of Figures

List of Figures

List of Tables

List of Tables

Appendix 3 - Laboratory Results

A3.1 Overview

This section presents the results of the Phase I and Phase II laboratory experiments. The results of each phase will be presented separately. The results will be organized based upon the work done at Michigan Tech and that done at the University of Toronto.

A3.2 Phase I Laboratory Experiment Results

A3.2.1 Results of Phase I Experiments Conducted at Michigan Tech

A3.2.1.1 Cyclical Temperature Experiment

Observations

The cyclic temperature experiment was initially designed to monitor changes in compressive strength after 14, 28, 56, 84, and 112 days of cyclic treatment (described in section 3.4.2.3). However, it was noticed that after 8 days of cyclic testing, the cylinders immersed in rock salt NaCl deicer solution were beginning to deteriorate. After 28 days, the cylinders had badly disintegrated. The experiment was repeated a second time, replacing the rock salt NaCl with food grade NaCl to ensure sulfate impurities were not the cause. Figure A3.1 shows three of the cylinders exposed to rock salt NaCl solution after 8 days, and Figure A3.2 shows three of the cylinders exposed to food grade NaCl solution after 8 days. After 28 days, the NaCl deicer experiments were aborted.

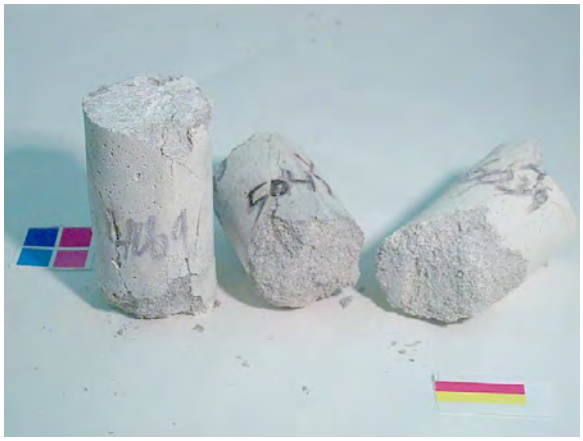

Figure A3.1. Cylinders exposed to rock salt NaCl solution after 8 days of cyclic temperature test. From left to right: 0.40, 0.50, and 0.60 *w/c* mortar cylinders.

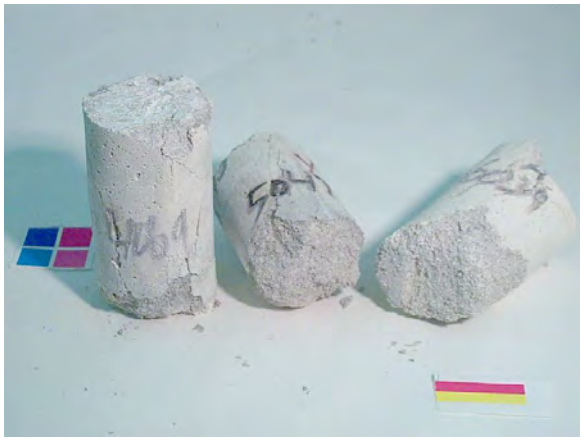

Figure A3.2. Cylinders exposed to food grade NaCl solution after 8 days of cyclic temperature test. From left to right: 0.40, 0.50, and 0.60 *w/c* mortar cylinders.

At 28 days the cylinders in the $MgCl_2$ and $CaCl_2$ solutions began to show some signs of cracking and expansion. By 56 days, the cylinders in the $MgCl_2$ and $CaCl_2$ solutions exhibited advanced deterioration. By 84 days the cylinders exposed to $MgCl_2$ and $CaCl_2$ solutions were severely deteriorated, as shown in Figures A3.3 and A3.4. It was decided that instead of running the testing out to the original 112 days, to end the test for all the cylinders at 84 days.

Figure A3.3. Cylinders exposed to $MgCl_2$ solution after 84 days of cyclic temperature test. From left to right: 0.40, 0.50, and 0.60 *w/c* mortar cylinders.

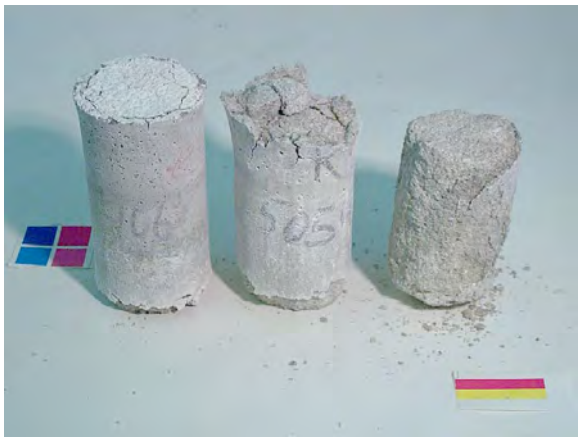

Figure A3.4. Cylinders exposed to $CaCl_2$ solution after 84 days of cyclic temperature test. From left to right: 0.40, 0.50, and 0.60 *w/c* mortar cylinders.

The cylinders exposed to the CMA solution were cycled to 84 days. Figure A3.5 shows the cylinders exposed to CMA at 84 days, with limited cracking, crumbling, and expansion evident near the top of the 0.60 *w/c* cylinder. The control cylinders exposed to limewater were in good condition at 84 days, as shown in Figure A3.6. Table A3.1 summarizes the visual ratings for all cylinders exposed to the cyclic temperature experiment over time for both the control (limewater) and deicer solutions.

Figure A3.5. Cylinders exposed to CMA solution after 84 days of cyclic temperature test. From left to right: 0.40, 0.50, and 0.60 *w/c* mortar cylinders.

Figure A3.6. Control cylinders exposed to limewater solution after 84 days of cyclic temperature test. From left to right: 0.40, 0.50, and 0.60 *w/c* mortar cylinders.

Table A3.1. List of visual ratings for all mortar cylinders from the cyclic temperature tests. Rating Scale: 0 - no visible change, 1 – some cracking, 2 - visible expansion and cracking, 3 - severe expansion and cracking, 4 - partial disintegration, 5 - total disintegration, *x* – test aborted.

Solution	Time in Days											
	w/c = 0.40				*w/c = 0.50*				*w/c = 0.60*			
	8	28	56	84	8	28	56	84	8	28	56	84
Limewater	0	0	0	0	0	0	0	0	0	0	0	0
$MgCl_2$	0	0	0-2	1-3	0	0-1	1-2	2-4	0	0-1	2-4	4-5
$CaCl_2$	0	0	0-2	2-3	0	0-1	1-3	3-4	0	2-3	3-4	4-5
NaCl	2-3	3-5	*x*	*x*	2-4	3-5	*x*	*x*	2-4	4-5	*x*	*x*
CMA	0	0	0	0	0	0	0	0	0	0	0	1

Split Tensile Strength Testing

Due to the large amounts of damage sustained during the cyclical testing, it seemed likely that the samples tested for strength would be self-selecting (i.e. the outer surfaces of more susceptible specimens scale off quickly, making them unusable for the split-tensile testing). The less susceptible specimens—with a greater immunity to distress—were the only ones able to be tested. Therefore, with the possible exception of the 0.40 *w/c* ratio specimens, this test would not be very useful in drawing conclusions about the damage done to the mortar cylinders as a result of exposure to the different deicers.

Petrographic Analysis

One of the 0.50 water to cement ratio (*w/c*) cylinders exposed to rock salt NaCl solution, and one of the control 0.50 *w/c* cylinders, were examined in thin section after 8 days of cyclic temperature testing. The thin sections represent a cross-section through the cylinder in an orientation parallel to the finished surface (i.e. the 2" [50 mm] finished end), to a depth of approximately ~3/4 inch [19 mm] from the finished surface. Figures A3.7 through A3.16 show various side-by-side image comparisons between the control and deicer-exposed cylinders. The control cylinder exposed only to limewater shows no signs of deterioration, while the cylinder exposed to the rock salt NaCl solution shows severe cracking. The cracks appear empty, with occasional secondary calcium hydroxide crystals.

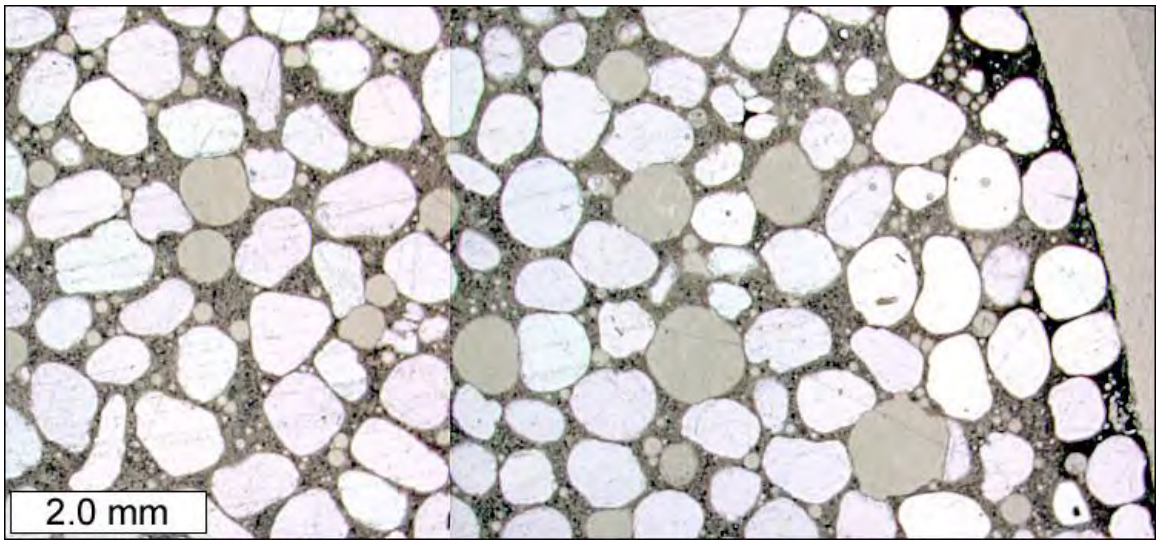

Figure A3.7. Plane polarized light image from control cylinder.

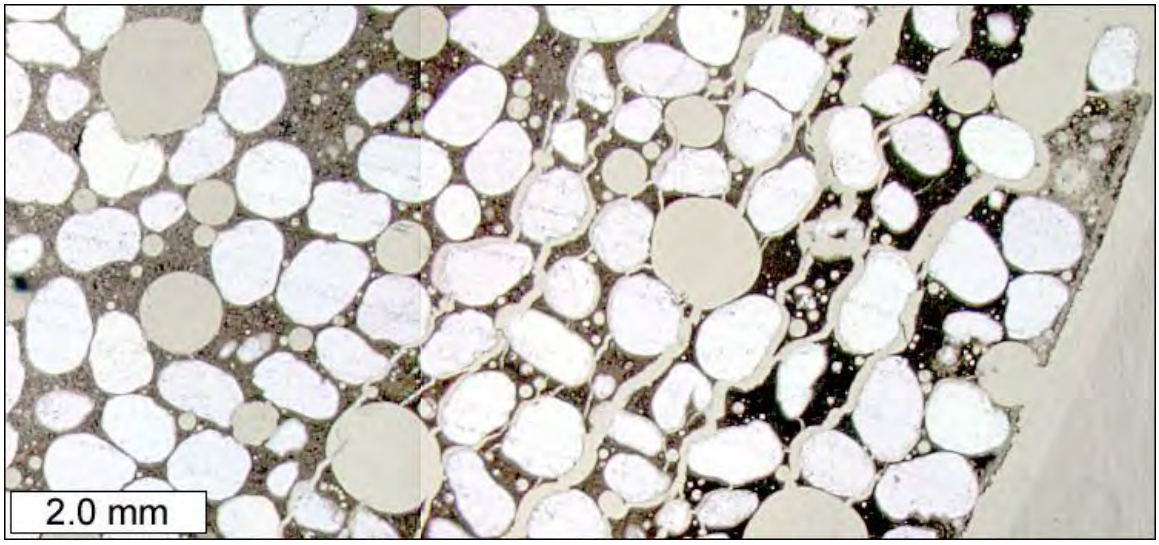

Figure A3.8. Plane polarized light image from rock salt NaCl deicer-exposed cylinder.

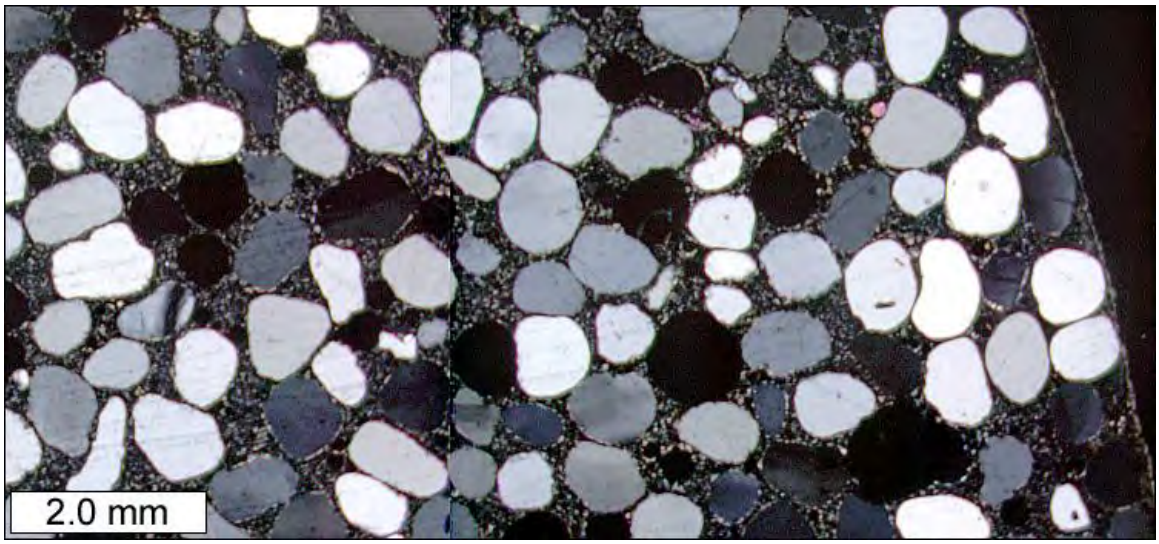

Figure A3.9. Cross polarized light image from control cylinder.

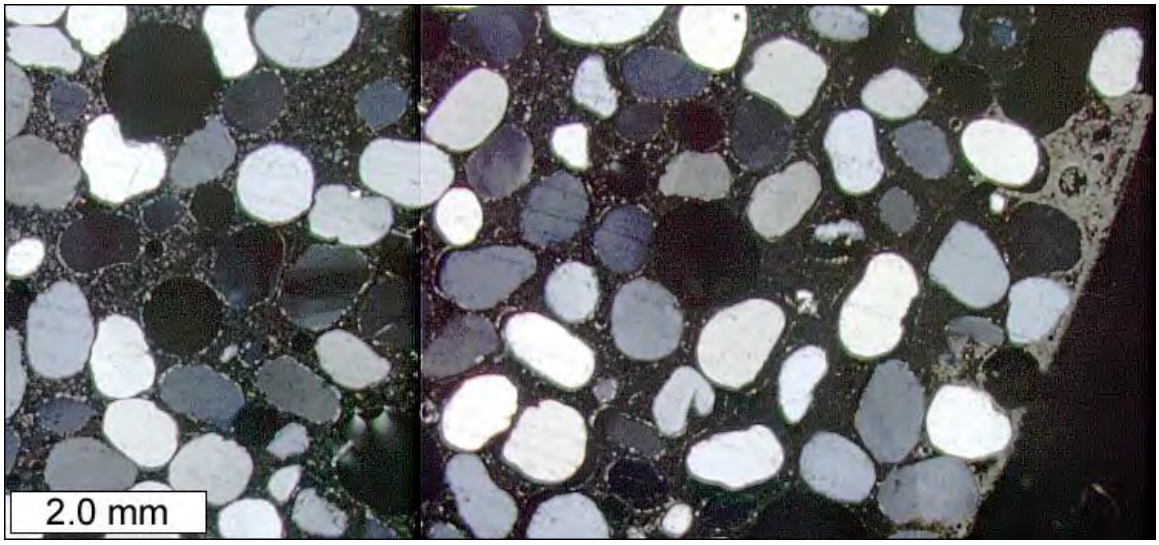

Figure A3.10. Cross polarized light image from rock salt NaCl deicer-exposed cylinder.

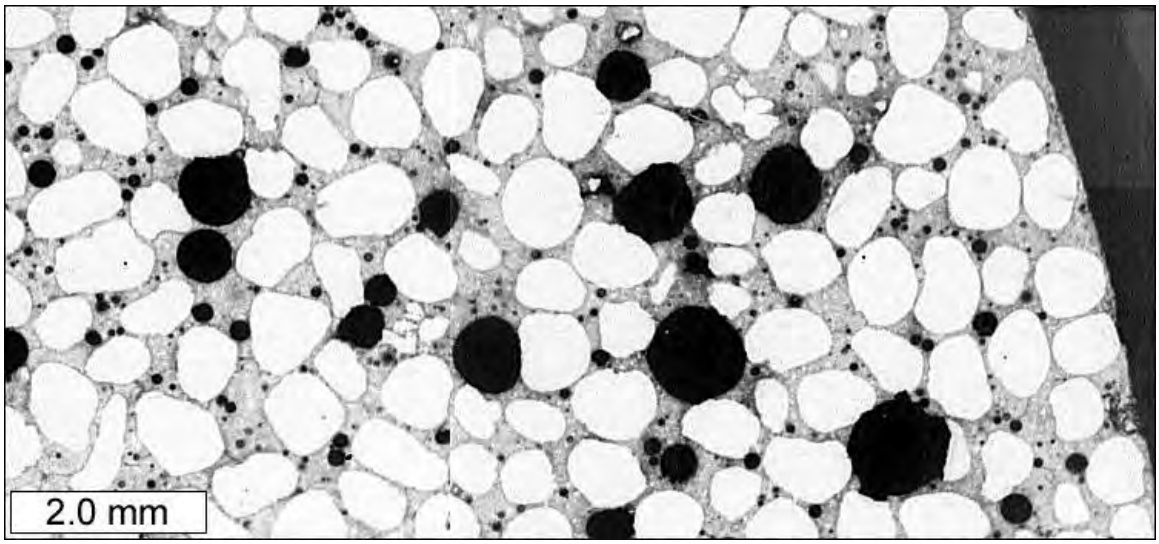

Figure A3.11. Epifluorescent image from control cylinder.

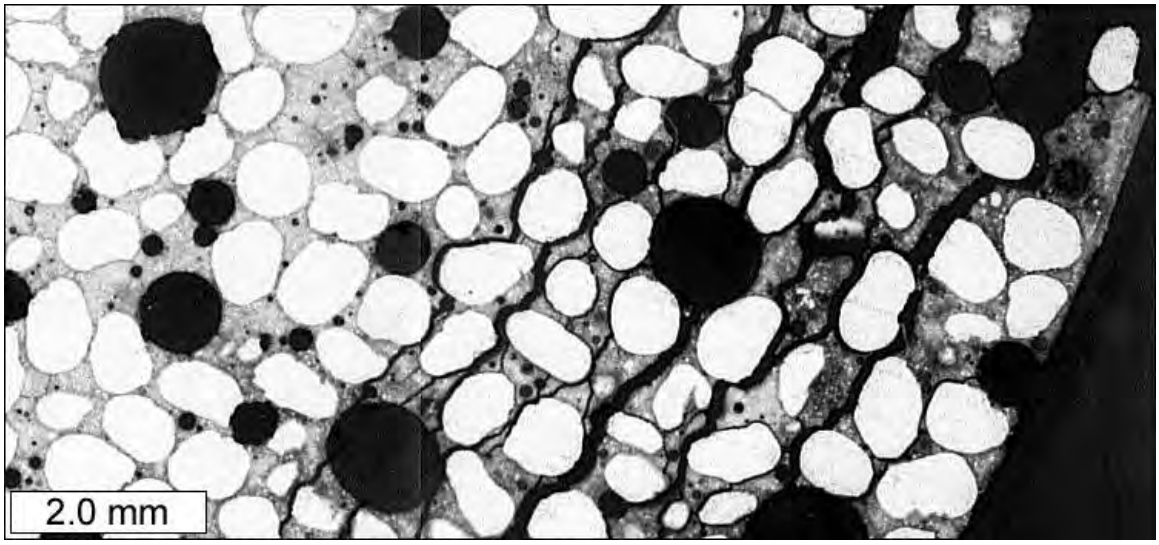

Figure A3.12. Epifluorescent image from rock salt NaCl deicer-exposed cylinder.

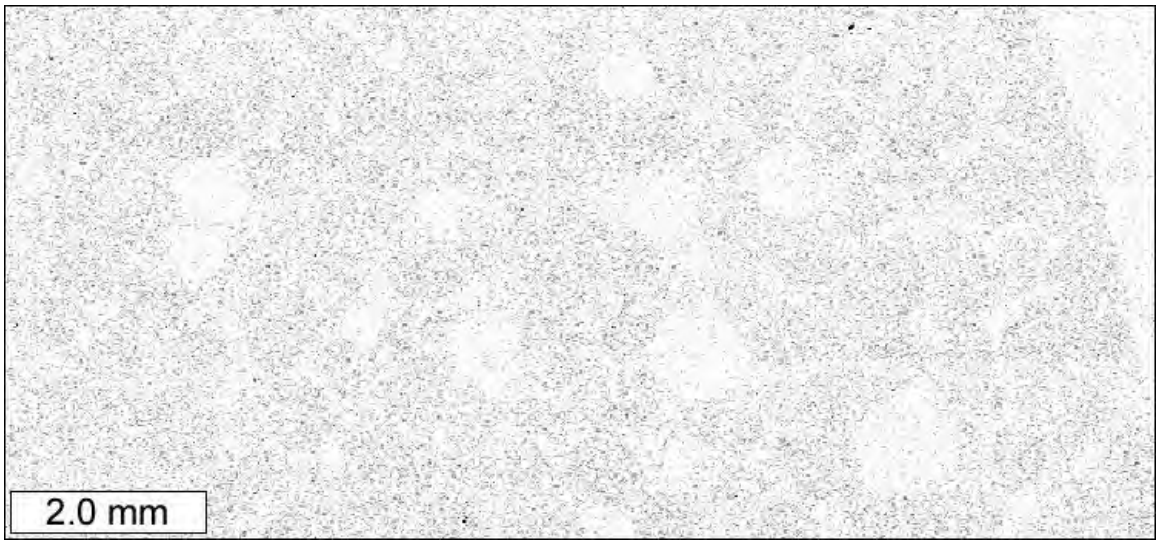

Figure A3.13. Sodium Kα X-ray map from control cylinder. Darker areas correspond to higher Kα X-ray counts.

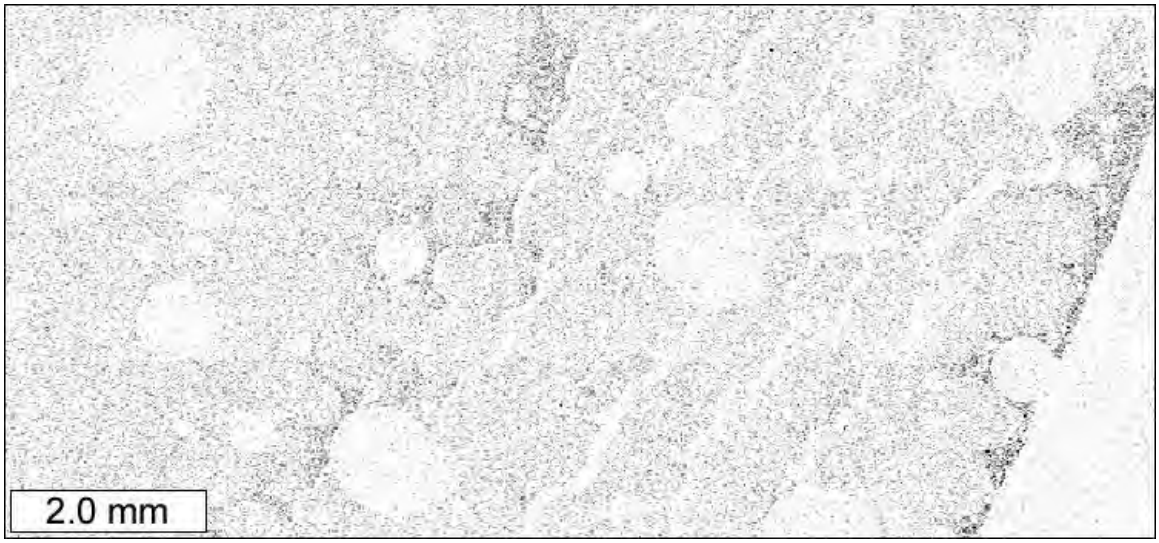

Figure A3.14. Sodium Kα X-ray map from rock salt NaCl deicer-exposed cylinder. Darker areas correspond to higher Kα X-ray counts.

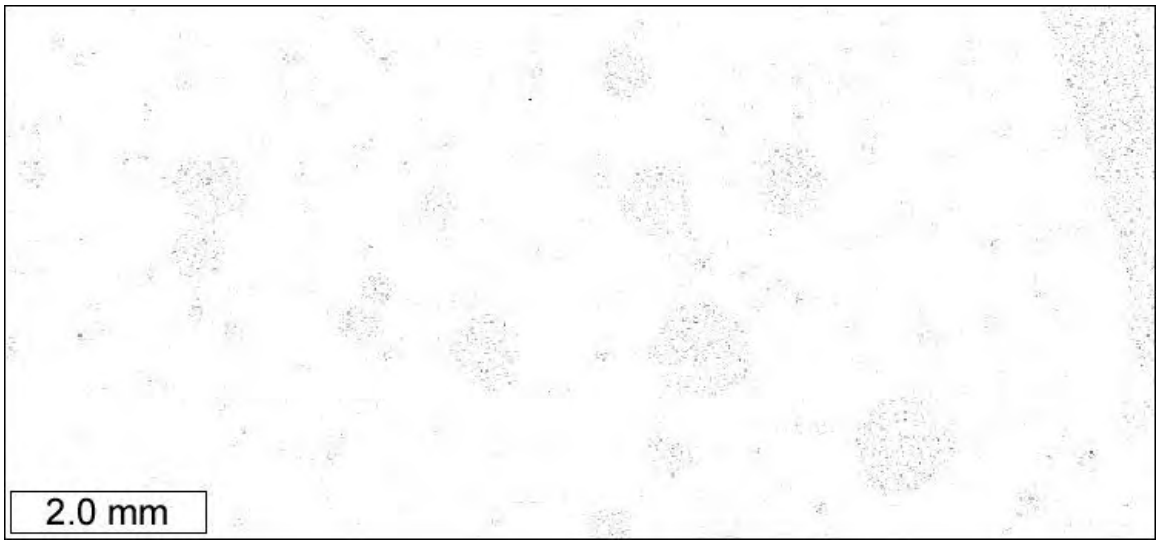

Figure A3.15. Chlorine Kα X-ray map from control cylinder. Darker areas correspond to higher Kα X-ray counts.

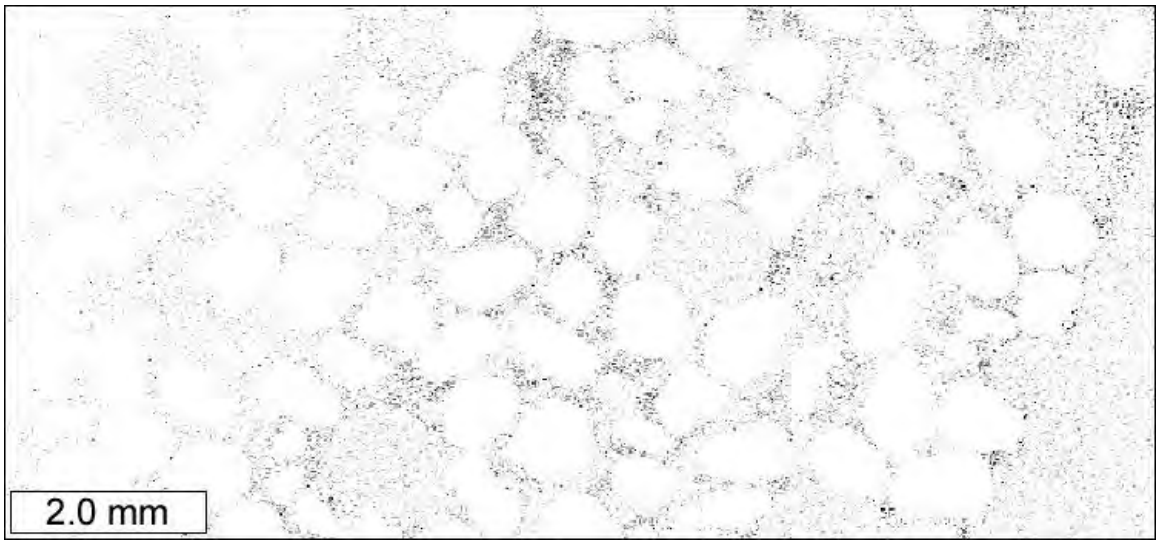

Figure A3.16. Chlorine Kα X-ray map from rock salt NaCl deicer-exposed cylinder. Darker areas correspond to higher Kα X-ray counts.

As the cyclical experiment progressed, and deterioration of the cylinders exposed to $CaCl_2$ and $MgCl_2$ solutions became evident, additional thin sections were prepared to represent the cylinders after the thawing, the lime-soak, and after the oven. The thin sections represent a cross-section through the cylinder in an orientation parallel to the finished surface (i.e. the 2" [50 mm] finished end), at a depth of approximately ~3/4 inch [19 mm] from the finished surface. The cylinders were selected during the early onset of deterioration. Three of the cylinders were selected from 0.60 *w/c* ratio mortars exposed to food grade NaCl at eight days, and three cylinders were selected from 0.40 *w/c* mortars exposed to food grade NaCl at ten days. The other six cylinders were selected from 0.50 *w/c* mortars exposed to $MgCl_2$ and $CaCl_2$ at twenty days. The deterioration of mortars exposed to the $MgCl_2$ and $CaCl_2$

solutions in the cyclic experiment looked very similar to the deterioration of mortars exposed to the $MgCl_2$ and $CaCl_2$ solutions from the constant cold temperature experiment, to be discussed later.

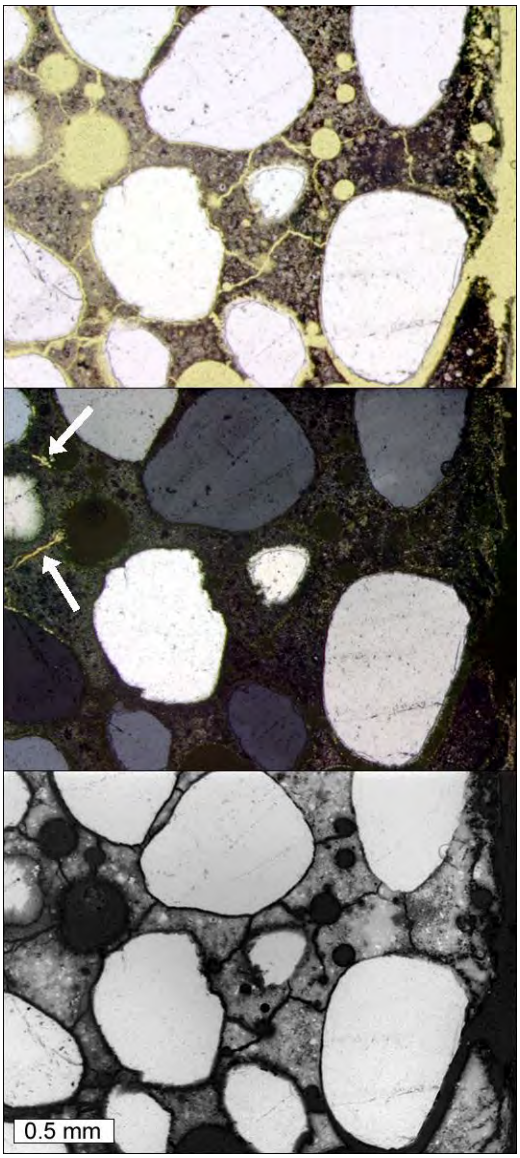

Figure A3.17. Petrographic microscope images of early onset of cracking in $MgCl_2$ exposed sample from cyclic experiment. White arrows indicate crystalline material filling cracks. From top to bottom: plane polarized light, cross polarized light, and epifluorescent mode.

Both the cyclic and constant cold temperature samples exhibited abundant cracks filled with calcium oxychloride or remnant calcium oxychloride. However, for the mortars exposed to the NaCl solution, the crack network appeared clean and empty, with occasional calcium hydroxide crystals. Figure A3.17 shows the early onset of cracking at 20 days in one of the $MgCl_2$ specimens. White arrows show the calcium oxychloride filling cracks at the left hand side of the image. Figure A3.18 shows the early onset of cracking at 8 days in one of the NaCl specimens. Secondary calcium hydroxide crystals appear in one of the air voids, but the cracks appear empty. In both Figures A3.17 and A3.18, the finished surface of the cylinders runs along the right-hand side of the image.

A3.2.1.2 Low Temperature Experiment

Observations

The constant low temperature experiment was designed to monitor chloride ingress at 28, 56, and 112 days at a temperature of 40 °F [4.4 ºC]. Some of the cylinders were coated with epoxy on all sides except for the top surface in order to monitor one-dimensional chloride diffusion. Other cylinders were not coated with epoxy, in order to monitor radial diffusion into the sides of the cylinders. As shown in Figure A3.19, the cylinders in the NaCl solution showed no deterioration after 84 days. Conversely, by 84 days, the cylinders in the $MgCl_2$ and $CaCl_2$ solutions were severely deteriorated, as shown in Figures A3.20 and A3.21. It was decided to end the constant temperature experiments for all cylinders at 84 days. The cylinders in the CMA solution showed little to no distress after 84 days as shown in Figure A3.22, although there was some staining evident in the 0.60 *w/c* cylinders. The control cylinders in the limewater solution, as shown in Figure A3.23, showed no signs of distress after 84 days. Table A3.2 summarizes the visual ratings for the cylinders over time for the low temperature exposure tests.

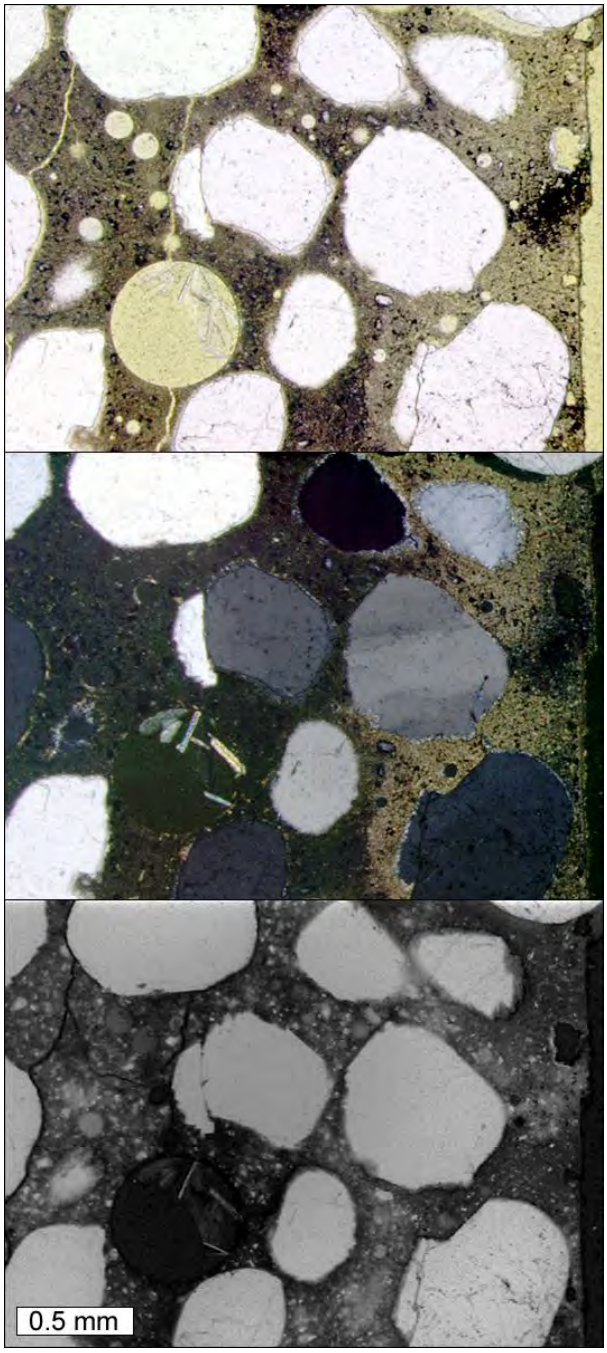

Figure A3.18. Petrographic microscope images of early onset of cracking in NaCl exposed sample from cyclic experiment. From top to bottom: plane polarized light, cross polarized light, and epifluorescent mode.

Figure A3.19. Cylinders exposed to NaCl solution after 84 days of constant low temperature test. From left to right: 0.40, 0.50, and 0.60 *w/c* mortar cylinders.

Figure A3.20. Cylinders exposed to $MgCl_2$ solution after 84 days of constant low temperature test. From left to right: 0.40, 0.50, and 0.60 *w/c* mortar cylinders.

Figure A3.21. Cylinders exposed to $CaCl_2$ solution after 84 days of constant low temperature test. From left to right: 0.40, 0.50, and 0.60 *w/c* mortar cylinders.

Figure A3.22. Cylinders exposed to CMA solution after 84 days of constant low temperature test. From left to right: 0.40, 0.50, and 0.60 *w/c* mortar cylinders.

Figure A3.23. Control cylinders exposed to limewater solution after 84 days of constant low temperature test. From left to right: 0.40, 0.50, and 0.60 *w/c* mortar cylinders.

Table A3.2. List of visual ratings for all mortar cylinders from the low temperature tests. Rating Scale: 0 - no visible change, 1 – some cracking, 2 - visible expansion and cracking, 3 - severe expansion and cracking, 4 - partial disintegration, 5 - total disintegration, *x* – test aborted.

Solution	Time in Days											
	w/c = 0/40				*w/c = 0/50*				*w/c = 0/60*			
	8	28	56	84	8	28	56	84	8	28	56	84
Limewater	-	0	0	0	-	0	0	0	-	0	0	0
$MgCl_2$	-	0-1	1-2	2-3	-	0-1	1-2	1-3	-	0-1	0-1	1-3
$CaCl_2$	-	0-1	2-3	3	-	0	2-3	3	-	0-1	1-3	2-3
NaCl	-	0	0	0	-	0	0	0	-	0	0	0
CMA	-	0	0	0	-	0	0	0	-	0	0	0

Split Tensile Strength Testing

Cylindrical specimens exposed to the constant low temperature treatment in selected chemicals were tested to determine the splitting tensile strength. Tests in accordance with ASTM C496 were performed on specimens that had been in the limewater and the four deicing chemicals for 28 days. Three specimens of each *w/c* ratio were tested, with the exception of calcium magnesium acetate (CMA). An error was made when drawing samples at 28 days for the CMA solution. A 0.40 *w/c* ratio specimen was taken in place of a 0.60 *w/c* ratio one. Therefore, four 0.40 *w/c* ratio specimens and two 0.60 *w/c* ratio specimens were tested for strength.

Tables A3.3 through A3.7 show the results of each strength test for the various specimens exposed to the constant low temperature treatment in selected chemicals. There was no apparent correlation between strength and deicer for a particular *w/c* ratio for anything other than calcium chloride. The calcium chloride, which was the most damaging salt in this particular experiment, decreased the tensile strength of the samples with a 0.60 *w/c* ratio by nearly 20%. There was no reduction apparent in the other specimens, but visible damage seemed fairly similar for all calcium chloride samples, regardless of *w/c* ratio.

Table A3.3. Splitting tensile strength of mortar cylinders exposed to limewater solution for 28 days in the constant low temperature test.

Limewater Specimens	*w/c* = 0.40		*w/c* = 0.50		*w/c* = 0.60	
	Max Load (lbs)	Max Tensile Stress (psi)	Max Load (lbs)	Max Tensile Stress (psi)	Max Load (lbs)	Max Tensile Stress (psi)
Sample 1	11607.6	924	9704.9	772	8009.2	637
Sample 2	11576.6	921	10396.9	827	8440.9	672
Sample 3	12738.9	1014	10160.7	809	8597.7	684
Average	11974.4	953.0	10087.5	802.7	8349.3	664.3

Table A3.4. Splitting tensile strength of mortar cylinders exposed to NaCl solution for 28 days in the constant low temperature test.

NaCl Specimens	*w/c* = 0.40		*w/c* = 0.50		*w/c* = 0.60	
	Max Load (lbs)	Max Tensile Stress (psi)	Max Load (lbs)	Max Tensile Stress (psi)	Max Load (lbs)	Max Tensile Stress (psi)
Sample 1	10597.2	843	10655.3	848	9867.45	785
Sample 2	11154.7	888	10812.0	860	8287.96	660
Sample 3	13304.2	1059	10311.7	821	9021.57	718
Average	11685.4	930.0	10593.0	843.0	9059.0	721.0

Table A3.5 Splitting tensile strength of mortar cylinders exposed to $MgCl_2$ solution for 28 days in the constant low temperature test.

$MgCl_2$ Specimens	*w/c* = 0.40		*w/c* = 0.50		*w/c* = 0.60	
	Max Load (lbs)	Max Tensile Stress (psi)	Max Load (lbs)	Max Tensile Stress (psi)	Max Load (lbs)	Max Tensile Stress (psi)
Sample 1	12695.4	1010	9525.8	758	8122.5	646
Sample 2	12490.3	994	9802.6	780	7501.1	597
Sample 3	9616.8	765	10618.5	845	8350.9	665
Average	11600.8	923.0	9982.3	794.3	7991.5	636.0

Table A3.6. Splitting tensile strength of mortar cylinders exposed to CMA solution for 28 days in the constant low temperature test.						
CMA Specimens	*w/c* = 0.40		*w/c* = 0.50		*w/c* = 0.60	
	Max Load (lbs)	Max Tensile Stress (psi)	Max Load (lbs)	Max Tensile Stress (psi)	Max Load (lbs)	Max Tensile Stress (psi)
Sample 1	11858.3	944	10242.0	815	9893.58	787
Sample 2	11446.9	911	10490.7	835	8897.69	708
Sample 3	10592.4	843	11021.1	877		
Sample 4	14278.8	1136				
Average	12044.1	958.5	10584.6	842.3	9395.6	747.5

Table A3.7. Splitting tensile strength of mortar cylinders exposed to $CaCl_2$ solution for 28 days in the constant low temperature test.						
CMA Specimens	*w/c* = 0.40		*w/c* = 0.50		*w/c* = 0.60	
	Max Load (lbs)	Max Tensile Stress (psi)	Max Load (lbs)	Max Tensile Stress (psi)	Max Load (lbs)	Max Tensile Stress (psi)
Sample 1	11752.8	935	10411.4	829	4363.4	347
Sample 2	11091.7	883	10238.1	815	7343.4	584
Sample 3	10189.7	811	9749.4	776	8367.33	666
Average	11011.4	876.3	10133.0	806.7	6691.4	532.3

Petrographic Analysis

Thin sections were prepared from the 0.50 *w/c* mortar cylinders subjected to 56 days of immersion in the five solutions. One cylinder was selected from each of the five solutions: magnesium chloride, calcium chloride, sodium chloride, calcium magnesium acetate, and limewater. The thin sections represent a cross-sectional plane oriented parallel to the finished surface at a depth of about 3/4 of an inch, [19 mm] from the finished surface. Figure A3.24 consists of epifluorescent mode images and Figure A3.25 consists of back-scattered electron images to illustrate the extensive crack networks of the magnesium chloride and calcium chloride immersed cylinders as compared to the cylinders immersed in the other three solutions. Near the exteriors of the magnesium chloride and calcium chloride cylinders, the cracks are empty. However, cracks further towards the interior of the cylinders are filled with a crystalline material bearing calcium and chlorine, likely calcium oxychloride or the altered remnants of calcium oxychloride. Figure A3.26 shows cross-polarized light images to emphasize the crystalline nature of the remnant calcium oxychloride filling the cracks. Figures A3.27 and A3.28 show close-up views of regions of the cement paste disrupted by cracks filled with calcium oxychloride for both the magnesium chloride and calcium chloride immersed samples. Figure A3.29 shows calcium oxychloride crystals that

have formed at the expense of secondary calcium hydroxide crystals in an air void, yet retained the shape of the original calcium hydroxide crystals. The deterioration of the magnesium chloride and calcium chloride immersed samples appears very similar. Both samples exhibit a region of calcium oxychloride filled cracks and voids associated with calcium hydroxide depleted cement paste. Figure A3.30 shows elemental maps for magnesium for all of the thin sections. Magnesium is sequestered at the exterior of the magnesium chloride immersed cylinders, likely resulting in a calcium chloride solution in the interior that is similar to the solution in the interior of the calcium chloride immersed cylinders. Figures A3.31 and A3.32 show brucite and magnesium chloride hydrate crystals filling cracks and voids at the exterior of the magnesium chloride immersed cylinder. Figure A3.33 shows elemental maps for chlorine for all of the thin sections. A chlorine gradient is clearly visible for all three of the chloride-based deicers. It should be noted that the epoxy used to stabilize the billets prior to thin sectioning also contains chlorine.

A complete set of the elemental maps and petrographic images collected from each of the thin sections is included in Figures A3.34 through A3.58. Figures A3.34 through A3.38 correspond to the cylinder immersed in magnesium chloride solution. Figures A3.39 through A3.43 correspond to the cylinder immersed in calcium chloride solution. Figures A3.44 through A3.48 correspond to the cylinder immersed in sodium chloride solution. Figures A3.49 through A3.53 correspond to the cylinder immersed in calcium magnesium acetate solution. And finally, Figures A3.54 through A3.58 correspond to the cylinder immersed in limewater. In all of these sets, back-scattered electron images and elemental maps of carbon and oxygen are provided to illustrate the extensive crack networks. Cross-polarized light images emphasize the crystalline nature of any infilling material and epifluorescent images emphasize areas of different density with darker areas being less dense than lighter areas. Micro-cracks can also be readily seen in the epifluorescent images.

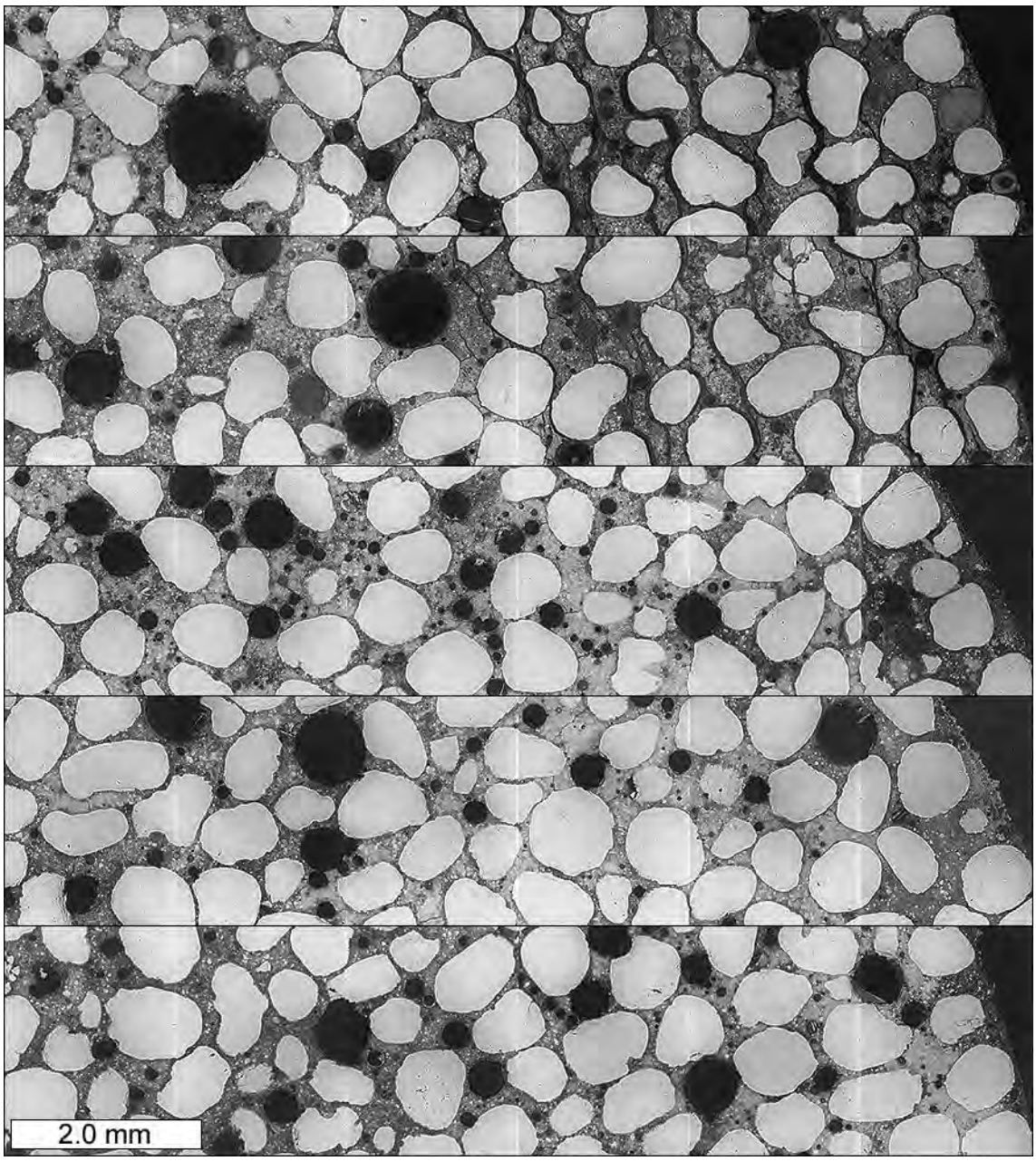

Figure A3.24. Epifluorescent mode images of thin sections prepared from mortar cylinders immersed in the following solutions, from top to bottom: magnesium chloride, calcium chloride, sodium chloride, calcium magnesium acetate, and limewater.

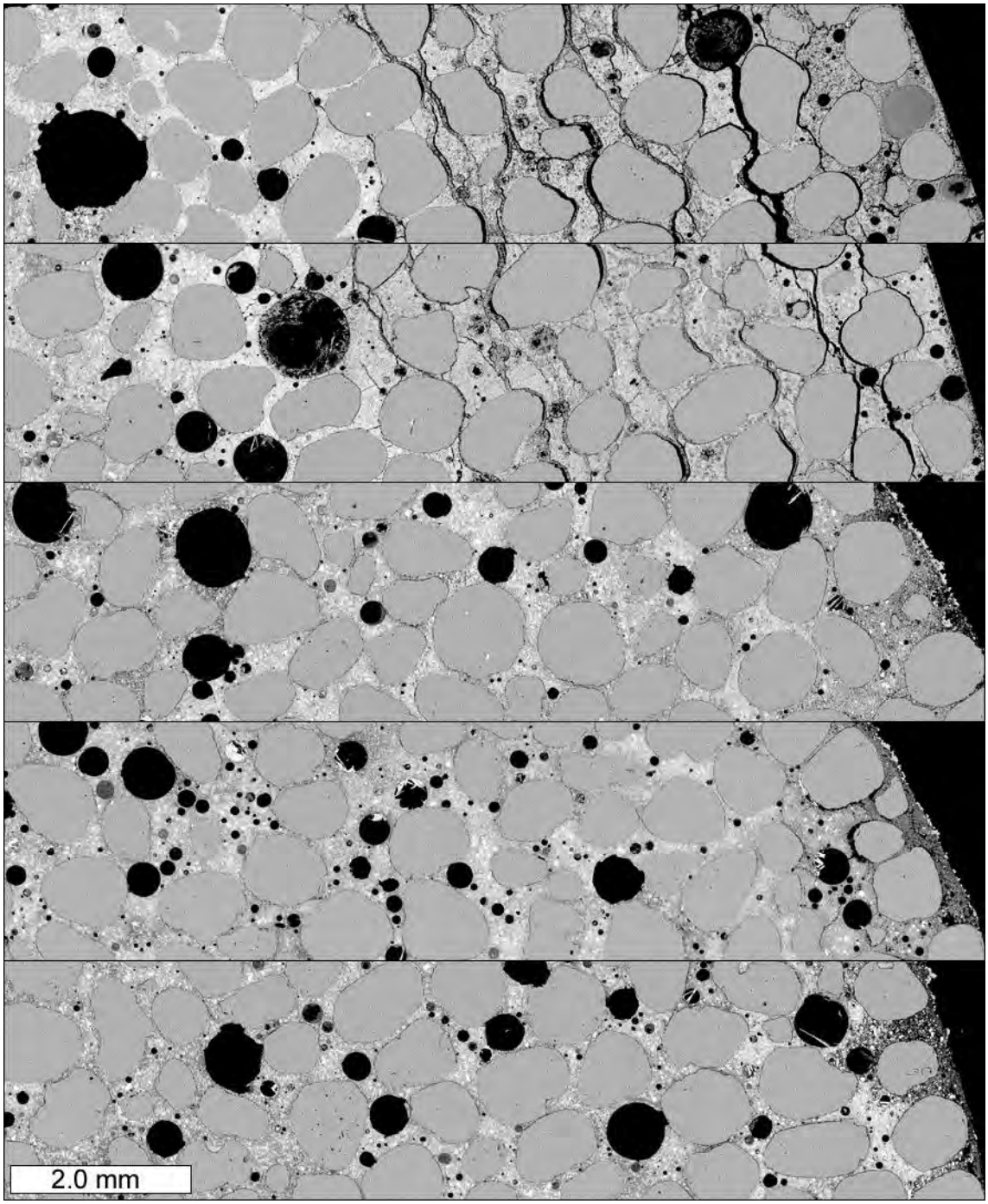

Figure A3.25. Back-scattered electron images of thin sections prepared from mortar cylinders immersed in the following solutions, from top to bottom: magnesium chloride, calcium chloride, sodium chloride, calcium magnesium acetate, and limewater.

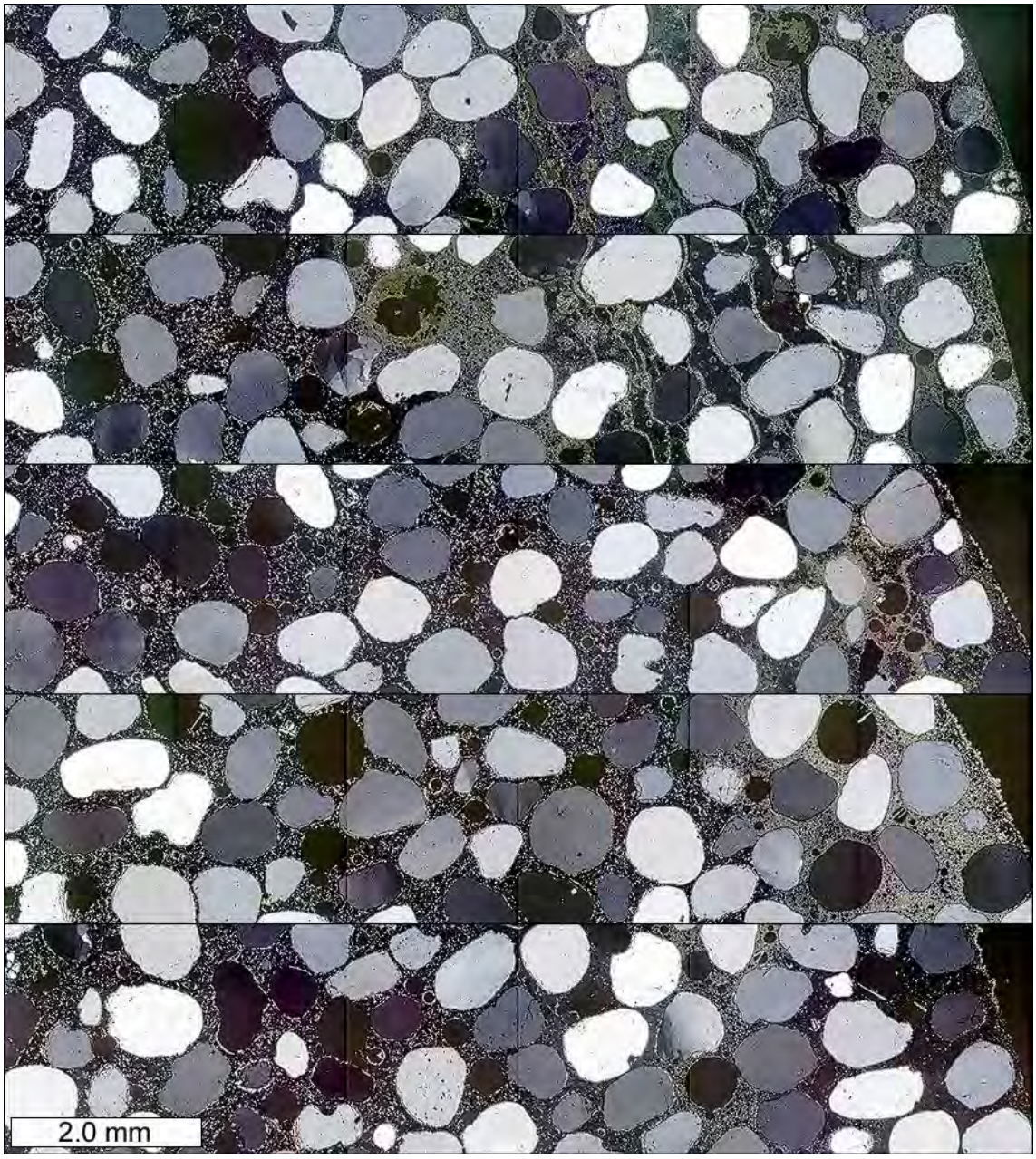

Figure A3.26. Cross-polarized light images of thin sections prepared from mortar cylinders immersed in the following solutions, from top to bottom: magnesium chloride, calcium chloride, sodium chloride, calcium magnesium acetate, and limewater.

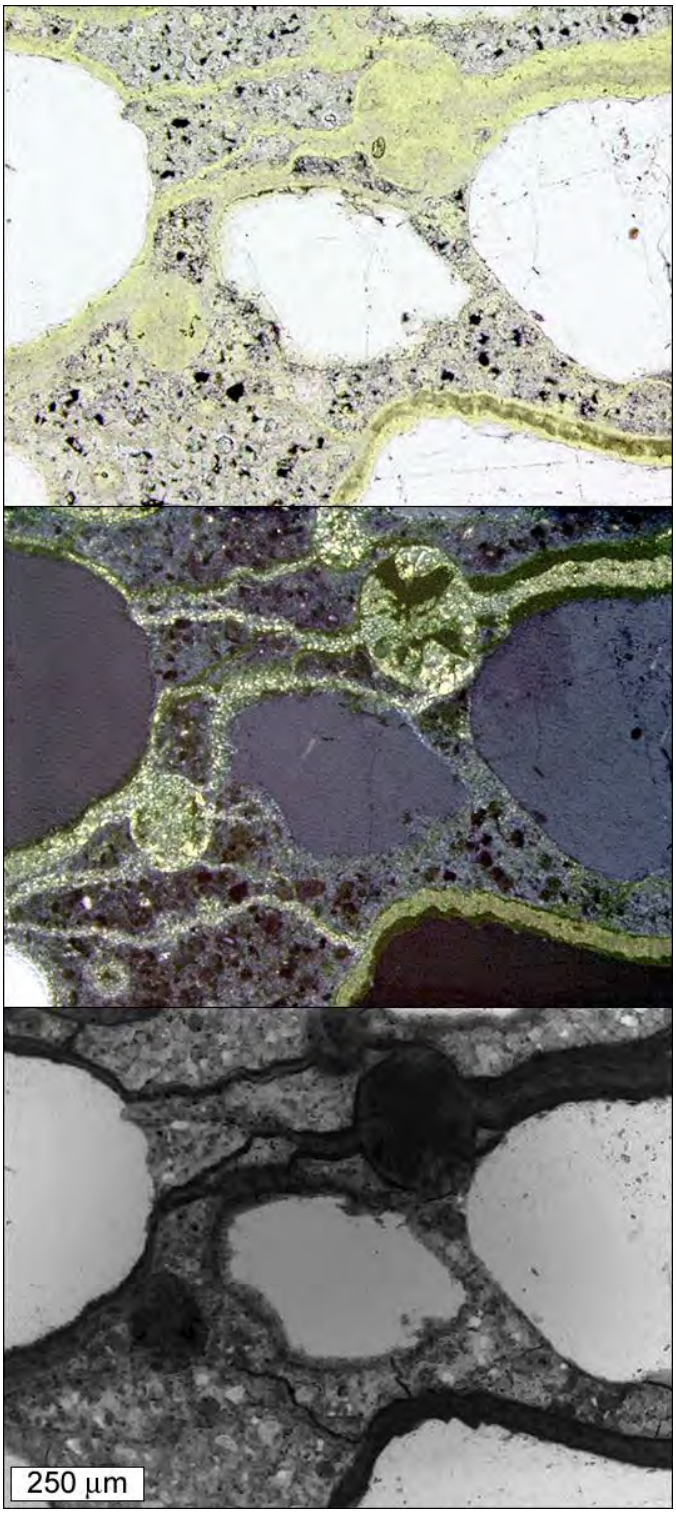

Figure A3.27. Cracks and air voids filled with remnant calcium oxychloride crystals in thin section prepared from magnesium chloride solution immersed sample. From top to bottom: plane polarized light, cross polarized light, and epifluorescent mode.

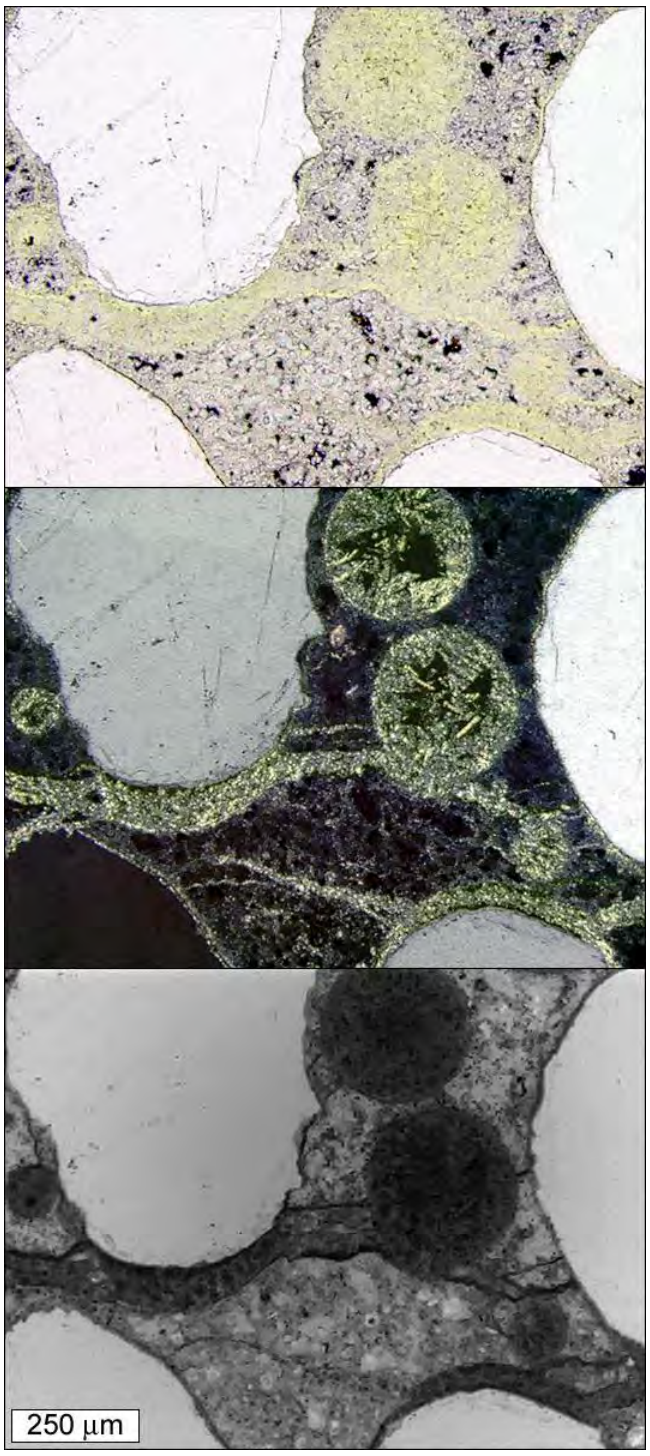

Figure A3.28. Cracks and air voids filled with remnant calcium oxychloride crystals in thin section prepared from calcium chloride solution immersed sample. From top to bottom: plane polarized light, cross polarized light, and epifluorescent mode.

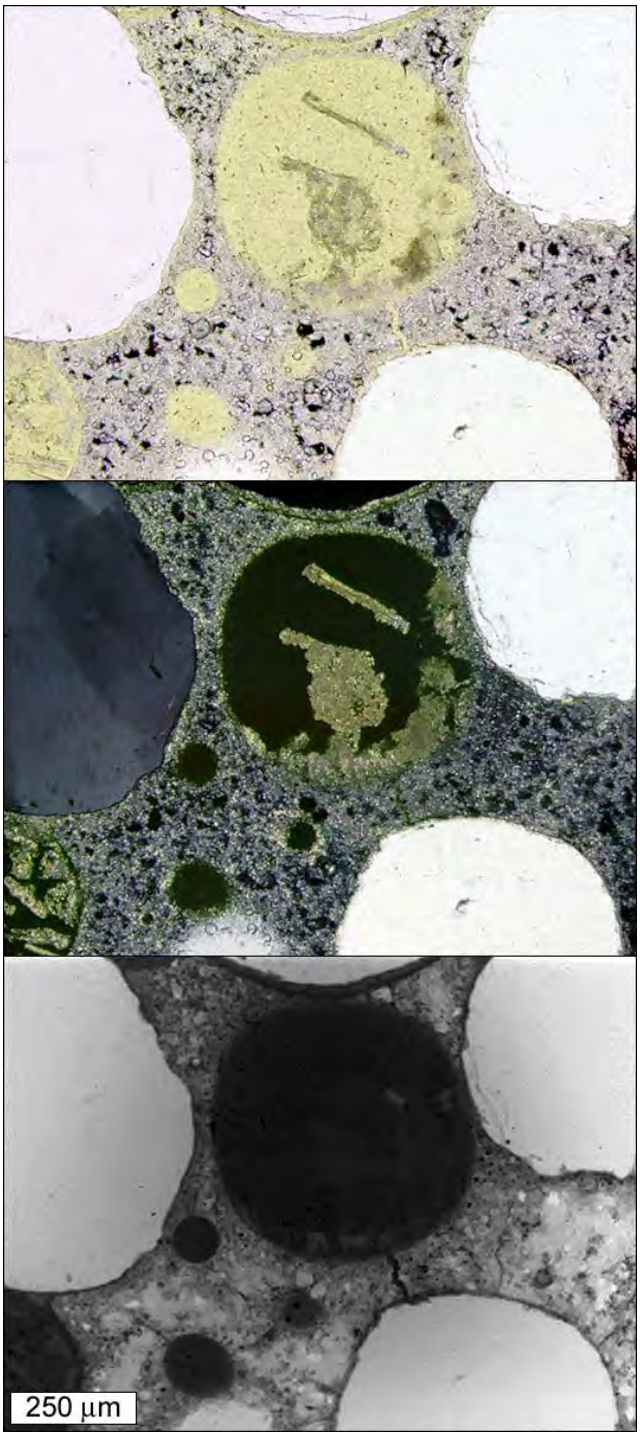

Figure A3.29. Remnant calcium oxychloride crystals that are pseudomorphs of secondary calcium hydroxide crystals initially formed in an air void from thin section prepared from magnesium chloride solution immersed sample. From top to bottom: plane polarized light, cross polarized light, and epifluorescent mode.

Figure A3.30. Elemental map for magnesium collected from thin sections prepared from mortar cylinders immersed in the following solutions, from top to bottom: magnesium chloride, calcium chloride, sodium chloride, calcium magnesium acetate, and limewater. Darker areas indicate a higher concentration.

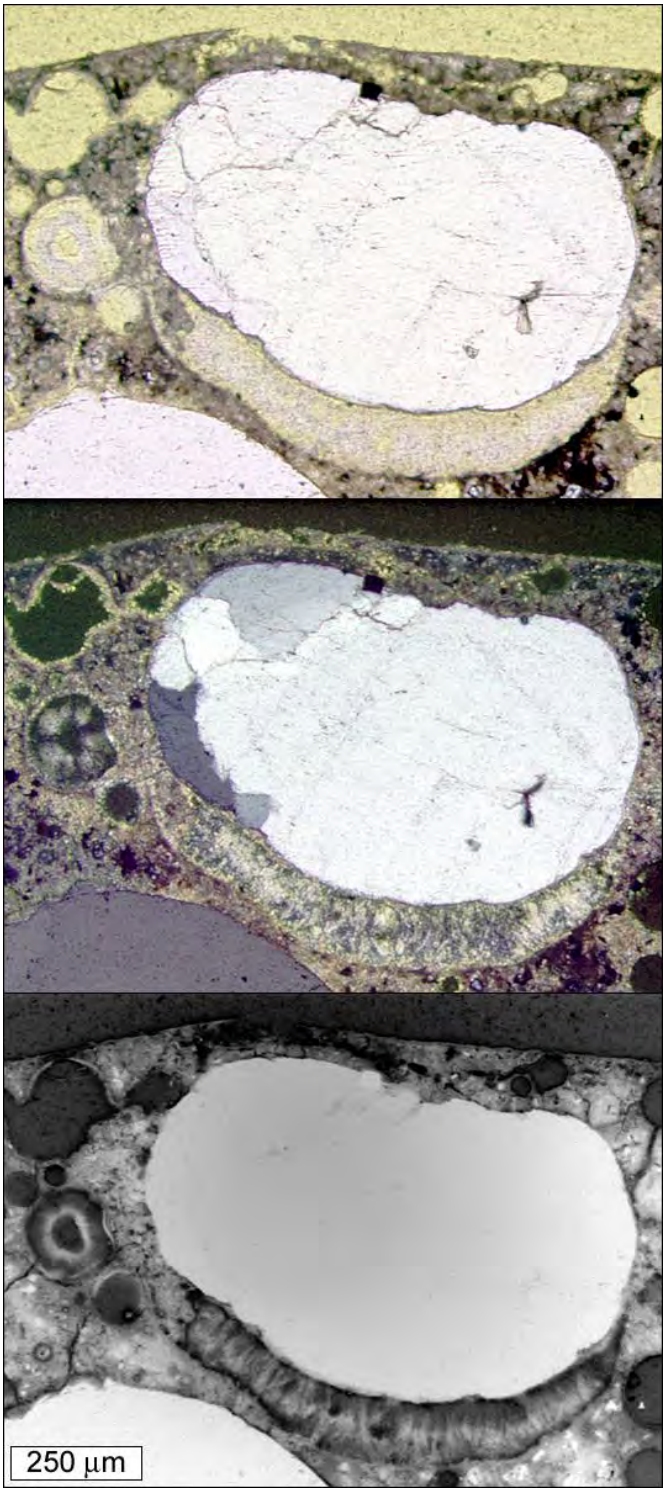

Figure A3.31. Brucite, (magnesium hydroxide) crystals in air void and seam beneath sand grain near exterior in thin section prepared from cylinder immersed in magnesium chloride solution. From top to bottom: plane polarized light, cross polarized light, and epifluorescent mode.

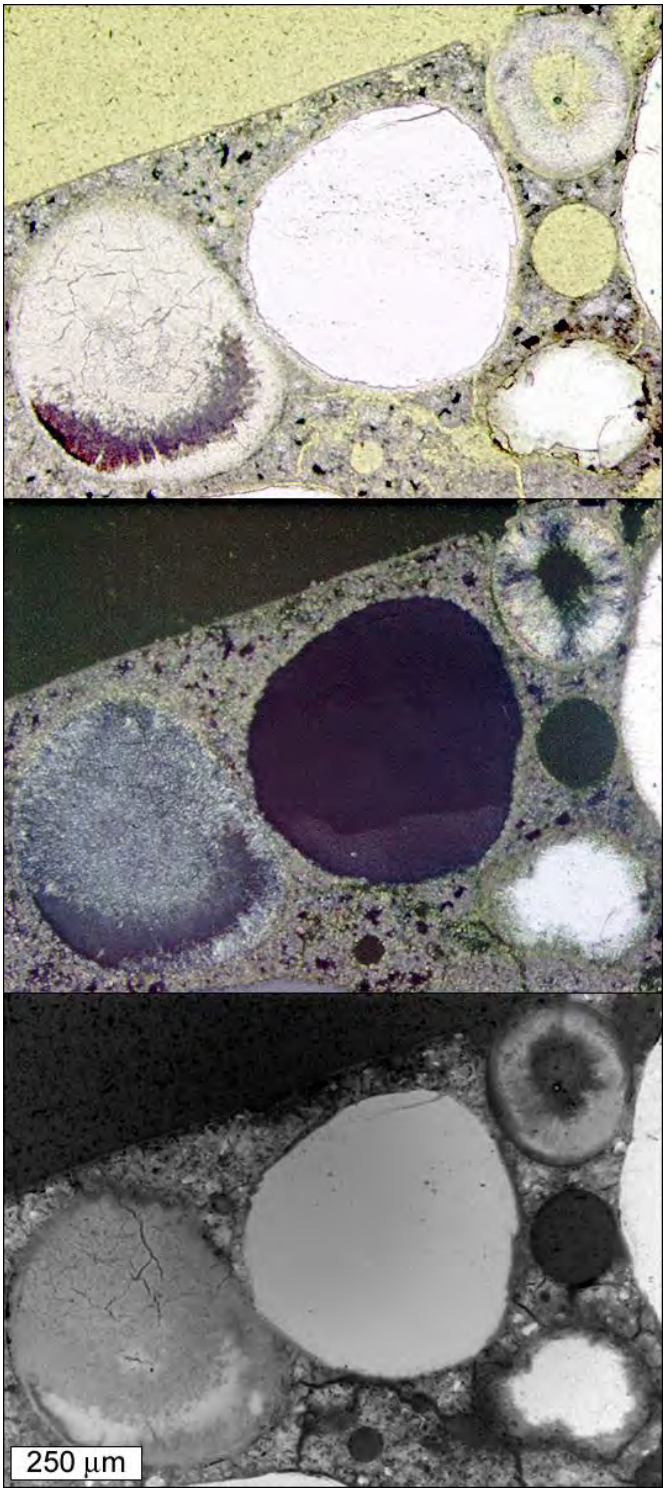

Figure A3.32. Magnesium chloride hydrate crystals in air voids near exterior in thin section prepared from cylinder immersed in magnesium chloride solution. From top to bottom: plane polarized light, cross polarized light, and epifluorescent mode.

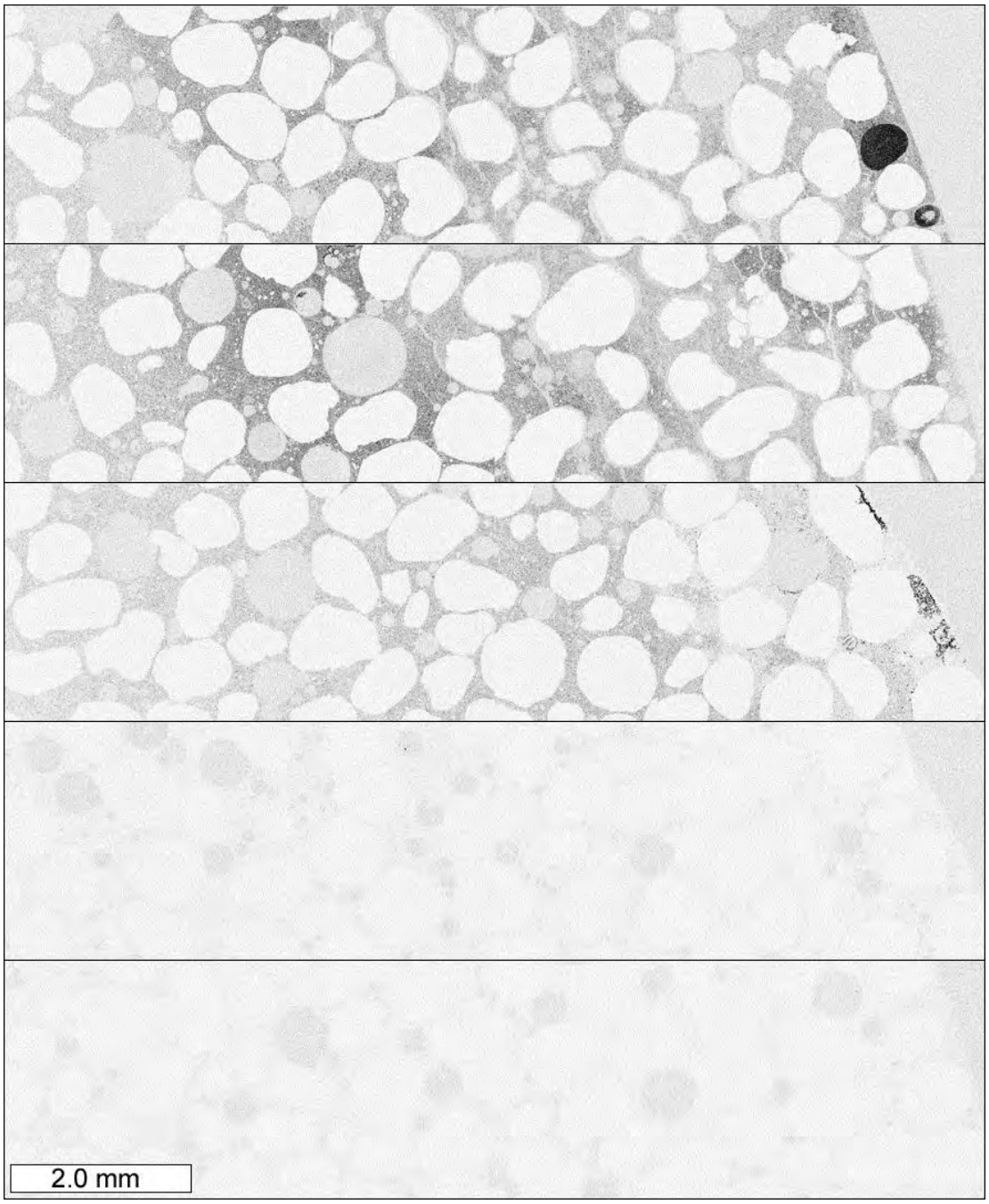

Figure A3.33. Elemental map for chlorine collected from thin sections prepared from mortar cylinders immersed in the following solutions, from top to bottom: magnesium chloride, calcium chloride, sodium chloride, calcium magnesium acetate, and limewater. Darker areas indicate a higher concentration.

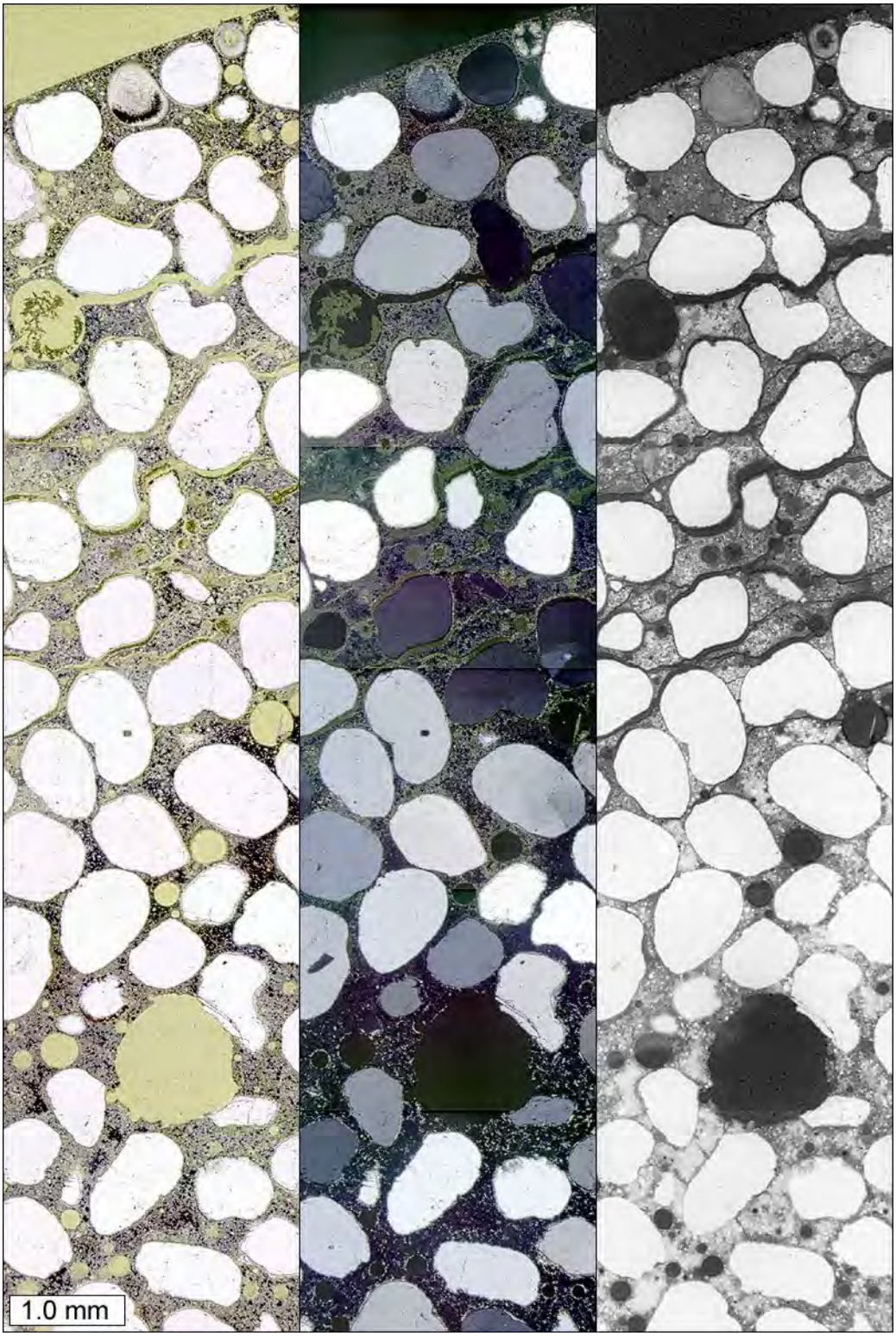

Figure A3.34. From left to right: plane polarized light, cross polarized light, and epifluorescent mode images of a thin section prepared from a cylinder immersed in magnesium chloride solution.

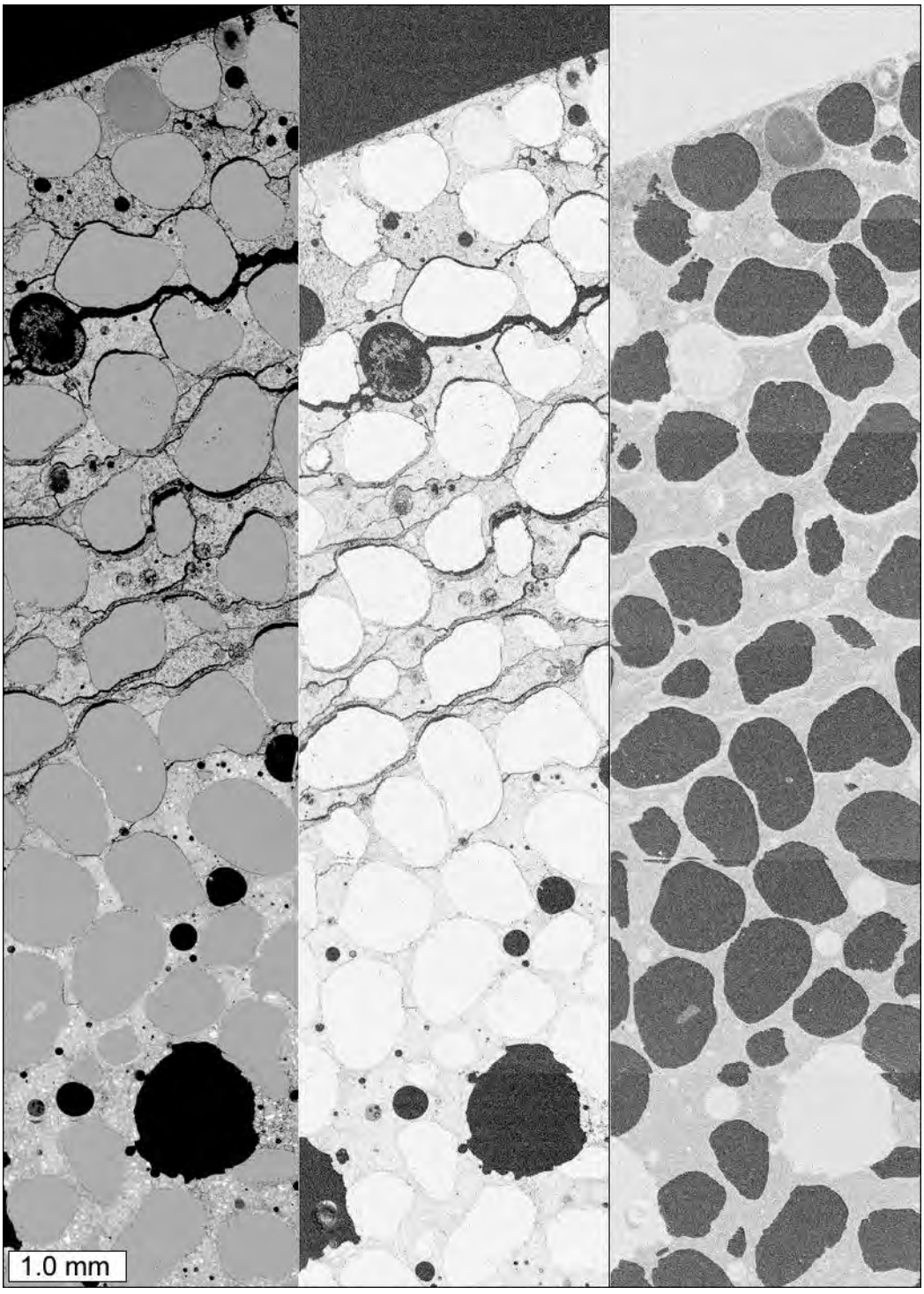

Figure A3.35. From left to right: back scattered electron image, elemental map for carbon, and elemental map for oxygen. Images were collected from a thin section prepared from a cylinder immersed in magnesium chloride solution. Darker areas in elemental maps indicate a higher concentration.

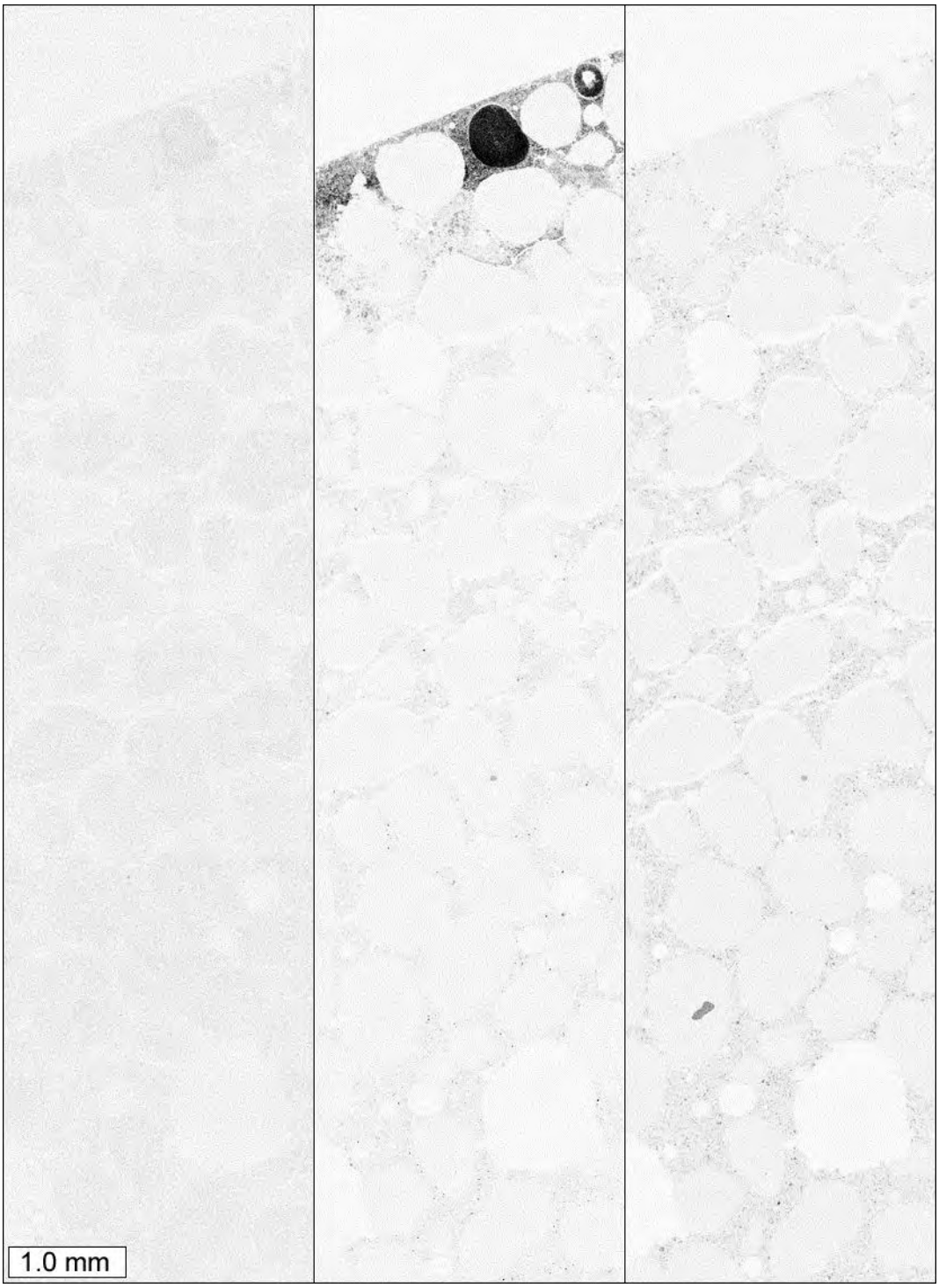

Figure A3.36. Elemental maps, from left to right: sodium, magnesium, and aluminum. The elemental maps were collected from a thin section prepared from a cylinder immersed in magnesium chloride solution. Darker areas indicate a higher concentration.

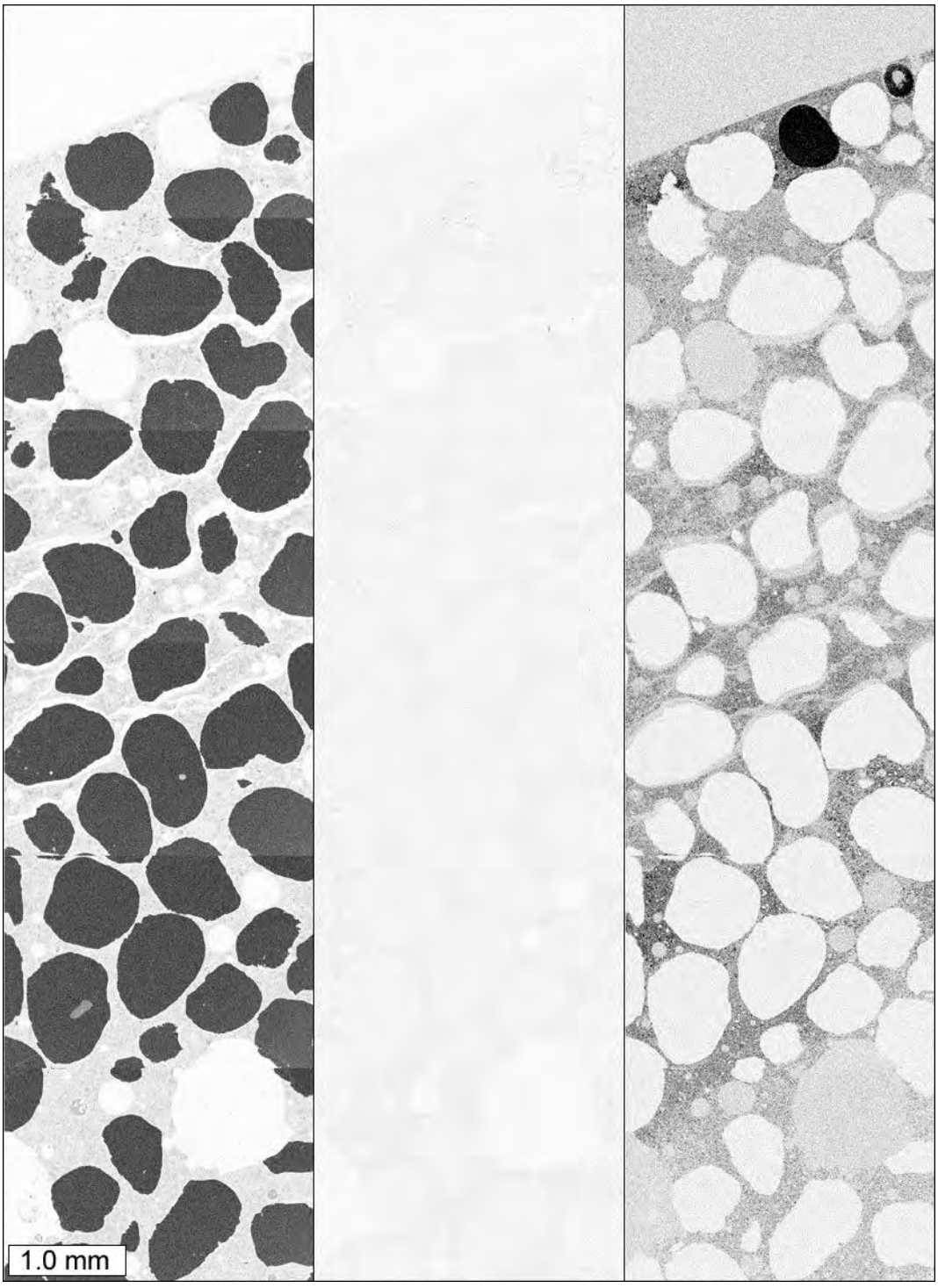

Figure A3.37. Elemental maps, from left to right: silicon, sulfur, and chlorine. The elemental maps were collected from a thin section prepared from a cylinder immersed in magnesium chloride solution. Darker areas indicate a higher concentration.

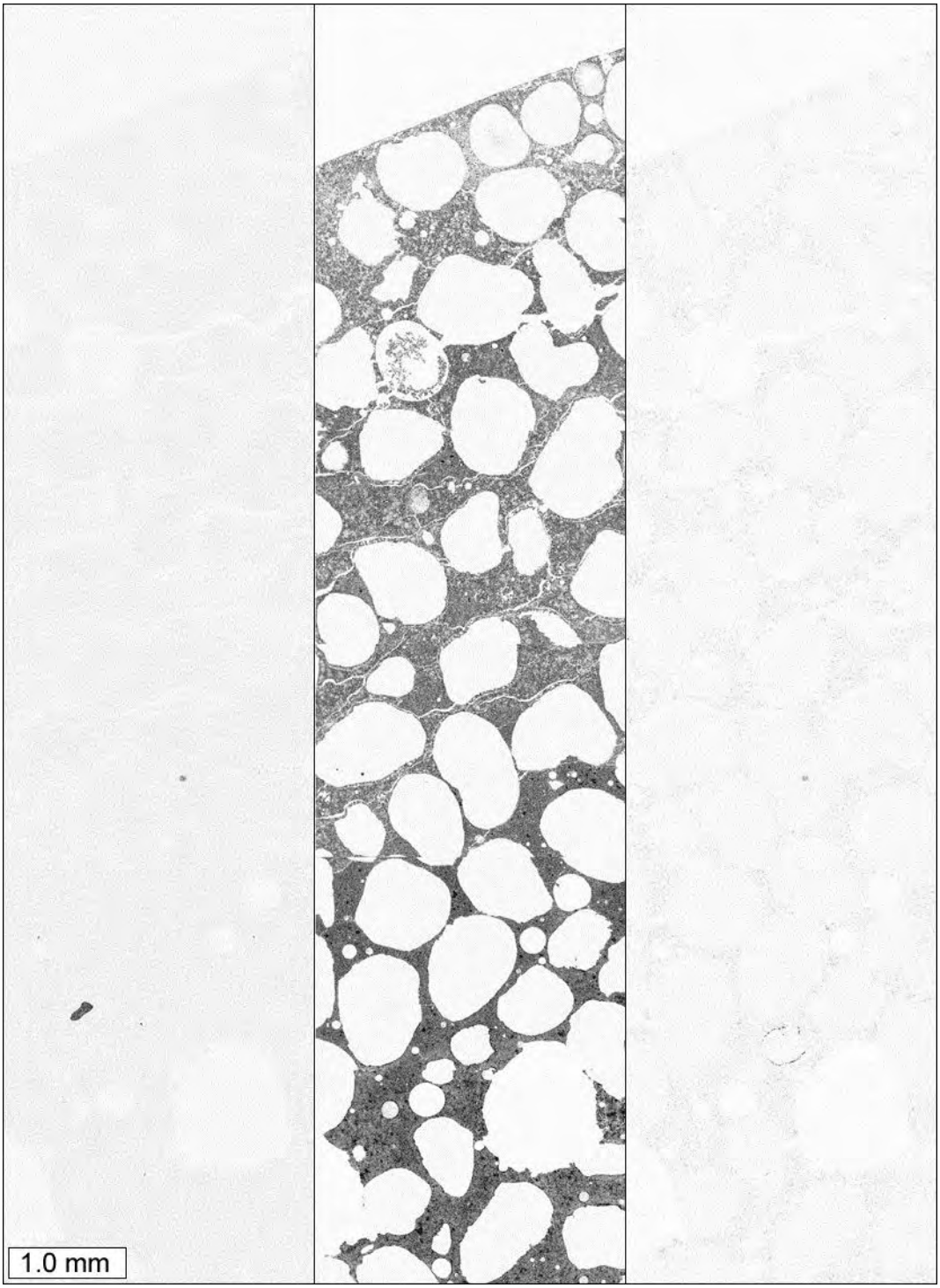

Figure A3.38. Elemental maps, from left to right: potassium, calcium, and iron. The elemental maps were collected from a thin section prepared from a cylinder immersed in magnesium chloride solution. Darker areas indicate a higher concentration.

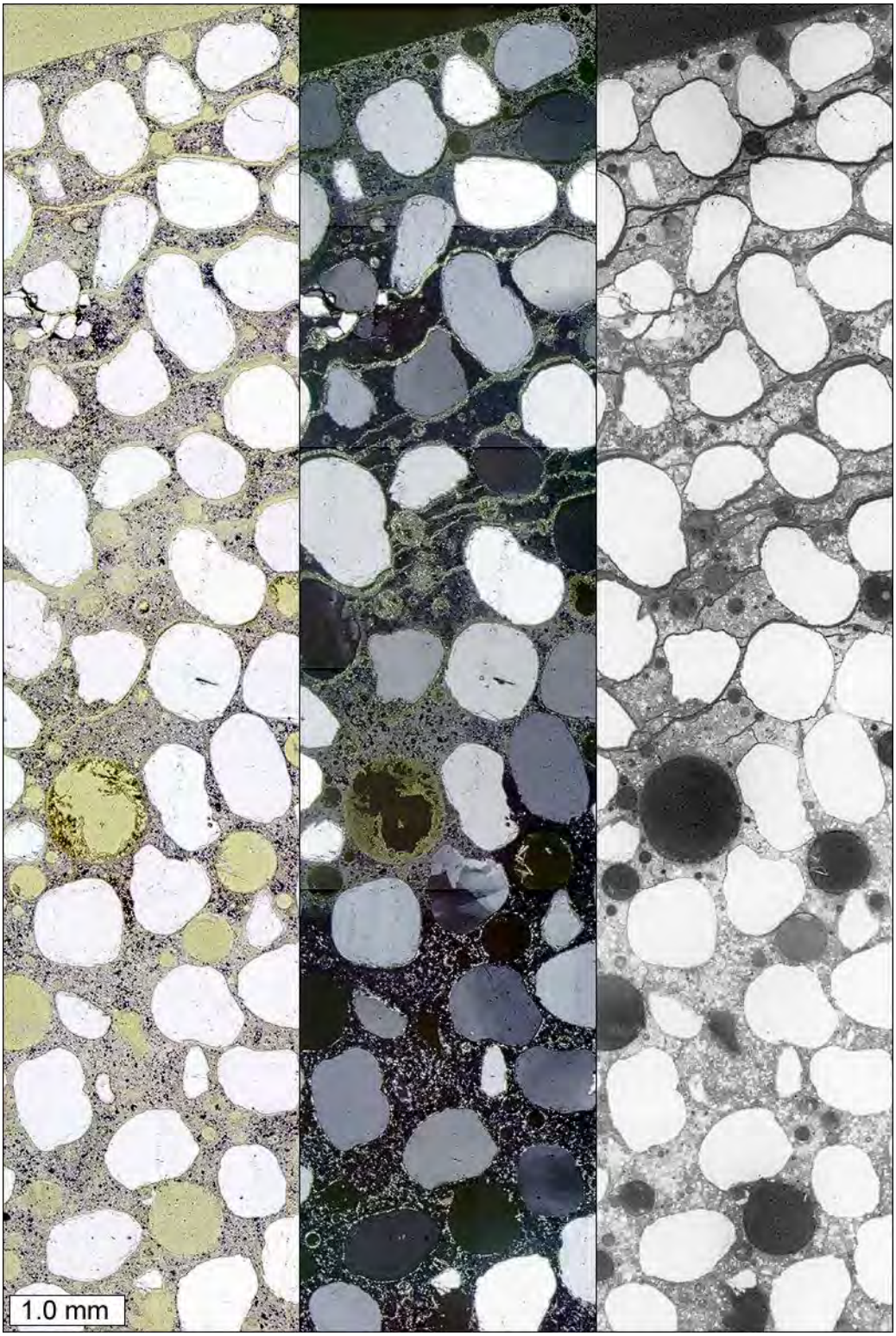

Figure A3.39. From left to right: plane polarized light, cross polarized light, and epifluorescent mode images of a thin section prepared from a cylinder immersed in calcium chloride solution.

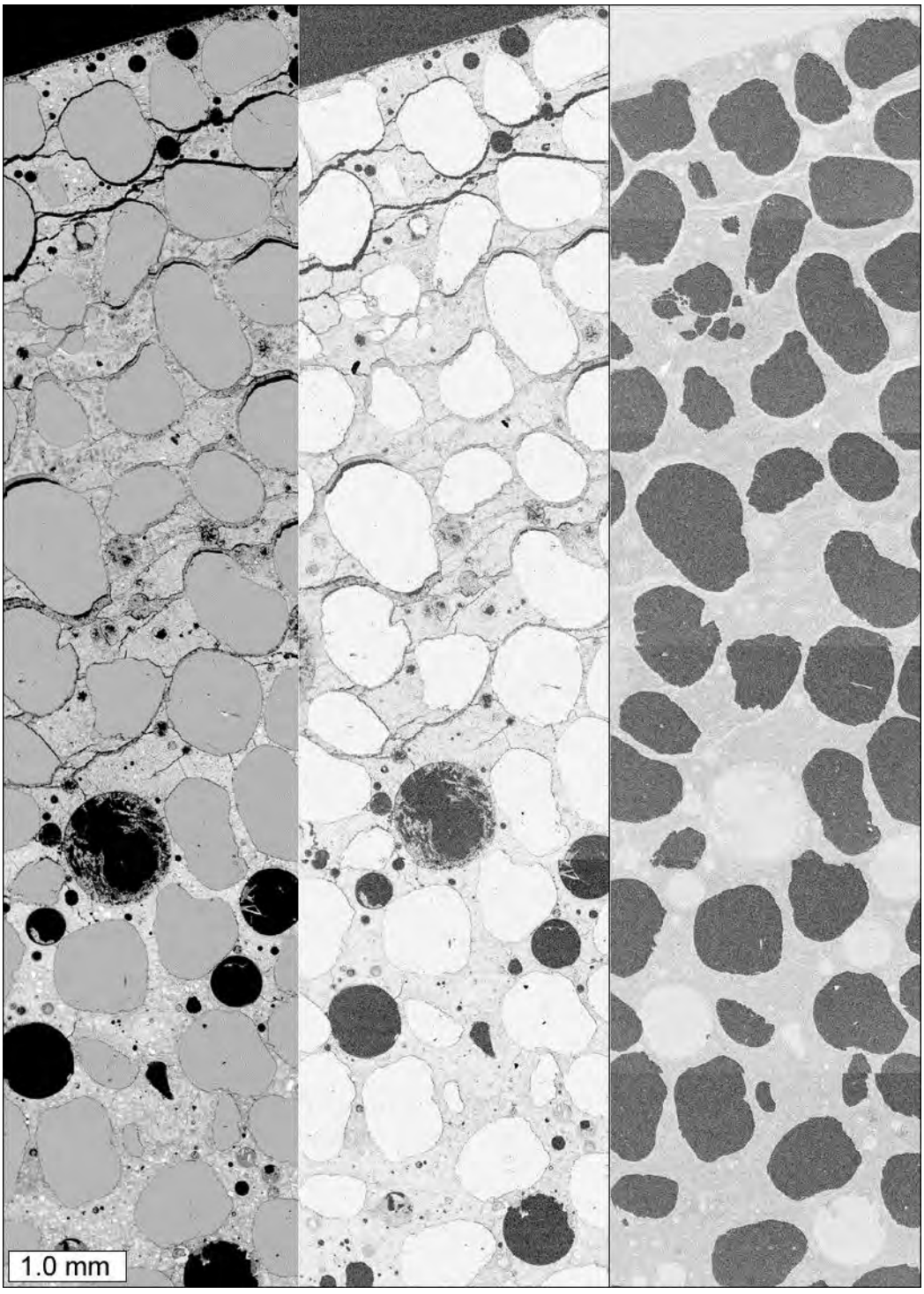

Figure A3.40. From left to right: back scattered electron image, elemental map for carbon, and elemental map for oxygen. Images were collected from a thin section prepared from a cylinder immersed in calcium chloride solution. Darker areas in elemental maps indicate a higher concentration. Darker areas in elemental maps indicate a higher concentration.

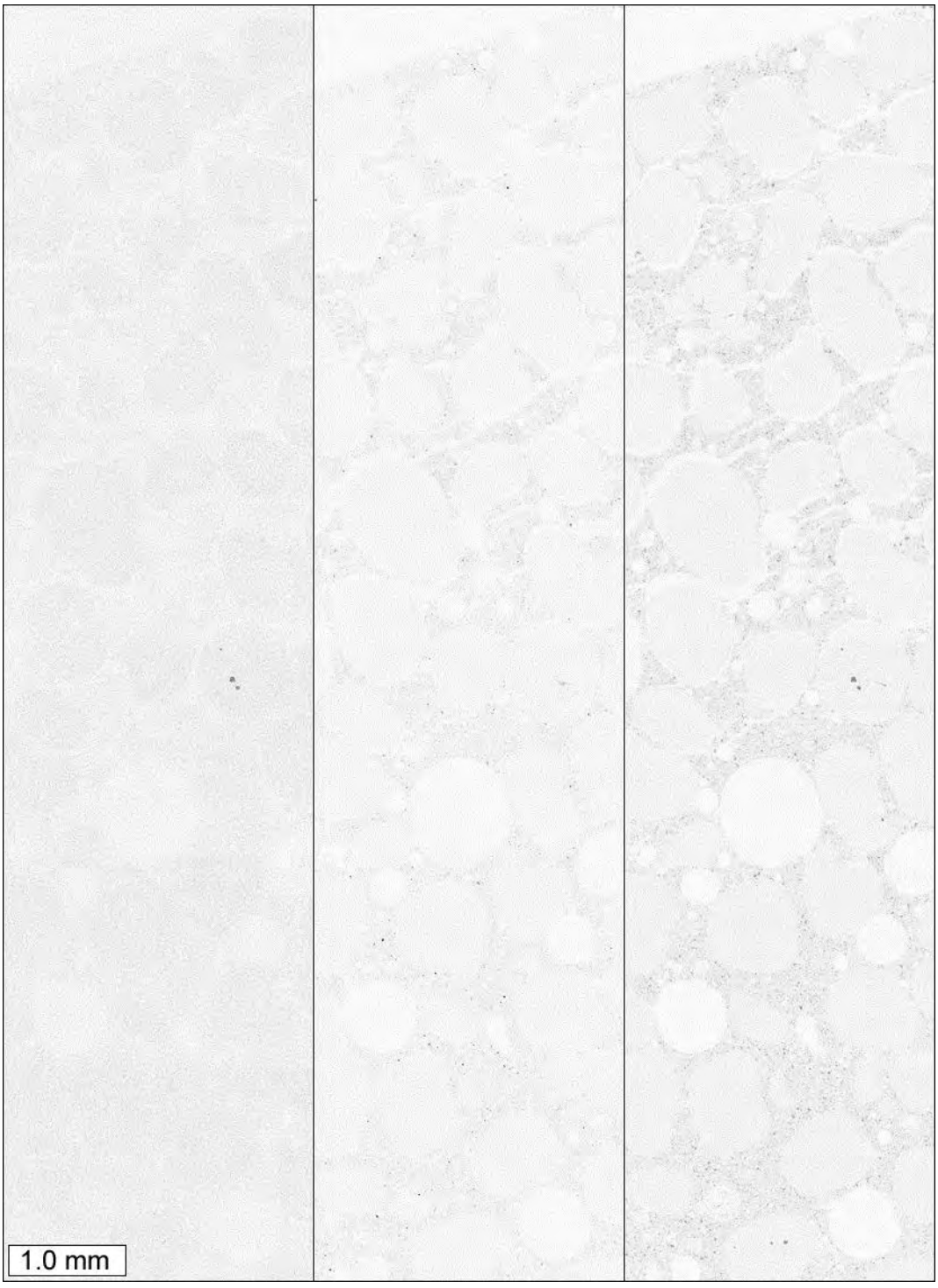

Figure A3.41. Elemental maps, from left to right: sodium, magnesium, and aluminum. The elemental maps were collected from a thin section prepared from a cylinder immersed in calcium chloride solution. Darker areas indicate a higher concentration.

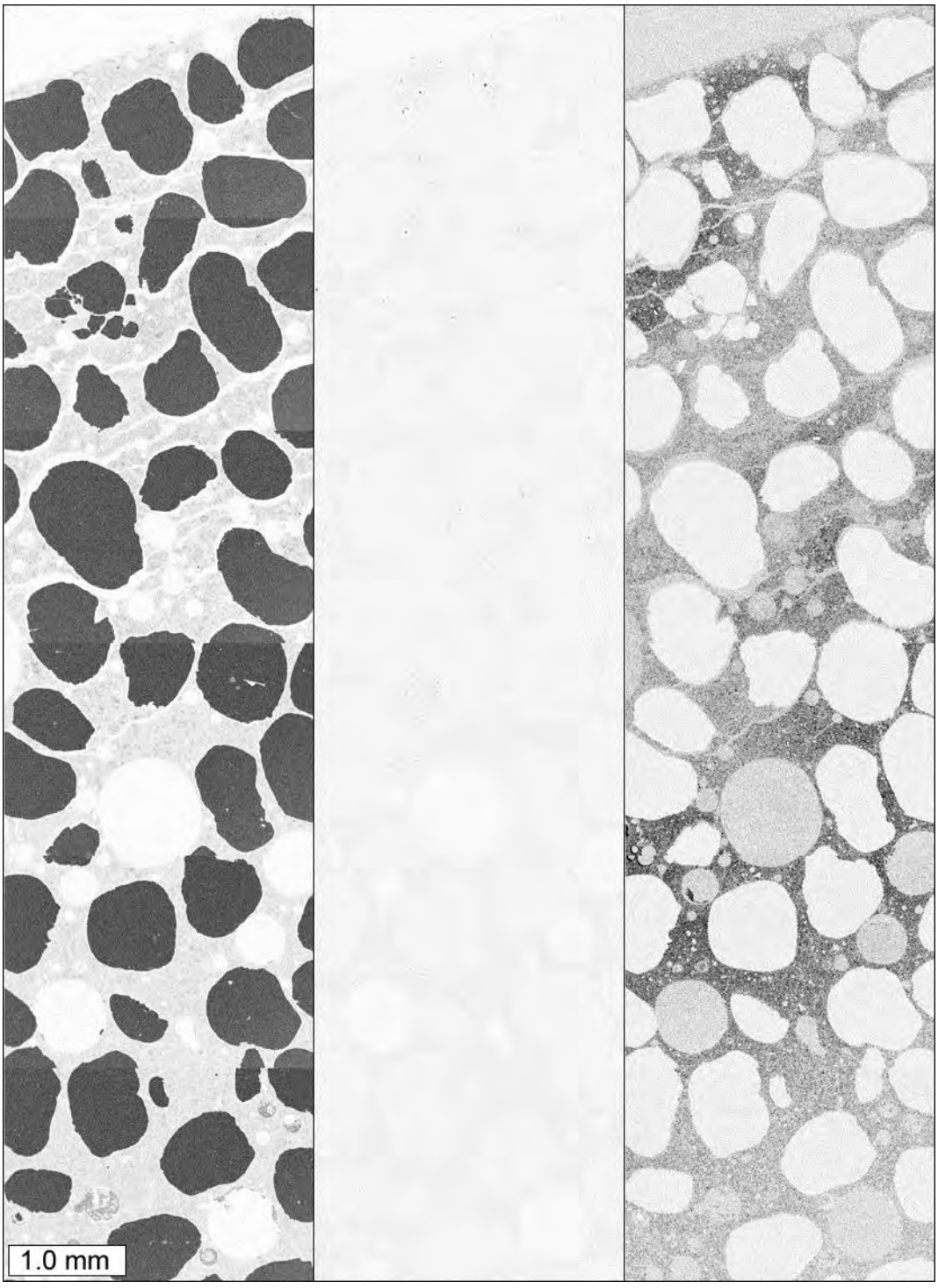

Figure A3.42. Elemental maps, from left to right: silicon, sulfur, and chlorine. The elemental maps were collected from a thin section prepared from a cylinder immersed in calcium chloride solution. Darker areas indicate a higher concentration.

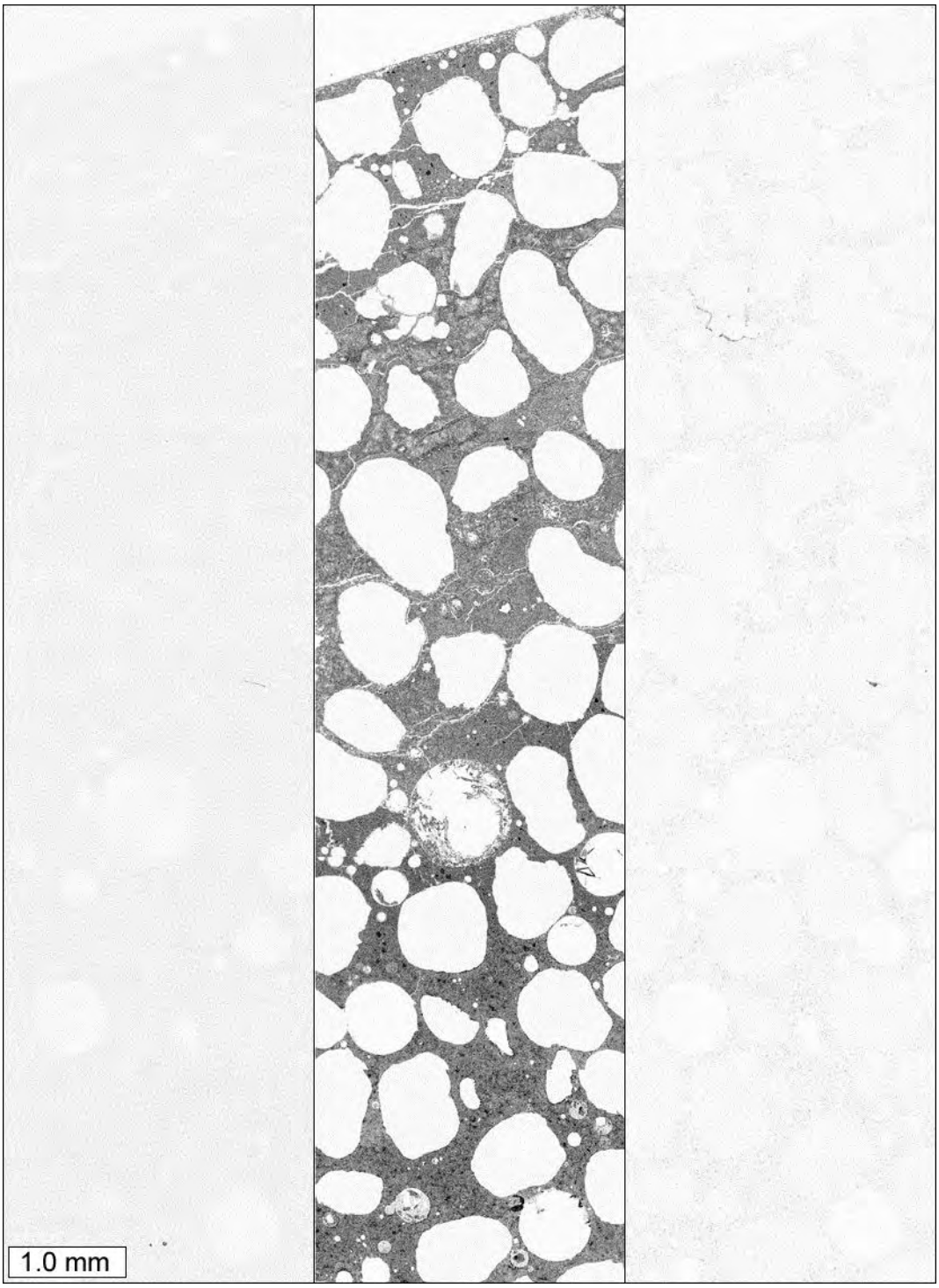

Figure A3.43. Elemental maps, from left to right: potassium, calcium, and iron. The elemental maps were collected from a thin section prepared from a cylinder immersed in calcium chloride solution. Darker areas indicate a higher concentration.

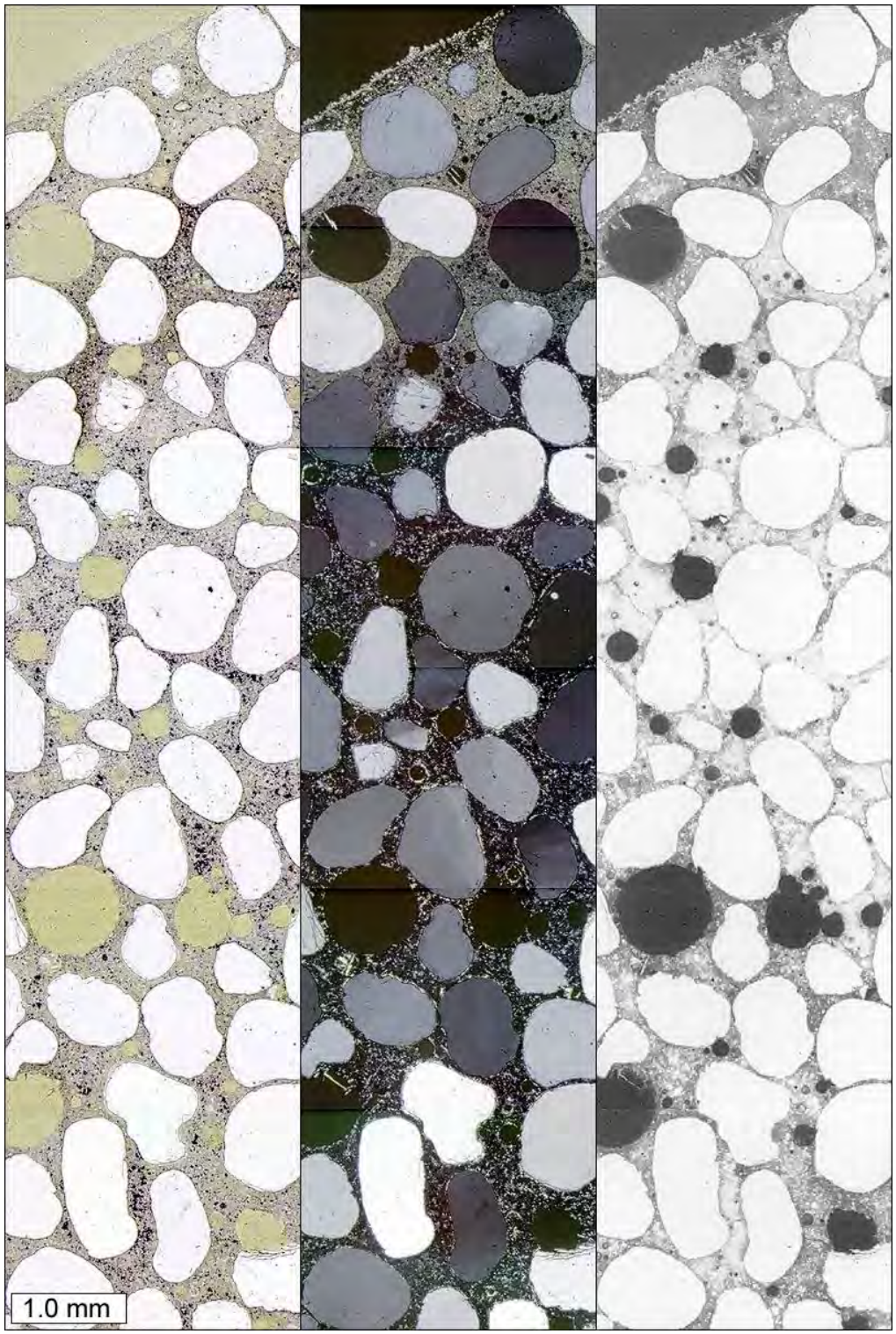

Figure A3.44. From left to right: plane polarized light, cross polarized light, and epifluorescent mode images of a thin section prepared from a cylinder immersed in sodium chloride solution.

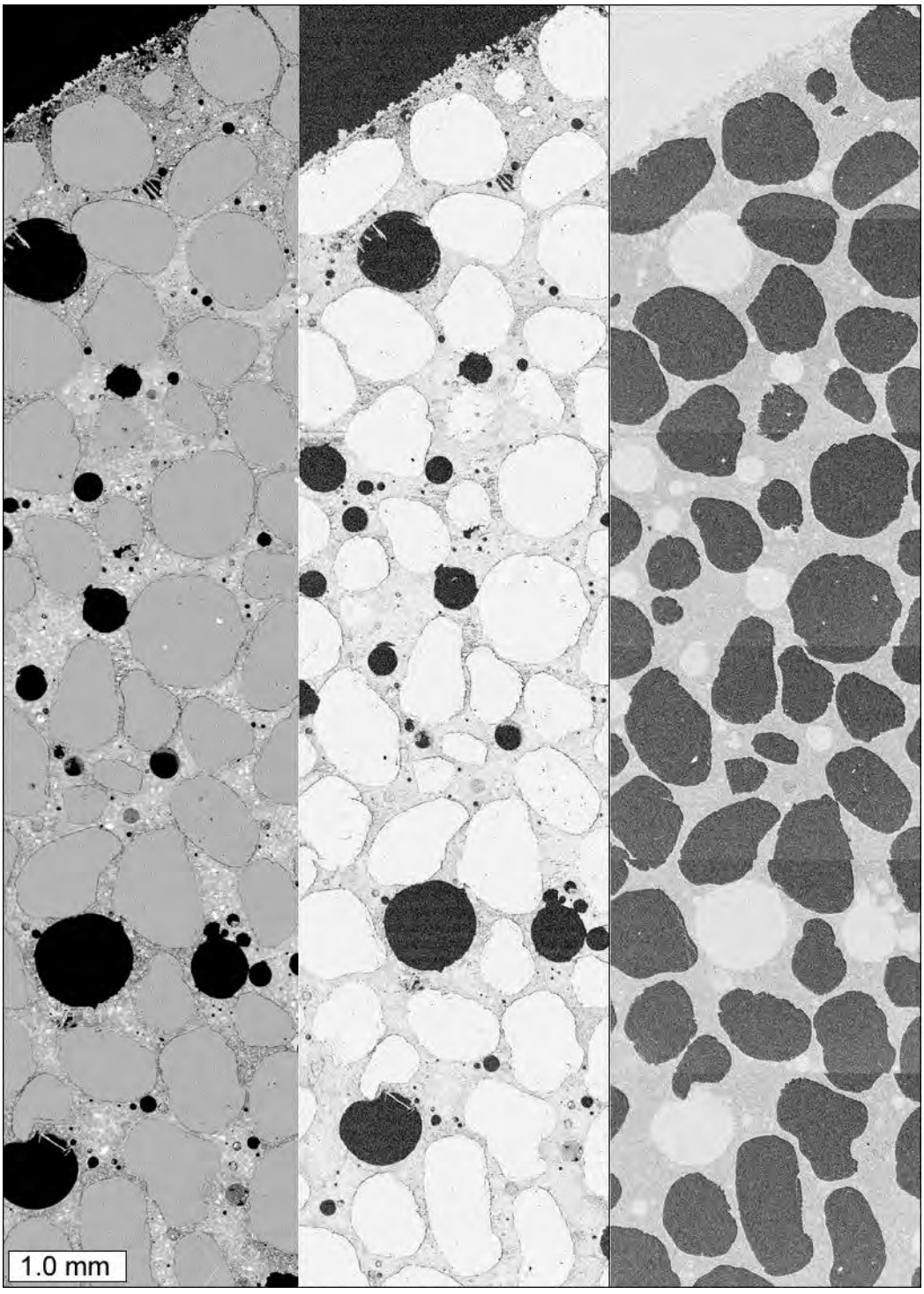

Figure A3.45. From left to right: back scattered electron image, elemental map for carbon, and elemental map for oxygen. Images were collected from a thin section prepared from a cylinder immersed in sodium chloride solution. Darker areas in elemental maps indicate a higher concentration.

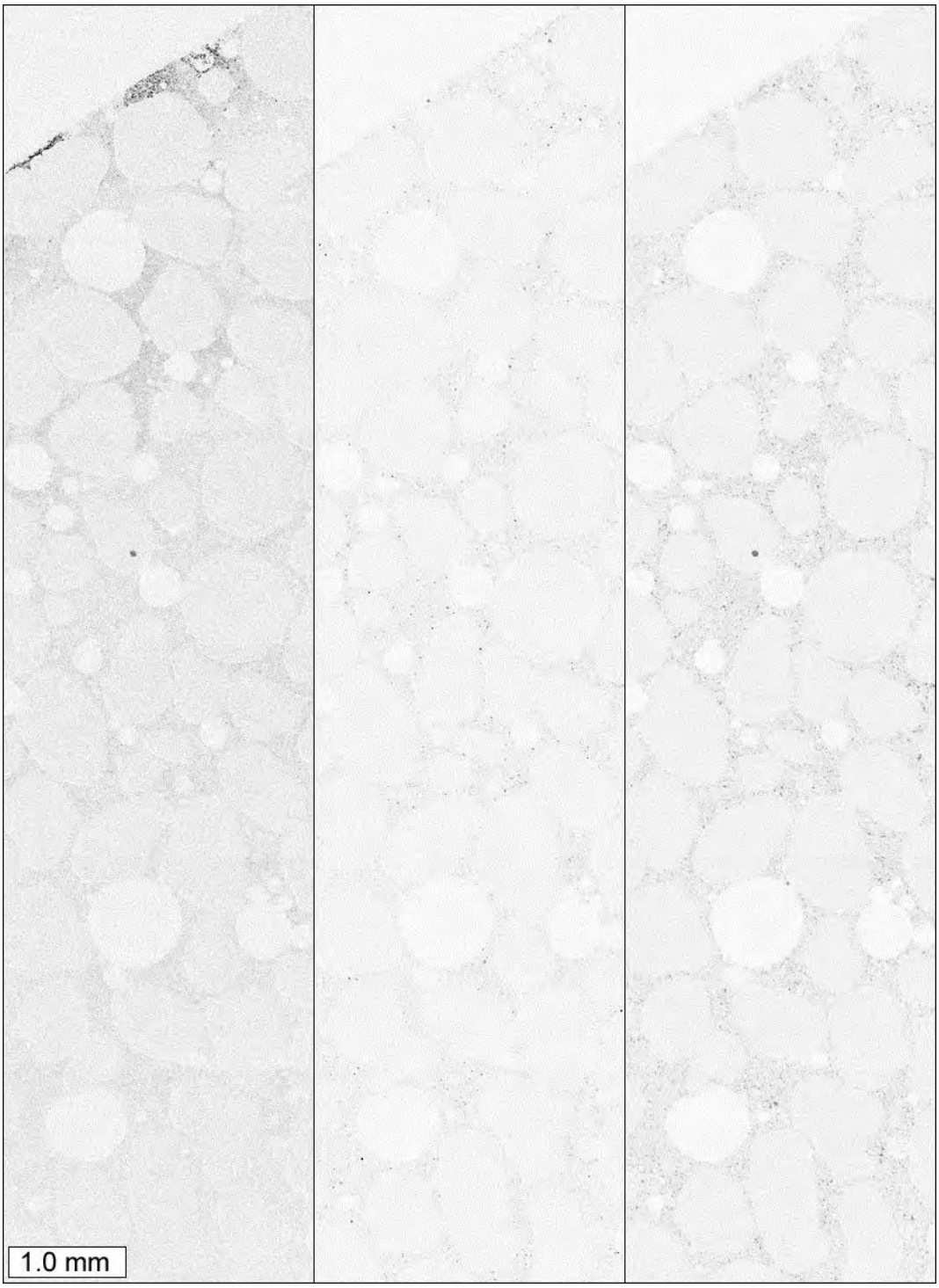

Figure A3.46. Elemental maps, from left to right: sodium, magnesium, and aluminum. The elemental maps were collected from a thin section prepared from a cylinder immersed in sodium chloride solution. Darker areas indicate a higher concentration.

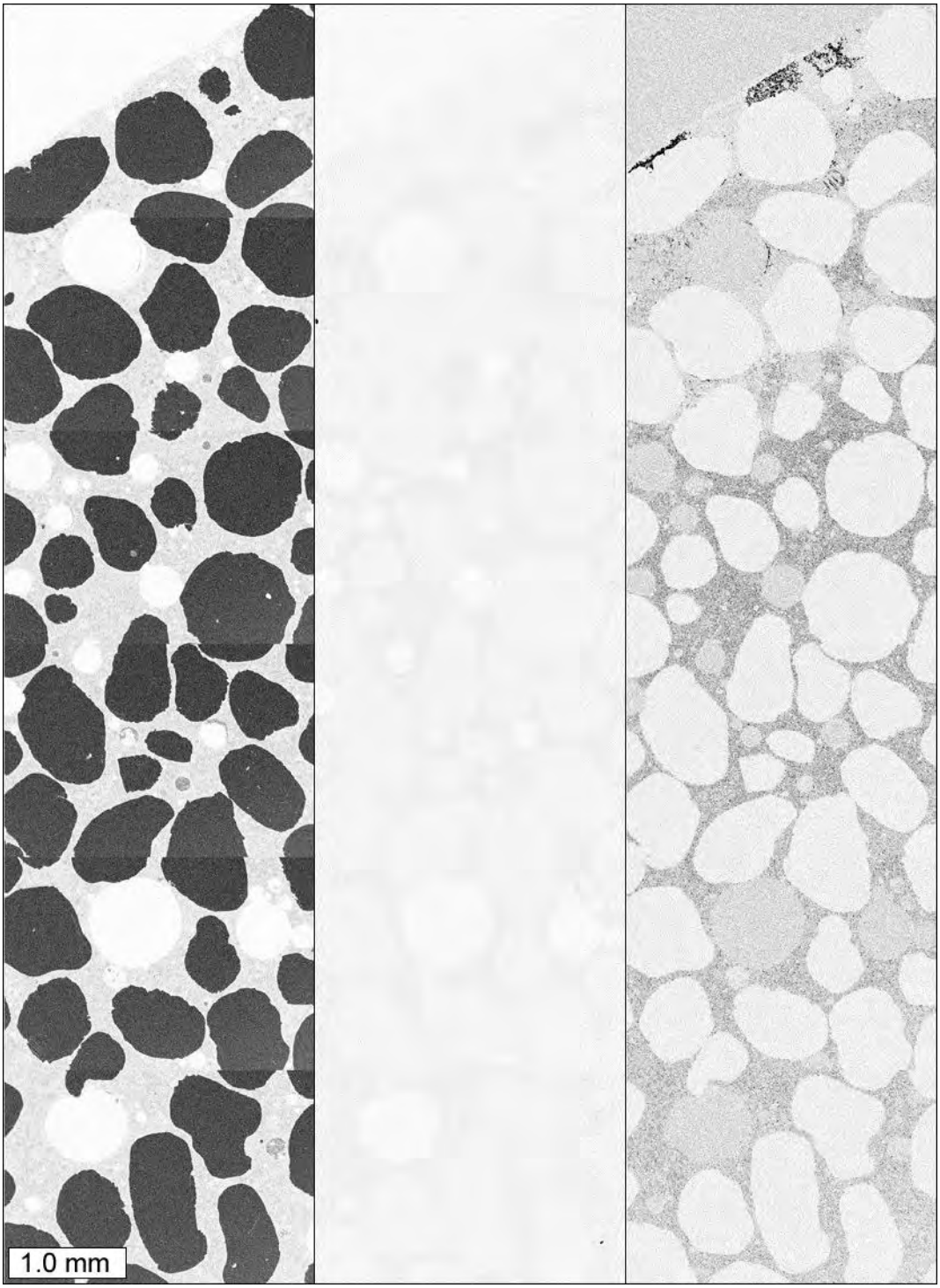

Figure A3.47. Elemental maps, from left to right: silicon, sulfur, and chlorine. The elemental maps were collected from a thin section prepared from a cylinder immersed in sodium chloride solution. Darker areas indicate a higher concentration.

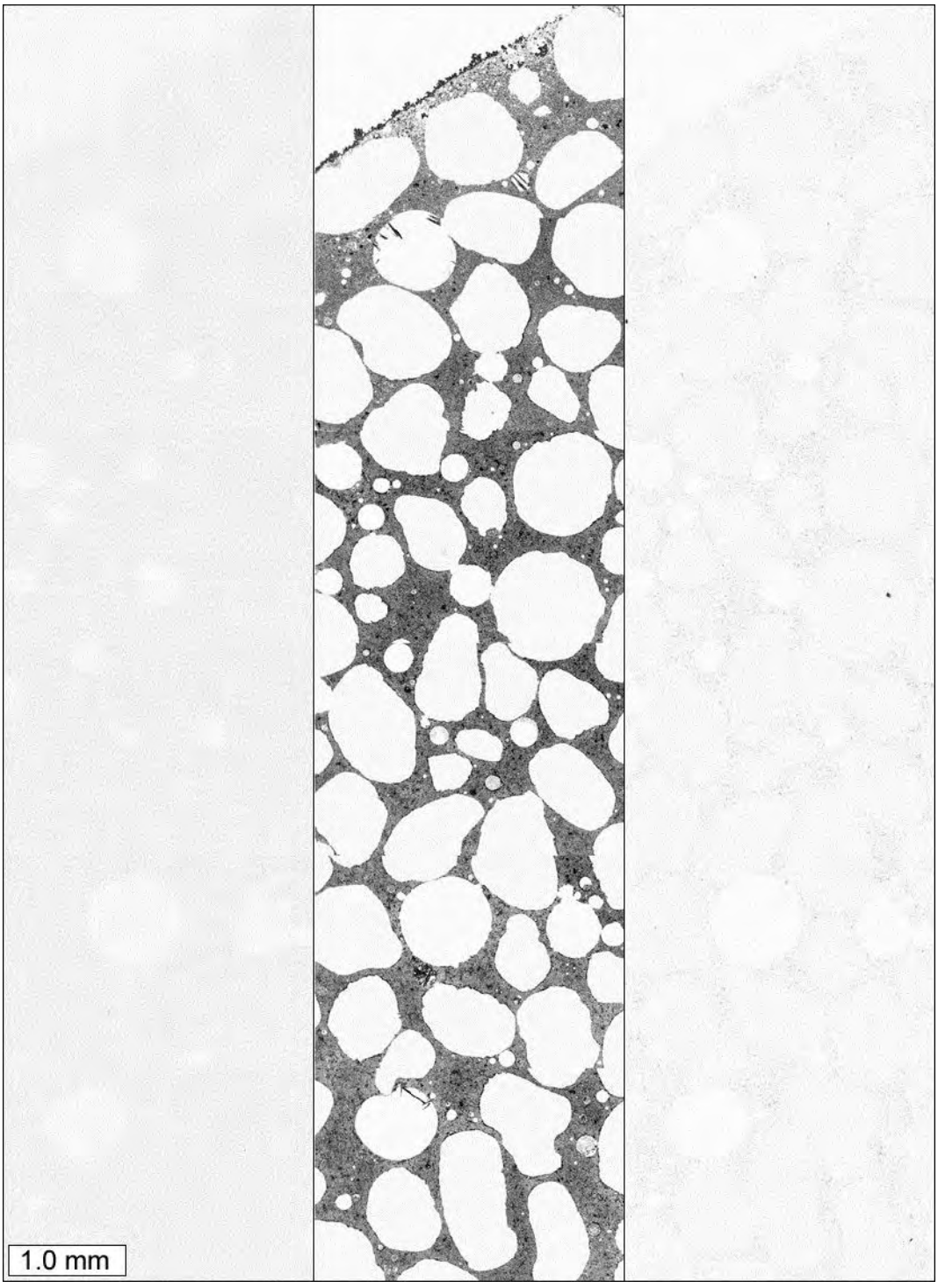

Figure A3.48. Elemental maps, from left to right: potassium, calcium, and iron. The elemental maps were collected from a thin section prepared from a cylinder immersed in sodium chloride solution. Darker areas indicate a higher concentration.

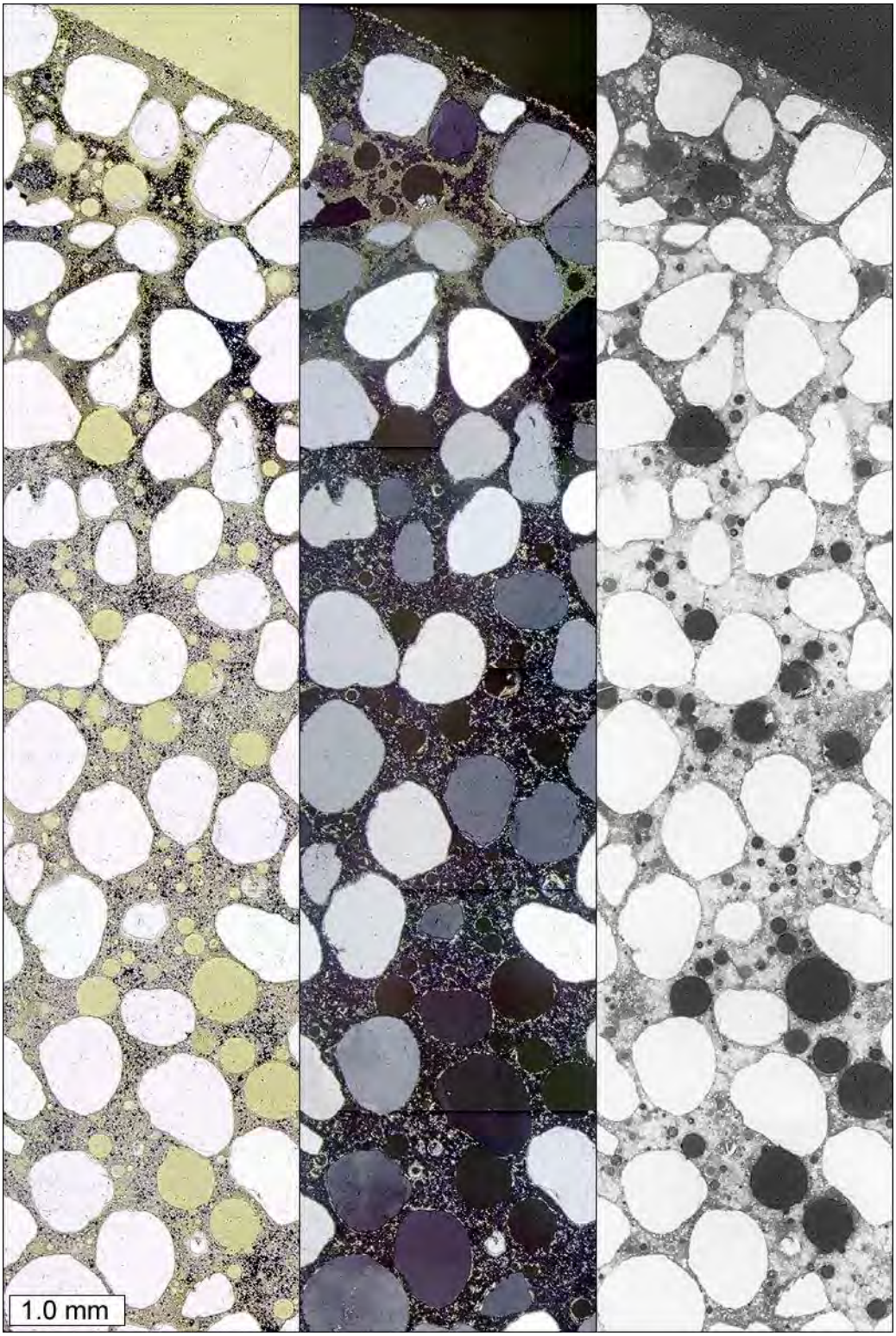

Figure A3.49. From left to right: plane polarized light, cross polarized light, and epifluorescent mode images of a thin section prepared from a cylinder immersed in calcium magnesium acetate solution.

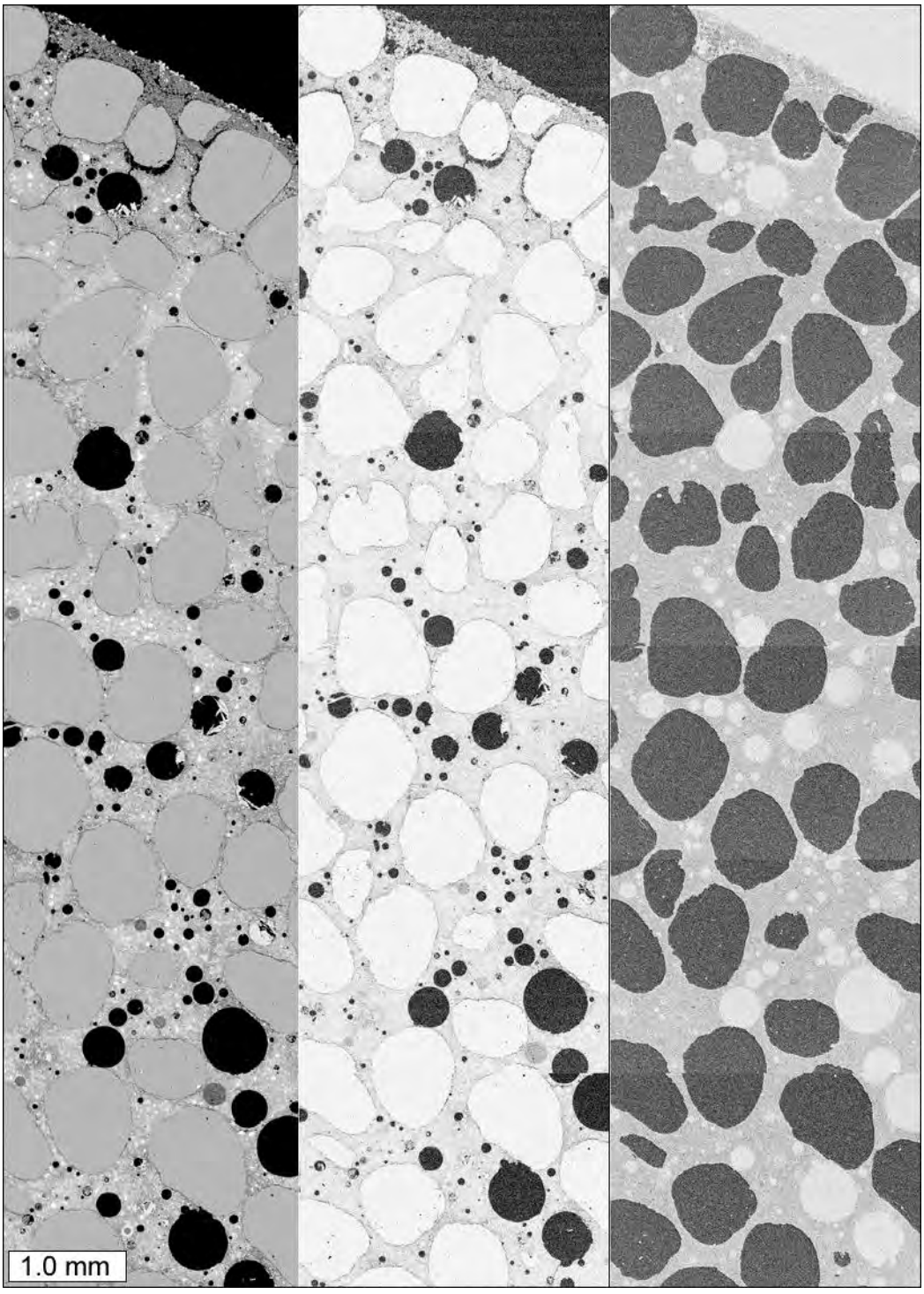

Figure A3.50. From left to right: back scattered electron image, elemental map for carbon, and elemental map for oxygen. Images were collected from a thin section prepared from a cylinder immersed in calcium magnesium acetate solution. Darker areas in elemental maps indicate a higher concentration.

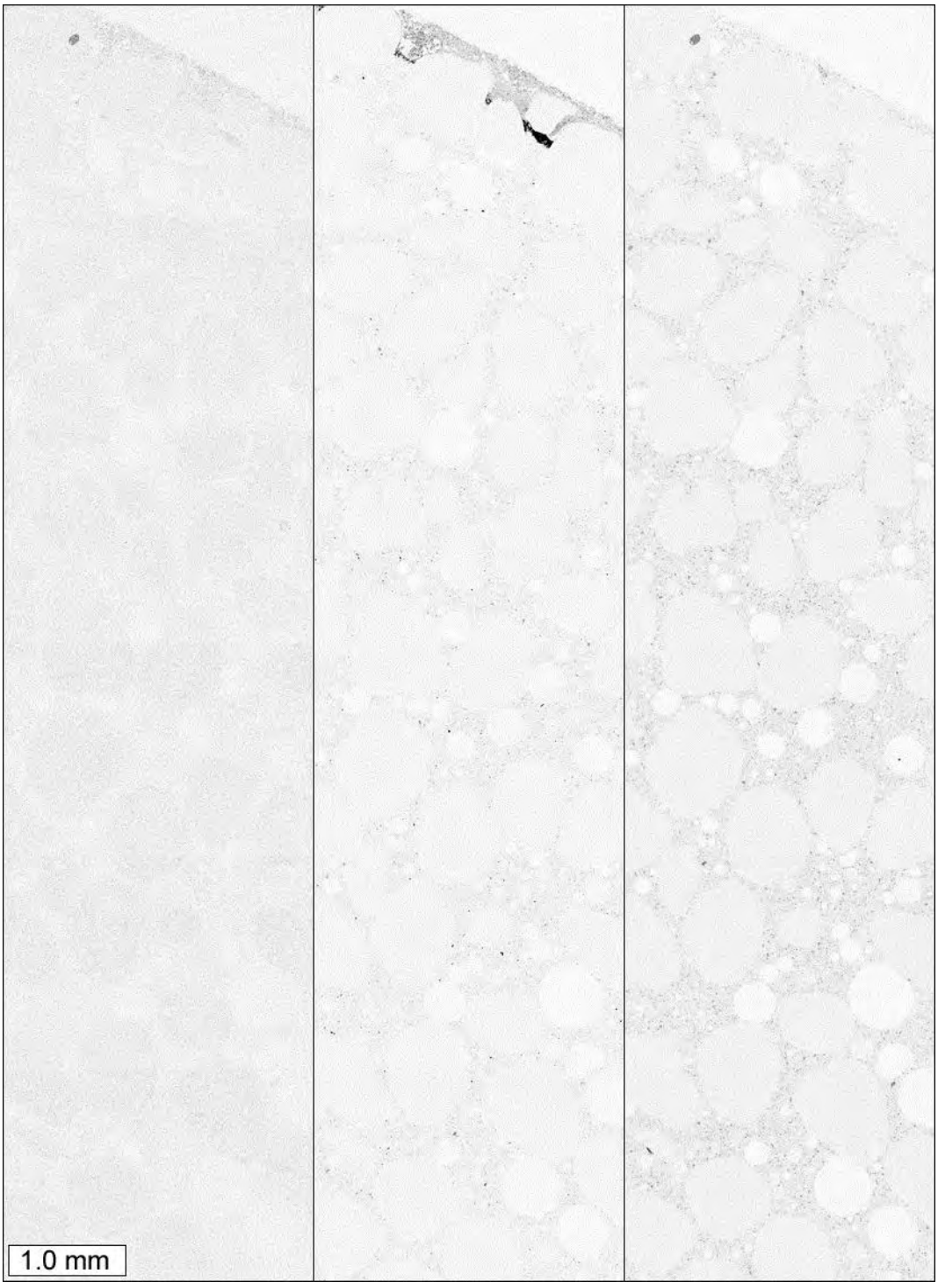

Figure A3.51. Elemental maps, from left to right: sodium, magnesium, and aluminum. The elemental maps were collected from a thin section prepared from a cylinder immersed in calcium magnesium acetate solution. Darker areas indicate a higher concentration.

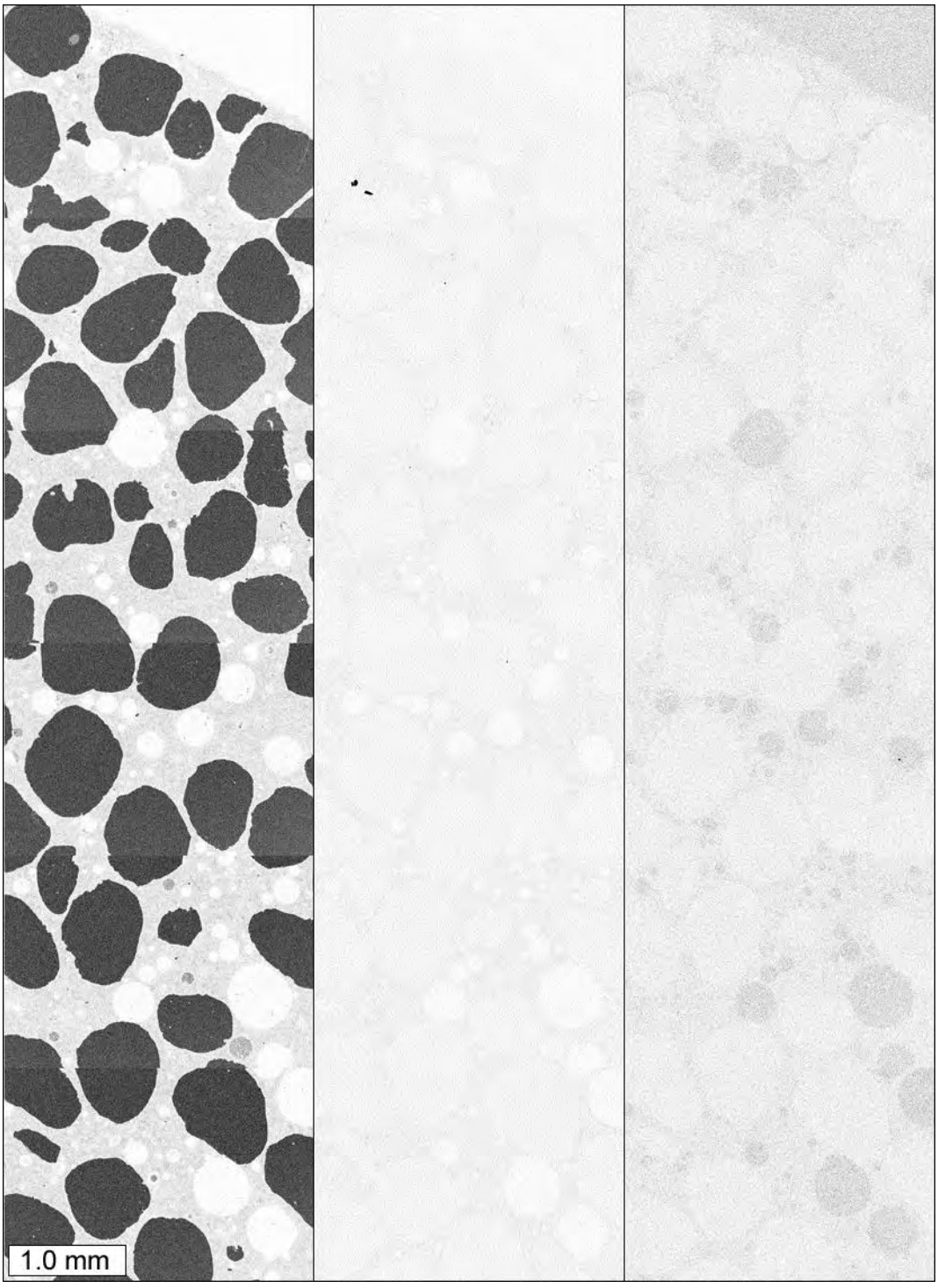

Figure A3.52. Elemental maps, from left to right: silicon, sulfur, and chlorine. The elemental maps were collected from a thin section prepared from a cylinder immersed in calcium magnesium acetate solution. Darker areas indicate a higher concentration.

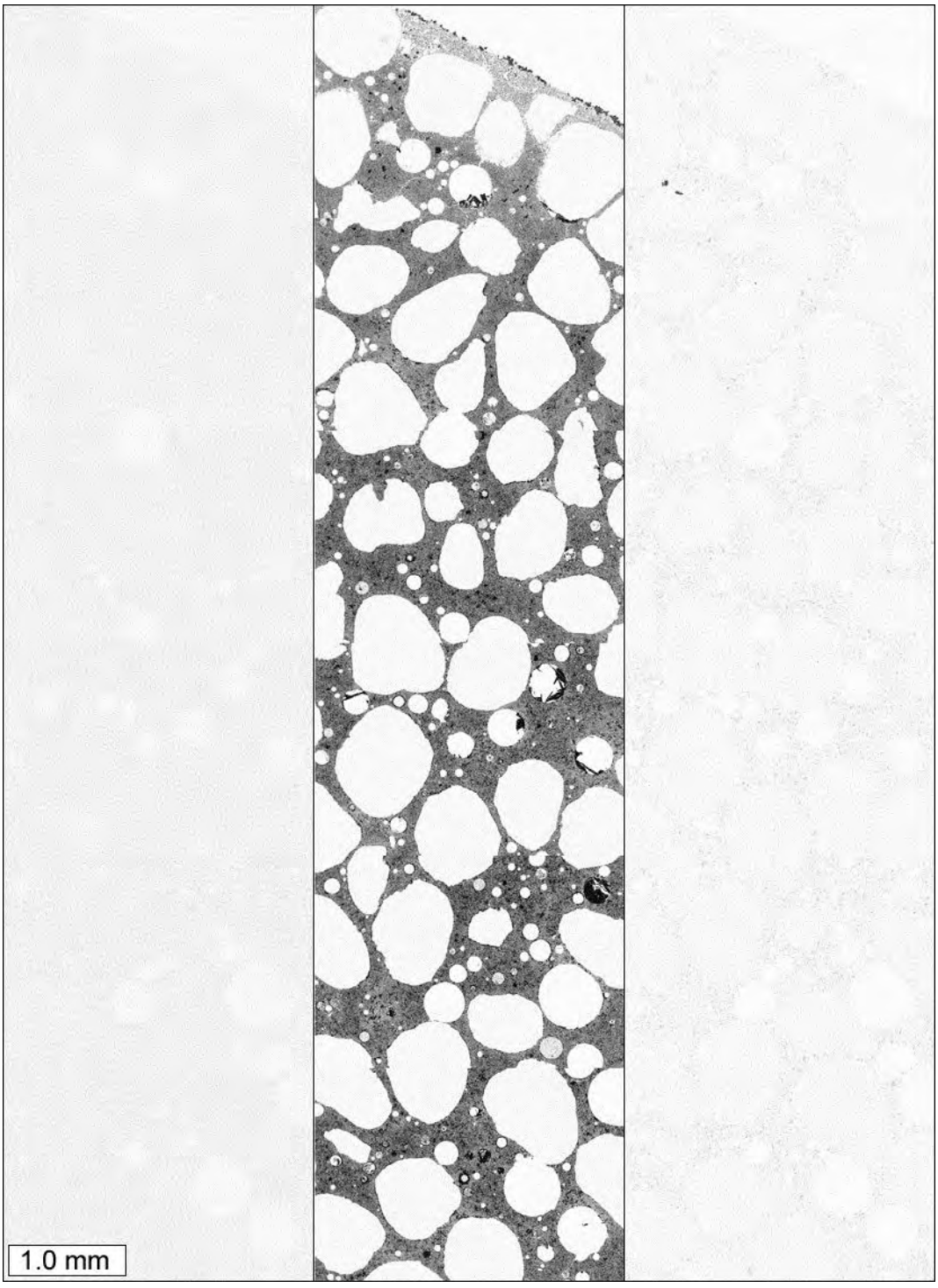

Figure A3.53. Elemental maps, from left to right: potassium, calcium, and iron. The elemental maps were collected from a thin section prepared from a cylinder immersed in calcium magnesium acetate solution. Darker areas indicate a higher concentration.

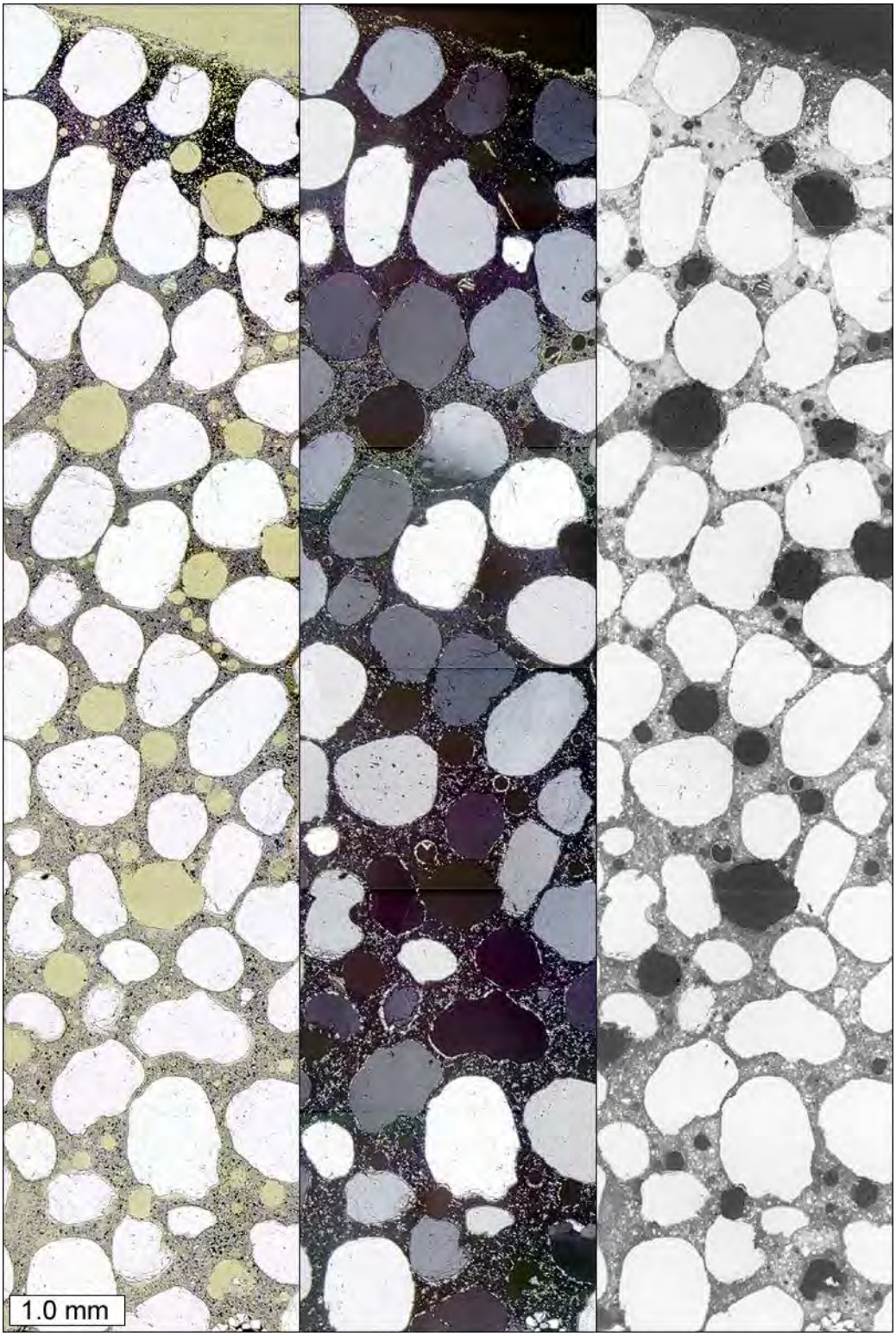

Figure A3.54. From left to right: plane polarized light, cross polarized light, and epifluorescent mode images of a thin section prepared from a cylinder immersed in limewater.

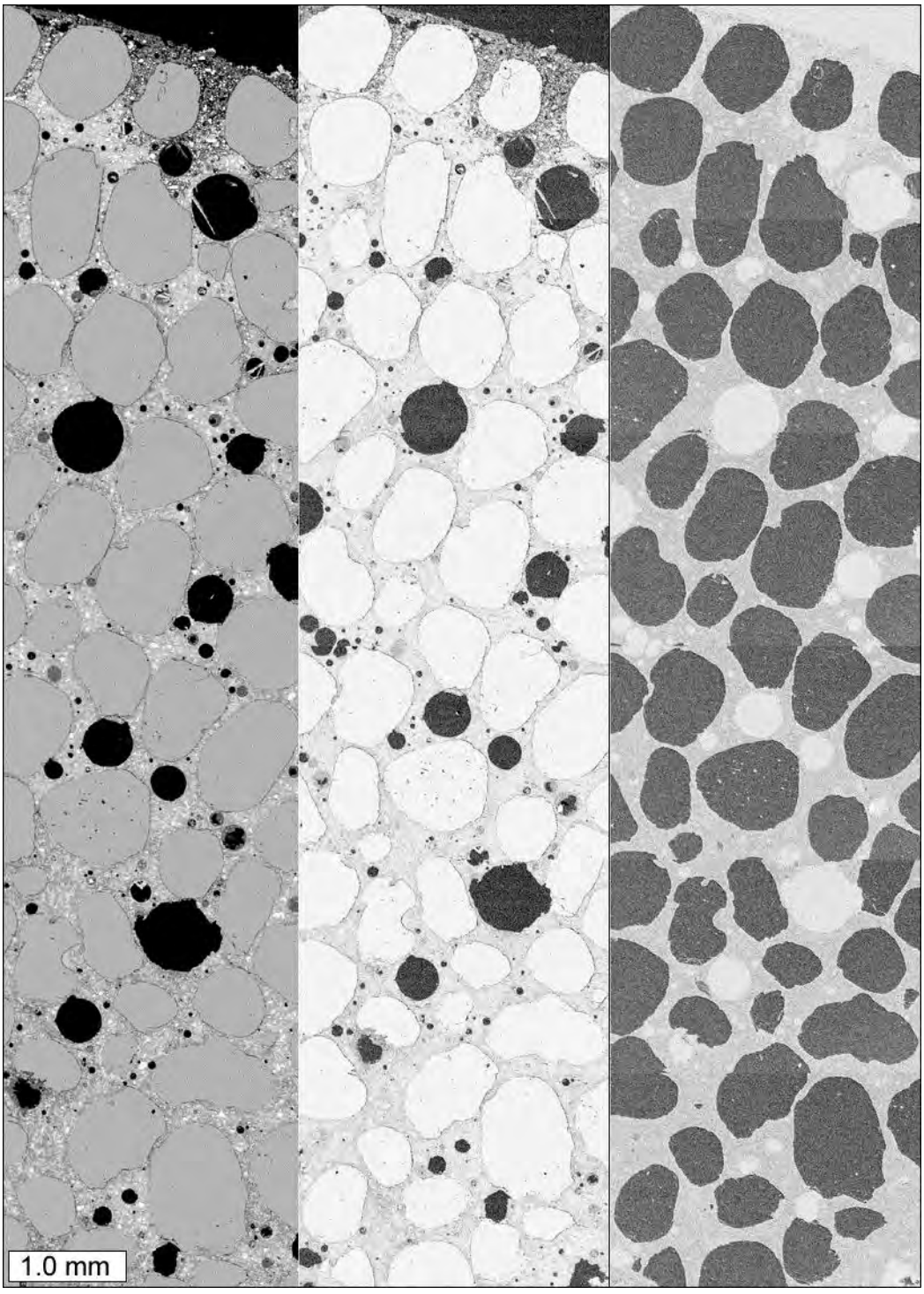

Figure A3.55. From left to right: back scattered electron image, elemental map for carbon, and elemental map for oxygen. Images were collected from a thin section prepared from a cylinder immersed in limewater. Darker areas in elemental maps indicate a higher concentration. Darker areas in elemental maps indicate a higher concentration.

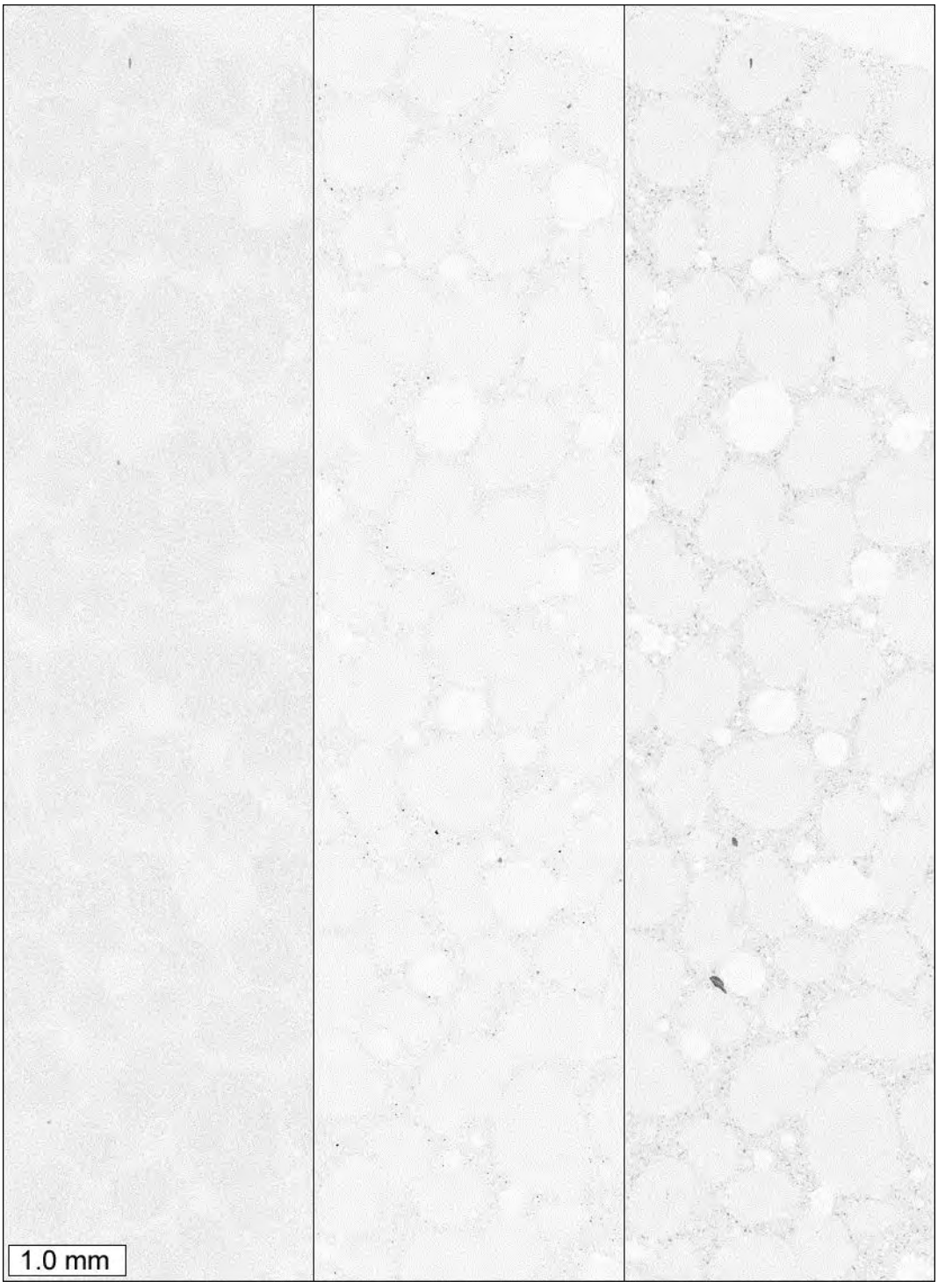

Figure A3.56. Elemental maps, from left to right: sodium, magnesium, and aluminum. The elemental maps were collected from a thin section prepared from a cylinder immersed in limewater. Darker areas in elemental maps indicate a higher concentration.

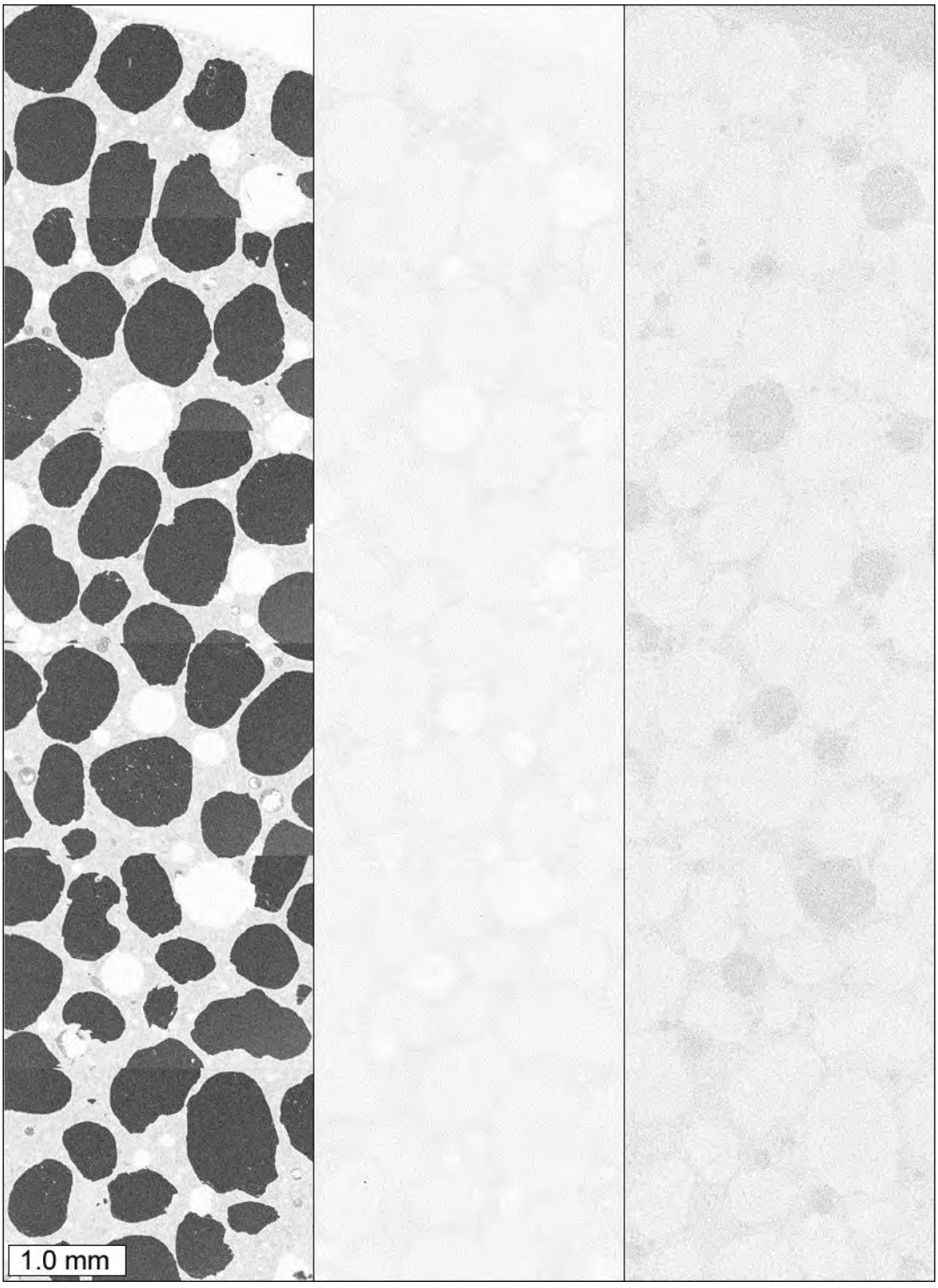

Figure A3.57. Elemental maps, from left to right: silicon, sulfur, and chlorine. The elemental maps were collected from a thin section prepared from a cylinder immersed in limewater. Darker areas indicate a higher concentration.

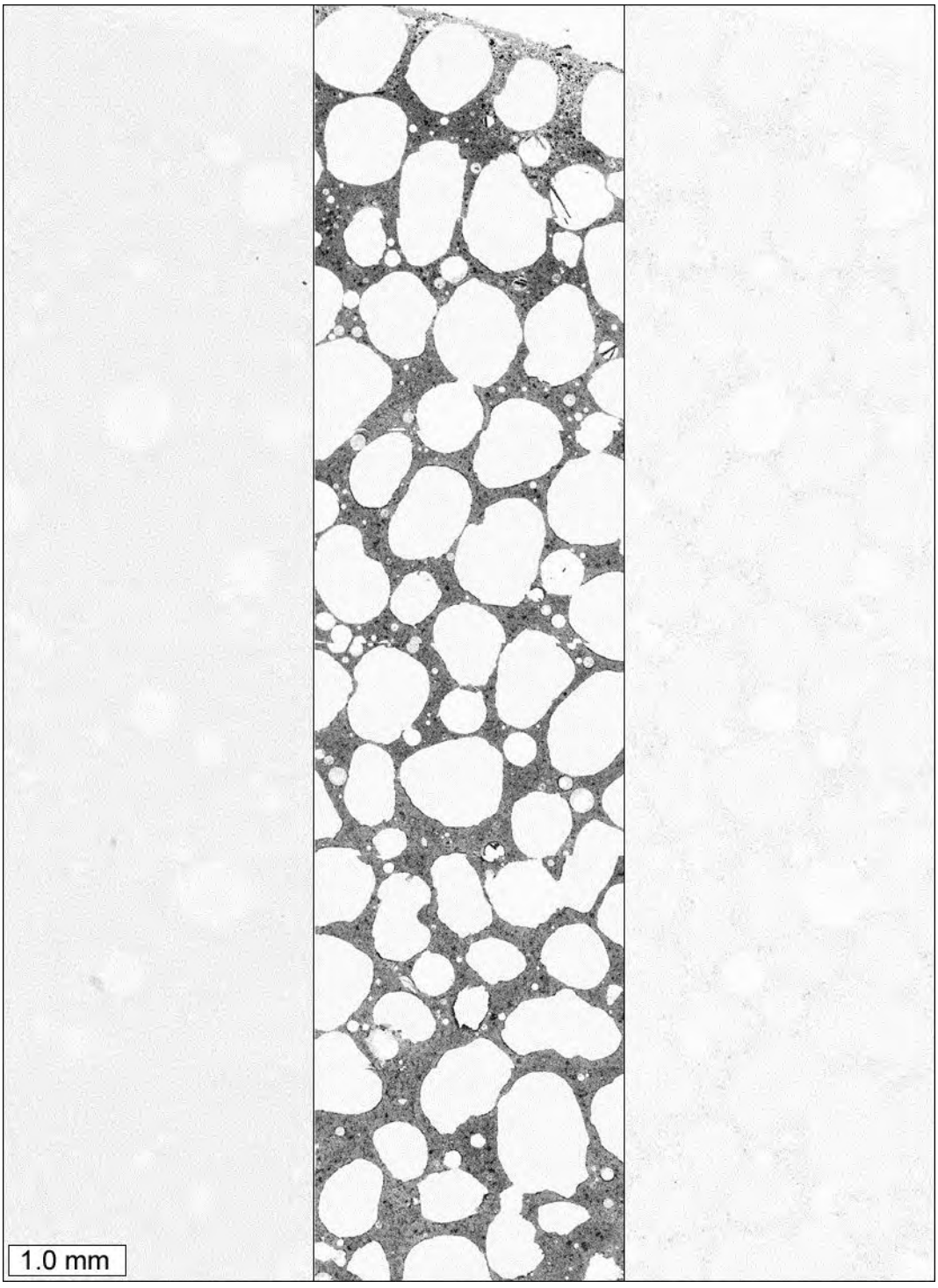

Figure A3.58. Elemental maps, from left to right: potassium, calcium, and iron. The elemental maps were collected from a thin section prepared from a cylinder immersed in limewater. Darker areas indicate a higher concentration.

A3.2.1.3 High Temperature Experiment

Observations

The constant high temperature experiment was run in the same manner as the constant low temperature experiment, but at an elevated temperature of 135 °F [57 ºC]. At 84 days the cylinders in the NaCl solutions showed no distress, as shown in Figure A3.59. The cylinders in the $MgCl_2$ solution began to show some cracking at 84 days, as shown in Figure A3.60. Figure A3.61 shows the $CaCl_2$ specimens after 84 days and no visible signs of distress are present. As shown in Figure A3.62, the cylinders in the CMA solution began to disintegrate after 28 days. It was decided to abort the CMA test at 28 days. At 84 days, the control samples in limewater were still unaffected as shown in Figure A3.63. Table A3.8 summarizes the visual ratings for the cylinders over time for all the limewater and deicer solution exposure tests.

Figure A3.59. Cylinders exposed to NaCl solution after 84 days of constant high temperature test. From left to right: 0.40, 0.50, and 0.60 *w/c* mortar cylinders.

Figure A3.60. Cylinders exposed to $MgCl_2$ solution after 84 days of constant high temperature test. From left to right: 0.40, 0.50, and 0.60 *w/c* mortar cylinders.

Figure A3.61. Cylinders exposed to $CaCl_2$ solution after 84 days of constant high temperature test. From left to right: 0.40, 0.50, and 0.60 *w/c* mortar cylinders

Figure A3.62. Cylinders exposed to CMA solution after 28 days of constant high temperature test. From left to right: 0.40, 0.50, and 0.60 *w/c* mortar cylinders.

Figure A3.63. Control cylinders exposed to lime solution after 84 days of constant high temperature test. From left to right: 0.40, 0.50, and 0.60 *w/c* mortar cylinders.

Table A3.8. List of visual ratings for all mortar cylinders from the high temperature tests. Rating Scale: 0 - no visible change, 1 – some cracking, 2 - visible expansion and cracking, 3 - severe expansion and cracking, 4 - partial disintegration, 5 - total disintegration, *x* – test aborted.

Solution	Time in Days											
	w/c = 0/40				*w/c = 0/50*				*w/c = 0/60*			
	8	28	56	84	8	28	56	84	8	28	56	84
Limewater	-	0	0	0	-	0	0	0	-	0	0	0
$MgCl_2$	-	0	0	0	-	0	0	0-1	-	0	0	0-1
$CaCl_2$	-	0	0	0	-	0	0	0	-	0	0	0
NaCl	-	0	0	0	-	0	0	0	-	0	0	0
CMA	-	4	*x*	*x*	-	4	*x*	*x*	-	4	*x*	*x*

Split Tensile Strength Testing

Split tensile testing has not been performed on these specimens. Given the turns that these experiments took, it does not seem prudent to invest resources in testing these specimens at this time.

Petrographic Analysis

The cylinders immersed at constant high temperature showed no external signs of deterioration after 84 days for any of the solutions, with the exception of the cylinders immersed in the calcium magnesium acetate solution. After 28 days, the exteriors of the cylinders exposed to the calcium magnesium acetate solution began to disintegrate into what could be best described as a mushy gray mass. After removal from the solution, the cylinders developed translucent whisker-like crystals intermixed with the disintegrated mortar. Figure A3.64 shows the crystals intermixed with the disintegrated mortar. A small quantity of the crystals were scraped and collected for X-ray diffraction (XRD). Figure A3.65 shows the X-

ray diffraction pattern from the crystals. The pattern provided a good match with calcium acetate hydrate. Some crystals were also examined with a scanning electron microscope. Figure A3.66 shows a secondary electron image of some of the crystals. Figure A3.67 shows an energy dispersive X-ray spectrum collected from a crystal with peaks for carbon, oxygen, and calcium. One of the 0.40 *w/c* cylinders was prepared in thin section. Figures A3.68, A3.69, and A3.70 show petrographic microscope images of a cross-section through the cylinder.

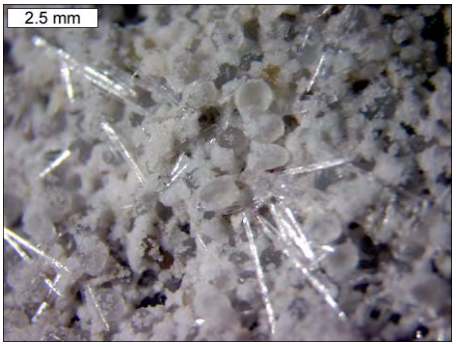

Figure A3.64. Stereomicroscope image of needles of translucent crystals on disintegrated mass of mortar.

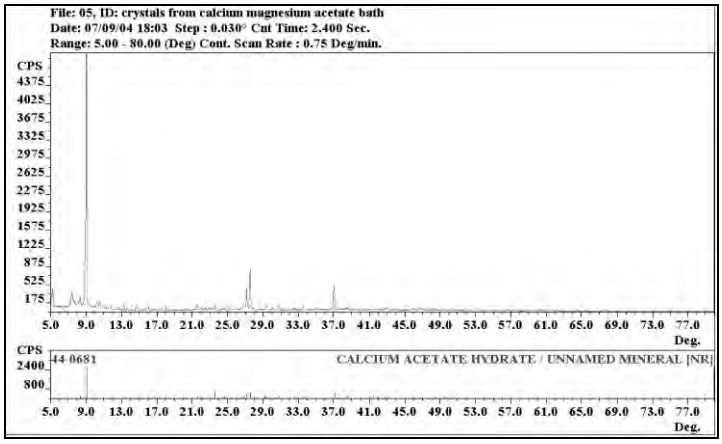

Figure A3.65. X-ray diffraction pattern showing match for calcium acetate hydrate.

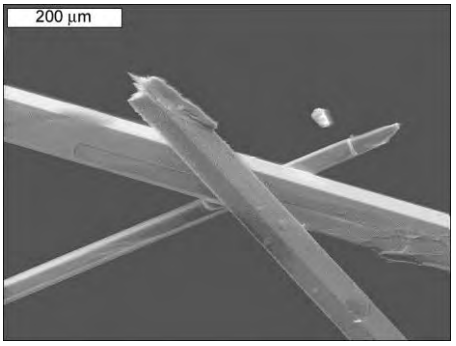

Figure A3.66. Secondary electron image of crystals plucked from disintegrated mortar.

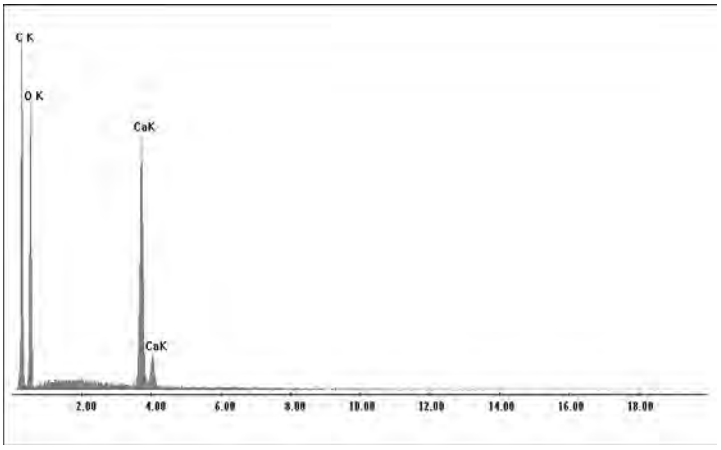

Figure A3.67. X-ray energy spectrum, (in units of kV) showing counts for carbon Kα, oxygen Kα, calcium Kα, and calcium Kβ X-rays, collected from crystals plucked from disintegrated mortar.

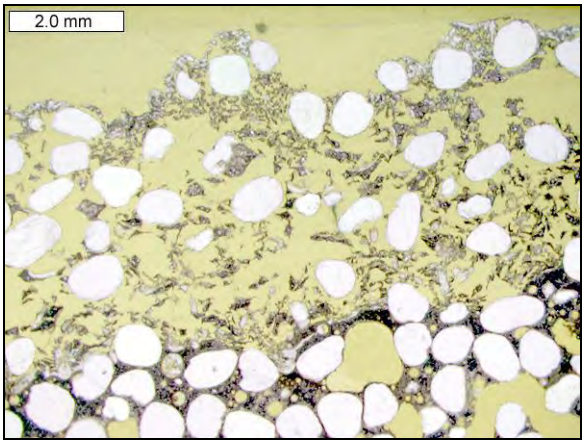

Figure A3.68. Petrographic microscope image, transmitted plane polarized light, of thin section prepared from cylinder from calcium magnesium acetate constant hot temperature experiment.

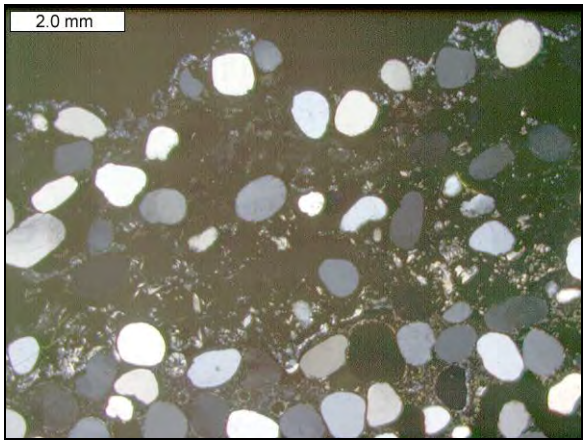

Figure A3.69. Petrographic microscope image, cross polarized light, of thin section prepared from cylinder from calcium magnesium acetate constant hot temperature experiment.

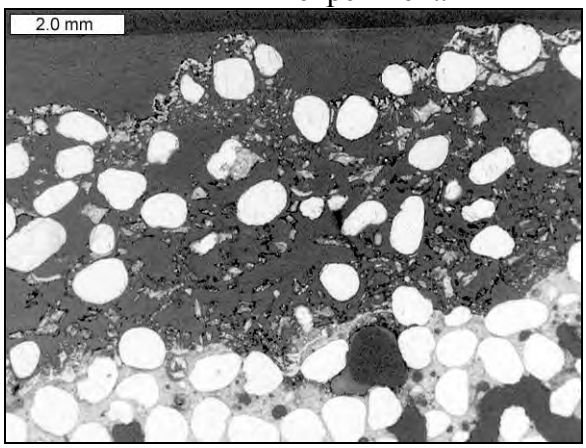

Figure A3.70. Petrographic microscope image, epifluorescent mode, of thin section prepared from cylinder from calcium magnesium acetate constant hot temperature experiment.

A3.2.1.4 Phase I Additional Experiments

Cyclical Temperature Experiments

Given the rapid failure of specimens treated in NaCl solution, it was determined that some follow-on tests should be performed to establish why these specimens failed so dramatically. To this end, two separate tests were conducted for NaCl and $MgCl_2$ only. First, the step of placing the specimens in the oven for 20 hours was replaced with allowing the specimens to sit at room temp for that same time. The second experiment was to eliminate the oven step and also eliminate the 2 hours of equilibration in limewater prior to the freezer step and the 20 hours in air. If the distress was associated with drying (i.e. salt crystallization or hydraulic pressure) then the distress should be reduced with the elimination of the oven. The elimination of the limewater conditioning step was done to isolate distress related to osmotic pressure that might result from interactions between the limewater and the ionic porewater of

the mortars. Given that the distress in the NaCl specimens occurred so quickly, it was thought that 14 days would be enough time to identify the effects of eliminating the oven and limewater steps, respectively. However, the specimens were exposed for up to 56 days.

Bypassing the oven step eliminated the rapid failures seen in the original NaCl cyclic tests. However with extended testing, it was shown that some distress would still manifest itself after 56 days. Eliminating both the oven and the limewater steps greatly reduced the distress even further. However, after 56 days, limited distress did still appear.

Further investigation of possible physical attack mechanisms was performed by reviewing additional literature. Although little was found regarding rapid heating and cooling of concrete, significant work was found regarding rapid and extreme temperature cycling of masonry (Grimm 1985). Based on this and other articles, it is postulated that specimens in the NaCl brine achieved a higher level of saturation as compared to the control specimens in limewater. Once saturated, the specimens in the NaCl brine froze completely, as did those in limewater. However, upon temperature cycling, the specimens in NaCl brine were subjected to high internal stresses from 1) salt crystallization, 2) the high coefficient of thermal expansion of salt relative to water, and 3) the restrained thermal expansion of ice, and subsequently of water, as the specimens progressed from -15 ºF to 135 ºF [-26 ºC to 57 ºC]. In the latter case, the restraint occurred in the specimens exposed to NaCl brine, as opposed to limewater, as the salt filled pores did not allow water to easily migrate from the specimens as the ice in the pore structure melted (Grimm 1985).

Additional Cold Temperature Experiment

It was determined that the cold temperature experiment showed the clearest damage and therefore this test was used to determine the effect of solution concentration on the observed distress. New constant low temperature $CaCl_2$ samples were exposed to $CaCl_2$ solutions at varying concentrations. For this experiment, solution concentrations were chosen at 3, 7, 10, and 14 weight percent salt. The specimens were left in solution for 54 days with random samples being removed every 7 days for inspection and analysis.

As can be seen clearly in Figures A3.71 through A3.75, concentration clearly has an affect on the observed damage at a given time for mortars exposed to the low temperature test.

Figure A3.71. Cylinders exposed to $CaCl_2$ solution after 56 days of constant low temperature test. From left to right: 0.40, 0.50, and 0.60 *w/c* mortar cylinders. Solution strength was 3% $CaCl_2$.

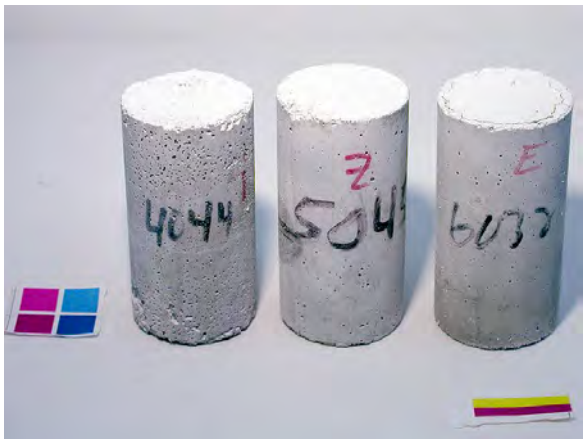

Figure A3.72. Cylinders exposed to $CaCl_2$ solution after 56 days of constant low temperature test. From left to right: 0.40, 0.50, and 0.60 *w/c* mortar cylinders. Solution strength was 7% $CaCl_2$.

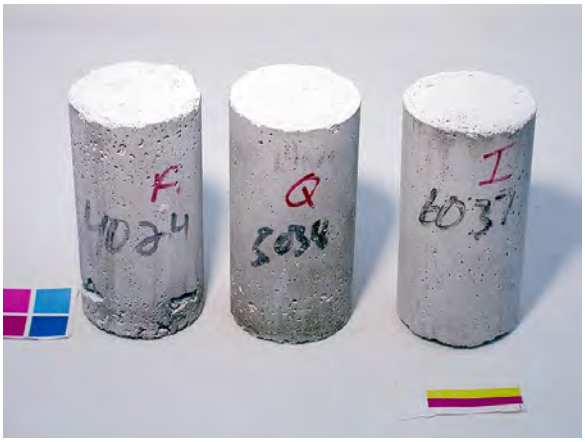

Figure A3.73. Cylinders exposed to $CaCl_2$ solution after 56 days of constant low temperature test. From left to right: 0.40, 0.50, and 0.60 *w/c* mortar cylinders. Solution strength was 10% $CaCl_2$.

Figure A3.74. Cylinders exposed to $CaCl_2$ solution after 56 days of constant low temperature test. From left to right: 0.40, 0.50, and 0.60 *w/c* mortar cylinders. Solution strength was 14% $CaCl_2$.

Figure A3.75. Cylinders exposed to $CaCl_2$ solution after 56 days of constant low temperature test. From left to right: 0.40, 0.50, and 0.60 *w/c* mortar cylinders. Solution strength was 17% $CaCl_2$.

A3.2.2 Results of Phase I Experiments Conducted at the University of Toronto

A3.2.2.1 Compressive Strength

Mortar cubes prepared for these tests were tested at 28 days of age and the average compressive strength of the mortar cubes was 6238 psi [43 MPa]. After exposure to the different deicers, the compressive strength decreased for those samples exposed to MBAP, $MgCl_2$ and $CaCl_2$. The compressive strength results are shown in Figure A3.76. The compressive strength decreased in the order $MgCl_2$, MBAP and $CaCl_2$ by 63, 62 and 23% respectively, when compared with the compressive strength of mortar cubes exposed to saturated calcium hydroxide solution. The mortar cubes exposed to NaCl did not show a decrease in compressive strength and to the contrary, their behavior was similar to those samples exposed to the calcium hydroxide solution. That is, the compressive strength increased with time as is expected with continuous hydration. The samples exposed to MBAP and $MgCl_2$ showed similar trends in their compressive strength evolution with time.

A3.2.2.2 Expansion

Exposure of mortar bars to MBAP, $MgCl_2$ and $CaCl_2$ resulted in considerable expansion while those subjected to NaCl showed negligible expansion even after 500 days of exposure, as illustrated in Figure A3.77. MBAP caused the highest expansion of all, 0.75% at 568 days followed by $MgCl_2$ and $CaCl_2$ with 0.37 and 0.29% respectively. Although MBAP and $MgCl_2$ caused the compressive strength to decrease to a similar degree, a similar correlation was not observed with the rate of expansion. The MBAP samples expanded almost twice as much as samples exposed to $MgCl_2$, with the same exposure period.

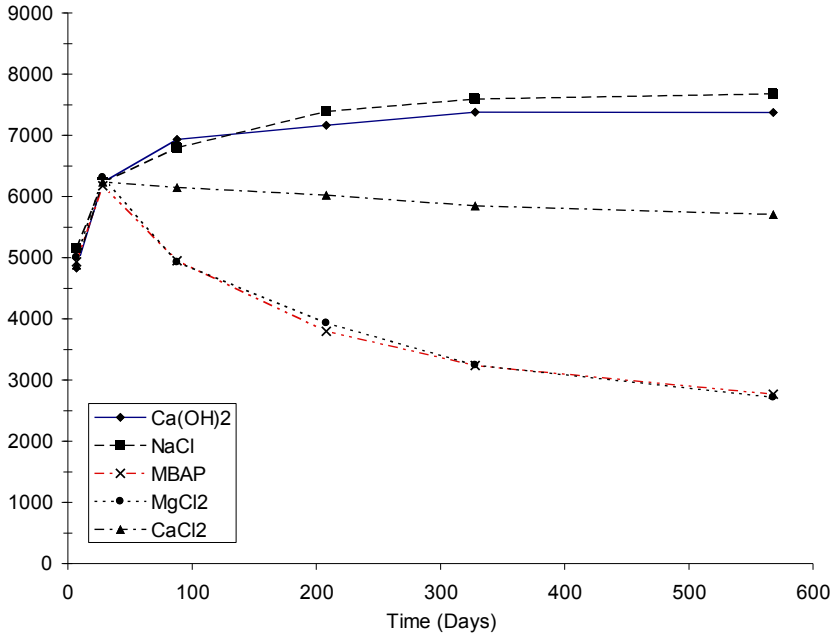

Figure A3.76. Compressive strength evolution with time of mortar cubes exposed to different deicers.

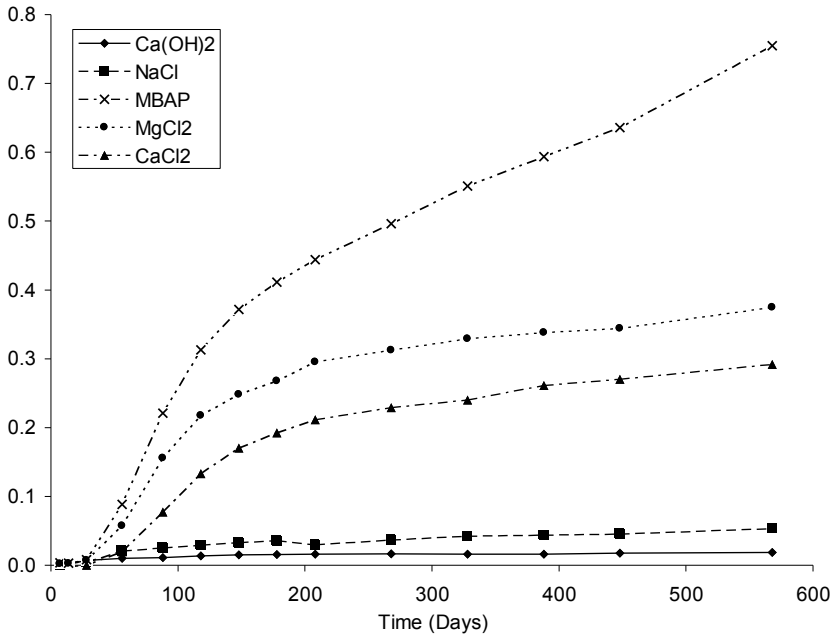

Figure A3.77. Length change of mortar bars with time for mortar bars exposed to different deicers.

A3.2.2.3 Mass Change

For those specimens exposed to MBAP, $MgCl_2$ and $CaCl_2$, expansion of mortar bars was accompanied by considerable mass gain as shown in Figure A3.78. The greatest mass gain was 5.9% observed for those samples exposed to MBAP, followed by $MgCl_2$ with 3.6% and $CaCl_2$ with 2.4% mass gain. The specimens exposed to NaCl and saturated calcium hydroxide solution did not show considerable mass gain with 1.4 and 1.1% recorded, respectively. The behavior of mass gain, especially for those samples exposed to MBAP, $MgCl_2$ and $CaCl_2$, can be divided into two events. The first being a steep mass gain slope up to 118 days of exposure followed by a less pronounced mass gain after 118 days.

A3.2.2.4 Visual Observations

Visual observations of the specimens exposed to MBAP and $MgCl_2$ that experienced loss of strength, expansion and mass gain revealed a clear feature. Defined zones of chemical interaction of 0 to 0.2 inches [0 to 5 mm] through the cross sectional area of the mortar bars were visible. These zones are easily identified by the changes in color from a light gray in the core of the specimen to a yellowish color at the surface. The presence of micro-cracks was confirmed using the stereo optical microscope.

At early ages (less than 118 days) a white layer developed on the surface of specimens exposed to MBAP and $MgCl_2$, and it was subsequently identified by X-ray diffraction as brucite. The deterioration front seemed to move deeper into the specimen with exposure time. Softening of the surface and debonding of sand grains were identified. None of these features were identified in samples exposed to either $CaCl_2$ or NaCl.

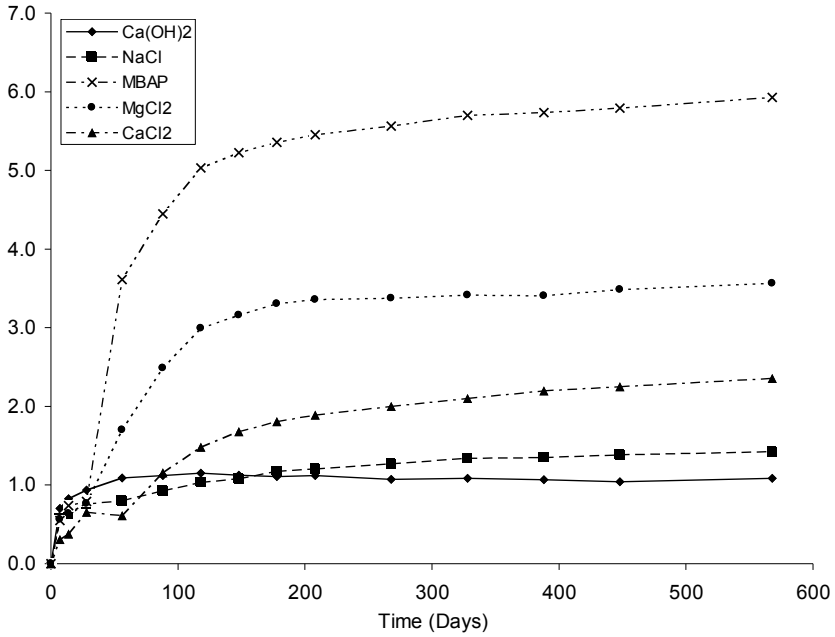

Figure A3.78. Mass change of mortar bars with time of mortar bars exposed to different deicers.

A3.2.2.5 Solution pH

Figure A3.79 shows the change in pH of the various exposure solutions during the exposure period. For the first 28 days, the samples were cured in calcium hydroxide saturated solution with a pH of approximately 12.7. Once the samples were immersed in the deicers, the pH of the exposure solution initially decreased, then increased. This is represented by the pronounced spike towards low pH seen at 28 days in Figure A3.79. For example, the pH of the MBAP and $MgCl_2$ solutions were 7.8 and 8.3, respectively, at the beginning of the salt solution exposure period and increased to up to approximately 8.6 after continued exposure of the mortar specimens to these same solutions. The $CaCl_2$ solution, initially acidic (e.g. pH of 5.6) after immersion of the specimens, increased to approximately 11.4 after exposure. The NaCl solution, with an initial pH of 7.6, increased to a pH of 12.4. This is much higher than that of the MBAP and closer to the pH of the calcium hydroxide solution at 12.7. It is expected that a solution pH less basic than a saturated solution calcium hydroxide solution (e.g. less than pH 10) will leach calcium hydroxide from the mortar samples until either reaching equilibrium with the pH of the pore solution or depleting the calcium hydroxide available for buffering the exposure solution.

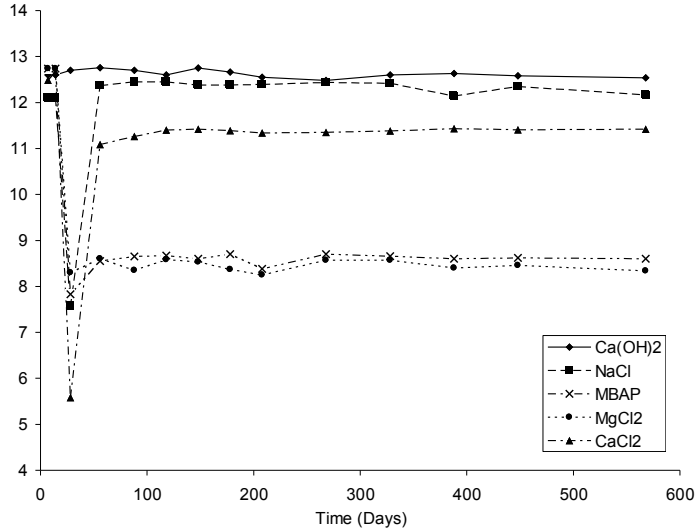

Figure A3.79. Measured pH change during deicer exposure period.

A3.2.2.6 Mercury Intrusion Porosimetry

The observed chemical interaction appeared to proceed inwards from the surface to the core of the specimens, so surface slices of 0.2 inch [5 mm] thickness were analyzed using MIP to determine the effect of the deicers on the porosity of the mortar bars, which in turn effects the diffusion and penetration of the deicers into the specimens for further chemical interaction. Table A3.9 presents the results for MIP at 248 days of exposure time. Those deicers such as MBAP and $MgCl_2$ that caused considerable expansion, mass gain and loss of compressive strength, showed an increase in the total volume of pores of up 20% when compared with the reference samples exposed to calcium hydroxide. On the other hand, those specimens exposed to NaCl and $CaCl_2$ did not show the same effect. However, the total pore surface area increased for those samples exposed to $CaCl_2$.

Table A3.9. Total porosity by Mercury Intrusion Porosimetry (MIP)

Exposure solution	Bulk density (lbs/ft^3) [kg/m^3]	Total pore surface area (ft^2/in^3) [m^2/cm^3]	Cumulative pore volume (%)
$Ca(OH)_2$	138.4 [2217]	7.4 [11.2]	9.4
NaCl	142.4 [2281]	9.6 [14.7]	8.8
MBAP	135.7 [2173]	9.0 [13.7]	11.5
$MgCl_2$	129.4 [2073]	9.5 [14.5]	10.7
$CaCl_2$	139.7 [2237]	10.3 [15.7]	9.1

A3.2.2.7 X-ray Diffraction

X-ray diffraction analysis of powder samples taken from the surface of the mortar bars up to a depth of 0.2 inches [5 mm] showed the formation of new phases and the depletion of others. In the case of the samples exposed to the saturated calcium hydroxide solution, no sign of chemical attack was found with the main calcium hydroxide peaks clearly defined in the diffractogram shown in Figure A3.80 as well as an ettringite, silica peaks from the Ottawa sand, and other minor phases that are the normal products of the hydration reactions.

Those samples exposed to NaCl solutions had phases similar to those exposed to calcium hydroxide solutions, the only difference being the presence of Friedel's salt. A typical X-ray diffraction pattern for a mortar specimen exposed to NaCl solution is shown in Figure A3.81. In the case of MBAP, besides Friedel's salt, some peaks of a phase resembling magnesium oxychloride (PDF 00-007-042 $Mg_3(OH)_5Cl{\bullet}4H_2O$), was identified as seen in Figure A3.82. This phase was not detected in the samples exposed to $MgCl_2$ but instead defined peaks of brucite were found as shown in Figure A3.83. For both MBAP and $MgCl_2$ the intensity of the main peaks of calcium hydroxide diminished suggesting depletion of this phase due to chemical attack, leaching or both.

The sample exposed to $CaCl_2$ did not show any new phases and although some depletion of calcium hydroxide was observed, calcium hydroxide was still present. It was expected that the expansion, gain in mass and the slow loss of compressive strength observed would be related to the formation of new phases yet this was not the case. Either the minor depletion of calcium hydroxide was due to leaching, or the amount of a newly formed phase by reaction of calcium chloride with calcium hydroxide was below the detection limit of the X-ray diffraction technique, or both. Figure A3.84 shows the X-ray diffraction pattern of the mortar sample exposed to $CaCl_2$ with Friedel's salt as the only new phase detected. Other phases are normal hydration reaction products.

Samples exposed to CMA at room temperature disintegrated approximately 30 days after immersion. As a result, measurements of length, mass, and compressive strength change were impossible. Figure A3.85 presents a photograph taken before complete disintegration of the mortar cubes exposed to CMA, illustrating how the mortar lost cohesiveness causing crumbling particles to pile up next to the specimen until nothing was left but debris. Within this time samples were taken for X-ray diffraction analysis and a compound identified as calcium acetate hydrate was present. X-ray diffraction results for this phase are shown in Figure A3.86.

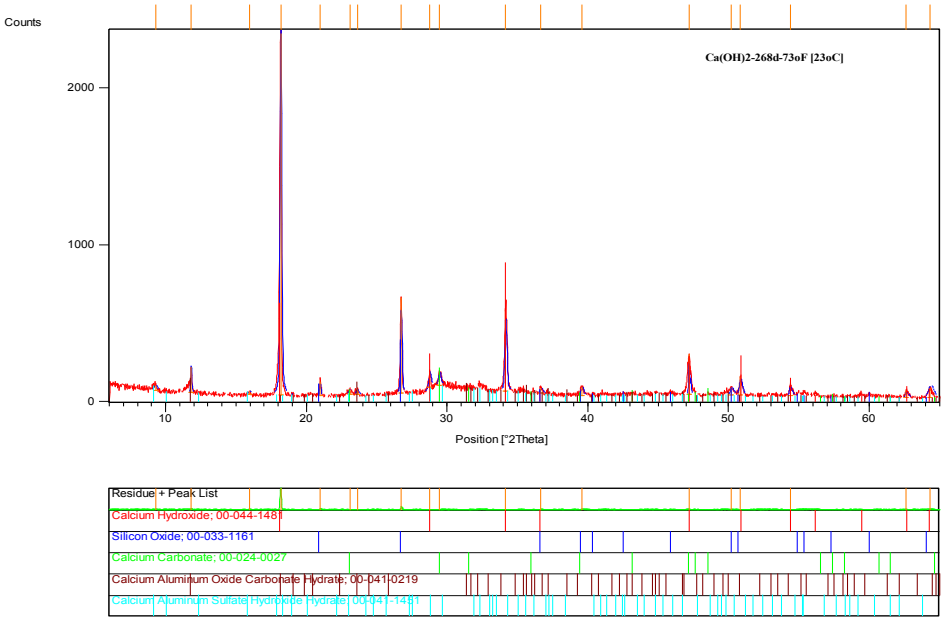

Figure A3.80. XRD diffractogram of mortar samples exposed to calcium hydroxide solution at 73.4 ºF [23 ºC] for 268 days.

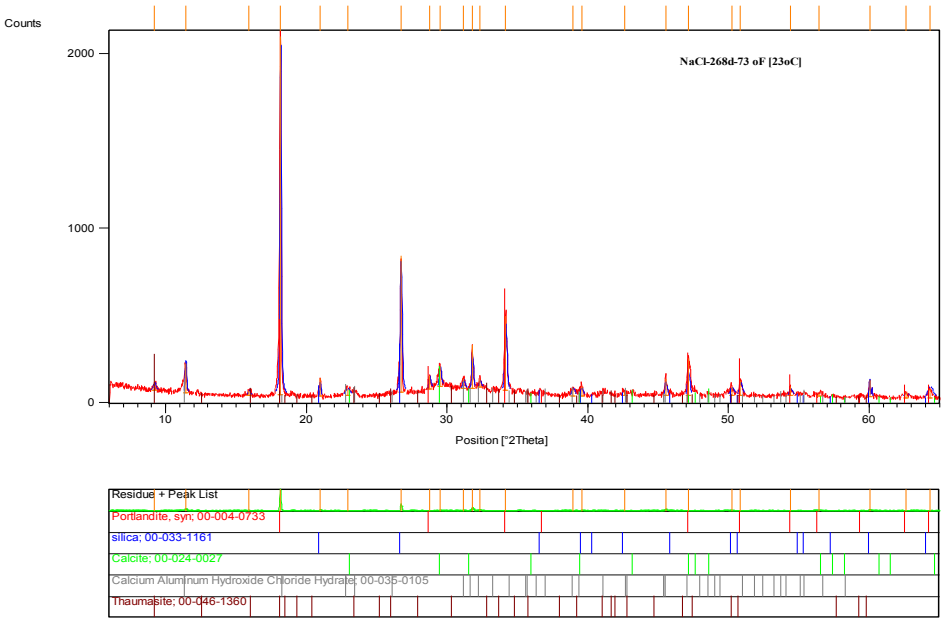

Figure A3.81. XRD diffractogram of mortar samples exposed to NaCl solution at 73.4 ºF [23 ºC] for 268 days.

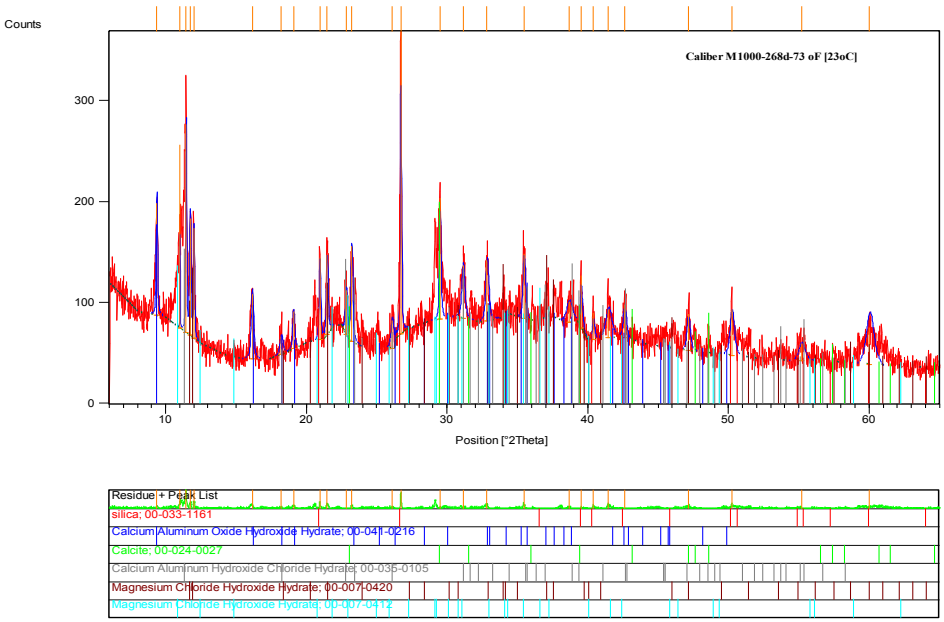

Figure A3.82. XRD diffractogram of mortar samples exposed to MBAP at 73.4 ºF [23 ºC] for 268 days.

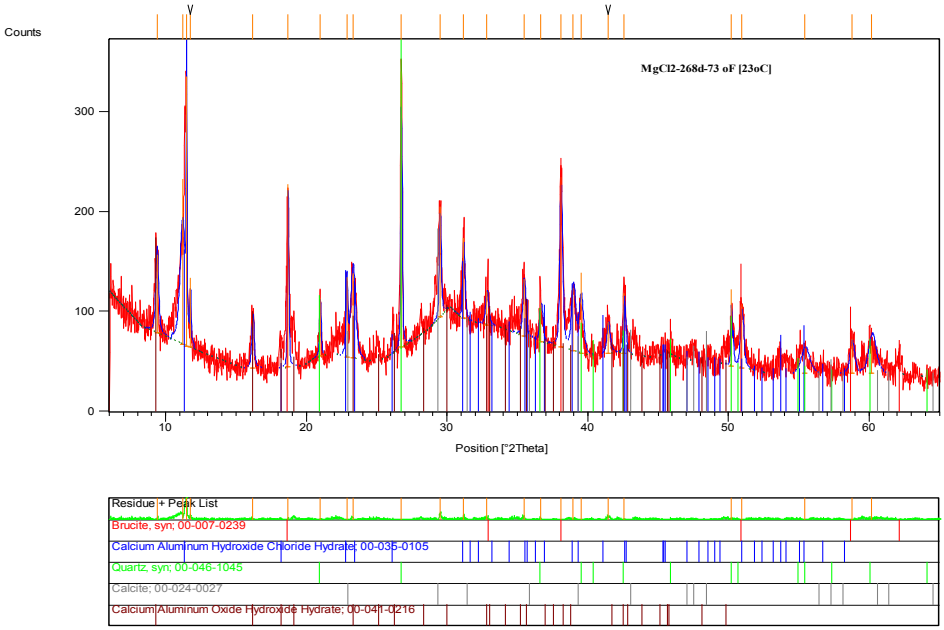

Figure A3.83. XRD diffractogram of mortar samples exposed to $MgCl_2$ at 73.4 ºF [23 ºC] for 268 days.

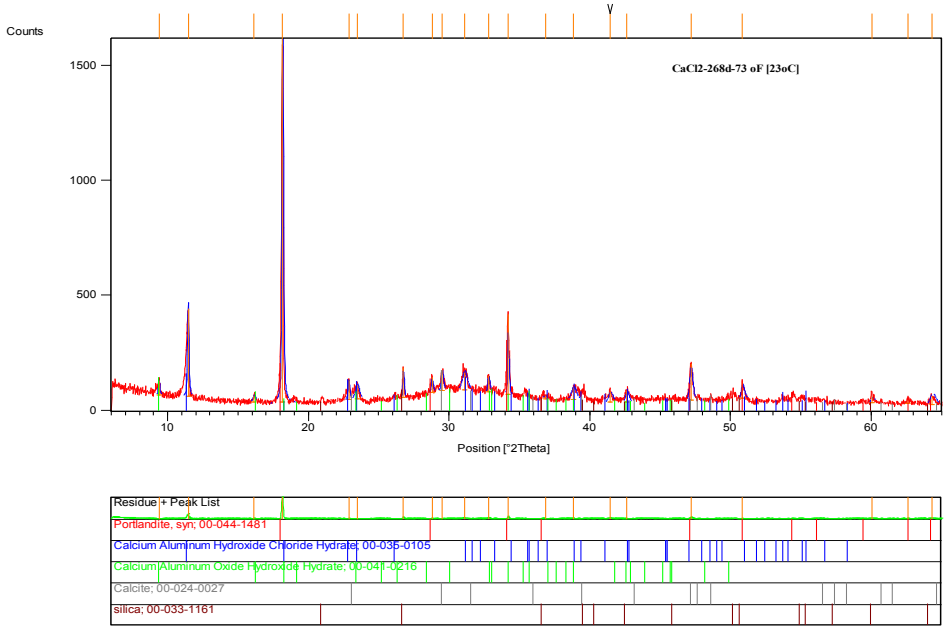

Figure A3.84. XRD diffractogram of mortar samples exposed to $CaCl_2$ at 73.4 ºF [23 ºC] for 268 days

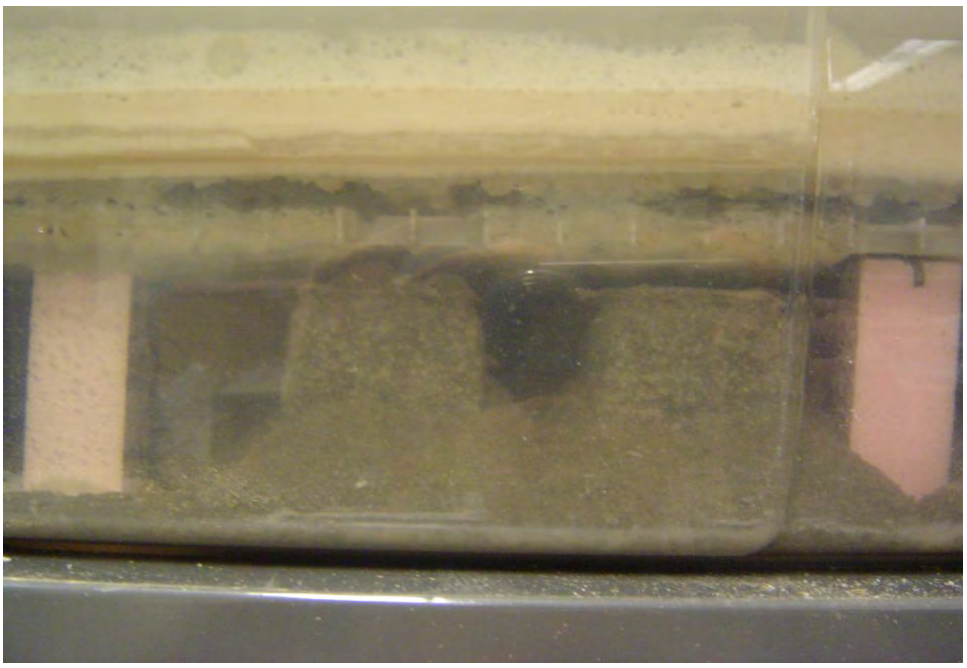

Figure A3.85. Disintegration of mortar cubes during exposure to CMA at 73.4 ºF [23 ºC].

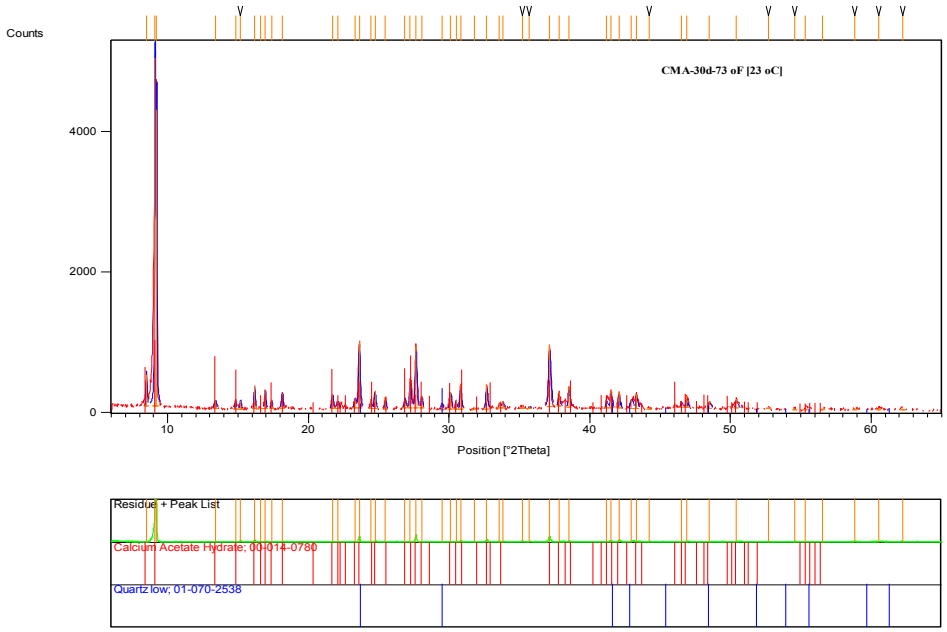

Figure A3.86. XRD diffractogram of mortar samples exposed to CMA at 73.4 ºF [23 ºC] for 30 days.

A3.2.2.8 Determination of Pessimum Concentration for $MgCl_2$ and $CaCl_2$

Mortar cubes were exposed to different concentrations of $MgCl_2$ and $CaCl_2$ at 41 ºF [5 ºC] to determine the effect of the exposure solution concentration on 30 day compressive strength of the mortar. The effect of concentration on compressive strength is shown in Figure A3.87. For those samples subjected to $MgCl_2$, the compressive strength increased for concentrations between 25 and 30% by mass of salt. There was no identifiable reason for this increase but additional tests gave similar results. At 20% $MgCl_2$, the compressive strength suffered a dramatic loss of up to 57%. For $CaCl_2$ solutions between 5 and 11% by mass of $CaCl_2$ the compressive strength was not effected at 30 days. Above 11% and up to 28%, the loss of compressive strength was considerable with 58% strength loss at 22% $CaCl_2$.

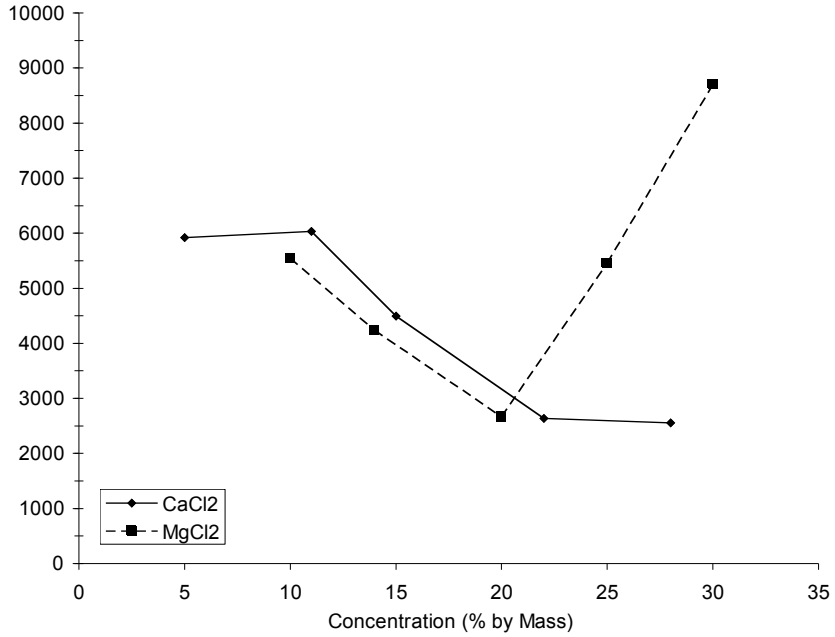

Figure A3.87. Effect of $MgCl_2$ and $CaCl_2$ on compressive strength after 30 days of exposure.

X-ray diffraction analysis of samples exposed to the pessimum concentration of $MgCl_2$ (i.e. 20%) and $CaCl_2$ (i.e. 22%) showed that the phase formed during the deterioration process of the mortar was a type of magnesium oxychloride (PDF 00-007-0412 $Mg_2(OH)_3Cl•4H_2O$) for $MgCl_2$ exposure and calcium oxychloride for $CaCl_2$ exposure. Diffraction results are shown in Figure A3.88 and Figure A3.89, respectively. Phase identification of calcium oxychloride is based on the main diffraction peaks at 8.215, 4.139 and 2.768 Å, similar to those reported by other researchers (Collepardi et al. 1994) of 8.34, 4.17 and 2.78 Å. Figures A3.90 and A3.91 show photographs illustrating the visual damage of specimens exposed to 20% $MgCl_2$ and 28% $CaCl_2$ respectively after 150 days of exposure.

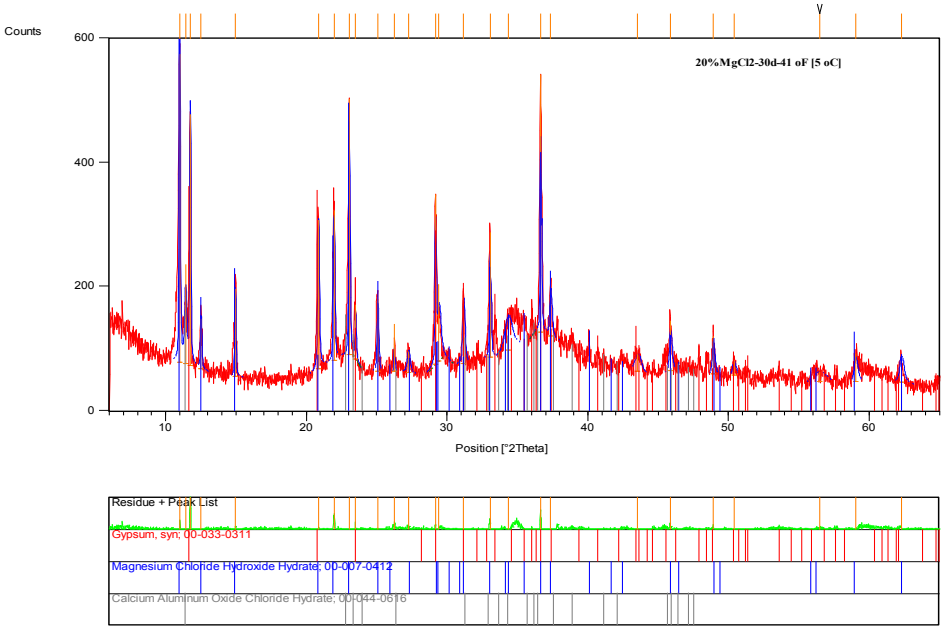

Figure A3.88. XRD diffractogram of mortar samples exposed to 20% $MgCl_2$ at 41 ºF [5 ºC] for 30 days.

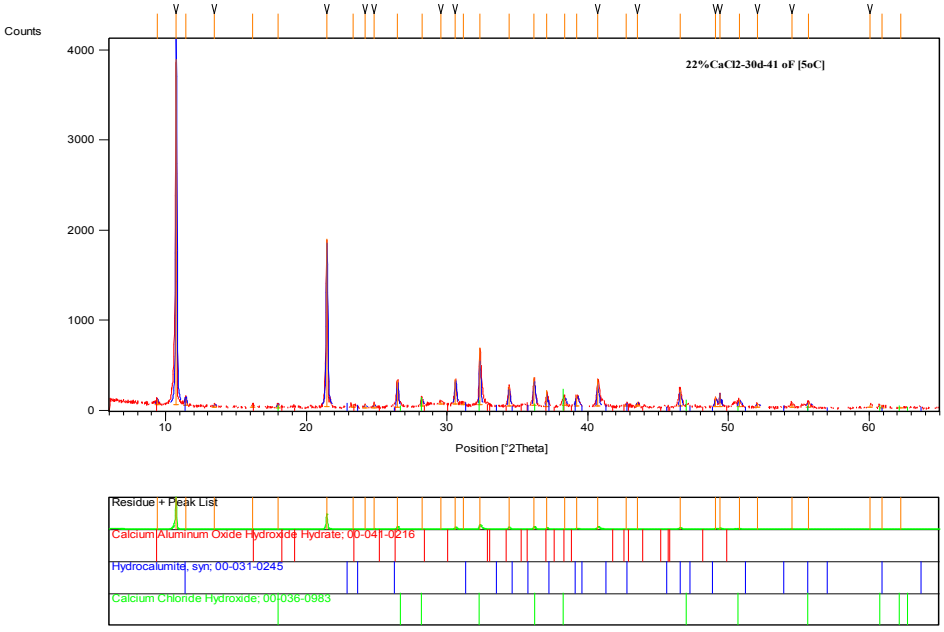

Figure A3.89. XRD diffractogram of mortar samples exposed to 22% $CaCl_2$ at 41 ºF [5 ºC] for 30 days.

Figure A3.90. Deteriorated disc sample exposed to 20% $MgCl_2$ after 150 days of exposure.

Figure A3.91. Deteriorated disc sample exposed to 28% $CaCl_2$ after 150 days of exposure.

A3.2.2.9 Other Observations

The characteristic features of deterioration due to $MgCl_2$ are swelling, cracking and exudation of a gel compound that with time turns into a mushy, semi-solid compound later identified as a mixture of magnesium oxychloride, brucite and bischofite ($MgCl_2 \bullet 6H_2O$).

Samples exposed to $CaCl_2$ developed cracks along the edges showing uniform expansion of the surface layer and distinctive needle-like crystals identified as calcium oxychloride.

Further tests on the effect of $MgCl_2$ concentration confirmed 20% $MgCl_2$ as the approximate pessimum concentration regardless of the exposure temperature as seen in Figures A3.92 and A3.93 where mortar bars exposed to 20% $MgCl_2$ expanded dramatically and gained mass considerably up to the point that the specimens bent and cracked, making it impossible to continue with measurements after 50 days of exposure.

Samples exposed to 30% $MgCl_2$ were found to actually show contraction and loss of mass, and as shown in Figure A3.93. The contraction and mass loss can be explained by the acidic nature of the exposure solution throughout the experiment as seen in Figure A3.94.

X-ray diffraction analysis of specimens exposed to 20% $MgCl_2$ confirmed the formation of magnesium oxychloride in these samples as shown in Figure A3.95. In addition, the white layer that precipitated on the surface was identified as a combination of magnesium oxychloride, bischofite and brucite. X-ray diffraction results for this mixture are shown in Figure A3.96.

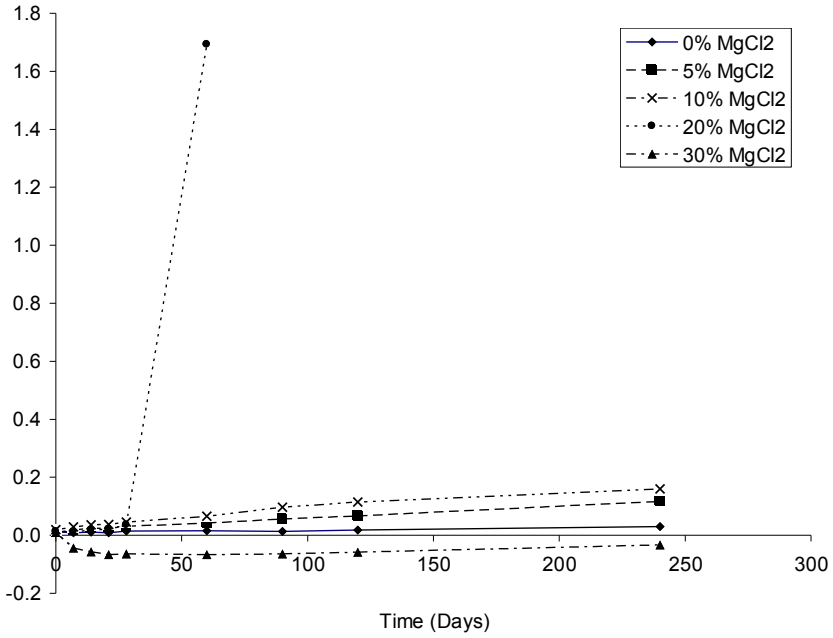

Figure A3.92. Length change due to the effect of different concentrations of $MgCl_2$.

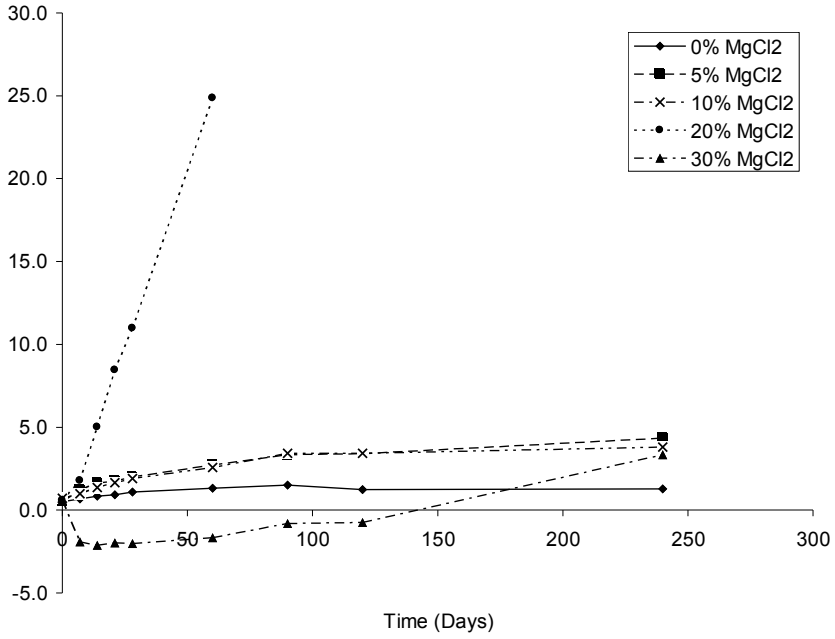

Figure A3.93. Mass change due to the effect of different concentrations of $MgCl_2$.

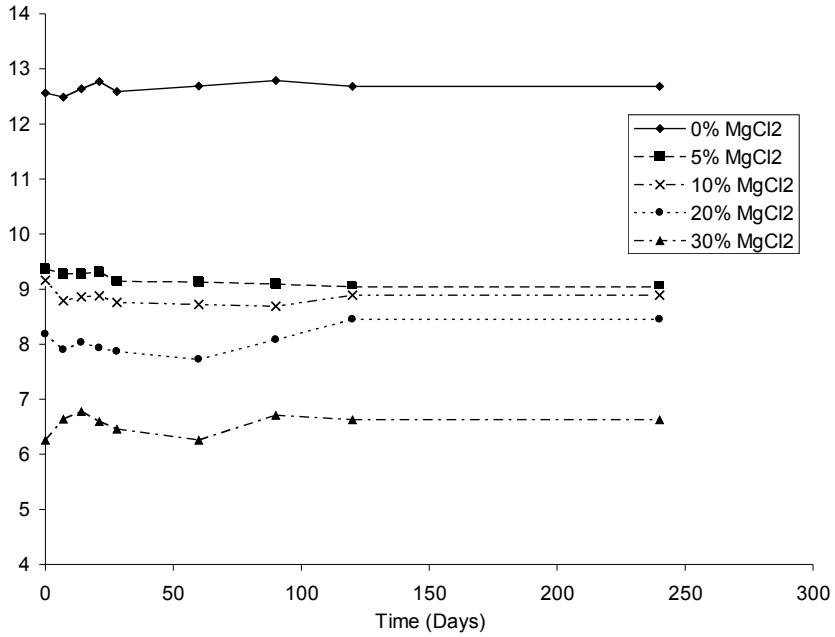

Figure A3.94. pH change with time of different concentrations $MgCl_2$ solution.

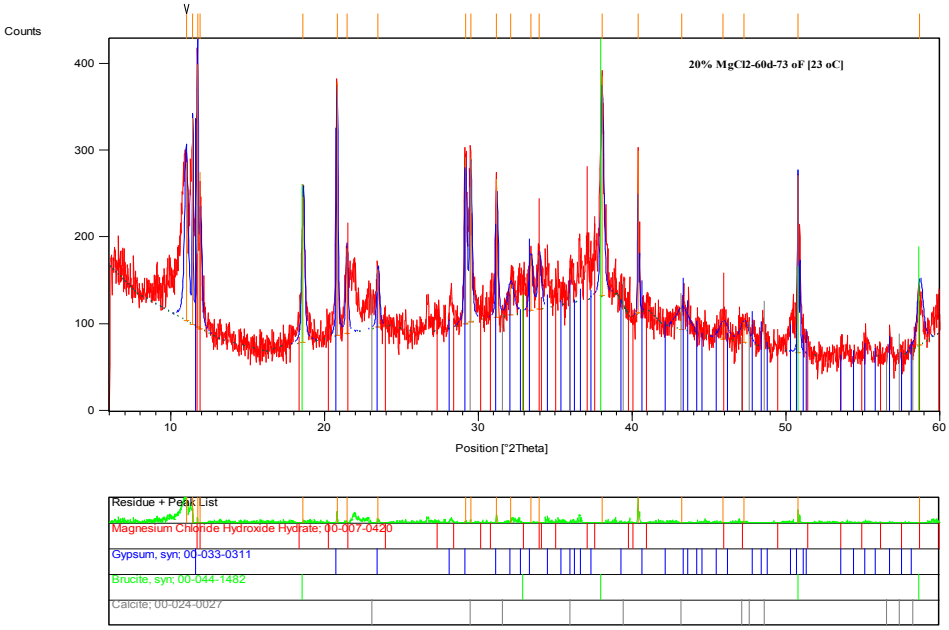

Figure A3.95. XRD diffractogram of mortar samples exposed to $MgCl_2$ at 73 ºF [23 ºC] for 60 days.

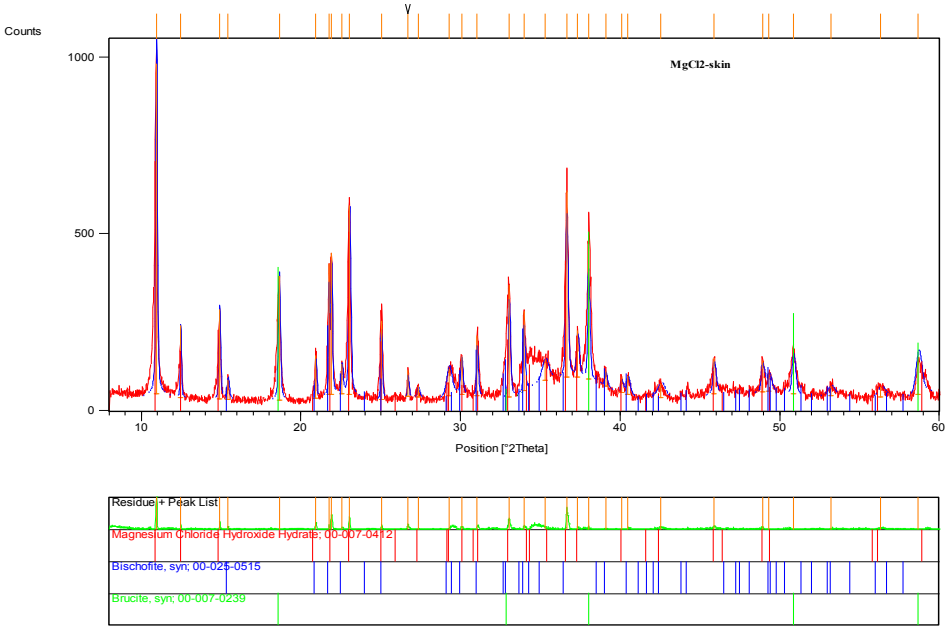

Figure A3.96. XRD diffractogram of a compound that precipitates at the surface after exposing mortar samples exposed to $MgCl_2$.

A3.3 Phase II Laboratory Experiment Results

A3.3.1 Results of Phase II Experiments Jointly Conducted at Michigan Tech and the University of Toronto

A3.3.1.1 Physical Characterization of Mortar and Concrete Mixtures

Mortar and concrete mixtures prepared by Michigan Tech for use in Phase II were analyzed at the University of Toronto to determine their sorptivity and bulk diffusion properties. The mortar mixtures were prepared and analyzed to provide baseline information regarding the characteristics of the mixtures used in Phase II. These mixtures included those made with plain Portland cement, ground granulated blast furnace slag (GGBFS), and fly ash. They are not the same mixture designs used in Phase I with the principal difference being the *w/c* used. The *w/c* of the mortars tested were the same as for the concrete mixtures (i.e. 0.45 and 0.55).

The specimens were discs saw cut from 4 x 2 inch [200 by 100 mm] cylinders without the finished surface. A total of 162 samples were provided to be used on three different tests: sorptivity as per ASTM C 1585, *"Measurement of Rate of Absorption of Water by Hydraulic Cement Concretes"*, bulk diffusion tests as per ASTM C 1556, *"Determining the Apparent Chloride Coefficient of Cementitious Mixtures by Bulk Diffusion"*, and the rapid chloride permeability test as per ASTM C1202, *"Electrical Indication of Concrete's Ability to Resist Chloride Ion Penetration"*. Tables A3.10 and A3.11 list the number and type of mixtures tested and the number of samples.

Table A3.10. Mortar samples tested for bulk diffusion, sorptivity, and rapid chloride permeability.

Number of Samples	Mixture	*w/cm*
12	GGBFS + OPC	0.55
12	GGBFS + OPC	0.45
12	OPC	0.55
12	OPC	0.45
12	15% fly ash + OPC	0.55
12	15% fly ash + OPC	0.45

Table A3.11. Concrete samples tested for bulk diffusion, sorptivity, and rapid chloride permeability.

Number of Samples	Mixture	*w/cm*
18	GGBFS + OPC	0.55
12	GGBFS + OPC	0.45
18	OPC	0.55
12	OPC	0.45
18	15% fly ash + OPC	0.55
12	15 % fly ash + OPC	0.45

A3.3.1.2. Bulk Diffusion

This test has two components; first, the determination of the apparent chloride diffusion coefficient on exposed sawn surfaces, and second, the determination of the apparent chloride diffusion coefficient on sealed, sawn surfaces. The type of salt, exposure solution concentration, and exposure temperature have been modified, relative to the standard procedure, to replicate the conditions used under Phase I of this project. That is, 15% magnesium chloride, 17% calcium chloride and 18% NaCl were the exposure solutions used at a constant 41 ºF [5 ºC] exposure temperature. For the first part five specimens were tested per mix for a total of 60 specimens.

For the second component only concrete mixtures with *w/c* of 0.55 were tested. The same exposure conditions as mentioned above were used. Two type of sealers were evaluated, a siloxane based product (12% oligomeric organosiloxane solids in water) and a silane based product (40% alkylalkoxysilane solids in 2-propanol). For this part six specimens were tested for a total of 18 specimens.

Concrete samples coated with siloxane did not allow the penetration of chloride ions; therefore, the experimental data cannot be fitted with Fick's 2nd law equation. Instead, Figures A3.97 - A3.99 are added for comparison purposes. Concrete samples coated with silane exhibited minor penetration of chloride ions.

The calculated bulk diffusion values (Da) for the exposed surfaces (no sealer) are shown in Tables A3.12 - A3.14 for concretes and Tables A3.15 - A3.17 for mortars. Table A3.18 shows the calculated diffusion parameters for a 0.55 *w/c* concrete sealed with silane. In Tables A3.12 - A3.18, Da is the bulk diffusion value, Cs is the calculate chloride concentration at the surface, r^2 is the correlation coefficient, and P(0.1%) is the depth in millimeters that chlorides penetrated to a concentration of 0.1% by mass of sample, an alternate way of determining chloride penetration resistance. Chloride penetration profiles are shown in Section A3.3.2.2.

Table A3.12. Summary of Results - Concrete samples – 17% $CaCl_2$. Da is the bulk diffusion value, Cs is the calculate chloride concentration at the surface, r^2 is the correlation coefficient, and P(0.1%) is the depth in millimeters that chlorides penetrated to a concentration of 0.1% by mass of sample.

Code*	*w/cm*=0.45			*w/cm*=0.55		
	PCC	FCC	SGC	PCC	FCC	SGC
Da (m^2/s)	4.28×10^{-12}	6.00×10^{-12}	3.60×10^{-12}	2.38×10^{-11}	1.27×10^{-11}	7.65×10^{-12}
Cs (%)	0.97	1.12	1.11	0.66	1.55	1.24
P [0.1%]	8.53	10.51	8.09	17.75	16.60	12.19
r^2	0.9803	0.9848	0.9987	0.9752	0.9875	0.9911

Table A3.13. Summary of Results - Concrete samples – 15% $MgCl_2$. Da is the bulk diffusion value, Cs is the calculate chloride concentration at the surface, r^2 is the correlation coefficient, and P(0.1%) is the depth in millimeters that chlorides penetrated to a concentration of 0.1% by mass of sample.

Code*	*w/cm*=0.45			*w/cm*=0.55		
	PCC	FCC	SGC	PCC	FCC	SGC
Da (m^2/s)	4.04×10^{-12}	6.73×10^{-12}	3.21×10^{-12}	2.35×10^{-11}	1.39×10^{-11}	7.89×10^{-12}
Cs (%)	1.12	0.85	1.45	0.59	0.82	0.84
P [0.1%]	8.62	10.29	8.20	16.97	14.60	11.08
r^2	0.9952	0.9839	0.9996	0.9944	0.9828	0.9961

Table A3.14. Summary of Results - Concrete samples – 18% NaCl. Da is the bulk diffusion value, Cs is the calculate chloride concentration at the surface, r^2 is the correlation coefficient, and P(0.1%) is the depth in millimeters that chlorides penetrated to a concentration of 0.1% by mass of sample.

Code*	*w/cm*=0.45			*w/cm*=0.55		
	PCC	FCC	SGC	PCC	FCC	SGC
Da (m^2/s)	2.5×10^{-11}	3.9×10^{-11}	1.0×10^{-11}	2.8×10^{-11}	4.6×10^{-11}	1.3×10^{-11}
Cs (%)	0.69	0.65	1.05	0.74	0.54	0.80
P [0.1%]	18.45	22.66	13.36	20.17	22.75	13.77
r^2	0.9920	0.9693	0.9964	0.9810	0.9920	0.9810

* Specimen Code
Da: Apparent Diffusion Coefficient
Cs: Surface Concentration
P (0.1%): Penetration depth for 0.1% chloride concentration
r^2: r-squared from fitting Fick's 2nd law equation to experimental data

PCC: portland cement concrete
FCC: portland cement + 15% fly ash concrete
SGC: GGBFS blended cement concrete

Table A3.15. Summary of Results - Mortar samples – 17% $CaCl_2$. Da is the bulk diffusion value, Cs is the calculate chloride concentration at the surface, r^2 is the correlation coefficient, and P(0.1%) is the depth in millimeters that chlorides penetrated to a concentration of 0.1% by mass of sample.

Code*	*w/cm*=0.45			*w/cm*=0.55		
	PCM	FCM	SGM	PCM	FCM	SGM
Da (m^2/s)	4.44×10^{-12}	2.30×10^{-12}	2.00×10^{-12}	1.00×10^{-11}	7.50×10^{-12}	2.50×10^{-12}
Cs (%)	1.82	2.38	2.86	1.20	1.76	2.24
P [0.1%]	10.82	7.74	7.45	13.83	13.12	7.97
r^2	0.9871	0.9981	0.9925	0.9911	0.9882	0.9988

Table A3.16. Summary of Results - Mortar samples – 15% $MgCl_2$. Da is the bulk diffusion value, Cs is the calculate chloride concentration at the surface, r^2 is the correlation coefficient, and P(0.1%) is the depth in millimeters that chlorides penetrated to a concentration of 0.1% by mass of sample.

Code*	*w/cm*=0.45			*w/cm*=0.55		
	PCM	FCM	SGM	PCM	FCM	SGM
Da (m^2/s)	4.40×10^{-12}	2.31×10^{-12}	2.51×10^{-12}	7.88×10^{-12}	6.23×10^{-12}	2.75×10^{-11}
Cs (%)	1.67	2.91	1.20	1.30	1.19	1.20
P [0.1%]	9.93	8.06	6.92	12.52	10.87	13.83
r^2	0.9969	0.9839	0.9994	0.9909	0.9921	0.9911

Table A3.17. Summary of Results - Mortar samples – 18% NaCl. Da is the bulk diffusion value, Cs is the calculate chloride concentration at the surface, r^2 is the correlation coefficient, and P(0.1%) is the depth in millimeters that chlorides penetrated to a concentration of 0.1% by mass of sample.

Code*	*w/cm*=0.45			*w/cm*=0.55		
	PCM	FCM	SGM	PCM	FCM	SGM
Da (m^2/s)	1.7×10^{-11}	2.2×10^{-11}	1.9×10^{-11}	-	3.3×10^{-11}	2.3×10^{-11}
Cs (%)	1.14	1.08	1.16	-	1.10	1.18
P [0.1%]	17.79	19.91	18.98	-	24.35	20.76
r^2	0.9707	0.9826	0.9838	-	0.9787	0.9859

* Specimen Code
Da: Apparent Diffusion Coefficient
Cs: Surface Concentration
P (0.1%): Penetration depth for 0.1% chloride concentration
r^2: r-squared from fitting Fick's 2nd law equation to experimental data

PCM: portland cement mortar
FCM: portland cement + 15% fly ash mortar
SGM: GGBFS blended cement mortar

Table A3.18. Summary of Results - Concrete samples – Silane Sealed. Da is the bulk diffusion value, Cs is the calculate chloride concentration at the surface, r^2 is the correlation coefficient, and P(0.1%) is the depth in millimeters that chlorides penetrated to a concentration of 0.1% by mass of sample.

Code*	*w/cm*=0.55 (17% $CaCl_2$)			*w/cm*=0.55 (15% $MgCl_2$)		
	PCC	FCC	SGC	PCC	FCC	SGC
Da (m^2/s)	1.3×10^{-11}	1.2×10^{-11}	0.4×10^{-11}	0.9×10^{-11}	1.8×10^{-11}	0.7×10^{-11}
Cs (%)	0.25	0.26	0.71	0.24	0.31	0.70
P [0.1%]	7.78	7.81	7.49	6.34	10.91	9.99
r^2	0.9773	0.9702	0.9960	0.9812	0.9901	0.9972

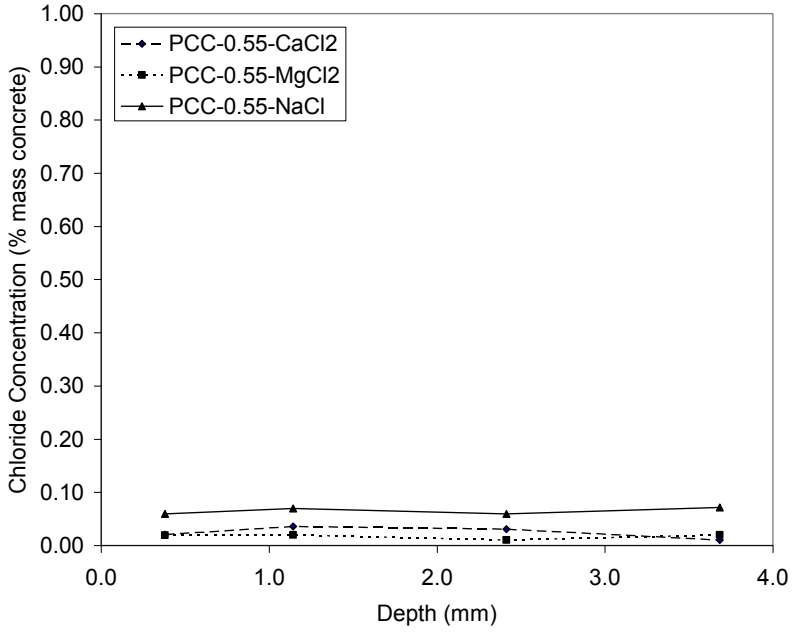

Figure A3.97. Portland cement concrete samples sealed with siloxane - chloride profiles

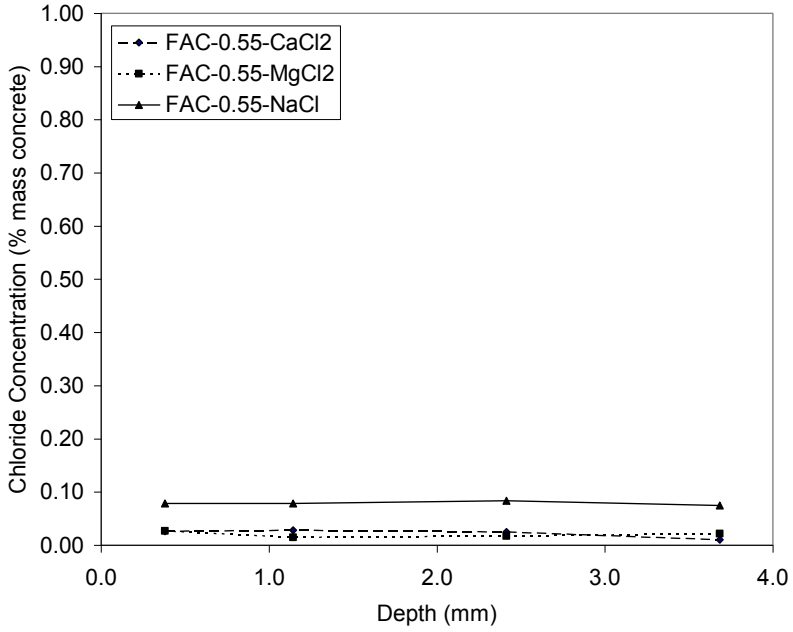

Figure A3.98. Portland cement with 15% fly ash concrete samples sealed with siloxane - chloride profiles

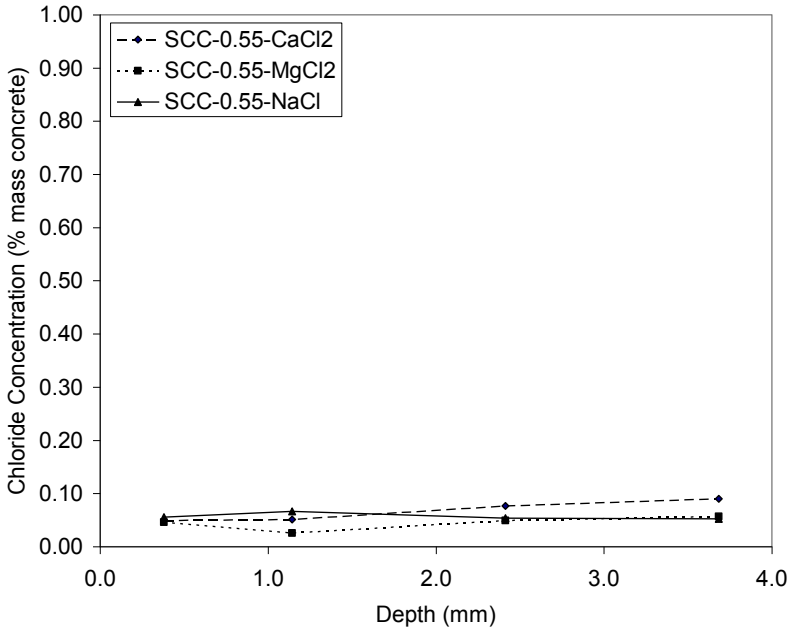

Figure A3.99. GGBFS blended cement concrete samples sealed with siloxane - chloride profile

A3.3.1.3. Sorptivity

For this test, five specimens were tested per mix for a total of 60 specimens. Besides the rate of absorption of water, three deicing salts were included for analysis: magnesium chloride, calcium chloride and sodium chloride. In general, the higher the rate of absorption, the more susceptible the sample is to penetration of the exposure solution. Table A3.19 summarizes the results of sorptivity testing for the mortar mixtures tested. Figures A3.100 - A3.113 present the plots of sorptivity trends for each mortar mixture, and for each solution tested. Table A3.20 summarizes the results of sorptivity testing for the concrete mixtures tested. Figures A3.114 – A3.127 present the plots of sorptivity trends for each concrete mixture, and for each solution tested.

Table A3.19. Sorptivity results for mortar samples

Exposure solution / Code*	*w/cm* = 0.45		*w/cm* = 0.55	
	Initial Absorption Si ($mm/s^{1/2}$) / [r^2]	Secondary Absorption S_s ($mm/s^{1/2}$) / [r^2]	Initial Absorption Si ($mm/s^{1/2}$) / [r^2]	Secondary Absorption S_s ($mm/s^{1/2}$) / [r^2]
Water				
PCMW	4.3×10^{-3} [0.99]	2.5×10^{-3} [0.99]	5.9×10^{-3} [0.99]	3.4×10^{-3} [0.98]
FCMW	3.3×10^{-3} [0.99]	1.9×10^{-3} [0.99]	4.0×10^{-3} [0.99]	2.5×10^{-3} [0.99]
SGMW	2.4×10^{-3} [0.97]	0.9×10^{-3} [0.99]	3.4×10^{-3} [0.98]	1.7×10^{-3} [0.99]
NaCl				
PCMN	4.6×10^{-3} [0.99]	2.5×10^{-3} [0.98]	7.1×10^{-3} [0.99]	3.0×10^{-3} [0.94]
FCMN	3.7×10^{-3} [0.99]	1.9×10^{-3} [0.99]	4.4×10^{-3} [0.99]	2.5×10^{-3} [0.98]
SGMN	2.4×10^{-3} [0.99]	0.8×10^{-3} [0.98]	4.3×10^{-3} [0.99]	1.2×10^{-3} [0.96]
$CaCl_2$				
PCMC	3.5×10^{-3} [0.99]	1.0×10^{-3} [0.98]	4.4×10^{-3} [0.99]	1.7×10^{-3} [0.99]
FCMC	1.7×10^{-3} [0.98]	0.5×10^{-3} [0.99]	2.0×10^{-3} [0.99]	0.6×10^{-3} [0.98]
SGMC	1.0×10^{-3} [0.95]	0.2×10^{-3} [0.99]	1.4×10^{-3} [0.96]	0.2×10^{-3} [0.98]
$MgCl_2$				
PCMM	0.4×10^{-3} [0.75]	0.5×10^{-3} [0.99]	1.0×10^{-3} [0.98]	1.1×10^{-3} [0.99]
FCMM	0.3×10^{-3} [0.64]	0.4×10^{-3} [0.99]	7.5×10^{-4} [0.99]	0.7×10^{-3} [0.99]
SGMM	0.3×10^{-3} [0.96]	0.3×10^{-3} [0.99]	6.7×10^{-4} [0.88]	0.3×10^{-3} [0.99]

*Specimen Codes

PCMW: portland cement mortar - tap water
PCMM: portland cement mortar – $MgCl_2$
FCMW: 15% fly ash mortar - tap water
FCMM: 15% fly ash mortar – $MgCl_2$
SGMW: GGBFS cement mortar - tap water
SGMM: GGBFS cement mortar – $MgCl_2$
PCMC: portland cement mortar – $CaCl_2$
PCMN: portland cement mortar - NaCl
FCMC: 15% fly ash mortar – $CaCl_2$
FCMN: 15% fly ash mortar – NaCl
SGMC: GGBFS cement mortar – $CaCl_2$
SGMN: GGBFS cement mortar – NaCl

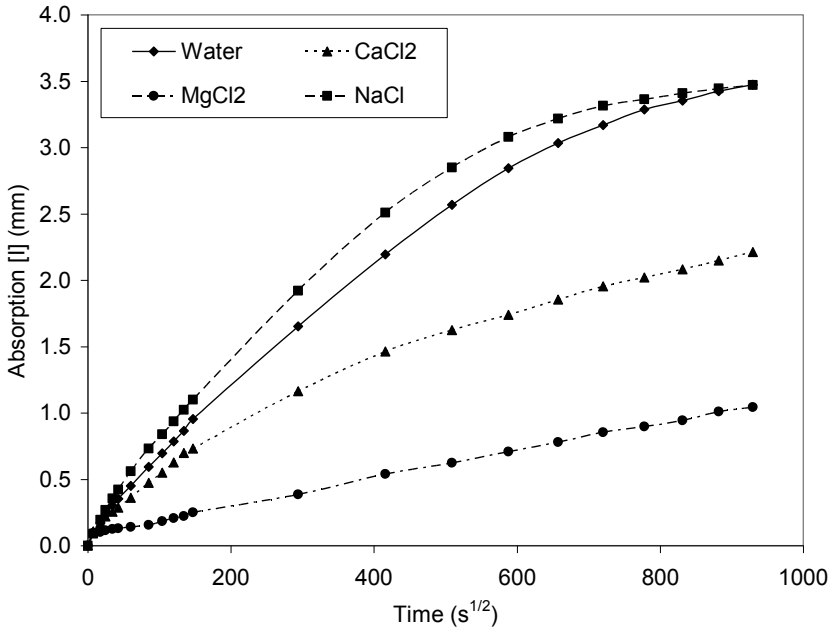

Figure A3.100. Sorptivity of portland cement mortar – *w/c* =0.55

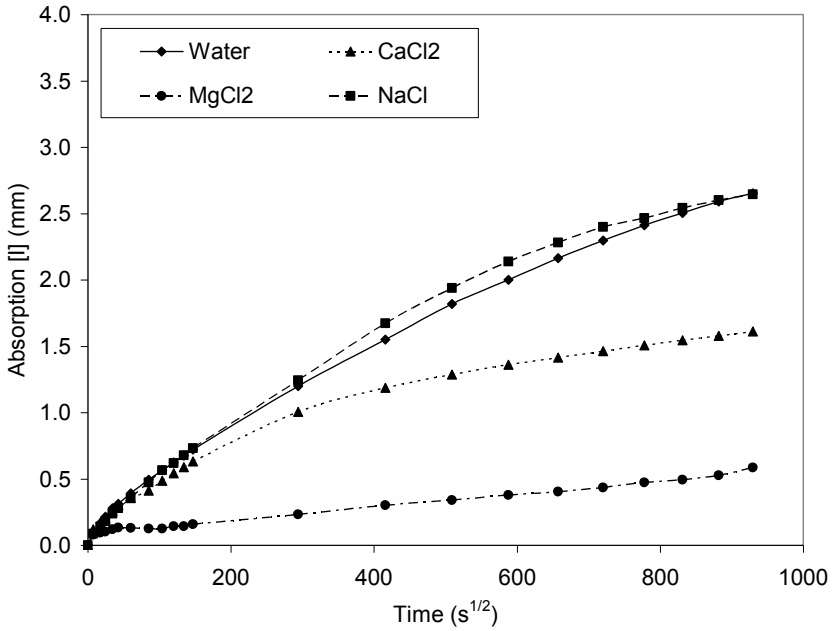

Figure A3.101. Sorptivity of portland cement mortar – *w/c*=0.45

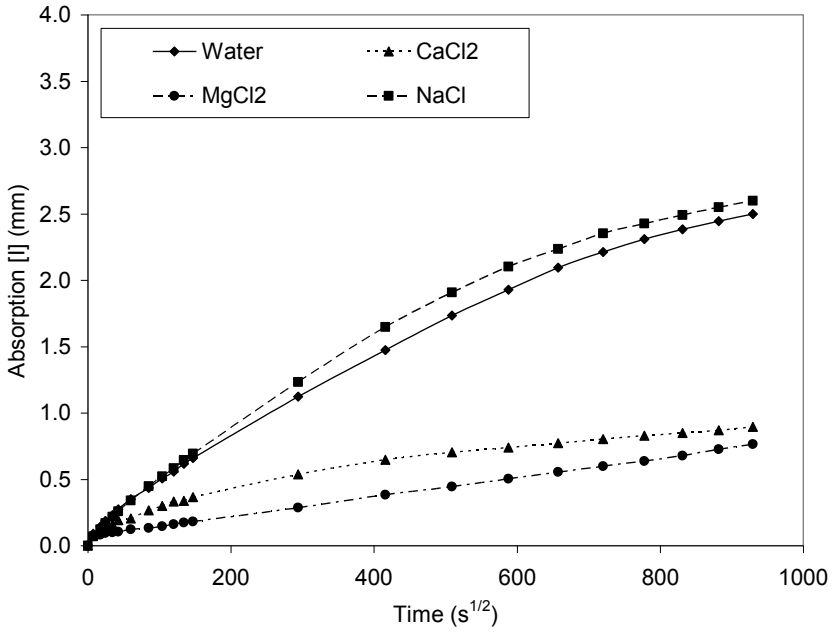

Figure A3.102. Sorptivity – fly ash mortar – *w/cm* = 0.55

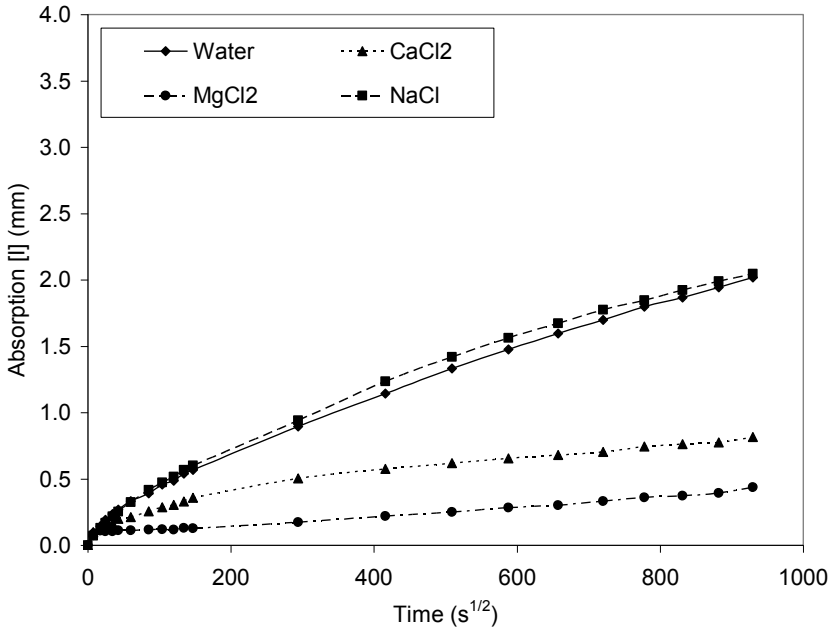

Figure A3.103. Sorptivity – fly ash mortar – *w/cm* = 0.45

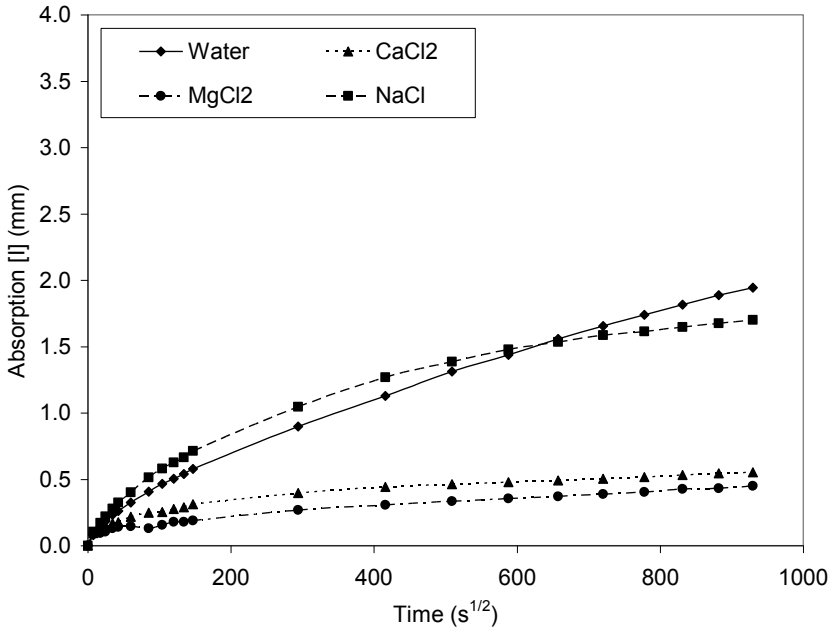

Figure A3.104. Sorptivity – GGBFS mortar – *w/cm* = 0.55

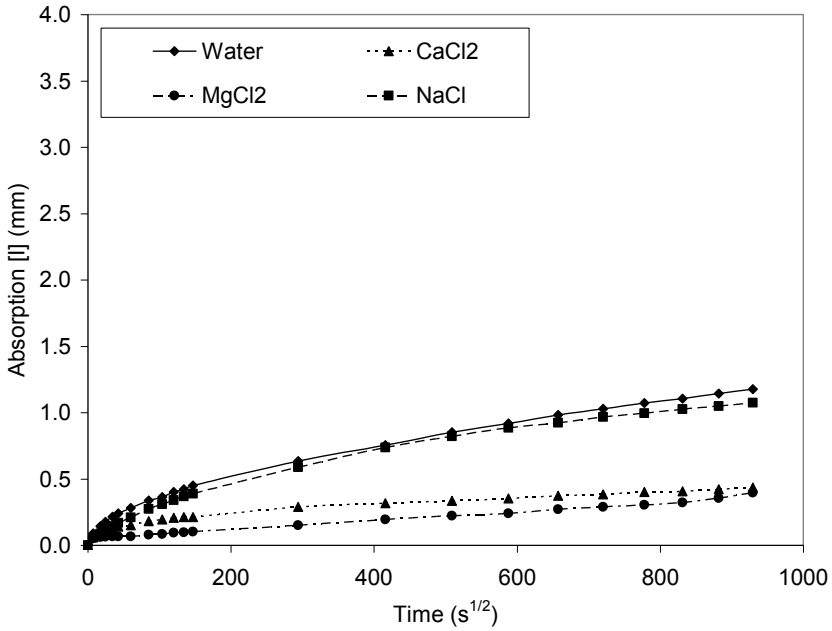

Figure A3.105. Sorptivity – GGBFS mortar – *w/cm* = 0.45

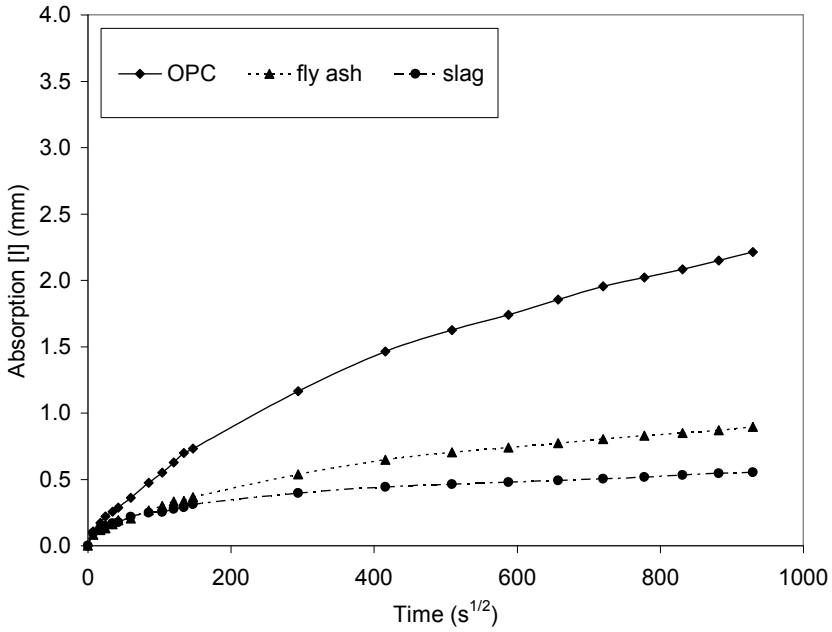

Figure A3.106. Sorptivity – mortar *w/cm* = 0.55 – $CaCl_2$

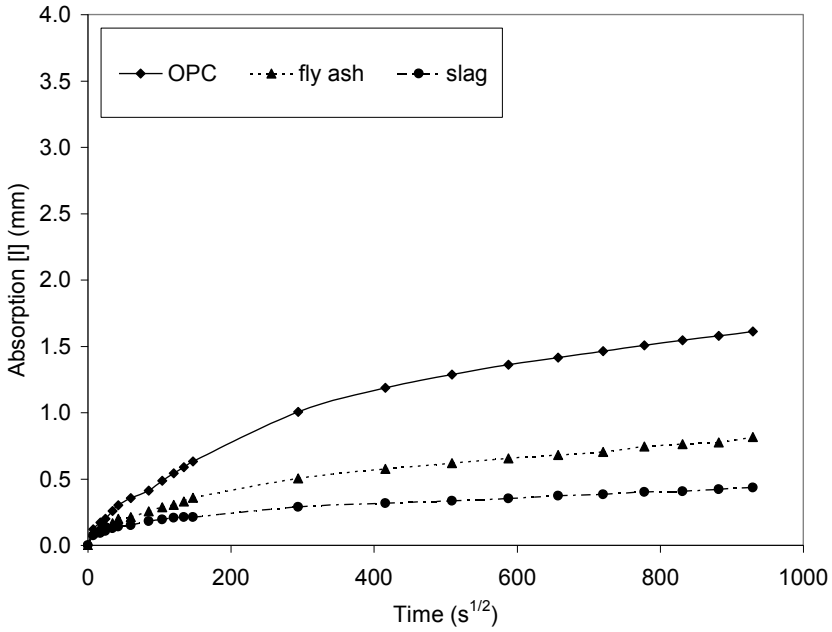

Figure A3.107. Sorptivity – mortar *w/cm* = 0.45 – $CaCl_2$

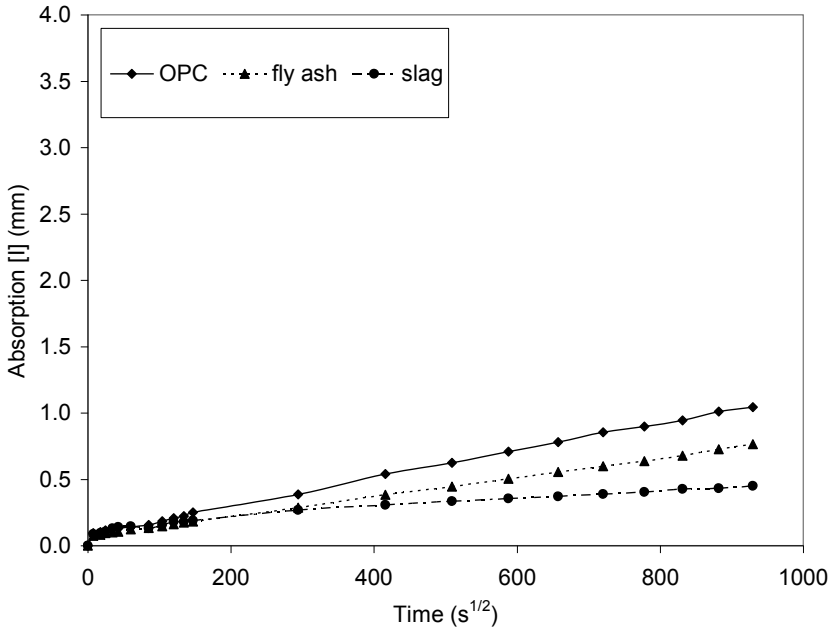

Figure A3.108. Sorptivity – mortar *w/cm* = 0.55 – $MgCl_2$

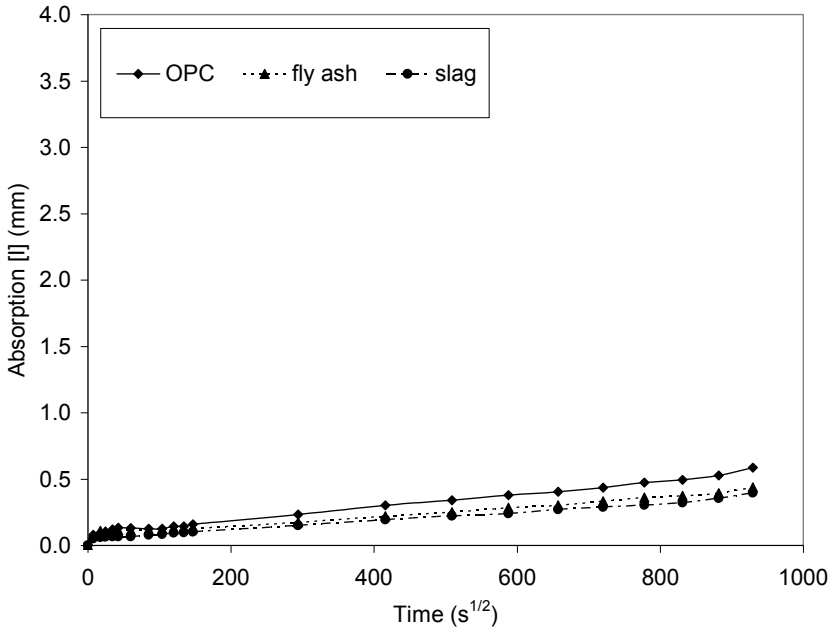

Figure A3.109. Sorptivity – mortar *w/cm* = 0.45 – $MgCl_2$

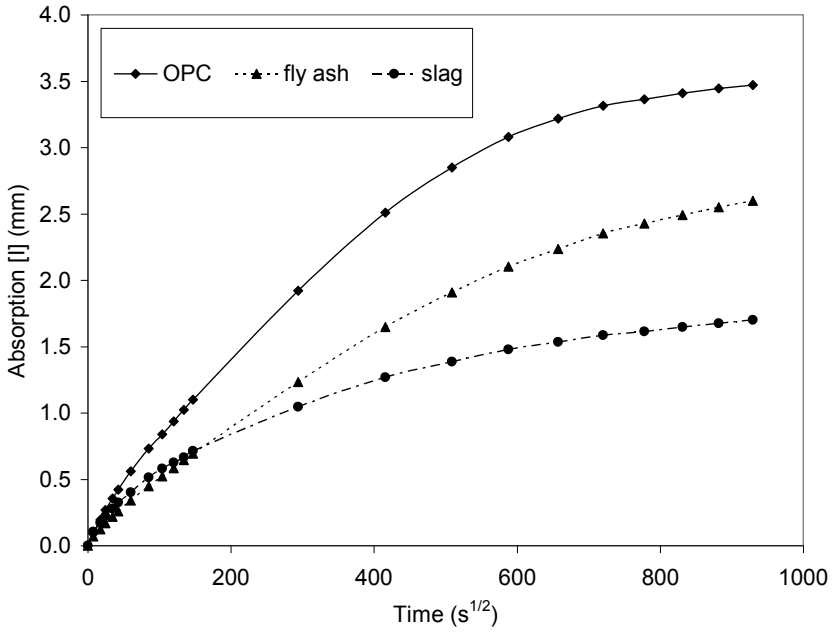

Figure A3.110. Sorptivity – mortar *w/cm* = 0.55 – NaCl

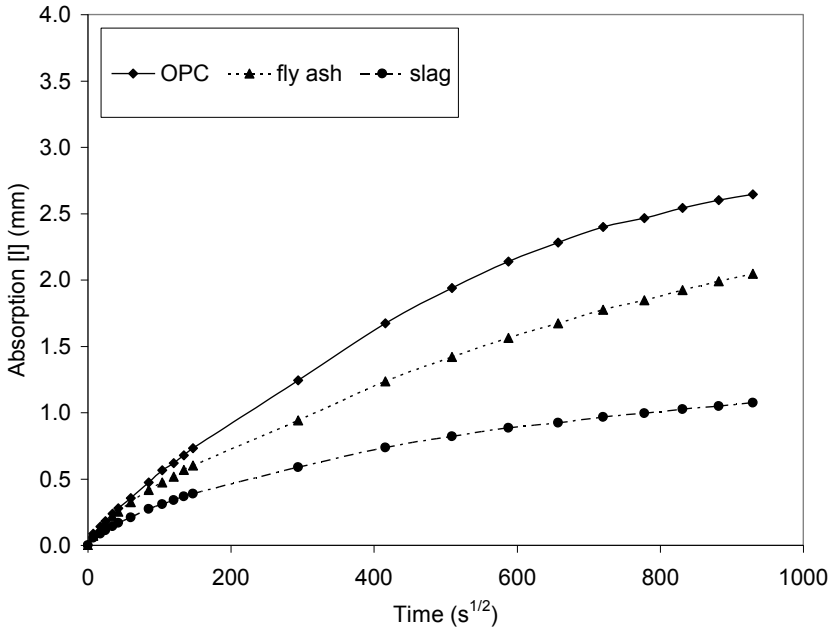

Figure A3.111. Sorptivity – mortar *w/cm* = 0.45 – NaCl

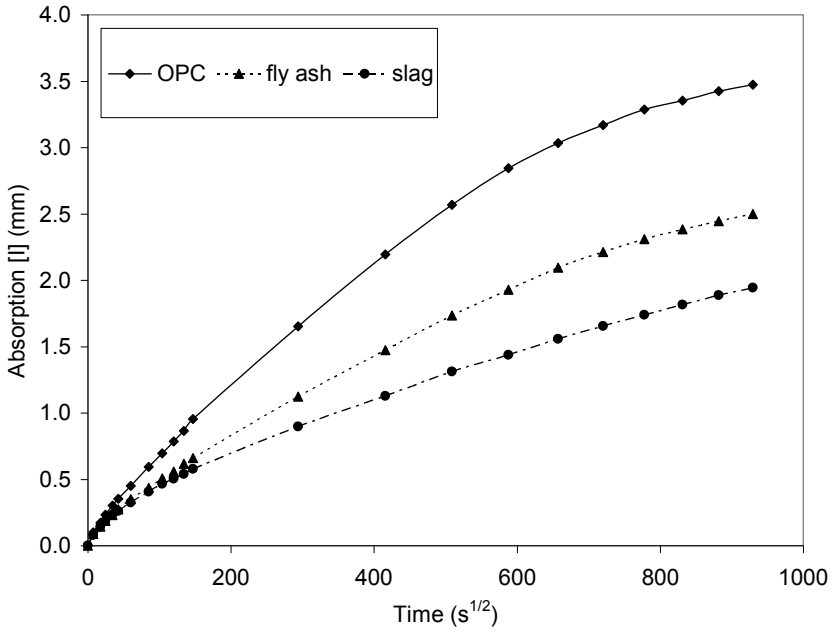

Figure A3.112. Sorptivity – mortar *w/cm* = 0.55 – water

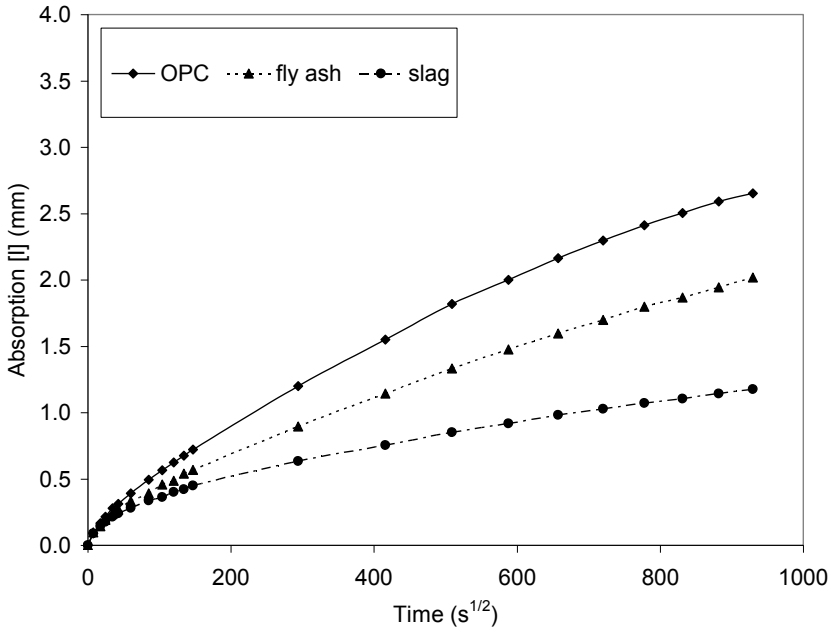

Figure A3.113. Sorptivity – mortar *w/cm* = 0.45 – water

Table A3.20. Sorptivity results for concrete samples

Exposure solution / Code*	*w/cm* = 0.45		*w/cm* = 0.55	
	Initial Absorption Si ($mm/s^{1/2}$) / [r^2]	Secondary Absorption S_s ($mm/s^{1/2}$) / [r^2]	Initial Absorption Si ($mm/s^{1/2}$) / [r^2]	Secondary Absorption S_s ($mm/s^{1/2}$) / [r^2]
Water				
PCW	3.0×10^{-3} [0.99]	1.9×10^{-3} [0.96]	6.2×10^{-3} [0.99]	2.7×10^{-3} [0.92]
FCW	2.7×10^{-3} [0.99]	1.8×10^{-3} [0.99]	6.6×10^{-3} [0.99]	2.1×10^{-3} [0.82]
SGW	1.8×10^{-3} [0.99]	1.1×10^{-3} [0.99]	2.8×10^{-3} [0.99]	1.8×10^{-3} [0.99]
$CaCl_2$				
PCC	1.2×10^{-3} [0.99]	4.9×10^{-4} [0.94]	3.0×10^{-3} [0.99]	1.7×10^{-3} [0.99]
FCC	2.4×10^{-3} [0.98]	8.1×10^{-4} [0.99]	4.3×10^{-3} [0.99]	2.4×10^{-3} [0.99]
SGC	1.1×10^{-3} [0.98]	2.2×10^{-4} [0.99]	1.5×10^{-3} [0.98]	6.1×10^{-4} [0.97]
$MgCl_2$				
PCM	6.6×10^{-4} [0.99]	7.4×10^{-4} [0.99]	1.3×10^{-3} [0.97]	1.2×10^{-3} [0.99]
FCM	4.6×10^{-4} [0.98]	3.3×10^{-4} [0.99]	1.4×10^{-3} [0.99]	1.3×10^{-3} [0.99]
SGM	4.2×10^{-4} [0.96]	1.9×10^{-4} [0.99]	6.7×10^{-4} [0.99]	2.5×10^{-4} [0.99]
NaCl				
PCN	1.8×10^{-3} [0.99]	1.4×10^{-3} [097]	4.0×10^{-3} [0.99]	2.6×10^{-3} [0.98]
FCN	2.9×10^{-3} [0.99]	1.5×10^{-3} [0.99]	4.4×10^{-3} [0.99]	2.7×10^{-3} [0.99]
SGN	1.5×10^{-3} [0.98]	5.7×10^{-4} [0.99]	2.2×10^{-3} [0.98]	9.3×10^{-4} [0.99]

PCW: portland cement concrete - tap water
PCM: portland cement concrete – $MgCl_2$
FCW: 15% fly ash concrete - tap water
FCM: 15% fly ash concrete – $MgCl_2$
SGW: GGBFS cement concrete - tap water
SGM: GGBFS cement concrete – $MgCl_2$
PCC: portland cement concrete – $CaCl_2$
PCN: portland cement concrete - NaCl
FCC: 15% fly ash concrete – $CaCl_2$
FCN: 15% fly ash concrete – NaCl
SGC: GGBFS cement concrete – $CaCl_2$
SGN: GGBFS cement concrete - NaCl

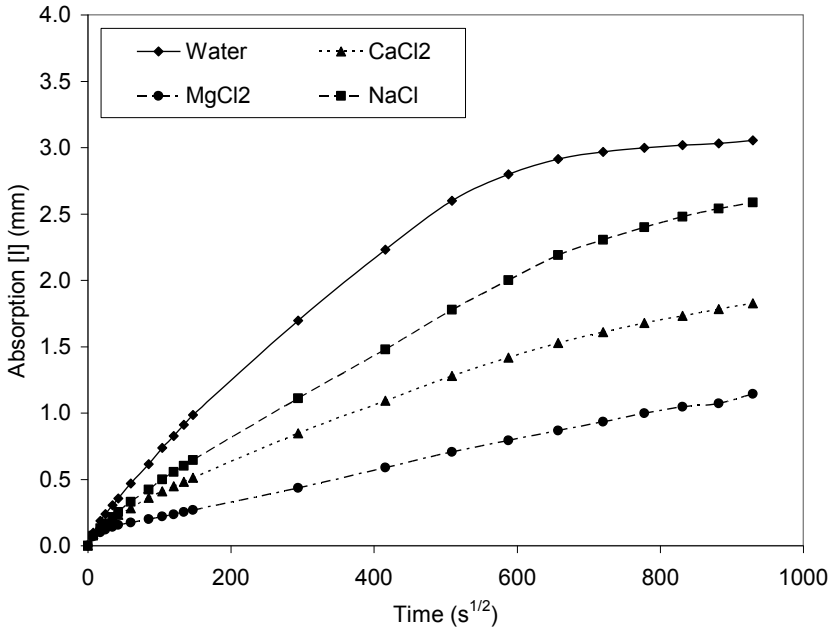

Figure A3.114. Sorptivity of portland cement concrete – *w/c* =0.55

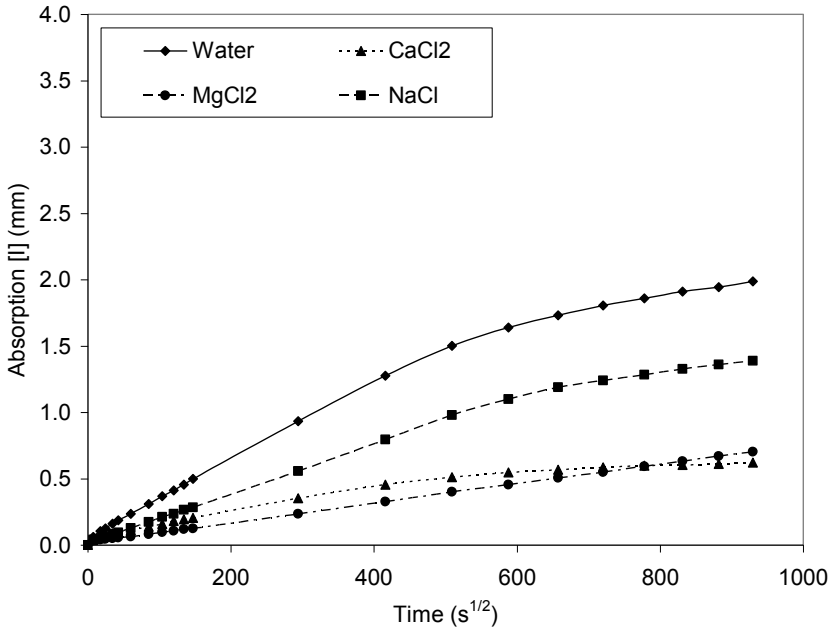

Figure A3.115. Sorptivity of portland cement concrete – *w/c*=0.45

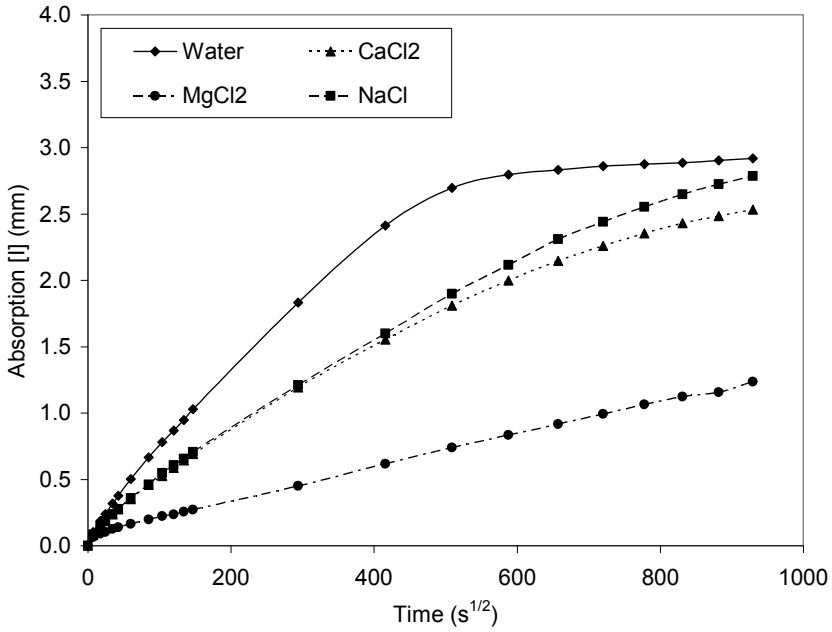

Figure A3.116. Sorptivity – fly ash concrete – *w/cm* = 0.55

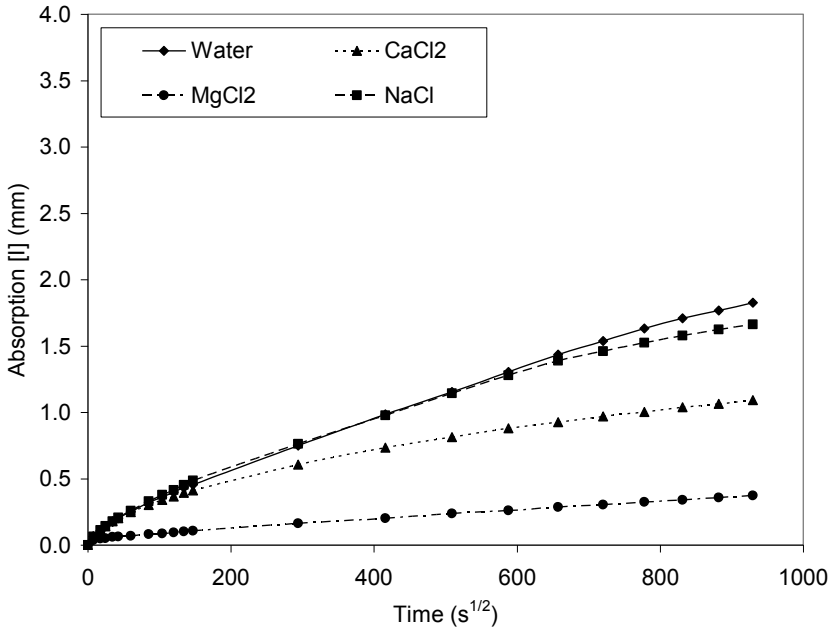

Figure A3.117. Sorptivity – fly ash concrete – *w/cm* = 0.45

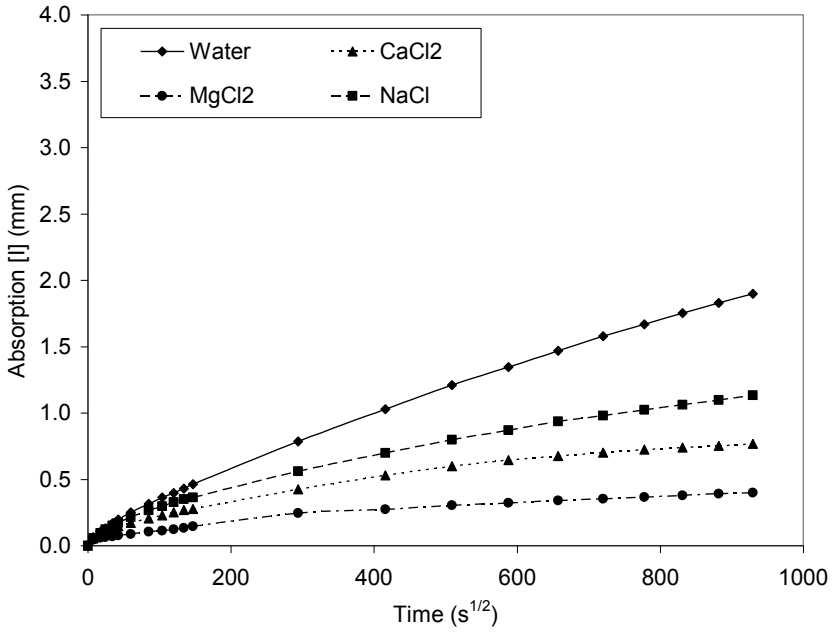

Figure A3.118. Sorptivity – GGBFS concrete – *w/cm* = 0.55

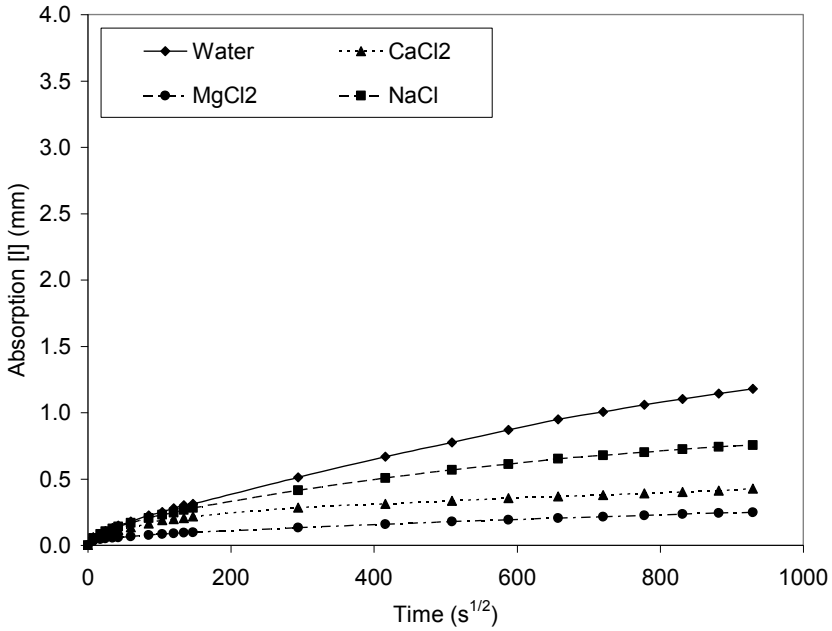

Figure A3.119. Sorptivity – GGBFS concrete – *w/cm* = 0.45

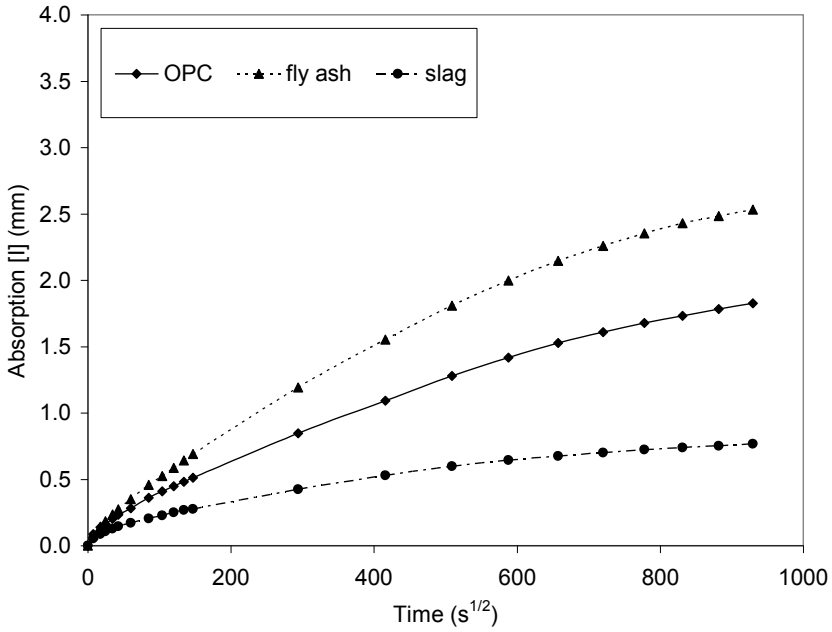

Figure A3.120. Sorptivity – concrete *w/cm* = 0.55 – $CaCl_2$

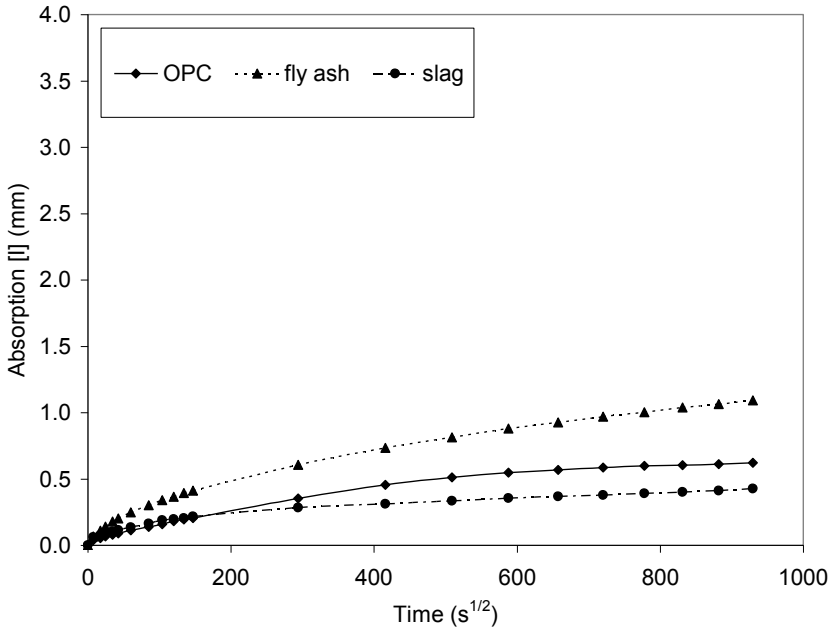

Figure A3.121. Sorptivity – concrete *w/cm* = 0.45 – $CaCl_2$

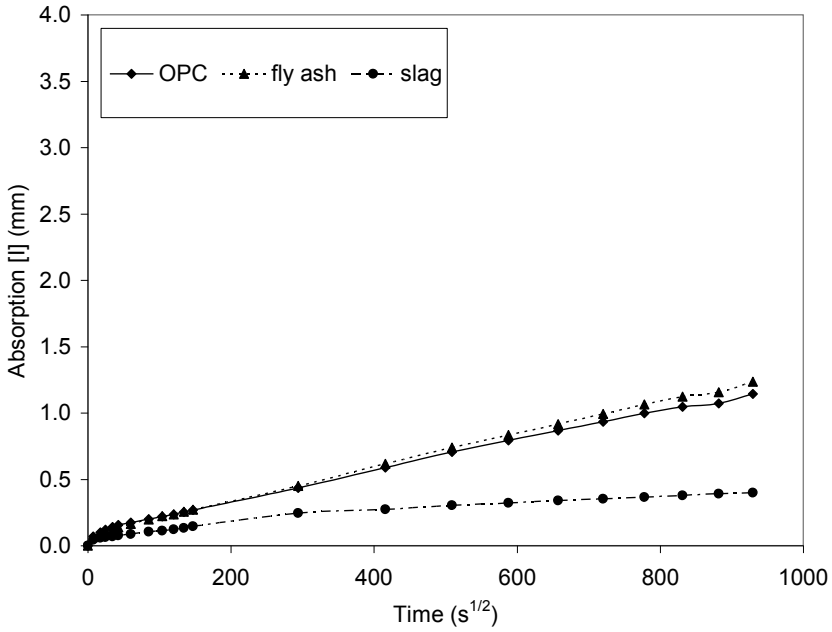

Figure A3.122. Sorptivity – concrete *w/cm* = 0.55 – $MgCl_2$

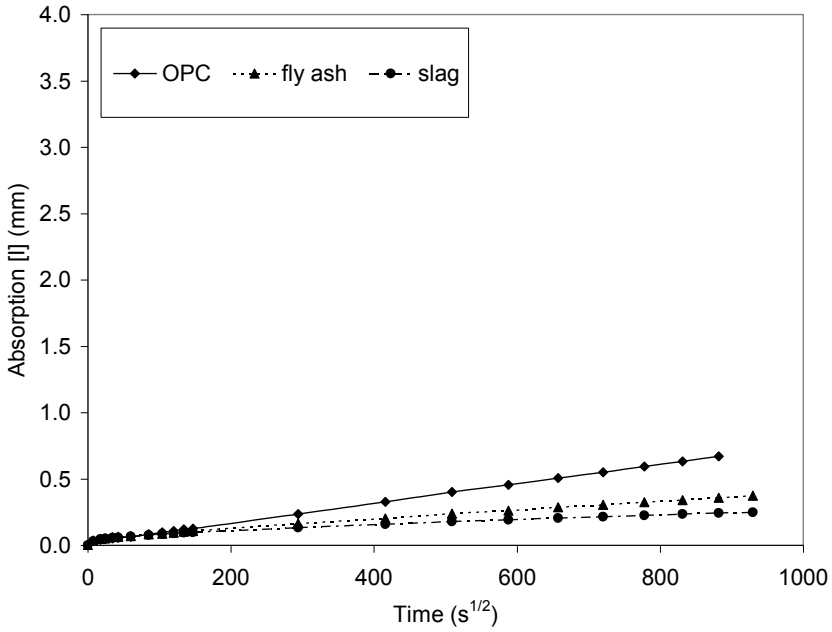

Figure A3.123. Sorptivity – concrete *w/cm* = 0.45 – $MgCl_2$

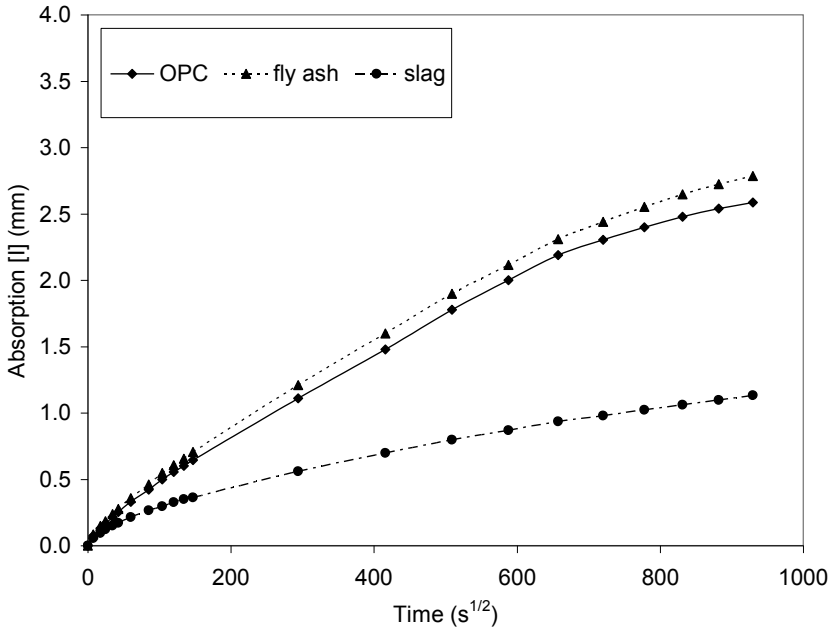

Figure A3.124. Sorptivity – concrete *w/cm* = 0.55 – NaCl

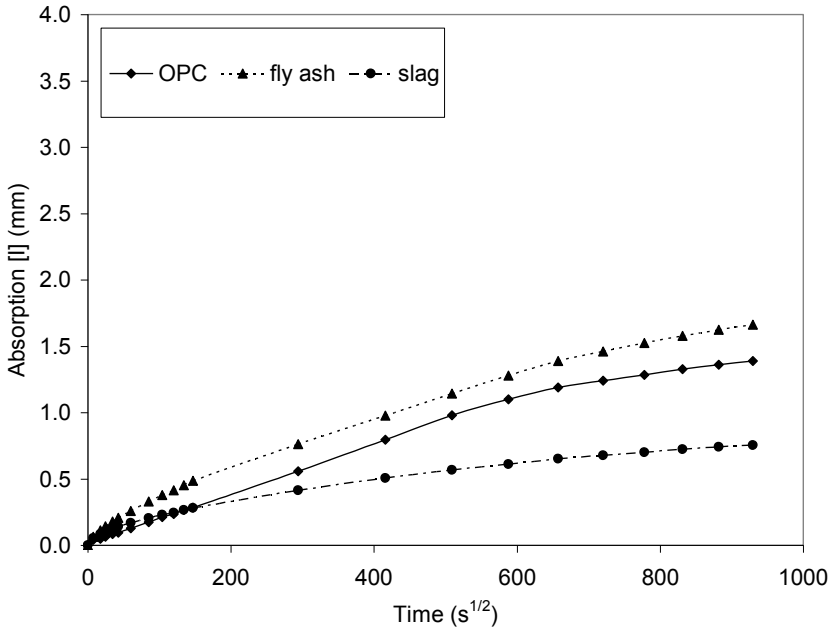

Figure A3.125. Sorptivity – concrete *w/cm* = 0.45 – NaCl

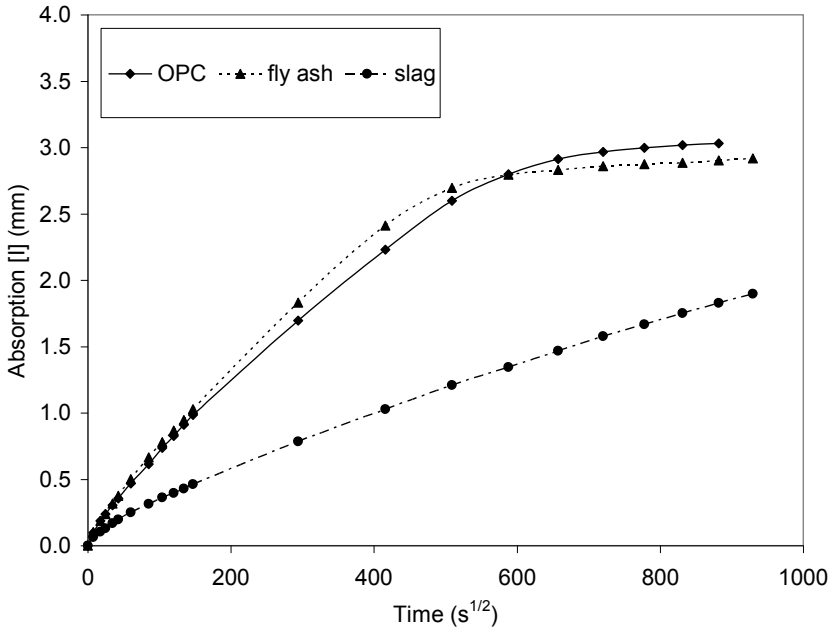

Figure A3.126. Sorptivity – concrete *w/cm* = 0.55 – water

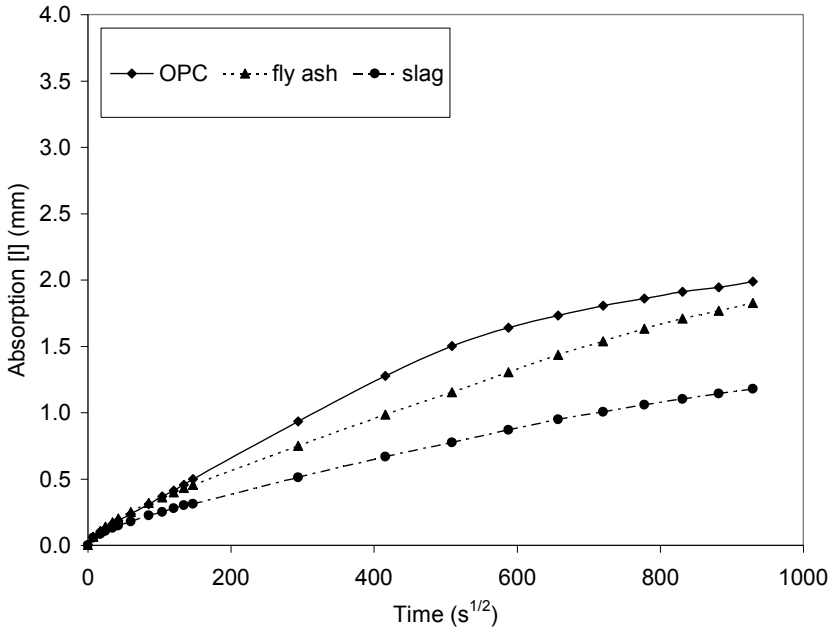

Figure A3.127. Sorptivity – concrete *w/cm* = 0.45 – water

A3.3.1.4. Rapid Chloride Permeability Test

This test gives a relative indication of the chloride penetrability and conductivity of the sample so all the mortar and concrete mixtures can be ranked relative to each other based on the charge passed during the test. To avoid misleading results due to heating of the specimen during the test, the total charge reported will be based on the 30 minutes charge (the 30 minute coulomb value was multiplied by 12 to obtain an equivalent 6 hour value). Two specimens per mixture were tested for a total of 24 specimens. Table A3.21 summarizes the results showing the charged passed and the chloride ion penetrability.

Table A3.21. Summary of RCPT testing performed on concrete and mortar mixtures for Phase II.

Code*	*w/cm* 0.45		*w/cm* 0.55	
	Charge (coulombs)	Chloride ion penetrability	Charge (coulombs)	Chloride ion penetrability
Mortar Samples				
PCM	5380	High	6151	High
FCM	5219	High	5871	High
SGM	3309	Moderate	4208	High
Concrete Samples				
PCC	4413	High	5236	High
FCC	3397	Moderate	4446	High
SGC	2787	Moderate	3103	Moderate

* Specimen Coding
PCC: portland cement concrete
FCC: portland cement + 15% fly ash concrete
SGC: GGBFS blended cement concrete
PCM: portland cement mortar
FCM: portland cement + 15% fly ash mortar
SGM: GGBFS blended cement mortar

A3.3.2 Results of Phase II Experiments Conducted at the Michigan Tech

A3.3.2.1 Macroscopic Observations

Random concrete and mortar specimens were removed from the various brine solutions after 60 days of exposure, with the remainder being removed after 500 days exposure. After removal from the brines, the specimens were blown dry with an air hose and cut with a kerosene cooled diamond saw. Specimens showing obvious external deterioration or other interesting features were photographed prior to drying. None of the specimens showed any obvious external signs of deterioration at 60 days. At 500 days, many of the specimens from the high-concentration $CaCl_2$, $MgCl_2$, and MBAP brines exhibited external cracking, examples of which are shown in Figure A3.128.

Figure A3.128. Photographs of 4 inch [100 mm] diameter 0.45 *w/c* ordinary portland cement (OPC) concrete specimens after 500 days in high concentration brines. From left to right: $CaCl_2$, $MgCl_2$, and MBAP brines.

A coating of mineral precipitates can be seen on the specimens in Figure A3.128. Mineral coatings were typically observed on specimens from the $CaCl_2$, $MgCl_2$, and MBAP brines. The mineral precipitates on the specimens from the $MgCl_2$ brine were white and very fine grained. Similar white precipitates were present on the specimens from the MBAP brine, but to a lesser degree. The mineral precipitates on the specimens from the $CaCl_2$ brine consisted of slender translucent crystals, examples of which are shown in Figure A3.129. External precipitates were not observed on specimens from the other brines, with the exception of specimens immersed in the low-concentration CMA brine. Figure A3.130 illustrates the white very fine-grained precipitate present on the surface of a specimen from the low-concentration CMA brine. Several circular deposits of black mold can also be observed along the sides of the specimen in Figure A3.130.

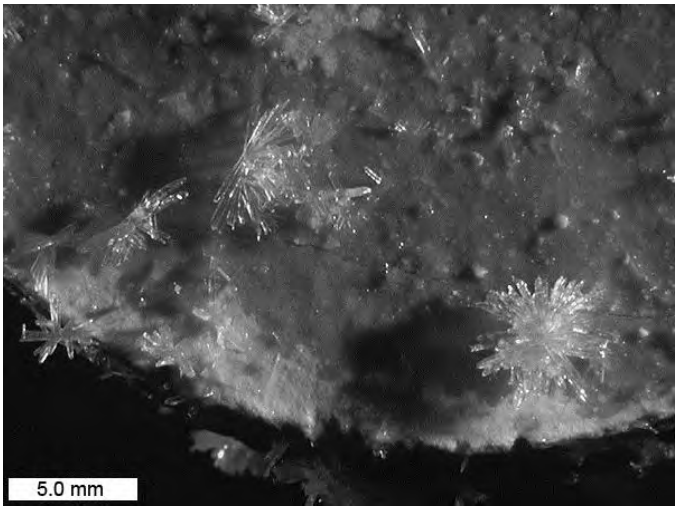

Figure A3.129. Crystals on exterior of concrete specimen after 500 days immersion in high-concentration $CaCl_2$ solution.

Figure A3.130. White precipitate on exterior of 4 inch [100 mm] diameter concrete specimen after 500 days immersion in low-concentration CMA solution.

During the sawing procedure a slab was removed from the middle of those specimens intended for chloride profiling and/or thin sectioning. These slabs were all oriented in a plane perpendicular to the flat-ends of the specimens. Specimens that were not to be used for chloride profiling were simply cut in half in the same orientation as the slabs. However, the three specimens shown in Figure A3.130 were treated differently than the rest. These specimens, all 0.45 *w/c* ordinary portland cement (OPC) concrete at 500 days, were immediately transferred, still damp with brine, to a 122 ºF [50 ºC] convection oven and dried overnight. After drying, the three specimens were vacuum impregnated with epoxy resin. After the epoxy had hardened, a slab was cut from each specimen in the same manner as previously described. The epoxy impregnation step was necessary to maintain the integrity of the slabs, which were intended for thin sectioning.

After cutting, the end-pieces were rinsed with kerosene and dried in the 122 ºF [50 ºC] convection oven. After drying, the cut-faces of the end pieces were scanned with a flatbed scanner in 24 bit RGB color at a resolution of 425 dpi [16.7 dpm]. The digital images were used to make visual estimates of the degree of alteration as exposed in the saw-cut cross-sections of the specimens. The perimeters of each specimen cross-section were outlined and any zones of visible alteration were outlined using Scion Image, (free software based on NIH Image for MacIntosh by Wayne Rasband of National Institutes of Health, USA). The number of pixels within any delineated zone of visible alteration was divided by the number of pixels within the entire specimen cross-section to yield an area percent value for the visible alteration.

Figure A3.131 shows example images from the 0.45 *w/c* mortar specimens from the five high-concentration brine solutions. Tables A3.22 through A3.26 summarize the visible alteration area percent values from all of the specimens measured. Figures A3.132 and

A3.133 plot the visible alteration area values versus time for the high-concentration brines and the low concentration brines, for all samples measured (i.e. mortars and concrete combined for all values of *w/c*). Figure A3.132 demonstrates that at the high-concentration, the $CaCl_2$, $MgCl_2$, and MBAP solutions were more aggressive than the NaCl and CMA solutions. At the low-concentration, all of the brines were less aggressive. For specimens exposed to the five high-concentration brines, Figures A3.134 and A3.135 plot the visible alteration area values versus time for all concrete specimens and mortar, respectively. A general trend of increased alteration was evident for the concrete specimens as compared to the mortar specimens. Figures A3.136 and A3.137 compare the visible alteration area values from 0.45 *w/c* specimens to values from 0.55 *w/c* specimens exposed in the same brines. A general trend of increased alteration was evident for the 0.45 *w/c* specimens as compared to the 0.55 *w/c* specimens. Figures A3.138 through A3.140 illustrate the effect of supplementary cementitious materials for specimens in the high-concentration $CaCl_2$, $MgCl_2$, and MBAP brines. A general trend of decreased alteration was evident when fly ash or GGBFS were used.

Figures A3.141 through A3.143 illustrate the effect of silane and siloxane sealants for specimens in the high-concentration $CaCl_2$, $MgCl_2$, and MBAP brines. A general trend of decreased alteration was evident when the sealants were used. Figures A3.144 and A3.145 illustrate the effect of pre-soaking 0.55 *w/c* mortar specimens in high-concentration NaCl brine prior to immersion in high-concentration $CaCl_2$ and $MgCl_2$ brines.

The slabs cut from the epoxy stabilized 0.45 *w/c* concrete specimens from the high-concentration $CaCl_2$, $MgCl_2$, and MBAP brines at 500 days were rinsed with kerosene, cut into billets with a smaller kerosene-cooled diamond saw, and dried for a period of one hour in the 122 ºF [50 ºC] convection oven. Next, the billets were mounted on glass work-slides and one surface ground flat and smooth with a mineral-oil cooled diamond cup wheel. The prepared surfaces were cleaned with kerosene, and the billets placed again in the oven for a period of one hour. After drying, most of the billets were brought to the vacuum epoxy impregnation unit and the prepared surfaces embedded in epoxy. However, one of the billets representing a cross-section through a corner of a specimen from the $MgCl_2$ brine was placed in a sealed Pyrex™ container while still warm. A time-lapse movie was recorded over a period of 17 hours to illustrate the phenomenon of the build-up of beads of moisture on the surface of the deteriorated portion of the specimen. Figure A3.146 shows the before and after images from the time-lapse movie. This phenomenon was also observed during the sample preparation of deteriorated mortar cylinders from high-concentration $CaCl_2$, and $MgCl_2$ brines in Phase I, and was attributed to the hygroscopic nature of salts present in the samples absorbing ambient humidity. The described experiment, which utilized a warm dried billet in a sealed container precludes the interpretation of hygroscopic salts absorbing moisture from the air, and suggests that the moisture may instead be the by-product of the instability of hydrated salt phases present in the samples.

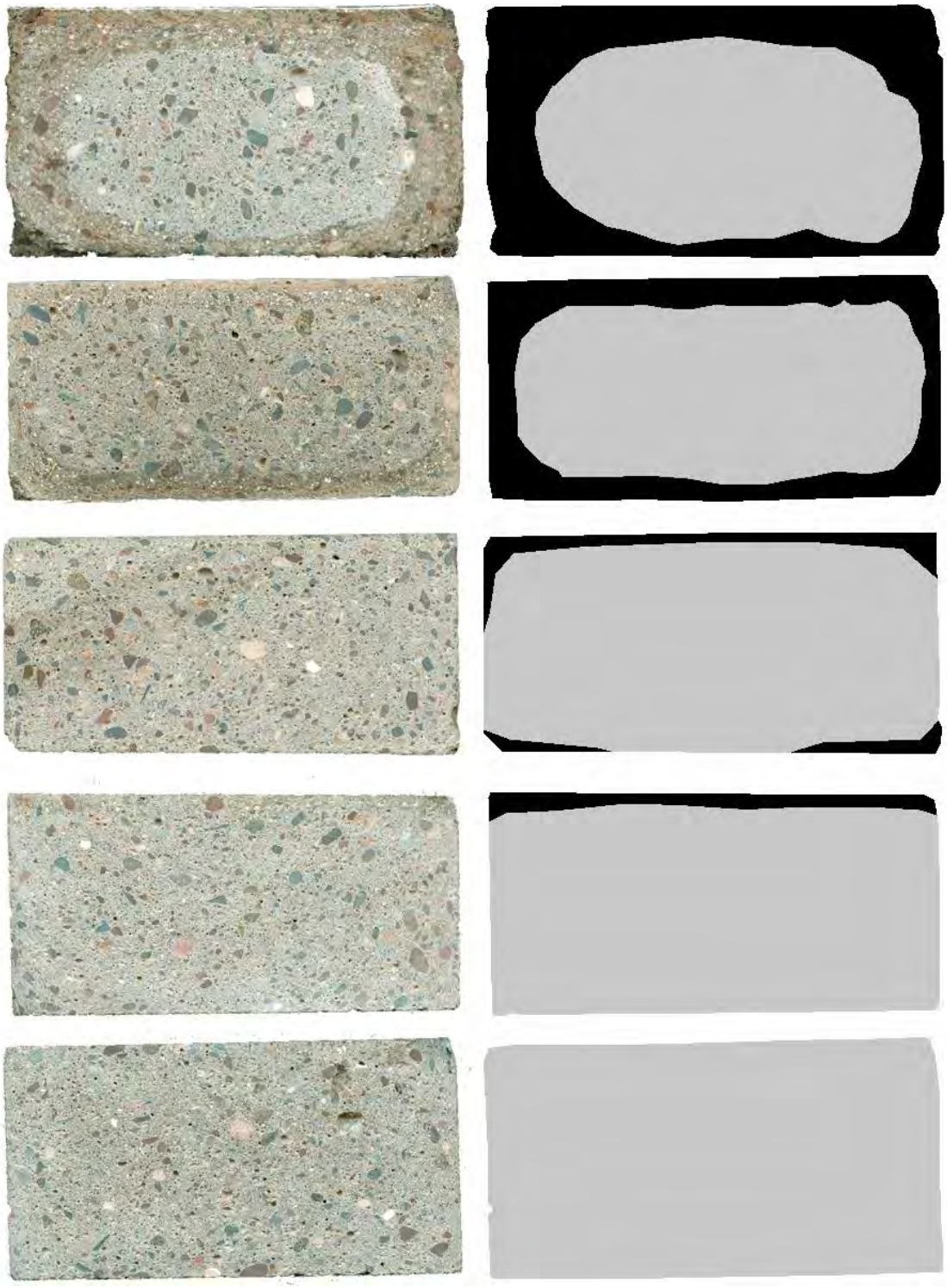

Figure A3.131. Visible alteration on saw-cut plane through 0.45 *w/c* mortar specimens, from top to bottom: $CaCl_2$, $MgCl_2$, MBAP, NaCl & CMA high concentration brines at 500 days.

Table A3.22. Measured visible alteration area percent values for specimens in limewater control and $MgCl_2$ brines at 60 and 500 days.

Sample ID	Visible alteration, area %	
	60 days	500 days
Limewater 0.45*w/c* PC	0.0	0.0
High Conc. $MgCl_2$ 0.45 *w/c* PC	14.8	60.3
High Conc. $MgCl_2$ 0.55 *w/c* PC	1.9	33.6
High Conc. $MgCl_2$ 0.55 *w/c* PC with SILANE SEAL	2.7	5.5
High Conc. $MgCl_2$ 0.55 *w/c* PC with SILOXANE SEAL	0.0	1.2
High Conc. $MgCl_2$ 0.45 *w/cm* FLY ASH	6.8	34.1
High Conc. $MgCl_2$ 0.55 *w/cm* FLY ASH	2.7	78.8
High Conc. $MgCl_2$ 0.45 *w/cm* GGBFS	5.5	32.7
High Conc. $MgCl_2$ 0.55 *w/cm* GGBFS	0.6	1.0
High Conc. $MgCl_2$ 0.45 *w/c* PC MORTAR	4.8	33.8
High Conc. $MgCl_2$ 0.55 *w/c* PC MORTAR	2.8	26.7
High Conc. $MgCl_2$ 0.45 *w/cm* FLY ASH MORTAR	6.4	31.5
High Conc. $MgCl_2$ 0.55 *w/cm* FLY ASH MORTAR	4.9	22.8
High Conc. $MgCl_2$ 0.45 *w/cm* GGBFS MORTAR	4.5	33.7
High Conc. $MgCl_2$ 0.55 *w/cm* GGBFS MORTAR	4.7	2.2
High Conc. $MgCl_2$ 0.55 *w/c* PC MORTAR NaCl pre-soak	0.0	36.6
High Conc. $MgCl_2$ 0.55 *w/c* PC MORTAR NaCl pre-soak SILANE SEAL	0.0	0.0
Low Conc. $MgCl_2$ 0.45 *w/c* PC	1.5	0.0
Low Conc. $MgCl_2$ 0.55 *w/c* PC	0.0	0.0
Low Conc. $MgCl_2$ 0.45 *w/c* PC MORTAR	1.1	3.9
Low Conc. $MgCl_2$ 0.55 *w/c* PC MORTAR	1.7	0.0

Table A3.23. Measured visible alteration area percent values for specimens in $CaCl_2$ brines at 60 and 500 days.

Sample ID	Visible alteration, area %	
	60 days	500 days
High Conc. $CaCl_2$ 0.45 *w/c* PC	7.4	76.4
High Conc. $CaCl_2$ 0.55 *w/c* PC	9.1	100.0
High Conc. $CaCl_2$ 0.55 *w/c* PC with SILANE SEAL	0.6	14.6
High Conc. $CaCl_2$ 0.55 *w/c* PC with SILOXANE SEAL	2.7	6.9
High Conc. $CaCl_2$ 0.45 *w/cm* FLY ASH	11.7	61.7
High Conc. $CaCl_2$ 0.55 *w/cm* FLY ASH	23.8	66.9
High Conc. $CaCl_2$ 0.45 *w/cm* GGBFS	1.9	23.3
High Conc. $CaCl_2$ 0.55 *w/cm* GGBFS	8.7	16.8
High Conc. $CaCl_2$ 0.45 *w/c* PC MORTAR	7.1	40.7
High Conc. $CaCl_2$ 0.55 *w/c* PC MORTAR	16.4	64.0
High Conc. $CaCl_2$ 0.45 *w/cm* FLY ASH MORTAR	10.1	30.6
High Conc. $CaCl_2$ 0.55 *w/cm* FLY ASH MORTAR	11.3	47.8
High Conc. $CaCl_2$ 0.45 *w/cm* GGBFS MORTAR	9.8	33.2
High Conc. $CaCl_2$ 0.55 *w/cm* GGBFS MORTAR	9.7	56.3
High Conc. $CaCl_2$ 0.55*w/c* PC MORTAR NaCl pre-soak	0.0	52.3
High Conc. $CaCl_2$ 0.55*w/c* PC MORTAR NaCl pre-soak with SILANE SEAL	0.0	12.5
Low Conc. $CaCl_2$ 0.45 *w/c* PC	0.0	0.0
Low Conc. $CaCl_2$ 0.55 *w/c* PC	1.2	0.3
Low Conc. $CaCl_2$ 0.45 *w/c* PC MORTAR	0.7	0.5
Low Conc. $CaCl_2$ 0.55 *w/c* PC MORTAR	4.9	1.7

Table A3.24. Measured visible alteration area percent values for specimens in MBAP brines at 60 and 500 days.

Sample ID	Visible alteration, area %	
	60 days	500 days
High Conc. MBAP 0.45 *w/c* PC	1.8	45.1
High Conc. MBAP 0.55 *w/c* PC	1.4	3.2
High Conc. MBAP 0.55 *w/c* PC with SILANE SEAL	0.0	0.0
High Conc. MBAP 0.55 *w/c* PC with SILOXANE SEAL	0.0	0.0
High Conc. MBAP 0.45 *w/cm* FLY ASH	0.6	10.5
High Conc. MBAP 0.55 *w/cm* FLY ASH	0.0	0.0
High Conc. MBAP 0.45 *w/cm* GGBFS	0.0	5.1
High Conc. MBAP 0.55 *w/cm* GGBFS	0.0	0.0
High Conc. MBAP 0.45 *w/c* PC MORTAR	1.2	6.2
High Conc. MBAP 0.55 *w/c* PC MORTAR	5.0	2.6
High Conc. MBAP 0.45 *w/cm* FLY ASH MORTAR	2.3	9.6
High Conc. MBAP 0.55 *w/cm* FLY ASH MORTAR	2.7	4.6
High Conc. MBAP 0.45 *w/cm* GGBFS MORTAR	3.6	3.0
High Conc. MBAP 0.55 *w/cm* GGBFS MORTAR	0.0	0.0
Low Conc. MBAP 0.45 *w/c* PC	1.6	3.5
Low Conc. MBAP 0.55 *w/c* PC	0.0	0.0
Low Conc. MBAP 0.45 *w/c* PC MORTAR	0.0	6.5
Low Conc. MBAP 0.55 *w/c* PC MORTAR	1.5	2.1

Table A3.25. Measured visible alteration area percent values for specimens in NaCl brines at 60 and 500 days.

Sample ID	visible alteration, area %	
	60 days	500 days
High Conc. NaCl 0.45 *w/c* PC	4.8	1.7
High Conc. NaCl 0.55 *w/c* PC	0.0	0.0
High Conc. NaCl 0.55 *w/c* PC with SILANE SEAL	4.3	1.3
High Conc. NaCl 0.55 *w/c* PC with SILOXANE SEAL	0.0	0.0
High Conc. NaCl 0.45 *w/cm* FLY ASH	2.1	1.5
High Conc. NaCl 0.55 *w/cm* FLY ASH	2.0	2.9
High Conc. NaCl 0.45 *w/cm* GGBFS	0.8	2.6
High Conc. NaCl 0.55 *w/cm* GGBFS	0.0	0.0
High Conc. NaCl 0.45 *w/c* PC MORTAR	1.5	7.4
High Conc. NaCl 0.55 *w/c* PC MORTAR	0.0	0.0
High Conc. NaCl 0.45 *w/cm* FLY ASH MORTAR	2.3	2.1
High Conc. NaCl 0.55 *w/cm* FLY ASH MORTAR	0.0	0.0
High Conc. NaCl 0.45 *w/cm* GGBFS MORTAR	0.0	0.0
High Conc. NaCl 0.55 *w/cm* GGBFS MORTAR	0.0	0.0
Low Conc. NaCl 0.45 *w/c* PC	0.0	0.5
Low Conc. NaCl 0.55 *w/c* PC	1.8	0.0
Low Conc. NaCl 0.45 *w/c* PC MORTAR	0.0	0.0
Low Conc. NaCl 0.55 *w/c* PC MORTAR	0.0	0.0

Table A3.26. Measured visible alteration area percent values for specimens in CMA brines at 60 and 500 days.

Sample ID	visible alteration, area %	
	60 days	500 days
High Conc. CMA 0.45 *w/c* PC	0.0	0.0
High Conc. CMA 0.55 *w/c* PC	0.0	1.1
High Conc. CMA 0.55 *w/c* PC with SILANE SEAL	0.0	0.0
High Conc. CMA 0.55 *w/c* PC with SILOXANE SEAL	0.0	0.0
High Conc. CMA 0.45 *w/cm* FLY ASH	0.0	0.0
High Conc. CMA 0.55 *w/cm* FLY ASH	0.0	0.0
High Conc. CMA 0.45 *w/cm* GGBFS	0.0	0.0
High Conc. CMA 0.55 *w/cm* GGBFS	0.0	0.0
High Conc. CMA 0.45 *w/c* PC MORTAR	0.0	0.0
High Conc. CMA 0.55 *w/c* PC MORTAR	0.0	0.0
High Conc. CMA 0.45 *w/cm* FLY ASH MORTAR	0.0	0.0
High Conc. CMA 0.55 *w/cm* FLY ASH MORTAR	0.0	0.0
High Conc. CMA 0.45 *w/cm* GGBFS MORTAR	0.0	0.0
High Conc. CMA 0.55 *w/cm* GGBFS MORTAR	0.0	0.0
Low Conc. CMA 0.45 *w/c* PC	0.0	0.0
Low Conc. CMA 0.55 *w/c* PC	0.0	0.0
Low Conc. CMA 0.45 *w/c* PC MORTAR	0.0	0.0
Low Conc. CMA 0.55 *w/c* PC MORTAR	0.0	0.0

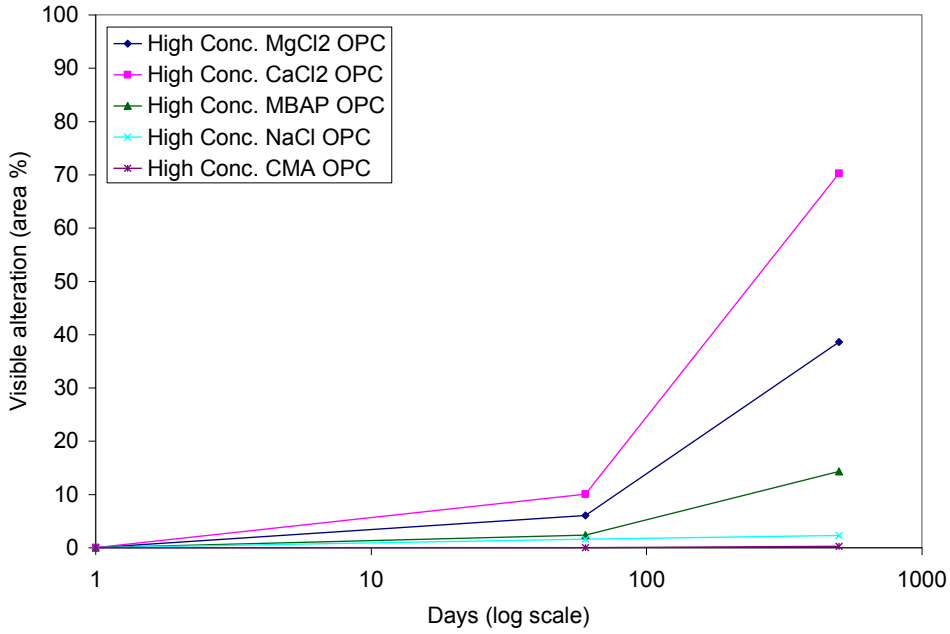

Figure A3.132. Average visible alteration versus time for high concentration brines with 0.45 and 0.55 *w/c* portland cement concrete specimens and mortar specimens

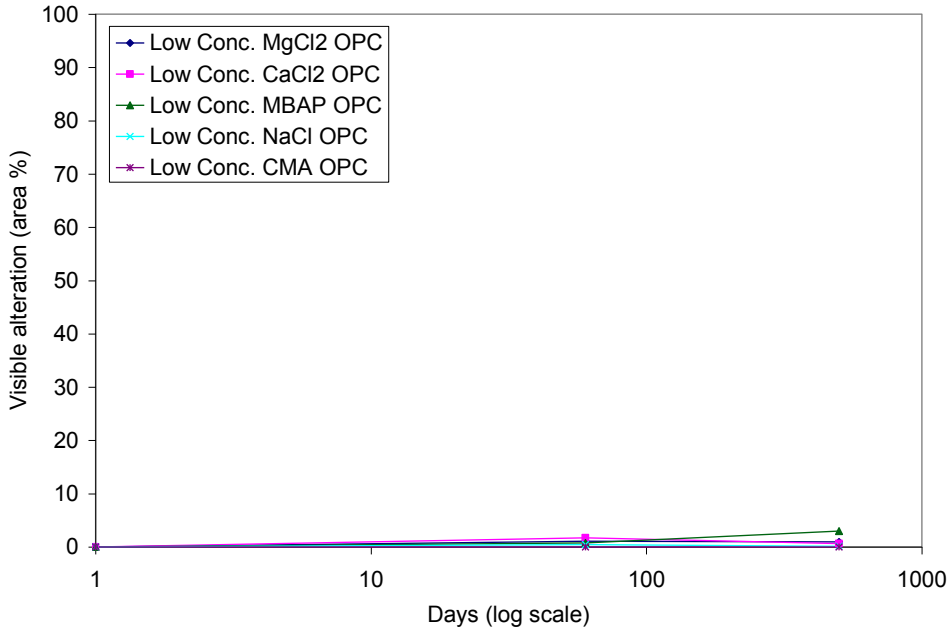

Figure A3.133. Average visible alteration versus time for low concentration brines with 0.45 and 0.55 *w/c* portland cement concrete specimens and mortar specimens.

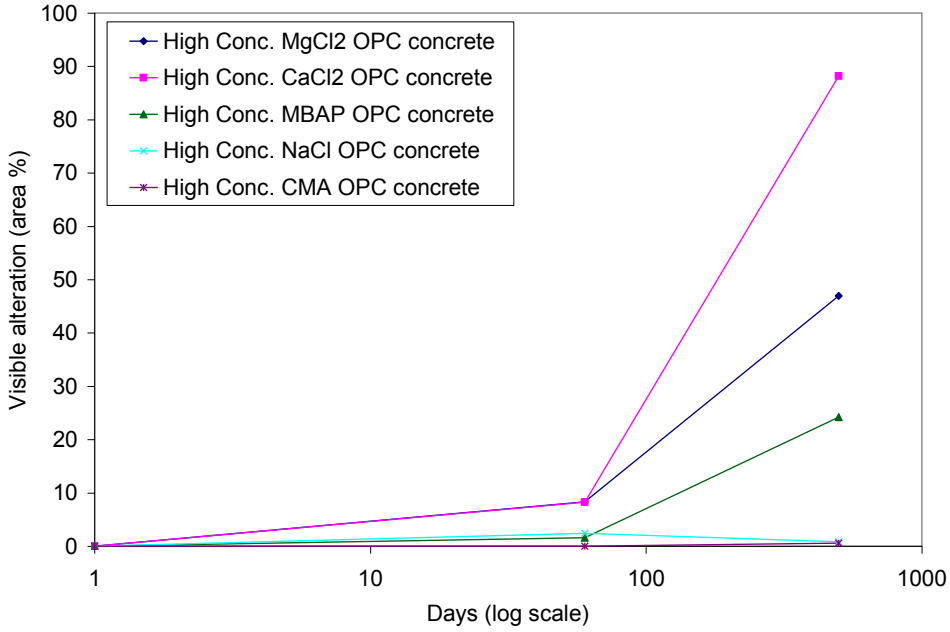

Figure A3.134. Average visible alteration versus time for high concentration brines with 0.45 and 0.55 *w/c* portland cement concrete specimens.

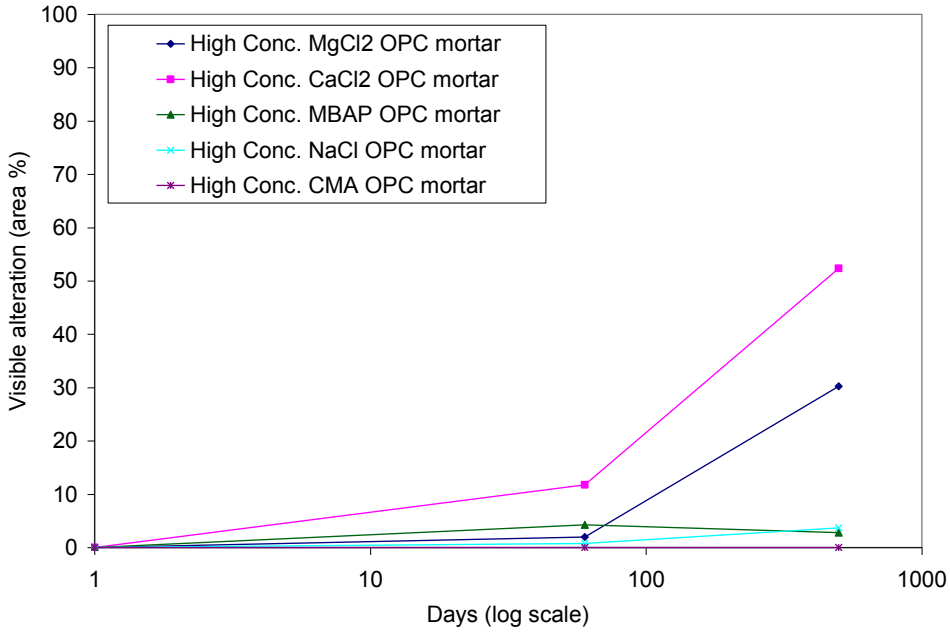

Figure A3.135. Average visible alteration versus time for high concentration brines with 0.45 and 0.55 *w/c* portland cement mortar specimens.

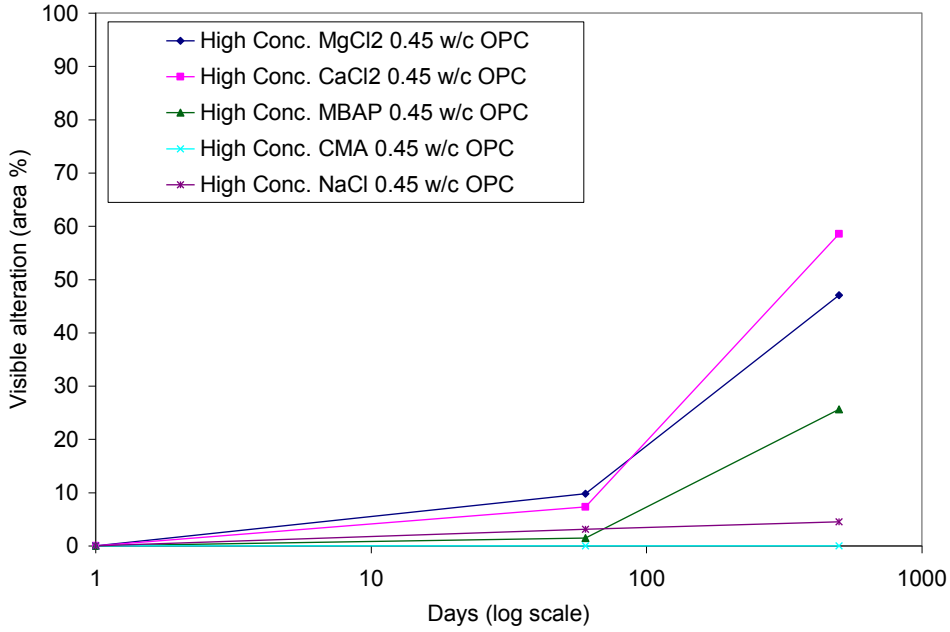

Figure A3.136. Average visible alteration versus time for high concentration brines with 0.45 *w/c* portland cement concrete specimens and mortar specimens.

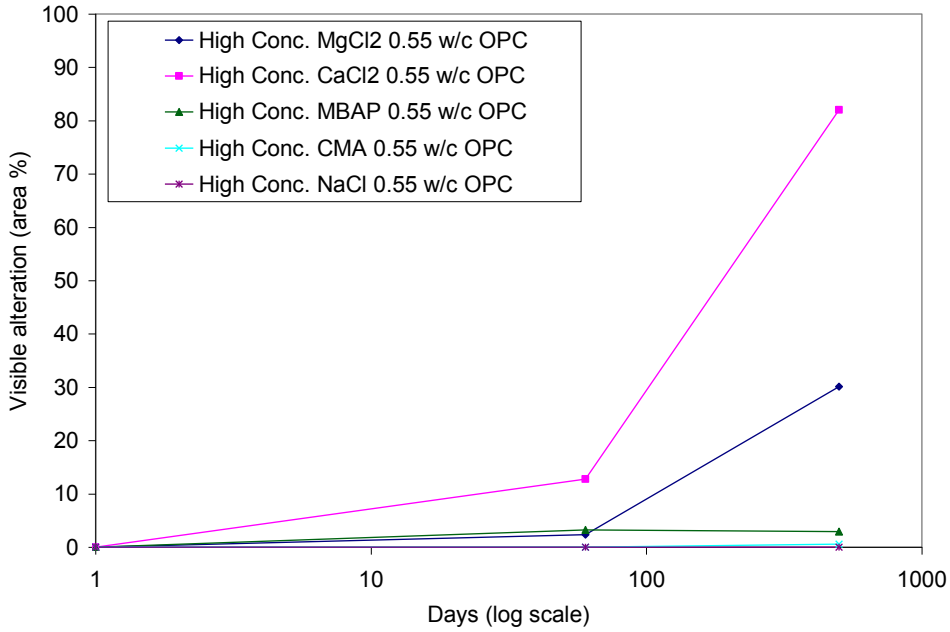

Figure A3.137. Average visible alteration versus time for high concentration brines with 0.55 *w/c* portland cement concrete specimens and mortar specimens.

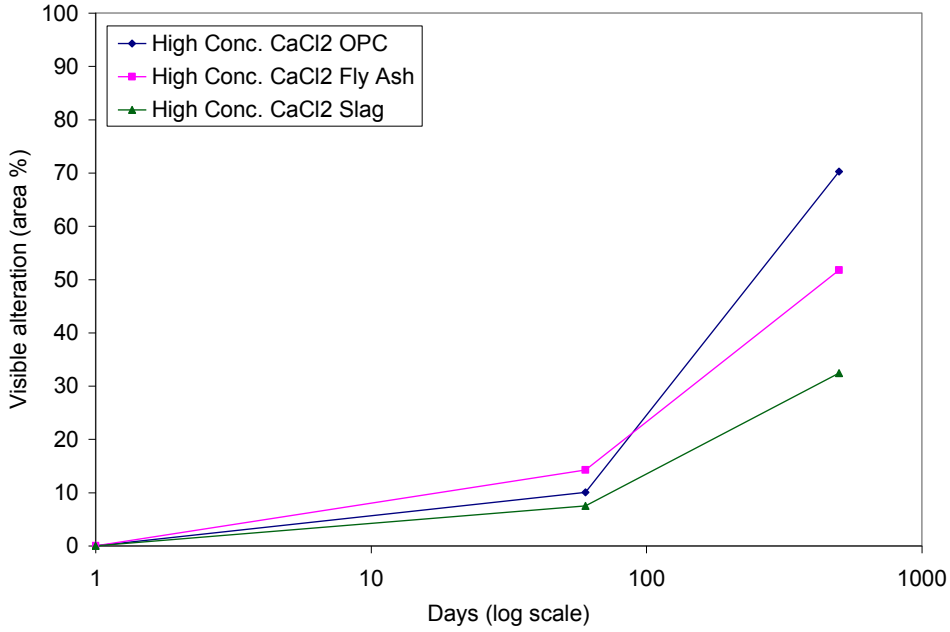

Figure A3.138. Average visible alteration versus time for 0.45 and 0.55 *w/cm* concrete specimens and mortar specimens made with straight portland cement, fly ash, and GGBFS after immersion in high concentration $CaCl_2$ brine.

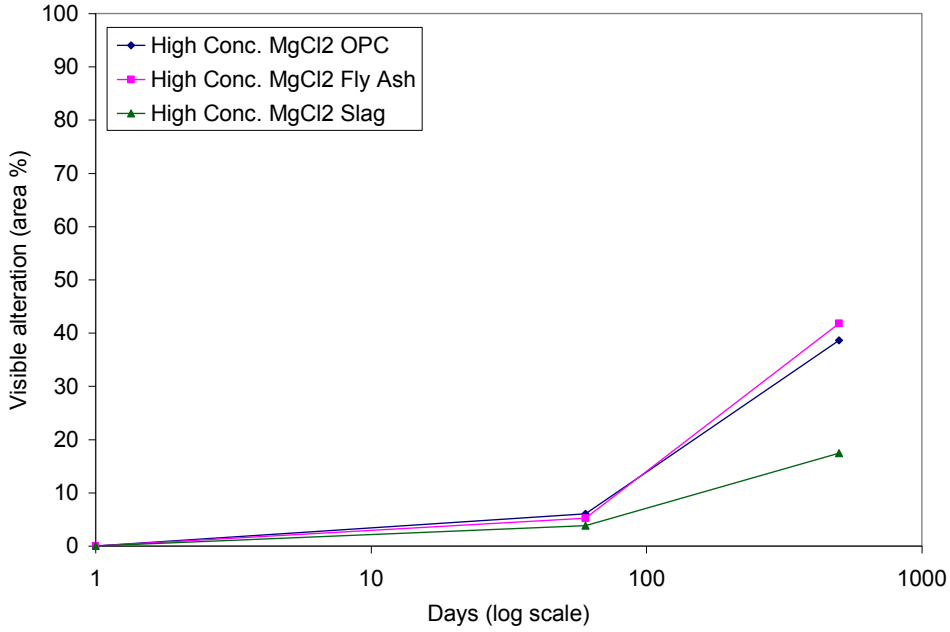

Figure A3.139. Average visible alteration versus time for 0.45 and 0.55 *w/cm* concrete specimens and mortar specimens made with straight portland cement, fly ash, and GGBFS after immersion in high concentration $MgCl_2$ brine.

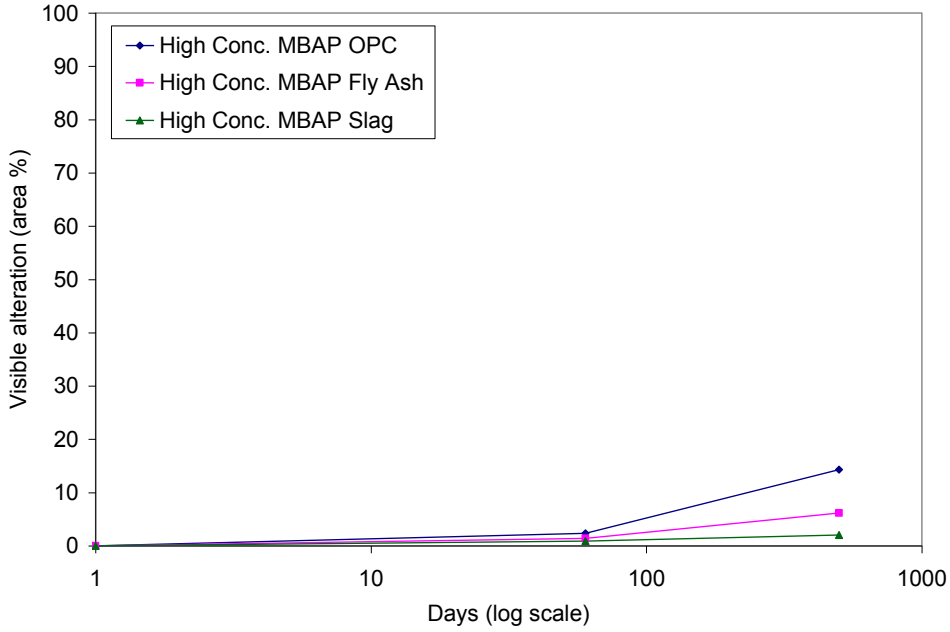

Figure A3.140. Average visible alteration versus time for 0.45 and 0.55 *w/cm* concrete specimens and mortar specimens made with straight portland cement, fly ash, and GGBFS after immersion in high concentration MBAP brine.

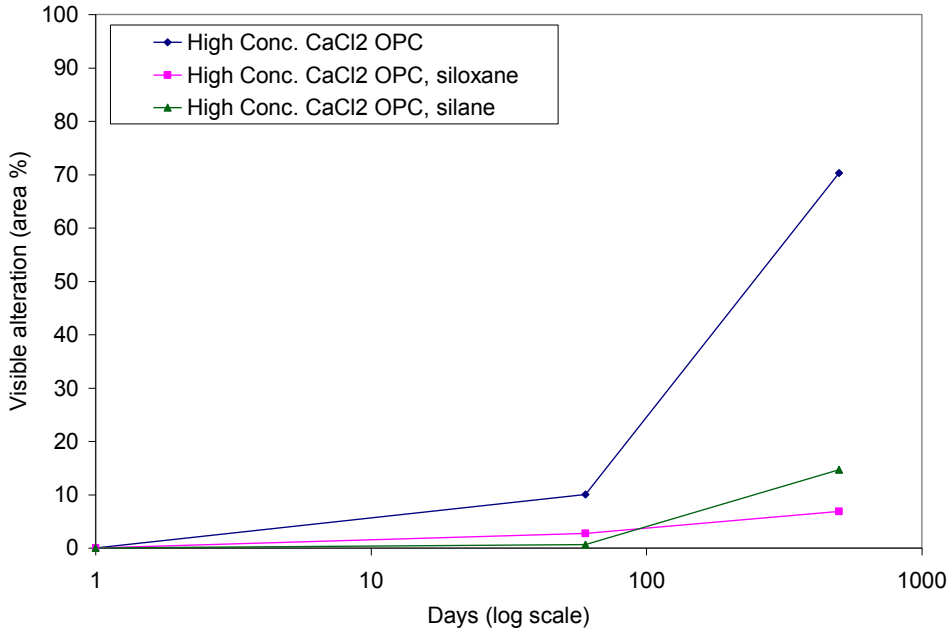

Figure A3.141. Average visible alteration versus time for 0.45 and 0.55 *w/c* portland cement concrete specimens and mortar specimens both with and without sealant after immersion in high concentration $CaCl_2$ brine.

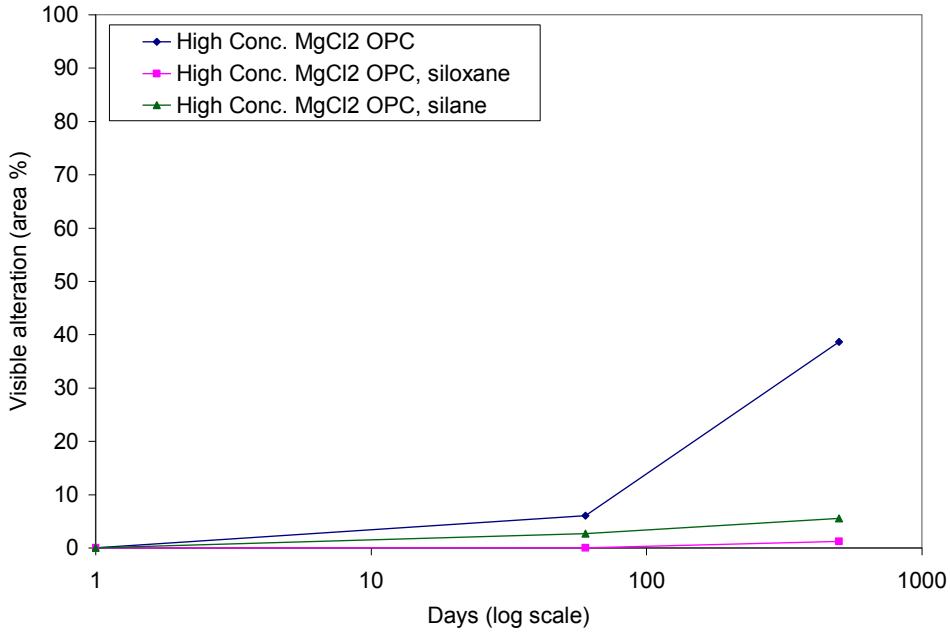

Figure A3.142. Average visible alteration versus time for 0.45 and 0.55 *w/c* portland cement concrete specimens and mortar specimens both with and without sealant after immersion in high concentration $MgCl_2$ brine.

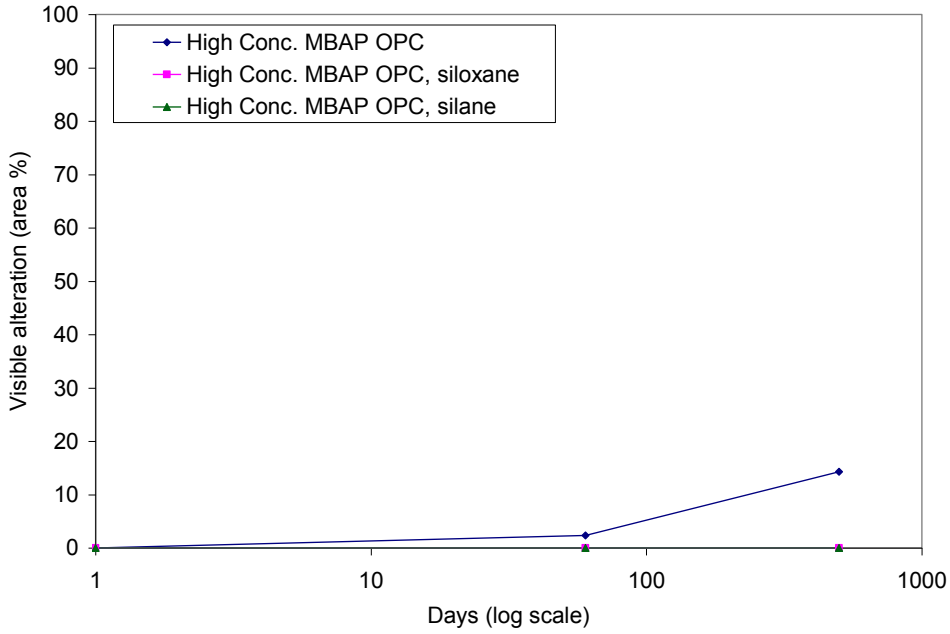

Figure A3.143. Average visible alteration versus time for 0.45 and 0.55 *w/c* portland cement concrete specimens and mortar specimens both with and without sealant after immersion in high concentration MBAP brine.

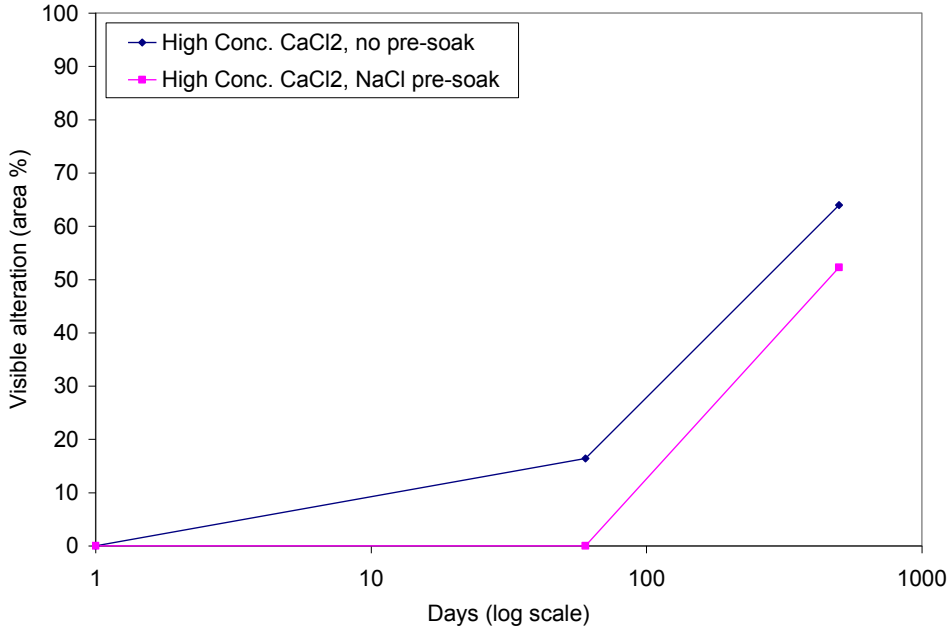

Figure A3.144. Visible alteration versus time for 0.55 *w/c* portland cement mortar specimens both with and without a NaCl pre-soaking period after immersion in high concentration $CaCl_2$ brine.

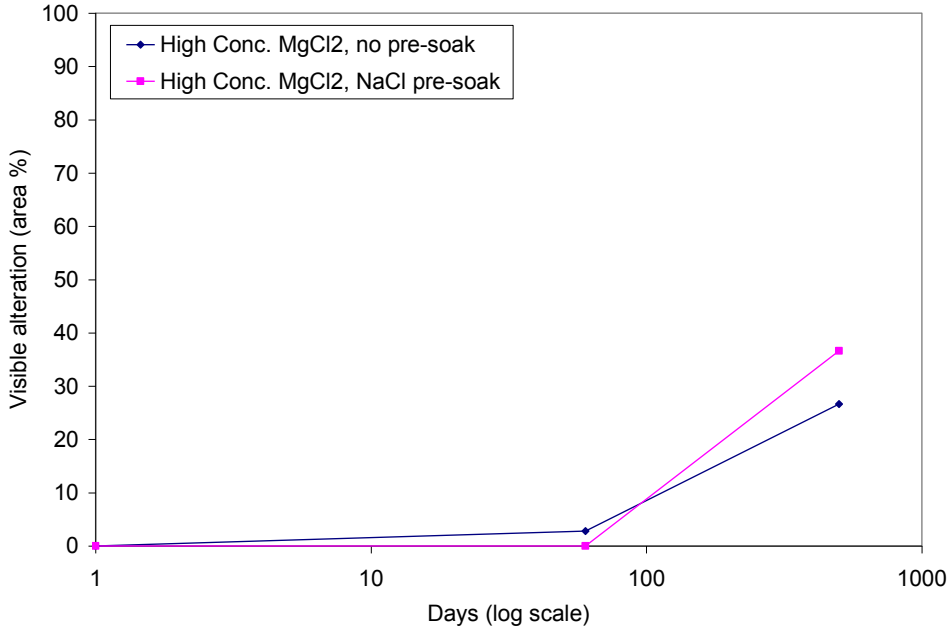

Figure A3.145. Visible alteration versus time for 0.55 *w/c* portland cement mortar specimens both with and without a NaCl pre-soaking period after immersion in high concentration $MgCl_2$ brine.

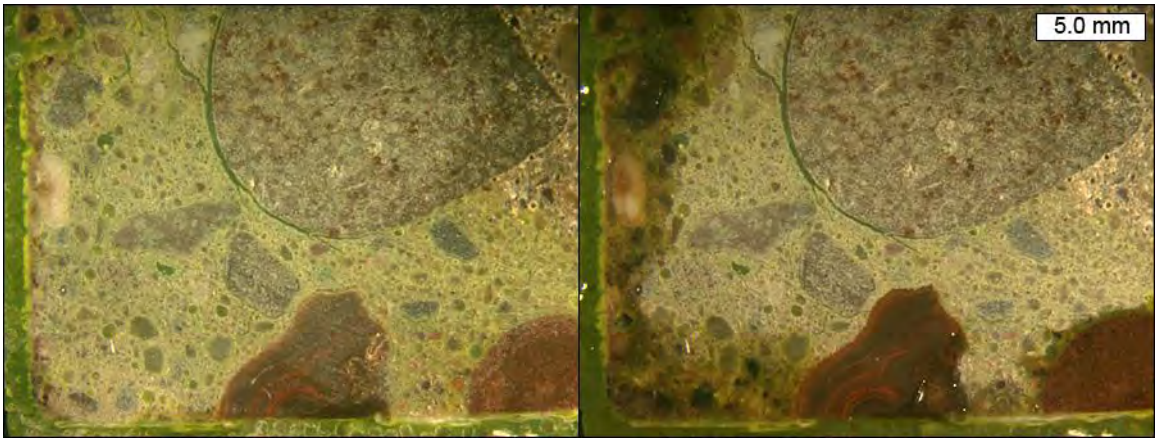

Figure A3.146. Before, (left) and after, (right) images from 17 hour time-lapse movie to show weeping in deteriorated zone on diamond-ground epoxy impregnated cross-section through corner of 0.45 *w/c* concrete specimen after 500 days exposure to high-concentration $MgCl_2$ brine.

A3.3.2.2 Chloride Profiling

Chloride profiling was performed using the X-ray microscope on smooth diamond-ground billets cut to represent a cross-section through the near-surface of the specimens immersed in the brine solutions. The billets came from the center of the specimens to avoid the effects of diffusion of Cl^- ions from the sides of the specimens. Two billets were used for the collection of profile data for each specimen in most cases. All of the specimens analyzed were removed from their respective brine solutions at 60 days, with two additional 0.45 *w/c* portland cement concrete specimens removed from the high-concentration NaCl brine and from the limewater control at 500 days. Another set of 0.55 *w/c* silane-sealed portland cement concrete specimens were also removed from the high-concentration $MgCl_2$ and $CaCl_2$ brines at 500 days. Tables A3.27 through A3.30 list the parameters derived by fitting the profile data collected from the specimens removed at 60 days to Fick's 2nd Law, as shown in Equation 2.1.

Figures A3.147 through A3.149 show profiles for 0.45 *w/c* concrete specimens immersed in the five different high-concentration brine solutions. Figure A3.147 shows profiles from the straight portland cement concrete specimens. Figure A3.148 shows profiles from the concrete specimens with fly ash, and Figure A3.149 shows profiles from the concrete specimens with GGBFS. The addition of GGBFS resulted in a marked decrease in the chloride concentration near the surfaces of the specimens. Chloride concentration profiles for concrete specimens with fly ash were similar to the profiles from specimens with straight portland cement.

Figures A3.150 through A3.152 show profiles for 0.45 *w/c* mortar specimens immersed in the five high-concentration brine solutions. Figure A3.150 shows profiles from the straight portland cement mortar specimens, Figure A3.151 shows profiles from the mortar specimens with fly ash, and Figure A3.152 shows profiles from the mortar specimens with GGBFS. The chloride concentrations reported for the mortar specimens are approximately double the values from the concrete specimens. A well-defined trend of higher chloride concentration near the surface was observed for mortar specimens immersed in the $MgCl_2$ and $CaCl_2$ brines relative to the other brines. At depth, chloride concentrations were consistently higher for the

mortar specimens immersed in the NaCl brine relative to the other brines. Chloride concentrations were lowest overall for specimens immersed in the MBAP brine.

Figure A3.153 shows profiles for the 0.45 *w/c* concrete specimens from the five low-concentration brine solutions. As might be expected, initial chloride concentrations were lower for concrete specimens from the low-concentration brines when compared to the same specimens from the high-concentration brines, (Figure A3.147) with the exception of the specimens immersed in the MBAP brines. Although the initial chloride concentrations were generally lower for concrete specimens in the low-concentration brines, the chloride concentrations at a depth of about ½ inch, [10 to 15 mm] were slightly elevated in the concrete specimens that had been exposed to the $CaCl_2$ and $MgCl_2$ low-concentration brines as compared to the same concrete specimens exposed to the $CaCl_2$ and $MgCl_2$ high-concentration brines. This trend was also observed in the mortar specimens. Figure A3.154 shows the profiles for the 0.45 *w/c* mortar specimens immersed in the low-concentration brines, as compared to Figure A3.150, which shows the profiles for the companion specimens immersed in the high-concentration brines.

Figure A3.155 shows the profiles for the 0.55 *w/c* portland cement concrete specimens exposed to the high-concentration brines. Compared to 0.45 *w/c* concrete specimens exposed to the same conditions, (Figure A3.147) the 0.55 *w/c* concrete specimens showed similar initial chloride concentrations but generally greater chloride penetration at depth. Figure A3.156 shows the profiles for the 0.55 *w/c* portland cement mortar specimens exposed to the high-concentration brines. The 0.55 *w/c* mortar specimens from the $CaCl_2$ and $MgCl_2$ brines showed much lower initial chloride concentrations than their counterparts from the 0.45 *w/c* mortar specimen experiment, (Figure A3.150). Overall, the 0.55 *w/c* mortar specimens showed greater penetration of chloride at depth when compared to 0.45 *w/c* mortar specimens exposed to the same conditions.

Figures A3.157 and A3.158 show profiles for 0.55 *w/c* concrete specimens treated with silane and siloxane after exposure to the five high-concentration brines. The sealants were very effective at impeding the ingress of chlorides at 60 days. However, at 500 days, chloride ingress was evident from the bases of the specimens, as shown in the profile data of Figures A3.159 and A3.160. These data sets could not be fit using Fick's 2nd Law.

Although some general trends were observed in the chloride profile data, there were often outliers or exceptions. Some of these inconsistencies, especially in the case of the concrete specimens, can in some cases be attributed to heterogeneities inherent to the material. For example, Figure A3.161 provides an example of the influence a large porous coarse aggregate particle can have on the ingress of chlorides. The scanned image and elemental map shown in Figure A3.161 were taken from a billet cut from a 0.45 *w/cm* fly ash concrete specimen exposed to high-concentration $MgCl_2$ brine. The scanning and elemental mapping were part of the procedure performed on all of the samples to assist in the location of suitable points in the cement paste for wt% chlorine analyses. For comparison, Figure A3.162 shows a scanned image of a billet and the corresponding elemental map from a 0.45 *w/cm* fly ash mortar specimen immersed in high-concentration $MgCl_2$ brine. During the selection of points for chloride profiling, areas such as the chloride-enriched zone adjacent to the large porous sandstone coarse aggregate particle of Figure A3.161 were avoided. Furthermore, bright spots in the chloride map due to diffraction events in the aggregate fraction were also

avoided. Figures A3.163 and A3.164 show the raw profile data collected from the same billets shown in Figures A3.161 and A3.162 respectively. As part of the profiling procedure, the measured wt% values for chloride in the hardened cement paste were converted to wt% chloride in the bulk concrete or mortar specimen based on mix design information prior to fitting with Fick's 2nd Law. Figures A3.165 and A3.166 show corrected profiles after fitting. The raw-data diffusion profiles shown in Figures A3.163 and A3.164 were similar since both originated from points in a 0.45 *w/cm* fly ash blend cement paste exposed to the same $MgCl_2$ brine. However, since the profile in Figure A3.165 came from the concrete specimen, and the profile in Figure A3.166 came from the mortar specimen, the weight-corrected chloride profile from the concrete specimen appears dramatically lower in concentration than the chloride profile from the mortar specimen. Chloride ions diffuse just as far in concrete as in mortar, if not farther in the case of concrete with porous coarse aggregate particles, but this fact is not always evident when the results are plotted in terms of wt% chloride in the bulk material.

As a check on the parameters determined by fitting the profiles to Fick's 2nd Law, the effective diffusion coefficient and initial concentration values from a 0.45 *w/c* concrete specimen exposed to high-concentration NaCl brine at 60 days were used to predict the chloride profile at 500 days. A companion concrete specimen was removed at 500 days, and the collected profile was compared to the predicted profile, as shown in Figure A3.167. Figure A3.168 shows a chloride profile collected from the 0.45 *w/c* concrete specimen immersed in limewater at 500 days. This data could not be fit using Fick's 2nd Law.

Table A3.27. Parameters derived from best fit of profile data from specimens immersed in $MgCl_2$ brines to Fick's 2nd Law.

Sample ID	Days	C_i (wt% Cl)	D_{eff} (m^2/s)	R^2
High Conc. $MgCl_2$ 0.45 *w/c* PC	60	1.65	1.87E-12	0.903
High Conc. $MgCl_2$ 0.55 *w/c* PC	60	1.29	1.20E-11	0.624
High Conc. $MgCl_2$ 0.55 *w/c* PC SILANE SEAL	60	0.39	9.47E-14	0.962
High Conc. $MgCl_2$ 0.55 *w/c* PC SILOXANE SEAL	60	0.12	5.90E-13	0.731
High Conc. $MgCl_2$ 0.45 *w/cm* FLY ASH	60	0.92	1.01E-11	0.832
High Conc. $MgCl_2$ 0.55 *w/cm* FLY ASH	60	0.57	2.87E-12	0.870
High Conc. $MgCl_2$ 0.45 *w/cm* GGBFS	60	0.81	3.62E-12	0.909
High Conc. $MgCl_2$ 0.55 *w/cm* GGBFS	60	0.56	3.32E-12	0.944
High Conc. $MgCl_2$ 0.45 *w/c* PC MORTAR	60	1.92	1.60E-12	0.944
High Conc. $MgCl_2$ 0.55 *w/c* PC MORTAR	60	1.41	2.45E-12	0.925
High Conc. $MgCl_2$ 0.45 *w/cm* FLY ASH MORTAR	60	2.12	1.51E-12	0.866
High Conc. $MgCl_2$ 0.55 *w/cm* FLY ASH MORTAR	60	1.54	2.41E-12	0.930
High Conc. $MgCl_2$ 0.45 *w/cm* GGBFS MORTAR	60	2.29	1.00E-12	0.936
High Conc. $MgCl_2$ 0.55 *w/cm* GGBFS MORTAR	60	1.56	9.92E-13	0.937
Low Conc. $MgCl_2$ 0.45 *w/c* PC	60	0.81	4.88E-12	0.869
Low Conc. $MgCl_2$ 0.55 *w/c* PC	60	0.46	1.14E-11	0.881
Low Conc. $MgCl_2$ 0.45 *w/c* PC MORTAR	60	0.88	6.52E-12	0.914
Low Conc. $MgCl_2$ 0.55 *w/c* PC MORTAR	60	1.21	5.33E-12	0.926

Table A3.28. Parameters derived from best fit of profile data from specimens immersed in $CaCl_2$ brines to Fick's 2nd Law.

Sample ID	Days	C_i (wt% Cl)	D_{eff} (m^2/s)	R^2
High Conc. $CaCl_2$ 0.45 *w/c* PC	60	1.39	2.96E-12	0.904
High Conc. $CaCl_2$ 0.55 *w/c* PC	60	1.33	4.30E-12	0.813
High Conc. $CaCl_2$ 0.55 *w/c* PC SILANE SEAL	60	0.02	2.49E-13	0.293
High Conc. $CaCl_2$ 0.55 *w/c* PC SILOXANE SEAL	60	0.11	1.00E-12	0.784
High Conc. $CaCl_2$ 0.45 *w/cm* FLY ASH	60	1.26	2.77E-12	0.834
High Conc. $CaCl_2$ 0.55 *w/cm* FLY ASH	60	1.47	1.02E-11	0.747
High Conc. $CaCl_2$ 0.45 *w/cm* GGBFS	60	0.76	1.77E-12	0.869
High Conc. $CaCl_2$ 0.55 *w/cm* GGBFS	60	0.92	2.30E-12	0.914
High Conc. $CaCl_2$ 0.45 *w/c* PC MORTAR	60	2.81	2.17E-12	0.969
High Conc. $CaCl_2$ 0.55 *w/c* PC MORTAR	60	1.24	4.04E-12	0.858
High Conc. $CaCl_2$ 0.45 *w/cm* FLY ASH MORTAR	60	2.57	2.74E-12	0.765
High Conc. $CaCl_2$ 0.55 *w/cm* FLY ASH MORTAR	60	1.77	2.27E-12	0.773
High Conc. $CaCl_2$ 0.45 *w/cm* GGBFS MORTAR	60	2.12	1.78E-12	0.892
High Conc. $CaCl_2$ 0.55 *w/cm* GGBFS MORTAR	60	1.64	2.36E-12	0.930
Low Conc. $CaCl_2$ 0.45 *w/c* PC	60	0.73	4.10E-12	0.901
Low Conc. $CaCl_2$ 0.55 *w/c* PC	60	0.44	8.77E-12	0.896
Low Conc. $CaCl_2$ 0.45 *w/c* PC MORTAR	60	1.08	3.82E-12	0.882
Low Conc. $CaCl_2$ 0.55 *w/c* PC MORTAR	60	0.98	6.61E-12	0.924

Table A3.29. Parameters derived from best fit of profile data from specimens immersed in MBAP brines to Fick's 2nd Law.

Sample ID	Days	C_i (wt% Cl)	D_{eff} (m^2/s)	R^2
High Conc. MBAP 0.45 *w/c* PC	60	0.72	3.71E-12	0.893
High Conc. MBAP 0.55 *w/c* PC	60	0.32	7.61E-12	0.856
High Conc. MBAP 0.55 *w/c* PC SILANE SEAL	60	0.10	2.60E-12	0.694
High Conc. MBAP 0.55 *w/c* PC SILOXANE SEAL	60	0.02	2.66E-12	0.223
High Conc. MBAP 0.45 *w/cm* FLY ASH	60	0.50	5.24E-12	0.850
High Conc. MBAP 0.55 *w/cm* FLY ASH	60	0.39	8.66E-12	0.865
High Conc. MBAP 0.45 *w/cm* GGBFS	60	0.49	3.33E-12	0.887
High Conc. MBAP 0.55 *w/cm* GGBFS	60	0.40	7.32E-12	0.792
High Conc. MBAP 0.45 *w/c* PC MORTAR	60	0.39	4.19E-12	0.878
High Conc. MBAP 0.55 *w/c* PC MORTAR	60	1.19	5.08E-12	0.957
High Conc. MBAP 0.45 *w/cm* FLY ASH MORTAR	60	0.52	4.90E-12	0.891
High Conc. MBAP 0.55 *w/cm* FLY ASH MORTAR	60	0.61	5.67E-12	0.897
High Conc. MBAP 0.45 *w/cm* GGBFS MORTAR	60	1.03	2.42E-12	0.880
High Conc. MBAP 0.55 *w/cm* GGBFS MORTAR	60	0.75	2.43E-12	0.953
Low Conc. MBAP 0.45 *w/c* PC	60	1.06	4.28E-12	0.970
Low Conc. MBAP 0.55 *w/c* PC	60	0.23	5.44E-12	0.869
Low Conc. MBAP 0.45 *w/c* PC MORTAR	60	0.58	5.87E-12	0.921
Low Conc. MBAP 0.55 *w/c* PC MORTAR	60	0.71	7.51E-12	0.848

Table A3.30. Parameters derived from best fit of profile data from specimens immersed in NaCl brines to Fick's 2nd Law.

Sample ID	Days	C_i (wt% Cl)	D_{eff} (m^2/s)	R^2
High Conc. NaCl 0.45 *w/c* PC	60	0.49	5.79E-12	0.929
High Conc. NaCl 0.55 *w/c* PC	60	0.65	1.27E-11	0.864
High Conc. NaCl 0.55 *w/c* PC SILANE SEAL	60	0.13	1.33E-12	0.739
High Conc. NaCl 0.55 *w/c* PC SILOXANE SEAL	60	0.30	3.00E-13	0.716
High Conc. NaCl 0.45 *w/cm* FLY ASH	60	0.62	6.52E-12	0.959
High Conc. NaCl 0.55 *w/cm* FLY ASH	60	0.63	1.90E-11	0.870
High Conc. NaCl 0.45 *w/cm* GGBFS	60	0.53	6.06E-12	0.825
High Conc. NaCl 0.55 *w/cm* GGBFS	60	0.63	8.99E-12	0.887
High Conc. NaCl 0.45 *w/c* PC MORTAR	60	1.14	7.20E-12	0.950
High Conc. NaCl 0.55 *w/c* PC MORTAR	60	1.02	1.40E-11	0.852
High Conc. NaCl 0.45 *w/cm* FLY ASH MORTAR	60	0.89	6.18E-12	0.899
High Conc. NaCl 0.55 *w/cm* FLY ASH MORTAR	60	0.58	7.33E-12	0.854
High Conc. NaCl 0.45 *w/cm* GGBFS MORTAR	60	1.08	4.53E-12	0.914
High Conc. NaCl 0.55 *w/cm* GGBFS MORTAR	60	0.82	4.33E-12	0.878
Low Conc. NaCl 0.45 *w/c* PC	60	0.32	7.17E-12	0.859
Low Conc. NaCl 0.55 *w/c* PC	60	0.36	1.34E-11	0.767
Low Conc. NaCl 0.45 *w/c* PC MORTAR	60	0.65	7.19E-12	0.884
Low Conc. NaCl 0.55 *w/c* PC MORTAR	60	0.54	7.61E-12	0.921

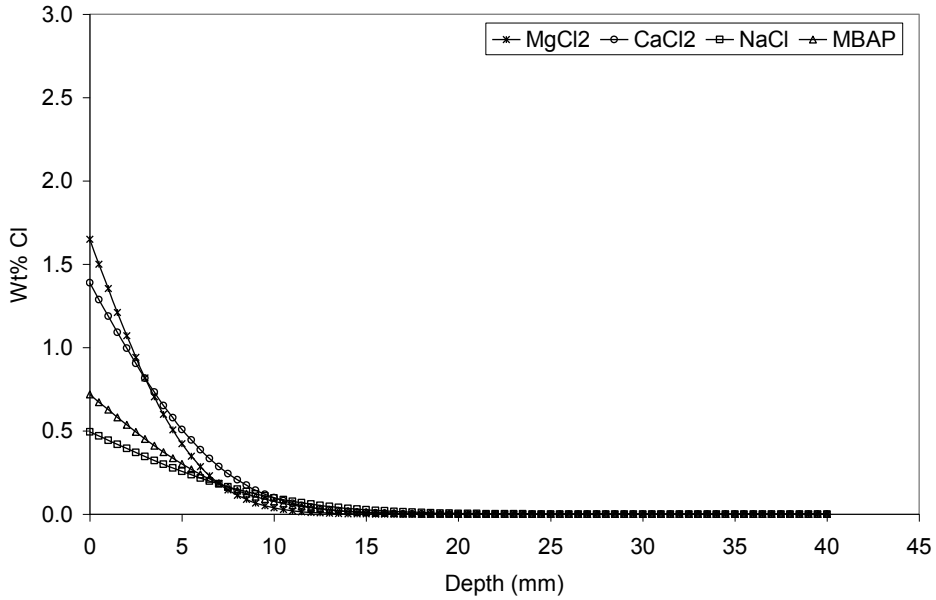

Figure A3.147. Fitted chloride profiles for 0.45 *w/c* straight portland cement concrete specimens immersed in high-concentration brines at 60 days.

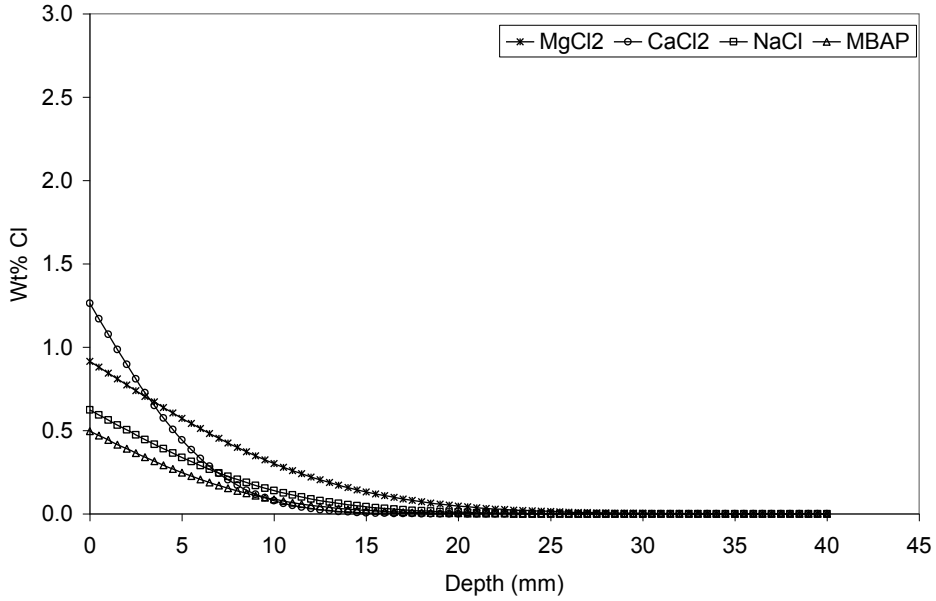

Figure A3.148. Fitted chloride profiles for 0.45 *w/cm* fly ash concrete specimens immersed in high-concentration brines at 60 days.

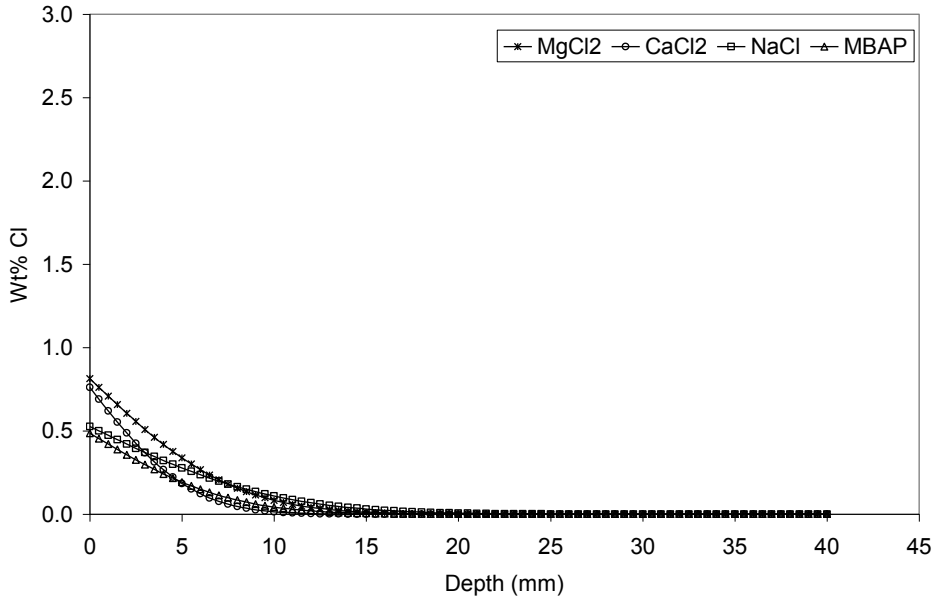

Figure A3.149. Fitted chloride profiles for 0.45 *w/cm* GGBFS concrete specimens immersed in high-concentration brines at 60 days.

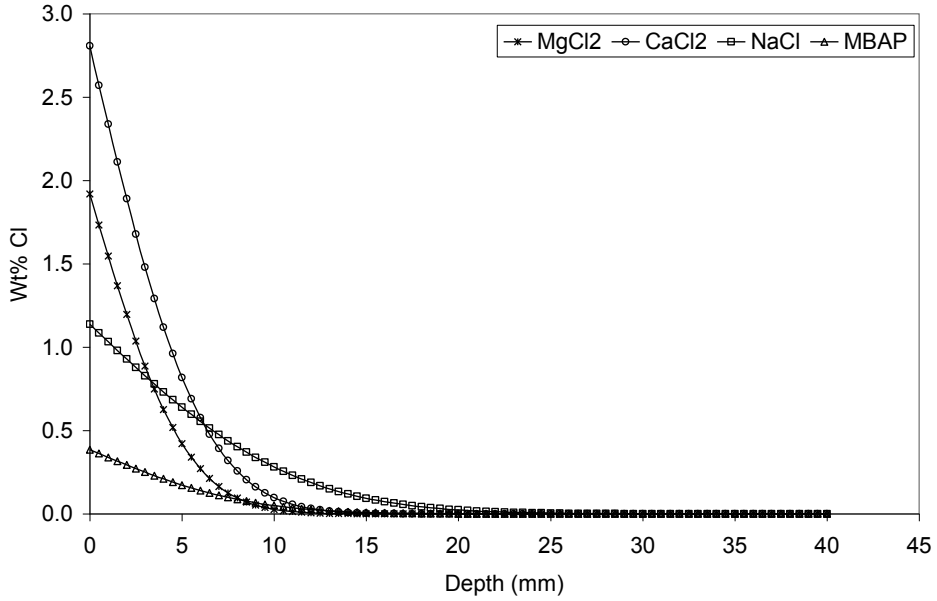

Figure A3.150. Fitted chloride profiles for 0.45 *w/c* straight portland cement mortar specimens immersed in high-concentration brines at 60 days.

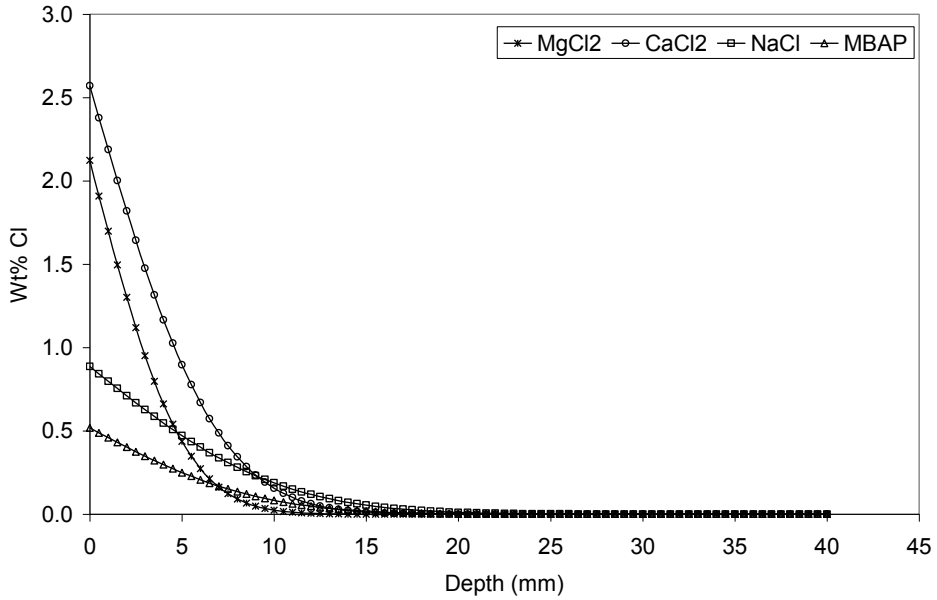

Figure A3.151. Fitted chloride profiles for 0.45 *w/cm* fly ash mortar specimens immersed in high-concentration brines at 60 days.

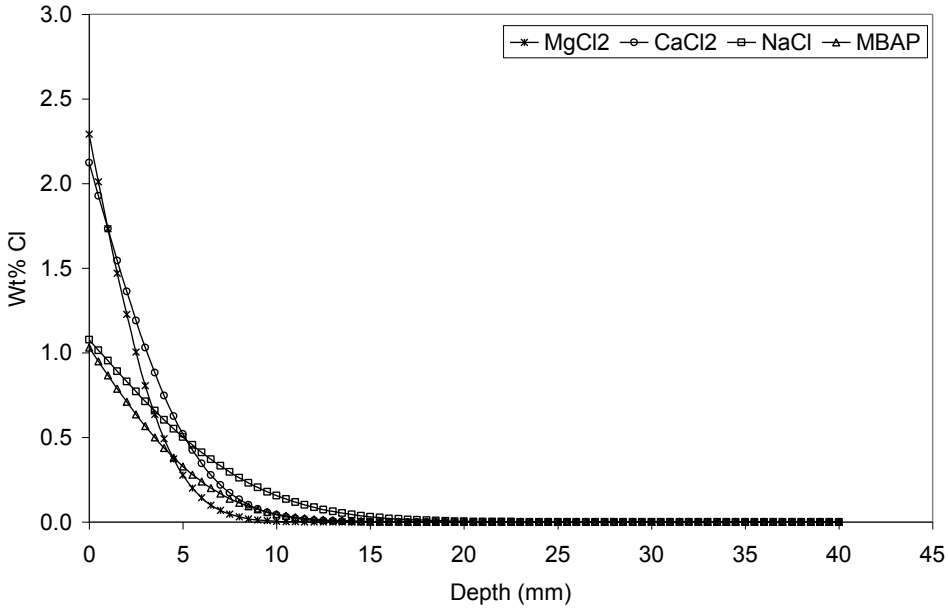

Figure A3.152. Fitted chloride profiles for 0.45 *w/cm* GGBFS mortar specimens immersed in high-concentration brines at 60 days.

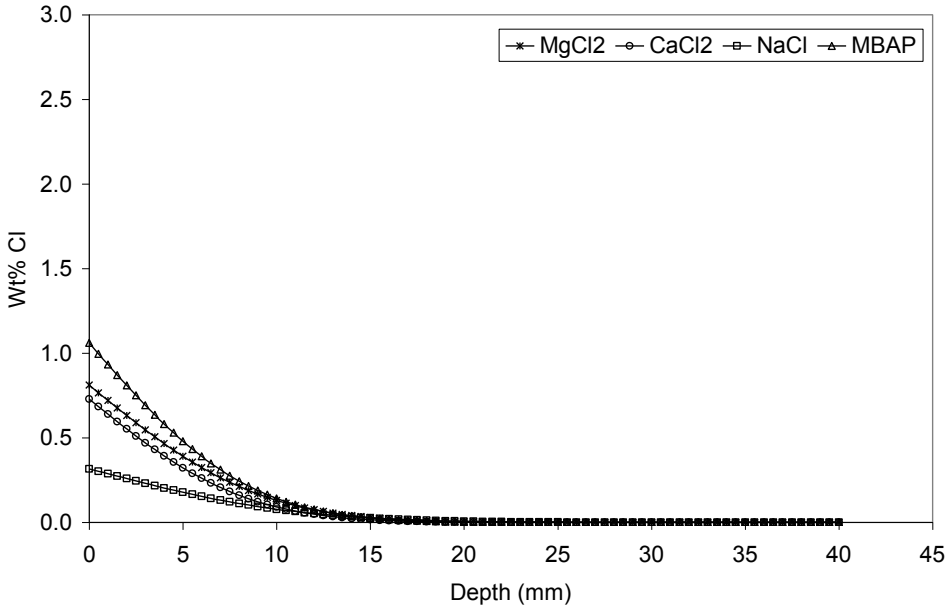

Figure A3.153. Fitted chloride profiles for 0.45 *w/c* straight portland cement concrete specimens immersed in low-concentration brines at 60 days.

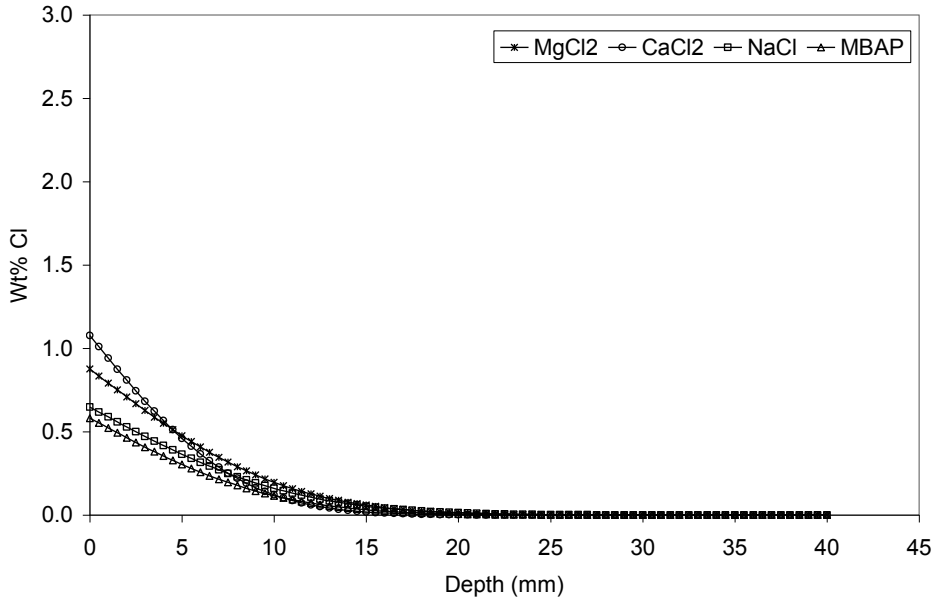

Figure A3.154. Fitted chloride profiles for 0.45 *w/c* straight portland cement mortar specimens immersed in low-concentration brines at 60 days.

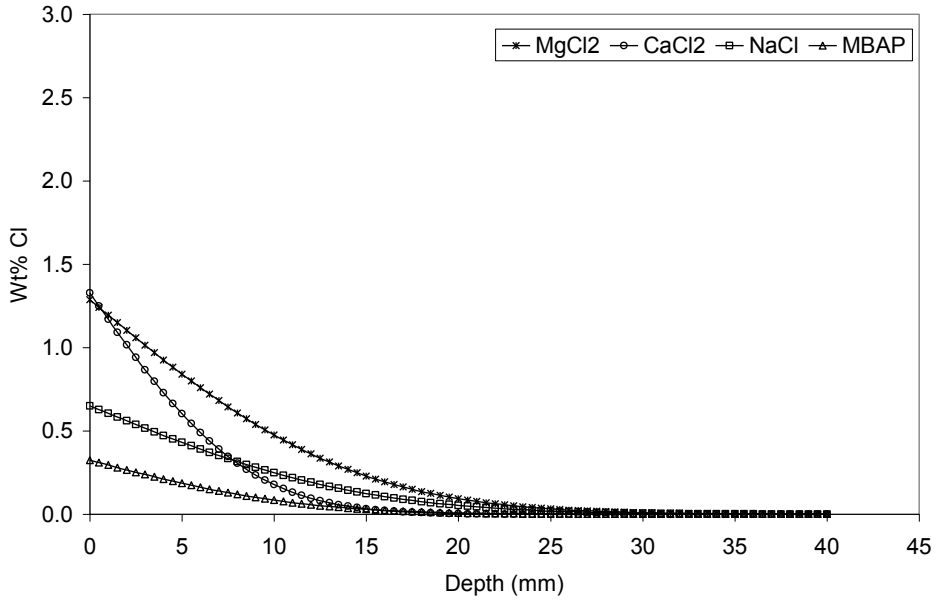

Figure A3.155. Fitted chloride profiles for 0.55 *w/c* straight portland cement concrete specimens immersed in high-concentration brines at 60 days.

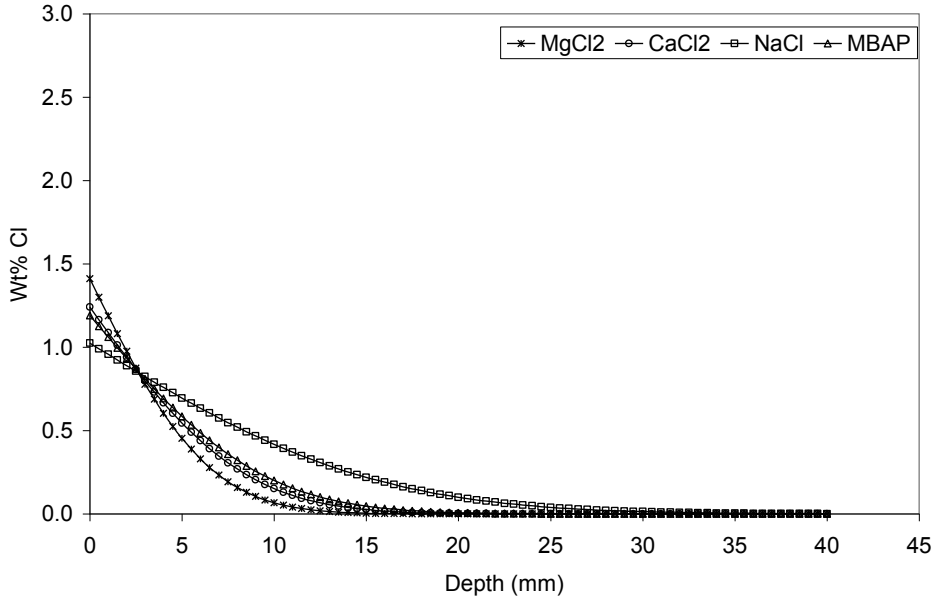

Figure A3.156. Fitted chloride profiles for 0.55 *w/c* straight portland cement mortar specimens immersed in high-concentration brines at 60 days.

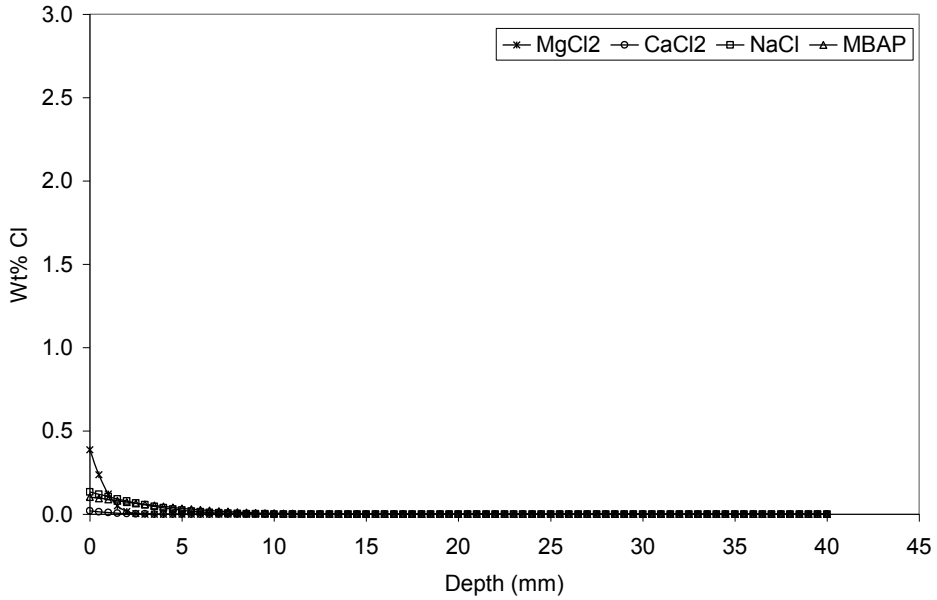

Figure A3.157. Fitted chloride profiles for 0.55 *w/c* straight portland cement concrete specimens sealed with silane and immersed in high-concentration brines at 60 days.

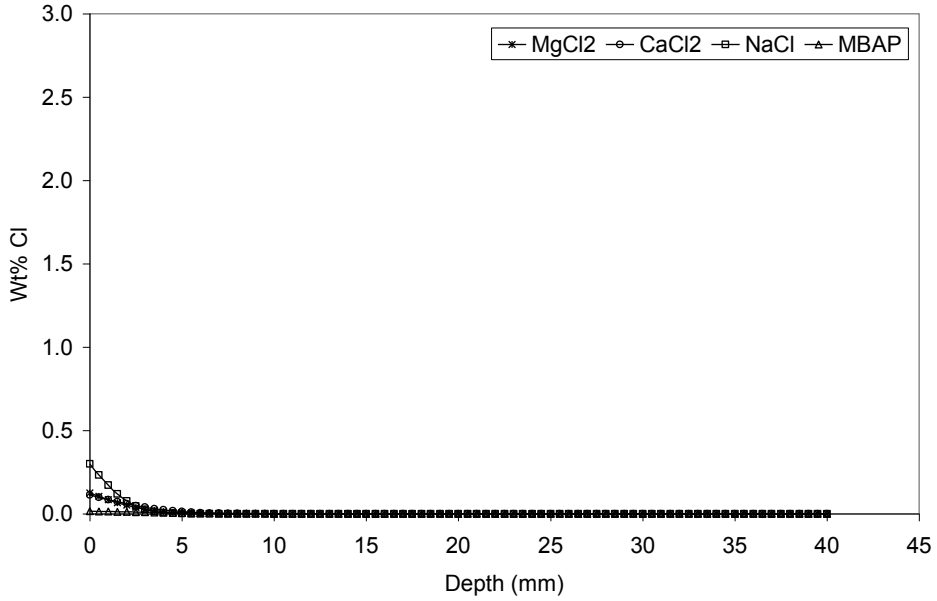

Figure A3.158. Fitted chloride profiles for 0.55 *w/c* straight portland cement concrete specimens sealed with siloxane and immersed in high-concentration brines at 60 days.

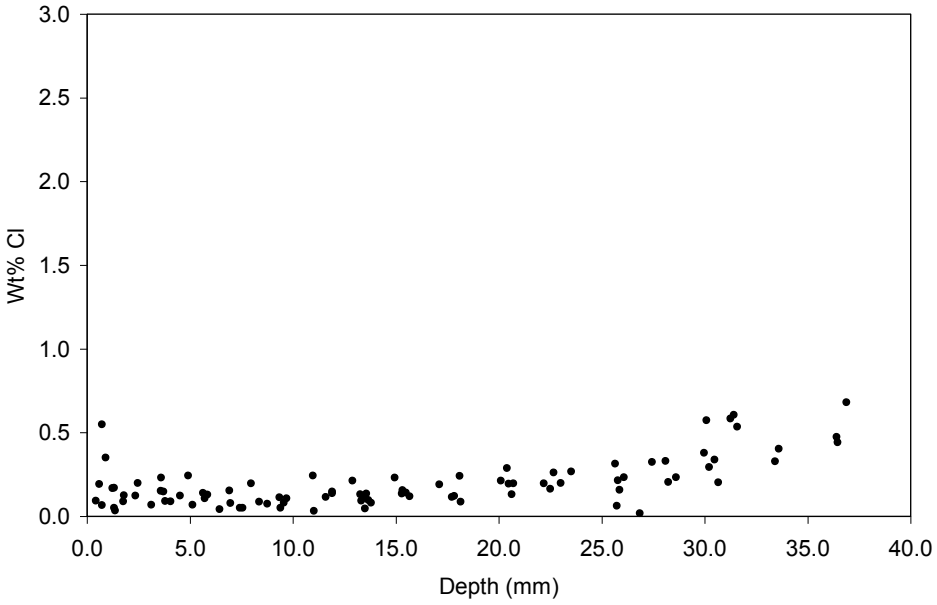

Figure A3.159. Non-fitted chloride profile from a 0.55 *w/c* straight portland cement concrete specimen sealed with silane and immersed in high-concentration $CaCl_2$ brine at 500 days.

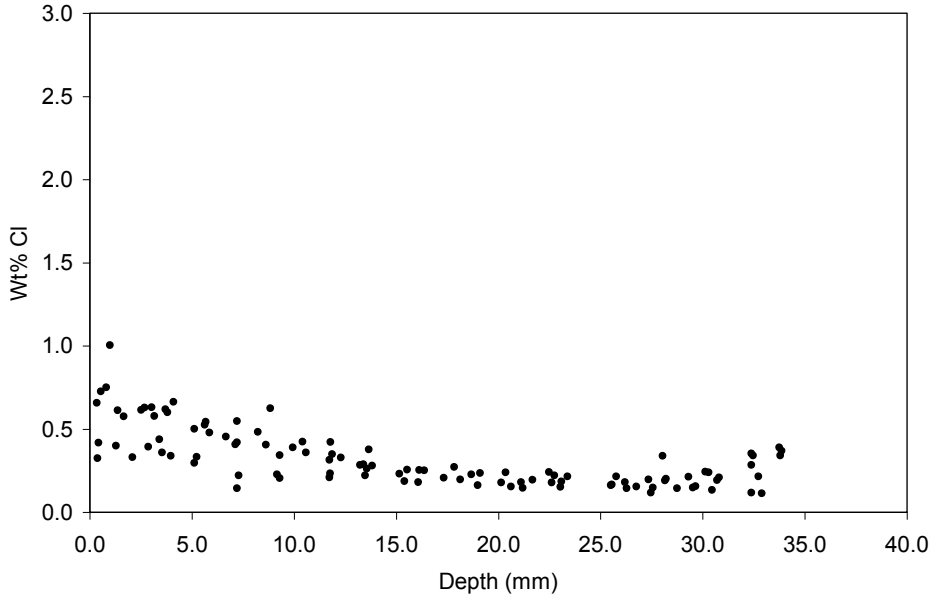

Figure A3.160. Non-fitted chloride profile from a 0.55 *w/c* straight portland cement concrete specimen sealed with silane and immersed in high-concentration $MgCl_2$ brine at 500 days.

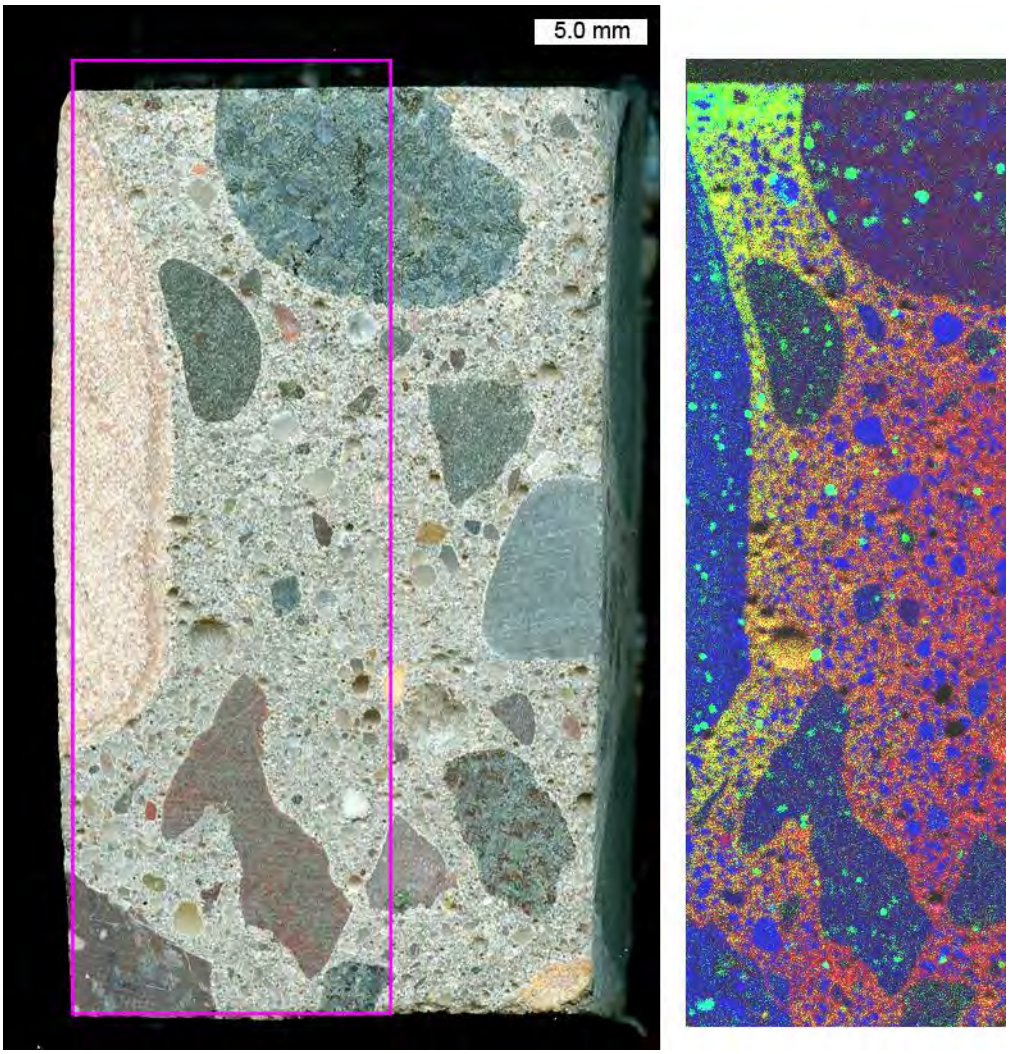

Figure A3.161. Scanned image, (left) and elemental map, (right) from diamond-ground billet cut to represent a cross-section through the near-surface of a 0.45 *w/cm* fly ash concrete specimen immersed in a high-concentration $MgCl_2$ brine for 60 days. In the elemental map, the R-channel was assigned to Ca, the G-channel was assigned to Cl, and the B-channel was assigned to Si.

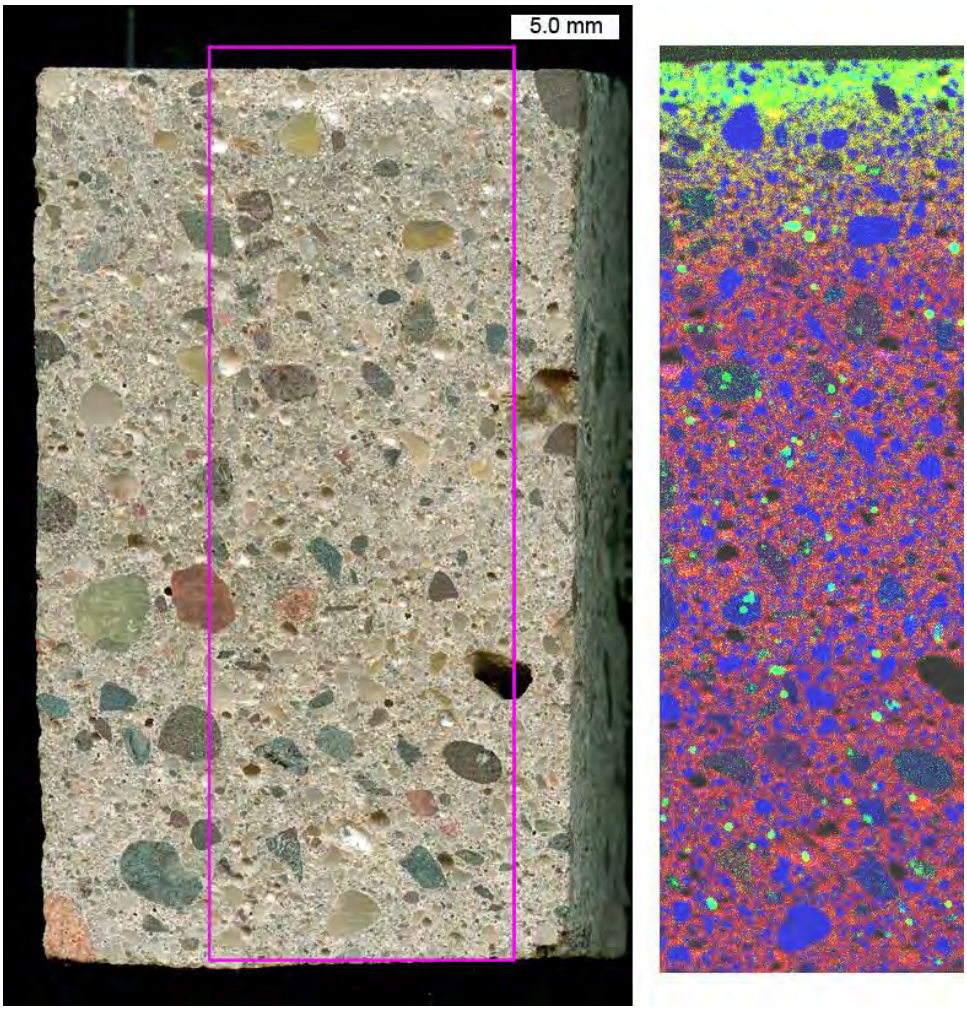

Figure A3.162. Scanned image, (left) and elemental map, (right) from diamond-ground billet cut to represent a cross-section through the near-surface of a 0.45 *w/cm* fly ash mortar specimen immersed in a high-concentration $MgCl_2$ brine for 60 days. In the elemental map, the R-channel was assigned to Ca, the G-channel was assigned to Cl, and the B-channel was assigned to Si.

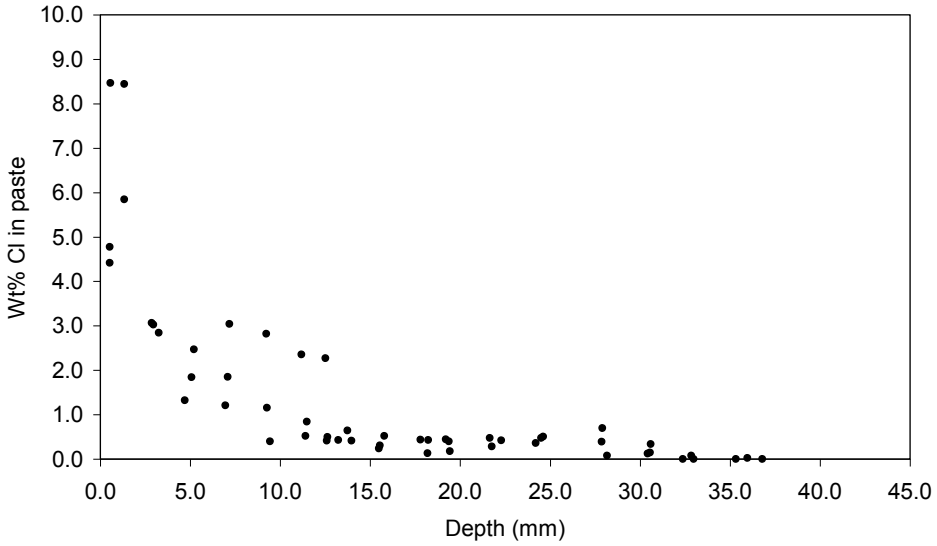

Figure A3.163. Raw profile data collected from area outlined in Figure A3.161 showing chloride concentration in paste from 0.45 *w/cm* fly ash concrete specimen immersed in high-concentration $MgCl_2$ brine for 60 days.

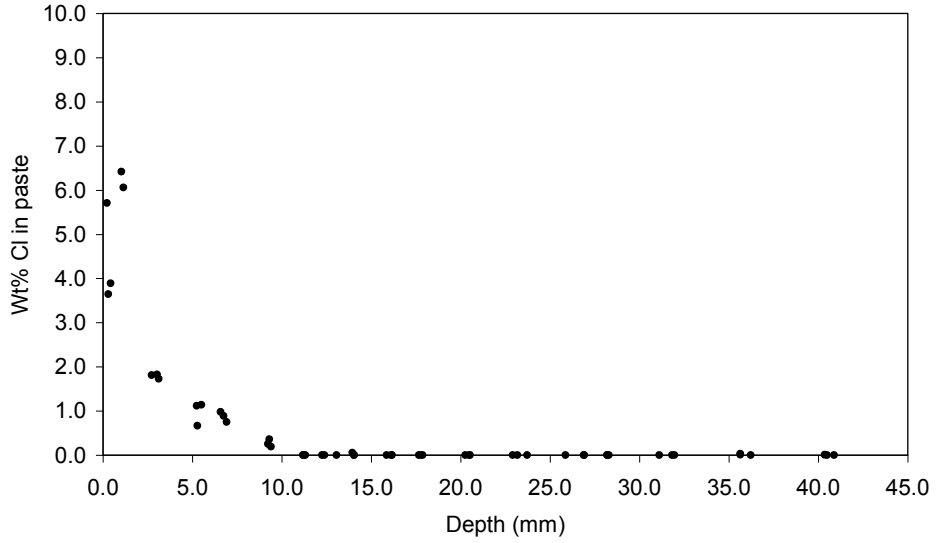

Figure A3.164. Raw profile data collected from area outlined in Figure A3.162 showing chloride concentration in paste from 0.45 *w/cm* fly ash mortar specimen immersed in high-concentration $MgCl_2$ brine for 60 days.

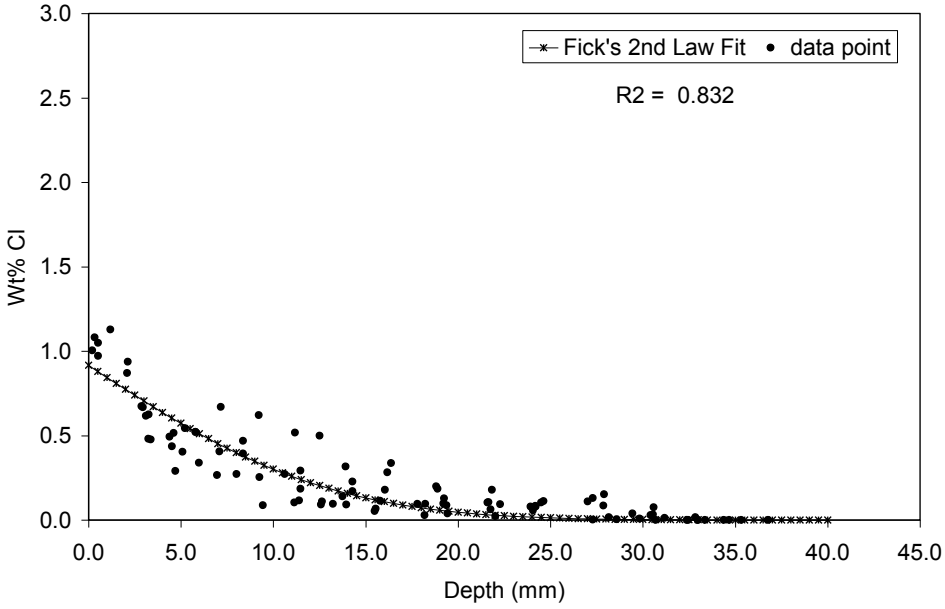

Figure A3.165. Fitted chloride profile from Figure A3.163 after correction to wt% Cl for bulk concrete. Data points listed from full pair of billets.

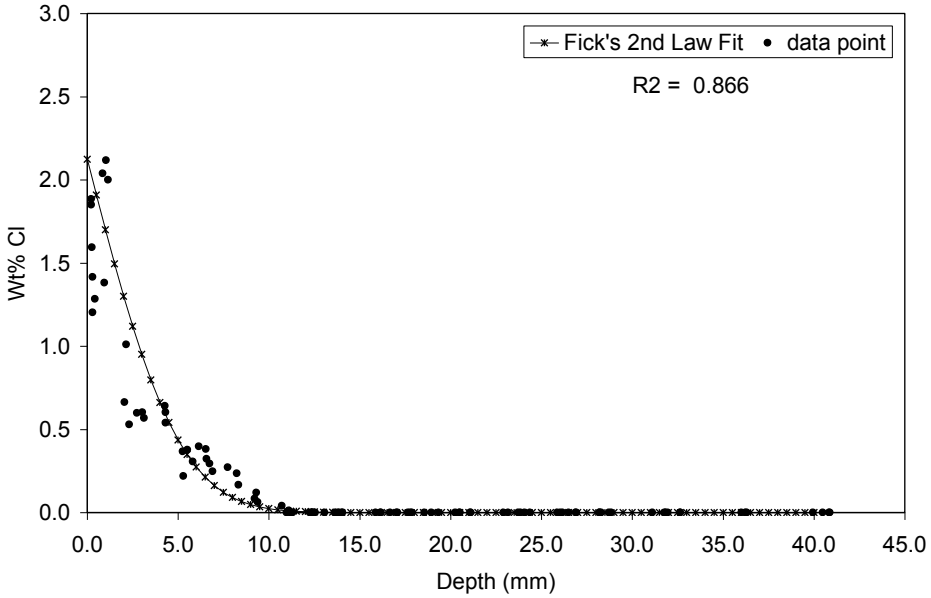

Figure A3.166. Fitted chloride profile from Figure A3.164 after correction to wt% Cl for bulk mortar. Data points listed from full pair of billets.

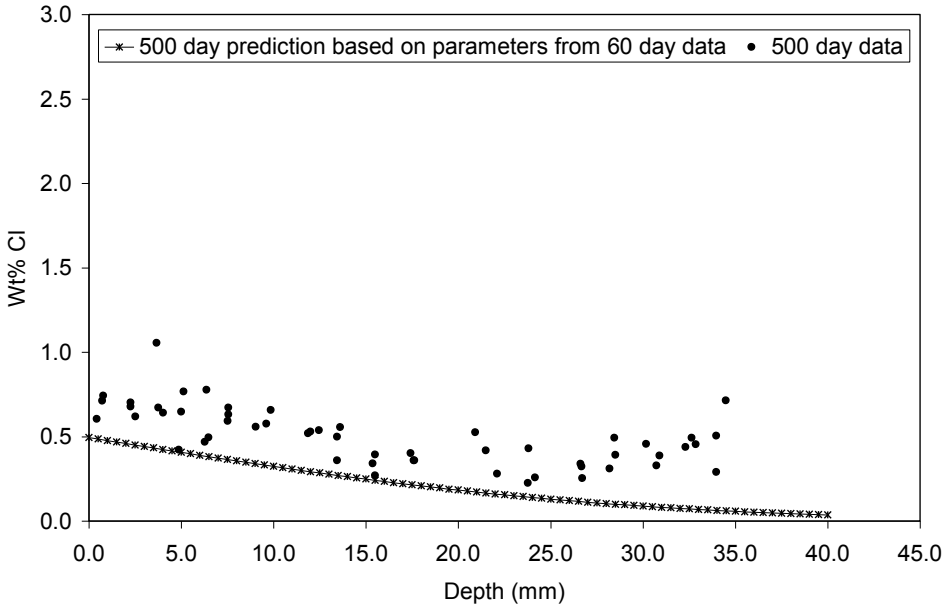

Figure A3.167. Prediction based on Fick's 2nd Law parameters from 60 day data plotted against actual 500 day data collected from a companion 0.45 *w/c* portland cement concrete sample immersed in high concentration NaCl brine.

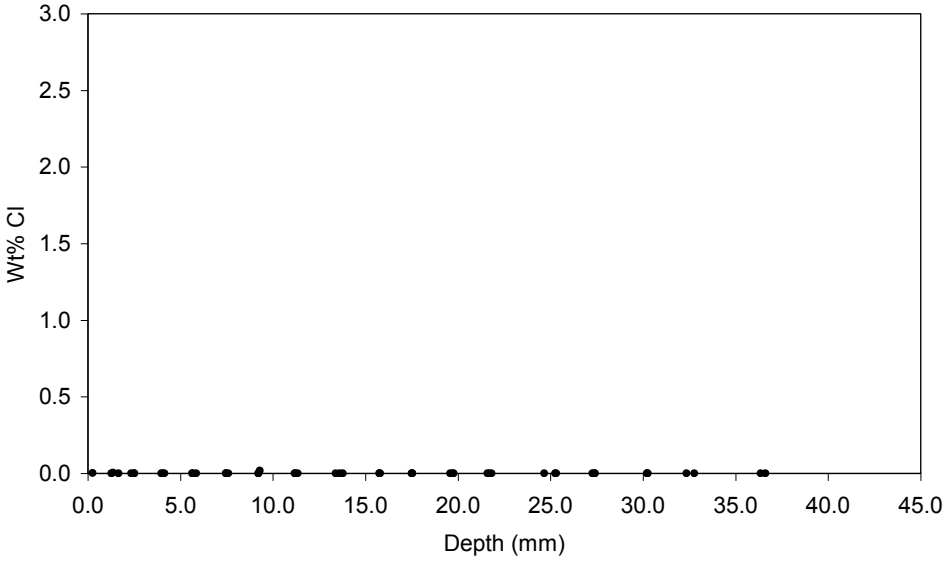

Figure A3.168. Non-fitted chloride profile from 0.45 *w/c* portland cement concrete specimen immersed in limewater for 500 days.

A3.3.2.3. X-ray Diffraction

Cement paste was extracted from the deteriorated concrete samples exposed for 500 days to the high concentration $MgCl_2$ and $CaCl_2$ brines. The paste was extracted by working portions of the deteriorated concrete through 50 mesh and 200 mesh sieves. The collected material was ground with a mortar and pestle, and examined by XRD. Mineral precipitates that formed on the external surfaces of the concrete samples exposed to the $MgCl_2$, $CaCl_2$, MBAP and CMA brines were also collected, ground and analyzed. XRD patterns in most cases were collected from the samples in both the wet and dry condition.

An XRD pattern from the wet paste extracted from the concrete exposed to the $CaCl_2$ brine is shown in Figure A3.169, along with an XRD pattern from the wet mineral precipitate collected from the exterior of the concrete exposed to the $CaCl_2$ brine. The patterns are very similar, and show that the primary phase is the 8.34, 4.13, 2.76 angstrom calcium oxychloride phase first described by Monosi and Collepardi (1990). They described the phase as $3CaO•CaCl_2•15H_2O$, but the XRD pattern listed for $3CaO•CaCl_2•15H_2O$, Joint Committee on Powder Diffraction Standards (JCPDS) Card No. 02-0280, does not match the XRD pattern they reported. The difference is shown in Figure A3.170. The calcium oxychloride crystals collected from the exterior of the concrete were subsequently oven dried at 122 ºF [50 °C] overnight and re-analyzed. At high-temperature, the calcium oxychloride reverted to $CaO•CaCl_2•2H_2O$, (JCPDS Card No. 02-1099) as shown in Figure A3.171. A time-lapse movie was recorded to observe the phase change from calcium oxychloride to $CaO•CaCl_2•2H_2O$. Figure A3.172 shows the before and after images from the time-lapse movie. Another time-lapse movie was recorded to observe the same $CaO•CaCl_2•2H_2O$ crystals after immersion in distilled water in equilibrium with atmospheric CO_2 at room temperature overnight. Figure A3.173 shows the before and after images from the time-lapse movie. The XRD pattern, (Figure A3.174) of the resultant material from the $CaO•CaCl_2•2H_2O$ immersion experiment showed that the $CaO•CaCl_2•2H_2O$ was converted to calcium carbonate ($CaCO_3$) (JCPDS Card No. 05-0586) (Note: calcium carbonate is cataloged by its mineral name, calcite, in the JCPDS diffraction database). A second sample of calcium oxychloride was subjected to a brine-cure treatment where it was heated to 122 °F [50 °C] overnight in a sealed container filled with $CaCl_2$ brine. Figure A3.175 shows before and after images of a time-lapse movie recorded of the hot brine-cure experiment. After treatment, the XRD pattern (Figure A3.176) showed that some calcium oxychloride remained, but there were also new peaks present for calcium hydroxide, JCPDS Card No. 04-0733 (Note: calcium hydroxide is cataloged by its mineral name, portlandite, in the JCPDS diffraction database). In another experiment, the extracted cement paste sample was allowed to air dry for one week and re-analyzed. Peaks for calcite ($CaCO_3$, JCPDS Card No. 05-0586) and quartz (SiO_2, JCPDS Card No. 46-1045) were observed in the dried paste, and no peaks were observed for calcium oxychloride or $CaO•CaCl_2•2H_2O$, as shown in Figure A3.177.

The XRD pattern from the wet paste extracted from the concrete exposed to the $MgCl_2$ brine, and the XRD pattern from the wet mineral precipitate collected from the exterior concrete exposed to the $MgCl_2$ brine showed very little similarity. Peaks for $Mg_3(OH)_5Cl•4H_2O$, (JCPDS Card no. 07-0420) were observed in the exterior mineral precipitate, but not in the wet paste. The calcium oxychloride phase was not observed in either of the XRD patterns.

The patterns are shown in Figure A3.178. The $Mg_3(OH)_5Cl•4H_2O$ crystals collected from the exterior of the concrete were subsequently oven dried at 122 °F [50 °C] overnight and re-analyzed. After the high-temperature experiment, some $Mg_3(OH)_5Cl•4H_2O$ remained, but new peaks for $MgCl_2•6H_2O$ (JCPDS Card No. 25-0515) were also observed, as shown in Figure A3.179. The extracted paste was allowed to air dry and was re-analyzed. The patterns from the wet extracted paste and the air-dried extracted paste were very similar, as shown in Figure A3.180. The wet paste sample dried very quickly in the diffractometer and displayed cracking after the first X-ray analysis was completed.

Wet mineral precipitates collected from the exterior of concrete that was exposed to the MBAP solution consisted primarily of $Mg_3(OH)_5Cl•4H_2O$, as shown in Figure A3.181.

Mineral precipitates collected from the exterior of concrete that was soaked in the low-concentration calcium magnesium acetate (CMA) solution consisted primarily of calcite, as shown in Figure A3.182.

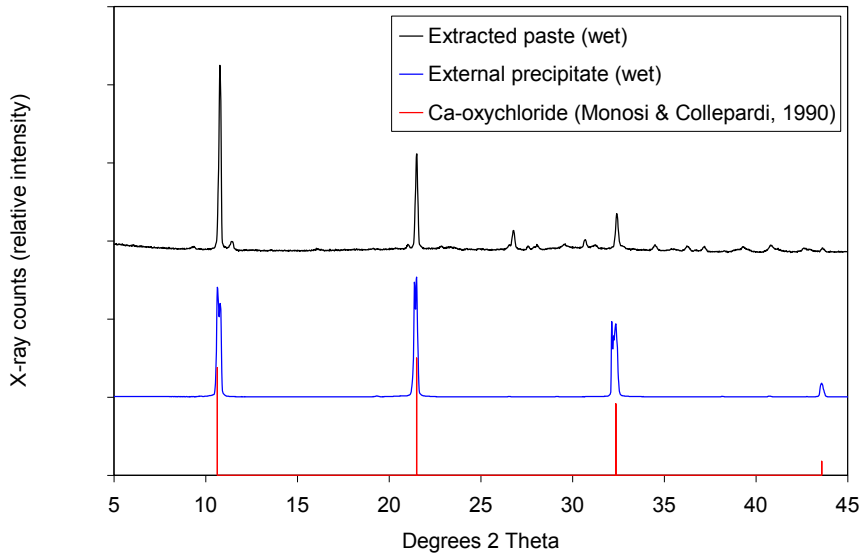

Figure A3.169. XRD patterns from the wet extracted paste and the wet exterior precipitate collected from concrete exposed to $CaCl_2$ brine for 500 days compared to the reference 8.34, 4.13, 2.76 angstrom peaks for Monosi and Collepardi's calcium oxychloride phase.

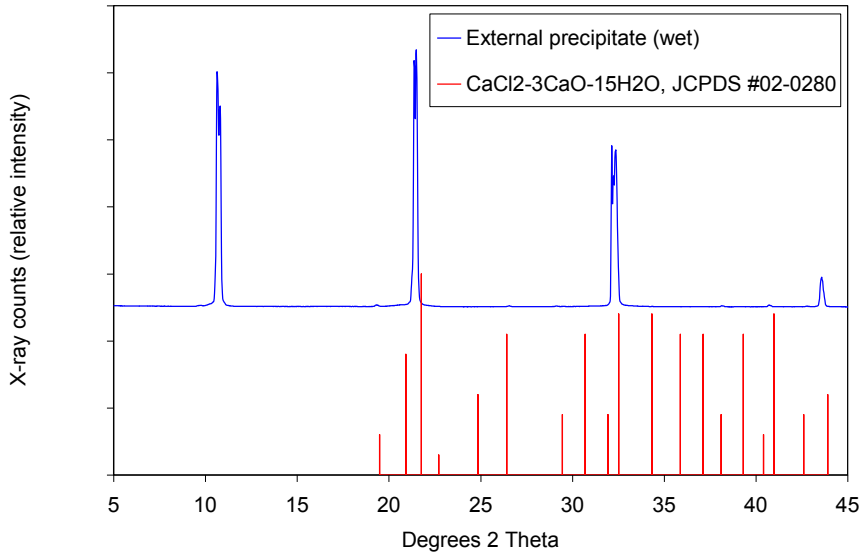

Figure A3.170. XRD pattern from the wet precipitate collected from the exterior of concrete exposed to $CaCl_2$ brine for 500 days compared to $3CaO•CaCl_2•15H_2O$ reference peaks.

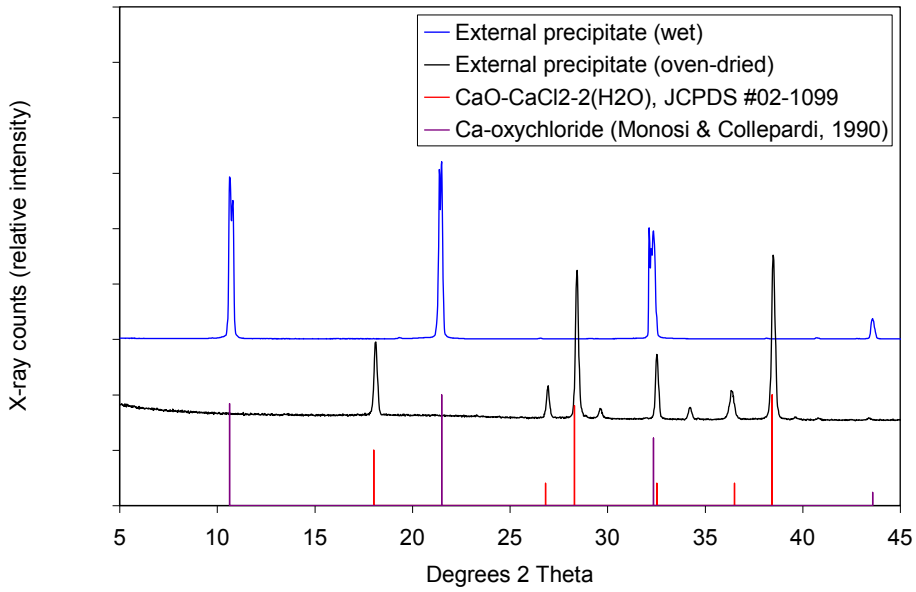

Figure A3.171. XRD patterns from the wet and oven-dried external precipitate collected from concrete exposed to $CaCl_2$ brine for 500 days compared to reference patterns for calcium oxychloride and $CaCl_2•Ca(OH)_2•2H_2O$.

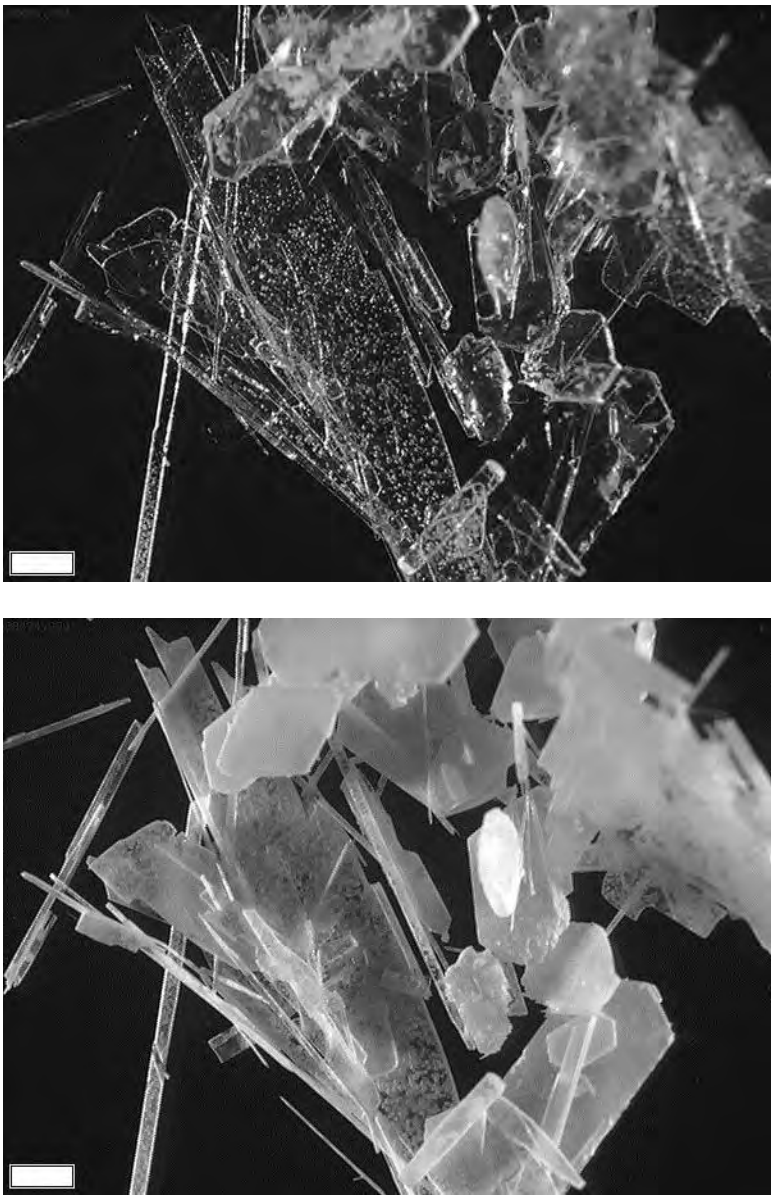

Figure A3.172. Fresh calcium oxychloride crystals before, (top) and after oven drying and conversion to $CaCl_2 \bullet Ca(OH)_2 \bullet 2H_2O$, (bottom) scale bar = 1mm.

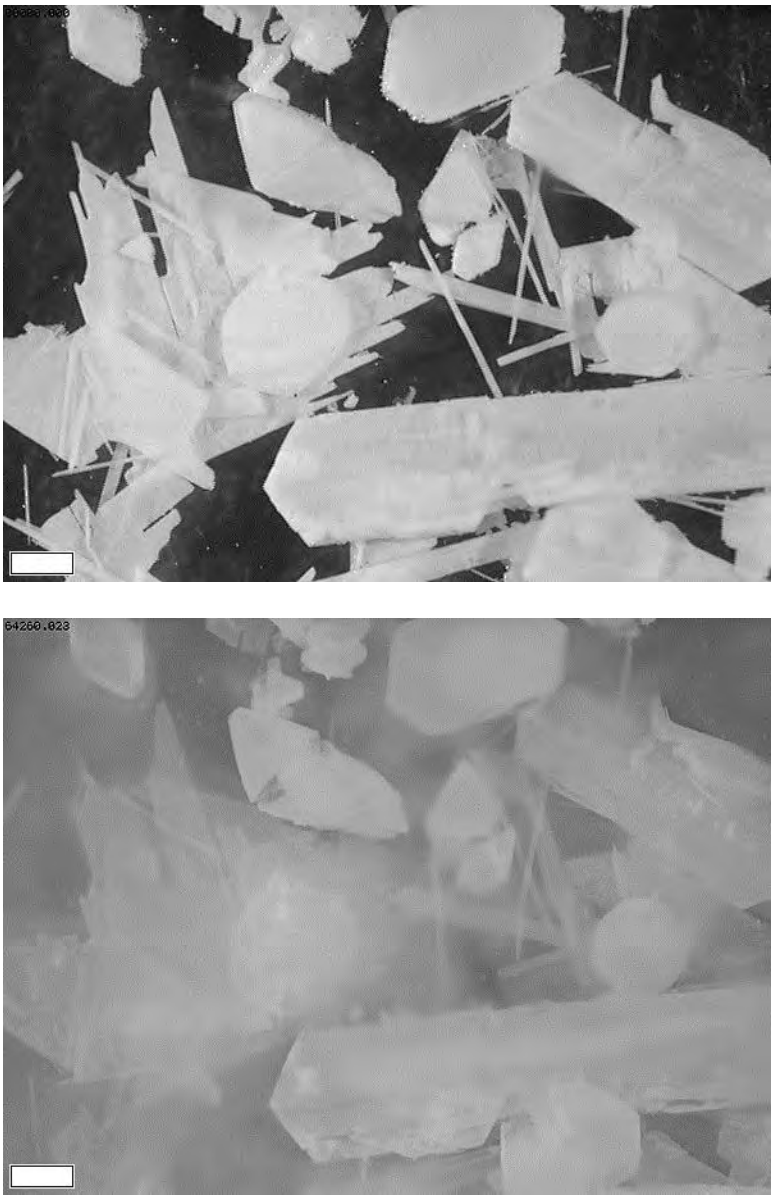

Figure A3.173. $CaCl_2 \cdot Ca(OH)_2 \cdot 2H_2O$ crystals before, (top) and after immersion in distilled water in atmospheric equilibrium with CO_2 at room temperature and subsequent alteration, (bottom) scale bar = 1mm.

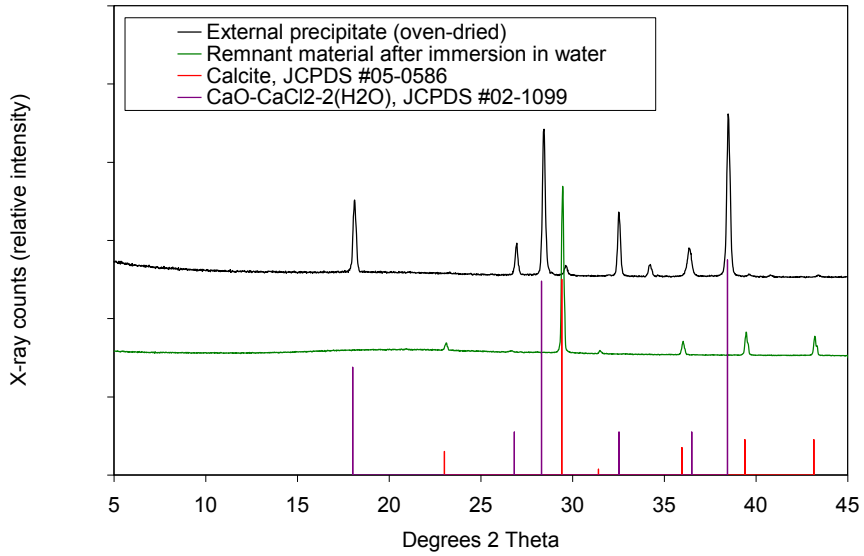

Figure A3.174. XRD patterns from oven-dried external precipitate crystals, and the resultant remnant material after immersion in room temperature water, as compared to a reference patterns for calcite and $CaCl_2 \bullet Ca(OH)_2 \bullet 2H_2O$.

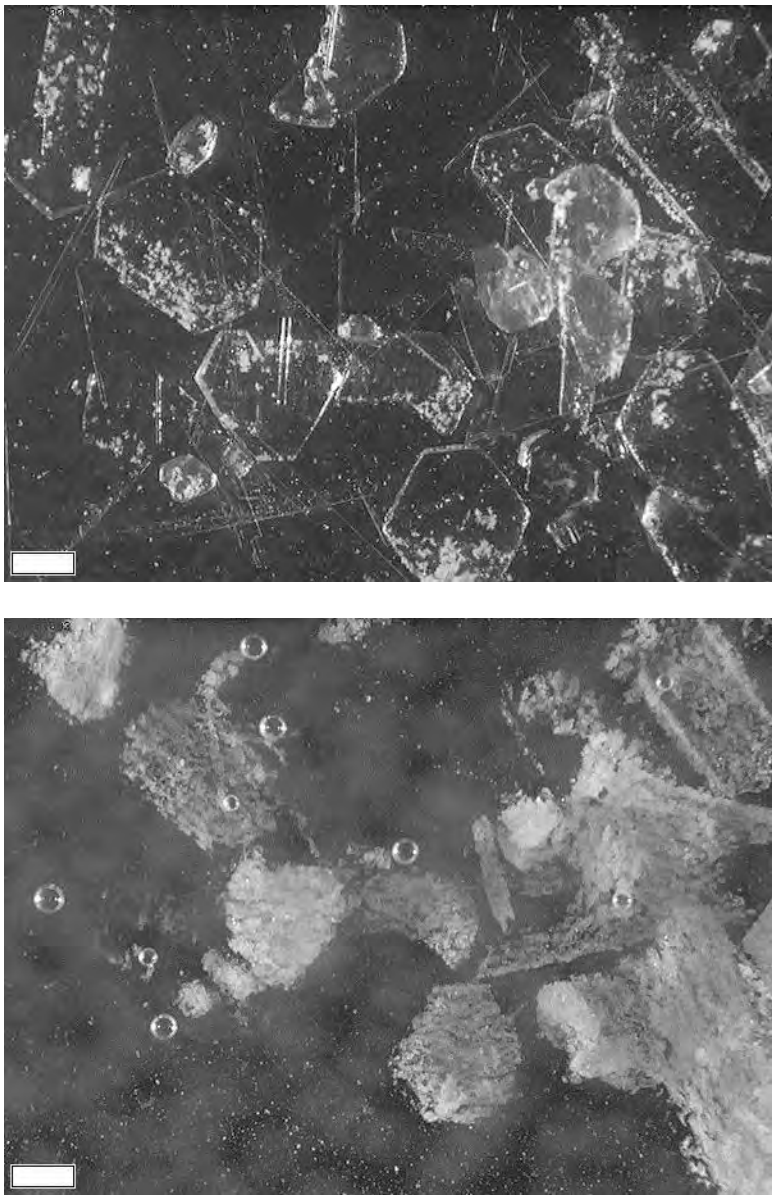

Figure A3.175. Fresh calcium oxychloride crystals before, (top) and after immersion in a sealed container of hot $CaCl_2$ brine, (bottom) scale bar = 1 mm.

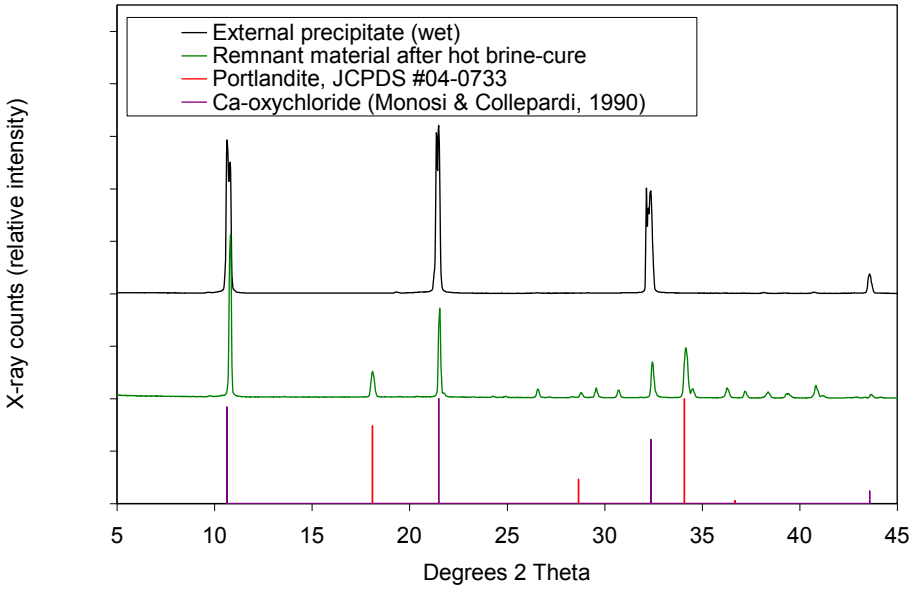

Figure A3.176. XRD patterns from wet external precipitate, and the resultant remnant material after curing in hot $CaCl_2$ brine, with reference patterns for calcium oxychloride and portlandite.

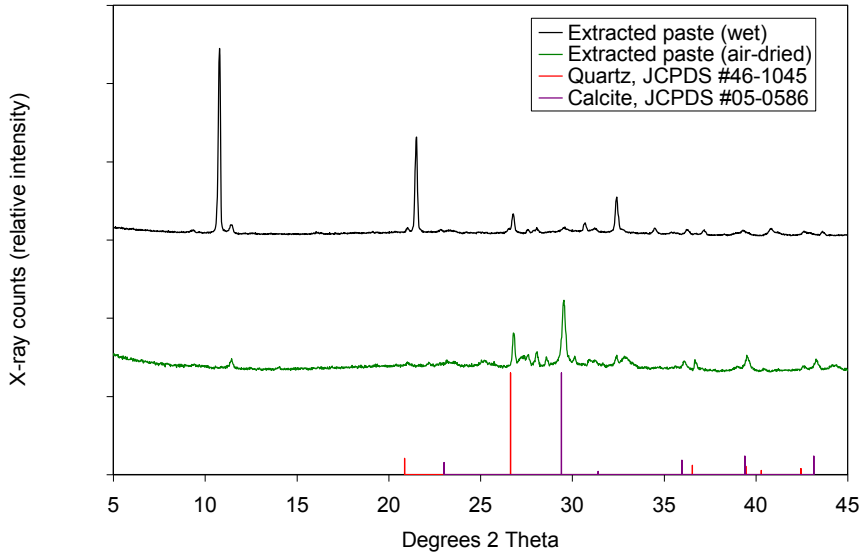

Figure A3.177. XRD patterns from the wet and air-dried extracted paste collected from concrete specimens exposed to $CaCl_2$ brine for 500 days, with reference patterns for calcite and quartz.

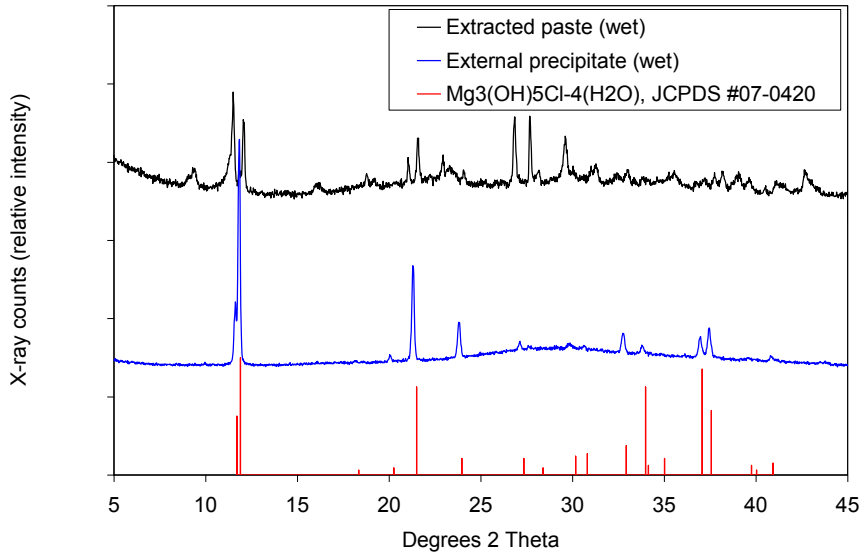

Figure A3.178. XRD patterns from the wet extracted paste and wet external precipitate collected from concrete exposed to $MgCl_2$ brine for 500 days, with reference pattern for $Mg_3(OH)_5Cl•4H_2O$.

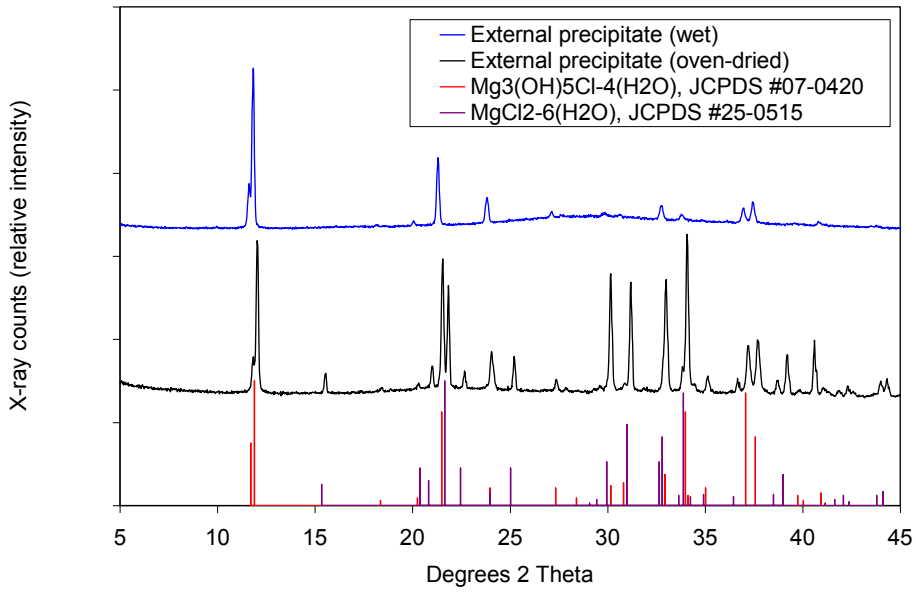

Figure A3.179. XRD patterns from the wet and oven dried external precipitate collected from concrete exposed to $MgCl_2$ brine for 500 days, with reference patterns for $Mg_3(OH)_5Cl•4H_2O$ and $MgCl_2•6H_2O$.

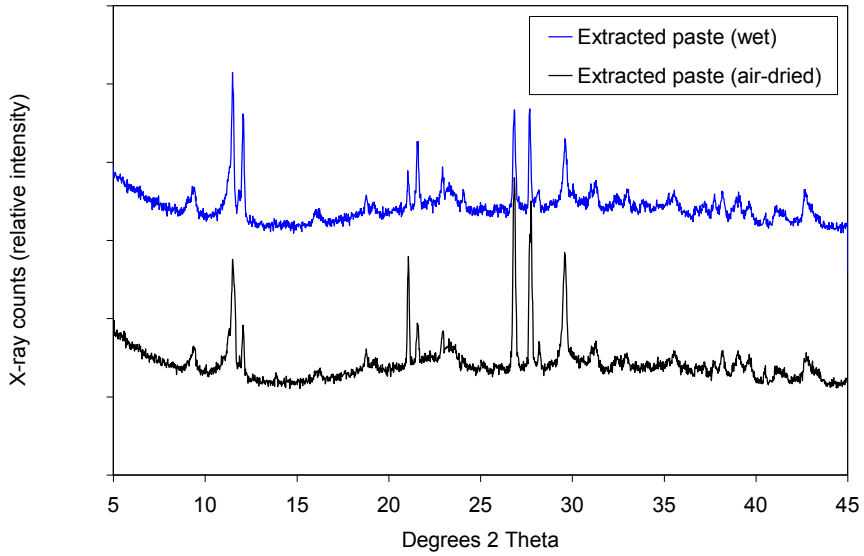

Figure A3.180. XRD patterns from the wet and air-dried extracted paste collected from concrete exposed to $MgCl_2$ brine for 500 days.

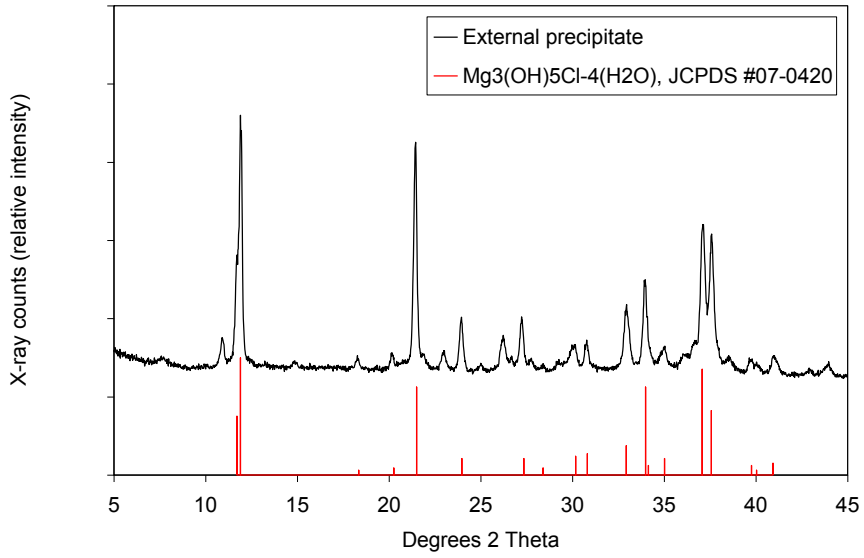

Figure A3.181. XRD pattern from the external precipitate collected from concrete exposed to MBAP solution for 500 days, with reference pattern for $Mg_3(OH)_5Cl{\bullet}4H_2O$.

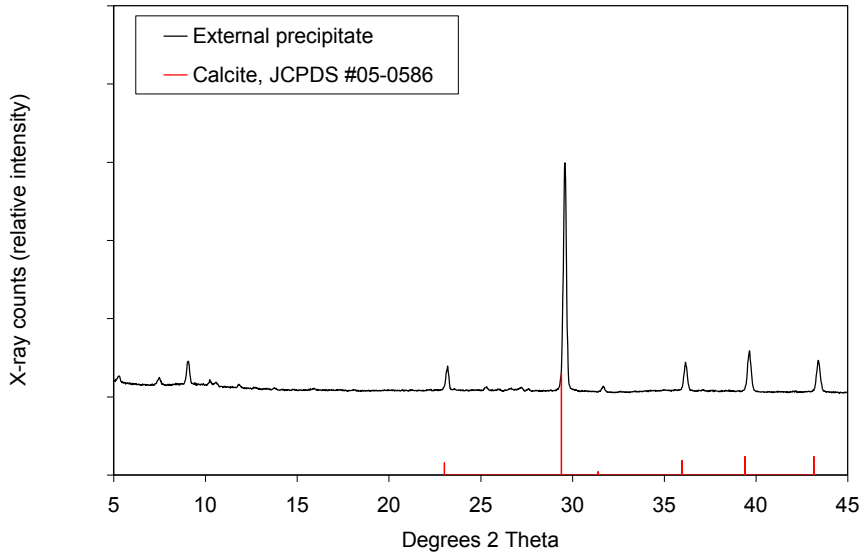

Figure A3.182. XRD pattern from the external precipitate collected from concrete exposed to CMA solution for 500 days, with reference pattern for calcite.

A3.3.2.4 Optical Microscopy

Sample Preparation

Thin sections were prepared from 0.45 *w/c* portland cement concrete specimens to represent all of the high-concentration brines and the limewater control after 500 days of immersion. Thin sections were also prepared from 0.45 *w/cm* concrete specimens with supplementary fly ash and GGBFS, but only those exposed to the $CaCl_2$, $MgCl_2$, and MBAP brine solutions for 500 days. An additional thin section was also prepared from a 0.55 *w/c* concrete specimen that had been sealed with silane and immersed in high-concentration $MgCl_2$ brine for 500 days. Specimens that were in an advanced state of deterioration, namely the 0.45 *w/c* specimens from the $CaCl_2$, $MgCl_2$, and MBAP brines, were dried in a 122 ºF [50 ºC] convection oven overnight, and then vacuum impregnated with epoxy. After stabilization, these specimens, along with the others, were cut into slabs with a kerosene cooled diamond saw. The slabs were further cut into billets, and the billets prepared in thin section using water-free methods.

Comparison of the 0.45 w/c Concrete Specimens from the Six Solutions

Figure A3.183 shows epifluorescent mode images from all of the 0.45 *w/c* straight portland cement concrete specimens. The images depict the specimens in cross-section, with the top surfaces of each specimen facing towards the right hand-side. Cracking planes sub-parallel to the surface are evident in the specimens exposed to the $CaCl_2$, $MgCl_2$, and MBAP brines, while the specimens exposed to the CMA and NaCl brines, and the specimen exposed to the limewater, do not show any cracking. Figure A3.184 shows further close-up epifluorescent mode images from the same areas outlined in pink from Figure A3.183. Figures A3.185

through A3.187 show close-up images of the cracks in the specimens exposed to $CaCl_2$, $MgCl_2$, and MBAP brines. In all of these specimens, a similar pattern of blocky birefringent crystals is observed in the cracks and air voids in the deteriorated regions. The crystals have the same birefringence colors as calcium hydroxide, but their blocky appearance departs from the usual calcium hydroxide morphology, which generally occurs as stacks of thin hexagonal plates, or as isolated thin hexagonal plates. The cement paste in the deteriorated portions is generally devoid of calcium hydroxide. The lack of calcium hydroxide in the paste is most noticeable when viewed under crossed-polars. The cement paste, usually speckled with bright patches of birefringent calcium hydroxide appears dark when calcium hydroxide is not present. Figures A3.188 through A3.190 show images of cement paste with abundant calcium hydroxide. These images were taken from areas just below the surfaces of the 0.45 *w/c* straight portland concrete specimens exposed to the NaCl, CMA, and limewater solutions. Secondary calcium hydroxide deposits are present in the air voids of the specimen immersed in limewater, as shown in Figure A3.190. The shape of these calcium hydroxide crystals, long and thin in cross-section, is a typical morphology for secondary calcium hydroxide, and in contrast to the blocky morphology demonstrated in the air voids and cracks of the deteriorated specimens (Figures A3.185 through A3.187).

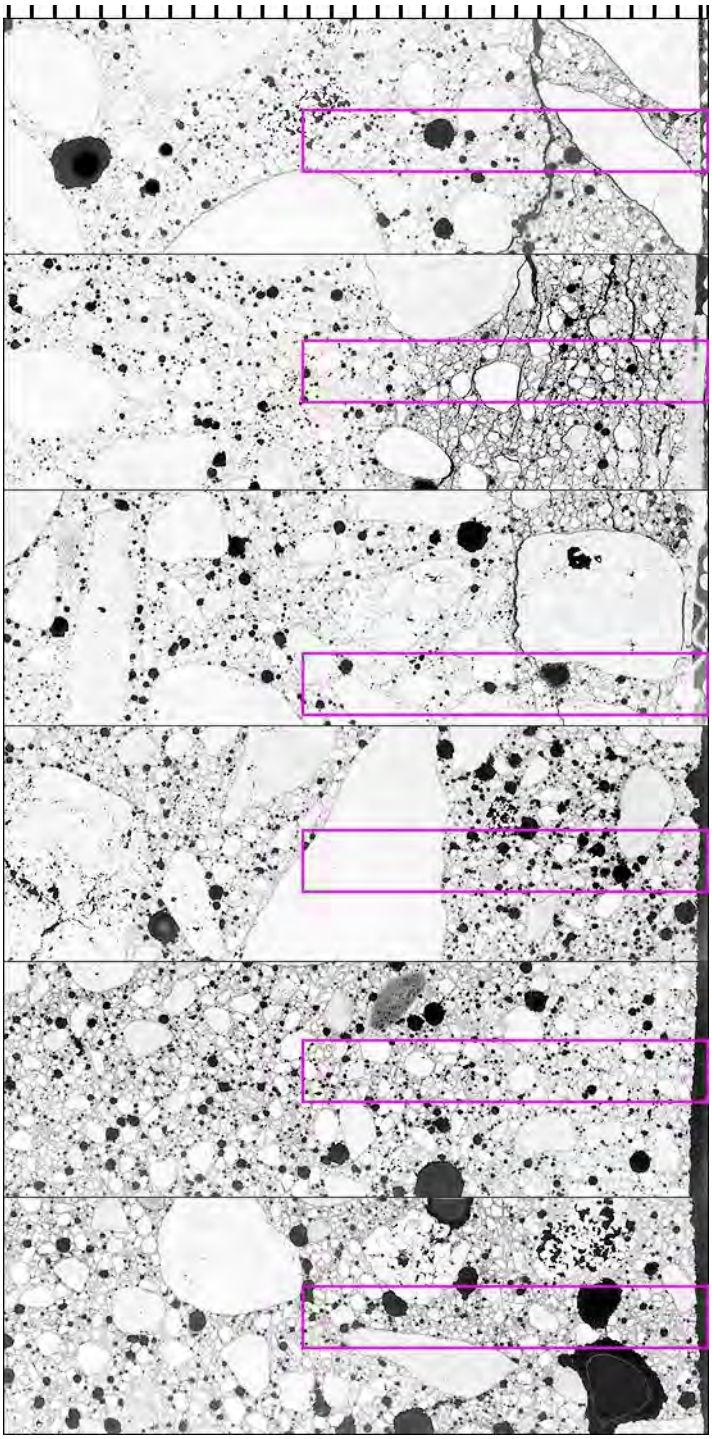

Figure A3.183. Epifluorescent thin section views of the 0.45 *w/c* concrete specimens immersed in solution for 500 days, exterior surfaces to the right. From top to bottom: CaCl2, MgCl2, MBAP, NaCl, CMA, and limewater, tic marks every mm. Pink boxes highlight close-up regions shown in Figure A3.184.

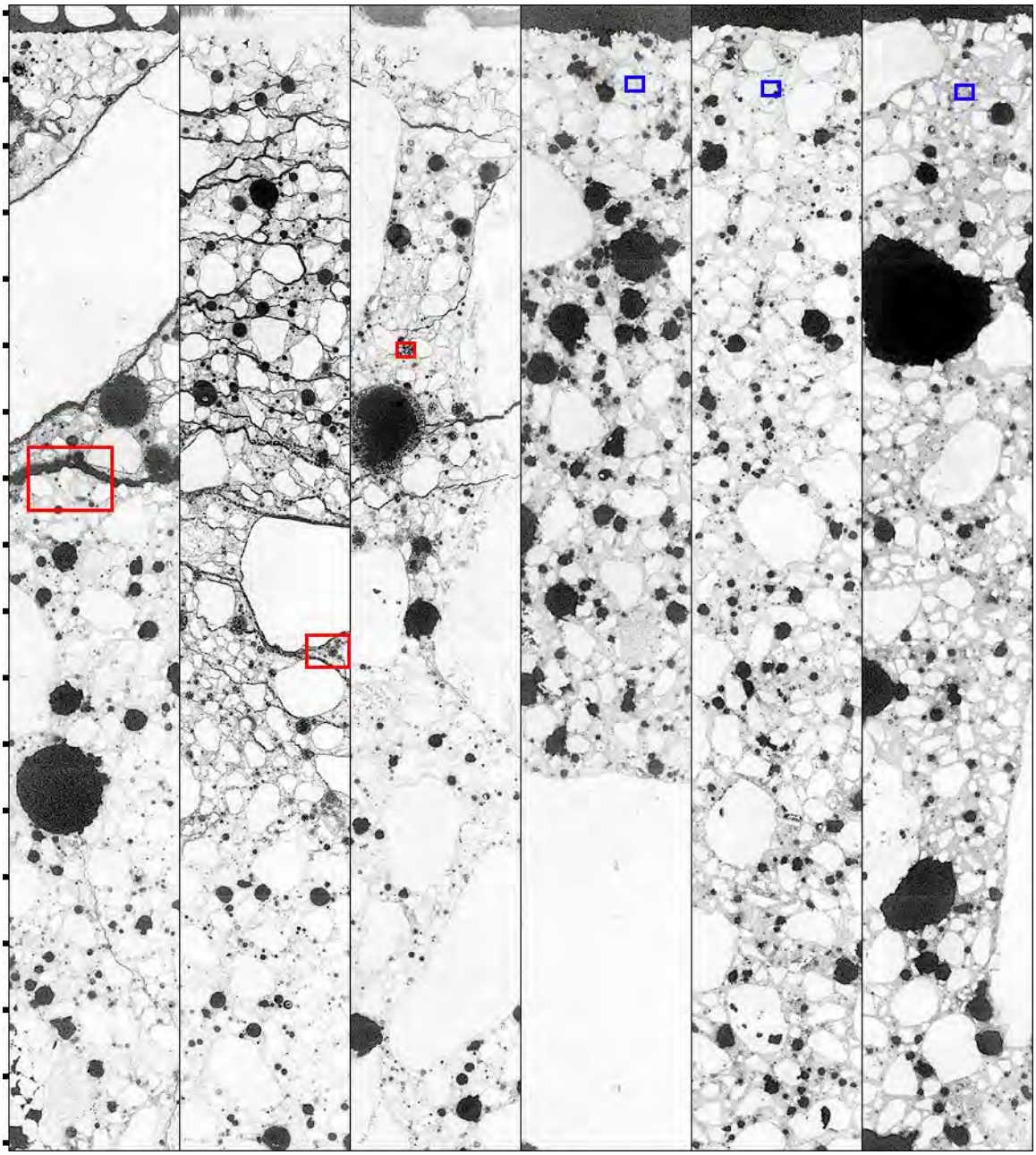

Figure A3.184. Close-up views of regions outlined in pink in Figure A3.183, but with exterior surfaces oriented towards the top. Cross-sectional epifluorescent mode images of the 0.45 *w/c* concrete specimens after 500 days of immersion in solution. From left to right: $CaCl_2$, $MgCl_2$, MBAP, NaCl, CMA, and limewater, tic marks every mm. Red boxes highlight locations of close-up images of deterioration in Figures A3.185 through A3.187. Blue boxes show locations of close-up images of calcium hydroxide in the cement paste in Figures A3.188 through A3.190.

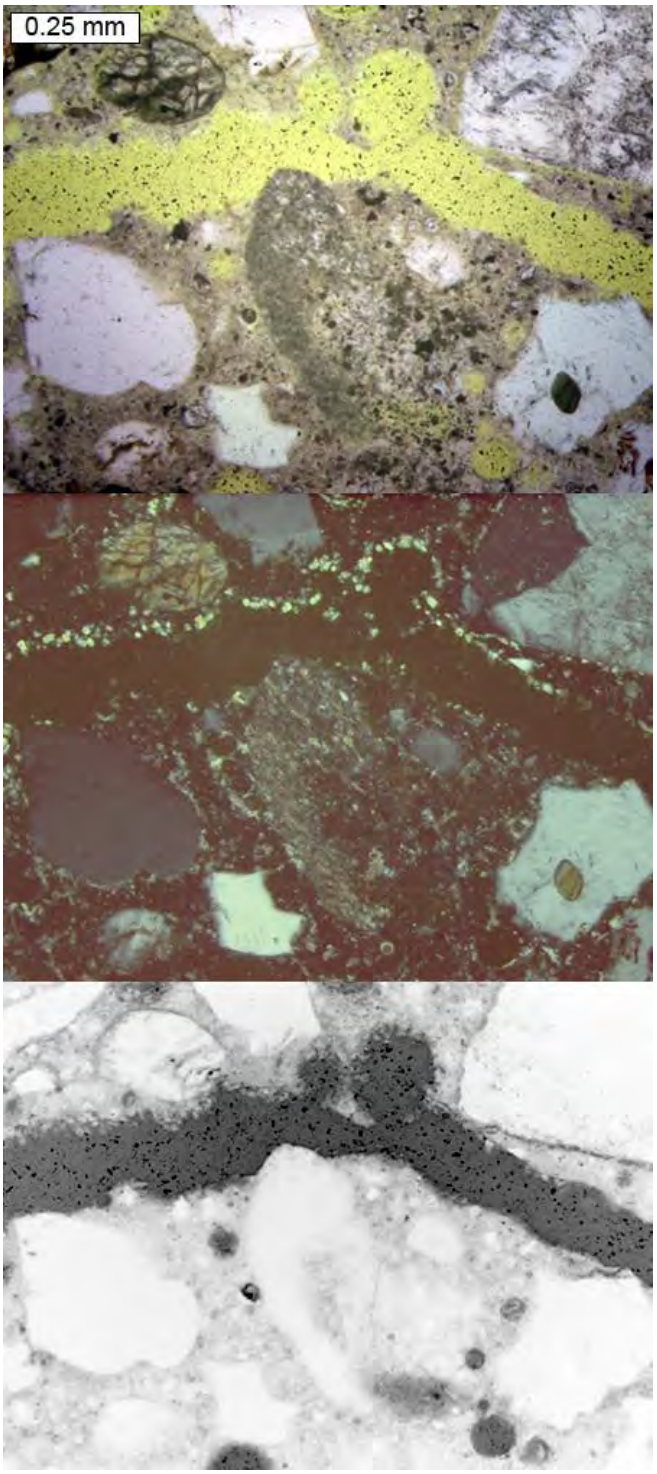

Figure A3.185. Close-up view of deteriorated portion from 0.45 *w/c* straight portland concrete specimen exposed to $CaCl_2$ brine. From top to bottom: transmitted light, crossed-polars, and epifluorescent mode images.

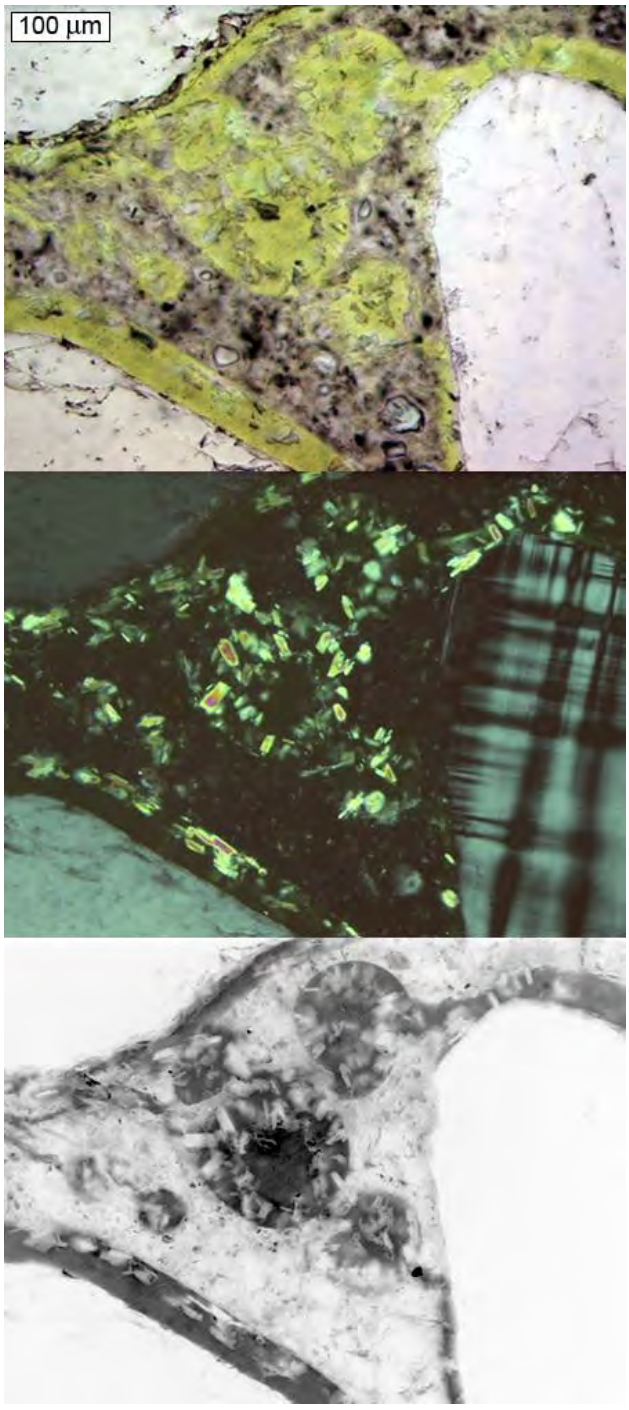

Figure A3.186. Close-up view of deteriorated portion from 0.45 *w/c* straight portland concrete specimen exposed to $MgCl_2$ brine. From top to bottom: transmitted light, crossed-polars, and epifluorescent mode images.

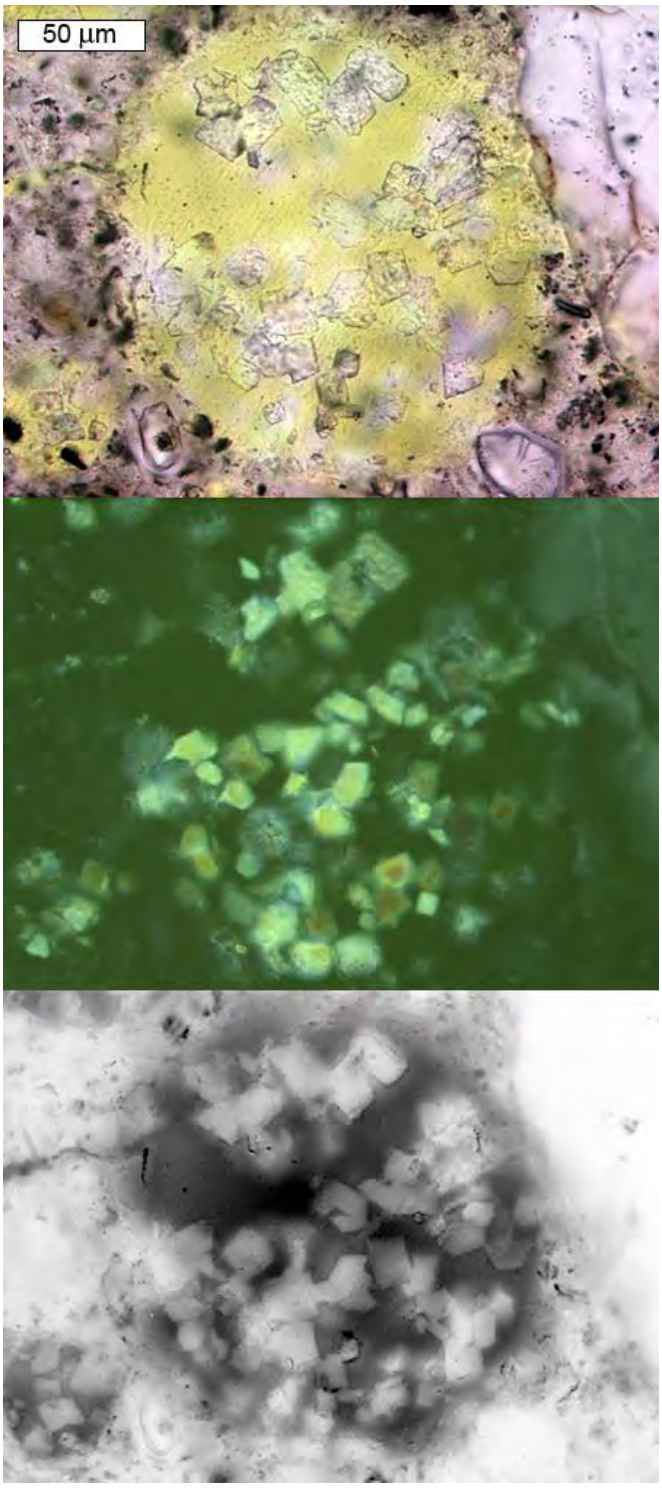

Figure A3.187. Close-up view of deteriorated portion from 0.45 *w/c* straight portland concrete specimen exposed to MBAP brine. From top to bottom: transmitted light, crossed-polars, and epifluorescent mode images.

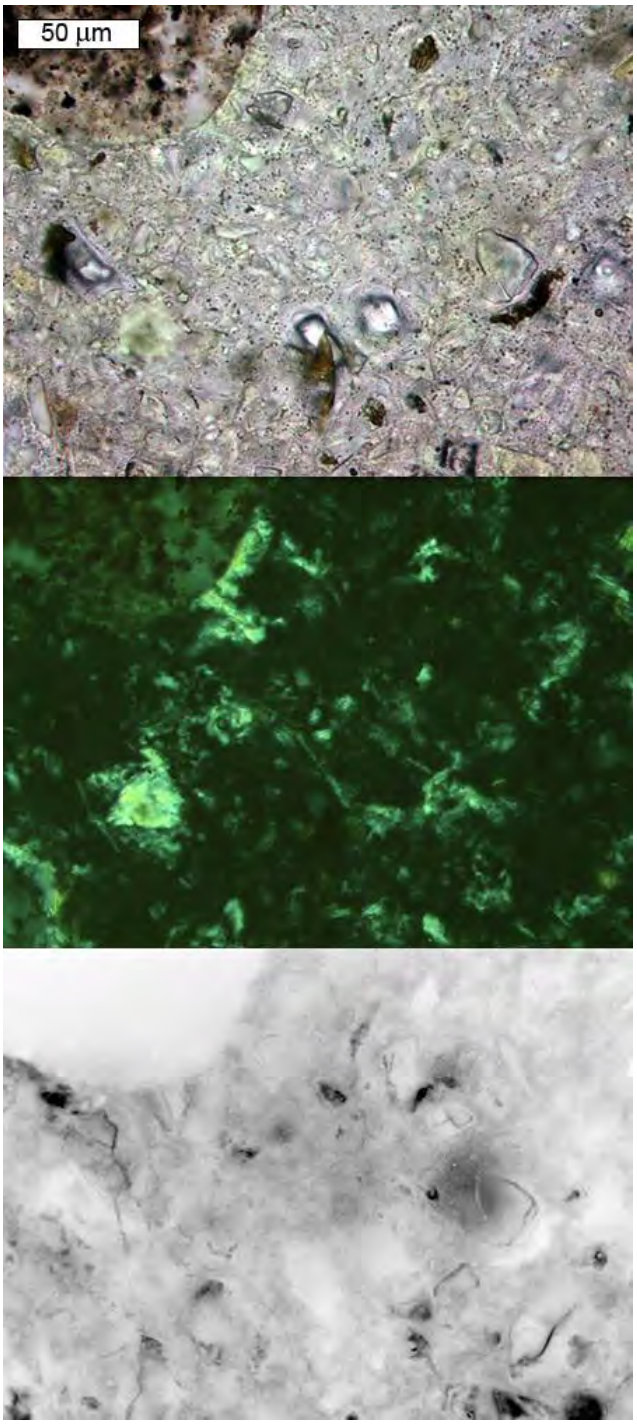

Figure A3.188. Cement paste just below the surface from 0.45 *w/c* straight portland cement concrete specimen exposed to NaCl brine. From top to bottom: transmitted light, crossed-polars, and epifluorescent mode images.

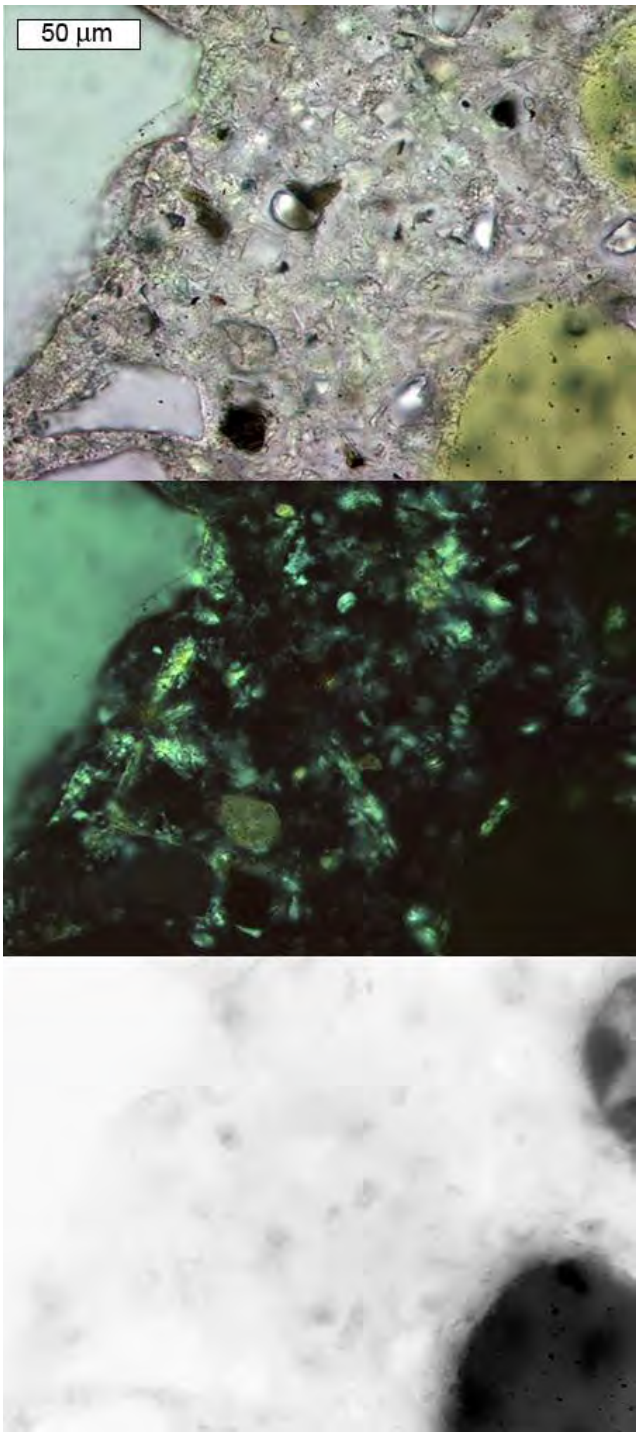

Figure A3.189. Cement paste just below the surface from 0.45 *w/c* straight portland cement concrete specimen exposed to CMA brine. From top to bottom: transmitted light, crossed-polars, and epifluorescent mode images.

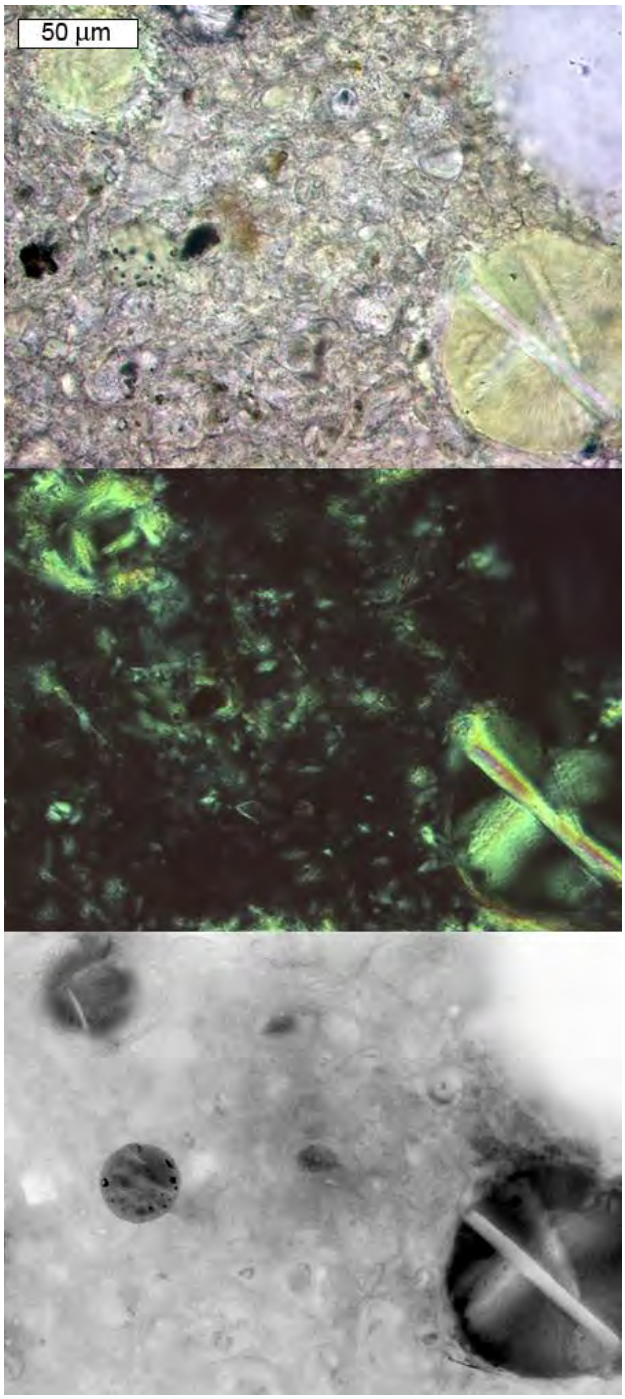

Figure A3.190. Cement paste just below the surface from 0.45 *w/c* straight portland cement concrete specimen exposed to limewater. Secondary calcium hydroxide deposits also present in air voids. From top to bottom: transmitted light, crossed-polars, and epifluorescent mode images.

Comparison of the 0.45 w/c Concrete Specimens Immersed in $CaCl_2$ Brine

Figure A3.191 shows epifluorescent mode images from the 0.45 *w/c* straight portland cement, fly ash, and GGBFS concrete specimens after 500 days immersion the high-concentration $CaCl_2$ brine. The images depict the specimens in cross-section, with the top surfaces of each specimen facing towards the right hand-side. Figure A3.192 shows further close-up epifluorescent mode images from the areas outlined in pink from Figure A3.191. In Figure A3.192, the straight portland cement concrete specimen shows the most severe cracking. Cracks are also present in the fly ash concrete specimen, but to a lesser degree. At the scale of the image in Figure A3.192, cracks are not observed in the GGBFS concrete specimen. The green-dashed lines in Figure A3.192 approximately mark the extent of calcium hydroxide depletion in the cement paste, which occurred in all three of the specimens. Above the green lines, calcium hydroxide is depleted from the cement paste, below the green lines, calcium hydroxide is present in the cement paste. Example images of depleted and non-depleted paste from the three specimens are included in Figures A3.193 through A3.195. The red lines show the horizons where images were taken of calcium hydroxide depleted-paste. The blue lines show the horizons where images were taken with calcium hydroxide still present in the paste. In the non-depleted regions of cement paste, calcium hydroxide appears most abundant and well-distributed in the straight portland cement concrete. Calcium hydroxide in the cement paste of the fly ash concrete appeared slightly less abundant overall than in the straight portland cement concrete, but tended to be more dispersed and occurred in larger patches. Calcium hydroxide was least abundant in the cement paste of the GGBFS concrete. All of the specimens exhibited blocky secondary calcium hydroxide crystals in air voids within the zone of calcium hydroxide-depleted cement paste, as shown in Figures A3.196 through A3.198. Blocky calcium hydroxide crystals were present in the large cracks of the straight portland cement concrete specimen, as previously shown, (Figure A3.185) but were not present in the tighter cracks of the fly ash and GGBFS concrete specimens, (Figures A3.197 and A3.198).

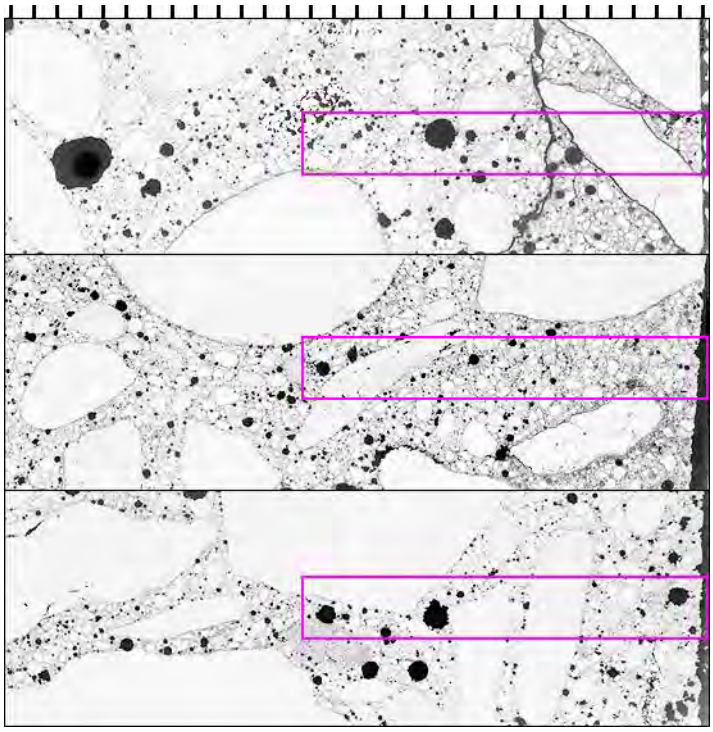

Figure A3.191. Epifluorescent thin section views of the 0.45 *w/c* concrete specimens immersed in $CaCl_2$ solution for 500 days, exterior surfaces to the right. From top to bottom: straight portland cement concrete, supplementary fly ash concrete, and supplementary GGBFS concrete, tic marks every mm. Pink boxes highlight close-up regions shown in Figure A3.192.

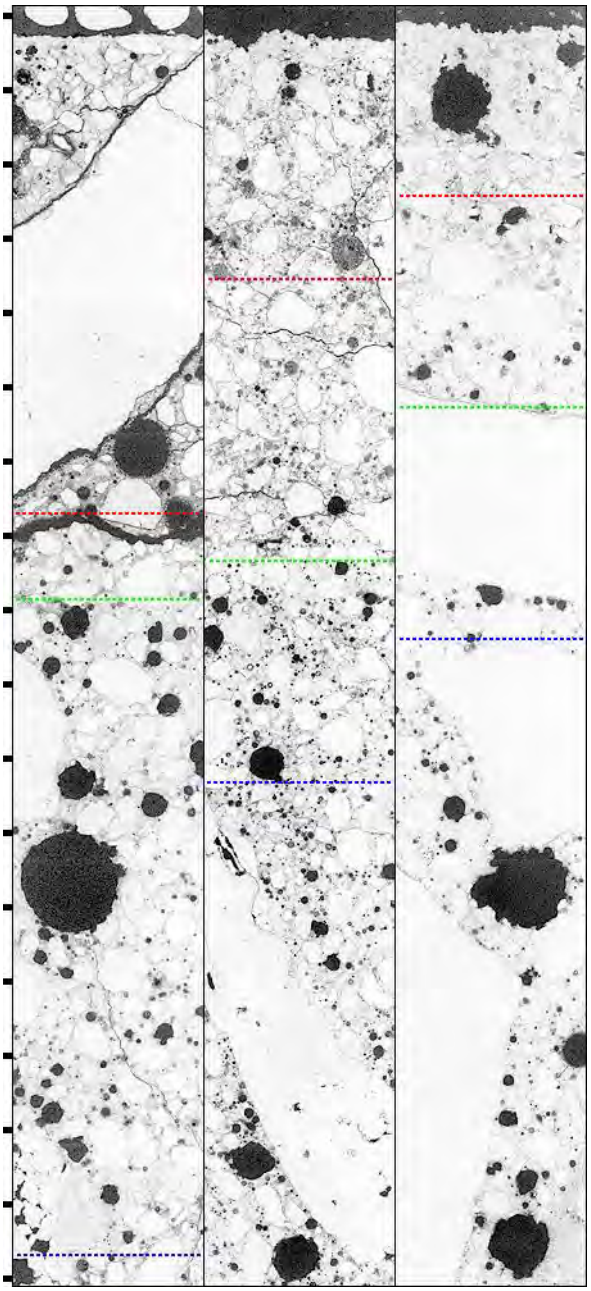

Figure A3.192. Close-up views of regions outlined in pink in Figure A3.191, but with exterior surfaces oriented towards the top. Cross-sectional epifluorescent mode images of the 0.45 *w/c* concrete specimens after 500 days of immersion in $CaCl_2$ solution. From left to right: straight portland cement concrete, supplementary fly ash concrete, and supplementary GGBFS concrete, tic marks every mm. Green lines show extent of calcium hydroxide depleted cement paste. Red lines show horizons where photos of depleted paste were taken. Blue lines show horizons where photos were taken of paste with calcium hydroxide still present.

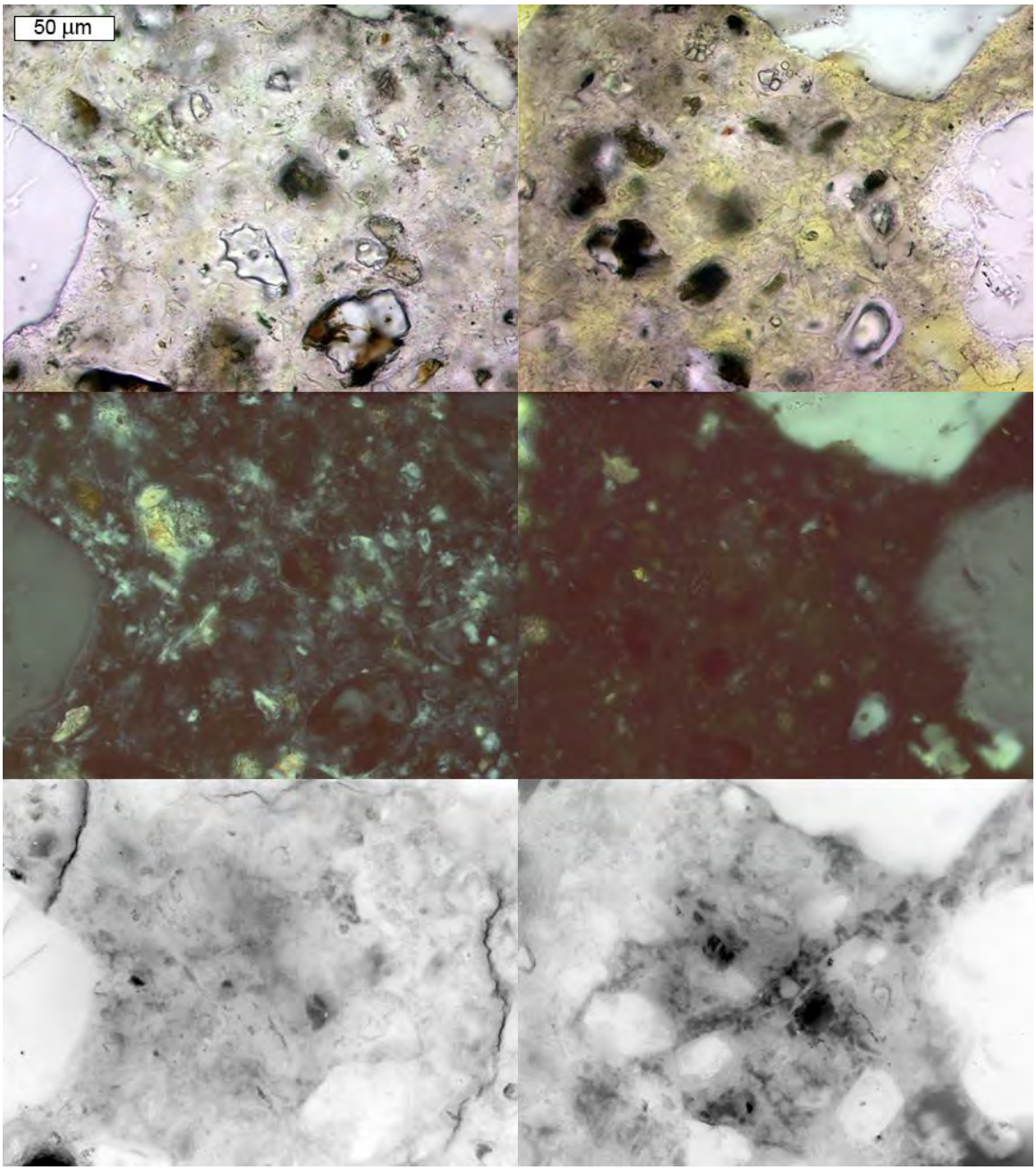

Figure A3.193. Regions of cement paste in 0.45 *w/c* straight portland cement concrete specimen exposed to $CaCl_2$ brine where calcium hydroxide is depleted, (right) and still present, (left). From top to bottom: transmitted light, crossed-polars, and epifluorescent mode images.

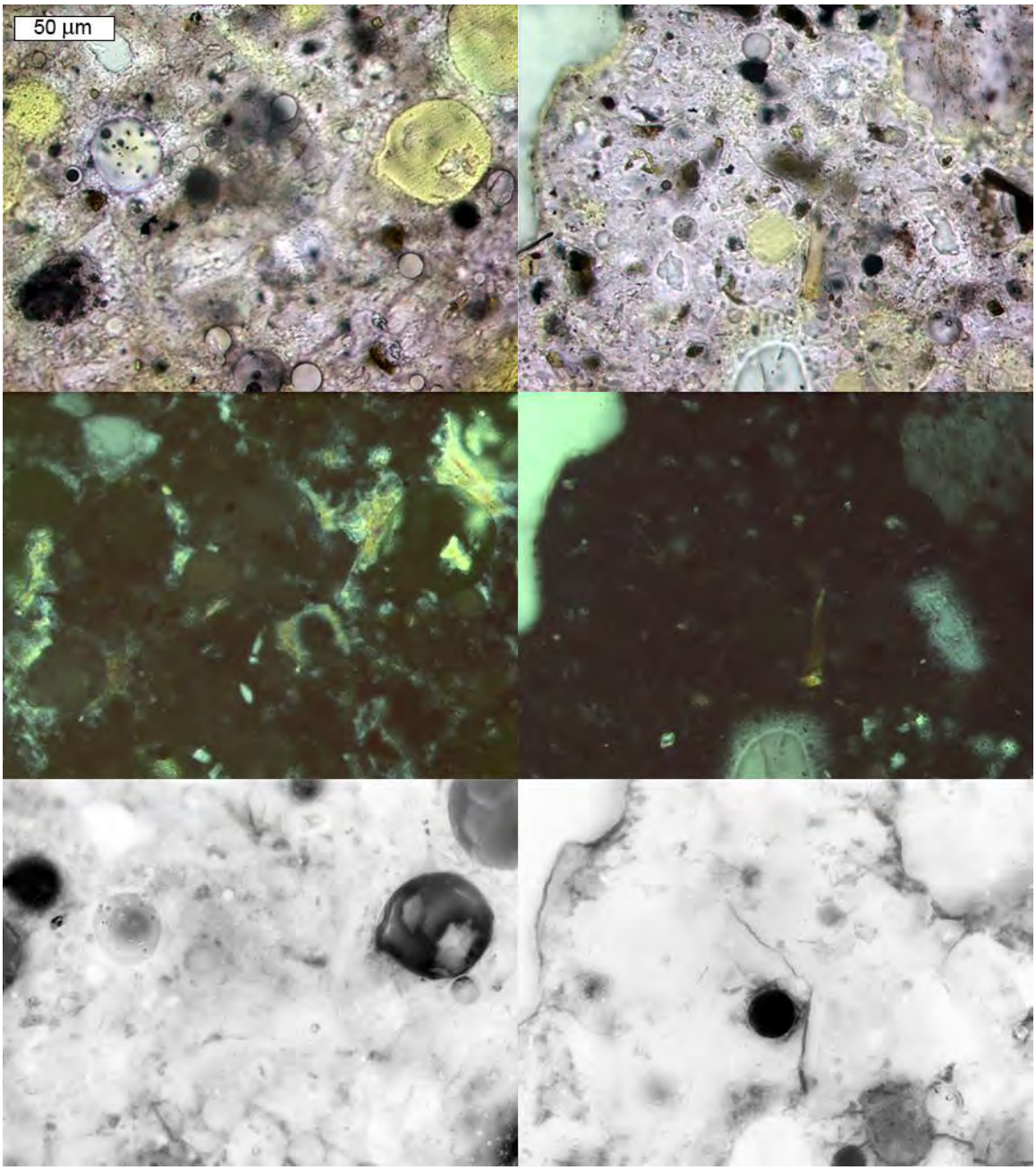

Figure A3.194. Regions of cement paste in 0.45 *w/c* fly ash concrete specimen exposed to $CaCl_2$ brine where calcium hydroxide is depleted, (right) and still present, (left). From top to bottom: transmitted light, crossed-polars, and epifluorescent mode images.

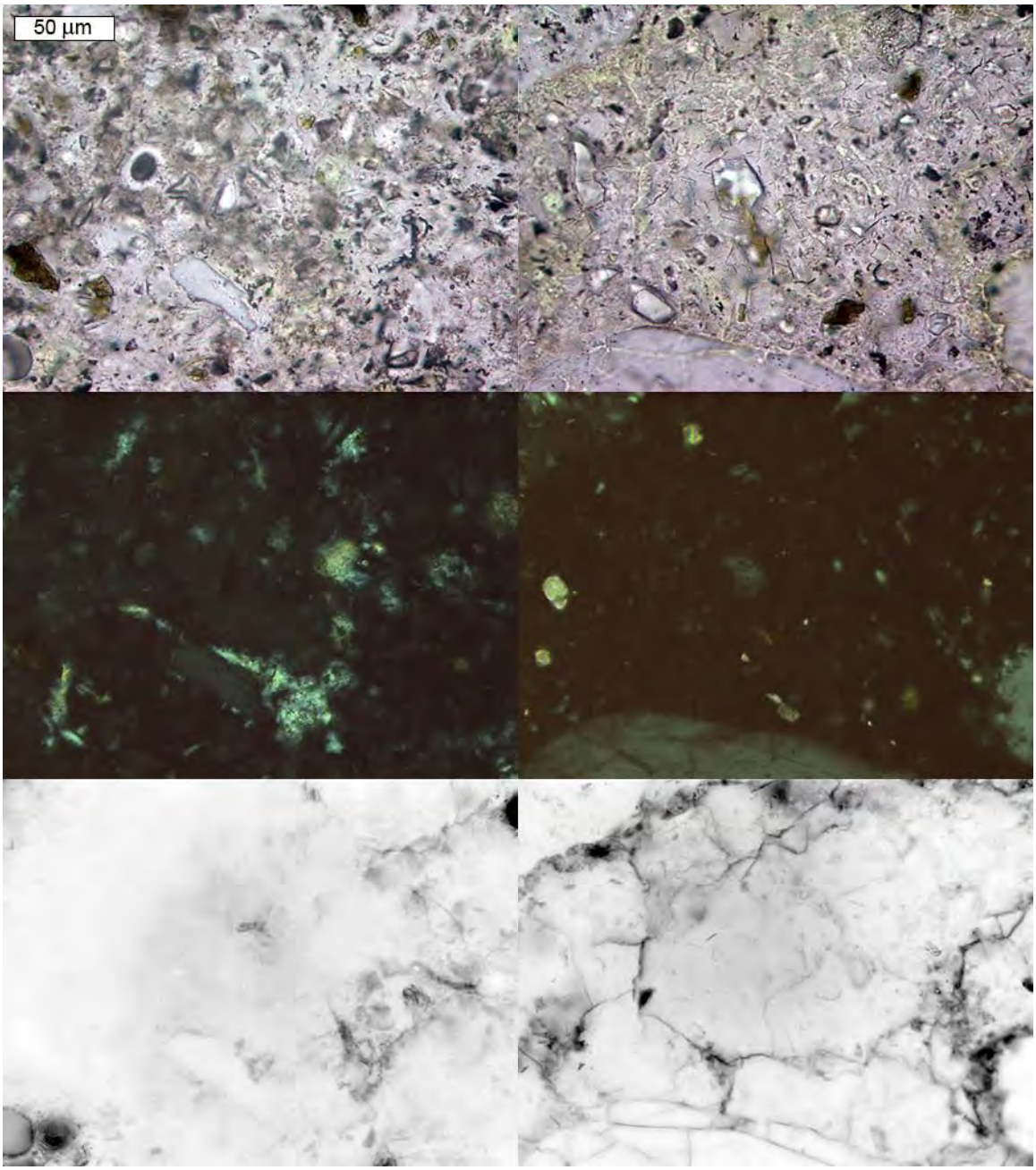

Figure A3.195. Regions of cement paste in 0.45 *w/cm* GGBFS concrete specimen exposed to $CaCl_2$ brine where calcium hydroxide is depleted, (right) and still present, (left). From top to bottom: transmitted light, crossed-polars, and epifluorescent mode images.

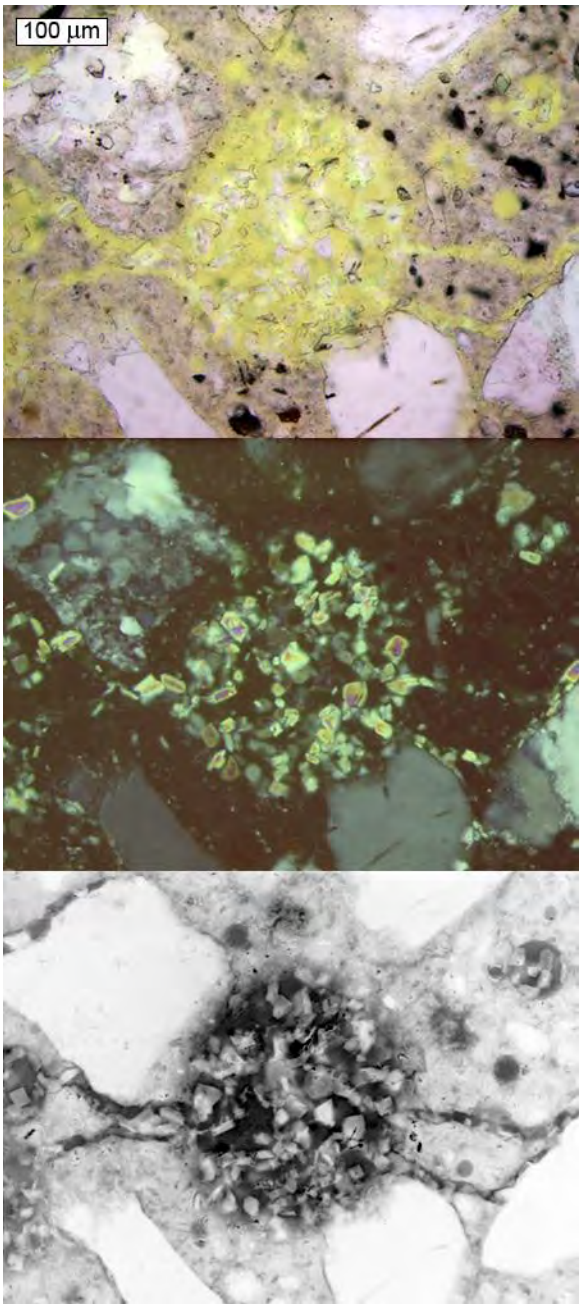

Figure A3.196. Deteriorated portion from 0.45 *w/c* straight portland cement concrete specimen exposed to $CaCl_2$ brine with blocky calcium hydroxide crystals. From top to bottom: transmitted light, crossed-polars, and epifluorescent mode images.

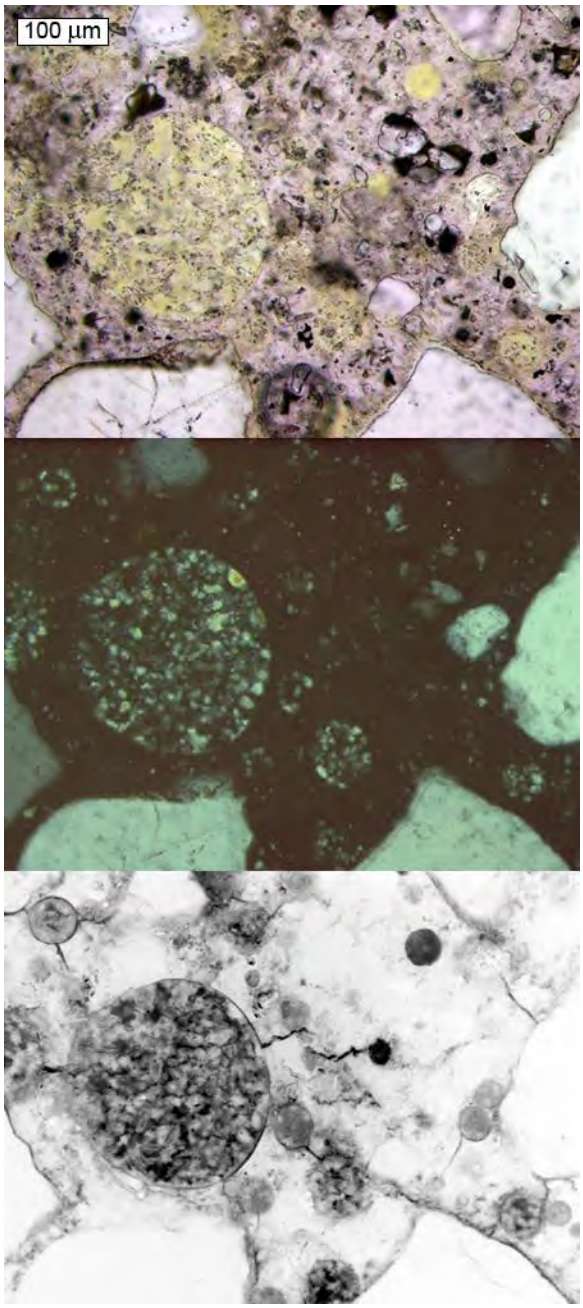

Figure A3.197. Deteriorated portion from 0.45 *w/cm* fly ash concrete specimen exposed to $CaCl_2$ brine with blocky calcium hydroxide crystals. From top to bottom: transmitted light, crossed-polars, and epifluorescent mode images.

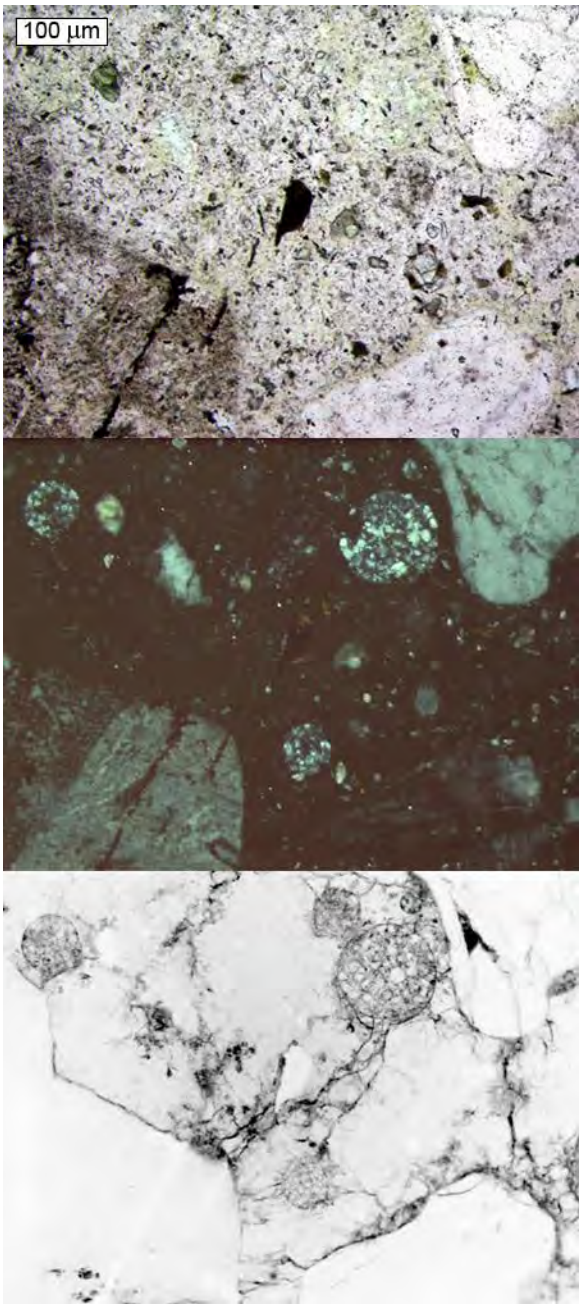

Figure A3.198. Secondary blocky calcium hydroxide crystals in air voids of 0.45 *w/c* GGBFS concrete specimen exposed to $CaCl_2$. From top to bottom: transmitted light, crossed-polars, and epifluorescent mode images.

Comparison of the 0.45 w/c Concrete Specimens Immersed in $MgCl_2$ Brine

Figure A3.199 shows epifluorescent mode images from 0.45 *w/c* straight portland cement, fly ash, GGBFS concrete specimens, and a 0.55 *w/c* straight portland cement concrete specimen treated with silane after 500 days immersion the high-concentration $MgCl_2$ brine. The images depict the specimens in cross-section with the top surfaces of each specimen facing towards the right hand-side. Figure A3.200 shows further close-up epifluorescent mode images from the areas outlined in pink from Figure A3.199. As with the straight portland cement specimens exposed to $CaCl_2$ brine, the straight portland cement concrete specimens exposed to $MgCl_2$ brine showed the most severe cracking, as can be seen in Figure A3.200. Cracks are also visible in the GGBFS concrete specimen, but to a lesser degree. At the scale of the image in Figure A3.200, cracks are not observed in the fly ash concrete specimen. The silane-sealed specimen appears to be in good condition in Figure A3.200. The same trend noted from the $CaCl_2$ brine of calcium hydroxide depletion, (Figures A3.201 through A3.203) coupled with blocky secondary deposits of calcium hydroxide in air voids and large cracks in the depleted zone, (Figures A3.204 through A3.206) was observed in the straight portland cement, fly ash, and GGBFS specimens exposed to $MgCl_2$ brine. However, in contrast to the same specimens exposed to the $CaCl_2$, the specimens exposed to the $MgCl_2$ brine all exhibited fibrous mineral precipitates on the surface and in the air voids and cracks near the surface, examples of which are shown in Figures A3.207 and A3.208. Figure A3.209 shows calcium hydroxide in the cement paste from a horizon just below the surface from the concrete specimen treated with silane. Neither calcium hydroxide depleted paste nor blocky secondary calcium hydroxide crystals were observed in the silane-sealed specimen.

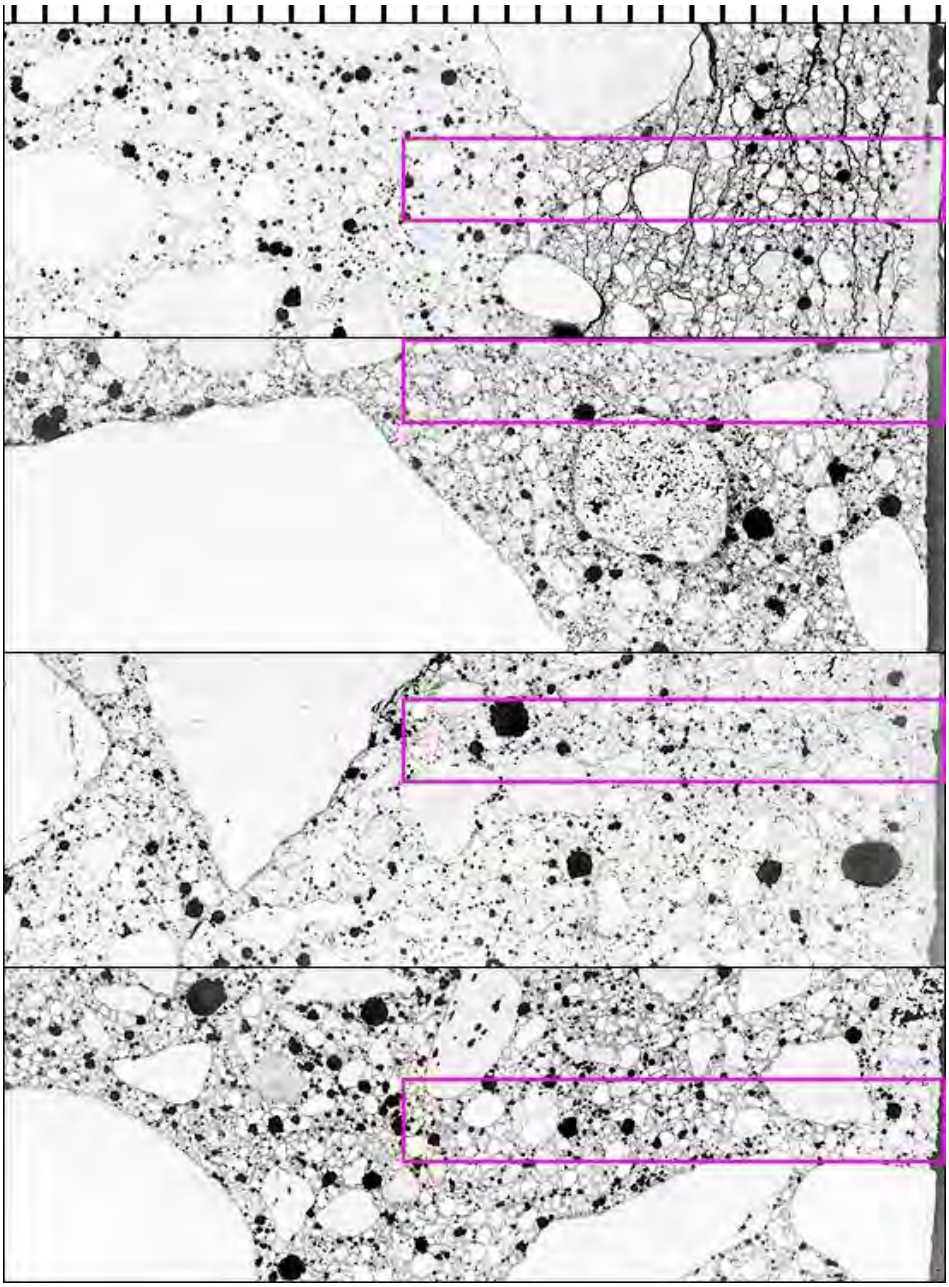

Figure A3.199. Epifluorescent thin section views of 0.45 *w/cm* concrete specimens, and a 0.55 *w/c* concrete silane-sealed specimen, all immersed in $MgCl_2$ solution for 500 days, exterior surfaces to the right. From top to bottom: straight portland cement concrete, supplementary fly ash concrete, supplementary GGBFS concrete, and the 0.55 *w/c* silane-sealed concrete, tic marks every mm. Pink boxes highlight close-up regions shown in Figure A3.200.

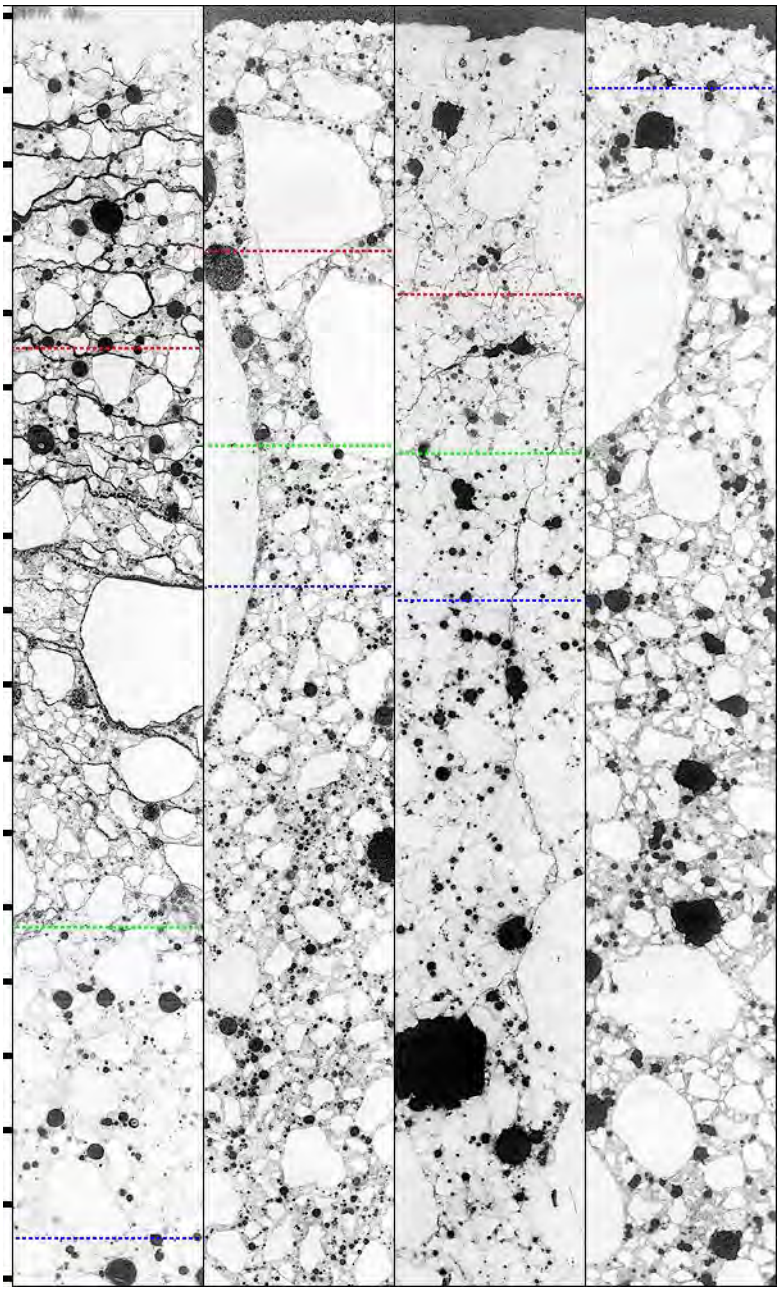

Figure A3.200. Close-up views of regions outlined in pink in Figure A3.199, but with exterior surfaces oriented towards the top. Cross-sectional epifluorescent mode images of 0.45 *w/cm* concrete specimens, and a 0.55 *w/cm* concrete specimen after 500 days of immersion in $MgCl_2$ solution. From left to right: straight portland cement concrete, supplementary fly ash concrete, supplementary GGBFS concrete, and the 0.55 *w/cm* silane-sealed concrete, tic marks every mm. Green lines show extent of calcium hydroxide depleted cement paste. Red lines show horizons where photos of depleted paste were taken. Blue lines show horizons where photos were taken of paste with calcium hydroxide still present.

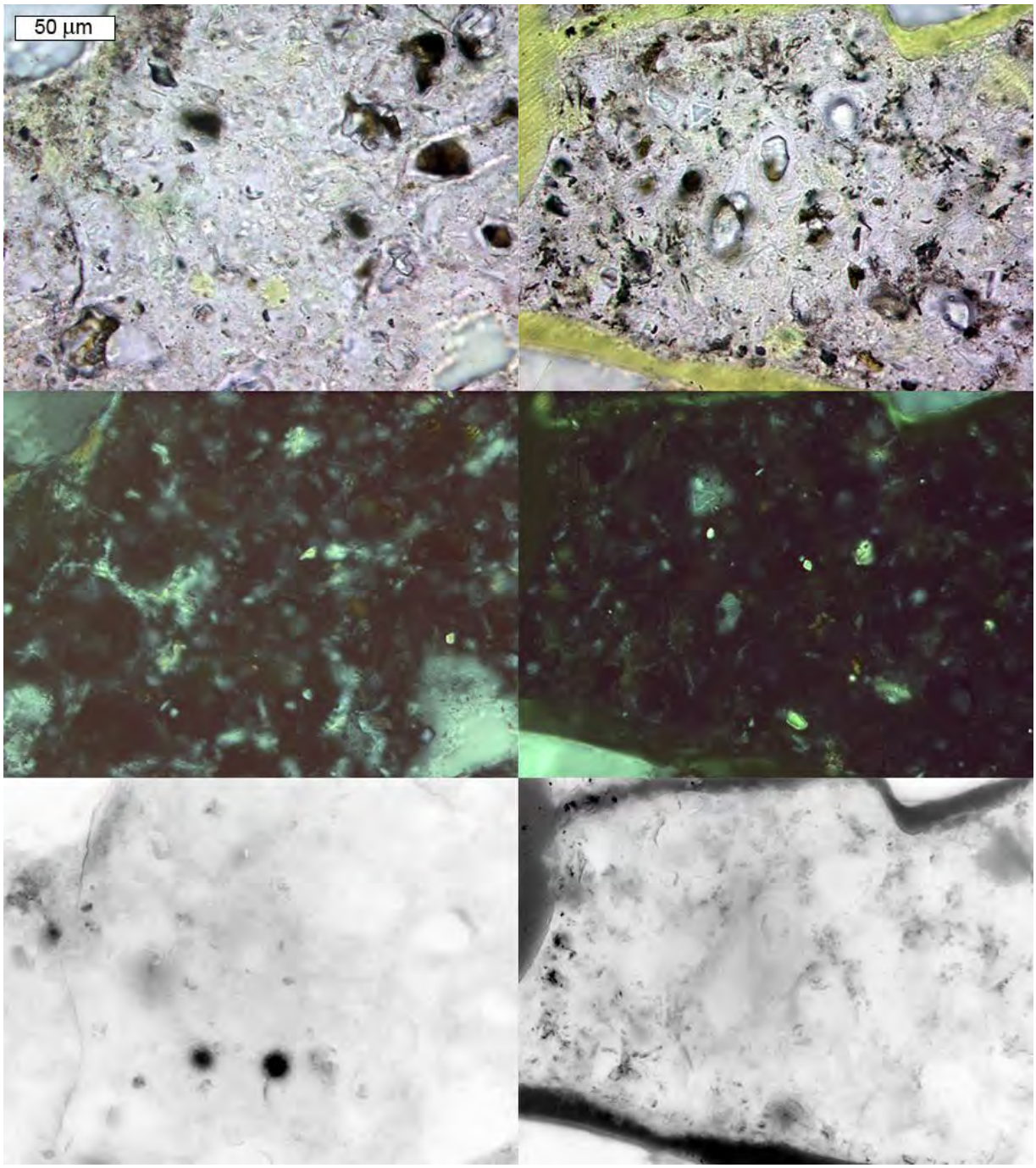

Figure A3.201. Regions of cement paste in 0.45 *w/c* straight portland cement concrete specimen exposed to $MgCl_2$ brine where calcium hydroxide is depleted, (right) and still present, (left). From top to bottom: transmitted light, crossed-polars, and epifluorescent mode images.

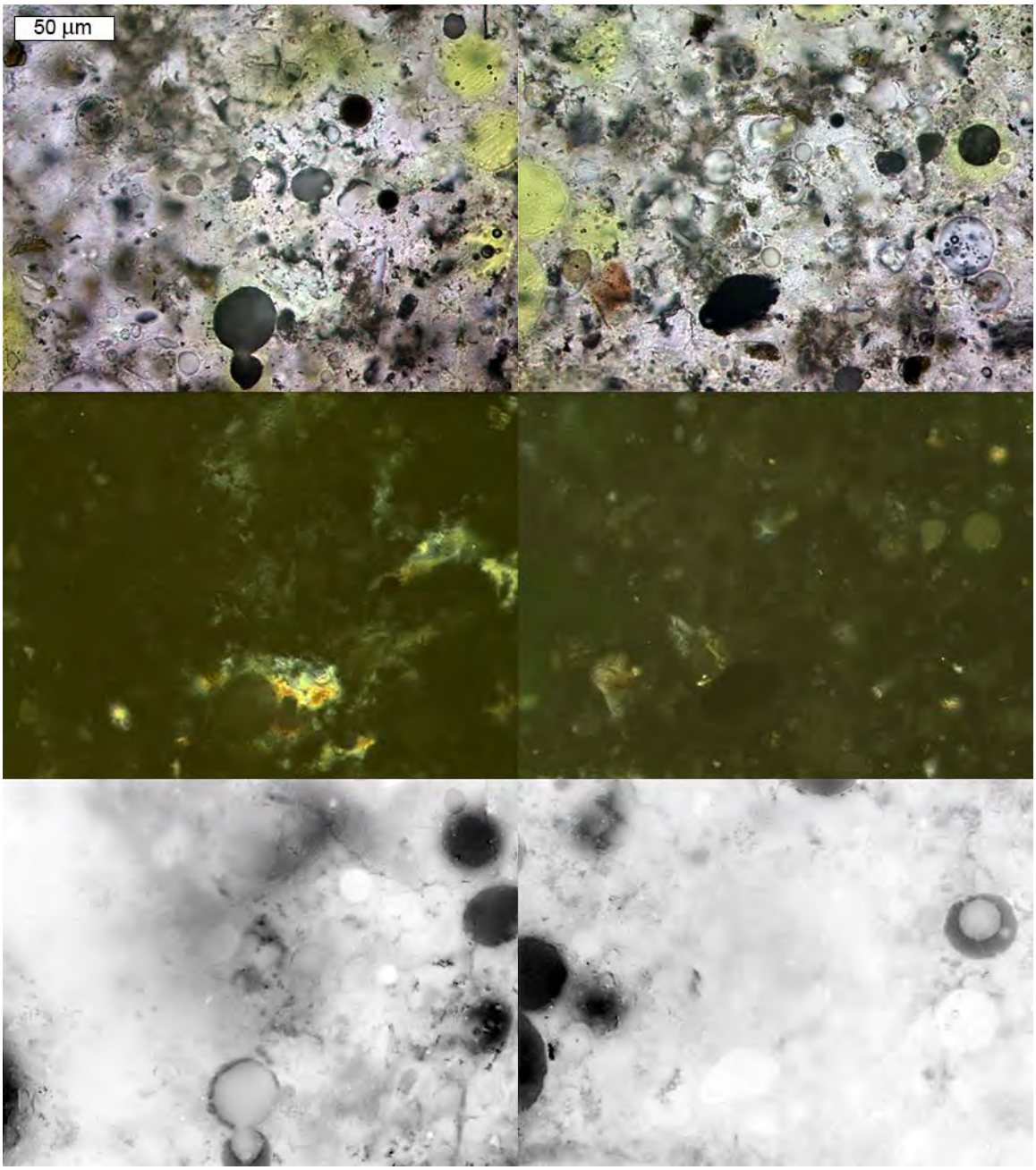

Figure A3.202. Regions of cement paste in 0.45 *w/cm* fly ash concrete specimen exposed to $MgCl_2$ brine where calcium hydroxide is depleted, (right) and still present, (left). From top to bottom: transmitted light, crossed-polars, and epifluorescent mode images.

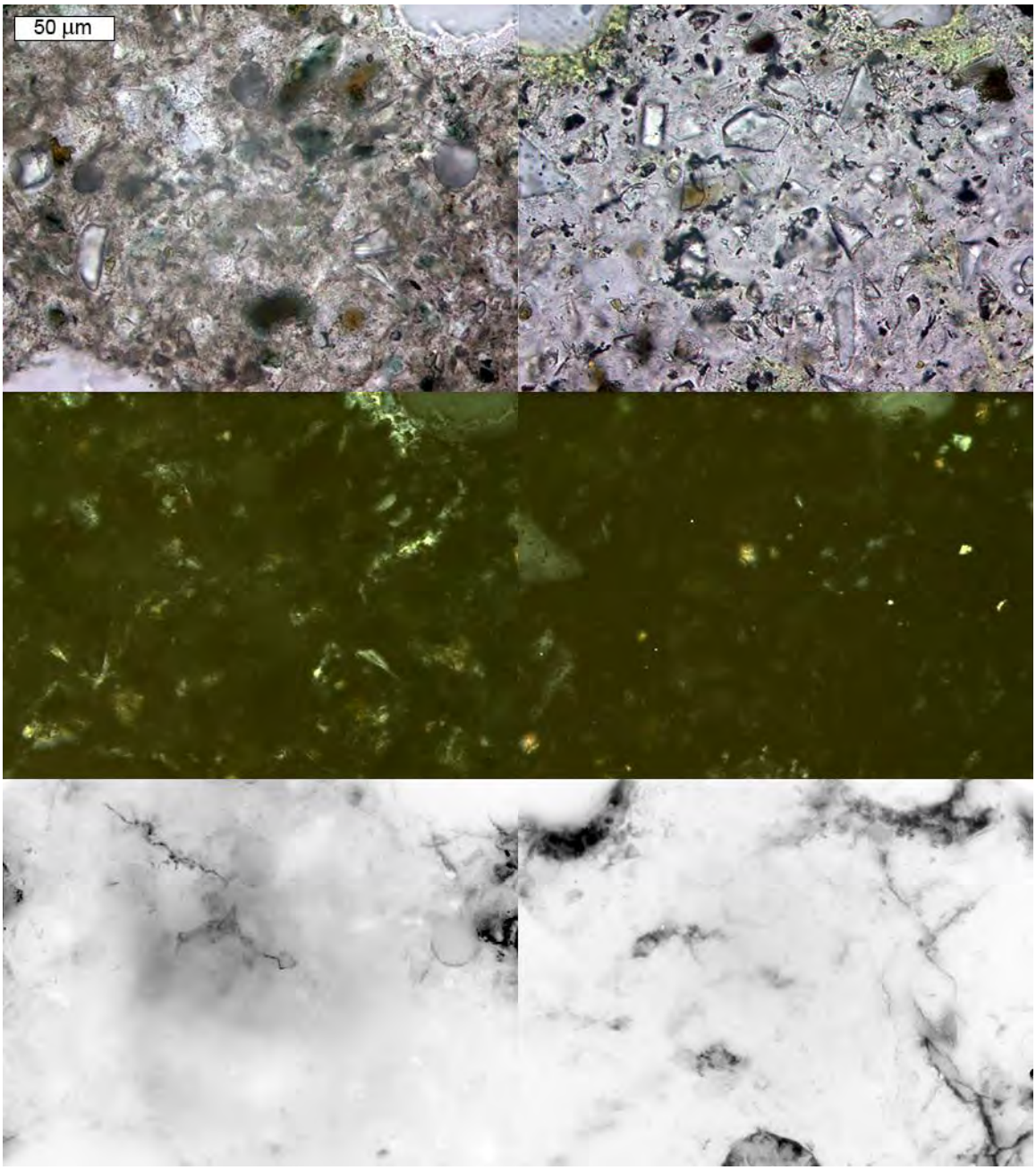

Figure A3.203. Regions of cement paste in 0.45 *w/cm* GGBFS concrete specimen exposed to $MgCl_2$ brine where calcium hydroxide is depleted, (right) and still present, (left). From top to bottom: transmitted light, crossed-polars, and epifluorescent mode images.

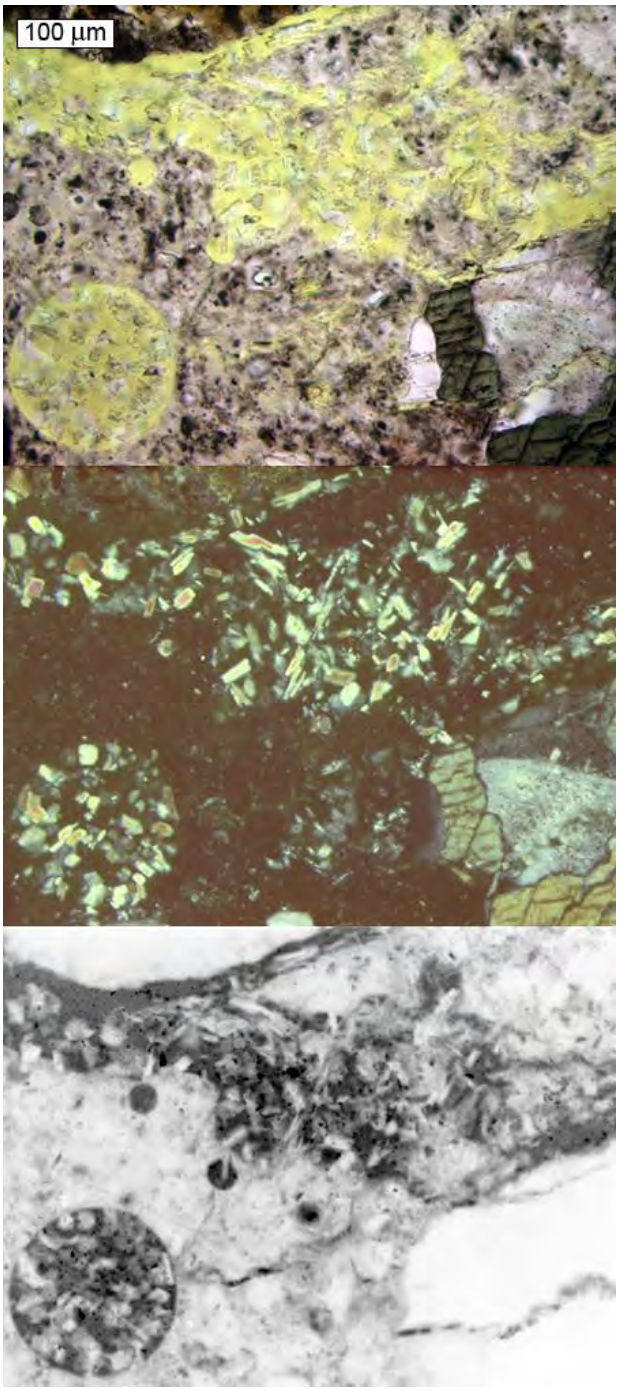

Figure A3.204. Deteriorated portion from 0.45 *w/c* straight portland cement concrete specimen exposed to $MgCl_2$ brine with blocky calcium hydroxide crystals. From top to bottom: transmitted light, crossed-polars, and epifluorescent mode images.

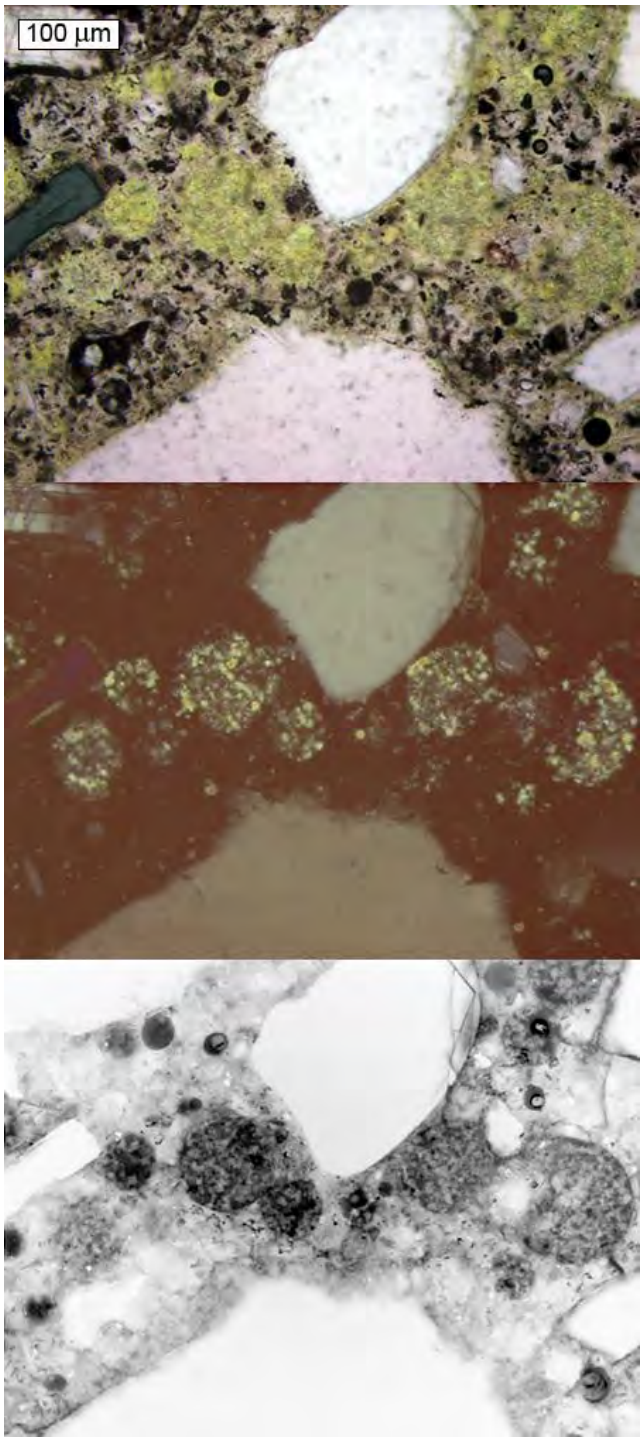

Figure A3.205. Secondary blocky calcium hydroxide crystals in air voids of 0.45 *w/cm* fly ash concrete specimen exposed to $MgCl_2$. From top to bottom: transmitted light, crossed-polars, and epifluorescent mode images.

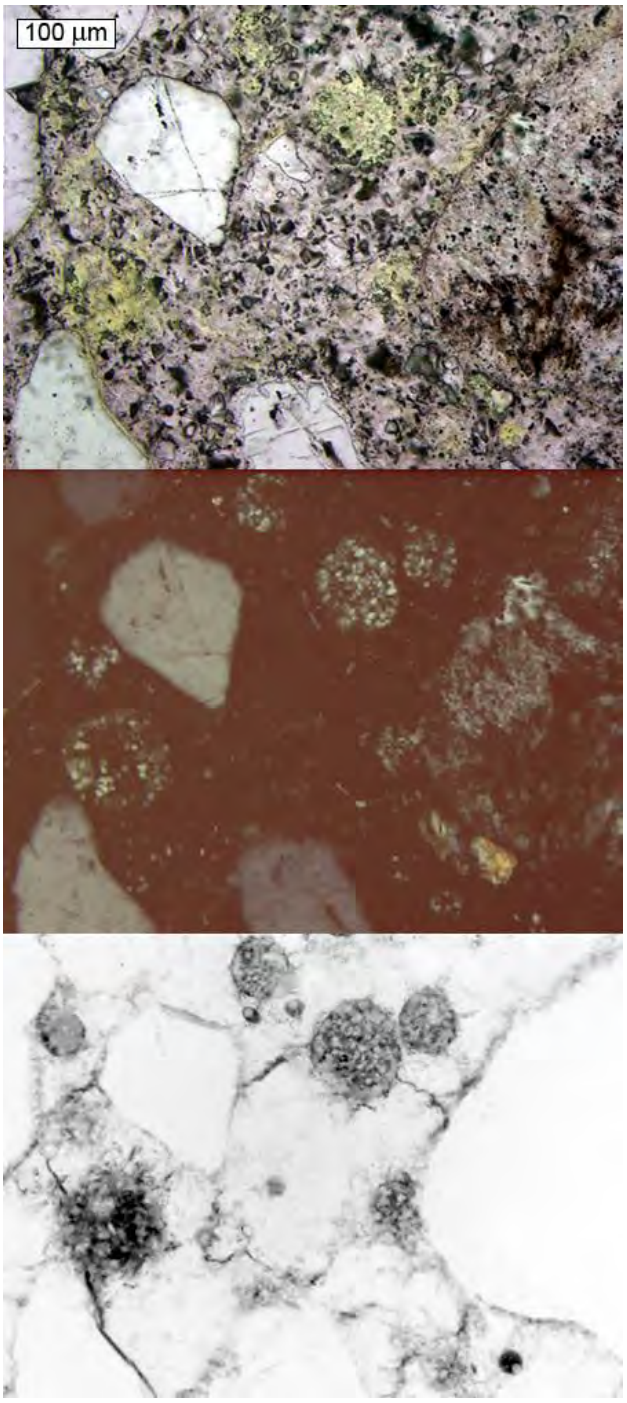

Figure A3.206. Deteriorated portion from 0.45 *w/cm* GGBFS concrete specimen exposed to $MgCl_2$ brine with blocky calcium hydroxide crystals in air voids. From top to bottom: transmitted light, crossed-polars, and epifluorescent mode images.

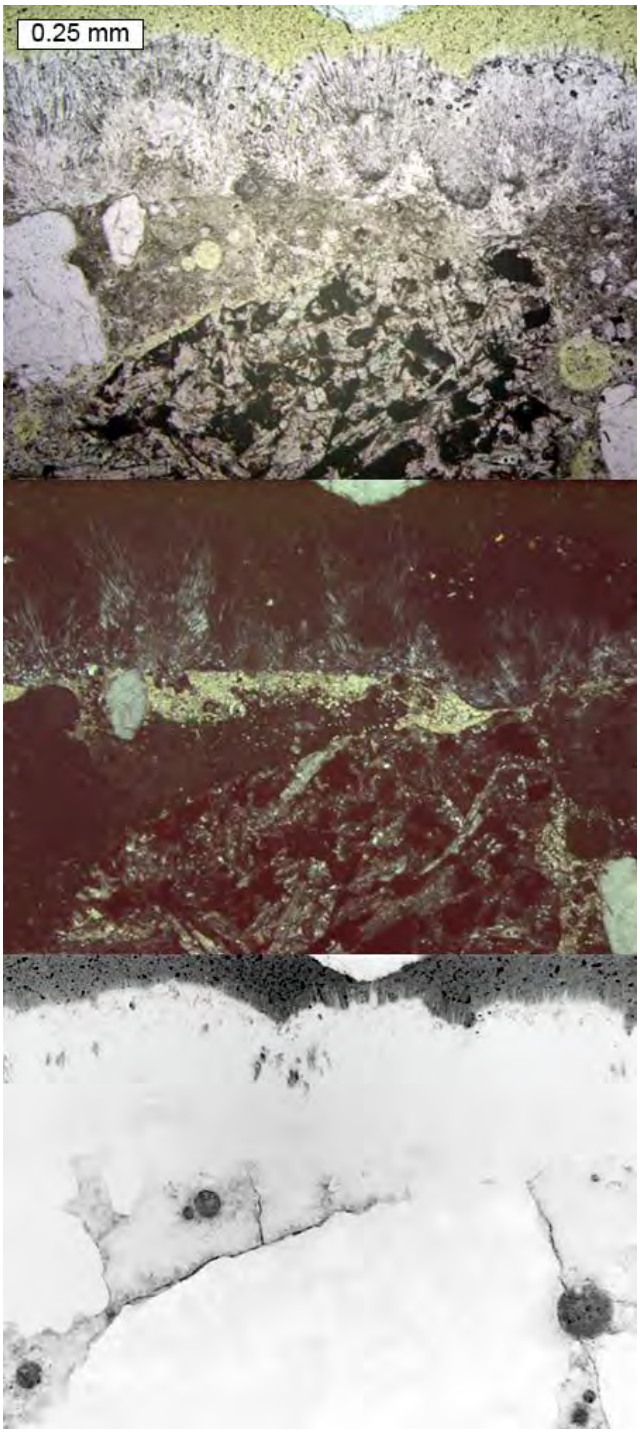

Figure A3.207. Fibrous crystals at surface of 0.45 *w/c* straight portland cement concrete specimen exposed to $MgCl_2$ brine. From top to bottom: transmitted light, crossed-polars, and epifluorescent mode images.

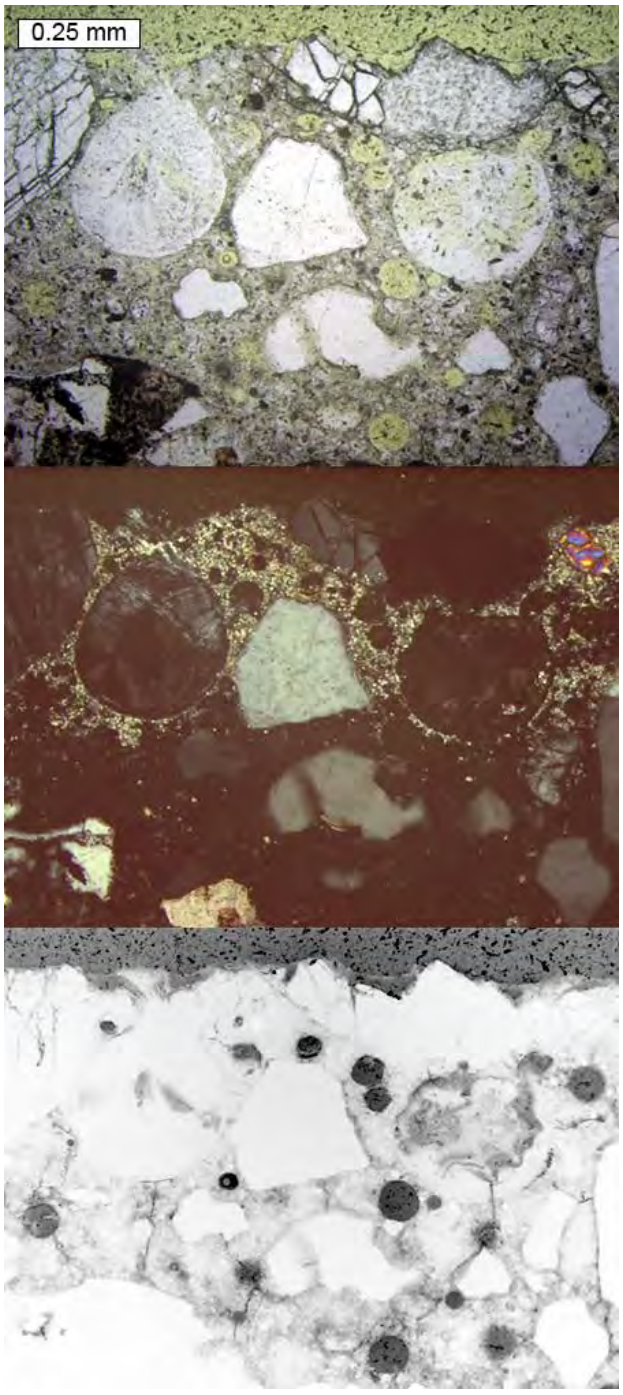

Figure A3.208. Fibrous crystals filling air voids near surface of 0.45 *w/cm* straight portland cement concrete specimen exposed to $MgCl_2$ brine. From top to bottom: transmitted light, crossed-polars, and epifluorescent mode images.

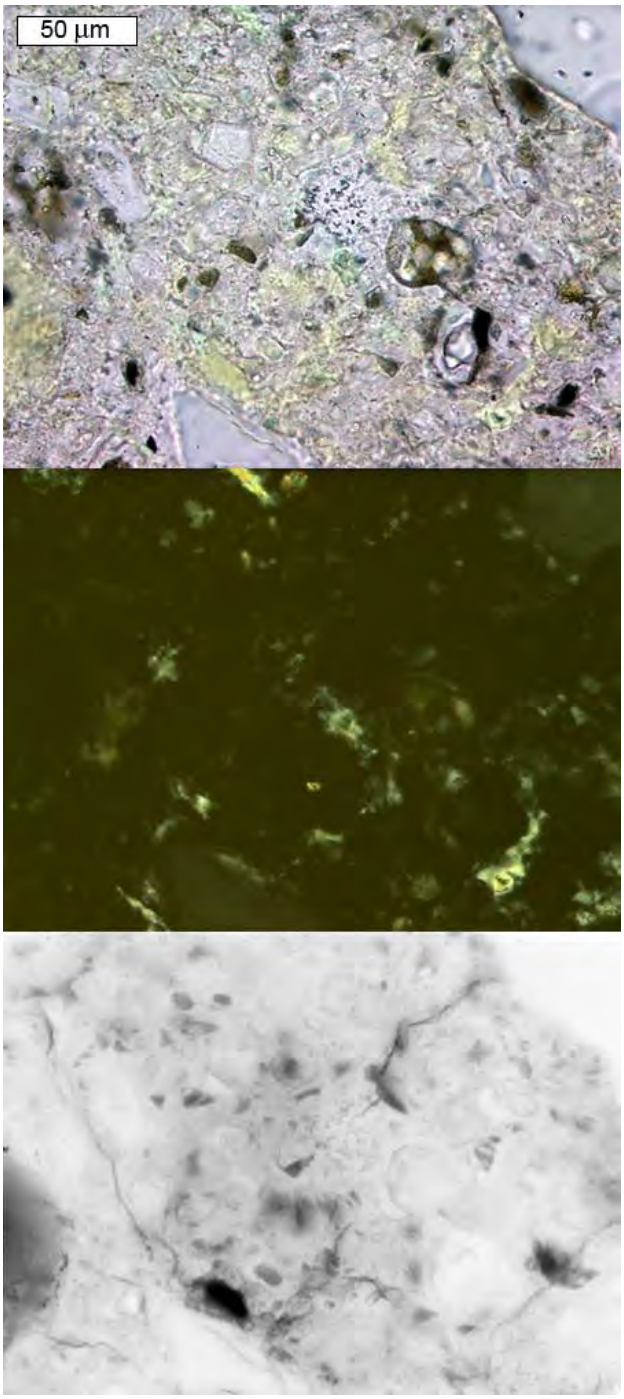

Figure A3.209. Cement paste just below the surface from 0.45 *w/c* straight portland cement concrete specimen sealed with silane and exposed to $MgCl_2$ brine. From top to bottom: transmitted light, crossed-polars, and epifluorescent mode images.

Comparison of the 0.45 w/c Concrete Specimens Immersed in MBAP Brine

Figure A3.210 shows epifluorescent mode images from 0.45 *w/c* straight portland cement, fly ash, and GGBFS concrete specimens after 500 days immersion the high-concentration MBAP brine. The images depict the specimens in cross-section with the top surfaces of each specimen facing towards the right hand-side. Figure A3.211 shows further close-up epifluorescent mode images from the areas outlined in pink from Figure A3.210. The only specimen to show signs of severe cracking was the straight portland cement concrete specimen, as shown in Figure A3.128. The same trend noted from the $CaCl_2$ and $MgCl_2$ brines of calcium hydroxide depletion, (Figures A3.212 through A3.214) coupled with blocky secondary deposits of calcium hydroxide in air voids and large cracks in the depleted zone, (Figures A3.215 through A3.217) was observed in the straight portland cement, fly ash, and GGBFS specimens exposed to MBAP brine. As with the specimens exposed to the $MgCl_2$ brine, all of the specimens from the MBAP brine exhibited fibrous mineral precipitates on the surface and in the air voids and cracks near the surface. An example of fibrous minerals filling a crack near the surface is included in Figure A3.218.

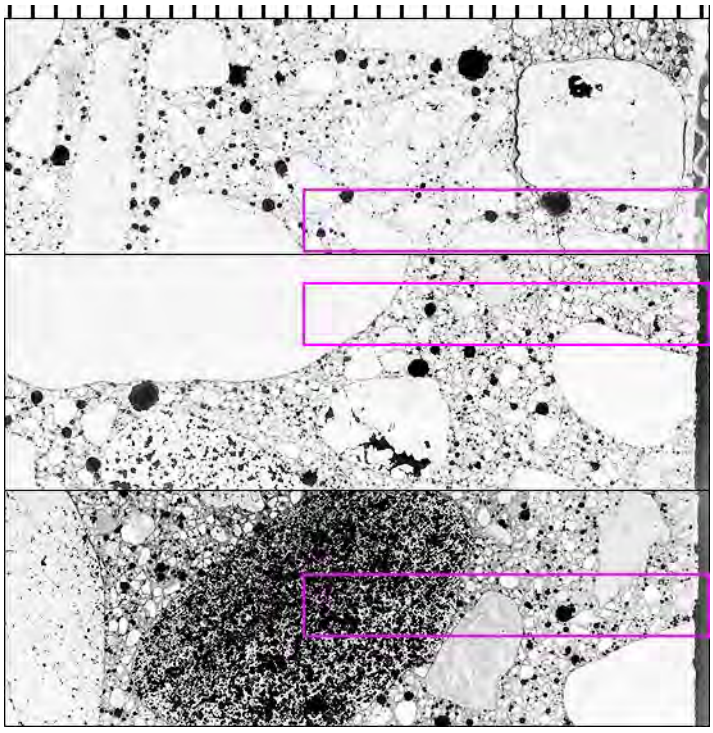

Figure A3.210. Epifluorescent thin section views of the 0.45 *w/c* concrete specimens immersed in MBAP solution for 500 days, exterior surfaces to the right. From top to bottom: straight portland cement concrete, supplementary fly ash concrete, and supplementary GGBFS concrete, tic marks every mm. Pink boxes highlight close-up regions shown in Figure A3.211.

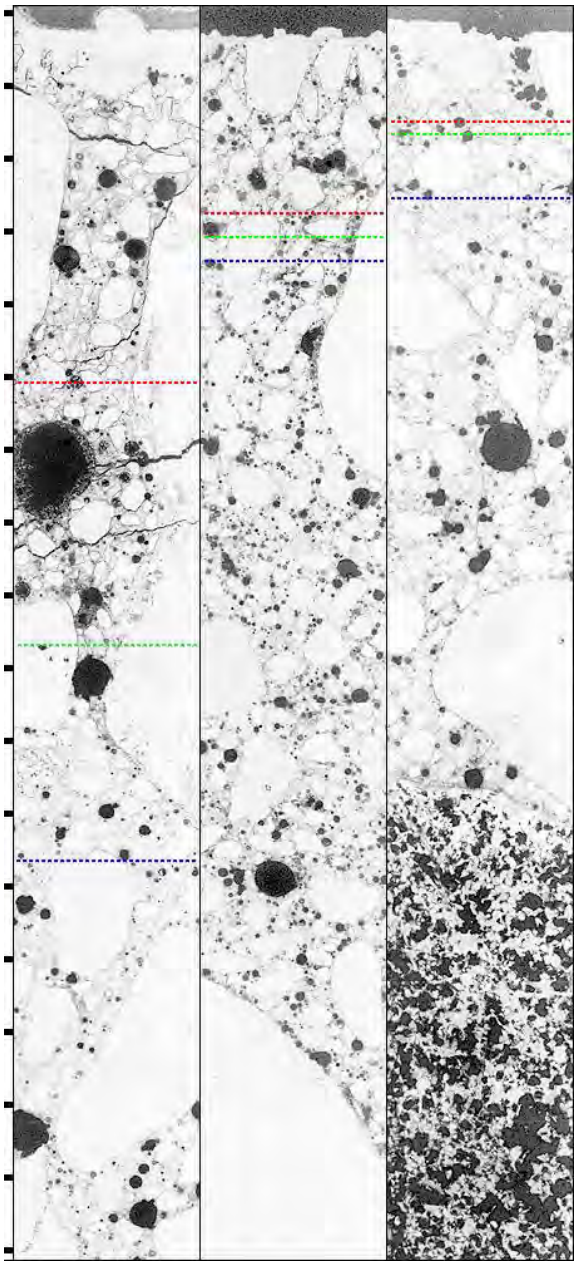

Figure A3.211. Close-up views of regions outlined in pink in Figure A3.210, but with exterior surfaces oriented towards the top. Cross-sectional epifluorescent mode images of the 0.45 *w/cm* concrete specimens after 500 days of immersion in MBAP solution. From left to right: straight portland cement concrete, supplementary fly ash concrete, and supplementary GGBFS concrete, tic marks every mm. Green lines show extent of calcium hydroxide depleted cement paste. Red lines show horizons where photos of depleted paste were taken. Blue lines show horizons where photos were taken of paste with calcium hydroxide still present.

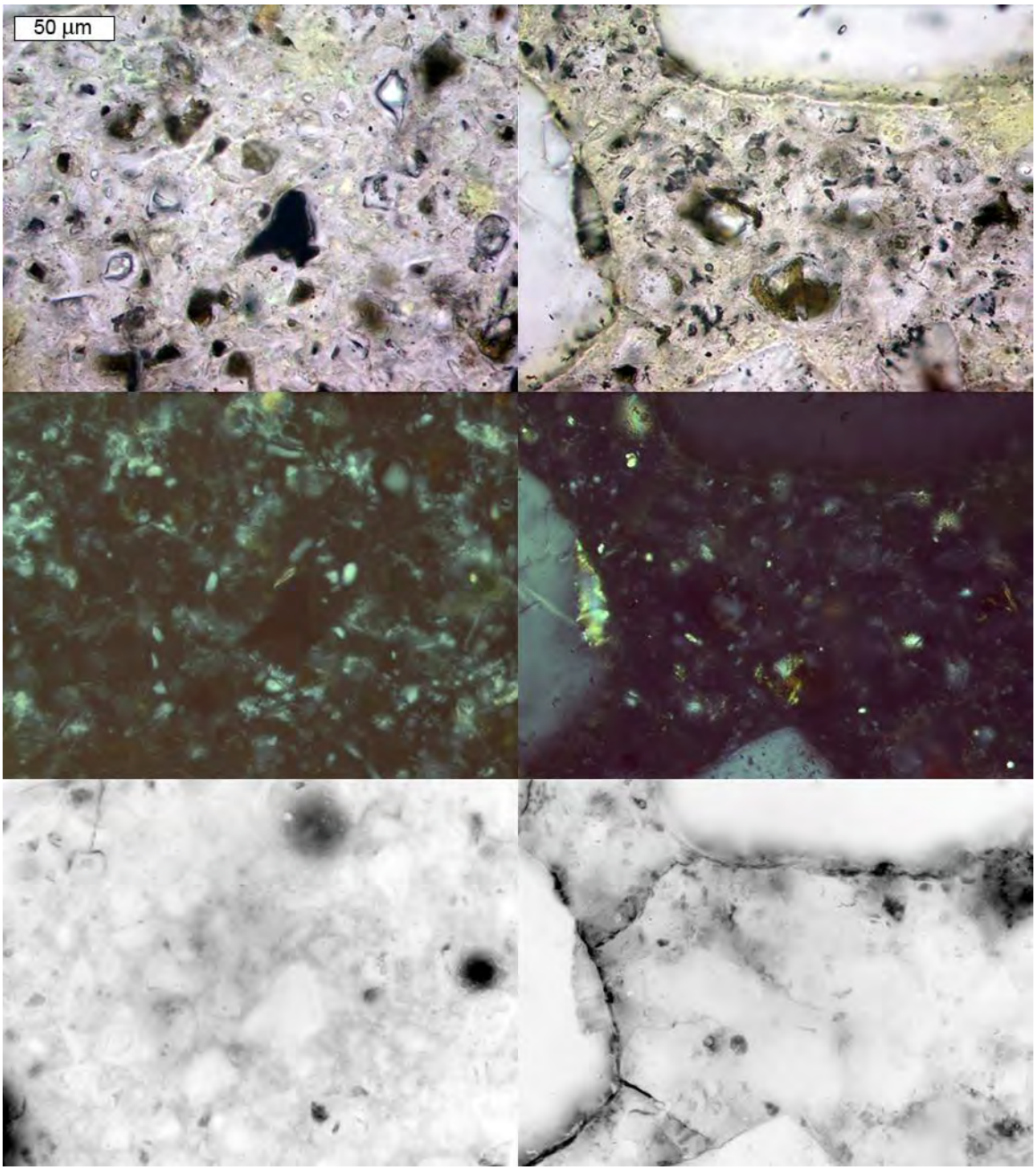

Figure A3.212. Regions of cement paste in 0.45 *w/c* straight portland cement concrete specimen exposed to MBAP brine where calcium hydroxide is depleted, (right) and still present, (left). From top to bottom: transmitted light, crossed-polars, and epifluorescent mode images.

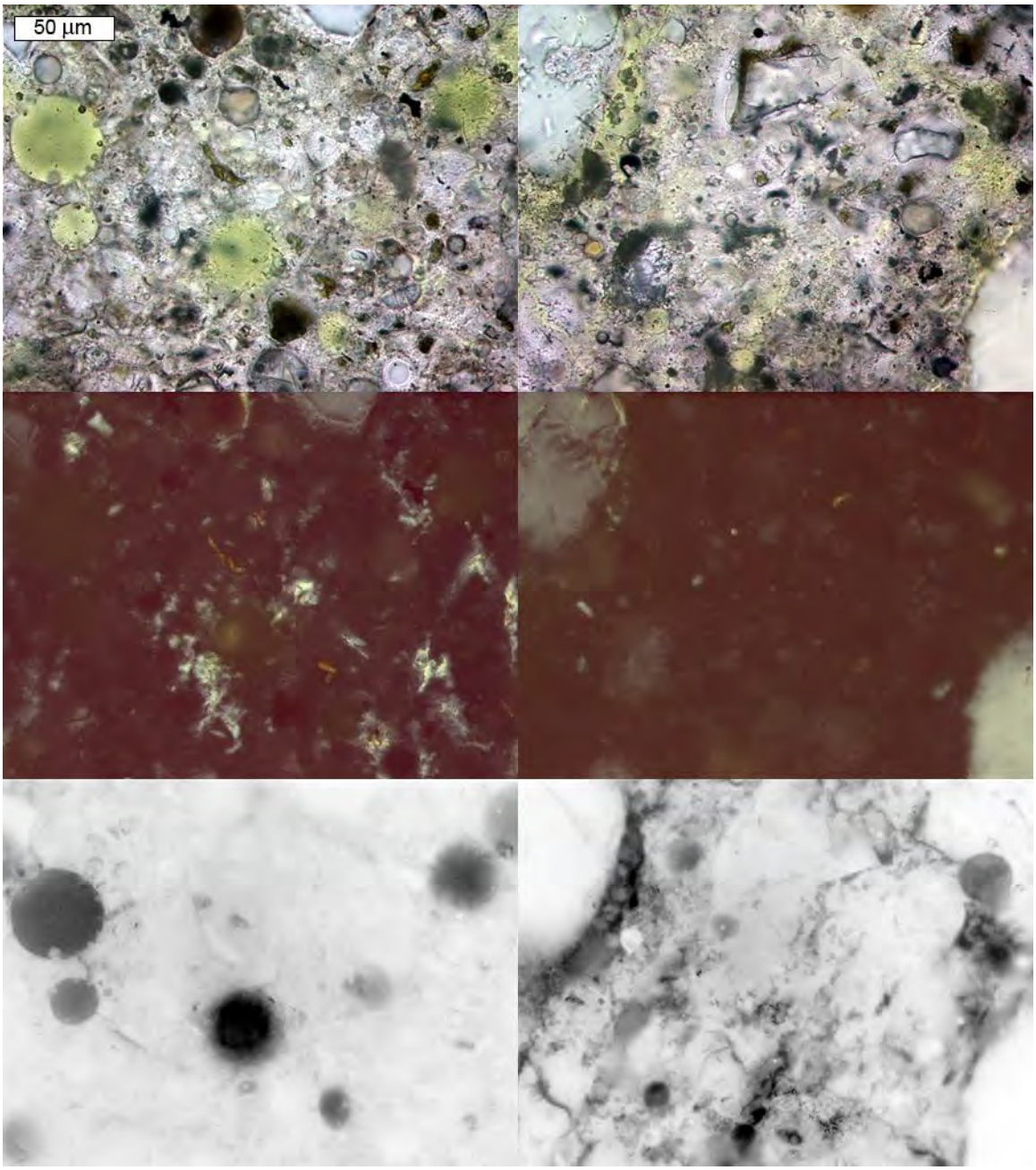

Figure A3.213. Regions of cement paste in 0.45 *w/cm* fly ash concrete specimen exposed to MBAP brine where calcium hydroxide is depleted, (right) and still present, (left). From top to bottom: transmitted light, crossed-polars, and epifluorescent mode images.

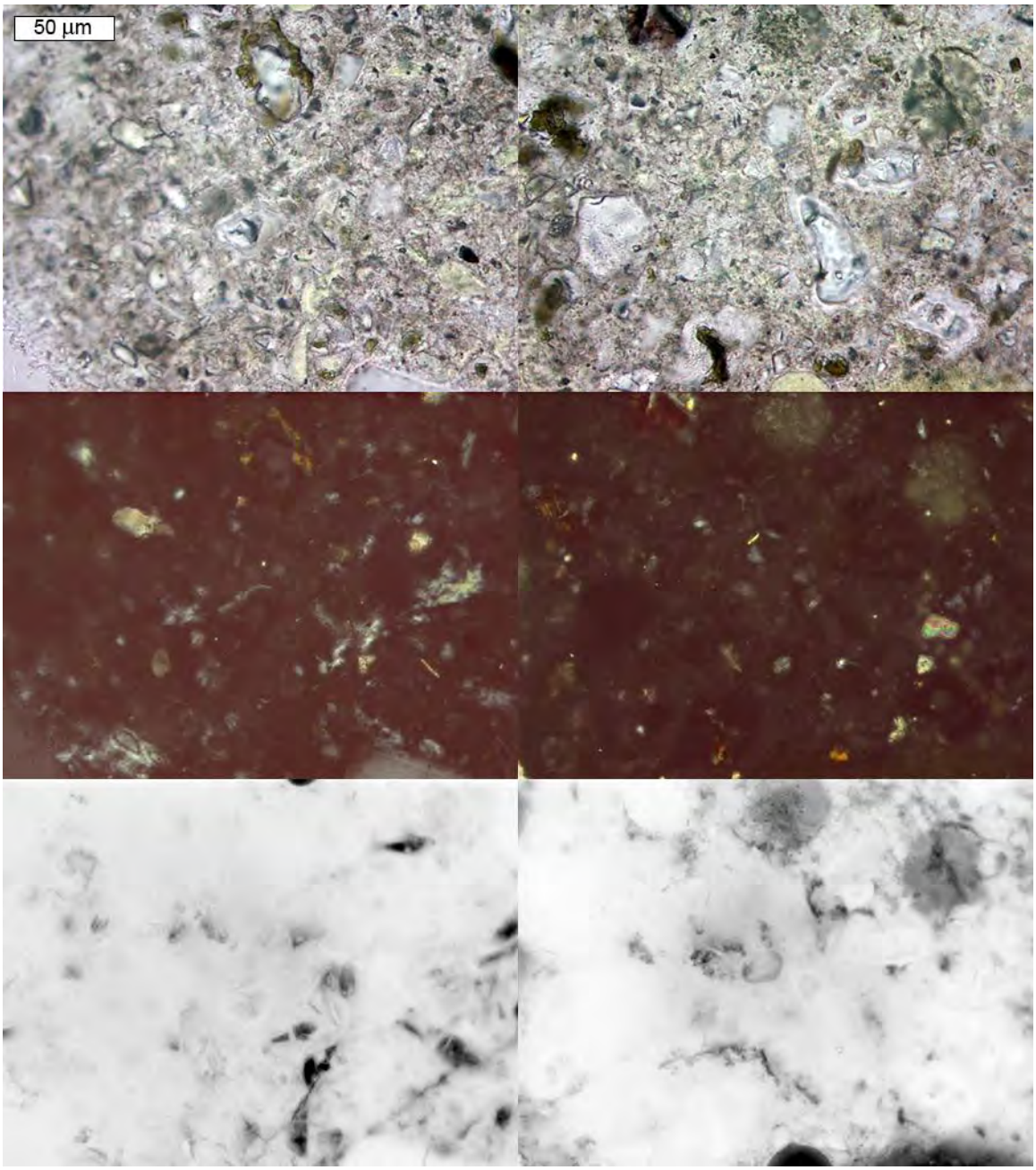

Figure A3.214. Regions of cement paste in 0.45 *w/cm* GGBFS concrete specimen exposed to MBAP brine where calcium hydroxide is depleted, (right) and still present, (left). From top to bottom: transmitted light, crossed-polars, and epifluorescent mode images.

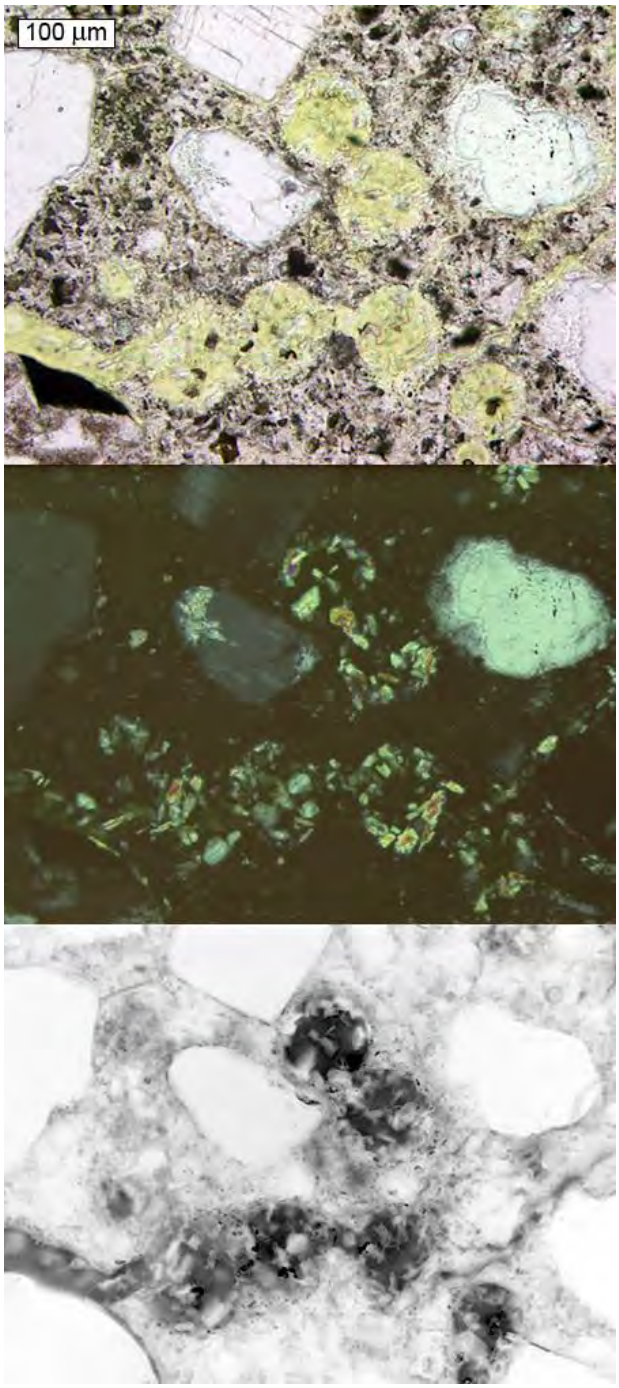

Figure A3.215. Deteriorated portion from 0.45 *w/c* straight portland cement concrete specimen exposed to MBAP brine with blocky calcium hydroxide crystals. From top to bottom: transmitted light, crossed-polars, and epifluorescent mode images.

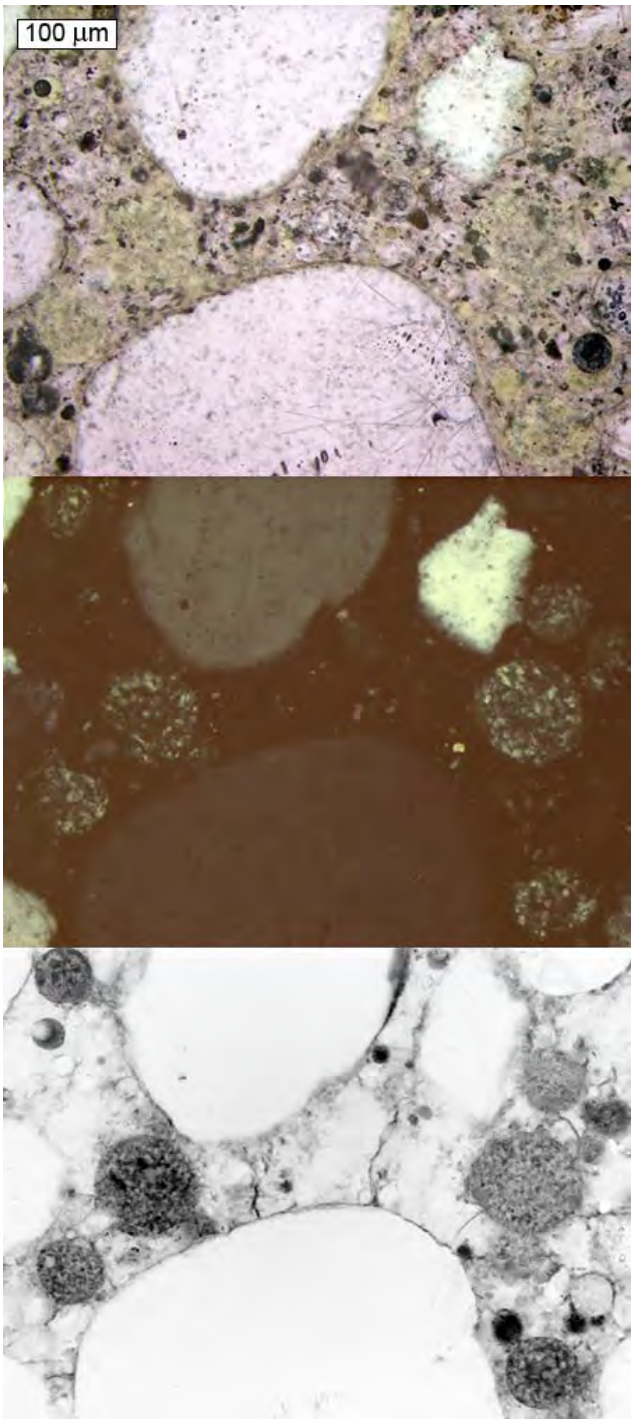

Figure A3.216. Secondary blocky calcium hydroxide crystals in air voids of 0.45 *w/cm* fly ash concrete specimen exposed to MBAP. From top to bottom: transmitted light, crossed-polars, and epifluorescent mode images.

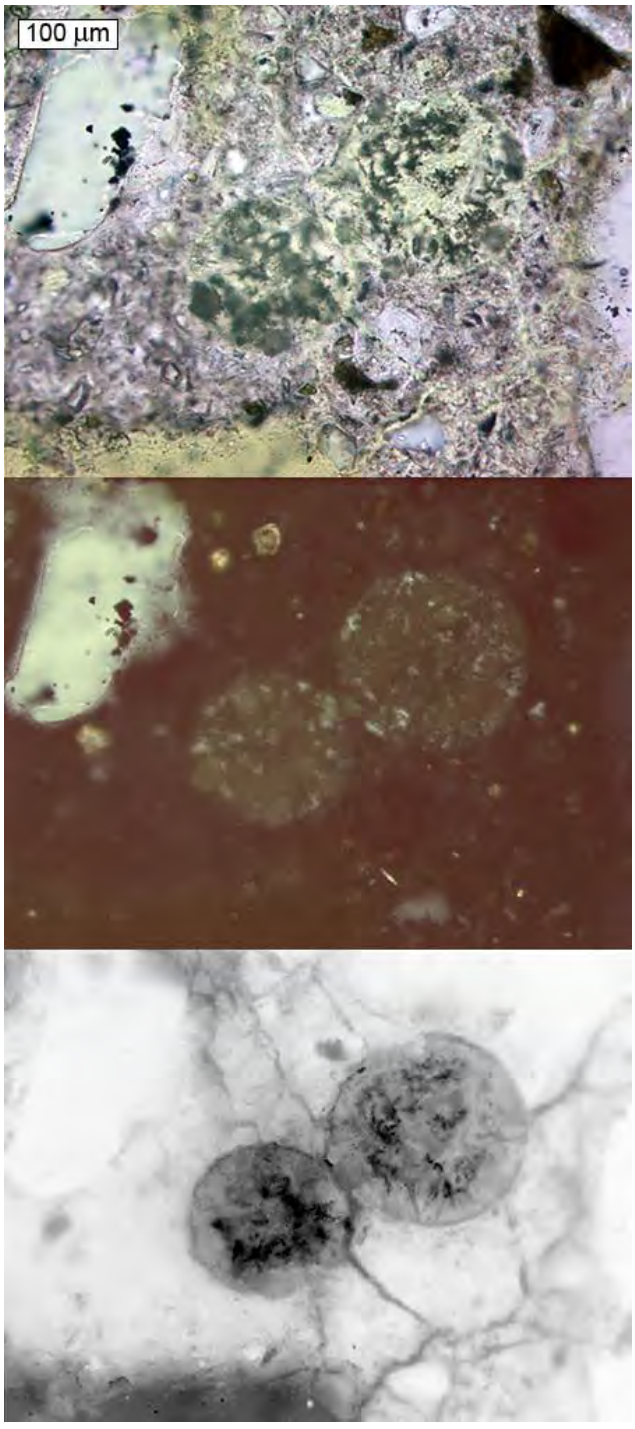

Figure A3.217. Secondary blocky calcium hydroxide crystals in air voids of 0.45 *w/cm* GGBFS concrete specimen exposed to MBAP. From top to bottom: transmitted light, crossed-polars, and epifluorescent mode images.

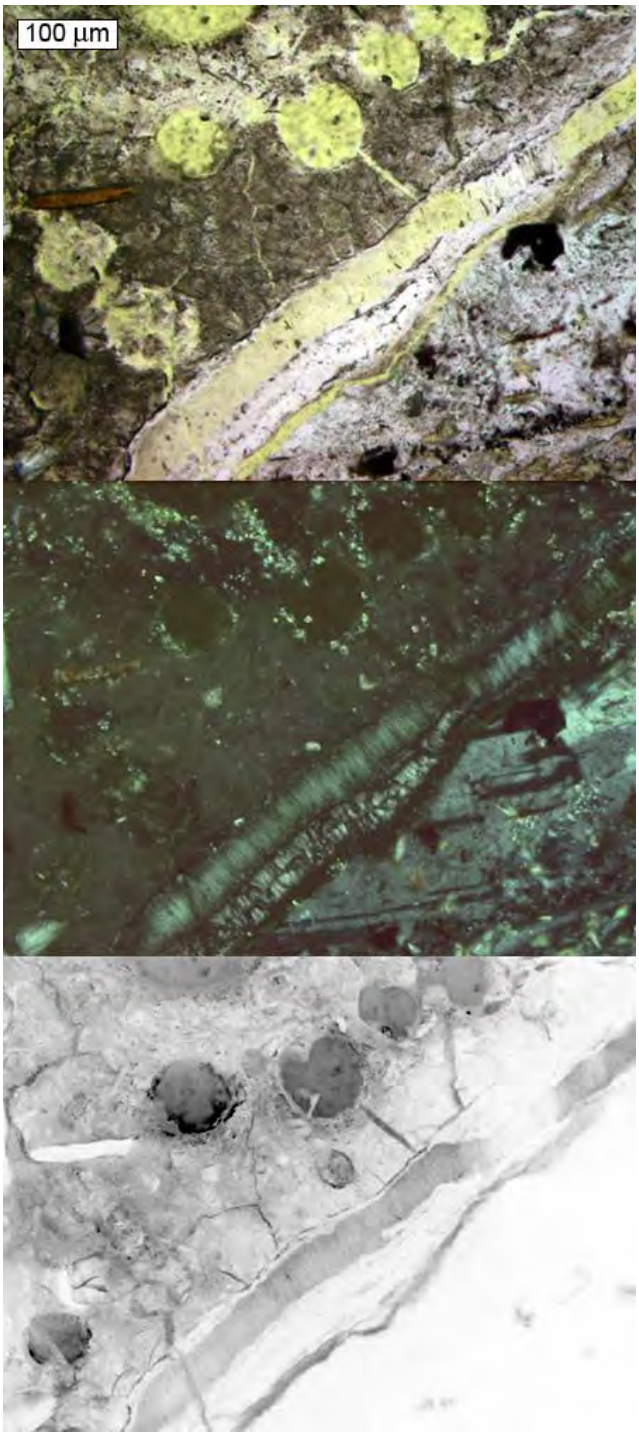

Figure A3.218. Fibrous crystals lining crack near surface of 0.45 *w/c* straight portland cement concrete specimen exposed to MBAP brine. From top to bottom: transmitted light, crossed-polars, and epifluorescent mode images.

A3.3.2.5. Scanning Electron Microscopy

The same thin sections prepared from the 0.45 *w/c* straight portland cement concrete specimens exposed to the high concentration brines and the limewater control for 500 days were examined with a scanning electron microscope (SEM). Figure 2.219 shows back-scattered electron (BSE) images from the same areas examined optically in Figure A3.184. Elemental maps were also collected, but only for the samples exposed to the $CaCl_2$, $MgCl_2$, and MBAP brines, and are shown in Figures 2.220 through 2.222.

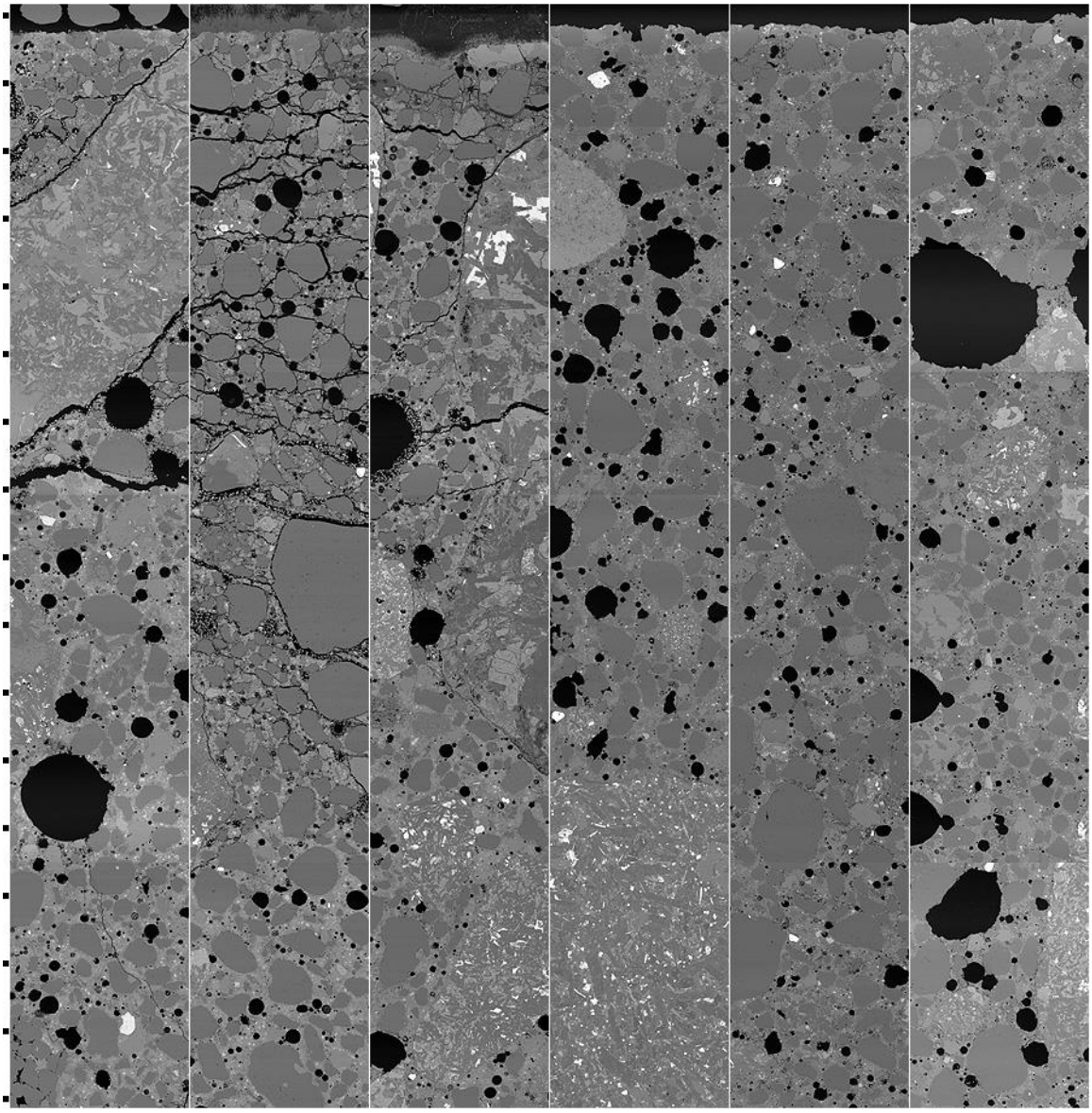

Figure A3.219. BSE images from 0.45 *w/c* concrete specimens exposed to high concentration brines and the limewater control after 500 days. From left to right, $CaCl_2$, $MgCl_2$, MBAP, NaCl, CMA, and limewater.

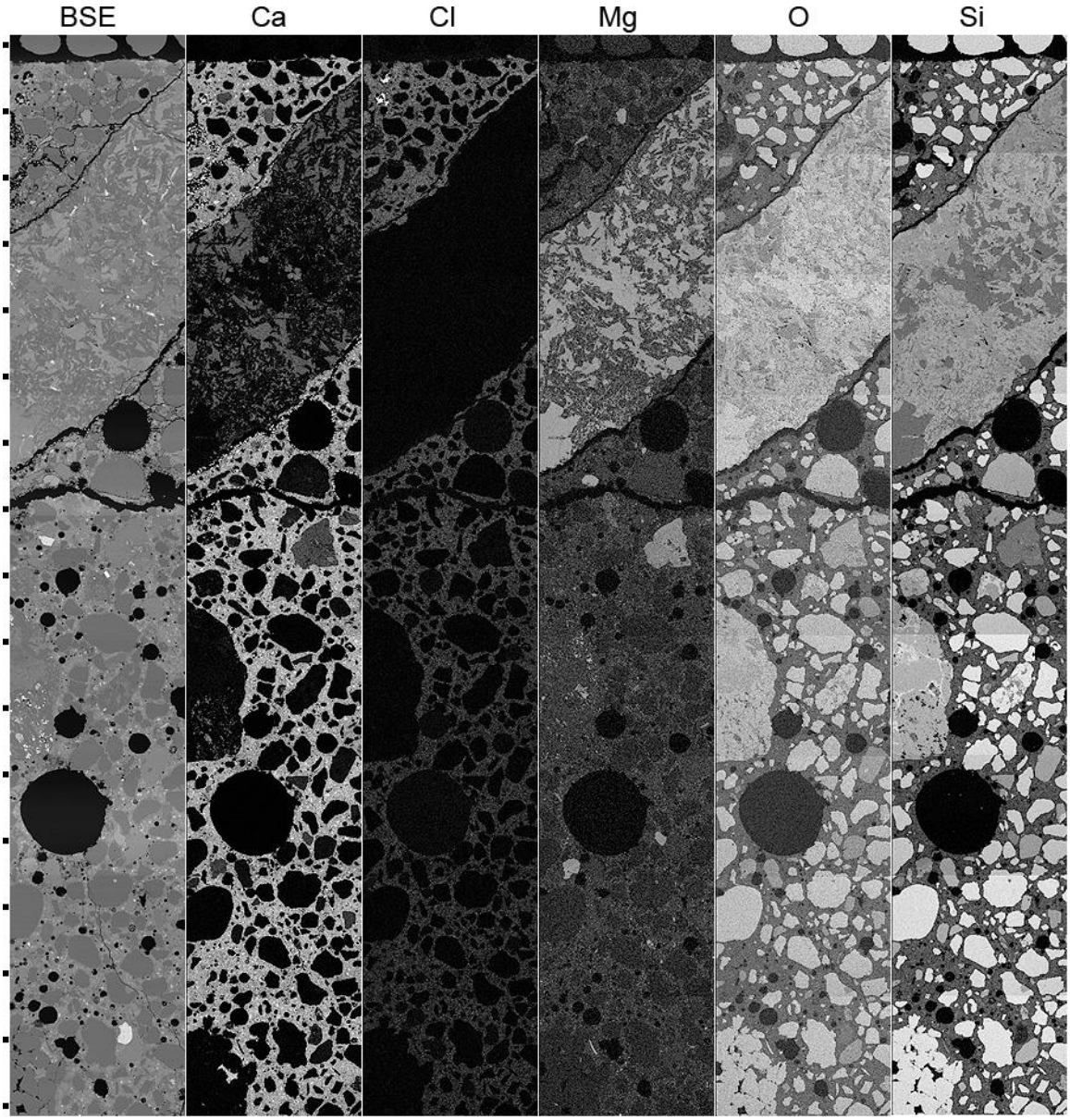

Figure A3.220. Elemental maps collected from 0.45 *w/c* concrete specimen immersed in $CaCl_2$ brine at 500 days. Brighter regions correspond to higher counts for characteristic elemental X-rays.

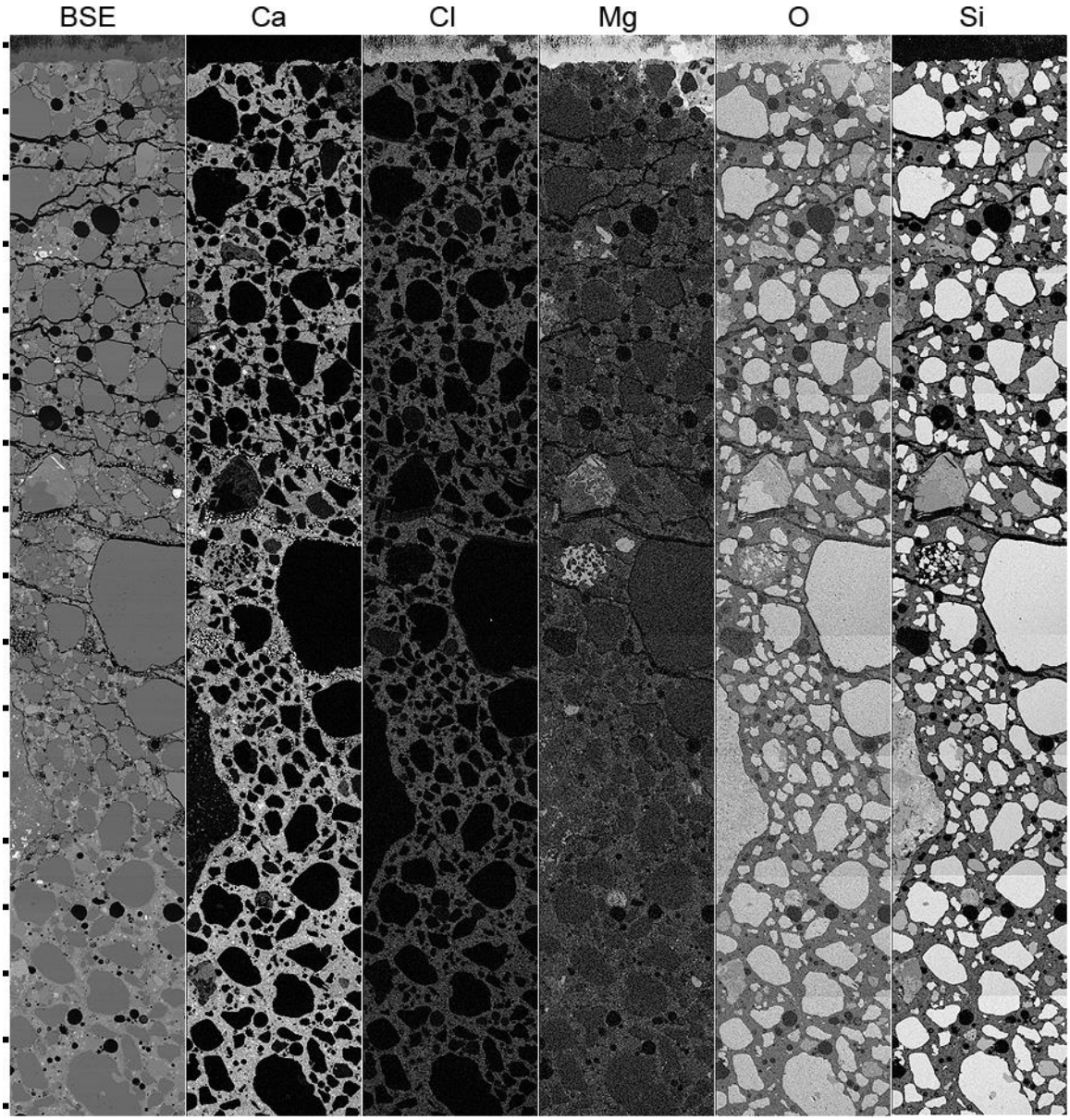

Figure A3.221. Elemental maps collected from 0.45 *w/c* concrete specimen immersed in $MgCl_2$ brine at 500 days. Brighter regions correspond to higher counts for characteristic elemental X-rays.

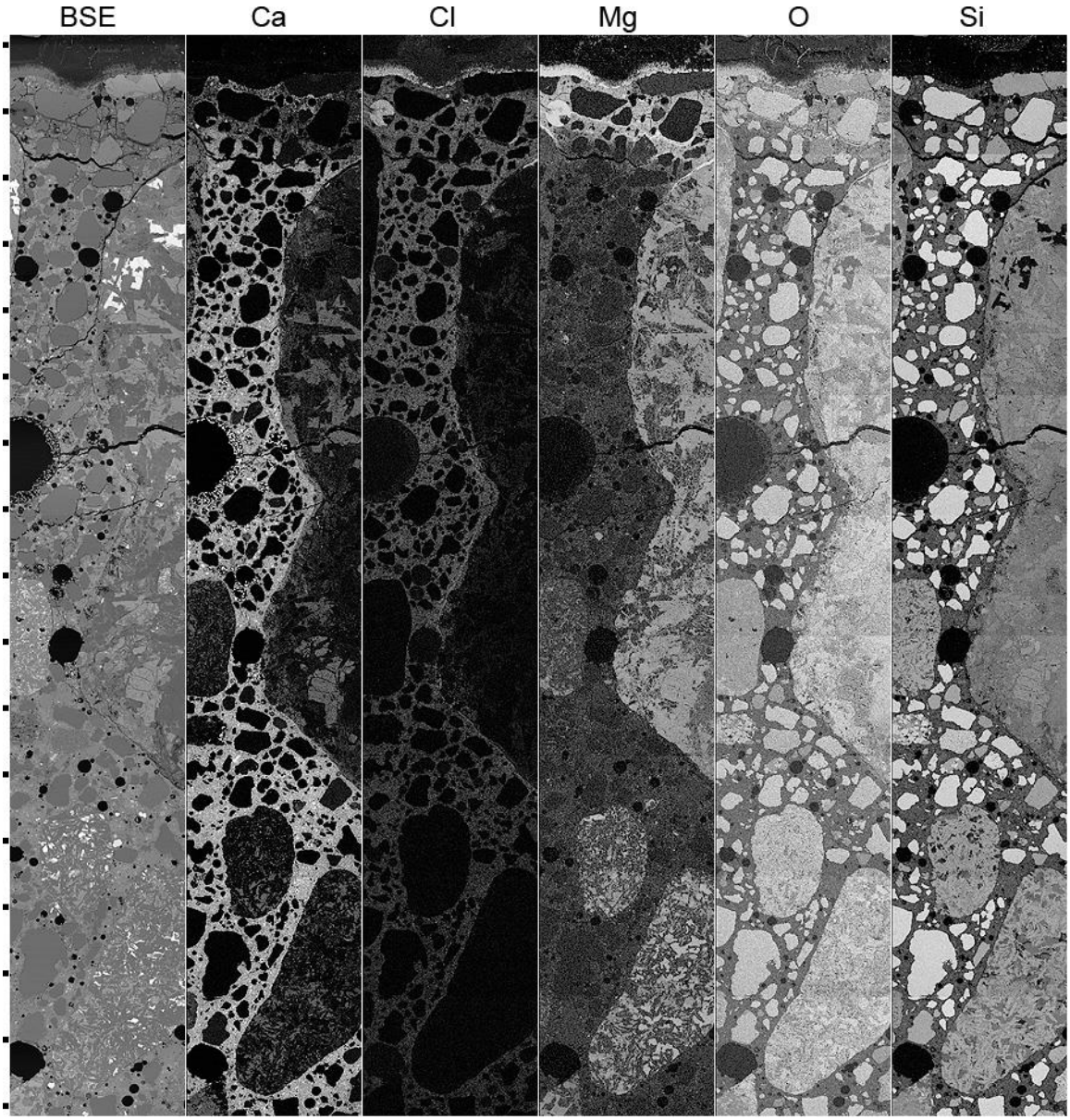

Figure A3.222. Elemental maps collected from 0.45 *w/c* concrete specimen immersed in MBAP brine at 500 days. Brighter regions correspond to higher counts for characteristic elemental X-rays.

All of the areas mapped show a chloride gradient with higher concentrations near the surface. All of the maps also show a slight calcium gradient, with higher concentrations in the cement paste at depth. Only the maps from $MgCl_2$ and MBAP immersed specimens show magnesium enrichment near the surface. Magnesium and chlorine concentrations are particularly high in the mineral precipitate crust at the surface. Energy dispersive spectroscopy (EDS) analyses were performed on the fibrous minerals near or at the surface of the specimens exposed to $MgCl_2$ and MBAP, and the results are summarized in Table A3.31. Figure A3.223 shows a BSE image of the multi-phase fibrous mineral crust, with compositions similar to magnesium chloride hydroxide hydrate and brucite, with possible Ca^{2+} substitution for Mg^{2+} and Cl^- substitution for OH^-.

Table A3.31. Typical EDS measurements from crystals in magnesium-enriched near-surface zone of specimens immersed in high concentration MBAP or $MgCl_2$ brines, compared to ideal mineral compositions for brucite and magnesium chloride hydroxide hydrate.

Element (Wt%)	Interior Fibrous Crystals	Exterior Fibrous Crystals	$Mg(OH)_2$	$Mg_3(OH)_5Cl•4H_2O$
H*	-	-	3.5	4.6
O*	-	-	54.9	54.5
C*	-	-	0.0	0.0
Na	0.2	0.2	0.0	0.0
Mg	38.5	28.8	41.7	27.5
Al	0.0	0.0	0.0	0.0
Si	0.2	0.1	0.0	0.0
P	0.1	0.0	0.0	0.0
S	0.0	0.1	0.0	0.0
Cl	1.6	13.4	0.0	13.4
K	0.0	0.0	0.0	0.0
Ca	0.9	0.0	0.0	0.0
Mn	0.0	0.0	0.0	0.0
Fe	0.1	0.0	0.0	0.0
Sum	41.6	42.6	100.0	100.0

* Not included in EDS analysis.

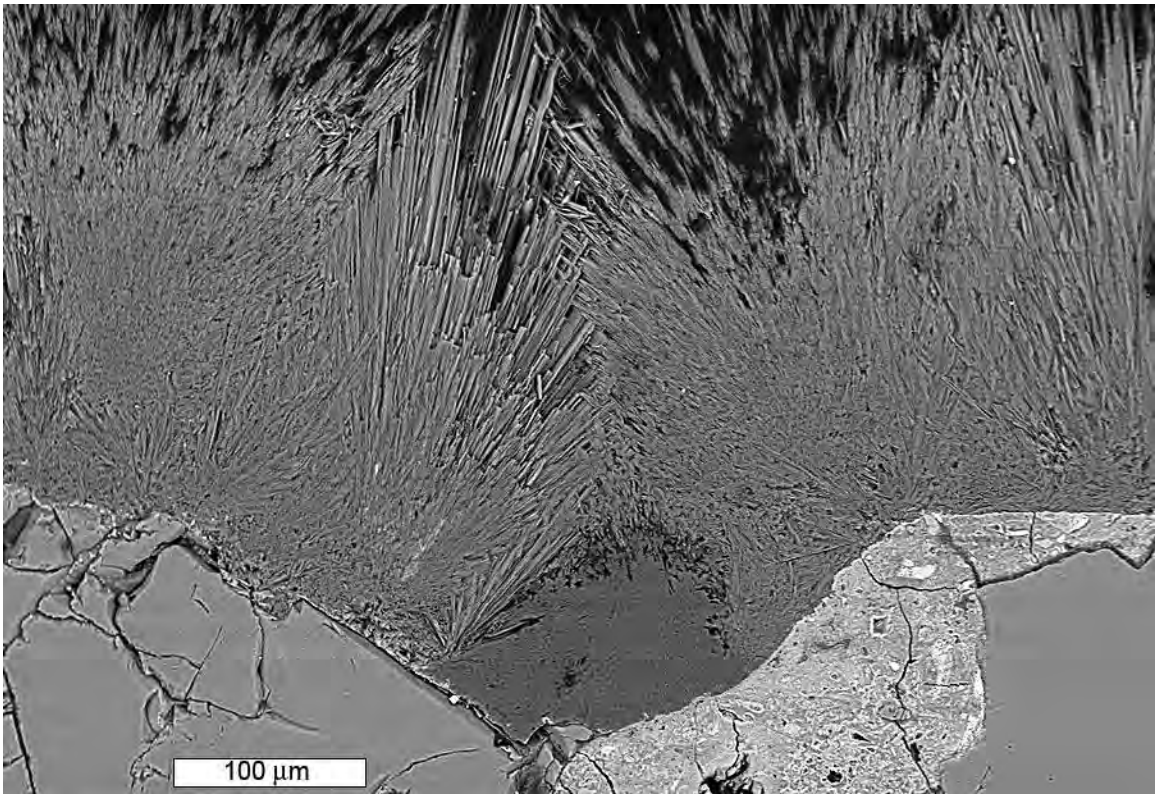

Figure A3.223. BSE image of magnesium chloride hydroxide hydrate (lighter) and brucite (darker) crystals at surface of 0.45 *w/c* concrete specimen exposed to $MgCl_2$ brine.

EDS analyses were also performed on the blocky secondary calcium hydroxide crystals observed by optical microscopy in all of the deteriorated specimens immersed in $CaCl_2$, $MgCl_2$, and MBAP brines. The results are summarized in Table A3.32. The small percentage of chlorine in the analyses may be due to minor Cl^- substitution for OH^- in the calcium hydroxide. A close examination of secondary deposits in the specimen immersed in $CaCl_2$ brine also revealed another bladed crystalline phase that had apparently replaced the blocky secondary crystals, but only near the surface. Figure 2.224 compares the blocky secondary calcium hydroxide crystals observed at depth to the bladed crystals near the surface. Table A3.33 shows the results of EDS analyses from the bladed crystals, which have a composition similar to calcium chloride hydroxide hydrate.

Table A3.32. Typical EDS measurements from blocky crystals in cracks and voids at depth in specimens immersed in high concentration $CaCl_2$, $MgCl_2$ and MBAP brines, compared to ideal mineral compositions for calcium hydroxide and calcite.

Element (Wt%)	Blocky Crystals	$Ca(OH)_2$	$CaCO_3$
H*	-	2.7	0.0
O*	-	43.2	48.0
C*	-	0.0	12.0
Na	0.0	0.0	0.0
Mg	0.0	0.0	0.0
Al	0.0	0.0	0.0
Si	0.0	0.0	0.0
P	0.1	0.0	0.0
S	0.0	0.0	0.0
Cl	3.4	0.0	0.0
K	0.1	0.0	0.0
Ca	50.9	54.1	40.0
Mn	0.0	0.0	0.0
Fe	0.0	0.0	0.0
Sum	54.5	100.0	100.0

* Not included in EDS analysis.

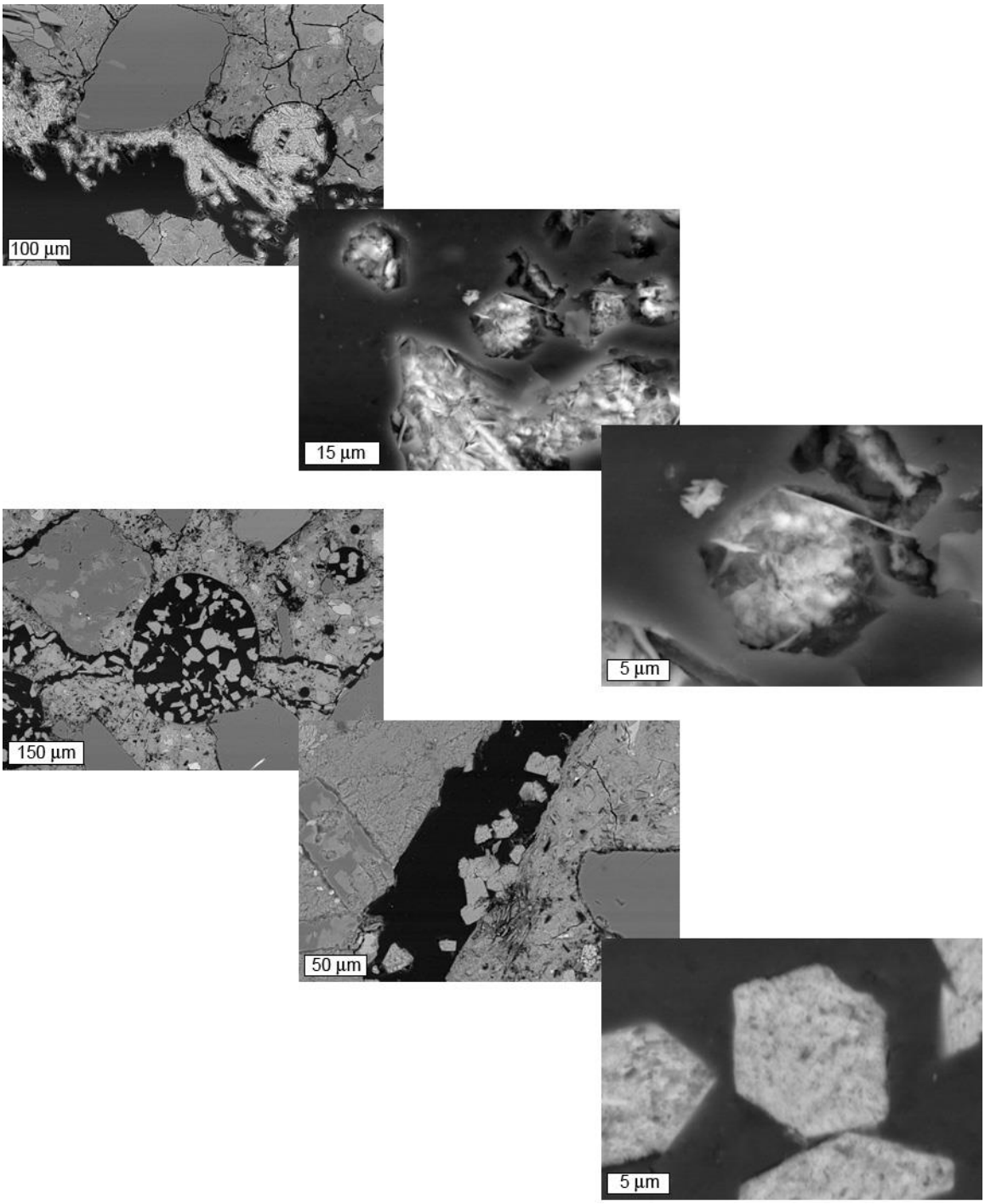

Figure A3.224. BSE images comparing bladed crystals observed near the top of the specimen exposed to $CaCl_2$ brine, (upper images) to secondary blocky calcium hydroxide crystals observed at depth (lower images).

Table A3.33. Typical EDS measurements from bladed crystals observed in cracks and voids in near-surface zone of specimen immersed in high concentration $CaCl_2$ brine, compared to ideal mineral composition for calcium chloride hydroxide hydrate.

Element (Wt%)	Bladed Crystals	$CaO•CaCl_2•2H_2O$
H*	-	1.8
O*	-	23.8
C*	-	0.0
Na	0.0	0.0
Mg	0.0	0.0
Al	0.0	0.0
Si	0.0	0.0
P	0.0	0.0
S	0.2	0.0
Cl	30.7	34.9
K	0.1	0.0
Ca	42.4	39.5
Mn	0.1	0.0
Fe	0.3	0.0
Sum	73.8	100.0

* Not included in EDS analysis.

A3.3.3 Results of Phase II Experiments Conducted at the University of Toronto

A3.3.3.1 ASTM C 666 Freeze Thaw Testing

The concrete prisms subjected to freeze-thaw testing showed behavior similar to the mortar samples tested in Phase I. That is, concrete prisms exposed to $MgCl_2$ and $CaCl_2$ expanded above 0.1%, which is considered by ASTM C 666 to represent failure. Figure A3.225 shows the length change of the specimens. While prisms exposed to NaCl did not expand more than 0.04% for 300 cycles, prisms exposed to $MgCl_2$ and $CaCl_2$ expanded considerably with 0.17 and 0.18% length change respectively. It was observed that the prisms subjected to $MgCl_2$ started to expand only after 150 cycles while those exposed to $CaCl_2$ expanded gradually from the start of the test. One deviation from the normal ASTM C 666 procedure was that specimens expanding more than 0.1% were not removed from the freeze-thaw chamber until all specimens were subjected to 300 cycles. This approach provided

deteriorated material for X-ray diffraction analysis to investigate the formation of new phases associated with this expansion. Note that the concentration of the exposure solution did not allow freezing during the test, eliminating physical attack as the sole mechanism of deterioration.

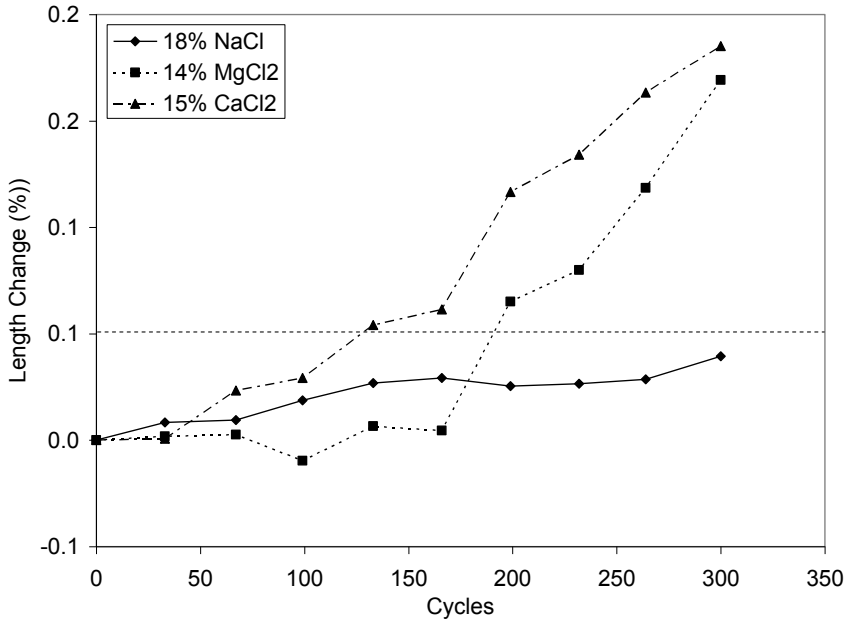

Figure A3.225. Length change of concrete prisms exposed to deicers under freezing and thawing cycles.

The determination of mass change during the ASTM C 666 test is not a requirement. However, Phase I results suggested that any formation of new phases seems to be accompanied with considerable changes in mass and therefore it was monitored. As seen in Figure A3.226, the specimens exposed to $MgCl_2$ gained considerable mass during the test. Those exposed to $CaCl_2$ had the opposite behavior with a recorded loss of mass. These two opposite reactions were evident after 100 cycles. The specimens exposed to NaCl showed negligible expansion even after 300 cycles. Although the observed length and mass change for the $MgCl_2$ and $CaCl_2$ specimens suggested that the minimum relative dynamic modulus of elasticity (i.e. 60% of the initial value) should have been reached after 100 cycles, this was not the case. Only after 250 cycles did the modulus drop below the minimum value for continuing the test. Figure A3.227 illustrates the gradual loss of the dynamic modulus of elasticity for those samples exposed to $MgCl_2$ and $CaCl_2$. For NaCl, no detrimental effect on the modulus was found even after 300 cycles of freezing and thawing.

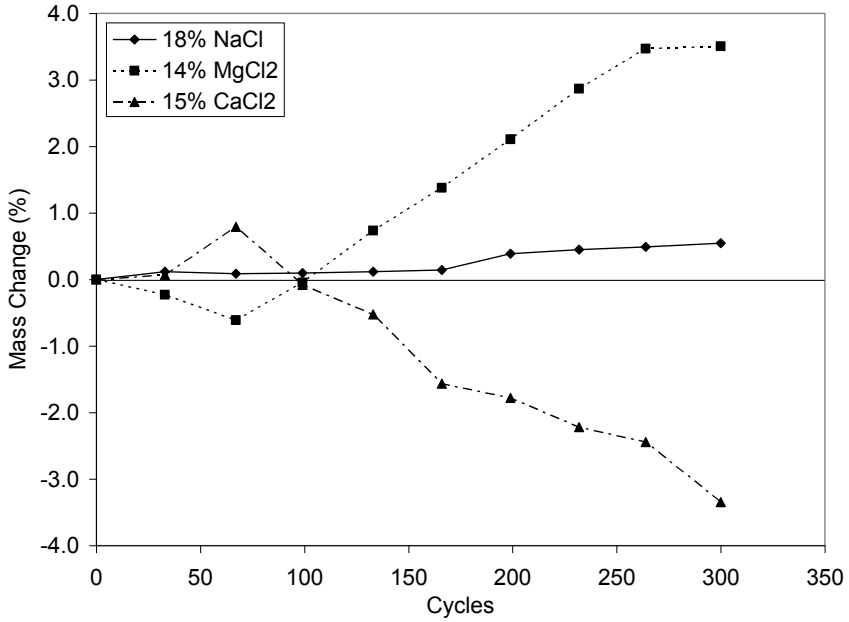

Figure A3.226. Mass change of concrete prisms exposed to deicers under freezing and thawing cycles.

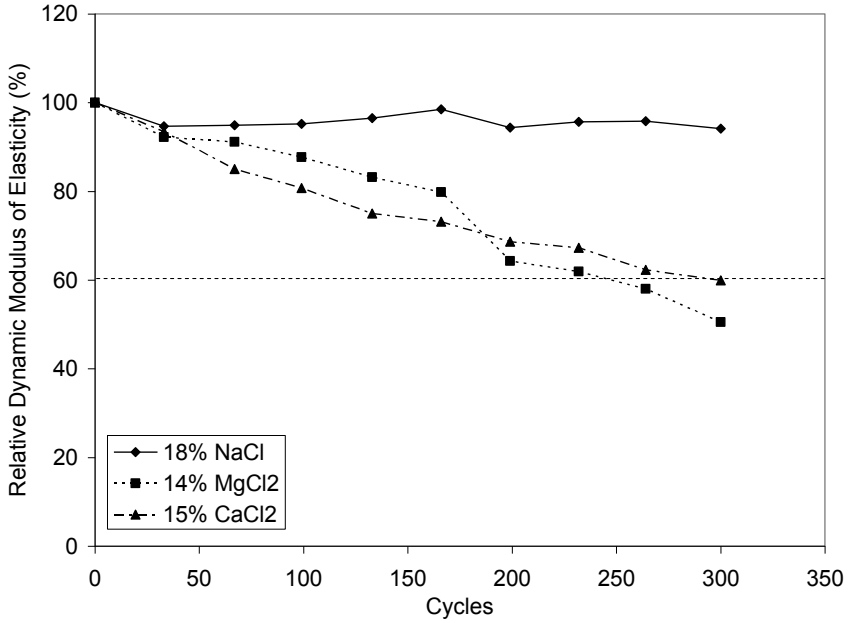

Figure A3.227. Relative dynamic modulus of elasticity of concrete prisms exposed to deicers under freezing and thawing cycles.

After determining the durability factor, it is clear that $MgCl_2$ and $CaCl_2$ solutions reduce the concrete's resistance to freezing and thawing when compared with NaCl as observed in Figure A3.228. The durability factors of 60 for $CaCl_2$ and 51 for $MgCl_2$ show the negative impact of these deicers on the resistance of concrete to freezing and thawing. Note that although there is no universally accepted limit for the durability factor, 80 is typically accepted as the threshold between durable and non-durable concrete.

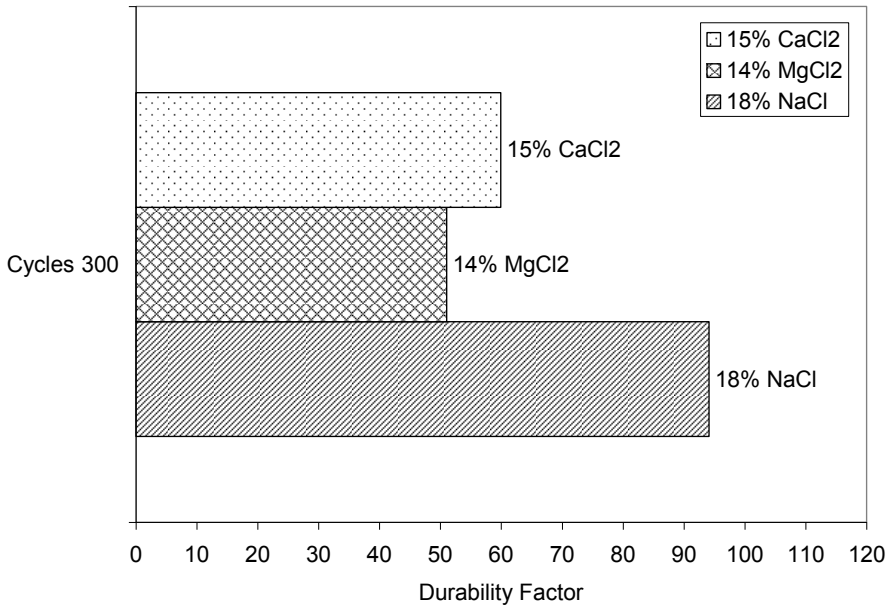

Figure A3.228. Durability factor of concrete prisms exposed to deicers under freezing and thawing cycles.

Figures A3.229 and A3.230 show photographs of the concrete prism specimens exposed to $CaCl_2$ and $MgCl_2$ and used for determining the resistance to freeze-thaw action. Both deicers caused the prisms to expand and crack along the edges but it was observed that in addition to this, the prisms exposed to $MgCl_2$ precipitated a white gel compound that started to fill the cracks. This could explain why the prisms exposed to $CaCl_2$ loss mass while those exposed to $MgCl_2$ gained mass even though both seem to undergo a similar deterioration process. The precipitation of this gel compound, identified as magnesium oxychloride, seemed to be associated with greater damage in the concrete prism as shown by the reduced durability factor for samples exposed to $MgCl_2$, as compared to the durability factor for specimens exposed to $CaCl_2$.

X-ray diffraction analysis of concrete samples taken from the edges of the concrete prisms again confirmed the formation of calcium oxychloride (Figure A3.231) and magnesium oxychloride (Figure A3.232) as the phases associated with concrete prisms deteriorating under the chemical attack of $CaCl_2$ and $MgCl_2$.

Figure A3.229. Photographs of concrete prisms subjected to 133 freezing and thawing cycles in 15% $CaCl_2$ solution.

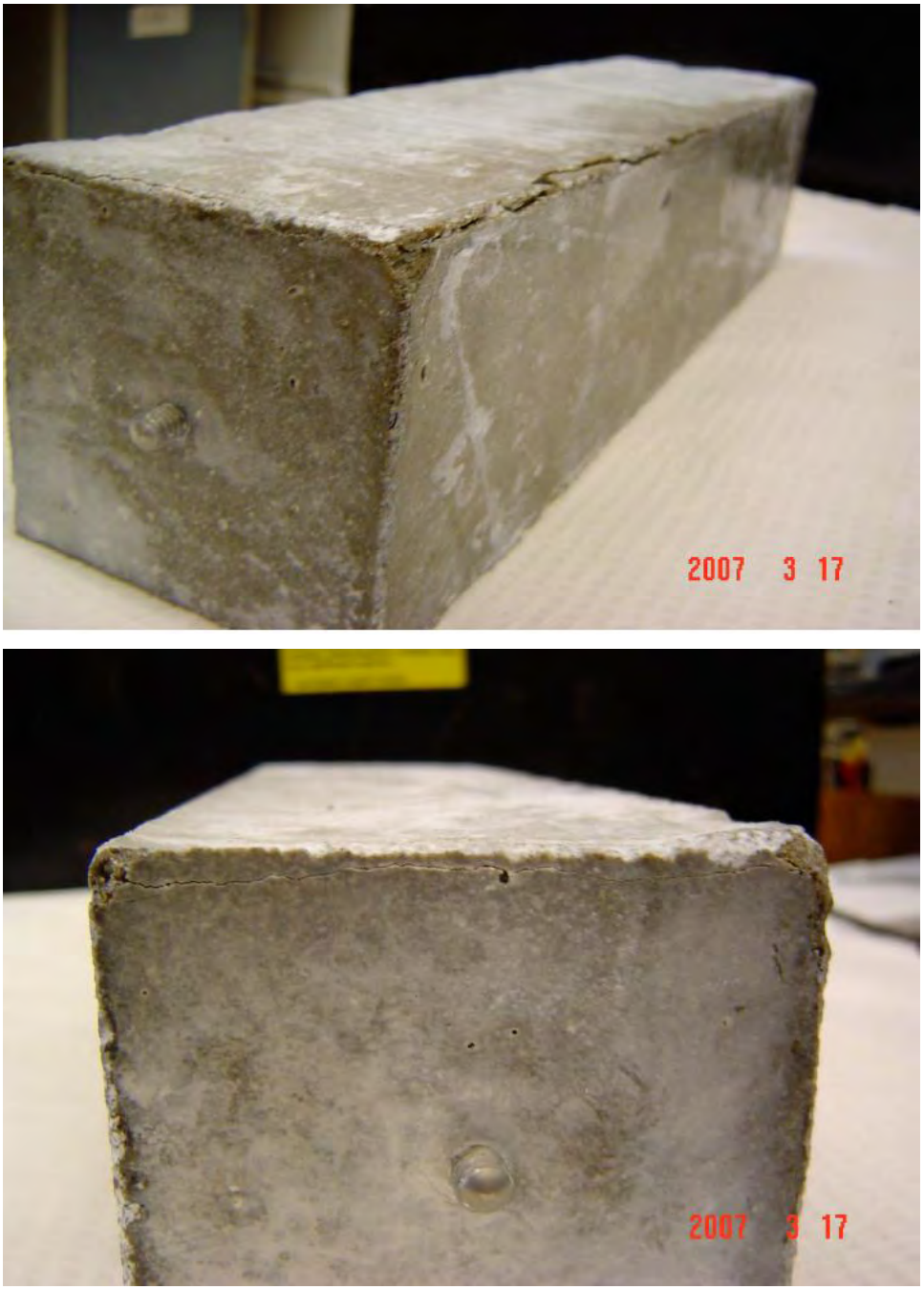

Figure A3.230. Photographs of concrete prisms subjected to 133 freezing and thawing cycles in 14% $MgCl_2$ solution.

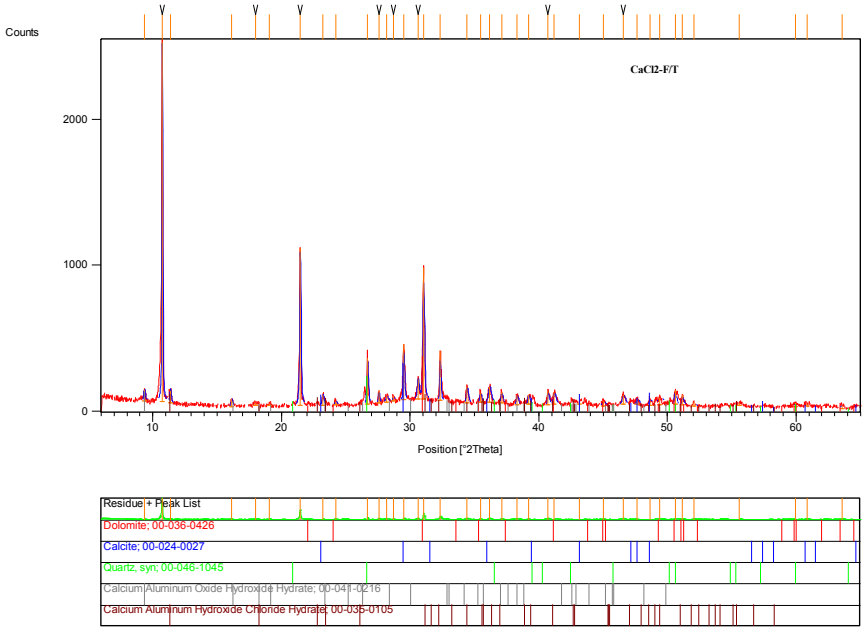

Figure A3.231. XRD diffractogram of concrete samples exposed to freezing and thawing cycles in the presence of 15% $CaCl_2$ for 300 cycles.

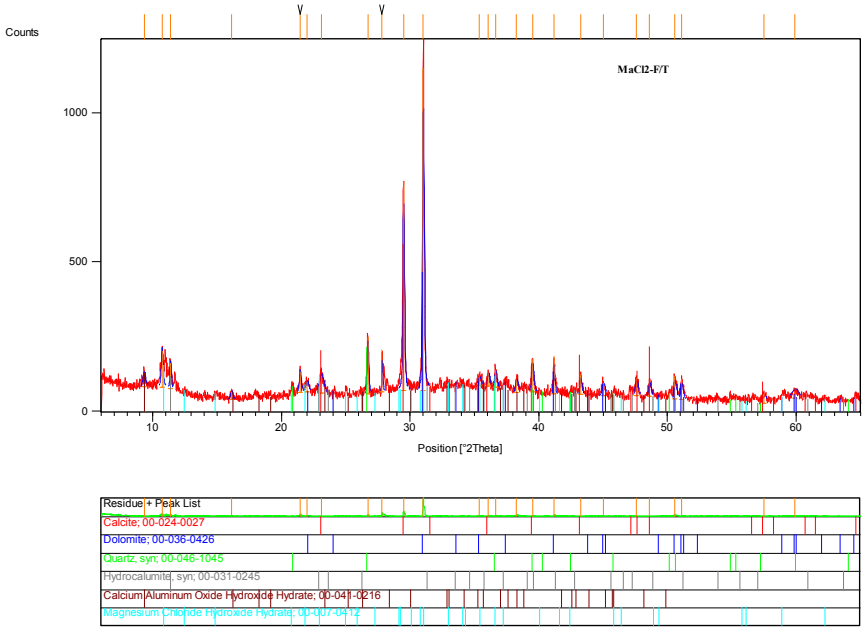

Figure A3.232. XRD diffractogram of concrete samples exposed to freezing and thawing cycles in the presence of 14% $MgCl_2$ for 300 cycles.

A3.3.3.2 Scaling Resistance

It was observed that after exposing concrete slabs to $CaCl_2$ solutions, the chemical interaction of this deicer with the concrete surface diminished the concrete's ability to properly withstand environmental conditions involving application of deicers during winter. After a year of ponding the surface of the slabs with 22% $CaCl_2$, the appearance of the surface did not suggest any problems and no signs of deterioration were observed. Once the slabs were subjected to freezing and thawing cycles in the presence of 4% $CaCl_2$, the surface started to scale gradually up to 50 cycles of exposure. At 50 cycles it was decided to continue the test as an unusual scaling pattern was developing on the surface with areas scaling deeper below the surface exposing the aggregate in localized areas of the slab. After 50 cycles, the amount of scaled material increased dramatically causing the surface to expose all the coarse aggregate and paste-aggregate debonding was evident. The test was discontinued once the scaling progressed so deep into the concrete that the solution could not be kept in place due to leakage down below the Styrofoam dike.

Parallel tests were run on slabs that were exposed to highly concentrated solutions of NaCl (23% by mass) and then tested with 3% NaCl solution. Those slabs did not show any sign of scaling (e.g. their visual rating was only 1 compared to 5 for specimens exposed to 22% $CaCl_2$ before the start of the salt scaling test.) Figure A3.233 compares the salt scaling resistance of slabs that were preconditioned by exposing them to 22% $CaCl_2$ before the start of the test, and those preconditioned in 23% NaCl until the start of the salt scaling test.

Figures A3.234, A3.235 and A3.236 show photographs of the concrete surface of slabs tested under the above conditions at different cycles, illustrating the unusual scaling of those preconditioned with 22% $CaCl_2$ and the excellent state of the slabs that were pretreated with 23% NaCl before starting the salt scaling test.

X-ray diffraction analysis was performed on concrete slabs subjected to the same pretreatment conditions, but kept for analysis instead of being tested for salt scaling resistance. The surface of the slab pretreated with 23% NaCl did not show any formation of new phases besides some Friedel's salt (Figure A3.237) but those slabs exposed to 22% $CaCl_2$ showed the distinctive peaks of calcium oxychloride in addition to Friedel's salt (Figure A3.238).

Those slabs pretreated with $MgCl_2$ and tested for salt scaling resistance did not scale and their visual rating and behavior was similar to those exposed to NaCl. No new phases were formed that were detectable by X-ray diffraction.

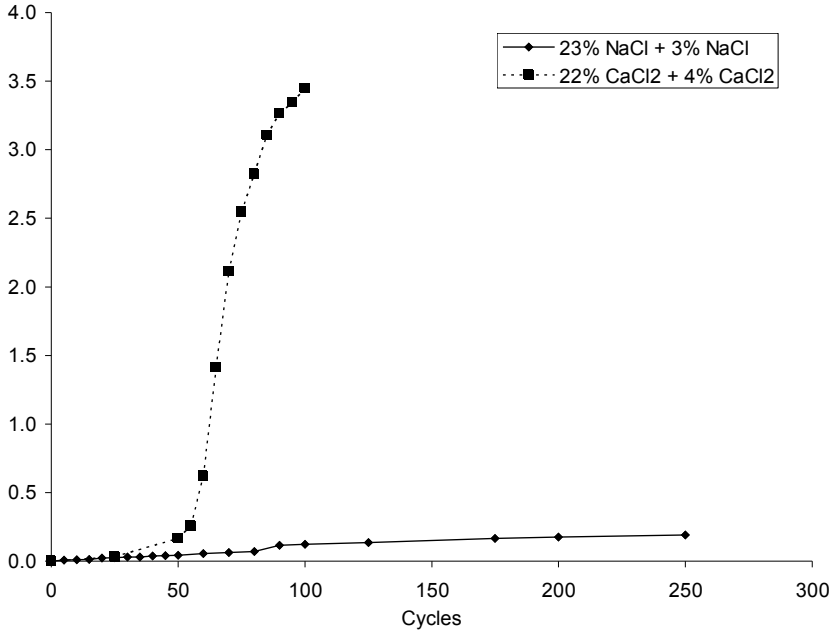

Figure A3.233. Scaled material of concrete slabs exposed to 22% $CaCl_2$ in comparison with those exposed to 23% NaCl before the start of the salt scaling test.

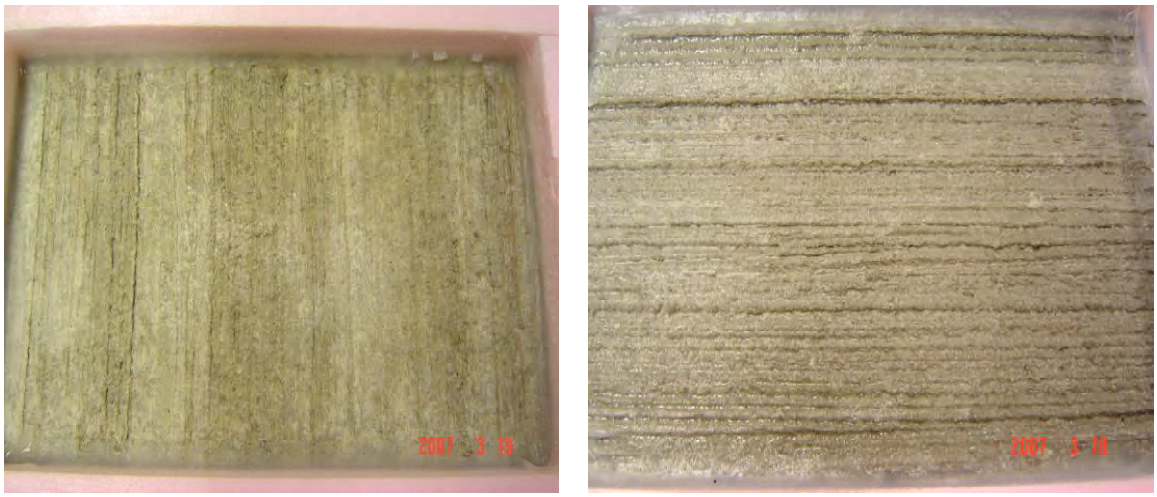

(a) (b)

Figure A3.234. Photographs of concrete surfaces at cycle 0 (a) pretreated with 23% NaCl and tested with 3% NaCl and (b) pretreated with 22% $CaCl_2$ and tested with 4% $CaCl_2$.

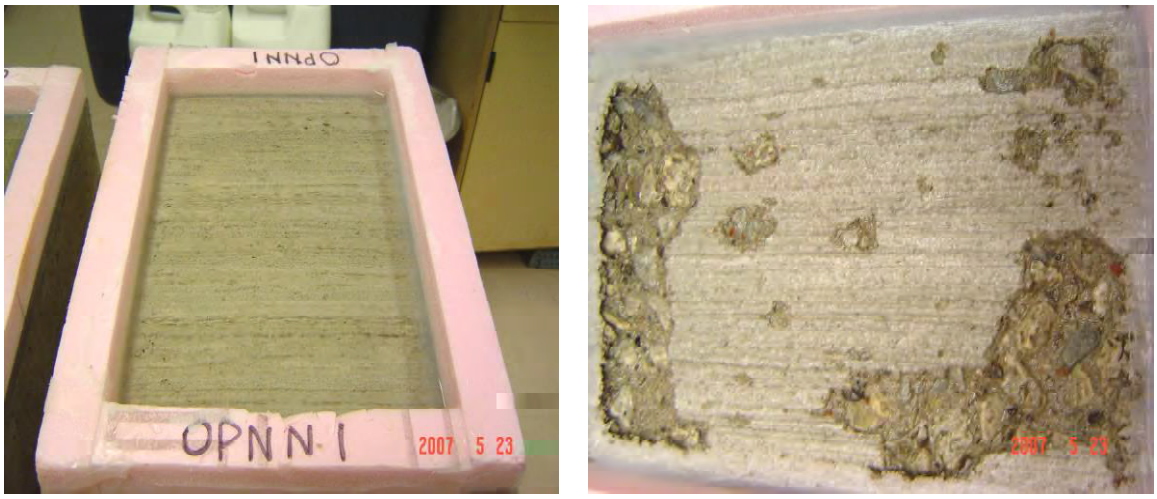

(a) (b)

Figure A3.235. Photographs of concrete surfaces at cycle 50 (a) pretreated with 23% NaCl and tested with 3% NaCl and (b) pretreated with 22% $CaCl_2$ and tested with 4% $CaCl_2$.

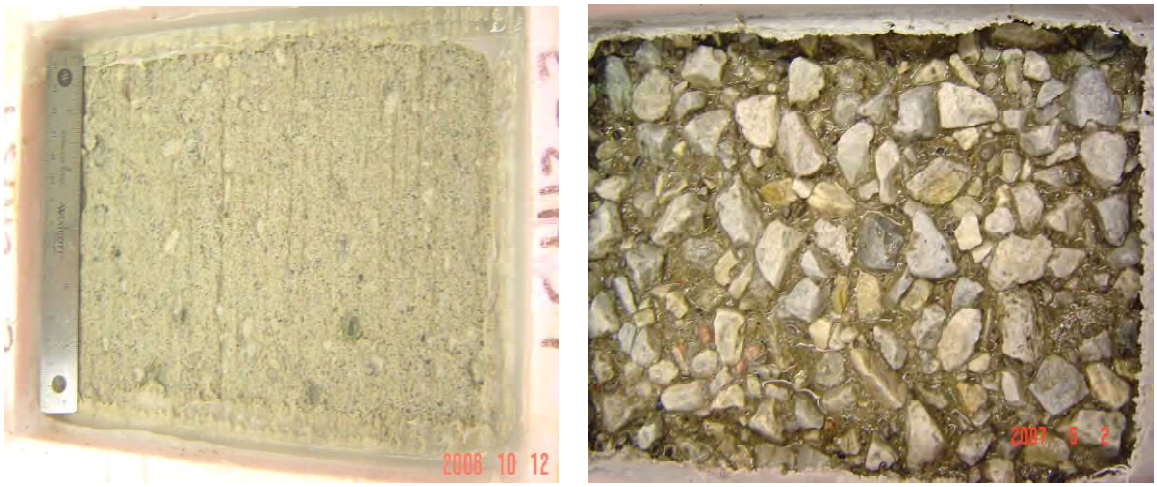

(a) (b)

Figure A3.236. Photographs of concrete surfaces at cycle 100 (a) pretreated with 23% NaCl and tested with 3% NaCl and (b) pretreated with 22% $CaCl_2$ and tested with 4% $CaCl_2$.

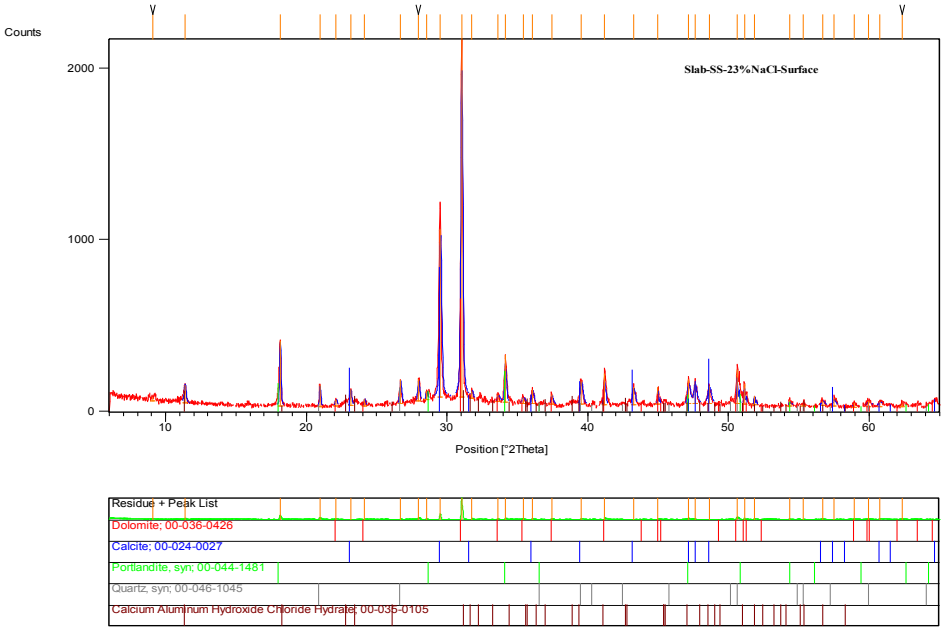

Figure A3.237. XRD diffractogram of concrete slabs ponded with 23% NaCl for 1 year at 41 ºF [5 ºC] and later used for determining their salt scaling resistance.

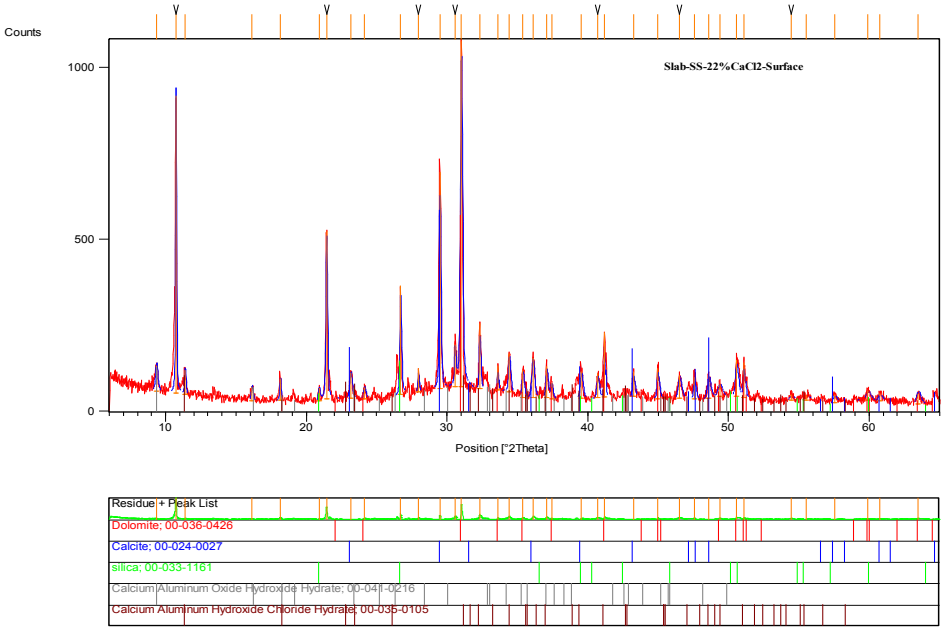

Figure A3.238. XRD diffractogram of concrete slabs ponded with 22% $CaCl_2$ for 1 year at 41 ºF [5 ºC] and later used for determining their salt scaling resistance.